

UNCLASSIFIED

AD NUMBER

ADB060927

LIMITATION CHANGES

TO:

Approved for public release; distribution is unlimited.

FROM:

Distribution authorized to U.S. Gov't. agencies only; Test and Evaluation; MAY 1980. Other requests shall be referred to Air Force Rocket Propulsion Agency, STINFO/XOJ, Edwards AFB, CA 93523.

AUTHORITY

AL/AFSC ltr, 23 Jan 1991

THIS PAGE IS UNCLASSIFIED

Report AFRPL-TR-81-26.

**LIGHTWEIGHT ADVANCED POST-BOOST VEHICLE
PROPULSION FEED SYSTEM DEVELOPMENT**

ROCKETDYNE DIVISION
ROCKWELL INTERNATIONAL
6633 CANOGA AVENUE
CANOGA PARK, CALIFORNIA 91304

August 1981

Final Report, September 1977-April 1980

Distribution limited to U.S. Government
agencies only, Test and Evaluation,
May 1980. Other requests for this docu-
ment must be referred to AFRPL (STINFO)/XOJ,
Edwards AFB, California 93523.

Prepared for:

AIR FORCE ROCKET PROPULSION LABORATORY
DIRECTOR OF SCIENCE AND TECHNOLOGY
AIR FORCE SYSTEMS COMMAND
EDWARDS AFB, CALIFORNIA 93523

2

LEVEL II

**DTIC
ELECTE
NOV 17 1981**

D

AD B060927

FILE COPY

NOTICES

When U.S. Government drawings, specifications, or other data are used for any purpose other than a definitely related Government procurement operation, the Government thereby incurs no responsibility nor any obligation whatsoever, and the fact that the Government may have formulated, furnished, or in any way supplied the said drawings, specifications, or other data, is not to be regarded by implication or otherwise, or in any manner licensing the holder or any other person or corporation, or conveying any rights or permission to manufacture, use, or sell any patented invention that may in any way be related thereto.

FOREWORD

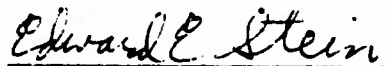
This report documents the results of Phase I, Feed System Analyses and Design and Phase II, Component and Subsystem Fabrication and Test of the Lightweight Advanced Post-Boost Vehicle Propulsion Feed System Program. The work was performed by Rocketdyne Division of Rockwell International, 6633 Canoga Avenue, Canoga Park, CA 91304, under Contract F04611-77-C-0068, Job Order 634100P1, with the Air Force Rocket Propulsion Laboratory, Edwards AFB, CA 93523. The contract was initiated in September 1977. The Air Force Rocket Propulsion Laboratory's Project Manager is Roy Silver. R. D. Paster was Rocketdyne's Program Manager, and Bill Stanley was the Project Engineer.

This technical report is approved for release and distribution in accordance with the distribution statement on the cover and on the DD Form 1473.


ROY A. SILVER
Project Manager


BERNARD R. BORNHORST, Chief
Strategic Systems Section

FOR THE COMMANDER


EDWARD E. STEIN
Deputy Chief
Liquid Rocket Division

SUBJECT TO EXPORT CONTROL LAWS

This document contains information for manufacturing or using munitions of war. Export of the information contained herein, or release to foreign nationals within the United States, without first obtaining an export license, is a violation of the International Traffic in Arms Regulations. Such violation is subject to a penalty of up to 2 years imprisonment and a fine of \$100,000 under U.S.C. 2778.

UNCLASSIFIED

SECURITY CLASSIFICATION OF THIS PAGE (When Data Entered)

19 REPORT DOCUMENTATION PAGE		READ INSTRUCTIONS BEFORE COMPLETING FORM
1. REPORT NUMBER (18) AFRPL-TR-81-26	2. GOVT ACCESSION NO. AD-B060	3. RECIPIENT'S CATALOG NUMBER 9272
4. TITLE (and Subtitle) LIGHTWEIGHT ADVANCED POST-BOOST VEHICLE PROPULSION FEED SYSTEM DEVELOPMENT		5. TYPE OF REPORT & PERIOD COVERED (9) Final Rep Sep 77 - Apr 80
7. AUTHOR(s)		PERFORMING ORG. REPORT NUMBER (14) RI/RD81-113
9. PERFORMING ORGANIZATION NAME AND ADDRESS Rockwell International Rocketdyne Division 6633 Canoga Ave. - Canoga Park, CA 91304		8. CONTRACT OR GRANT NUMBER(s) (15) F4611-77-C-0968
11. CONTROLLING OFFICE NAME AND ADDRESS Air Force Rocket Propulsion Laboratory/LKCC Edwards Air Force Base, CA 93523		10. PROGRAM ELEMENT, PROJECT, TASK AREA & WORK UNIT NUMBERS JON 634100P1 (17) 001
14. MONITORING AGENCY NAME & ADDRESS (if different from Controlling Office)		12. REPORT DATE (11) August 1981
		13. NUMBER OF PAGES 443 (15) 444
		18. SECURITY CLASS. (of this report) Unclassified
		15a. DECLASSIFICATION/DOWNGRADING SCHEDULE
16. DISTRIBUTION STATEMENT (of this Report) Distribution limited to U.S. Government agencies only, Test and Evaluation, May 1980. Other requests for this document must be referred to AFRPL(STINFO)/ XOJ, Edwards AFB, CA 93523.		
17. DISTRIBUTION STATEMENT (of the abstract entered in Block 20, if different from Report) Approved for Public Release; Distribution Unlimited		
18. SUPPLEMENTARY NOTES		
19. KEY WORDS (Continue on reverse side if necessary and identify by block number) Post-Boost Propulsion Systems, Propellant Feed Systems, Propellant Tanks, Expulsion Bladders, Ellipsoids, Composite Materials, Pressurization, Hot Gases, Catalysis, Pressure Regulators, Electronic Equipment, Design, Analyses, Fabrication, Test and Evaluation, Random Vibration, Structural Response		
20. ABSTRACT (Continue on reverse side if necessary and identify by block number) An advanced development contract was conducted in support of the Air Force Ballistic Missile program to demonstrate a lightweight liquid-bipropellant feed system for application in an advanced post-boost propulsion system. The feed system is composed of composite-wrapped aluminum propellant storage tanks and a catalytically reacted warm-gas pressurization subsystem. Tank capability was demonstrated in workhorse expulsion characterization tests (expulsion efficiency of 98.1 to 99.3 percent) and fabrication and		

DD FORM 1 JAN 73 1473

EDITION OF 1 NOV 65 IS OBSOLETE

UNCLASSIFIED

SECURITY CLASSIFICATION OF THIS PAGE (When Data Entered)

390299

UNCLASSIFIED

SECURITY CLASSIFICATION OF THIS PAGE(When Data Entered)

20. Abstract (Continued)

expulsion of a flight weight propulsion storage assembly (PSA). The latter was accomplished with a representative pressurization subsystem consisting of a composite-wrapped aluminum pressurant tank with Tridyne pressurant (helium, oxygen, and hydrogen), an electronically controlled pressure regulator, a catalytic reactor, and valves. The reactor supplied warm-gas pressurant to the PSAs at up to 1158 F. The delivered propellant pressure was controlled to 300 \pm 1.4 psia during pulsed propellant flow by continuous modulation of the pressurant flow.

The feed system was sized to deliver 1400 pounds of N₂O₄ and MMH with each PSA weighing 59 pounds, and the PS weighing 41 pounds. The resultant weight savings was 27 to 35 percent when compared to more conventional systems.

Accession For	
NTIS GRA&I	<input type="checkbox"/>
DTIC TAB	<input checked="" type="checkbox"/>
Unannounced	<input type="checkbox"/>
Justification	
By	
Distribution/	
Availability Codes	
Dist	Avail and/or Special
B	

DTIC
ELECTE
NOV 17 1981
S D D

UNCLASSIFIED

SECURITY CLASSIFICATION OF THIS PAGE(When Data Entered)

SUMMARY

An advanced development program was conducted in support of the Air Force Ballistic Missile Program to analyze, design, fabricate, and test a lightweight feed system for application in an advanced postboost propulsion system. The objective of this program was to demonstrate, through component and system-level testing, an advanced liquid-bipropellant feed system that was significantly lighter weight than those developed during the earlier feed system technology programs, while maintaining the emphasis placed on high reliability and low life cycle cost. The demonstration tests included propellant expulsion performance and structural dynamic response.

The flightweight and prototype (test) designs of the propellant storage assemblies (PSAs) and pressurization subsystem (PS) are presented with their operating characteristics. The feed system was sized to deliver 1400 pounds of N_2O_4 and MMH at equal volumetric flowrates. Each PSA is comprised of a composite-wrapped aluminum tank, a reversing aluminum diaphragm for positive expulsion, pressurant inlet and propellant outlet isolation valves, a fill and drain valve, a vacuum service valve, and a vacuum gage tube leak detector. The tank is oblate with a contour that deviates slightly from an ellipse to achieve stresses compatible with the nonisotropic characteristics of the composite wrap. The contour also enhances uniform reversal of the diaphragm and provides an increasing margin of diaphragm stability during the expulsion cycle, compared to a constant-radius contour. The diaphragm has step-thickness changes to preclude local folds from propagating along the diaphragm surface to the major axis and to minimize center-of-gravity excursions.

Diaphragm design requirements were defined, manufacturing processes were developed, and repeatable expulsion performance was verified experimentally in a flanged, plastic workhorse tank. Eight diaphragms were expelled at low pressure (25 psig) with ambient temperature gas, including two that were preceded by acceleration to 15 g's while in a pressurized, partially reversed condition. There were no tight folds or cracks resulting from normal diaphragm operating conditions. The expulsion efficiency for four tests with

the selected design configuration was 98.1 to 98.2 percent at a diaphragm ΔP of 25 psi with the tank both horizontal and vertical. Up to 90 percent expelled, the ΔP was less than 4 psi. The maximum CG displacement from the polar (expulsion) axis was 1.0 inches for both tests with the polar axis vertical and 1.9 inches for both tests with the axis horizontal.

Three diaphragms were expelled and one was exposed to structural dynamic testing in a flanged, metal workhorse tank. The expulsion efficiency attained with the plastic tank was verified at design pressure (300 psia) with warm (up to 1192 F) gas pressurant. Both tests were 99.3 percent at a ΔP of 50 to 54 psi. The effectiveness of the mechanical design of the pressurant inlet section of the tank in thermally isolating the tank shell was demonstrated during pulsed and continuous expulsion duty cycles.

Unpressurized ground random vibration, and pressurized flight shock and random vibration tests were conducted with the fourth diaphragm in the metal workhorse tank. The diaphragm survived the first two environments, but three fatigue cracks developed during pressurized flight random vibration. Two axes were tested simultaneous with the tank mounted at 45 degrees relative to the shaker motion. Although diaphragm fatigue life is a problem, its magnitude is unknown for four reasons. First, the vibration environments were derived from MX requirements, but they were applied as inputs (at the fixture) rather than responses (on the tank), which increased the test levels. Since the diaphragm in the flightweight tank was not tested, the comparative influence of the workhorse tank on the diaphragm is not known. Shaker limitations prevented full level shock tests. Finally, the unintentional presence of a noncondensable gas on the liquid side of the diaphragm may have contributed to the failure.

The fundamental response characteristics of the diaphragm were determined using strain gages. Peak strains rolled-off significantly at frequencies above 225 Hz. Maximum diaphragm strain gage measurements during ground random vibration (22μ - in/in peak) were considered too low to cause any damage, even for 10 hours duration. Higher peak strains (up to 380μ - in/in) were

recorded during the shock test, but a maximum of four cycles was observed, which also should not cause significant damage. Full shock levels were not achieved above 110 Hz, however, and contributions to fatigue damage due to shock are therefore possible. Peak strains were $650 \mu - \text{in/in}$ during pressurized flight random, which, when coupled with concentration factors associated with folds, is sufficient to predict failure. Metallurgical evaluations confirmed the crack initiation and propagation was due to fatigue, and failed to provide any evidence of abnormal material properties that would have an appreciable effect on fatigue life. Since potential diaphragm fatigue-life problems related to vibration of 1100-0 aluminum had been identified during the metal workhorse tank vibration test and other AFRPL feed system technology contracts, it was decided to resolve the problem by changing the scope of one of the other contracts, and additional diaphragm structural dynamic tests were deleted from this contract.

A composite-wrapped lightweight propellant tank was fabricated and tested. Fabrication processes were developed for Kevlar/epoxy wrapping of an aluminum liner assembly in a heated enclosure. Experiments were conducted that demonstrated that laser holography is an extremely useful technique for locating unbonded regions as small as 0.25 inches between the tank liner and composite wrap. Fabrication and testing of this tank confirmed the weight savings (27 to 35 percent) achievable with a wrapped tank and a 98 percent expulsion efficiency. The inert weight of 59 pounds could be reduced even further by redesigning the "universal" mounting ring, which weighed 12 pounds, to meet specific application requirements.

External leakage with an internal pressure of 315 psig was less than 10^{-8} sec helium. A pulsed-flow expulsion test was conducted at design pressure with warm gas pressurant (up to 1042 F). This test demonstrated the structural integrity of the tank, expulsion performance and the adequacy of the design in minimizing the heat transferred to the tank shell. The maximum composite outer surface temperature was 202 F, which had no apparent degrading effect. The final pressurant gas bulk temperature was 150 F for a 61 F initial

temperature. The propellant (water) temperature increased 14 F, with half of this value occurring during the last 8 seconds of the 665-second duty cycle.

The structural dynamic response characteristics of the tank shell were determined during unpressurized ground random vibration (1 g rms, 5 to 500 Hz), unpressurized and pressurized random vibration (13 g rms, 10 to 2000 Hz) and pressurized shock tests. There were no significant tank resonances below 80 Hz. The maximum transfer function gains during ground random were 3 to 5.5 at frequencies between 400 and 500 Hz on the mounting ring, normal to the polar axis, and 3 to 6 at frequencies between 100 and 500 Hz on the aluminum polar bosses, both normal to and along the polar axis. The maximum gain measured on the composite was 2 at 400 Hz. During flight random, the maximum gains were 5 to 10 at frequencies between 400 and 1500 Hz on the mounting flange, normal to the polar axis, and on the pressurant polar boss, along the polar axis. Gains between 10 and 26 at frequencies between 400 and 1000 Hz were measured on the composite. There was no significant difference in response due to pressurizing the tank to 75 psig. No structural damage was found as a result of the vibration and shock tests.

A liner-to-liner EB weld crack occurred as the burst pressure was attained during a hydrostatic pressure test after the expulsion and vibration/shock tests. There was no evidence of any other damage. The crack was the result of a tensile overload caused by crevice-type corrosion extending half way through the weld. A continuous line of porosity extending past the crack accentuated the corrosion. The corrosion was due to residual water from the expulsion test conducted five months earlier.

The PS consists of a composite-wrapped aluminum pressurant tank, Tridyne pressurant fluid (gaseous mixture of helium, oxygen, and hydrogen), a fill and drain valve, a pressure switch leak detector, a pressurant isolation valve, an electronically controlled pressure regulator, a relief valve, and a catalytic reactor. Propellant pressure is sensed by a pressure transducer and the error signal is conditioned electronically using proportional and lead-lag compensation. The electronics assembly output current drives a

torquemotor in the regulator assembly. The torquemotor positions the pilot valve which in turn controls the pressure acting on the diaphragm to position the regulator's main valve. Thus, the pressure and flow to the reactor are modulated to compensate for duty cycle variations in system pressure drops. The PS weighs 41 pounds.

A catalytic reactor and two electronically controlled regulators were fabricated and tested, first as components to optimize performance, and then as part of the pressurization subsystem used with the flanged metal workhorse and welded flightweight tanks. When tested with the workhorse tank, the temperature rise of the Tridyne from the inlet to the outlet of the reactor was 99 percent of theoretical, during the major portion of the continuous-expulsion duty cycle. The temperature rise during a pulsed duty cycle with the workhorse tank was 91 to 95 percent of theoretical. During a different pulsed cycle with the flightweight tank, the reactor's performance was 75 to 90 percent. Steady state conditions were never reached with the pulsed cycles. Inefficiencies were due to incomplete reaction and heat loss. The response of the 1.2-inch diameter, 2.0-inch long catalyst bed was very fast. During initial tank pressurizations, reactor outlet gas temperatures of 1050 to 1223 F were achieved in 4 seconds. Vibration and shock tests did not cause any breakage of the catalyst.

The final pressurant gas bulk temperature in the workhorse propellant tank was 185 to 201 F at the end of the continuous expulsion duty cycle. The initial temperature was 69 F. The final bulk temperature during the pulsed cycle was 90 F, with an initial temperature of 59 F. At the completion of a different pulsed expulsion of the flightweight tank, the bulk temperature was 150 F, with an initial temperature of 61 F.

The electronically controlled regulator was very accurate during both component and subsystem tests. These tests were conducted after vibration and shock tests. Initial pressurization of the workhorse propellant tank (to 300 psia) resulted in a 2.1 psi overshoot, but it dissipated in 0.1 seconds. Peak-to-peak oscillations of 1.0 psi were observed for a short

time during the initial portion of the hold period, prior to initiation of propellant expulsion. During pulsed expulsion of the flightweight tank, the propellant pressure was maintained within ± 0.4 psi except during the last high-flow pulse. During this pulse, the error was ± 1.4 psi.

CONTENTS

Summary	1
Introduction	19
Engineering Analyses and Design	22
Flightweight Propellant Storage Assembly	22
Plastic Workhorse Propellant Storage Assembly	97
Metal Workhorse Propellant Storage Assembly	99
Flightweight Pressurization Subsystem	101
Prototype Pressurization Subsystem	140
Flightweight Feed System	149
Feed System Parametrics	183
Composite-Wrapped Aluminum PSA Design Layouts	183
All-Aluminum and Titanium PSA Design Layouts	185
Parametric Data	188
Propellant Storage Assembly Fabrication and Test	221
Plastic Workhorse Tank	221
Aluminum Workhorse Tank	266
Flightweight Tank	323
Pressurization Subsystem Fabrication and Test	374
Catalytic Reactor	374
Electronically Controlled Regulator	394
Pressurization Subsystem	407
Design Update and New Technology	422
Materials Processing Development	423
Diaphragm Forming	423
Composite Wrapping	427
Propellant Storage Assembly	430
Pressurization Subsystem	432
Conclusions	434
Recommendations	435
<u>Appendix A</u>	
Technical Requirements	437

ILLUSTRATIONS

1. Propellant Feed System Schematic	20
2. PSA Design Layout	26
3. PSA Girth Joint	27
4. Inlet Polar Boss	29
5. Outlet Polar Boss	30
6. Handling Fixture	32
7. Feed System Installation--Looking Forward	34
8. Feed System Installation--Other Views	35
9. Comparison of Contours	37
10. Critical Structural Areas	40
11. Composite Running Loads	44
12. Composite Stresses	46
13. Buckling Coefficient	49
14. Buckling Pressure Illustration	49
15. Diaphragm Reversal Geometry	53
16. Cylinder Rolling Outside-In	54
17. Curvature Parameter	56
18. Stress-Strain Diagram	58
19. Comparison of Diaphragm Rolling Mode Pressure Prediction With Test Data	59
20. Nominal Diaphragm Reversal Mode	60
21. Worst-Case Diaphragm Reversal Mode	62
22. Diaphragm Pressure Differential Required for Buckling	64
23. Fill and Drain Valve	65
24. Vacuum Service Valve	65
25. Propellant Outlet Valve	67
26. Pressurant Inlet Valve	68
27. PSA Leak Detector	71
28. Tank Temperature Response for MDC I	82
29. Tank Temperature Profile at End of MDC I	83
30. Tank Temperature Response for MDC II	84
31. Tank Temperature Profile at End of MDC II	85

32. Missile X Stage IV Structural Dynamics Summary	87
33. Propellant Tank Structural Model	88
34. Second-Mode Normalized Displacements for Propellant Tank	89
35. Dynamic Response of Propellant Tank Shell	90
36. Diaphragm Structural Model	91
37. Fluid Compliance Model	93
38. First-Mode Normalized Displacements for Diaphragm	93
39. PSA Assembly Sequence	95
40. Plastic Workhorse PSA	98
41. Metal Workhorse PSA	100
42. Pressurization Subsystem Assembly	102
43. Pressurant Temperature Transient for MDC II	106
44. Pressurant Temperature Transient for MDC I	107
45. Flightweight Pressurant Tank Assembly	110
46. Pressurant Isolation Valve	112
47. Pressure Switch Leak Detector	114
48. Flightweight Regulator Assembly--Bottom and End Views	116
49. Flightweight Regulator Assembly--Top View	117
50. Flightweight Controller Assembly	118
51. Sectioned Flightweight Regulator Assembly--Side View	119
52. Flow Limiter Schematic	120
53. Sectioned Flightweight Regulator Assembly--End View	121
54. Torquemotor Current	122
55. Pressure Regulator Schematic	124
56. Relief Valve Schematic	124
57. Sectioned Relief Valve	125
58. Sectioned Flightweight Controller Assembly	127
59. Flightweight Electronics Schematic	130
60. Gain Schedule	131
61. Flightweight Catalytic Reactor	133
62. Reactor Nodal Model	135
63. Catalyst Bed Temperature Profile	137
64. Reactor Temperature Transients During Initial Pressurization	138
65. Reactor Temperature Transients During MDC I	139

66.	Prototype Pressurant Tank	141
67.	Prototype Regulator Assembly	143
68.	Sectioned Prototype Regulator Assembly	144
69.	Variable Gain Controls	146
70.	Electronic Components	147
71.	Prototype Catalytic Reactor	148
72.	Reduced Block Diagram	152
73.	Regulator Dynamic Performance for Initial Pressurization	155
74.	Regulator Dynamic Performance for Start of MDC I	157
75.	Regulator Dynamic Performance for Start of MDC II	158
76.	Regulator Dynamic Performance for Middle of MDC II	159
77.	Regulator Dynamic Performance for End of MDC II	160
78.	Feed System Center of Gravity	165
79.	Sample Manufacturing Planning Sheet	166
80.	Fault Logic Diagram for Fire or Explosion Internal to Feed System During Storage	174
81.	Fault Logic Diagram for Excess Pressure Buildup in Feed System During Storage	175
82.	Parametric Propellant Tank Layouts for $a/b = 1.4$	184
83.	Parametric Propellant Tank Layouts for $a/b = 1.2, 1.9$	186
84.	All-Aluminum and Titanium Flightweight Tank Layouts	187
85.	Parametric PSA Weights as a Function of Material and Propellant Weight and Pressure	189
86.	Parametric PSA Weights as a Function of a/b and Propellant Weight at Pressures of 400 and 500 psia	190
87.	Parametric PSA Weights as a Function of a/b and Propellant Weight at Pressures of 250 and 300 psia	191
88.	Parametric PSA Weights as a Function of Pressurant Temperature	192
89.	Parametric PSA Envelopes as a Function of Propellant Weight and a/b	194
90.	Parametric PSA Costs as a Function of a/b , Metal Fabrication Process, and Propellant Weight and Pressure	196
91.	Parametric PSA Costs as a Function of Rate and Quantity	197
92.	Parametric Diaphragm Pressure Differential as a Function of Expulsion Efficiency, Thickness and Material	199
93.	Parametric Additional Propellant Requirements as a Function of Delivered Propellant Weight and Expulsion Efficiency	200

94.	Parametric Diaphragm Weights as a Function of Propellant Weight, Thickness, and Material for $a/b = 1.2$	201
95.	Parametric Diaphragm Weights as a Function of Propellant Weight, Thickness, and Material for $a/b = 1.4$	202
96.	Parametric Diaphragm Weights as a Function of Propellant Weight, Thickness, and Material for $a/b = 1.9$	203
97.	Parametric Pressurant Weight as a Function of Propellant Weight and Mission Duty Cycle	204
98.	Parametric Pressurant Weight as a Function of Propellant Weight and Pressure for PSA Inlet Temperature = 1425 and 1025 F	205
99.	Parametric Pressurant Weight as a Function of Propellant Weight and Pressure for PSA Inlet Temperature = 625 and 227 F	206
100.	Parametric Pressurant Volume as a Function of Propellant Weight and Mission Duty Cycle	208
101.	Parametric Pressurant Volume as a Function of Propellant Weight and Pressure for PSA Inlet Temperature = 1425 and 1025 F	209
102.	Parametric Pressurant Volume as a Function of Propellant Weight and Pressure for PSA Inlet Temperatures = 625 and 225 F	210
103.	Parametric Pressurant Tank Weight as a Function of Storage Pressure, Material, and Propellant Weight for PSA Inlet Temperature = 1025 F	211
104.	Parametric Pressurant Tank Weight as a Function of Storage Pressure, Material, and Propellant Weight for PSA Inlet Temperatures = 625 and 225 F	212
105.	Parametric Pressurant Tank Diameter as a Function of Storage Pressure and Propellant Weight for PSA Inlet Temperature = 1025 F	213
106.	Parametric Pressurant Tank Diameter as a Function of Storage Pressure and Propellant Weight for PSA Inlet Temperatures = 625 and 225 F	214
107.	Parametric Pressurant Tank Costs	215
108.	Parametric Pressurization Subsystem Weights	216
109.	Parametric Feed System Weights	219
110.	Plastic Tank Design Modification	223
111.	Thickness Distribution	226
112.	Pressure Differential at Tank Centerline	232
113.	Flight NTO Tank CG Displacement From Polar Axis	233
114.	Test Schematic	236
115.	Plastic Tank Test Setup	237

116.	Development of Buckles	238
117.	Diaphragm ΔP for Plastic Tank Tests 1 and 2	239
118.	CG Shift for Plastic Tank Test 1	240
119.	Sketch of Diaphragm Number 1 After First Part of Expulsion	241
120.	Diaphragm Number 1 After First Part of Test	242
121.	CG Shift for Plastic Tank Test 2	244
122.	Diaphragm Differential Pressure as a Function of Percent Expulsion	246
123.	Center-of-Gravity Movement During Third Test	248
124.	Center-of-Gravity Movement During Fourth Test	249
125.	Wires Attached to Plastic Tank	251
126.	Orientation of Diaphragm Rolling Radius After Pulses	253
127.	Centrifuge Test Setup	255
128.	Tank Pressure and Accelerations During Test 7	258
129.	Movement of Deflected Section of Diaphragm During Test 7	259
130.	Diaphragm Shape Prior to Expulsion During Test 7	260
131.	Tank Pressure and Accelerations During Test 8	262
132.	Movement of Deflected Section of Diaphragm During Test 8	263
133.	Diaphragm Shape During Expulsion Portion of Test 8	265
134.	Aluminum Workhorse PSA	267
135.	Feed System Schematic	270
136.	Feed System Test Setup	271
137.	Pressure Transients During Initial Pressurization	272
138.	Tank Outlet Pressure During First Pulse	272
139.	Maximum Tank Outer Wall Temperatures	276
140.	Diaphragm Differential Pressure at Tank Polar Axis	278
141.	Propellant Side of Diaphragm 1	279
142.	Wrinkle in Diaphragm 1	280
143.	Test Temperature Transients	283
144.	Tank Wall Thermocouple Locations	284
145.	Tank Wall Temperature Transients for Test	286
146.	Diaphragm Differential Pressure	287
147.	Pulse Series	289
148.	Diaphragm Crack	290
149.	Test Temperature Transients	292

150.	Tank Wall Temperature Transients for Test 3	293
151.	Shock/Vibration Test Setup	295
152.	Control Accelerometer Response	299
153.	Response of Flange at Top (X axis)	300
154.	Response of Flange at Top (Y axis)	301
155.	Response of Flange at Side (X axis)	302
156.	Response of Flange at Side (Y axis)	303
157.	Response of Gas Side Polar Boss (X axis)	304
158.	Response of Gas Side Polar Box (Y axis)	305
159.	Response of Liquid Side Polar Boss (X axis)	306
160.	Response of Liquid Side Polar Boss (Y axis)	307
161.	Post-Test View of Diaphragm	310
162.	Post-Test View of Tear and Cracks	311
163.	Post-Test View of Tear	312
164.	Post-Test View of Crack No. 1	313
165.	Post-Test View of Rub Marks	314
166.	Control Accelerometer Response (Fixture Base, V)	316
167.	Strain Gage 2 PSD	317
168.	Strain Gage 3 PSD	318
169.	Strain Gage 7 PSD	319
170.	Strain Gage 8 PSD	320
171.	Comparative Diaphragm	321
172.	Inlet Liner	325
173.	Inlet Polar Boss and Diffuser Plate Parts	326
174.	Outlet Liner Assembly	327
175.	Outlet Liner Assembly	328
176.	Tank Liner Assembly	329
177.	Girth Ring Assembly	330
178.	Flight Tank	333
179.	Subscale NDI Tank	337
180.	Holographic Setup	339
181.	Optical Holograms of Wrapped Tank	341
182.	Tank Wall Temperature Transients	344
183.	Reactor Temperatures	345

184.	Tank Outer-Wall Thermocouple Locations	346
185.	Tank Wall Temperature Transients	347
186.	Structural Dynamic Test Setup	348
187.	Flight Weight Tank Accelerometer Locations	350
188.	Pressurant Boss X-Axis PSD	351
189.	Propellant Boss X-Axis PSD	352
190.	Composite Wrap PSD - Near Pressurant Boss	353
191.	Flange Top Y-Axis Gain	354
192.	Flange Bottom Y-Axis Gain	355
193.	Pressurant Boss Y-Axis Gain	357
194.	Propellant Boss Y-Axis Gain	358
195.	Pressurant Boss X-Axis Gain	359
196.	Propellant Boss X-Axis Gain	360
197.	Composite Wrap Gain - Near Pressurant Boss	361
198.	Flange Top Y-Axis Gain	362
199.	Flange Bottom Y-Axis Gain	363
200.	Pressurant Boss X-Axis Gain	364
201.	Composite Wrap Gain - Near Pressurant Boss	365
202.	Composite Wrap Gain - Near Flange	366
203.	Test Fixture Flight Shock Spectrum	368
204.	Pressurant Boss X-Axis Shock Spectrum	369
205.	Pressurant Boss Y-Axis Shock Spectrum	370
206.	Propellant Boss X-Axis Shock Spectrum	371
207.	Propellant Boss Y-Axis Shock Spectrum	372
208.	Catalytic Reactor Parts	375
209.	Assembled Catalytic Reactor	376
210.	Interchangeable Reactor Parts	377
211.	Test Schematic	379
212.	Test Stand	380
213.	Thermocouple Locations Relative to Catalyst Beds	383
214.	Reactor Temperature Increase Transients	385
215.	Catalyst Comparison	393
216.	Ground Random Vibration	398
217.	Stage II/III Random Vibration	399

218.	Regulator Test Schematic	402
219.	Initial Pressurization	404
220.	Flow Test No. 1	405
221.	Flow Test No. 2	406
222.	Flow Test No. 5	408
223.	Electronically Controlled Regulator	409
224.	Pressure Transients During Initial Pressurization	412
225.	Tank Outlet Pressure Transient During Initial Pressurization	414
226.	Tank Outlet Pressure Prior to First Pulse	415
227.	Catalytic Reactor Thermocouples	416
228.	Regulator Transients From Second Through Third High-Flow Pulse	419
229.	Pressure Transients During Next-to-Last High-Flow Pulse	420

TABLES

1. PSA Design Characteristics	23
2. Tank Liner Contour	39
3. Stress Summary	41
4. Maximum Structural Loads	42
5. Tank Deflections	48
6. Buckling Pressures	51
7. Comparison of Diaphragm Rolling and Buckling ΔP 's	61
8. Welds	72
9. DEAP Analogous Parameters	78
10. Dynamic Response of Girth Ring	90
11. Maximum Diaphragm Stresses	92
12. PSA Materials	94
13. Pressurization Subsystem Design Characteristics	101
14. Feed System Pressure Schedule With N_2O_4 PSA	104
15. Tridyne Pressurant Temperatures and Pressures	108
16. Pressure Transducer Accuracy	128
17. Feed System Design Characteristics	150
18. Initial Conditions for Feed System Dynamic Performance Predictions	154
19. Feed System Dynamic Error Summary	161
20. Feed System Weights (Pounds)	162
21. Feed System Center of Gravity	164
22. Unit Production Cost	167
23. Hazard Classification	169
24. Preliminary Hazard Analysis	170
25. Failure Modes/Effects Analysis	176
26. Failure Rates	178
27. PSA Range of Parameters	193
28. Valves and Leak Detector Envelopes	195
29. Pressurization Subsystem Range of Parameters	207
30. Pressurization Subsystem Component Envelopes	217
31. Pressurization Subsystem Envelopes	217
32. Feed System Unit Production Costs	220

13.	Diaphragm-to-Diaphragm Thickness Variations	225
14.	Diaphragm Meridional Thickness Variations	225
35.	Diaphragm Thickness Variations	226
36.	Diaphragm Nominal Thicknesses	227
37.	Chem-Mill Tolerances	227
38.	Chem-Mill Variations	228
39.	Diaphragm No. 5 Thickness	228
40.	Plastic Tank Tests	229
41.	Test Event Durations	273
42.	Ground Random Vibration Acceleration Levels	308
43.	Catalytic Reactor Test Objectives	381
44.	Test Data Summary	384
45.	MDC II Simulation	391
46.	MDC II Data Summary	392
47.	Ground Shocks	400
48.	Summary of Diaphragm Forming Problems	425

INTRODUCTION

An advanced development program was conducted in support of the Air Force Ballistic Missile program. Recent exploratory development programs, which were initiated to minimize risk during weapon system development of an advanced post-boost propulsion system (PBPS), emphasized low life-cycle cost and high reliability. However, changing requirements demanded greater emphasis be placed on the reduction of inert weight. The propellant feed system is a major contributor to PBPS weight and has the most potential for reduction. The feed system is also the most critical in terms of 15-year operational life.

The objective of this technology program was to demonstrate an advanced, liquid-bipropellant feed system incorporating design features that: (1) significantly reduced advanced post-boost propulsion feed system weight, (2) maintained or improved upon the high reliability demonstrated by the Minuteman III Propulsion System Rocket Engine (PSRE), (3) provided for deployment in a mobile environment without maintenance and with minimal condition monitoring, (4) was compatible with the launch dynamic and nuclear environments, and (5) provided a low life-cycle cost. The baseline system, shown schematically in Fig. 1, employs a positive-expulsion tankage configuration with warm-gas pressurization. The propellant storage assemblies (PSA's) include lightweight, filament-wrapped propellant tanks with aluminum diaphragms to contain and expel the dinitrogen tetroxide (N_2O_4) and monomethylhydrazine ($N_2H_3CH_3$, MMH) propellants; propellant and pressurant isolation valves; vacuum service valves; fill and drain valves; and vacuum gage tube leak detectors. The warm-gas pressurization subsystem consists of Tridyne pressurant (mixture of gaseous oxygen, hydrogen, and helium), a filament-wrapped pressurant tank, a fill and drain valve, an isolation valve, a pressure switch leak detector, an electronically controlled pressure regulator with integral relief valve, and a catalytic reactor. This system resulted in a 27 to 35% weight reduction relative to those developed on the AFRPL low-cost feed system programs with a lower production cost due to design simplicity.

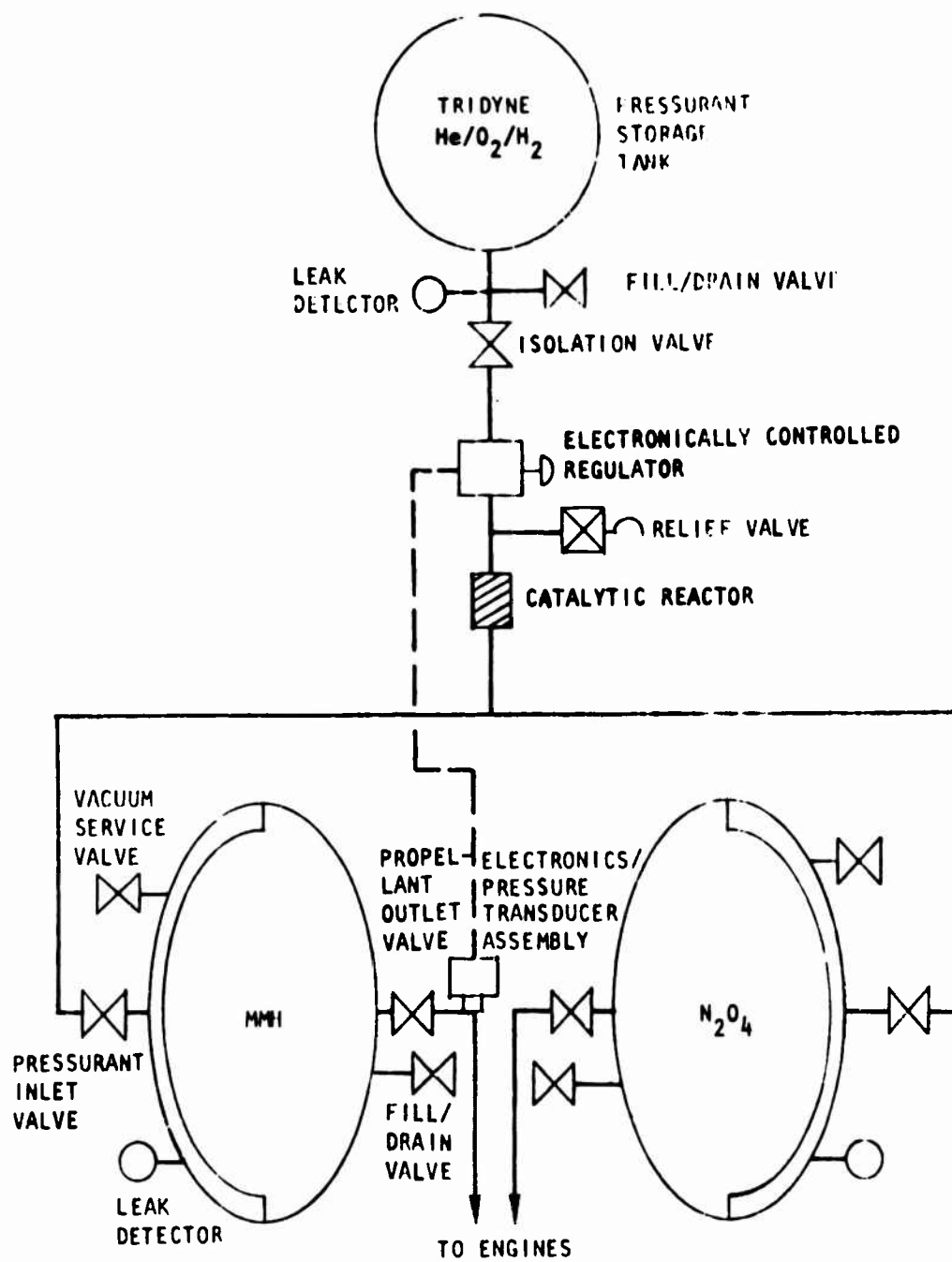


Figure 1. Propellant Feed System Schematic

The program plan to accomplish the stated objective was divided into three phases. Design and analyses were accomplished in Phase I to generate detailed designs and operating characteristics of the flightweight feed system and prototype test hardware. Parametric design layouts and component weight, envelope, and cost data were also completed. Hardware was fabricated and tested at the component and subsystem levels during the Phase II effort. The program was cancelled at the completion of Phase II. Phase III would have included the fabrication and testing of two complete feed systems and the fabrication, acceptance testing, and delivery of two flightweight PSA's to AFRPL for long-term storability and operation demonstrations.

ENGINEERING ANALYSIS AND DESIGN

Detailed engineering analyses and design were performed on the originally proposed feed system to further define the operating parameters and design characteristics. The purpose was to enable selection of the optimum weight design, subject to the technical requirements and program goals. The feed system was separated into two major subsystems, the two propellant storage assemblies and the pressurization subsystem. In addition to the flight-weight PSA, analyses and detailed designs were conducted for the prototype plastic and aluminum workhorse tanks. Both flightweight and prototype pressurization subsystem analyses and designs were also conducted. Functional compatibility of the subsystems during steady-state and transient operating modes was analyzed and a typical stage installation design was prepared.

FLIGHTWEIGHT PROPELLANT STORAGE ASSEMBLY

The two propellant storage assemblies provide for storage and delivery of N_2O_4 and MMH propellants to the engines. The identical tanks are sized to deliver a total of 1400 pounds of propellants to the engines.

Each tank consists of a composite-wrapped aluminum liner with an aluminum diaphragm for positive expulsion. In addition, each PSA includes pressurant inlet and propellant outlet isolation valves, a fill and drain valve, a vacuum service valve, a leak detector, and a mounting ring.

This section includes descriptions of the flightweight PSA envelope, component designs, static stress analyses, diaphragm reversal, operating temperatures, structural dynamic response, and fabrication sequence. Table 1 summarizes PSA design characteristics.

TABLE 1. PSA DESIGN CHARACTERISTICS

<u>Capacities, Ft³</u>	
Propellant	10.57
Liner Inner Wall	10.66
<u>Pressures, psi</u>	
Delivered Propellant	300.0
Maximum Pressurant (at $\eta_{Exp} = 99\%$)	324.2
Design	350.0
Proof	385.0
Burst	475
<u>Dimensions (pressurized), inches</u>	
Length	40.1
Width	40.1
Height	31.2
<u>Efficiencies, %</u>	
Volumetric	99.2
Expulsion (at $\Delta P = 25$ psi)	98.1

Tank Sizing

In sizing the propellant tanks to deliver 1400 pounds of propellants to the engines, several factors were considered, including line volume, storage temperature, expulsion efficiency, and propellant vapor ullage volume. Equation 1 shows the relationship between these parameters.

$$\text{Volume} = \frac{W_L + W_D}{\frac{\rho_{T1}}{K_U} - (1 - \eta_{Exp}) (\rho_{T2})} \quad (1)$$

where

- W_L = Weight in lines at minimum operating temperature
- W_D = Weight delivered to engines
- ρ_{T1} = Density at maximum storage temperature
- K_U = Ullage factor
- η_{Exp} = Expulsion efficiency
- ρ_{T2} = Density at minimum operating temperature

The weights of the oxidizer and fuel in the lines between the tank outlet valves and the engine inlet valves are 4.6 and 2.6 pounds, respectively. The delivered propellant weights are 866.3 pounds of N_2O_4 and 533.7 pounds of MMH. The oxidizer densities are 92.46 and 86.03 lb/ft³ and fuel densities are 55.53 and 52.93 lb/ft³ at 40 and 120 F, respectively. The ullage factor is 1.01, i.e., the propellant vapor volume is 1% of the tanked liquid volume at 120 F. An expulsion efficiency of 0.97 was selected for sizing, although 0.981 was achieved with a diaphragm pressure differential of 25 psi.

The resultant fluid volumes contained within the diaphragm and propellant outlet liner are 10.57 ft³ (18,267 in.³) per tank. The tank liner internal volume, which also includes the diaphragm, pressurant ullage, and inlet and outlet plates, is 10.66 ft³ (18,413 in.³) in the unpressurized condition.

Internal dimensions of the virgin tank liner are 36.21 by 36.21 by 25.62 inches in the unpressurized condition, resulting in a diameter ratio of 1.41. The larger diameter corresponds to the outlet half and therefore neglects the offset in the inlet half where the diaphragm is attached. The smaller diameter results from extrapolating the contours at the poles to the centerlines of the pressurant inlet and propellant outlet ports. When pressurized to 350 psia, the major axis grows to 36.24 inches and the minor axis to 26.16 inches. The envelope dimensions of the virgin PSA, including valves and the mounting ring, are 40.02 by 40.02 by 30.66 inches unpressurized. The PSA major and minor axes also grow by 0.03 and 0.54 inch, respectively, when pressurized.

Tank Design Description

The PSA design is presented in Fig. 2 and details of the girth joint are shown in Fig. 3. The tank liner assembly is comprised of pressurant inlet and propellant outlet half liners, joined by a girth weld at the equator (Fig. 3). Both the inlet and outlet half liners are constructed of 5086-0 aluminum for propellant compatibility and ductile weld properties. The thickness of the liners is nominally 0.32 inch, but it thickens locally at the equator to provide sufficient material for the girth joint and mount ring attachment (Fig. 3), and at the polar openings for welding to their respective polar bosses (Fig. 2). The polar boss material is 5086-H34 to provide the bending strength at the 6.0-inch-diameter helical wrap opening.

The outlet half liner has 36 equally spaced meridional ribs on the inside surface to ensure flow passages from the girth to the outlet plate at the end of the expulsion cycle, when the diaphragm is against the outlet half liner. The ribs are formed by chem-milling the area between them, starting 0.25 inches from the equator. The ribs are 0.03 inches high and 0.18 inches wide.

The diaphragm is made of 1100-0 aluminum to provide sufficient ductility during the reversal mode. It is welded to the outlet half liner as shown in Fig. 3. This weld is independently adequate to transmit all forces during internal pressure sizing of the diaphragm against the inlet half liner prior to propellant loading and during reversal of the diaphragm to expel propellants. At the equator the diaphragm skirt is sandwiched between the liners for additional structural support.

The diaphragm is contained within and contacts the inside surface of the inlet liner. In the area of the inlet polar boss, the diaphragm is flat and contacts the pressurant diffuser frontplate, the inlet support plate, and the inlet liner ring as shown in Fig. 2. The diaphragm has a stepped wall thickness ranging from 0.026 inch at the pole to 0.044 inch near the equator to provide additional stability during the reversal mode. The thickness at the equator weld joint is 0.061 inch.

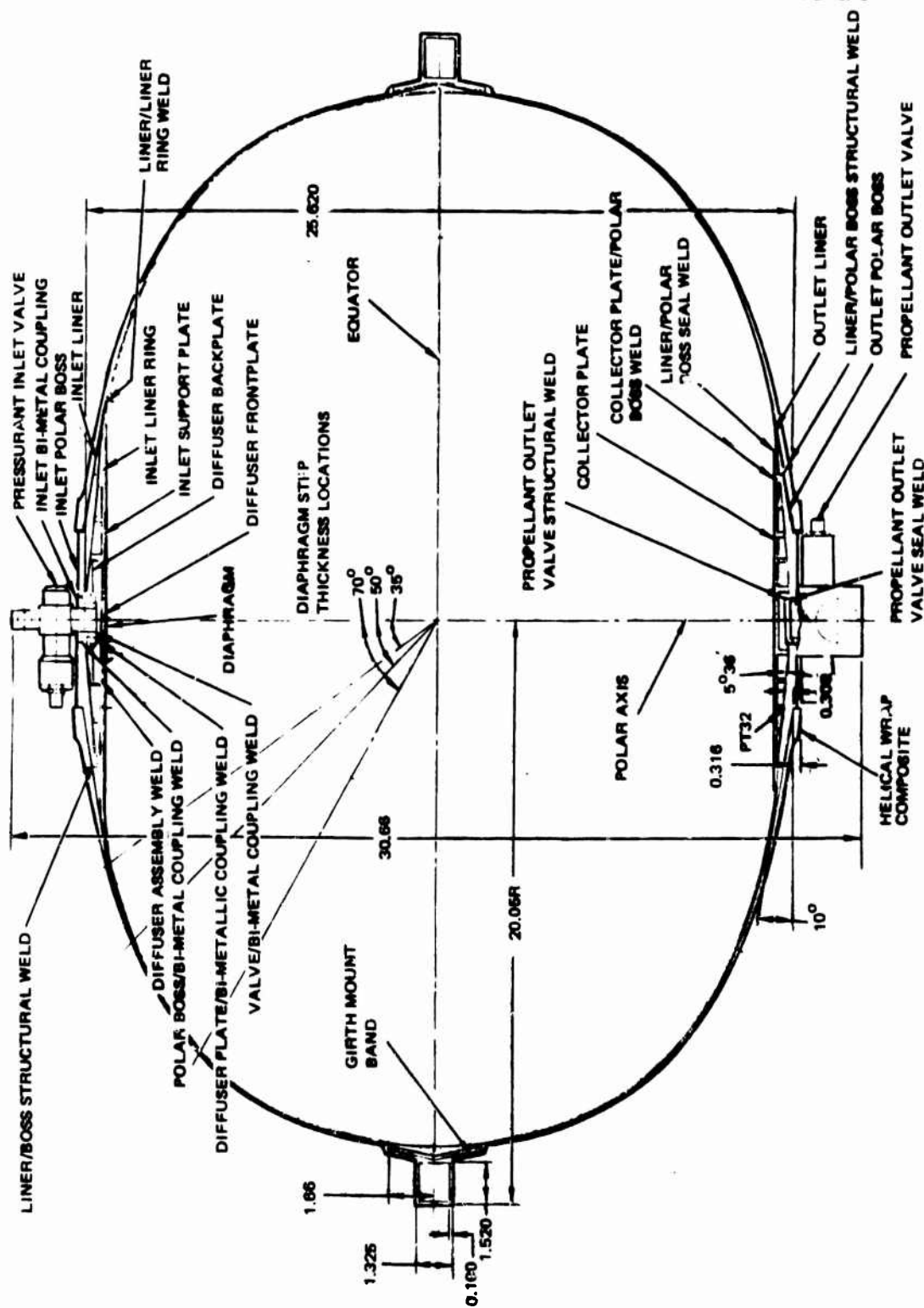


Figure 2. PSA Design Layout

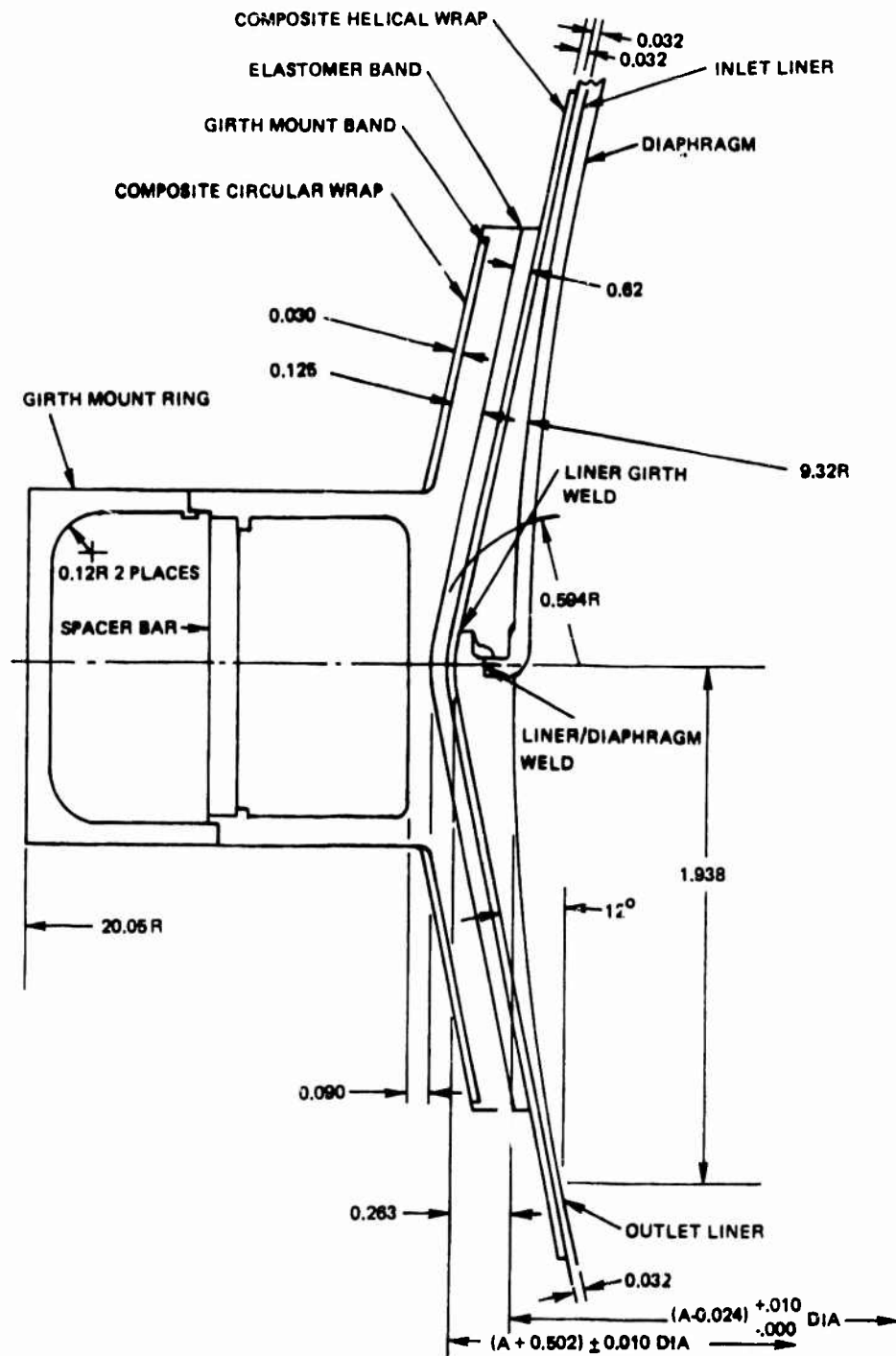


Figure 3. PSA Girth Joint

The inlet diffuser plate assembly, consisting of a welded frontplate and backplate (Fig. 2), provides a plenum that receives the pressurant gas and diffuses it before it impacts the diaphragm. It is made from 304L stainless steel to withstand the warm pressurant gas (1025 to 1051 F). The diffuser backplate is welded to the lower steel section of the bimetallic 5086 aluminum/304L steel tube as shown in Fig. 2. The upper aluminum section of the tube is welded to the inlet polar boss. The bimetallic tube thus permits joining of the steel and aluminum components. The pressurant inlet valve has a 304L stainless-steel outlet tube that fits within and is welded to the steel section of the bi-metal tube. Contact between these tubes is minimal to provide thermal insulation between the warm pressurant gas and the aluminum polar boss. This design will minimize the tank liner and composite overwrap temperatures.

Both the inlet support plate and inlet liner ring are made from 5086-0 aluminum. The liner ring is welded to the inlet half liner and mechanically holds the support plate in place.

The inlet polar boss, which is welded to the tank liner, also serves as the mounting structure for the leak detector and vacuum service valve as shown in Fig. 4. The 304L stainless-steel leak detector is welded to one end of a bi-metal tube, while the other end is welded to the polar boss. The 5086 aluminum vacuum service valve is threaded and mounted in a 5086 adapter plate that is welded to the polar boss. A 5086 valve cap is welded to the adapter plate.

The polar boss in the propellant outlet half liner is welded to the liner at two locations and is used for mounting the propellant outlet valve and the propellant fill and drain valve as shown in Fig. 2 and 5. The propellant outlet valve has a 5086 aluminum inlet tube that is welded to the polar boss in two places. The 5086 fill and drain valve body and its cylindrical cap also are welded to the polar boss. End plates are then welded to the valve body and outer cap.

The outlet polar boss also supports a collector plate (Fig. 2) that provides a pattern of holes and channels to ensure propellant outlet flow passages.

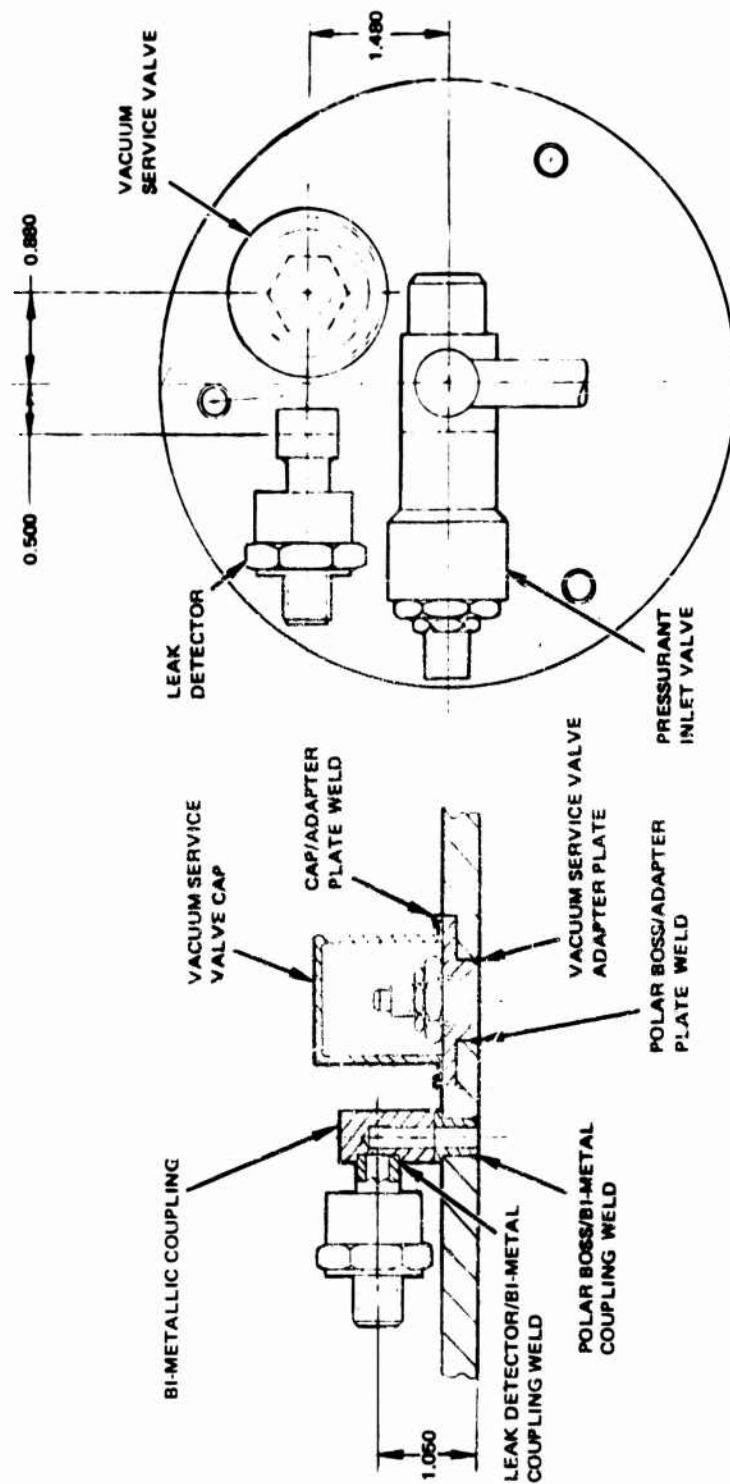


Figure 4. Inlet Polar Boss

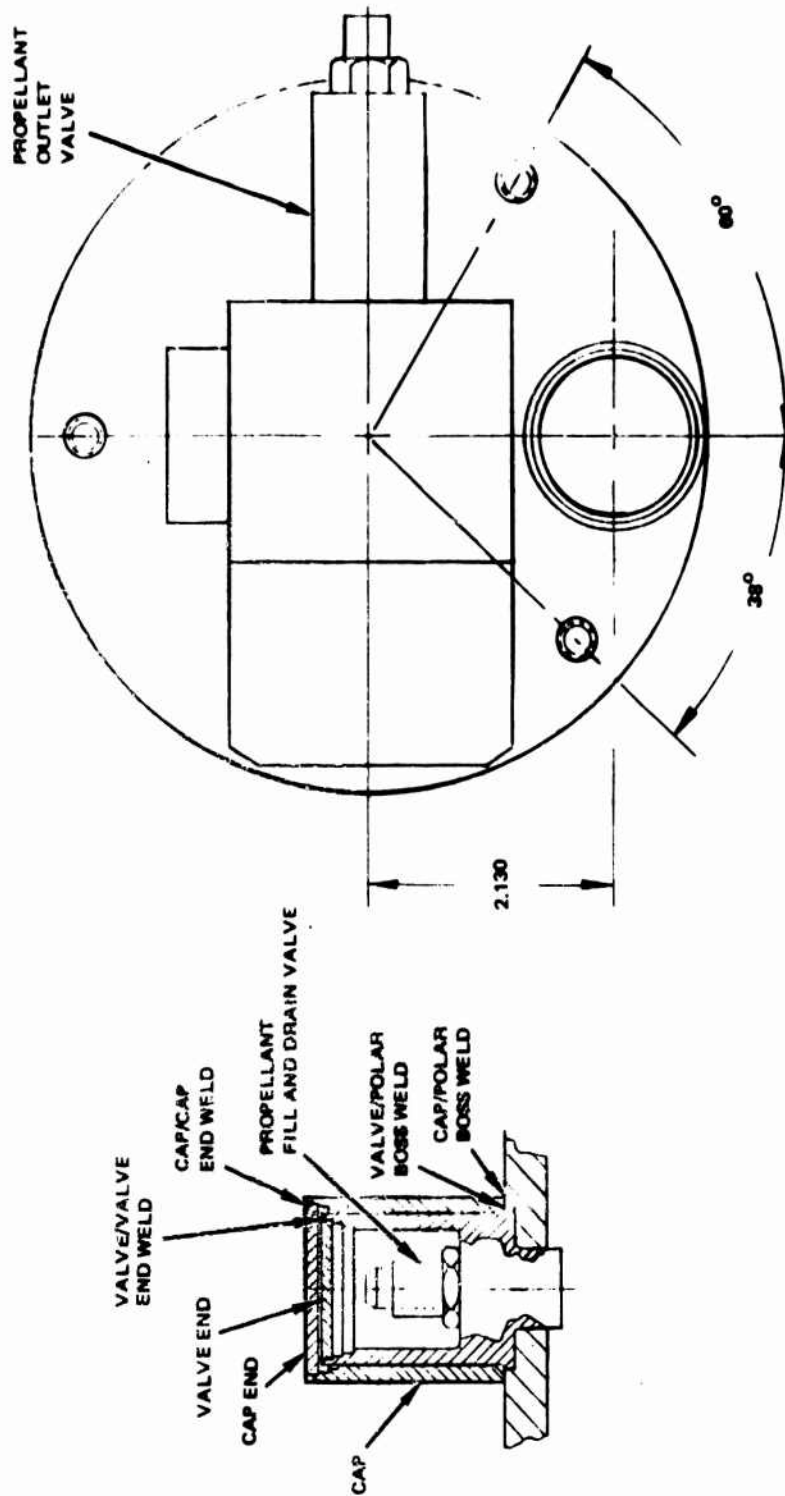


Figure 5. Outlet Polar Boss

This plate prevents the diaphragm from covering the outlet port. The collector plate, made from 5086 aluminum, is welded to the polar boss at its outer diameter.

Both inlet and outlet polar bosses have threaded holes to attach the removable handling fixtures shown in Fig. 6. The fixtures are designed to fit over the valves and leak detector to permit appropriate attachment for filament winding and subsequent pressure testing through the vacuum service valve and the propellant fill and drain valve.

Prior to filament winding, the liner assembly surface is prepared for bonding the composite overwrap to the liner. The Kevlar 49 fiber, wet with epoxy resin, is helically wound around the liner assembly to form the composite structure. The thickness of the composite wrap varies from 0.032 inch at the equator to 0.411 inch near the polar boss opening. An elastomeric girth band is placed around the wrapped tank assembly for fitup between the girth mount band and the tank as shown in Fig. 3. This band also is used to help isolate the tank from forces transmitted by the tank support links.

The 2219-T62 aluminum girth mount ring assembly is a box-section design to provide the required stiffness under externally applied static and dynamic loads. It is assembled around the elastomer band and held in position by a circular-wound composite wrap. The wide part of the assembly, which is in contact with the tank, consists of a one-piece, full-circumference ring that is slit and fitted with a mechanically attached coupling to permit proper adjustment to the tank. Four spacer bars are welded inside the ring at the PSA mounting points for support. The larger diameter C-section is welded to complete the assembly. The 12-degree angle of the outside liner surfaces at the equator provides a structural resistance to side slippage of the ring under mount load components parallel to the polar axis. The box section stiffness prevents excessive deflections of the mount ring in the twist and inward radial directions, relative to the tank axis, which would cause buckling of the thin-wall tank structure.

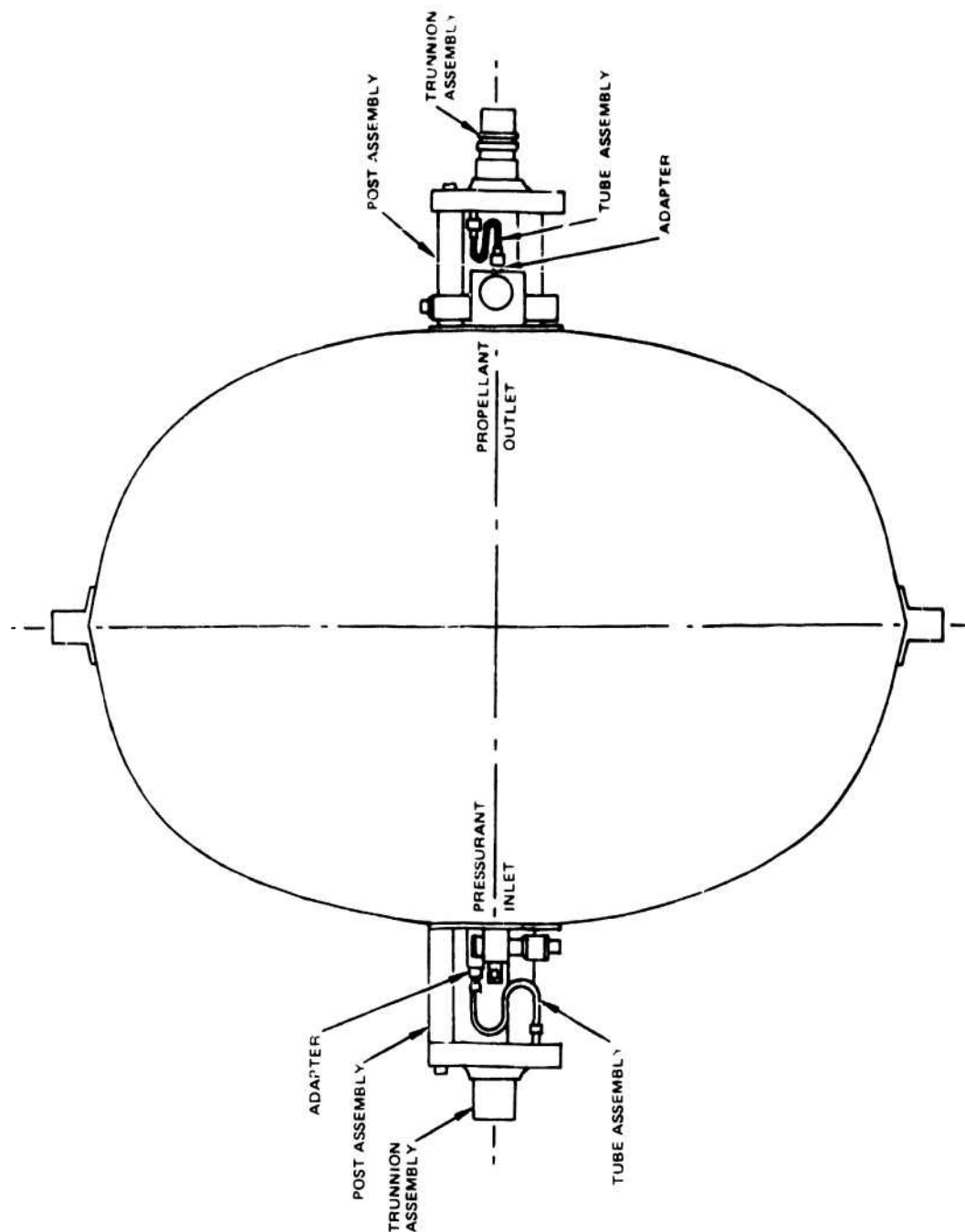


Figure 6. Handling Fixture

Attach locations of the tank supporting links are shown in the view of the tank presented in Fig. 7 and 8. Links 1 and 2 take the stage radial and axial loads, respectively, on each side of the tank. Links 3 and 4 at the aft end and the pin at the forward end take the transverse lateral loads. Links 3 and 4 also act as stabilizers to prevent tank rotation under radial loads about the stage lateral axis at the link 1 joint. The pin at the forward end has slots to permit sliding and precludes redundancy with links 3 and 4.

Static Stress Analysis

Static stress analyses were conducted to optimize the tank contour and determine stress levels and deflections associated with the load-bearing parts. The primary areas of concern were the girth joint, the polar bosses, and the composite. In addition, inward buckling under vacuum propellant-loaded conditions was analyzed.

Tank Contour. Initially, the propellant tank design was an oblate spheroid, i.e., an elliptical contour-of-revolution about the minor axis, with propellant expulsion in the direction of the minor axis. An internal surface diameter ratio (a/b) of approximately 1.4 was selected to fit the required envelope; it also represents a good compromise between minimum weight and a uniformly reversing diaphragm. A spherical tank would result in the minimum weight for a given contained volume, but the constant radius of curvature contour does not enhance uniform reversal of the diaphragm. Initial buckling of a spherical diaphragm is equally likely at any surface location of a constant-thickness section. An elliptical shape, however, results in an increase in the pressure differential required for the undesirable buckling mode to occur as you move away from the minor axis. This is caused by the decreasing radius of curvature and provides an increasing margin of stability as the diaphragm reverses. Because of the large radius of curvature at the minor axis, the initial reversing

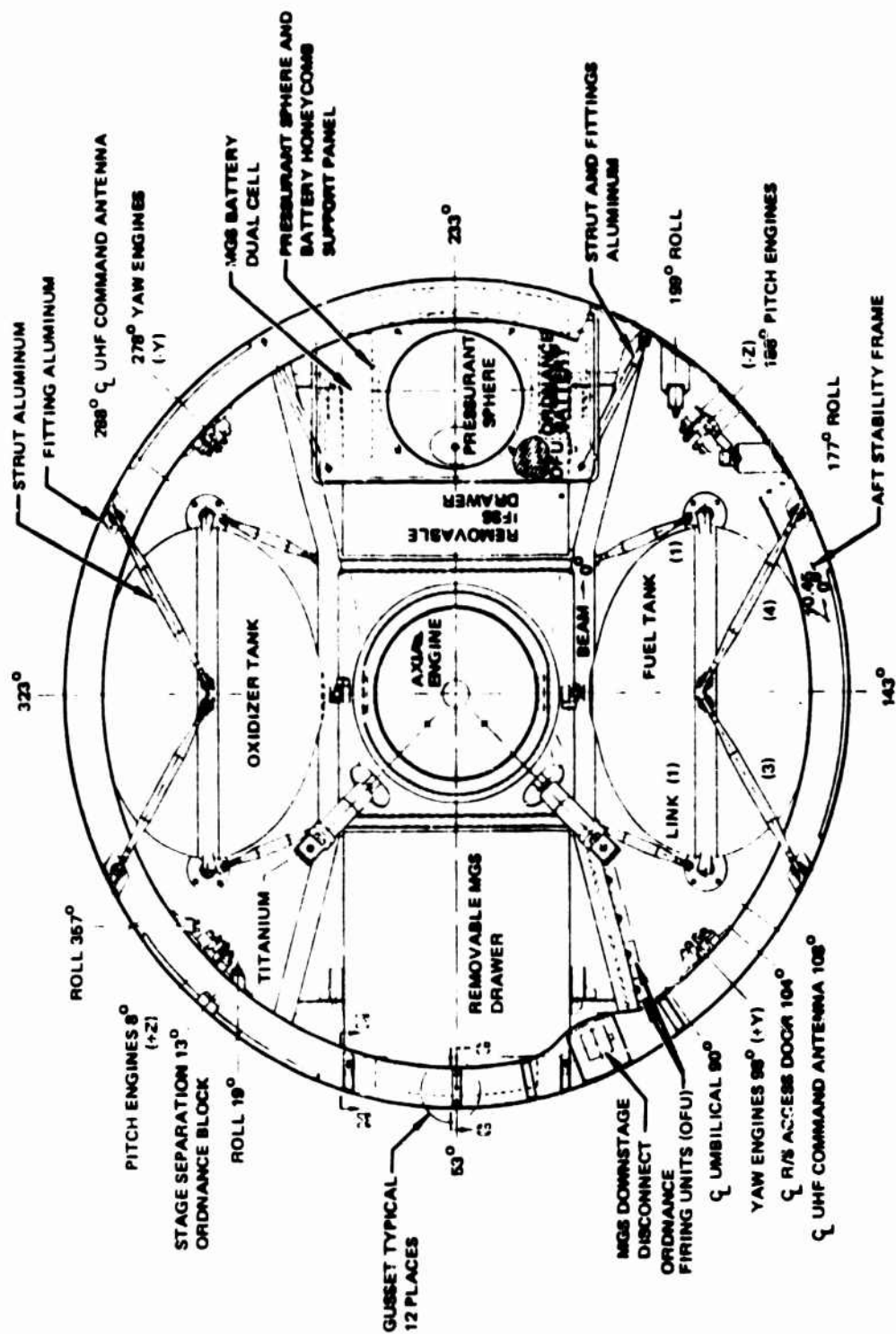


Figure 7. Feed System Installation--Looking Forward

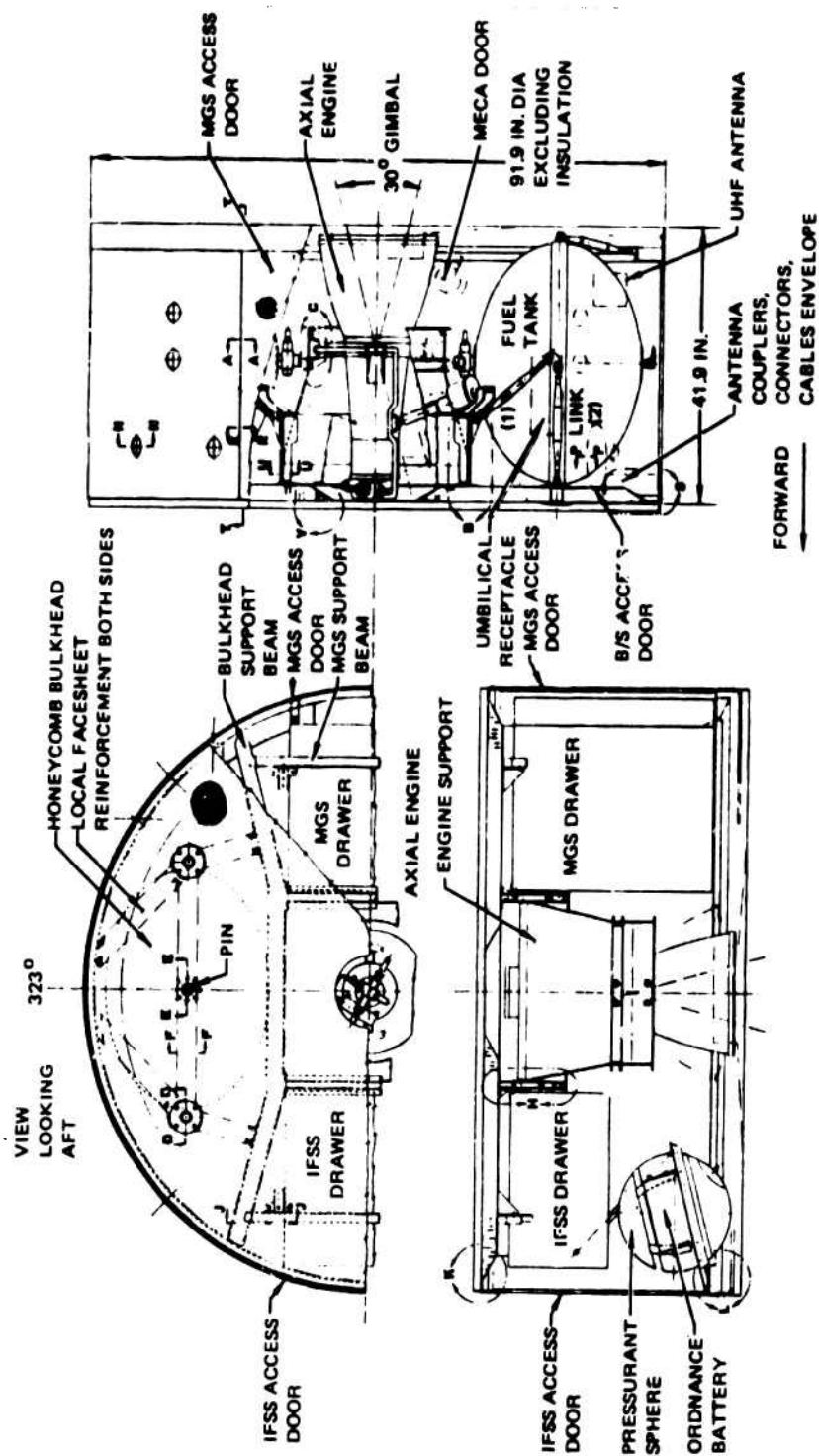


Figure 8. Feed System Installation--Other Views

(buckling) starts there and then progresses outward in concentric circles via the rolling mode to areas of decreasing radius of curvature. The rolling mode occurs because a smaller pressure differential is required compared to buckling.

The composite-wrap design analysis by Defense Products Division of Brunswick Corp. resulted in a change of the contour from an oblate spheroid (elliptical cross-section). The new shape is still oblate and in fact is nearly elliptical. Compared to the original ellipse, the new contour has smaller major and minor diameters and bulges outward midway between the two, as shown in Fig. 9. This contour is based on an analysis that relates the meridional and tangential (hoop) curvatures and the local filament wind angle so that the resultant stress is directed parallel to the fiber. As a result of this "balanced loading," there is no tendency for the fiber to slip when the tank is pressurized.

The membrane load relationship for a shell is expressed by

$$\frac{N_t}{N_m} = 2 - \frac{r_t}{r_m} \quad (2)$$

where

N_t = Tangential running load

N_m = Meridional running load

r_t = Tangential curvature

r_m = Meridional curvature

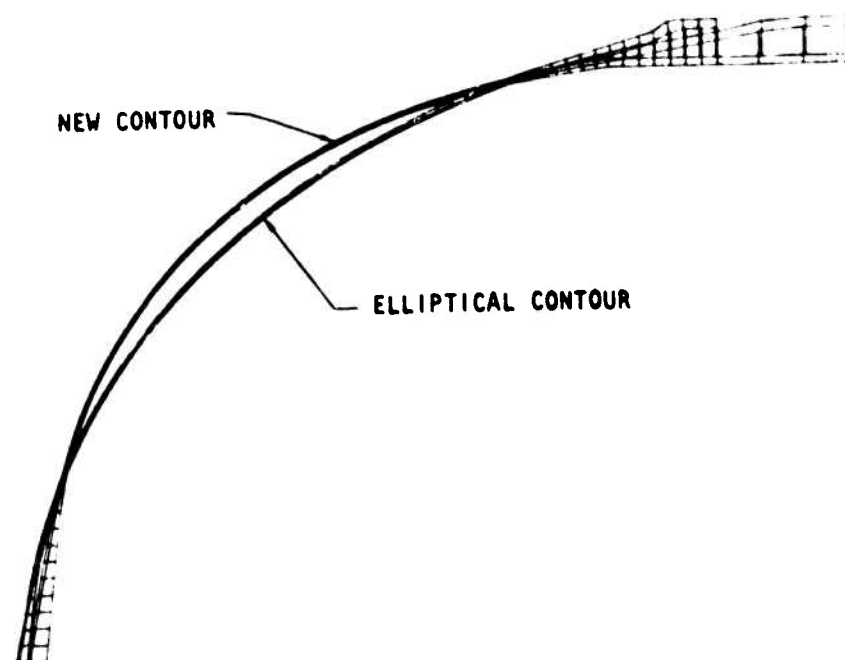


Figure 9. Comparison of Contours

This leads to the following contour equation:

$$R'' R = [1 + (R')^2] \left[\frac{N_t}{N_m} - 2 \right] \quad (3)$$

where

R = Radial distance from polar axis

R' = First derivative of R with respect to Z

R'' = Second derivative of R with respect to Z

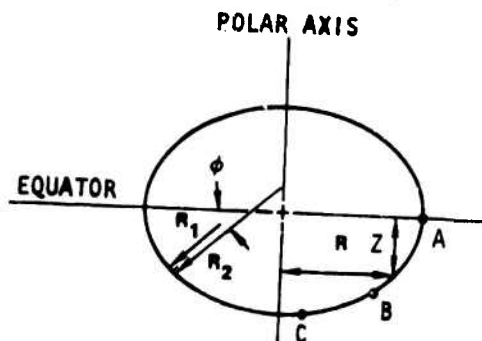
Z = Axial coordinate

The contour coordinates of the inside surface of the liner are presented in Table 2, which also defines the colinear radii of curvature R_1 and R_2 . Radius R_1 is the curvature of the contour at a point in the meridional plane. Radius R_2 is the length of the line perpendicular to the contour from the contour to the intersection of the polar axis. These two radii were used to establish the buckling and rolling of the diaphragm during expulsion.

Liner and Polar Boss Stresses. Based on Rocketdyne's stage weight optimization analyses in support to the MX Stage IV proposal, a delivered propellant pressure of 300 psia was selected. This results in a maximum tank pressure at the end of the expulsion cycle of 324 psia. An intentionally high tank design pressure of 350 psia was selected, however, because the relief valve is set at this value. The proof and burst pressure safety factors (1.1 and 1.25, respectively) were applied to 350 psia to yield values of 385 and 437.5 psia. Referenced to 324 psia, the safety factors are 1.19 and 1.35, respectively.

TABLE 2. TANK LINER CONTOUR

Point	Coordinates, Inches		Composite Thickness, Inch	Liner Thickness, Inch	R ₁ , inches	R ₂ , inches	θ, degrees
	R	Z					
1	18.104	0.000	0.0320				
2	17.563	3.500	0.0334				
3	17.398	4.156	0.0337	0.032			
4	17.182	4.808	0.0342	0.032	9.235	18.162	16.284
5	16.919	5.441	0.0347	0.032	9.392	18.391	20.519
6	16.611	6.054	0.0354	0.032	9.539	18.654	24.692
7	16.261	6.643	0.0362	0.032	9.716	18.984	28.792
8	15.872	7.205	0.0371	0.032	9.926	19.374	32.807
9	15.446	7.739	0.0382	0.032	10.171	19.927	36.726
10	14.986	8.243	0.0395	0.032	10.454	20.346	40.540
11	14.496	8.716	0.0409	0.032	10.776	20.936	44.240
12	13.979	9.157	0.0425	0.032	11.143	21.602	47.816
13	13.438	9.566	0.0443	0.032	11.558	22.350	51.262
14	12.876	9.943	0.0464	0.032	12.028	23.138	54.570
15	12.297	10.287	0.0488		12.558	24.123	57.735
16	11.703	10.600	0.0515	0.036	13.156	25.164	60.749
17	11.097	10.882	0.0546		13.834	26.323	63.609
18	10.483	11.134	0.0582		14.602	27.609	66.310
19	9.863	11.357	0.0623		15.478	29.035	68.848
20	9.240	11.554	0.0672	0.041	16.480	30.614	71.220
21	8.617	11.725	0.0730		17.636	32.355	73.421
22	7.997	11.872	0.0800		18.983	34.265	75.449
23	7.500	11.957	0.0833	0.046	20.573	36.340	77.301
24	6.700	12.072	0.0990				
25	6.400	12.110	0.1100				
26	6.000	12.150	0.1300				
27	4.800	12.150	0.1690				



The structural areas of the tank liner and diaphragm assembly felt to be the most critical are the girth weld and the polar bosses. Figure 10 illustrates the girth weld areas while Table 3 gives the type of stresses, the operating conditions, the induced stresses, the allowable strengths, and the resulting safety factors. It can be seen that ample margin exists for all critical areas. The proof "sizing" condition occurs during proof test of the wrapped tank in which the liner yields to match the expansion of the overwrap.

Analysis of diaphragm Section D and the liner/diaphragm weld (E) was conservative in that friction between the liners and diaphragm was ignored. Also, a weld efficiency of 80% was assumed.

The load directions associated with each mounting link were shown in Fig. 7 and 8. The maximum magnitudes of the loads as presented in Table 4 are 15 g's axial and 4.4 g's radial and lateral.

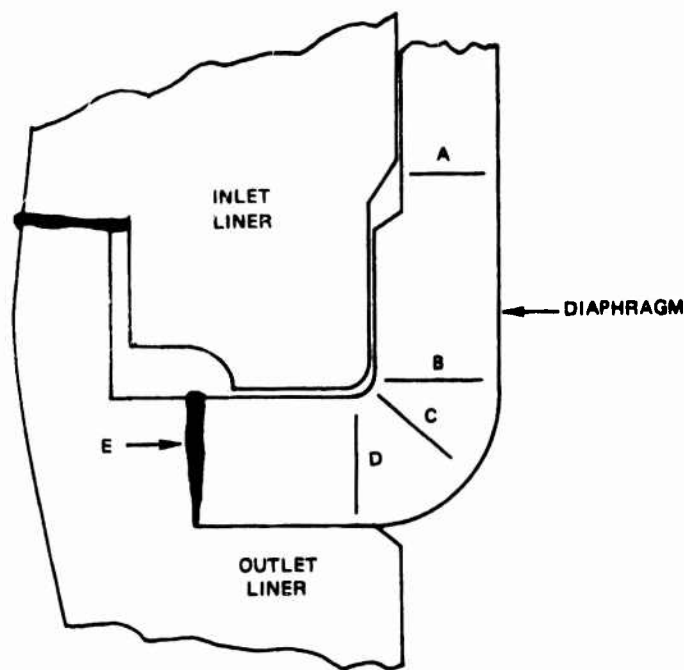


Figure 10. Critical Structural Areas

TABLE 3. STRESS SUMMARY

Area	Induced Stress, psi	Ultimate Strength, psi	Safety Factor	Mode/Condition
Polar Boss at Helical Wrap Opening	22,600	38,000	1.68	<ul style="list-style-type: none"> • Bending and Tensile • Proof Sizing
Diaphragm Section A	6,000	12,000	2.00	<ul style="list-style-type: none"> • Tensile • Proof Sizing • Yield
Section B	4,886	12,000	2.46	<ul style="list-style-type: none"> • Tensile • Proof Sizing • Yield
Section C	6,910	12,000	1.74	<ul style="list-style-type: none"> • Shear • Collapse Mode
Section D	8,460	12,000	1.42	<ul style="list-style-type: none"> • Shear • Proof Sizing
Section E	6,080	12,000	1.58	<ul style="list-style-type: none"> • Bending • Proof Sizing • Yield

TABLE 4. MAXIMUM STRUCTURAL LOADS

Acceleration, g's		Pressure, psia	Diaphragm Reversal, %	Load Condition
Axial	Lateral			
- 2.0	±4.4	0	0	Ground Handling
-15.0	±1.6	350	12	Stage IV Separation
- 1.0	±0.26	350	50	Expulsion
- 1.5	±0.39	350	90	Expulsion

When the girth mount is analyzed as a free ring, i.e., without being supported by the tank wall pressurized to 350 psia, the maximum twist deflection is 1.7 degrees, well within the yield point of the material. When considering the support provided by the tank, the deflections reduce substantially (almost an order of magnitude), so that the girth ring mounting concept should prove to be a reliable method with high structural margins.

Composite Helical Wrap Stresses. For balanced loading, neglecting any structural contributions of the resin matrix

$$\frac{N_t}{N_m} = \tan^2 \alpha \quad (4)$$

where

N_t = Tangential running load

N_m = Meridional running load

α = Local wind angle

This angle is defined by the following equation

$$\alpha = \sin^{-1} \left(\frac{r_E}{r_a} \right) \quad (5)$$

where r_E is the distance of the center of the winding band to the polar axis at its closest approach and r_a is the local value of this distance. As indicated by Eq. 5, the wrap angle increases along the contour from the equator (approximately 11 degrees) to the polar axis (90 degrees).

The load-sharing contribution of the aluminum liner also was neglected. At the design operating pressure, the liner is plastic and carries only about 10% of the load. It therefore serves primarily as a permeation barrier and wrap support.

In comparing the ellipse with the new balanced load contour, the envelopes are not significantly different. However, the tangential and meridional curvatures, and therefore the tangential and meridional running loads, are significantly different. The running loads were calculated from the following equations

$$N_t = \frac{p r_t}{2} \left(2 - \frac{r_t}{r_m} \right) \quad (6)$$

$$N_m = \frac{p r_t}{2} \quad (7)$$

where

p = Pressure

r_t = Tangential curvature

r_m = Meridional curvature

and are presented in Fig. 11.

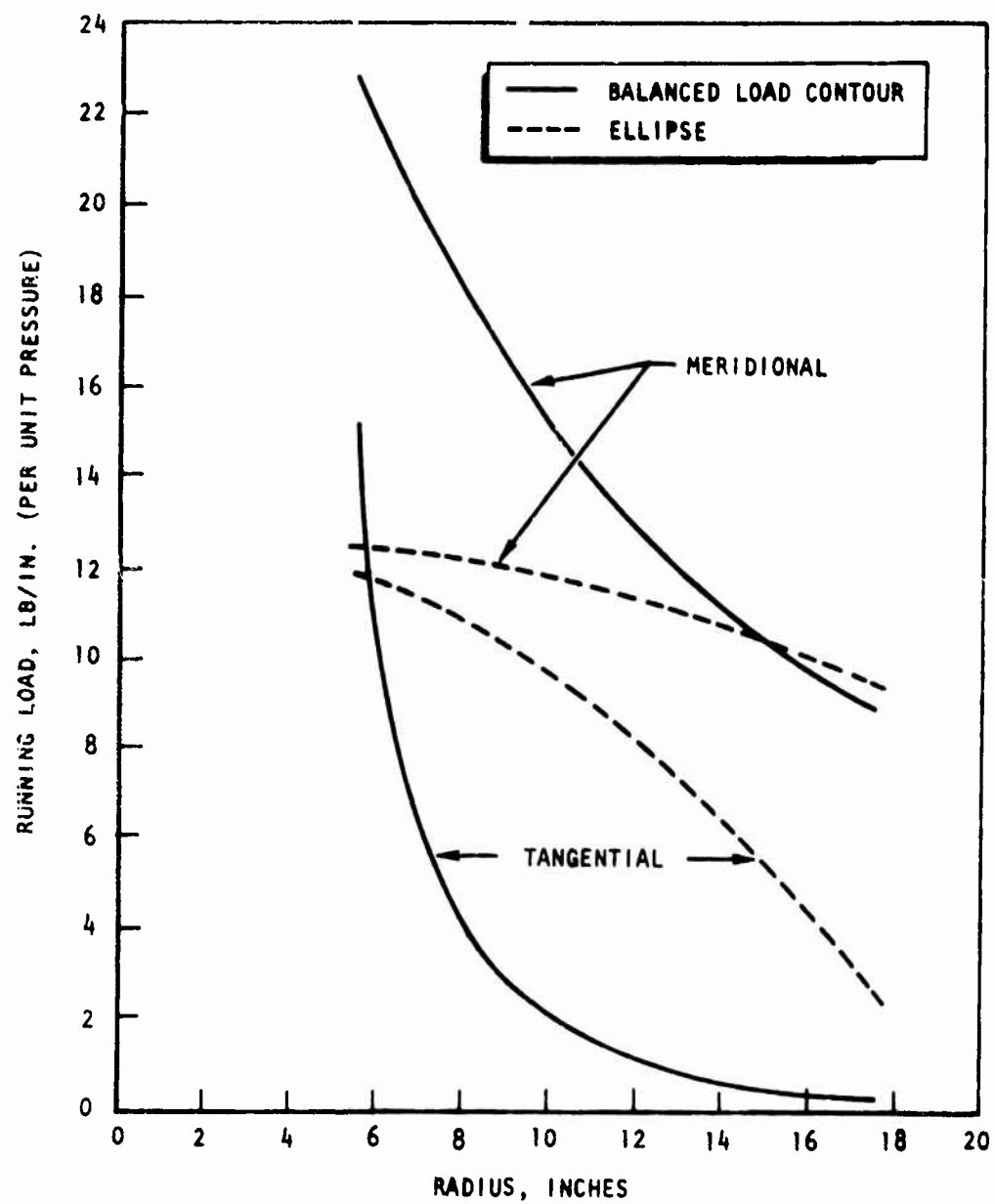


Figure 11. Composite Running Loads

The stresses were found by dividing the running loads by the local composite thickness, which varies according to

$$t = t_{Ref} \left(\frac{R_{Ref}}{R} \right)^{\frac{\cos \alpha_{Ref}}{\cos \alpha}} \quad (8)$$

where

R = Radial distance from polar axis

Subscript "Ref" = Reference value

The calculated thicknesses were presented in Table 2. The resulting stress curves (Fig. 12) show how the balanced-load contour takes best advantage of the fiber characteristics. At the larger radii, the wind angle is relatively small so that the meridional stress is high and the hoop stress is low. As the radius decreases, the wind angle increases and the fiber carries lower meridional loads and higher hoop loads. In contrast, the hoop stresses for an ellipse peak at an intermediate radius where the fiber is still at a relatively low wind angle. This overstressing causes excessive deflections and shear stresses in the non-isotropic composite material and results in a low burst pressure (approximately 100 psia). This problem would not occur with an all-metal elliptical contour, however, because of its isotropic material properties.

Brunswick test data show single-filament Kevlar fiber stresses to be approximately 500 ksi. This value is discounted to 320 ksi as a conservative allowable design fiber stress when helical winding several filaments per band. This accounts for differing filament tensions which affect their local load-sharing characteristics and filament damage (nicks and scratches) during handling and application. Because of the relatively low tank pressure, only two layers of filaments with the

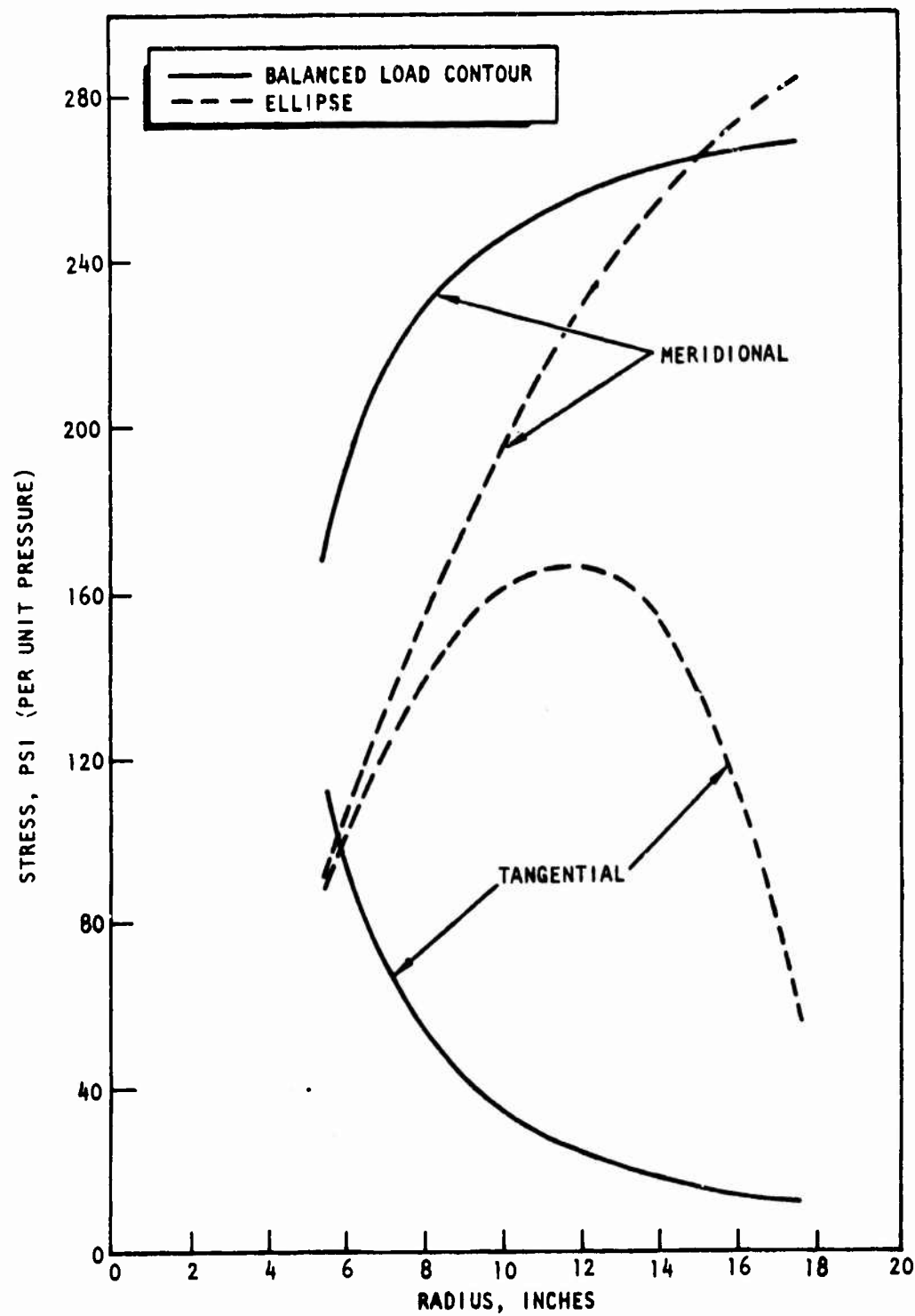


Figure 12. Composite Stresses

minimum recommended wrap density (filaments per inch) is required. Even with this minimum wrap, the tank pressure required for the actual stress to reach the allowable stress is 600 psia. Since the design burst pressure is 437.5 psia (233 ksi stress), additional design margin is provided. Since very little directly applicable test data are available relating to environmental effects (aging and temperature), this margin has been allocated to meet any degradation from these sources. Whether it is adequate is not known, but some information is available with respect to thermal effects.

The maximum time that the composite temperature is above 200 F is approximately 6 minutes and occurs during Mission Duty Cycle (MDC) 11. The worst-case maximum local temperature is 285 F during MDC I. Previous testing of single filaments maintained at this temperature (285 F) for 30 minutes in an oxidizing air environment showed a degradation of approximately 72 ksi, compared to the 87-ksi available margin. The data are not directly applicable, however, because single filaments were used. It should be noted that because of the balanced-load helical wind design, there should not be any movement of the filaments if the epoxy resin softens due to heating during the expulsion cycle.

Tank Deflections. Deflections of the wrapped tank under internal pressure were evaluated and the results are presented in Table 5 for the geometry presented previously in Table 2. Deflections of the liner internal surface at three points are tabulated for proof and design pressures. At any point, defined by the coordinates R and Z, there is an outward ΔR and ΔZ . Under proof pressure testing there is some yielding of the aluminum liner while the overwrap deflects, as evidenced by comparing the deflections at proof and post-proof pressures. The ΔR deflection at the girth was designed to have a negligible value to minimize the stress on the diaphragm weld. The large ΔR at the pole during proof testing requires

TABLE 5. TANK DEFLECTIONS

Location	Virgin (0 psig)		Proof (385 psig)		Post-Proof (0 psig)		Operating (350 psig)	
	R	Z	ΔR	ΔZ	ΔR	ΔZ	ΔR	ΔZ
A (Equator)	16.104	0.000	0.016	0.000	0.005	0.000	0.015	0.000
B	13.979	9.157	0.009	0.087	0.015	0.017	0.006	0.078
C (Near Polar Axis)	6.700	12.072	0.024	0.291	0.010	0.013	0.022	0.268

balancing the pressure across the diaphragm to prevent its movement. The post-proof deflections indicate the amount of diaphragm sizing to the liner that is required prior to loading propellants. These values are minimal and will not appreciably cold work the annealed aluminum diaphragm. At the 350-psig design conditions, all deflections are elastic. The deflection at each pole is 0.268 inch at 350 psig.

The loads created at the poles by the pressurant and propellant tubing as the tank deflects due to pressurization is dependent on the tubing design, i.e., bends and attachment to the stage structure. Since these aspects of the tubing design were not considered, the polar boss was designed for a moment of 160 in.-lb, which is the value required to yield a 0.5-inch-diameter, 0.028-inch-wall, 300-series stainless-steel tube.

Tank Buckling. An important design consideration was the inward buckling of the composite-wrapped tank wall under vacuum loaded propellant storage conditions. The lightweight, thin-wall structure has a large curvature and is susceptible to this failure mode. The critical buckling pressure is a function of modulus of elasticity (E), wall thickness (t), Poisson's ratio (ν), and normal radius (R).

$$P = \frac{K 2E}{[3(1 - \nu^2)]^{0.5}} \left(\frac{t}{R}\right)^2 \quad (9)$$

The coefficient K accounts for variations from the theoretical relationship based on test data. A value of 0.301 was taken from the Von Karman and Tsien results shown in Fig. 13. Column A of Table 6 shows the buckling pressure for theoretical spheres of radius R_2 at the contour points shown in Fig. 14.

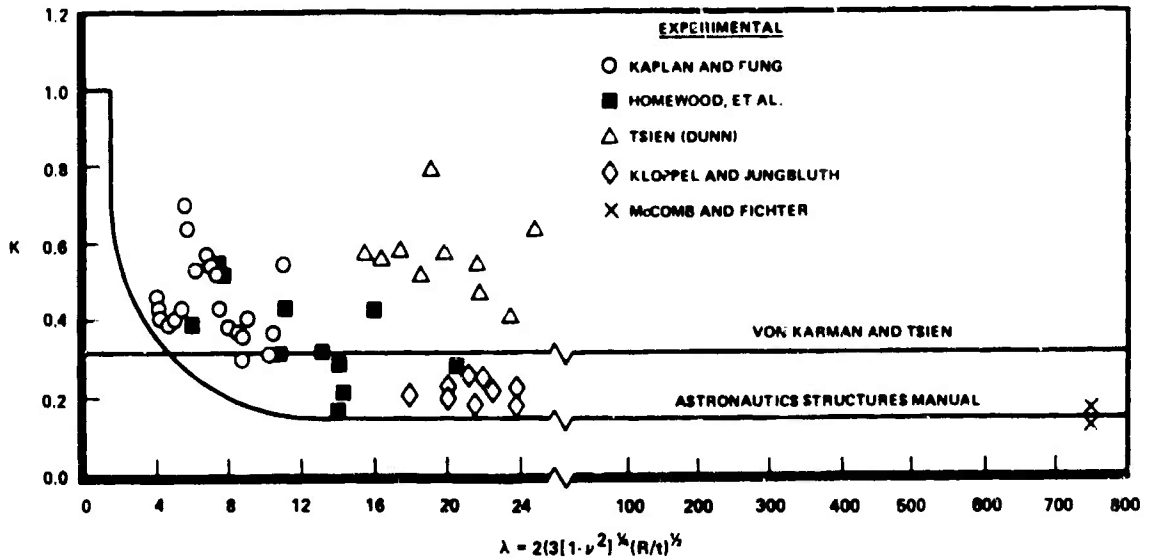


Figure 13. Buckling Coefficient

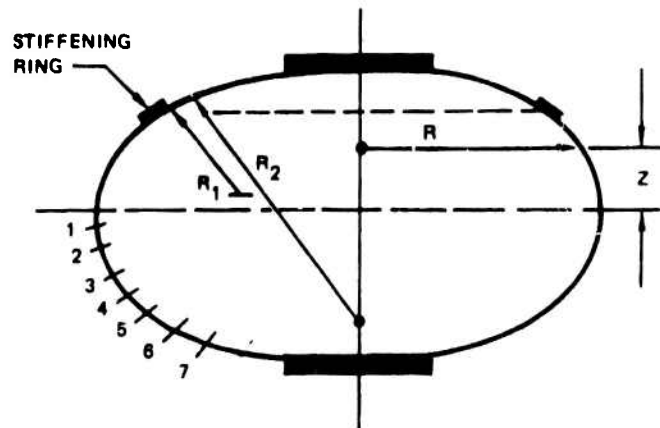


Figure 14. Buckling Pressure Illustration

These are conservative values since the stiffening effect of the smaller R_1 is not considered. The results indicate that buckling can occur between point 5 and the polar boss, i.e., less than atmospheric pressure is required. Column B assumes that stiffening rings of composite material, which are bonded to the wrapped tank, would force the buckling mode from R_2 to R_1 . The results indicate ample pressure margin even at location 7 (36.19 psi). Column C shows how the tank liner thickness could be varied to maintain a buckling pressure of 18.75 psi without stiffeners. This results in a weight increase of about 1.0 pound. The tank liners were therefore modified to the thickness contour shown in column C with a minimum of 0.032 inch.

Based on the factors considered, this analysis is believed to be conservative; however, it should be noted that the values shown assume a perfect bond between the liners and composite overwrap. This bond is very important to resisting buckling, e.g., without any bond, the buckling pressures at the most critical locations (near the poles) would be 20% of the values listed. For a very large, 5-inch-diameter unbonded area near the pole, the buckling pressures were estimated to be 60% of the stated values (Table 6). The critical pressure increases as the size of unbonded area decreases. Only a 5% reduction in buckling pressures was calculated for a 1-inch-diameter unbonded area, which is considered to be larger than will occur during fabrication. The effects of environmental factors, especially aging and thermal cycling, are not known, however. Although the fabrication process might result in no unbonded areas or only very small ones, environmental factors could deteriorate the bond.

Diaphragm Reversal Analysis

The desired reversing mode of the diaphragm is to "dish buckle" at the pole, followed by axisymmetric rolling away from the liner wall in increasingly larger diameters until "snap-through" occurs at the equator. The diaphragm curvature and stepped wall thickness both ensure this mode of reversal.

TABLE 6. BUCKLING PRESSURES

Location	R	Z	A		B		C	
			R ₂ Mode		R ₁ Mode		R ₂ Mode	
			R ₂	P _{CR}	R ₁	P _{CR}	t	P _{CR}
1	17.182	4.808	18.391	23.2	9.392	88.95	0.026	18.75
2	16.261	6.643	19.374	21.6	9.926	82.20	0.027	↓
3	14.986	8.243	20.936	19.6	10.776	73.95	0.029	
4	13.438	9.566	23.188	17.4	12.028	64.66	0.032	
5	11.703	10.600	26.323	15.1	13.834	54.66	0.036	
6	9.863	11.357	30.614	13.0	16.480	44.85	0.041	↓
7	7.997	11.872	36.340	11.6	20.573	36.19	0.046	18.75

Dimension in inches; pressures in psia

Initial buckling occurs at 1.2 psi, followed by the rolling mode at approximately 2 to 3 psi until 90% of the propellant is expelled. From this point, the diaphragm pressure differential (ΔP) increases steadily to 25 psi at an expulsion efficiency of 98.1%.

The polar region is flat to a half angle of 26 degrees and has a thickness of 0.026 inch. The wall thickness is then stepped to 0.034 inch between 35 and 50 degrees, to 0.039 inch between 50 and 70 degrees, and to 0.044 inch between 70 degrees and the radius at the equator. The radius is 0.061 inch thick. The results of the analyses indicate that the ΔP to roll is less than that required for buckling at any location after the thinnest section buckles. Also, the ΔP required to buckle increases along the contour from the pole to the equator. This helps resist the propagation of random buckles that might cause critical folds and tearing of the diaphragm.

Figure 15 relates the reversal positions of the diaphragm, i.e., height (Z) and angular location (θ), and the diaphragm's percent volume reversal. It should be noted that the percent volume reversal is not the same as percent propellant expelled because of the propellant vapor ullage, which is dependent on temperature.

The equation used to calculate the pressure required to buckle the diaphragm is the same as that utilized in analyzing tank buckling (Eq. 9). The larger of the two colinear radii of curvature (R_2 , the length of the line perpendicular to the contour from the contour to the intersection of the polar axis) was used to yield a low, conservative value to compare to the desirable rolling-mode pressure.

Rolling Mode Analysis. The predicted pressures for rolling were based on Ref. 1. Figure 16 illustrates a cylinder rolling outside-in. The force required to roll is a result of the energy to bend the cylinder and that required to increase the cylinder's diameter.

$$F = \frac{A\sigma_y}{2} \left[\frac{1}{c} + \frac{2ct}{D} \right] \quad (10)$$

where

$$A = \pi Dt$$

$$\sigma_y = \text{yield stress}$$

$$c = \text{curvature parameter}$$

The terms $(1/c)$ and $(2ct/D)$ represent the bending and hoop stresses, respectively. Because one term is inversely proportional and one is directly

Ref. 1. Guist, LeRoy R., and Donald P. Marble: Prediction of the Inversion Load of a Circular Tube, NASA TN D-3622, September 1966.

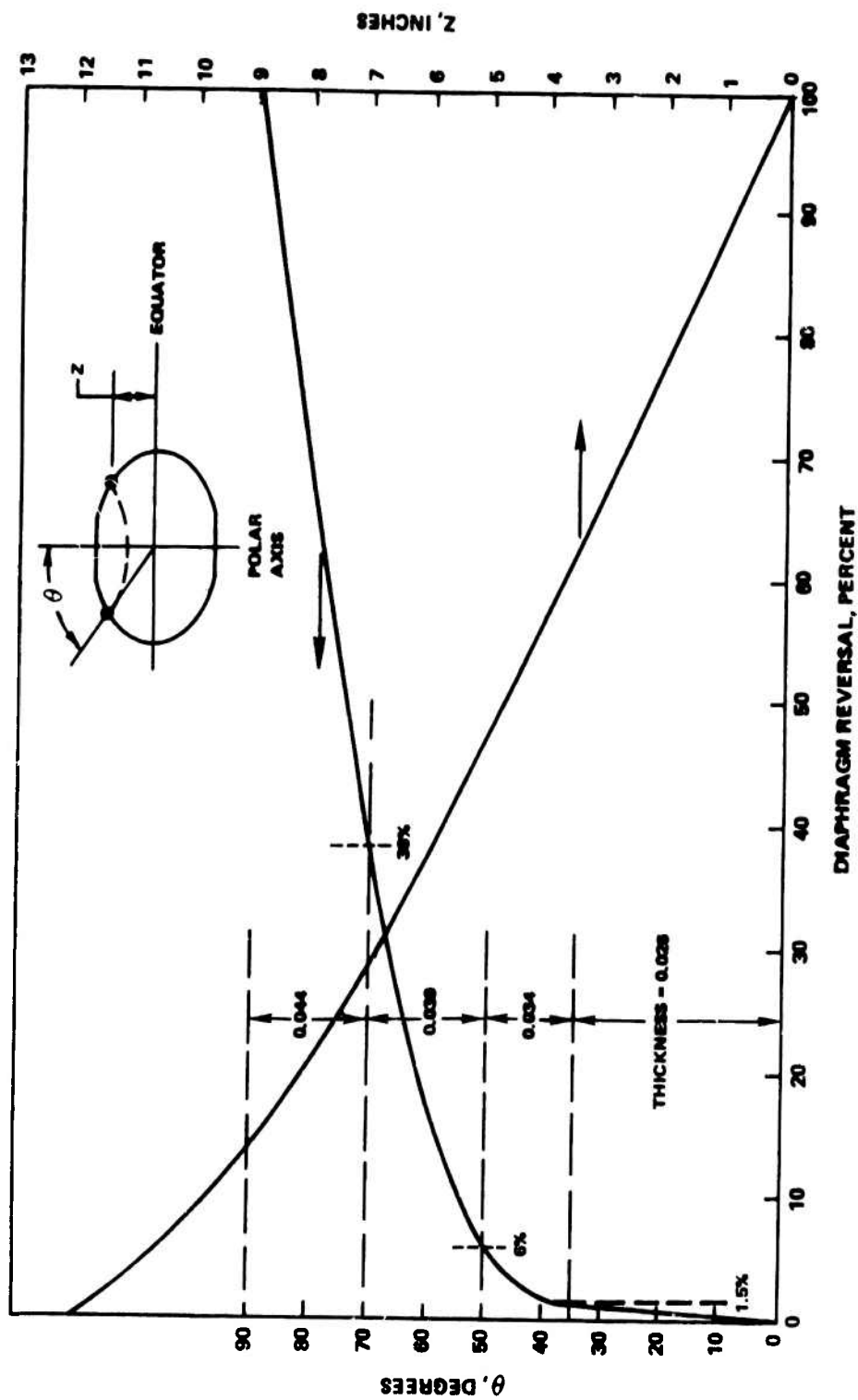


Figure 15. Diaphragm Reversal Geometry

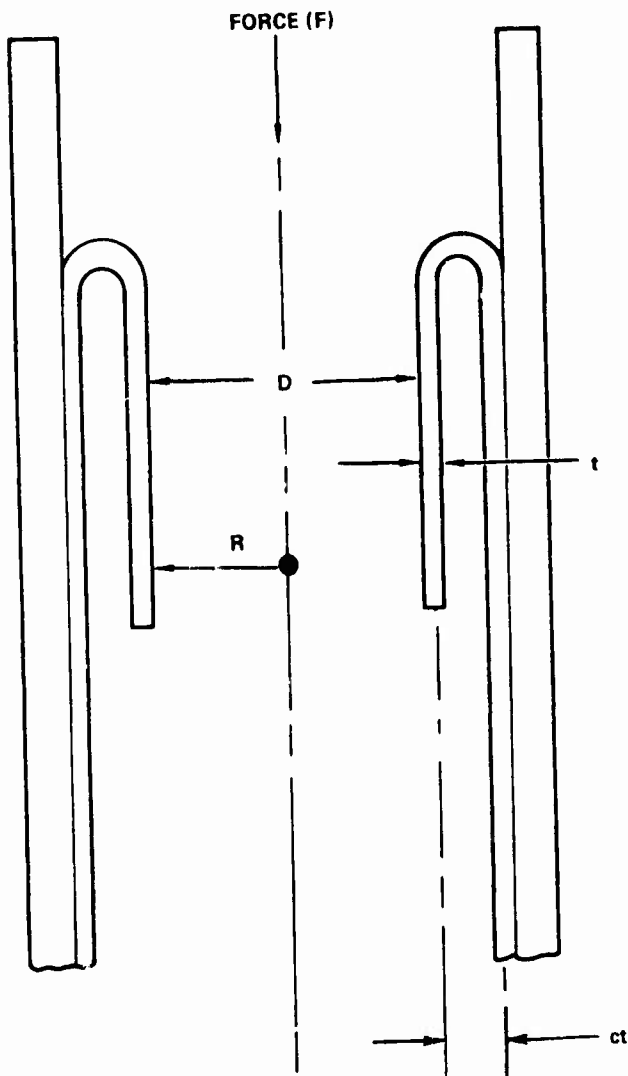


Figure 16. Cylinder Rolling Outside-In

proportional to c , the term in brackets in Eq. (10) has a minimum value with respect to c . Hypothesizing the rolling process will occur at this minimum value requires that

$$c = c_m = (D/2t)^{0.5} \quad (11)$$

A cube root was substituted for the square root in the relationship expressed in Eq. (11) to match the Ref. 1 data reproduced in Fig. 17. The ratio of diaphragm thickness to diameter is less than approximately 0.003 along the curved portion of the diaphragm, which is at the lower range of the t/D values in Fig. 17. Also, the contoured diaphragm geometry is not the same as bending a tube outside-in except at the equator. At other locations, the bend angle is less than 180 degrees. Because of this, the term $(2ct/D)$ was modified by making it a sinusoidal function of half the bend angle $(\theta/2)$. These two modifications imply that

$$c_m = \left[\frac{D}{2t \sin(\theta/2)} \right]^{1/3} \quad (12)$$

and

$$F = \frac{A\sigma_y}{2} \left[\frac{1}{2c^2} + \frac{2ct \sin(\theta/2)}{D} \right] \quad (13)$$

substituting

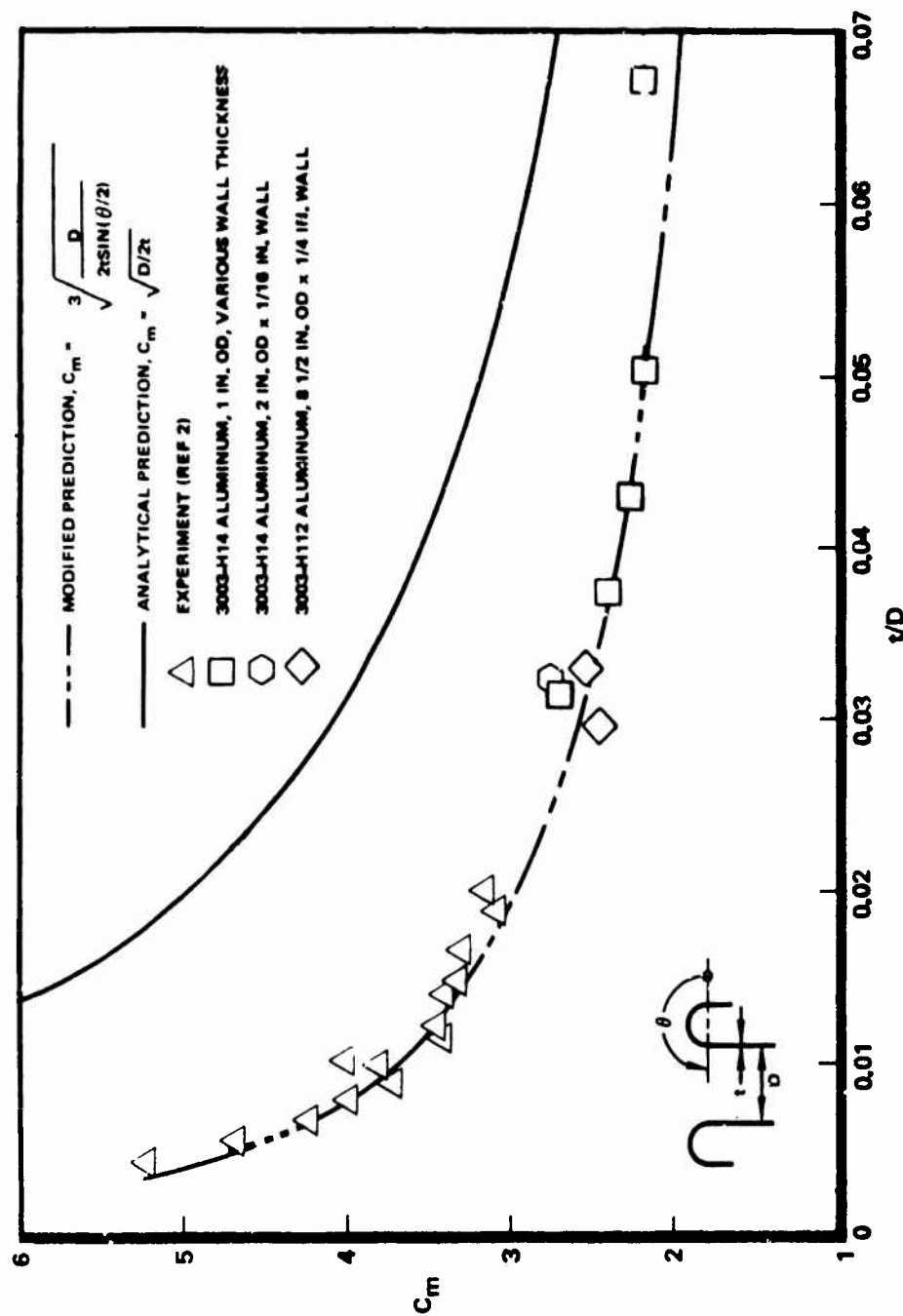
$$F = \frac{P\pi D^2}{4} \quad (14)$$

into Eq. (13) where

$$P = \text{pressure}$$

results in

$$P = \frac{t}{D} \sigma_y \left[\left(\frac{2t \sin(\theta/2)}{D} \right)^{1/3} + 2 \left(\frac{2t \sin(\theta/2)}{D} \right)^{2/3} \right] \quad (15)$$



Ref. 2. Kroell, C. K.: "A Simple, Efficient, One-Shot Energy Absorber," Shock, Vibration, and Associated Environments, Part III, Bulletin 30, 30th Symposium on Shock, Vibration, and Associated Environments. Detroit, Michigan, Oct. 10-12, 1981.

Figure 17. Curvature Parameter

To verify Eq. 15, Rocketdyne's IR&D half-scale plastic tank diaphragm was analyzed and compared to the test data. The stress-strain diagram for the diaphragm material (1100-0) is presented in Fig. 18 and indicates that cold working occurs at relatively low values of stress, such as during the rolling mode. Therefore, a conservative yield stress of 12,000 psi was assumed. Figure 19 indicates a close comparison between Eq. 15 and the test data.

Predicted Diaphragm Reversal Mode. The reversal mode of the diaphragm with nominal thicknesses is presented in Fig. 20 as a function of percent reversal. Initially, the thin (0.026 inch) flat portion near the polar axis buckles at a differential pressure of 1.2 psi. The buckling ΔP increases from 1.2 to 2.0 psi along the curved surface between the flat section and the first step increase. Because the rolling mode ΔP is approximately 2.0 psi at the step, a transition to the rolling mode occurs. Because of the step thickness change, the rolling mode becomes the preferred mode in the 0.034-inch-thick section, i.e., the ΔP for rolling is less than that required for buckling. On the thick side of this first step, 3.4 psi is required for buckling and the value increases as you move toward the next step because of the decreasing local radius of curvature. The ΔP to sustain rolling decreases from 2.7 psi, however, because of the increasing diameter of the diaphragm.

At the start of the 0.039-inch-thick section, 8.4 psi is required for buckling, but only 2.7 psi for rolling. It can be seen that the margin between buckling and rolling continues to increase with percent reversal because of the diaphragm's thickness, diameter, and local radius of curvature.

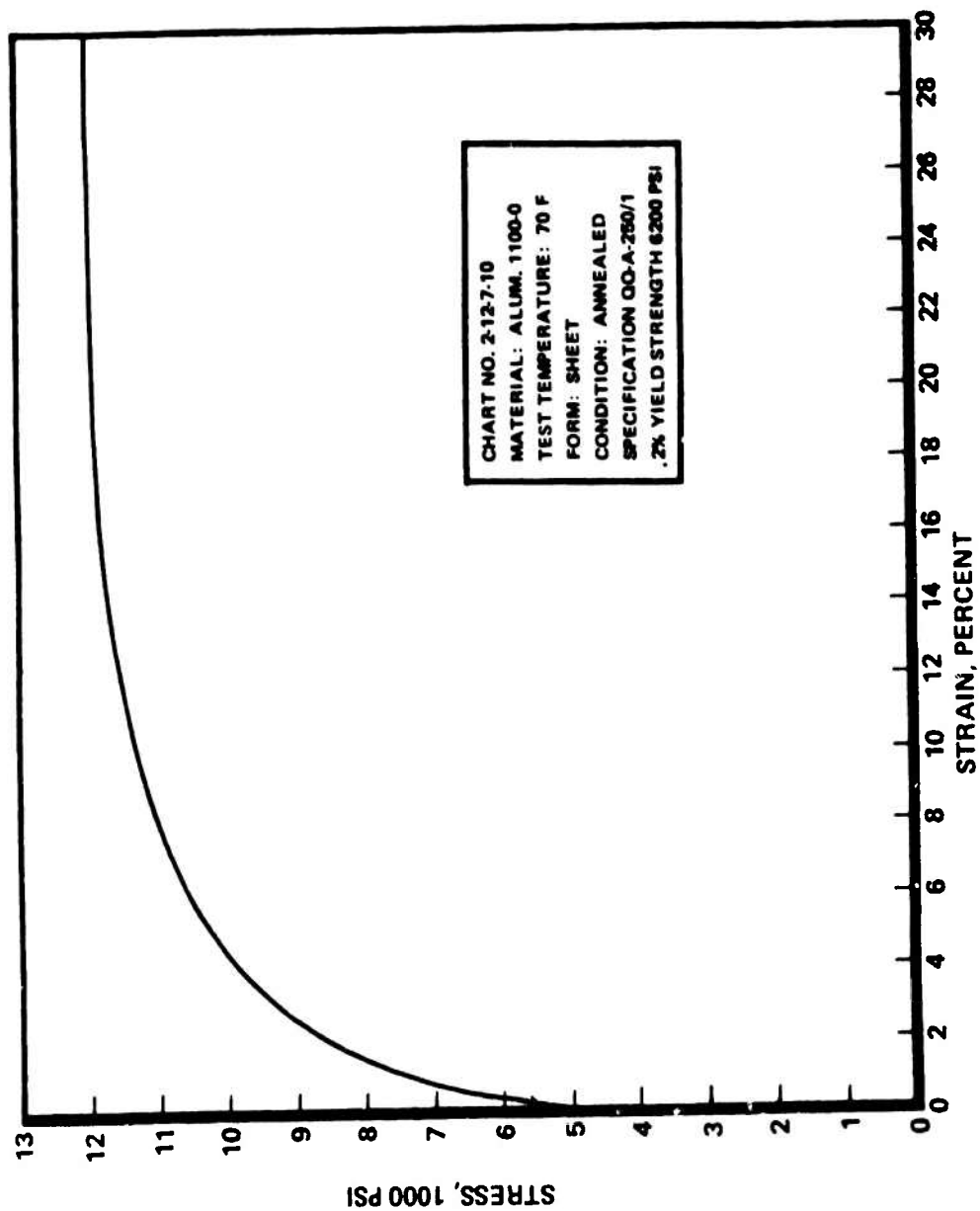


Figure 18. Stress-Strain Diagram

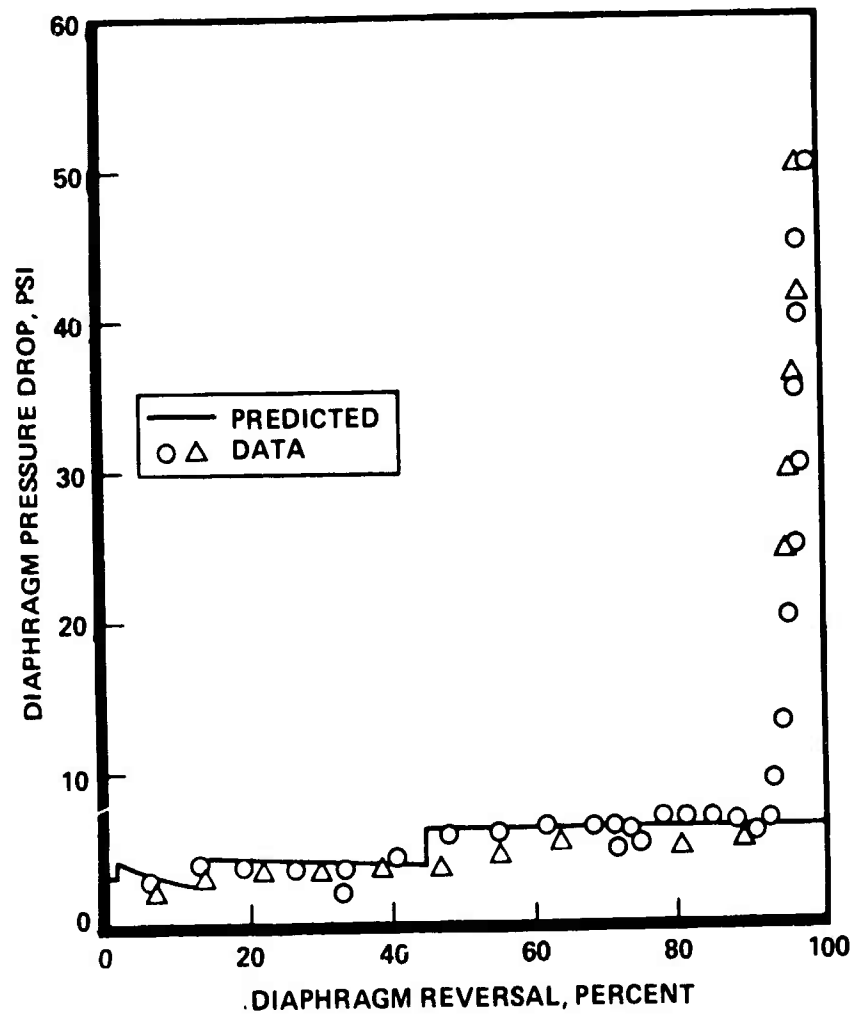


Figure 19. Comparison of Diaphragm Rolling Mode Pressure Prediction With Test Data

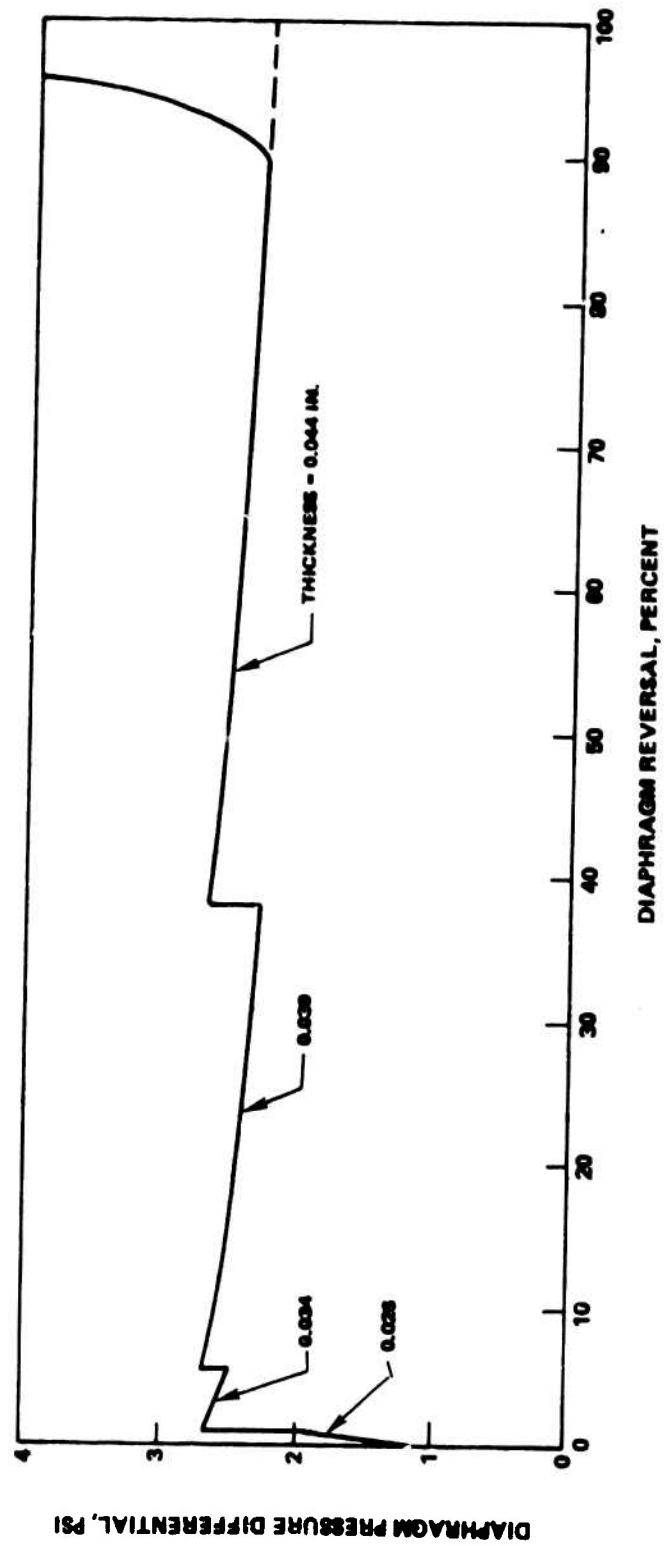


Figure 20. Nominal Diaphragm Reversal Mode

At the start of the thickest section (0.044 inch), the buckling ΔP is 18.4 psi, compared to 2.7 for rolling. At the end of the expulsion cycle, the ΔP deviates from the rolling mode as the diaphragm is pressed against the tank liner to expel the remaining propellant. Table 7 summarizes the predicted ΔP 's.

Predicted Worst-Case Reversal Mode. The worst-case reversal mode, i.e., the smallest margin between buckling and rolling, also was considered. For this analysis, a buckling coefficient of 0.14 was used (Fig. 13, Astronautics Structures Manual, lower bound of data for the values of λ between approximately 50 and 100). Also, the thinnest diaphragm permitted by manufacturing tolerances was used. The resulting reversal mode is presented in Fig. 21. Of greatest significance is the analytical prediction of buckling in the nominal 0.034-inch-thick section. It should be noted, however, that reversal of this section is complete at 6.0 percent (by volume) and for low storage temperatures will only be collapsing the propellant vapor volume. A comparison of ΔP 's for this case was included in Table 7.

TABLE 7. COMPARISON OF DIAPHRAGM ROLLING AND BUCKLING ΔP 's

Nominal Thickness, inch	Location	Nominal Thicknesses		Minimum Thicknesses	
		ΔP Roll, psi	ΔP Buckle Spherical $K=0.301$, psi	ΔP Roll, psi	ΔP Buckle Spherical $K=0.14$, psi
0.026	Flat Section	--	1.2	--	0.5
0.026	Curved Section at Step	2.0	2.0	1.9	0.9
0.034	At 0.026 Step	2.7	3.4	2.5	1.4
0.039	At 0.034 Step	2.7	8.4	2.5	3.5
0.044	At 0.039 Step	2.7	18.4	2.5	7.8

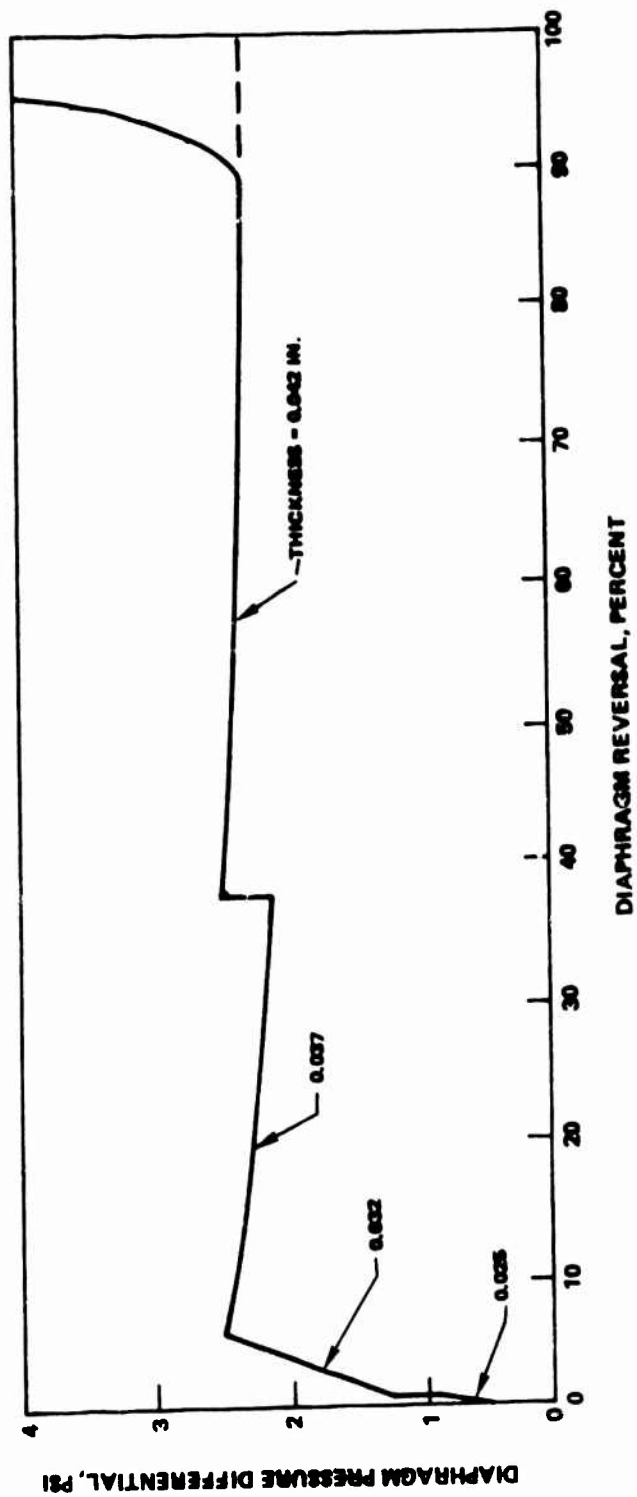


Figure 21. Worst-Case Diaphragm Reversal Mode

The effect of the local radius of curvature and thickness, including tolerances, on buckling ΔP for the curved and conical sections is presented in Fig. 22. These data correspond to a worst-case buckling coefficient of 0.14.

Valves

Each PSA has four valves. Two are mounted in the propellant outlet boss and used for filling and draining the propellant, and isolating the propellant during storage. The other two are mounted in the pressurant inlet boss and are used to evacuate the volume between the diaphragm and pressurant inlet half liner, and isolate the PSA from the pressurization subsystem.

Propellant Fill and Drain. The tank will be filled through the valve shown in Fig. 23. It is a Pyronetics model 1811 valve, with modifications to the body for welding into the propellant outlet polar boss. It has a metal-to-metal seal that is closed mechanically by rotating the retainer nut to pull the center poppet against the outer body seat. The seat has a minimum 100 cycle life. Separate fittings are provided for the N_2O_4 and MMH. The proof pressure is 600 psia and the burst pressure is 800 psia. Two caps are welded over this valve for dual-weld containment.

Vacuum Service. The vacuum service valve is used to evacuate the cavity between the diaphragm and pressurant inlet half liner before the tank is filled with propellant. The vacuum helps maintain contact between the diaphragm and liner, provides a means of detecting a leak, and permits vacuum filling of the tank by equalizing the pressure across the diaphragm.

Figure 24 shows a fully developed Pyronetics model 1146-1 valve with the same type of mechanically actuated metal-to-metal seat as the fill and drain valve. The seat has a minimum 100 cycle life. The proof and burst pressures are 6000 and 8000 psig, respectively. The valve is screwed into the pressurant inlet boss and a cap is welded over it.

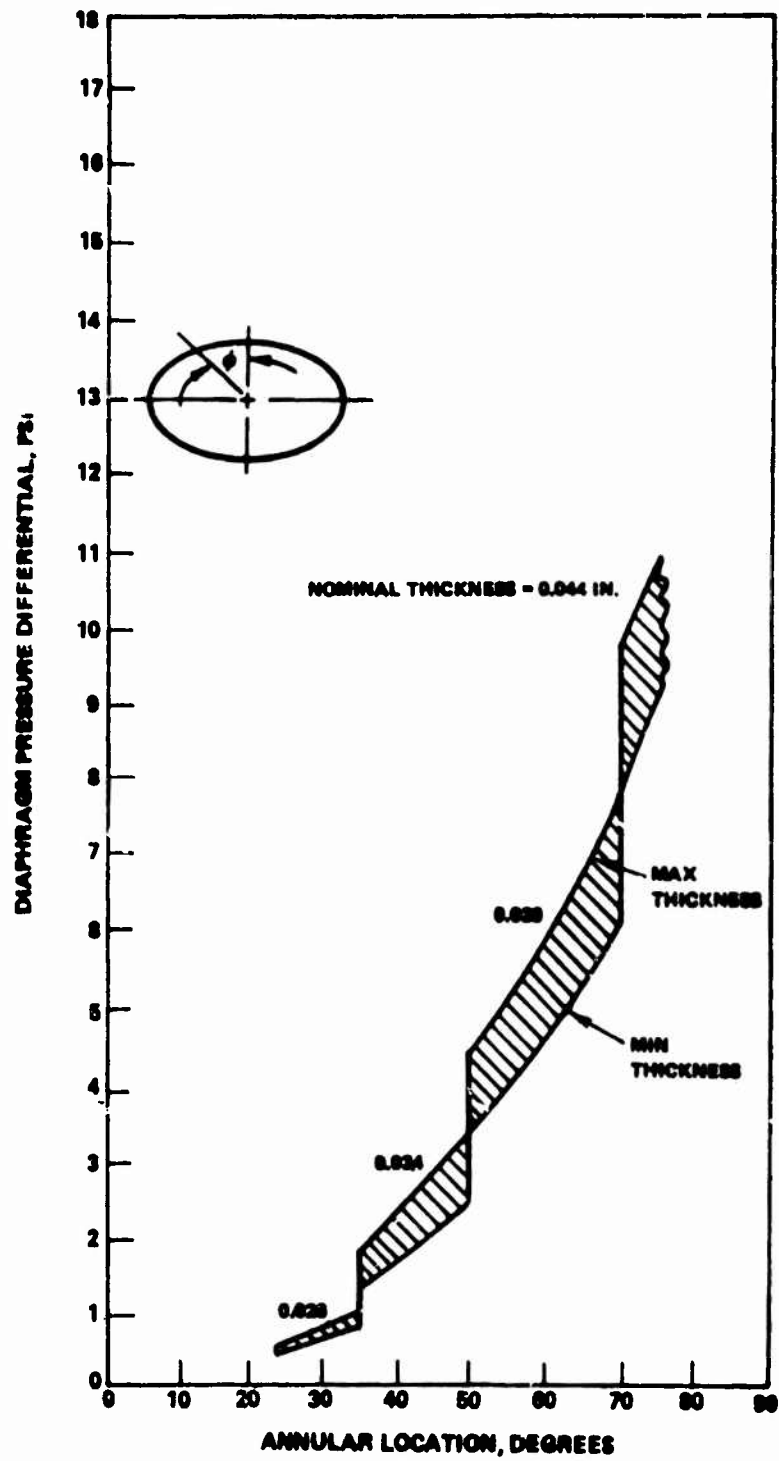


Figure 22. Diaphragm Pressure Differential Required for Buckling

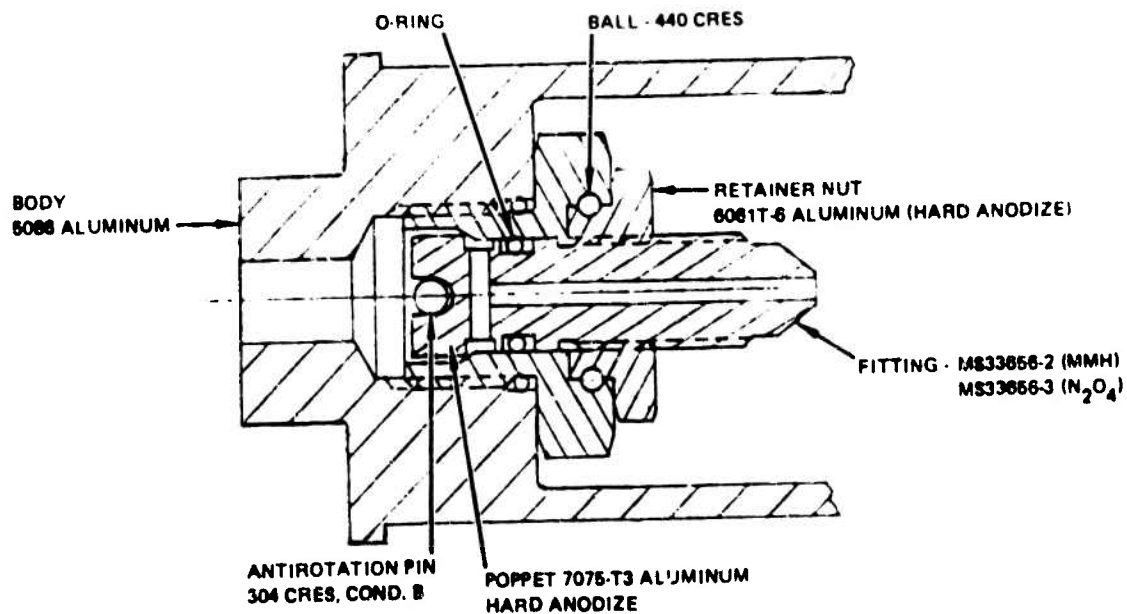


Figure 23. Fill and Drain Valve

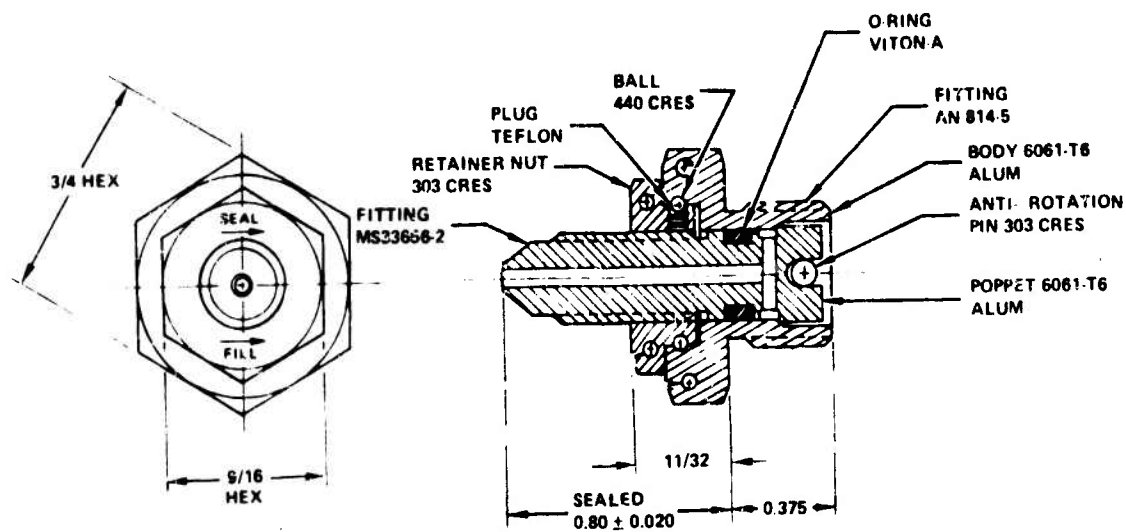


Figure 24. Vacuum Service Valve

Propellant Outlet. A pyrotechnically actuated valve is used for propellant isolation. The fully developed Pyronetics model 1498 valve with modified inlet and outlet ports was selected for this application. This valve is shown in Fig. 25 after actuation. The cap on the inlet nipple is sheared off by a ring slide that encircles the cap. The slide is driven by a piston and a protrusion on the slide locks in a plug, which prevents the slide from rebounding after actuation. The piston and housing are tapered to provide a metal-to-metal locking seal. The trigger mechanism consists of a squib activated by a 28-volt signal.

Pressurant Inlet. A fully developed Pyronetics model 1470 valve with modified inlet and outlet ports was selected to isolate the PSA from the pressurization subsystem. This valve prevents loss of the vacuum between the diaphragm and tank liner. Like the propellant isolation valve, it is pyrotechnically actuated. Figure 26 shows a sectioned drawing before actuation.

The end caps on both the inlet and outlet nipples are sheared by the single-piece piston, which has an oversized hole to permit flow after actuation. Both piston and housing are tapered to provide a metal-to-metal locking seal.

Leak Detector

The dual-wall containment provided by the diaphragm and pressure inlet half liner offers the potential for detecting leakage in either of these parts by monitoring the pressure in the cavity between them. This volume is evacuated so the propellant can be vacuum loaded without collapsing the diaphragm. It remains at vacuum until the tank is pressurized to initiate the expulsion cycle.

A consideration in the selection of a pressure measurement device was the ability to apply proof pressure to the instrument, after installation, without impairing its subsequent performance in measuring vacuum-level pressures. Devices that could not withstand proof pressure were disregarded because they

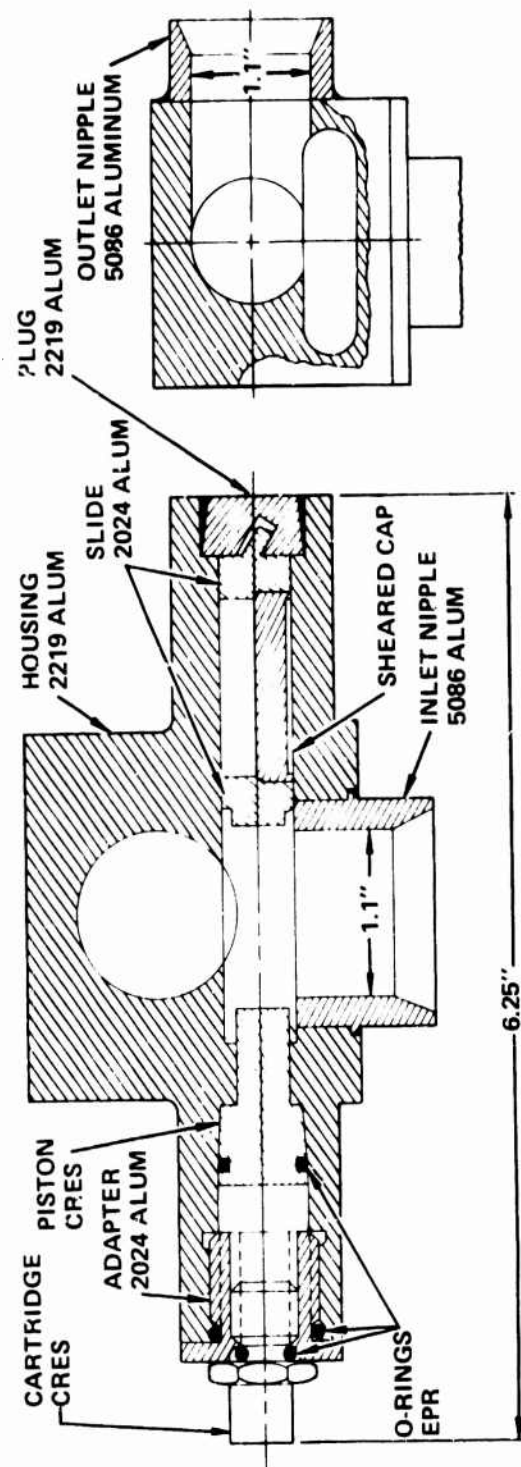


Figure 25. Propellant Outlet Valve

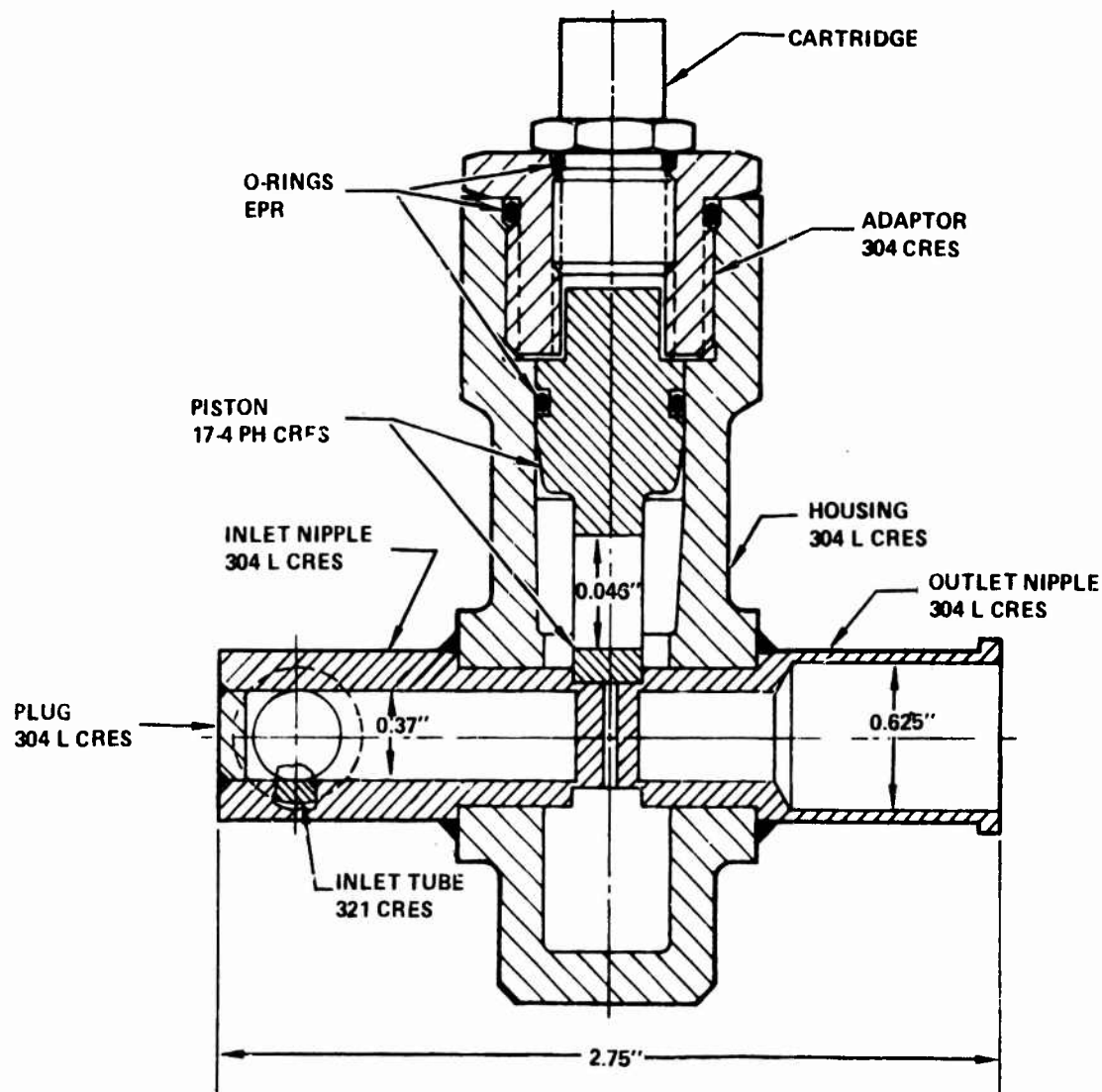


Figure 26. Pressurant Inlet Valve

would have to be installed after proofing with a subsequent low-pressure leak test. Also, to avoid any design and development problems associated with incorporating a mechanical stop behind the diaphragm on a pressure switch, a simple off-the-shelf vacuum gauge was selected for leak detection. This approach also provides an alternative for comparative evaluation with the pressure switch utilized in one of AFRPL's other feed system programs.

The selected instrument is a Teledyne Hastings-Raydist model VT-4 vacuum gauge with a model DV-34 gage tube. It has a usable range of 0.002 to 0.39 psia and a best sensitivity range of 0.004 to 0.10 psia. The accuracy is 2% of the full-scale angular meter deflection, which has a logarithmic scale. The maximum pressure and temperature are 600 psig and 575 F.

Operation is based on a noble metal thermopile circuit. The hot junctions are heated directly by an alternating current while the cold junctions are kept at ambient temperature by the mounting studs. Thus, a d-c voltage is generated between the hot and cold junctions. An increase in pressure increases the thermal conductivity of the gas and tends to decrease the temperature of the hot junctions and the output of the thermopile. A third unheated couple is connected in opposition to the heated couples and responds to sudden ambient temperature changes, providing compensation for transient temperature effects.

The maximum gage tube thermopile temperature is approximately 480 F in a high vacuum and its d-c voltage output is 10 mv. The power requirement of the tube is 0.01 watt (0.029 amp, 0.32 volts ac). The instrument has a continuous-use life of 3 years and therefore intermittent operation is recommended. The response time is less than 0.2 second.

The vacuum gage selected requires 115-volt a-c power; however, 230-volt a-c and battery-operated units are available. A recorder and alarm also are available. The gage tube requires a Bendix connector type PC-06W-8-4S and adapter cable type OM-1-MSF.

Figure 27 presents the dimensions of the vacuum gage tube, which is purchased off-the-shelf. The external case of the valve is made from 304L stainless steel and therefore requires a bi-metal aluminum/stainless-steel transition tube for welding to the 5086-0 polar boss on the tank.

Leakage Integrity

The leak-free integrity of the PSA is maintained by using properly selected materials and joining processes in combination with partial dual-wall propellant containment to minimize the opportunity for leakage. The diaphragm and propellant outlet half of the liner provide the primary containment of the propellant. The minimum original material thickness is 0.025 inch. The 1100-0 aluminum diaphragm and 5086-0 aluminum liner are joined at the equator with an EB weld as shown in Table 8 (number 10). Dual-weld containment is provided by joining the pressurant inlet half of the liner (5086-0 aluminum) to the propellant outlet half at the equator with another EB weld (number 22). Applicable section techniques are also presented in Table 8.

Only visual, penetrant, and low-pressure leak testing are available for inspecting the diaphragm/liner weld. Meaningful ultrasonic inspection is unlikely and X-ray would not be directly useful. The step adjacent to the weld will be used as a dimensional aid to visual/manual tracking of the weld and for verification afterward. Restraining tooling will be used and relatively slow speeds are planned. With match-machined parts, pre-weld (and perhaps post-weld) samples, and in-process inspection checkoff and monitoring of critical parameters, full joint fusion can be obtained.

Similar comments also are applicable to the liner-to-liner weld, except that X-ray will be used with the film on the opposite side of the tank. However, this will not reliably detect mistracking or lack of fusion. A scribe line will be placed parallel to the joint as a tracking aid. Verification of tracking and penetration by grinding to joint depth may be used as a supplementary method on this joint.

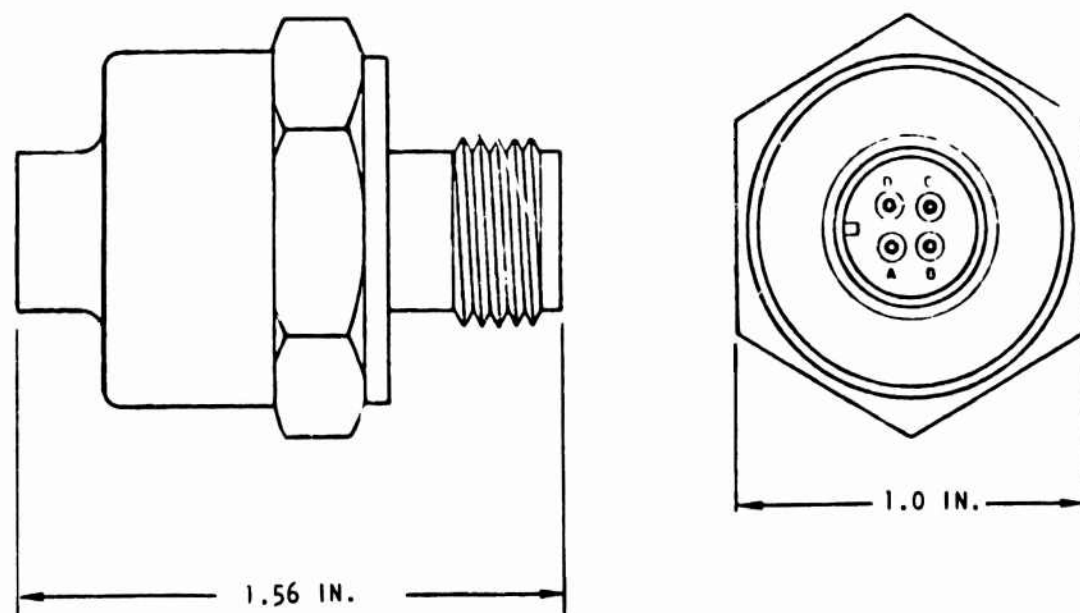


Figure 27. PSA Leak Detector

TABLE 8. WELDS

Weld No.	Weld Location	Type of Joint	Weld Process	Inspection Method	Class	Joint Materials
1	Fill and Drain Valve/ Polar Boss	Square Butt	EB	X-Ray	I	5086/5086
2	Fill and Drain Valve Cap/Polar Boss	Corner	TIG	Penetrant	II	
3	Fill and Drain Valve/ End Plate					
4	Fill and Drain Valve Cap/End Plate					
5	Outlet Valve/Polar Boss	Square Butt	EB			
6	Outlet Valve/Polar Boss					
7	Collector Plate/ Polar Boss					
8	Outlet Liner/Polar Boss			X-Ray	I	
9	Outlet Liner/Polar Boss	Lap	TIG	Penetrant	II	
10	Liner/Diaphragm	Square Butt	EB	Penetrant, Helium	I	
11	Leak Detector/ Bi-Metal Coupling	Corner	TIG	Penetrant	I	304L/304L

TABLE 8. (Cont)

Weld No.	Weld Location	Type of Joint	Weld Process	Inspection Method	Class	Joint Materials
12	Polar Boss/Leak Detector Bi-Metal Coupling	Square Butt	TIG	Penetrant	II	5086/5086
14	Polar Boss/Vacuum Service Valve Adapter Plate	Square Butt	EB			
15	Vacuum Service Valve Cap/Adapter Plate	Edge	TIG			
16	Inlet Valve/Bi-Metal Coupling	Square Butt	EB	X-Ray	I	304L/304L
17	Polar Boss/Bi-Metal Coupling					
18	Diffuser Plate/Bi-Metal Coupling			Penetrant	II	
19	Diffuser Assembly Weld			Penetrant	II	
20	Inlet Liner/Polar Boss			X-Ray	I	5086/5086
21	Inlet Liner/Liner Ring	Lap	TIG	Penetrant	II	5086/5086

TABLE 8 . (Conc)

Weld No.	Weld Location	Type of Joint	Weld Process	Inspection Method	Class	Joint Materials
22	Liner Girth Weld	Square Butt	EB	X-Ray	I	5086/5086
23	Mount Ring/Mount Band					
24	Mount Ring/Mount Band					

No. 13 Deleted

Dual-weld containment at the propellant outlet valve/polar boss (both 5086 aluminum) is provided by two EB welds (numbers 5 and 6). The fill and drain valve (5086 aluminum) is joined to the outlet boss with an EB weld (number 1). As a backup, a 5086 aluminum cap is TIG welded around the valve to the boss (number 2). To make this weld prior to wrapping the tank and to provide dual-weld containment against leakage through the valve, the end plates are TIG welded over the valve and cap (numbers 3 and 4). The third set of redundant welds at the outlet are at the joint between the polar boss and liner. An EB weld (number 8) is used for structural integrity and a TIG weld (number 9) for sealing.

Because the propellant is contained by the diaphragm, only single welds were required at the pressurant inlet joints. The end of the 304L stainless steel pressurant isolation valve outlet nipple is EB welded (number 16) to the 304L section of the bi-metal coupling. The other end of the coupling (5086 aluminum) is EB welded (number 17) to the inlet polar boss (5086 aluminum). The third weld required is the EB weld (number 20) to join the inlet liner and polar boss. Two additional welds are required for the leak indicator. The 5086 aluminum instrumentation boss is joined to the polar boss using a TIG weld (number 12) and the 304L section of the bi-metal coupling is TIG welded (number 11) to the 304L stainless-steel indicator. Two more welds are required for the vacuum service valve. The 5086 aluminum adapter plate is EB welded (number 14) to the polar boss, and the 5086 aluminum valve cap is joined to the adapter with a TIG weld (number 15).

Six more welds are required for assembly of the pressurant inlet and propellant outlet plates, and the mounting ring. These welds, not related to leakage integrity, are discussed in the Fabrication section.

Thermal Analysis

The primary thermal considerations in the design of the propellant tank were to minimize the diaphragm, liner, and composite overwrap temperatures, and

to maximize the final pressurant gas temperature. Minimizing material temperatures was desirable to utilize a lightweight, low-cost aluminum diaphragm and liner, and to keep from approaching the composite cure temperature. Maximizing the final pressurant temperature results in reduced pressurization component weights. Fortunately, these two requirements are compatible in that both can be achieved by minimizing the heat transfer rate between the gas and tank.

Pressurant Inlet Diffuser. The reacted Tridyne enters the tank at steady-state temperatures between 1025 and 1051 F, depending on storage conditions. After passing through the stainless-steel inlet tube, the gas is distributed by a stainless-steel shower-head-type diffuser plate. A worst-case analysis was conducted to show the adequacy of the diffuser plate. Laminar stagnation heat transfer was assumed for a single large stream impinging on the diaphragm without propellant behind it. A gas temperature of 1025 F was utilized with a 0.026-inch-thick diaphragm initially at 70 F. It took 6.4 seconds for the diaphragm to reach 300 F. In addition to slowing down the impingement velocity, the diffuser plate will spread the flow over a large diaphragm surface area. Further, initial diaphragm reversal will occur almost instantaneously to ensure contact with the propellant since less than 2 psi is required. This will permit the diaphragm to be cooled with propellant. Consequently, no local diaphragm heating problems are anticipated.

Conduction of heat from the steel inlet tube and diffuser plate to the aluminum polar boss assembly is controlled by minimizing the area of contact. Of greatest importance is contact with the inlet tube because it has the highest gas velocity. An additional heat transfer advantage inherent in the tank design concept is that reversal of the diaphragm is in line with the inlet port, which avoids flow of warm gas along the tank wall.

Propellant Tank Model. The transient thermal analysis of the PSA was accomplished with a specialized model used in conjunction with Rocketdyne's Differential Equation Analyzer Program (DEAP), which provides a basic tool for

the solution of second-order partial differential equations. The general hyperbolic differential equation can be represented as

$$\nabla \cdot (K \nabla \phi) + \tilde{W} \cdot \nabla \phi + s\phi + q = \lambda \frac{\partial^2 \phi}{\partial t^2} + \rho c \frac{\partial \phi}{\partial t} \quad (16)$$

where the significance of each term is presented in Table 9. Normally, several of the coefficients in Eq. 16 will be zero, resulting in the specialization of the equation to a parabolic equation ($\lambda = 0$) or an elliptic equation ($\lambda = 0$ and $\rho c = 0$). The usefulness of this equation for solution of physical problems can be seen in Table 9, which lists the analogous parameters for mechanical, thermal, mass diffusion, acoustic, magnetic, and electrical physical systems.

This program is a descendent of the Lockheed Thermal Analyzer Program (TAP). The computer program logic of TAP was revised and the program capabilities enlarged at Rocketdyne to produce DEAP, which has retained the capability to solve any existing TAP problem with only minor changes to the data deck.

The DEAP computer program solves problems related to the behavior of a continuous physical system through the analogy of a lumped parameter (or nodal) representation that is solved by difference methods. The difference solution method used is a three-time-level method. This method is a modification of the DuFort Frankel Method, which is stable for any computational time increment and is well suited for nonlinear problems, i.e., where the coefficients of Eq. 16 are functions of the dependent variable.

The physical system can be represented by a lumped network with up to 999 nodes and 2999 connectors; and the problem may include conduction, convection, radiation, phase changes, heat sources, and heat sinks. Functional variations of all the parameters with respect to time, temperature, or any other specified combination of variables also are available for problems involving variable material properties, ablation, variable coolant flow, etc.

TABLE 9. DEAP ANALOGOUS PARAMETERS

Basic Equation: $\nabla \cdot (K \nabla \phi) + \tilde{W} \cdot \nabla \phi + s\phi + q = \lambda \frac{\partial^2 \phi}{\partial t^2} + \rho c \frac{\partial \phi}{\partial t}$

Difference Equation: $\sum Y\phi - \phi \sum Y + \sum Y_{FA}\phi + S\phi + Q = \underbrace{L \frac{d^2 \phi}{dt^2}}_{\text{Inertial Term}} + \underbrace{C \frac{d\phi}{dt}}_{\text{Inertial Capacitance Term}}$

Type of Parameter	Thermal Heat Flow	Potential Fluid Flow	Acoustic System	Mechanical Translation	Mechanical Rotation
Dependent Variable (ϕ)	Temperature	Potential function	Pressure	Displacement	Angular displacement
Applied Force (Q,S)	Heat generation terms	Source or sink terms	Source or sink terms	Force compliance	Force compliance
Internal Admittance (Y)	Conductance	Flow path	Propagation rate	Compression	Compression
Transport Admittance (YF)	Flow	None	None	None	None
Inertial (L)	None	None	Density (mass)	Mass	Mass
Capacitance (C)	Thermal capacity	None	None	Frictional resistance	Frictional resistance
Equation Type	Parabolic	Elliptic	Hyperbolic	Hyperbolic	Hyperbolic

The PSA nodal model utilized with DEAP simulated the complete tank and diaphragm geometry, but symmetry about the polar axis was assumed. The model also included a representation of the feed line from the catalytic reactor to the tank inlet boss. The liquid propellant in the tank was simulated with a single node whose time-dependent capacitance (i.e., mass) was determined by initial conditions and the expulsion duty cycle.

The warm-gas pressurant was simulated by a series of flow nodes with a specified temperature at the catalytic reactor outlet. The temperature loss of the pressurant as it flowed through the line was calculated using suitable convective film coefficients. The feed line was assumed to be insulated so that only during the initial flow transient was there significant temperature loss in the line.

The pressurant gas flowrate required to maintain a constant delivered propellant pressure was calculated by the program from the following relationship

$$\dot{w} = \frac{P}{RT} \dot{V} + \frac{Q}{C_p T} \quad (17)$$

where

- P = Pressurant pressure
- R = Gas constant
- T = Pressurant inlet temperature
- \dot{V} = Expulsion flowrate
- Q = Heat loss from pressurant
- C_p = Specific heat of pressurant

The first term represents the gas flow required to maintain the pressure profile, a function of diaphragm ΔP , as the pressurized volume increases due to the expulsion of propellants. The second term represents the gas flow needed to offset the heat loss. The volumetric expulsion rate is

input to the program in the form of a table. Both pressurant gas temperature and cooldown rate are calculated and vary with time.

Heat loss from the pressurant gas to the tank and propellant was the primary calculation since this factor affects the hardware temperatures and the total pressurant required. The biggest uncertainty in determining the heat loss was calculating the heat transfer film coefficient. Problems were associated with gas mixing and not knowing the velocity of the gas along the diaphragm and liner surfaces. This was further complicated by the variations in vehicle acceleration imposed by the engines. Because of these uncertainties, both forced and natural convective film coefficients were considered.

To minimize the forced convection film coefficient, gas injection velocity was minimized by use of a diffuser plate. Utilizing this velocity in conjunction with the tank geometry and assuming laminar pipe flow relationships resulted in a convective film coefficient of 6.7×10^{-6} Btu/in.²-sec-F for the highest pressurant flow and 0.33×10^{-6} Btu/in.² sec-F for the lowest flow. Forced convection was assumed to be the governing process and was used to calculate pressurant requirements. Natural convection coefficients were higher, however, and therefore were used to determine the worst-case hardware temperatures to be presented.

The alternate approach utilized the natural convection data of Ref. 3 to estimate film coefficients within the tank. The use of the natural convection data is complicated by the fact that during the actual mission the gravitational forces vary from slightly more than 1 g during axial engine operation down to about 0.003 g based on an integrated average of the ACS engines. Utilizing this range of g values, the Rayleigh number varies from approximately 4.3×10^9 to 1.2×10^7 . The resultant film coefficients for maximum and minimum pressurant flows are 15×10^{-6} and 2.2×10^{-6} Btu/in.²-sec-F, respectively.

Ref. 3. Means, J.D., and R.D. Ulrich: "Transient Convection Heat Transfer During and After Gas Injection into Containers," ASME Journal of Heat Transfer, May 1975.

Convective film coefficients were multiplied by the exposed surface areas of the tank liner and diaphragm nodes to obtain the corresponding values of admittance and the resultant heat losses, based on the temperature differences between the ullage gas node and corresponding material nodes. The number of nodes exposed to the warm gas increased with time as the diaphragm rolled away from the liner. This effect was accomplished by the use of an input table in which the exposed surface area was a function of the percent diaphragm reversal. Full surface exposure was assumed at 50% expulsion.

The liquid propellant film coefficient was obtained from the natural convection relationship in Ref 4. The resulting value of 1.6×10^{-4} Btu/in.²-sec-F, which is an order of magnitude larger than the ullage gas values, ensures that the diaphragm temperature is controlled primarily by the propellant temperature.

Heat Transfer Predictions. The results for MDC I at a storage temperature of 100 F are presented in Fig. 28. The initial pressurization was performed in the first 10 seconds and was followed by a 128-second coast. At the end of the 122.5-second expulsion, the gas bulk temperature was 358 F. Because of this high value, there is usable Tridyne in the pressurant storage tank which is sized for MDC II. The warmest liner/composite temperature was 285 F, which occurs in the thin section approximately midway between the pole and equator. The aluminum inlet boss temperature shown is near the inlet valve, and the diaphragm temperature is the maximum value. The long coast after completion of the expulsion is academic to show the soakout transient. Figure 29 shows the temperature profiles at the end of the long expulsion for a portion of the tank liner/composite.

Figures 30 and 31 show similar data for MDC II. Because of the long, pulsed propellant demand, the tank temperature profile is more uniform and results in a lower maximum liner/composite temperature (253 F). The gas temperature at the end of the cycle is 290 F.

Ref. 4. McAdams, W.H.: Heat Transmission, Third Edition, McGraw-Hill, New York, 1954.

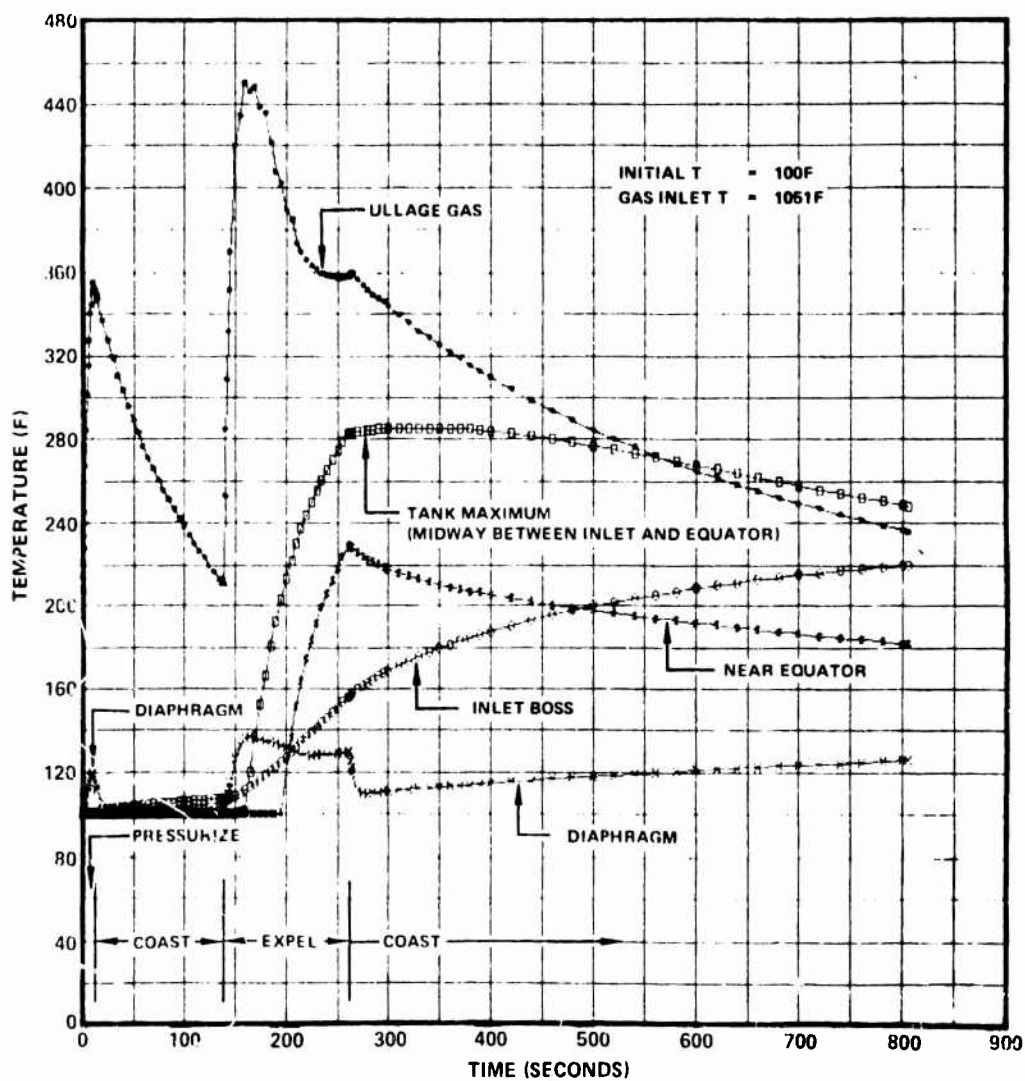


Figure 28. Tank Temperature Response for MDC I

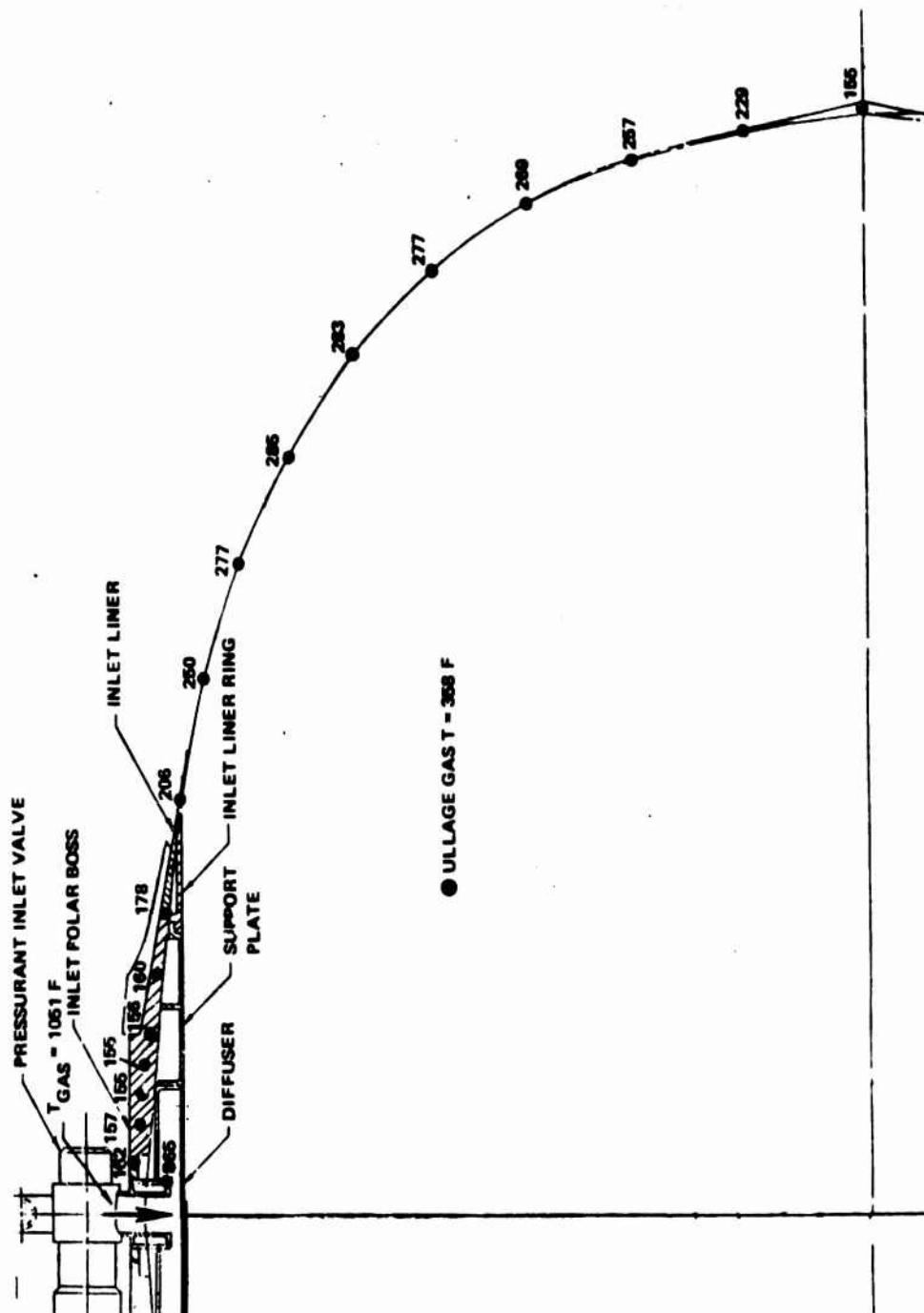


Figure 29. Tank Temperature Profile at End of MDC I



Figure 30. Tank Temperature Response for MDC II

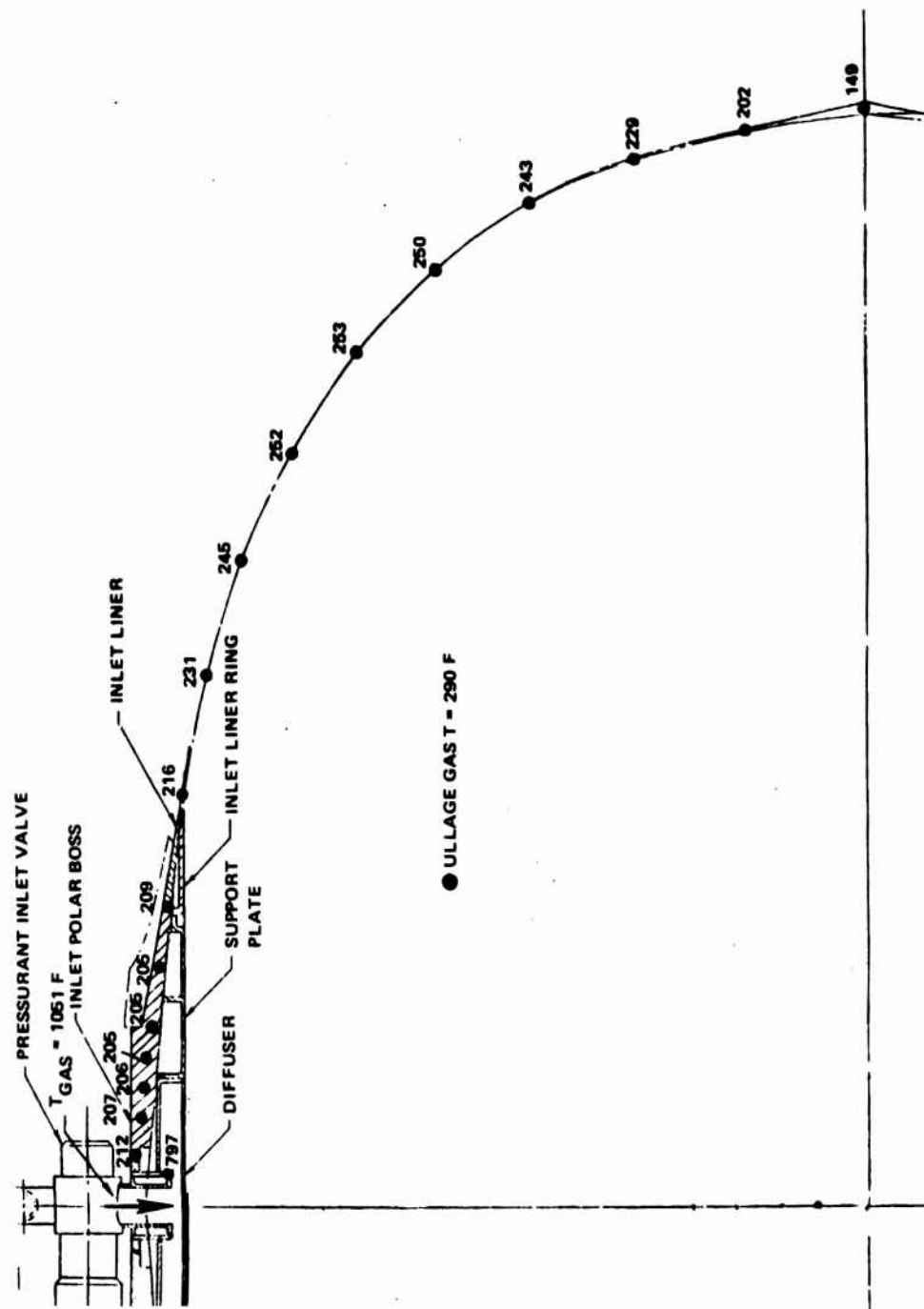


Figure 31. Tank Temperature Profile at End of MDC II

Structural Dynamic Analysis

Structural dynamic analyses of the composite-wrapped propellant tanks were conducted using the finite-element techniques available within the STARDYNE Analysis System formulated by Mechanics Research Inc. This system is comprised of a compatible set of digital computer routines that encompass the total range of static and dynamic response analyses. Capabilities include static, thermal, and inertial loading; eigenvector or mode shape extractions utilizing either Inverse Iteration, LANZOS, or Householder Q-R algorithms; and sinusoidal, random, acoustic, shock, and transient responses.

A comparison of response stresses in the mount structures of the fuel, oxidizer, and pressurant tanks was made to support Rocketdyne's MX proposal effort using a Stage IV system model. The vibration criteria applicable to the stage structure were similar in shape but had higher levels than the interstage structure requirements for this contract. The results of system response analyses, summarized in Fig. 32, indicated the oxidizer tank supports had the highest response stresses of the components included in the propellant feed system. The oxidizer tank, being the heavier of the two propellant tanks in the loaded condition, was therefore selected as the critical component for detailed dynamic response analysis.

Propellant Tank Liner, Wrap and Mount Ring. A worst-case analysis of the propellant tank structural shell was accomplished by combining the flight and ground random vibrations into an envelope of the maximum specifications from 1 to 2000 Hz. This spectrum and the separation shock were applied to the complete tank model shown in Fig. 33 through the mount attach points. Based on earlier analyses, the critical condition of 12% diaphragm reversal, which is the approximate condition during separation shock, was included in the model, assuming full fluid compliance.

The first 88 natural frequencies with "participation factors" greater than 0.1 in any one axis direction (26 to 1125 Hz) were included in the analysis. A typical normalized displacement is illustrated in Fig. 34 for the second mode (51 Hz).

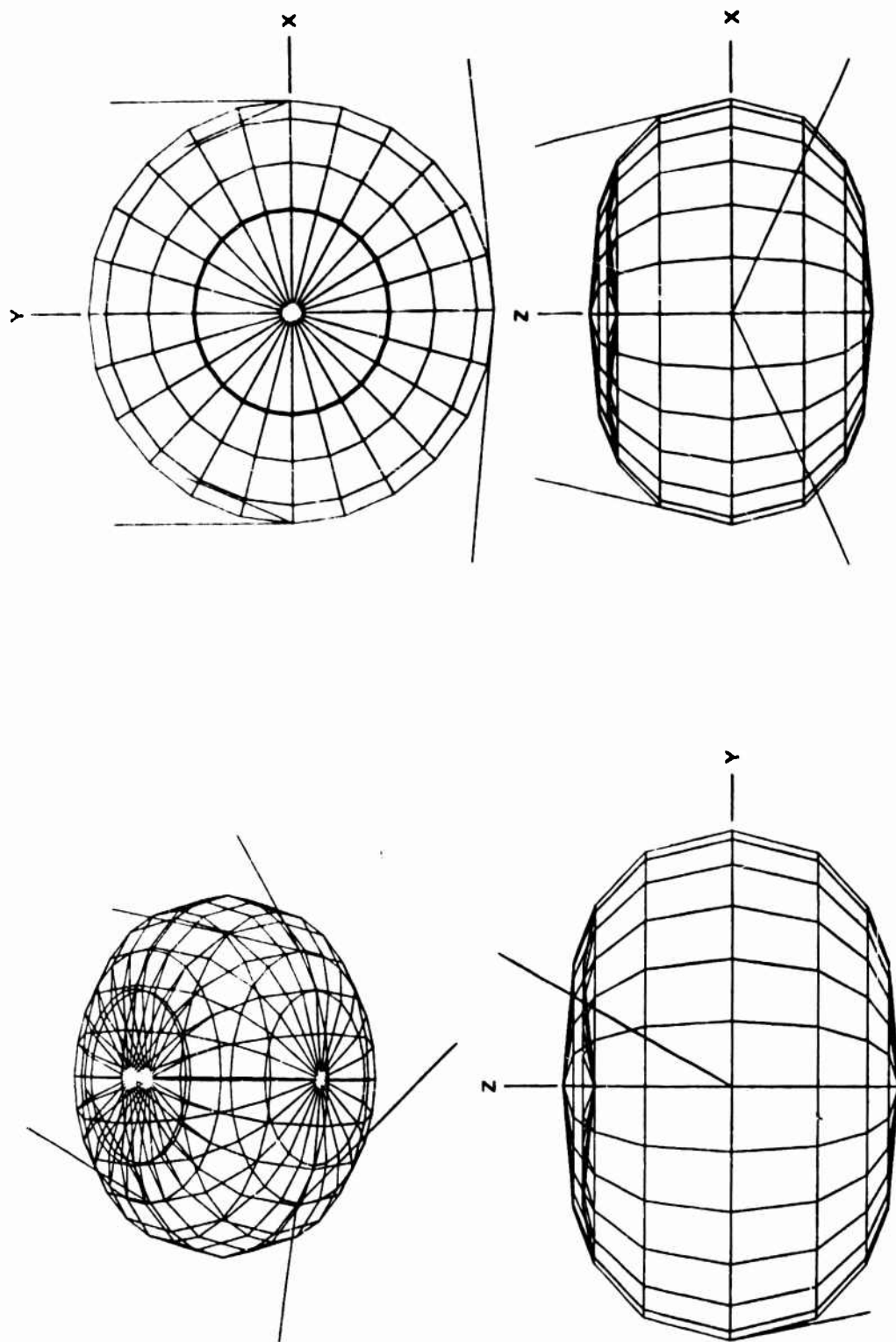


Figure 33. Propellant Tank Structural Model

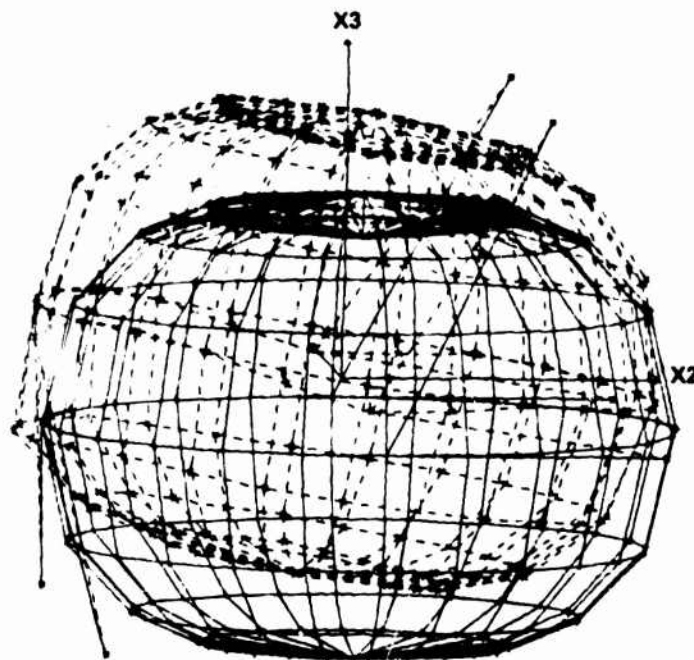


Figure 34. Second-Mode Normalized Displacements for Propellant Tank

The combined structural dynamic and static pressure stresses versus radius are shown in Fig. 35 to have a substantial margin of safety when compared to the allowable Kevlar/epoxy composite stresses. The girth ring also is shown to have substantial margin for both shock and peak random response stresses in Table 10. The deflections shown are for the slotted point of attachment. These results are conservative not only because the multiple vibration requirements were enveloped, but shock-mounted support links were later incorporated to accommodate the diaphragm. In conclusion, there are no anticipated structural dynamic problems with the propellant tank structural shell or the girth ring mounting structure.

Propellant Tank Diaphragm. A separate model of the aluminum diaphragm, partial structural shell, girth ring and tank mount links was created to assess the response of the diaphragm at both the 12 and 37.5% reversal conditions. Figure 36 is a graphic display of the 12% reversal model.

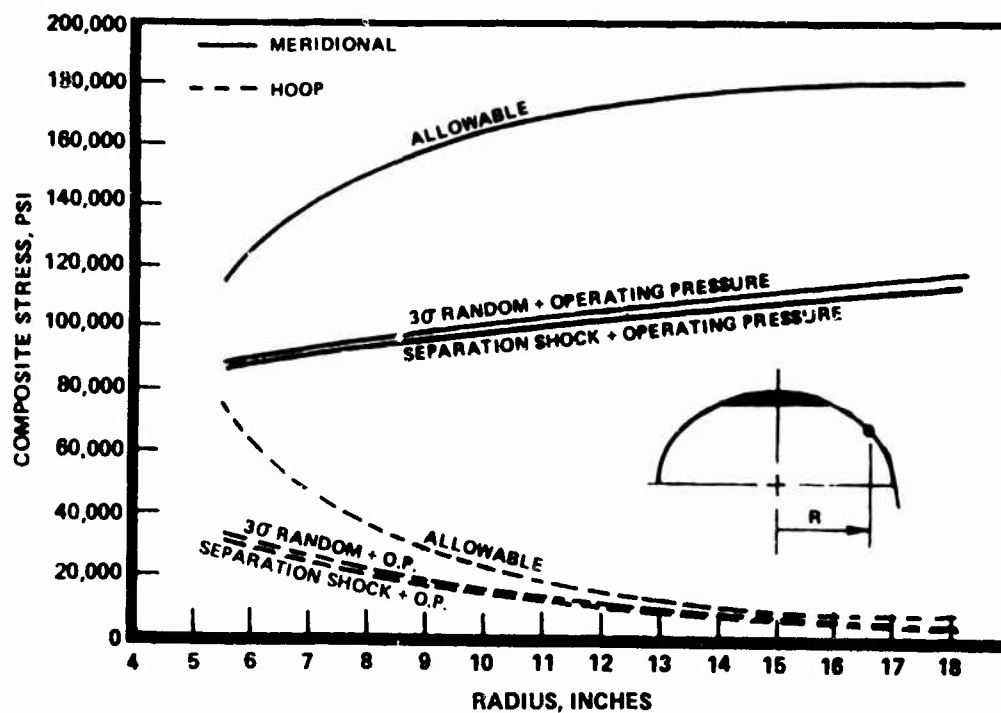


Figure 35. Dynamic Response of Propellant Tank Shell

TABLE 10. DYNAMIC RESPONSE OF GIRTH RING

Allowable Stress	Shock Response			Random Response		
	Maximum Deflection, inch	Maximum Stress, psi	Margin of Safety	Maximum Deflection, inch	Maximum 3σ Stress, psi	Margin of Safety
65,000	0.253	17,200	2.8	0.390	51,200	0.3

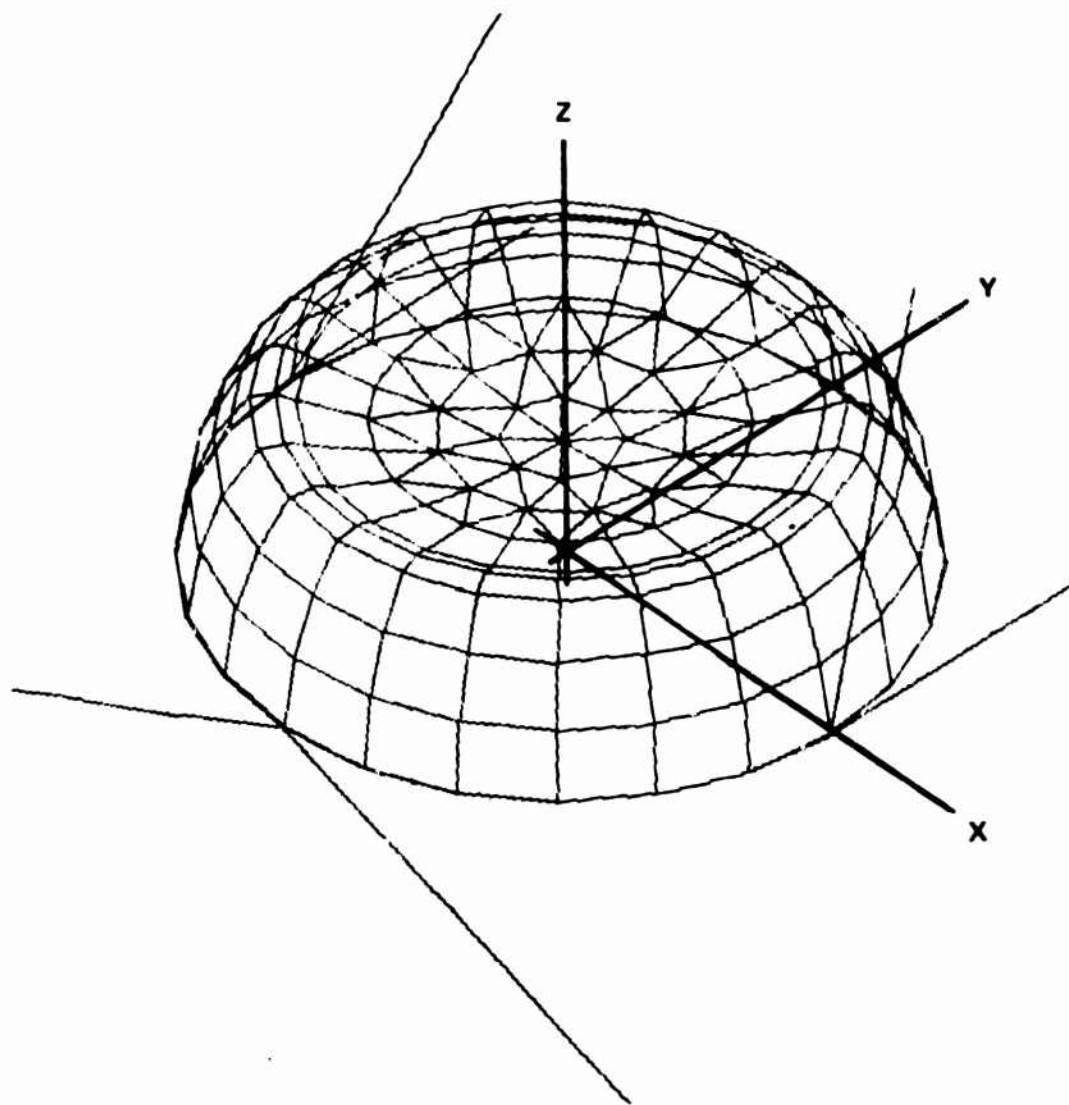


Figure 36. Diaphragm Structural Model

The effective fluid used in the analysis was calculated by constructing the simple fluid model of Fig. 37 and calculating the generalized weight term (59 pounds) for the first fluid mode (1190 Hz). This weight was then distributed over the surface of the diaphragm model and 67 mode shapes, such as the one shown in Fig. 38, were extracted from 53 to 4889 Hz.

Responses of the 12% reversed diaphragm to both peak vibration and separation shock indicated significant yielding of the diaphragm. A design change was then initiated, which led to shock-mounted support links. The diaphragm was re-analyzed and shown to exhibit no significant yielding. The range of the first 67 mode frequencies was 39 to 4763 Hz. The shock mounting was accomplished by isolating the tank structure from the stage structure with a shearing type elastomer material integral with the support links.

Similarly, the response analysis of the 37.5% reversed diaphragm to Stage IV random vibration showed the diaphragm to possess a finite fatigue life without the shock mounting and an infinite life with the mount. A summary of the maximum diaphragm stresses appears in Table 11.

TABLE 11. MAXIMUM DIAPHRAGM STRESSES

12% Reversed	Allowable	Hard-Mounted	Shock-Mounted
3 σ Vibration	15,000 psi	22,900 psi	15,500 psi
Separation Shock	15,000 psi	17,660 psi	9,930 psi
37.5% Reversed			
RMS Vibration	4,000 psi	5,125 psi	290 psi

Fabrication

The PSA components, materials, and process specifications are shown in Table 12. The PSA assembly sequence is presented schematically in Fig. 39, and the welds were presented in Table 8. The welds required for dual

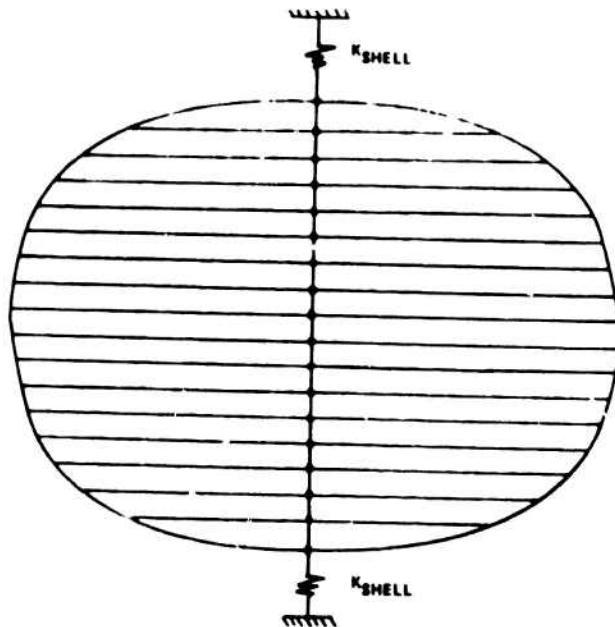


Figure 37. Fluid Compliance Model

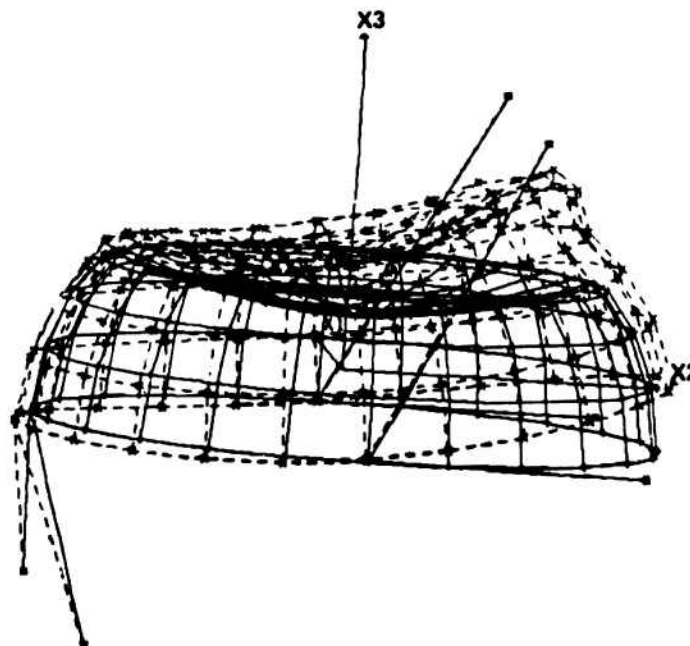


Figure 38. First-Mode Normalized Displacements for Diaphragm

TABLE 12. PSA MATERIALS

Part	Material	Specification
Girth Mount Coupling	6061-T6 Aluminum	
Girth Mount Spacer	2219-T62 Aluminum	STO 170 LB0048-T62
Girth Mount Ring	2219-T62 Aluminum	STO 170 LB0048-T62
Fill and Drain Valve End	5086-0 Aluminum	QQ-A-250/7-0
Fill and Drain Valve Cap End	5086-0 Aluminum	QQ-A-250/7-0
Fill and Drain Valve Cap	5086-0 Aluminum	QQ-A-250/7-0
Fill and Drain Valve	5086 Aluminum	
Cylindrical Wrap	KEVLAR 49/Epoxy	
Leak Detector	304L CRES	
Leak Detector Bi-Metal Coupling	6061/304L	
Vacuum Service Valve Cap	5086-0 Aluminum	QQ-A-250/7-0
Vacuum Service Valve	5086 Aluminum	
Vacuum Service Valve Adapter	5086-H34 Aluminum	QQ-A-250/7-H34
Girth Ring Elastomer	Elastomer	
Girth Mount Ring Band	2219-T62 Aluminum	STO 170 LB0048-T62
Pressurant Inlet Valve	304L CRES	
Propellant Outlet Valve	5086 Aluminum	
Helical Wrap	KEVLAR 49/Epoxy	
Inlet Bi-Metal Coupling	6061/304L	
Inlet Polar Boss	5086-H34 Aluminum	QQ-A-250/7-H34
Inlet Liner Ring	5086-0 Aluminum	QQ-A-250/7-0
Inlet Support Plate	5086-0 Aluminum	QQ-A-250/7-0
Inlet Diffuser Backplate	304L CRES	QQ-S-766 CL304L COND A
Inlet Diffuser Frontplate	304L CRES	QQ-S-766 CL304L COND A
Outlet Collector Plate	5086-0 Aluminum	QQ-A-250/7-0
Outlet Polar Boss	5086-H34 Aluminum	QQ-A-250/7-H34
Diaphragm	1100-0 Aluminum	QQ-A-250/1-0
Inlet Liner	5086-0 Aluminum	QQ-250/7-0
Outlet Liner	5086-0 Aluminum	QQ-A-250/7-0

containment of the propellant were included in the Leakage Integrity section. Six additional welds are required for joining the pressurant inlet plates, the propellant outlet plate, and the girth ring. Figure 39 is divided into the pressurant inlet, propellant outlet, and PSA assemblies as indicated, starting at the bottom of the chart.

The assembly sequence for the propellant outlet polar boss assembly is initiated by welding the outlet valve and fill and drain valve to the polar boss. The outlet valve requires two welds. The 5086 aluminum outlet plate is then welded to the 5086 aluminum polar boss to complete the boss assembly. The boss assembly is subsequently welded to the outlet liner at two locations and is followed by joining the diaphragm and outlet liner with girth welds.

The assembly sequence for the pressurant inlet polar boss assembly is initiated by welding the leak detector to its bi-metal coupling and welding the coupling to the polar boss. The vacuum service valve adapter is also welded to the polar boss and the valve is threaded into the adapter.

Next the pressurant inlet valve is welded to its bi-metal coupling and inserted in the polar boss opening. The coupling is then welded to the polar boss. This is followed by welding of the 304L stainless-steel pressurant inlet backplate to the 304L section of the coupling and to the 304L frontplate. The inlet support plate is fitted between the backplate, the polar boss, and the 5086-0 aluminum contour transition ring after the latter is welded to the pressurant inlet half liner. Welding of the polar boss to the liner completes the inlet liner assembly.

The inlet and outlet liner assemblies are then joined by welding at the equator. At this point the metal tank is mounted in handling yokes and shipped. After surface preparation, the Kevlar filaments are helically wound while wet with epoxy resin. The elastomer band is placed over the equator and the girth ring is positioned over the elastomer and the coupling fastened. The composite is then circular wrapped over the girth ring and the tank is put through the cure cycle. After appropriate tests are conducted, the tank is

vacuum filled with propellants and the caps are welded over the fill and drain and vacuum service valves.

PLASTIC WORKHORSE PROPELLANT STORAGE ASSEMBLY

The plastic workhorse tank is used for initial diaphragm testing. It is designed for low-pressure water expulsion tests to view the reversal mode and evaluate alternate diaphragm designs to establish the optimum configuration for the flightweight tank.

Figure 40 shows the assembly. Warm plexiglass G half shells are drawn to contour to mate with 6061 T651 aluminum contour rings at their inner surfaces and aluminum flange rings at their outer surfaces, and then polished to optical quality. Aluminum inlet and outlet plugs are bonded to the shells at their poles.

The flange rings are designed to minimize their rotation under the internal pressure of 50 psig and ensure O-ring sealing under the large bending moment resulting from the large flange width. The large width is used to minimize the stress in the nonductile plexiglass and preclude high stress concentrations. Butyl O-ring seals are located at the inner and outer surfaces of the contour rings.

The 321 CRES pressurant inlet post has a shoulder and is threaded for mechanical attachment to the inlet plug with a washer and nut. It is also threaded for attachment to the 6061 T651 aluminum diffuser plate. This plate diffuses the pressurant before it impinges on the diaphragm and is welded to a 6061 T651 aluminum transition ring that duplicates the flightweight tank contour. The inlet plug also has a small threaded port to provide for monitoring the pressurant.

The propellant outlet post fitting is the same as the inlet post and permits threaded attachment of the 6061 T651 aluminum collector plate. The plate geometry is the same as the flightweight configuration. The small port in the

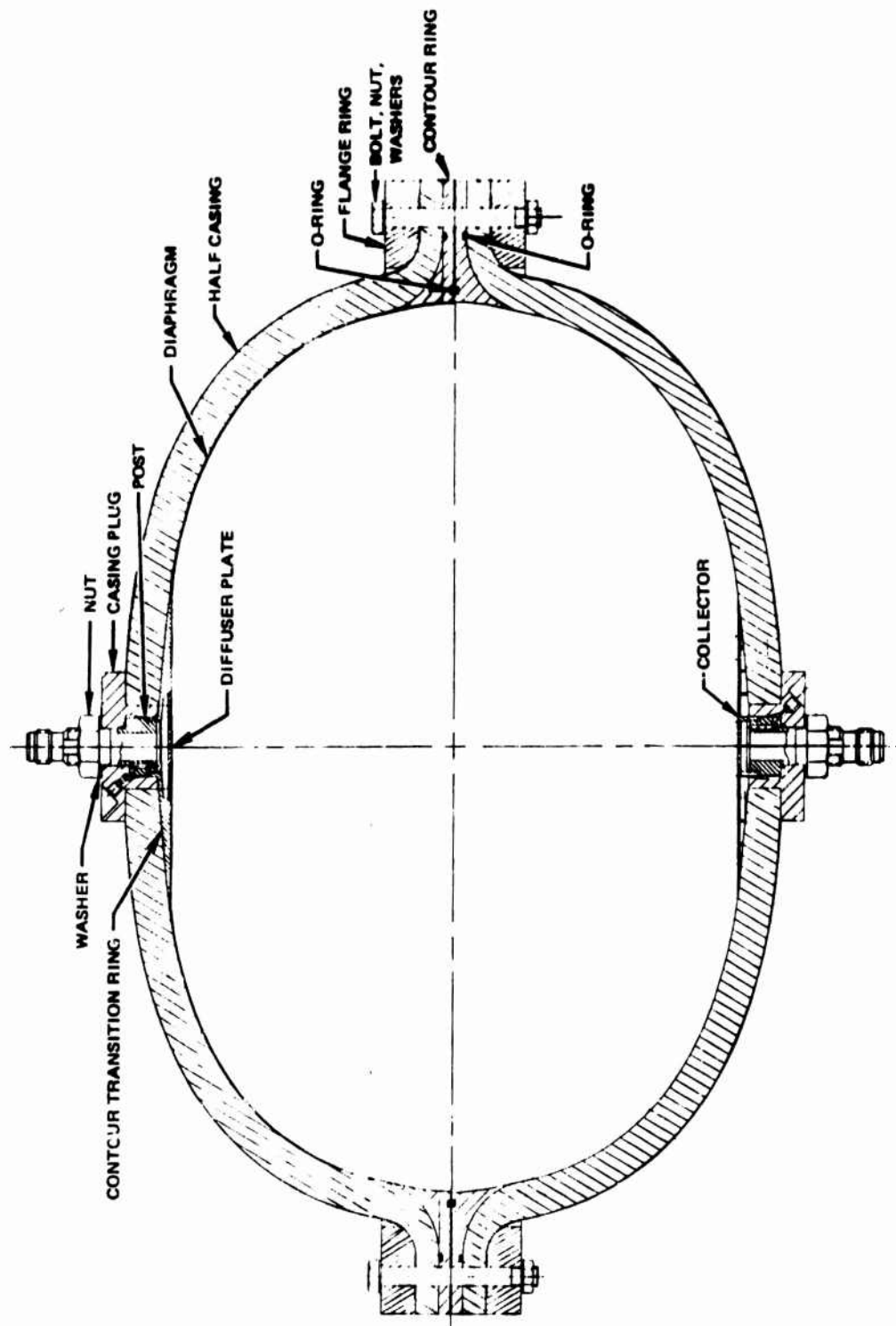


Figure 40. Plastic Workhorse PSA

outlet plug provides for monitoring the outlet pressure. Pressurant inlet and propellant outlet fittings are made from AN815-16J fittings and are welded to their respective posts.

The diaphragms are made of 1100-0 aluminum and duplicate the flightweight configuration except for the flange area, which in this case is designed for bolted attachment. The diaphragms are easily replaceable by simple disassembly of the tank shell halves.

METAL WORKHORSE PROPELLANT STORAGE ASSEMBLY

The metal workhorse tank has a "heavy" aluminum shell instead of a thin liner overwrapped with composite. It will be fabricated to provide a reusable tank for evaluating tank performance under life cycle environmental conditions including pressure, temperature, and structural dynamics. Figure 41 shows the tank assembly, which is girth-flanged for bolting and disassembly as required for test evaluations. The optimized 1100-0 aluminum diaphragm configuration determined from the plastic tank tests will be used with this tank.

The assembly is comprised of two aluminum half-shells with welded flanges and polar bosses made from 2219 T62 aluminum. The pressurant diffuser assembly is welded to the 304L CRES inlet fitting, which is bolted to the inlet boss. The welded 304L CRES outlet collector assembly is welded to the 304L CRES outlet fitting, which is welded to the outlet boss. Both polar bosses contain 321 CRES fittings to monitor inlet and outlet pressures.

Tank shells are draw formed from plate stock in the annealed condition and trimmed. They are then heat treated and EB welded. EB welding, as opposed to fusion welding, only partly reduces the material strength at the joint so that allowable ultimate and yield strength levels of 42 ksi and 28 ksi, respectively, are achieved. This permits tank wall reduction to about 0.450 inch at the poles and 0.250 inch at the girth.

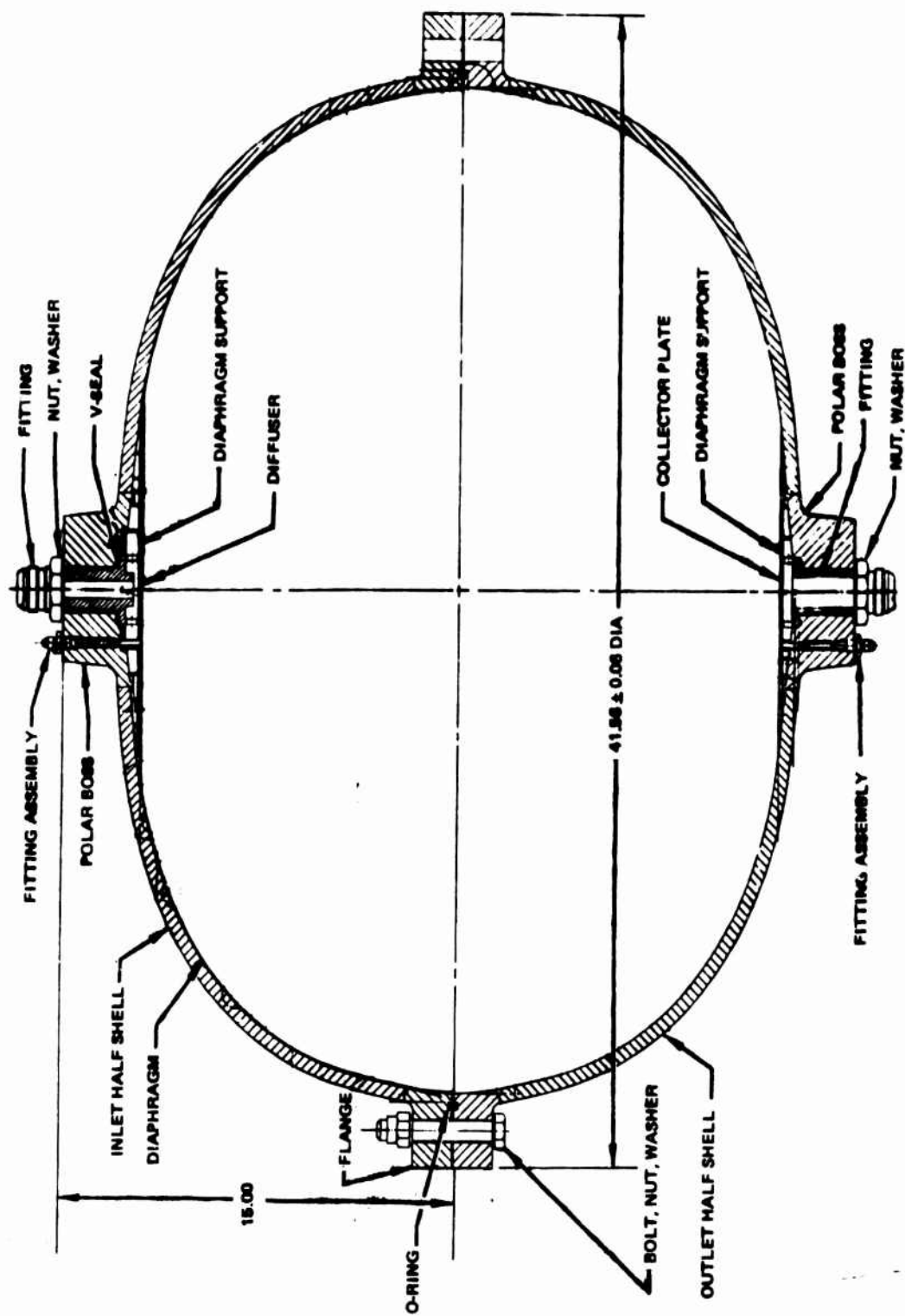


Figure 41. Metal Workhorse PSA

FLIGHTWEIGHT PRESSURIZATION SUBSYSTEM

The flightweight pressurization subsystem, which is used to pressurize the two PSA's, consists of Tridyne pressurant fluid (a gaseous mixture of helium, oxygen, and hydrogen), a composite-wrapped storage tank, a fill and drain valve, a pressure switch leak detector, a pyrotechnically actuated isolation valve, an electronically controlled pressure regulator, a catalytic reactor, and associated flow lines. A schematic of these components was shown in Fig. 1 and a top-level assembly drawing is presented in Fig. 42. Each of these components are described in this section of the report. Pressurization subsystem design characteristics are summarized in Table 13.

TABLE 13. PRESSURIZATION SUBSYSTEM DESIGN CHARACTERISTICS

<u>Envelope, inches</u>		
Pressurization Subsystem Length	26.5	
Pressurization Subsystem Width	18.9	
Pressurization Subsystem Height	18.7	
Pressurization Tank Diameter		
(at 4000 psia)	18.7	
Catalyst Bed Length	2.05	
Catalyst Bed Diameter	1.25	
<u>Volume, in.³</u>		
Pressurant Tank (at 4000 psia)	2910.0	
Catalyst Bed	2.49	
<u>Pressurant Composition, %</u>	<u>Molar</u>	<u>Mass</u>
Helium	91.10	77.3
Oxygen	2.97	20.1
Hydrogen	5.93	2.5
<u>Pressures, psia</u>	<u>Minimum</u>	<u>Maximum</u>
Pressurant Storage	3629	4370
Tank Blowdown	400	554
Regulator Outlet	341	359
Pressurant in PSA	306	324
<u>Temperatures, F</u>		
Reactor Outlet	1035	1061
PSA Inlet	1025	1051
Pressurant in PSA, End of MDC I	445	
Pressurant in PSA, End of MDC II	350	

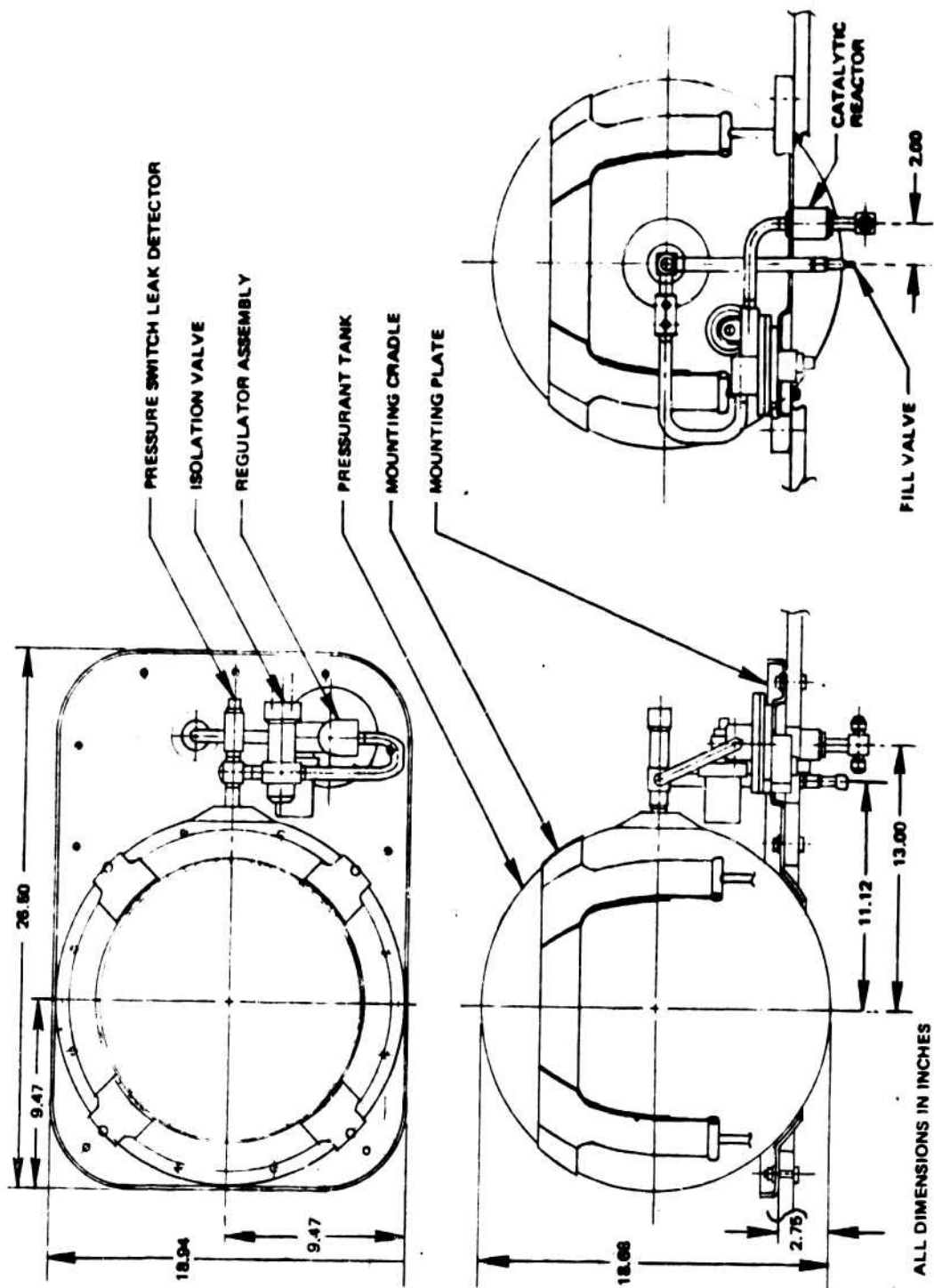


Figure 42. Pressurization Subsystem Assembly

Tridyne Pressurant

The weight of Tridyne pressurant required is dependent on several factors including the catalytic reaction temperature rise, the storage pressure, the final blowdown pressure, the pressurized volume, and the final gas temperature in the PSA (which is a function of the mission duty cycle (MDC)).

Reaction Temperature And Composition. The coldest temperature at the inlet to the catalytic reactor is -181 F, which corresponds to expansion from 3777 psia at 40 F to 359 psia with a polytropic exponent of 1.33. The pressurant gas temperature at the inlet to the PSA's was assumed to be 1025 F for 40 F storage conditions. With a 10-degree drop in the lines, the reactor outlet temperature was established at 1035 F. The required reaction temperature rise is therefore 1216 F. Assuming a reaction efficiency of 0.995, the complete reaction temperature rise is 1222 F and the corresponding Tridyne molar composition is 0.911 He/0.0297 O₂/0.0593 H₂. The respective mass composition is 0.7733/0.201/0.0254. A stoichiometric O₂/H₂ mixture is utilized.

Subsystem Pressures. A storage pressure of 3777 psia at 40 F corresponds to 4000 psia at 70 F and 4222 psia at 100 F. The nominal 4000 psia was selected as a reasonable compromise between weight, volume, and accepted design practices. The weight savings in going from 4000 to 5000 psia is very small. The biggest advantage at the higher pressure is reduced volume; however, envelope constraints were not imposed on the pressurization subsystem. The pressure selection is therefore more properly dependent on the stage configuration.

The 359 psia at the reactor inlet occurs at the end of the expulsion cycle for an assumed 99% expulsion efficiency. The feed system pressure schedule is presented in Table 14. All of the pressures are in psia.

TABLE 14. FEED SYSTEM PRESSURE SCHEDULE WITH N_2O_4 PSA

Expulsion Efficiency, %	90	97	98	99
Delivered Propellant	300.0	300.0	300.0	300.0
Propellant in PSA	303.1	303.1	303.1	303.1
Pressurant in PSA	306.1	314.1	318.1	324.1
Pressurant at PSA Inlet	306.7	314.7	318.7	324.7
Pressurant at Reactor Outlet	307.2	315.2	319.2	325.2
Pressurant at Regulator Outlet	340.8	348.8	352.8	358.8

Pressurized Volume. Each propellant tank has an unpressurized propellant capacity of 10.57 ft^3 . In addition to displacing 97% of twice this volume, the pressurant must account for PSA growth, the initial volume between the diaphragm and the pressurant inlet half of the PSA, and the volumes within the other pressurization subsystem components. The total volume downstream of the isolation valve is 20.76 ft^3 .

Design Margin. The nominal expulsion efficiency has been conservatively established as 97%; however, it is anticipated that 98 or 99% can be achieved. The diaphragm ΔP is the limiting parameter, and since its gradient is very steep, a certain amount of uncertainty exists in predicting expulsion efficiency. As a result, design margins were provided. The predicted pressurant pressure in the PSA at 97% is 314 psia, but 324 psia (predicted at 99%) was used in pressurant requirement calculations. The PSA was designed at 350 psia. In addition, the regulator requires a minimum inlet pressure of approximately 375 psia, but the final pressurant tank pressure was set at 400 psia to provide additional margin.

Thermal Analysis. The DEAP nodal heat transfer model of the PSA (described in Flightweight PSA section) was used to determine the pressurant flowrates and the final bulk temperature within the PSA for the single-burn MDC I and the pulsed MDC II. The maximum pressurant requirement corresponds to the coldest storage temperature (40 F), which results in a PSA inlet temperature

of 1025 F. The relatively long MDC II permits the most heat transfer from the gas to the tank and propellant, and results in the lowest final bulk gas temperature. Unlike the PSA thermal analyses, nominal rather than maximum predicted film coefficients were used.

Figure 43 shows the transient temperatures for a 10-second initial pressurization and a typical 128-second coast, followed by MDC II. During pressurization, the pressurant temperature peaked at approximately 505 F. During coast, this temperature dropped to approximately 355 F in spite of the flow required to maintain the pressure as heat was transferred from the gas during periods of zero expulsion. During pulsing, the gas temperature peaked at approximately 455 F and then gradually decreased as the diaphragm reversed to expose additional heat transfer surface area. The final gas temperature, used in pressurant requirement calculations, was 350 F and reflects the increased flowrate demand due to the increasing diaphragm pressure drop.

MDC I also was simulated and the results are presented in Fig. 44. During the early portion of the 122.5-second-duration expulsion, the gas temperature peaked at nearly 520 F (at a mission time of approximately 170 seconds), and clearly demonstrates the effect of the increase in exposed surface area. The bulk gas temperature at the end of expulsion is approximately 445 F. Because the pressurization subsystem is sized for MDC II, a coast period was added to determine how long the PSA's could be pressurized as heat was removed from the gas. The results indicate that a small amount of attitude control engine burn capability could be accommodated, if required for a particular mission, for up to approximately 300 seconds after termination of the main burn.

Pressurant Requirements. When all of these factors are taken into account, the pressurant requirement is 5.12 pounds. At 4000 psia and 70 F, the corresponding volume is 1.68 ft^3 (2910 in.^3). Pressurization subsystem pressures and temperatures at the start and end of MDC II are summarized in Table 15 as a function of storage temperature.

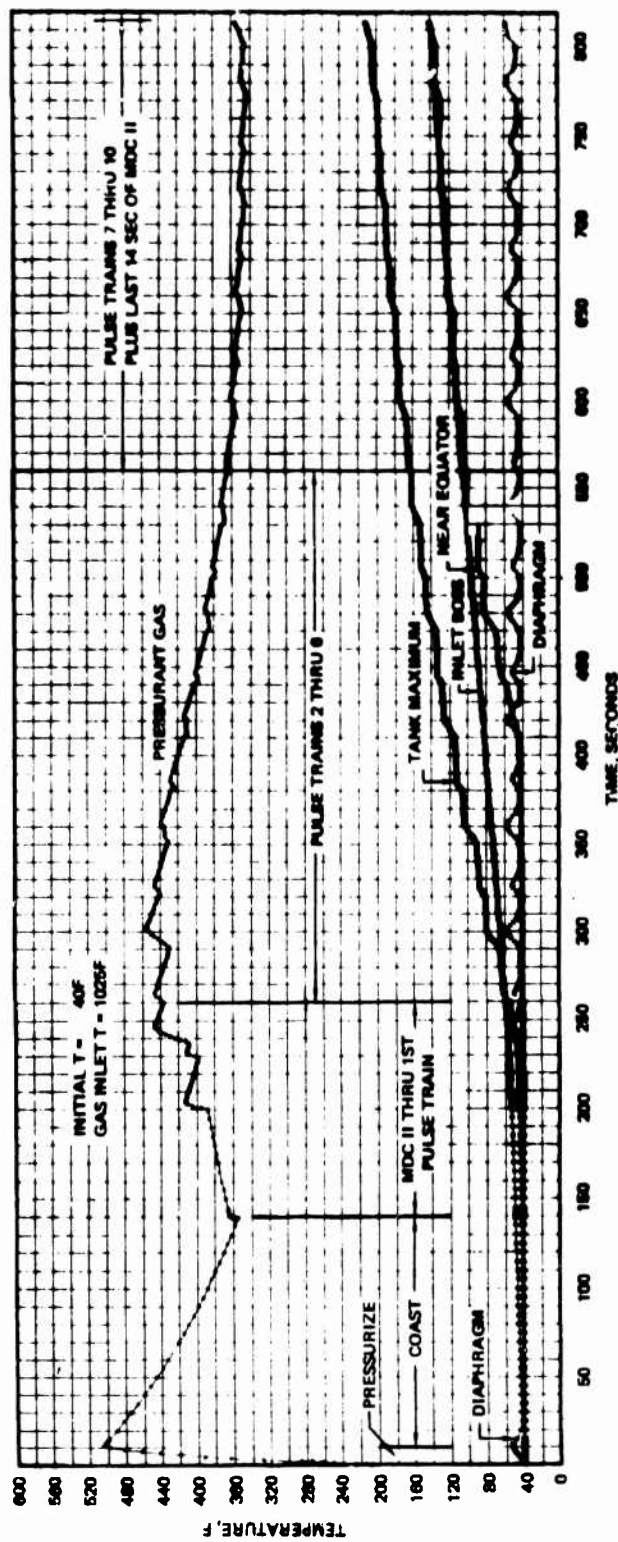


Figure 43. Pressurant Temperature Transient for MDC II

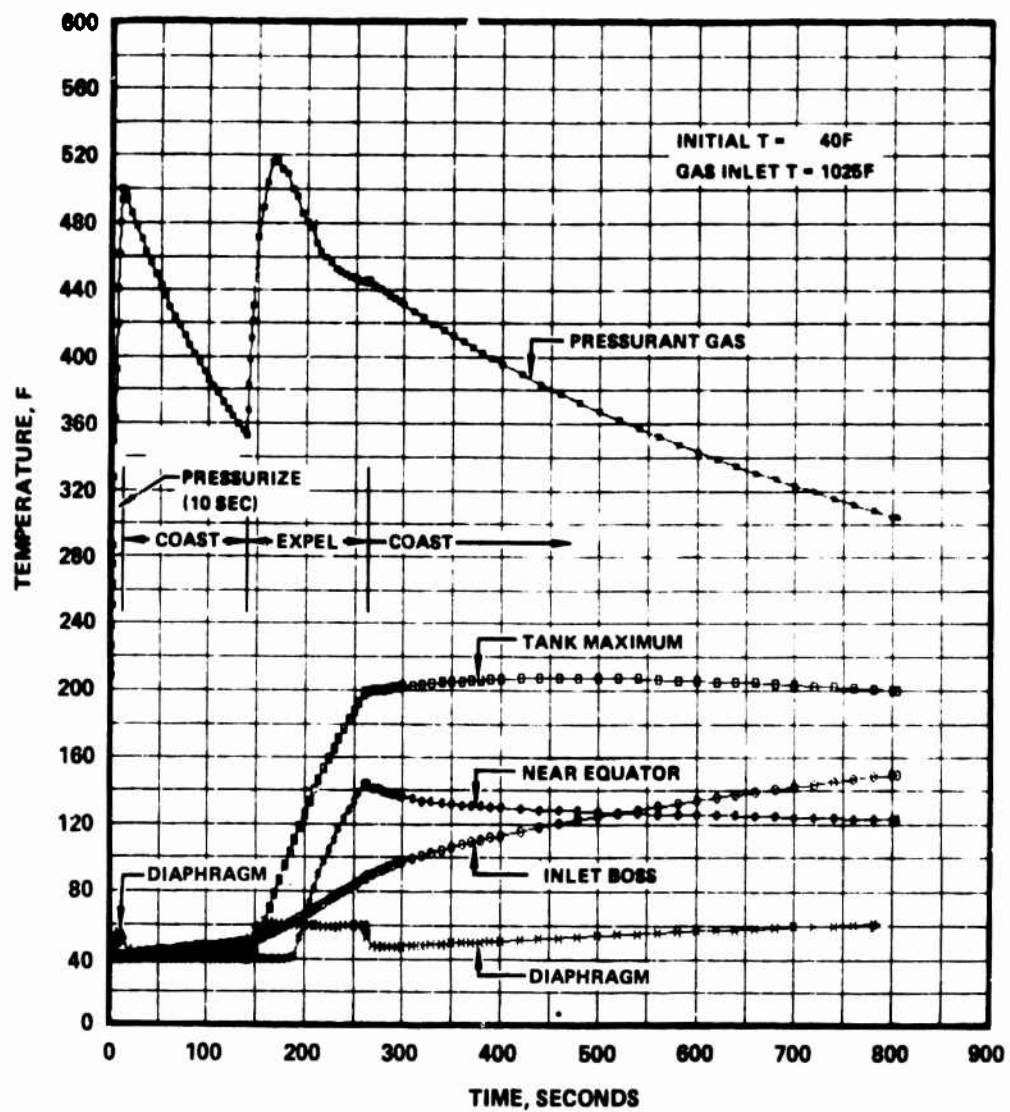


Figure 44. Pressurant Temperature Transient for MDC I

TABLE 15. TRIDYNE PRESSURANT TEMPERATURES AND PRESSURES

Location	Time	Storage Temperature, F											
		20			40			70			100		
		Temperature, F	Pressure, psia	Temperature, F	Pressure, psia	Temperature, F	Pressure, psia	Temperature, F	Pressure, psia	Temperature, F	Pressure, psia	Temperature, F	Pressure, psia
Storage Tank Gas	Initial	20	3629	40	3777	70	4000	100	4222	120	4370	--	--
	Final	--	--	-174	400	-148	475	-122	554	--	--	--	--
Reactor Inlet Gas	Initial			-180	341	-167	341	-154	341				
	Final				359		359		359				
Reactor Outlet Gas	Initial			1035	307	1048	307	1061	307				
	Final				325		325		325				
Pressurant Gas in PSA	Initial			40	306	70	306	100	306				
	Final			350	324	372	324	394	324				
Propellant	Initial			40	303	70	303	100	303				
	Final			46	303	76	303	106	303				
Final values assume diaphragm $\Delta P = 21$ psi													

Pressurant Storage Tank

The pressurant tank has a contained volume of 2910 in.³ at 4000 psia and 70 F. A spherical shape was selected for weight and volume effectiveness. This is also a common shape for filament winding. The design proof and burst pressures are 6000 and 8000 psig, respectively.

The tank, which was designed by the Defense Products Division of Brunswick Corp., is shown in Fig. 45. Pressurant is contained in an all-welded 5086-0 aluminum shell assembly that is fabricated from two half shells with thicknesses of 0.050 inch that are welded at the girth. Thicker-wall bosses are welded into the polar openings of the half shells. One of these bosses has a threaded port to permit Tridyne flow. A plug assembly is inserted into this port and welded. This assembly consists of an aluminum plug and a co-extruded aluminum/300 series stainless-steel transition tube. The aluminum end of the 0.083-inch-thick wall, 5/8-inch-diameter tube is welded to the plug and the steel end to a four-way 300 series stainless-steel tee.

After the aluminum shell assembly has been fabricated, it is filament wound with du Pont Kevlar 49/epoxy resin for structural strength, then coated with polyurethane, which provides a moisture barrier. The composite is approximately 0.44 inch thick, yielding a tank O.D. of 18.68 inches at 4000 psia and 70 F. The change in volume with pressure is approximately 13 in.³ per 1000 psi.

The pressurant tank is retained in an elastomeric-lined cradle and mounting plate, which are fastened together with tee bolts (Fig. 42). The elastomer allows for expansion and contraction of the tank caused by changes in pressurant pressure resulting from environmental conditions and blowdown during operation.

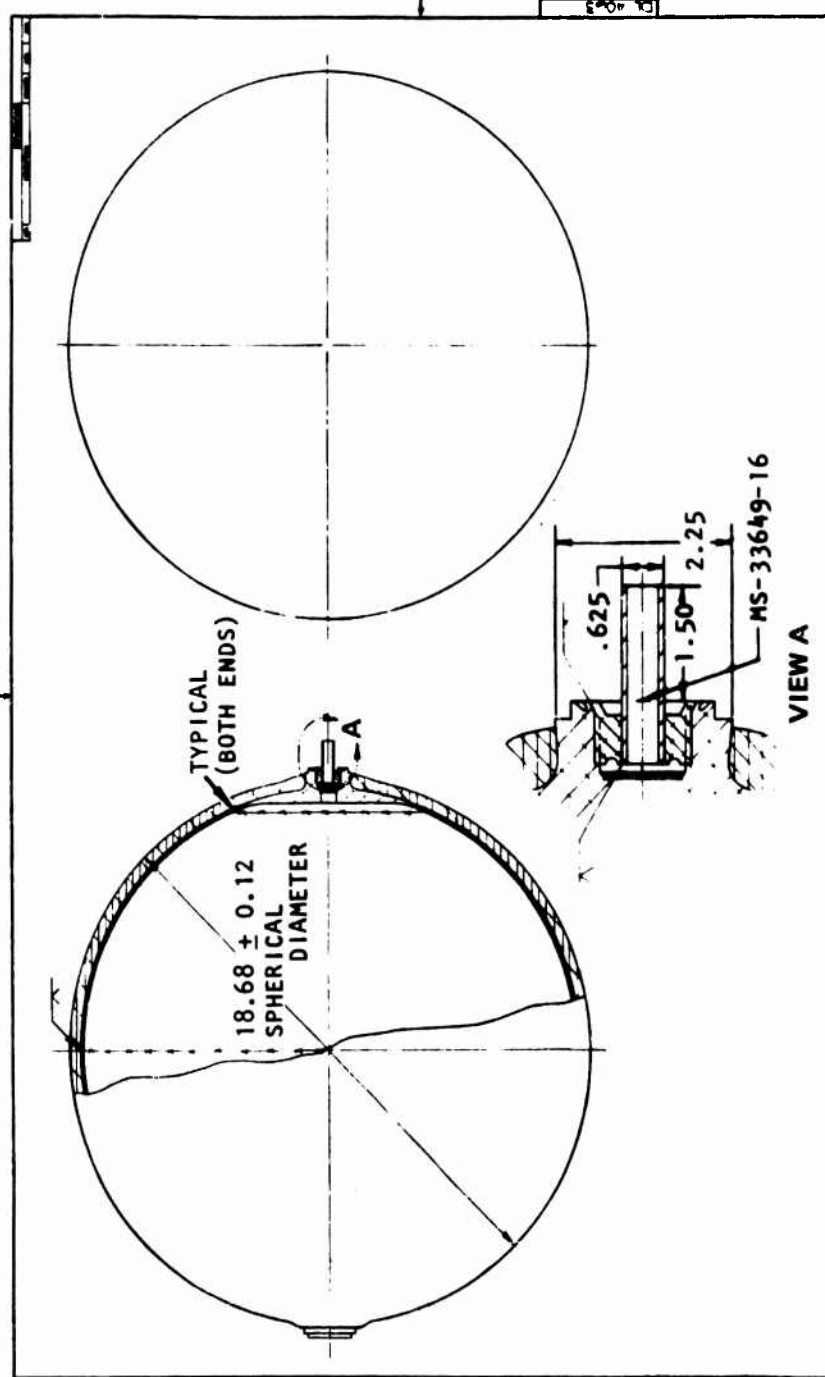


Figure 45. Flightweight Pressurant Tank Assembly

Valves

The pressurization subsystem includes a fill and drain valve and an isolation valve.

Fill and Drain. The fill and drain valve is a fully developed Pyronetics model number 1176-1, which is the same as the PSA vacuum service valve (Fig. 24) except that it is made from 303 stainless steel. The proof pressure is 7500 psi and the burst pressure is 12,500 psi. The valve is welded to a 5/8-inch-diameter, 0.083-inch-thick wall, 300 series stainless-steel tube that extends from the four-way tee at the pressurant tank outlet to provide easy access. A cap is welded over the inlet port for redundant sealing.

Isolation. The isolation valve (Fig. 46) is a fully developed Pyronetics model number 1470, modified for 5/8-inch-diameter tube stubs instead of 1/2-inch-diameter threaded fittings. This is the same model valve used as the PSA pressurant inlet valve (Fig. 21). One tube end is welded to the four-way tee at the pressurant tank outlet and the other end is welded to a 5/8-inch-diameter, 0.083-inch-thick wall, 300 series stainless-steel tube that attaches to the regulator inlet.

Leak Detector

A pressure switch is utilized to detect any decay in pressure of pressurant fluid during storage. The switch is located between the pressurant tank and the isolation valve and would therefore detect fluid leakage from the tank or through the isolation valve or fill and drain valve. The switch would be set to indicate the occurrence of a leak at approximately 3539 ± 90 psia. The upper value of the tolerance (3629 psia) corresponds to the storage pressure at the minimum temperature (20 F).

The selected pressure switch is a Gulton model number 2109-0901, modified for a higher setting. This instrument was developed for and is operational on the Minuteman III PSRE at a pressure setting of 2960 psia. The pressure

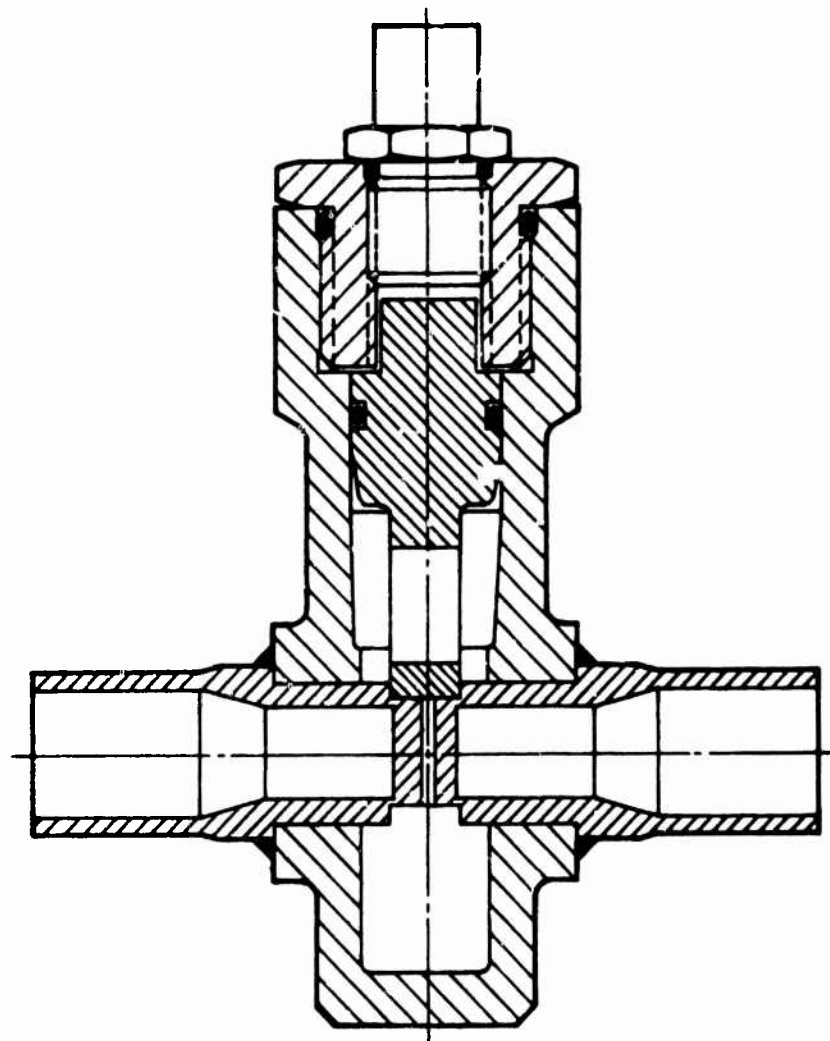


Figure 46. Pressurant Isolation Valve

switch design utilizes a helical Bourdon tube as the sensing element. As pressure is applied, the sensing element rotates (unwinds) about the centerline, causing the wiper arm to slide over segments of a precious metal switching element. Contact with each segment provides a switching function relative to the applied input and the desired switching point. Sufficient tube travel (approximately $3/8$ inch) is generated so that the switch setting and accuracy can be maintained without amplifying mechanisms.

Figure 47 shows the switch, which has an external case of 304L stainless steel and is welded to the four-way tee at the pressurant tank outlet.

Electronically Controlled Regulator

The pressure of the MMH delivered to the engines is regulated with an electrically controlled, continuously modulating regulator designed by the Air and Fuel Division of Parker-Hannifin Corp. The pressure control components include a regulator assembly with an integrally packaged filter, flow limiter, and relief valve in the pressurant line and a controller assembly with an electronics package and pressure transducer located at the MMH PSA outlet.

To compensate for variations in reactor, line, and propellant tank pressure drops during the expulsion cycle (especially the diaphragm), remote sensing with a pressure transducer is utilized. The transducer senses the delivered MMH pressure; the electronics compare this pressure to the reference setting, condition the error signal, and supply a controlling current to the regulator assembly. The small pressure tolerance ($\pm 1\%$) is maintained during transients with proportional and integral compensation of the error signal by the electronics package. The electronics also contain controller gain scheduling to achieve dynamic stability as the regulator inlet Tridyne pressure decays from 4000 to 400 psia and the downstream pressurized volume simultaneously increases from approximately 1 to 20 ft³. An additional feature of the electronics is the ability to provide a smooth ramped initial pressurization by controlling the reference pressure signal.

Current supplied by the electronics package to the regulator assembly powers a torquemotor used to position a small pilot valve that regulates the dome pressure. The dome pressure acts on a diaphragm to position the main valve and regulate the Tridyne pressure supplied to the two PSA's.

The pressure of the N_2O_4 delivered to the engines is controlled indirectly. Both PSA's have a common pressurant supply and, as a result, variations in

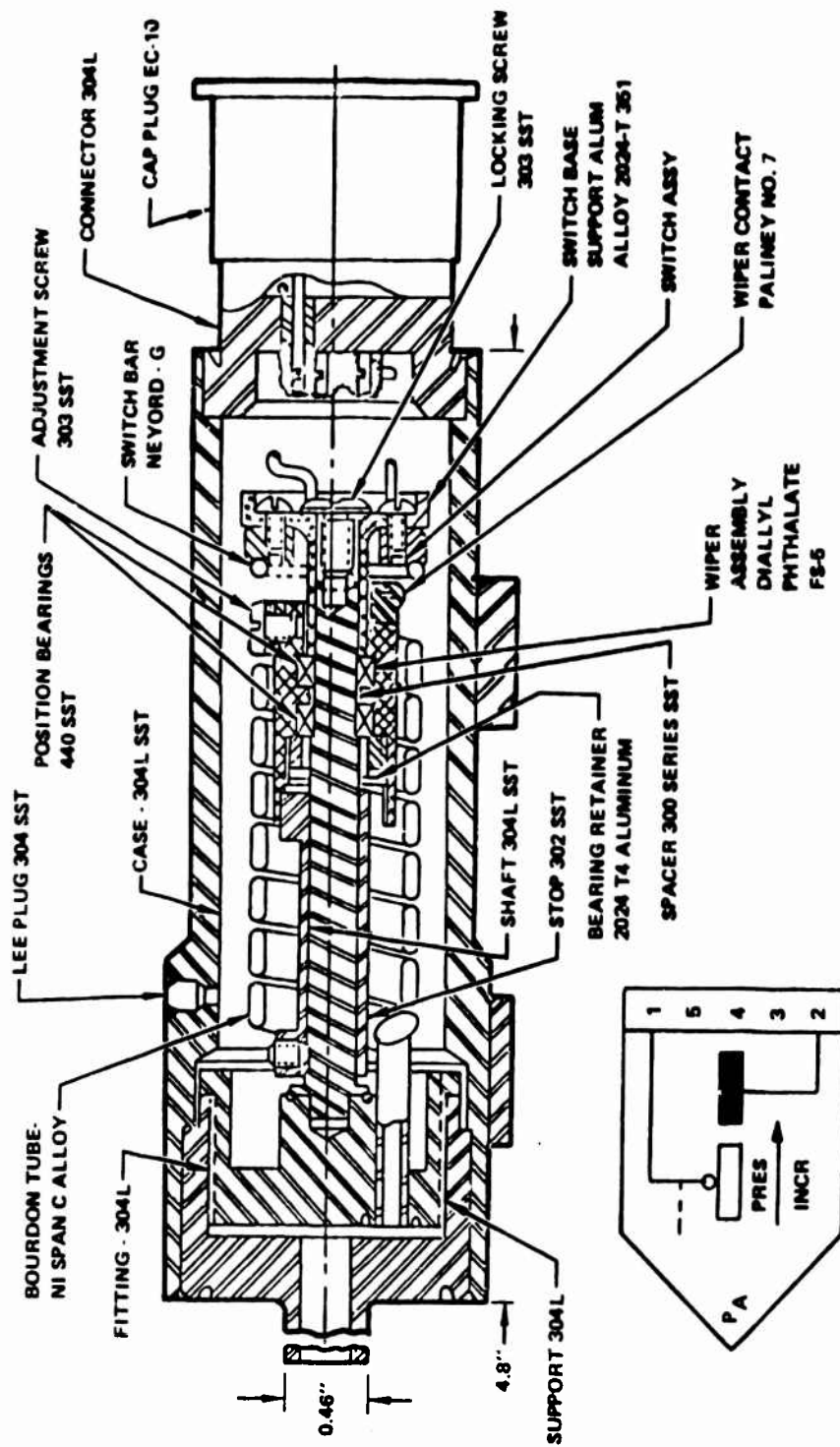


Figure 47. Pressure Switch Leak Detector

the N_2O_4 and MMH pressures will depend on differences in their respective component pressure losses. Variations in the propellant pressures will primarily result from differences in diaphragm thicknesses and the resulting effects on diaphragm pressure drops.

The regulator body has a stainless-steel lower body, including the inlet and outlet ports, and an A356-T61 cast aluminum cover. An all-bolted assembly is utilized with O-ring seals. The relief valve has an A356-T61 cast aluminum cover. This valve is bolted to the regulator main valve outlet port. Top-level assembly drawings are shown in Fig. 48 and 49.

Controller assembly components shown in Fig. 50 are contained in an aluminum housing. Recommendations for modifications to the design to improve nuclear survivability are contained in the Flightweight Feed System section of this report.

Inlet Filter. The inlet filter is a cylindrical type, flowing from the outside to the inside. It is fabricated from 304L stainless-steel, double-dutch-twill wire mesh, supported on the inside by a perforated tube to prevent collapsing. It has a 25-micron absolute rating. Its installation is shown in Fig. 51.

Flow Limiter. A flow limiter is located immediately downstream of the filter and limits the maximum flow, if the regulator fails open, to a lower value than the main valve would permit. This allows a relief valve of smaller size to be used. The main valve flow area must be oversized to minimize pressure errors during rapid transients, but the flow limiter will not inhibit this function of the main valve because it has a slower response.

Figure 52 shows the flow limiter, which consists of a spring and a single moving part containing fixed flow-measuring orifices. The sliding poppet is spring loaded open so that the pressure drop created by the design flow through the fixed orifices does not create a sufficient force to cause any

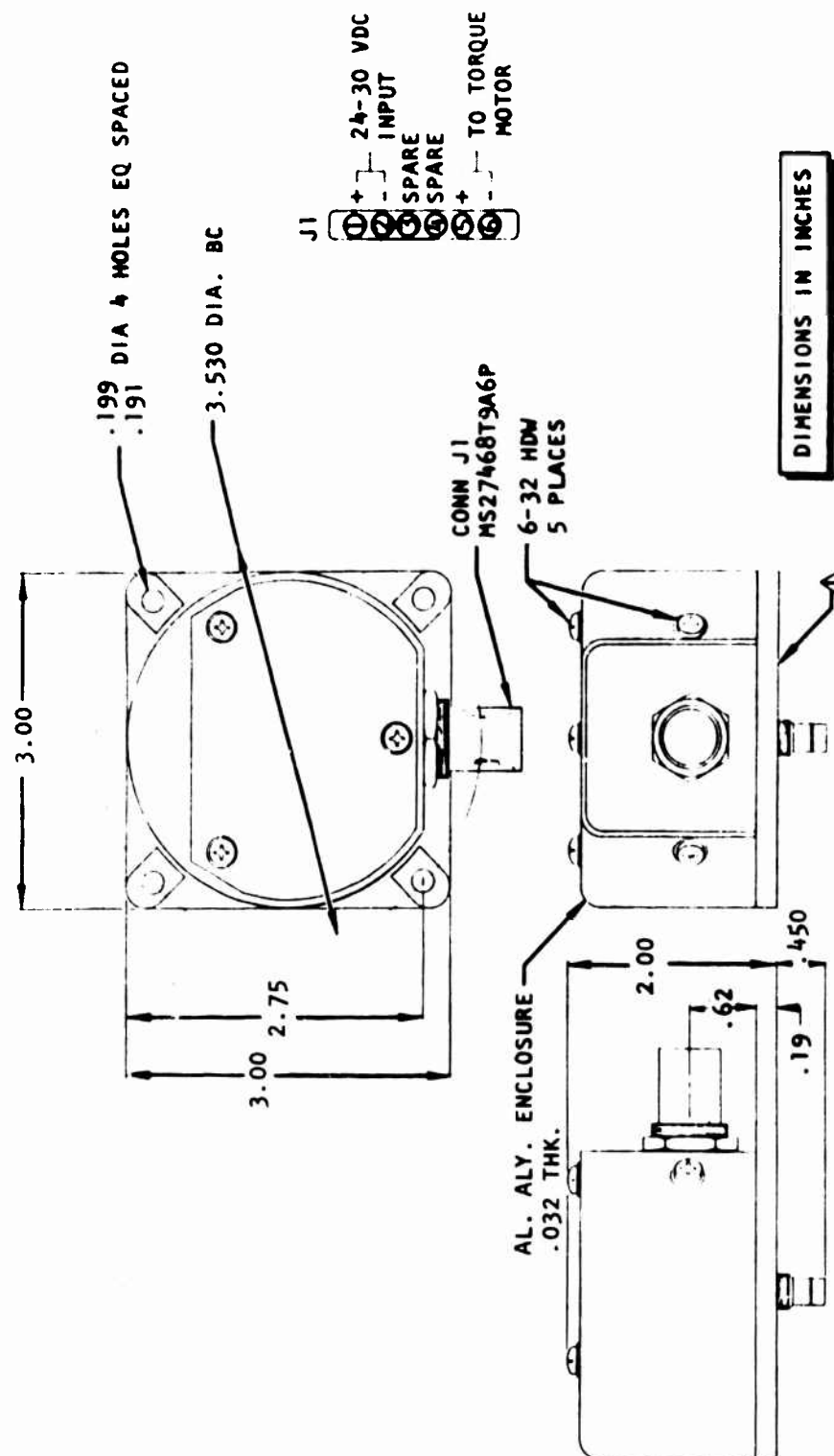
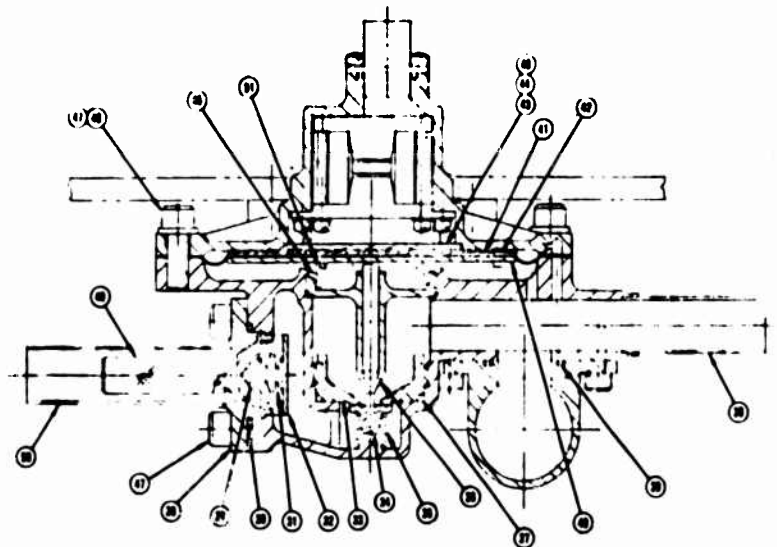


Figure 50. Flightweight Controller Assembly



QTY	NOMENCLATURE	MATERIAL	ITEM NO.
1	SPRING	302 CRES	51
1	TUBE	304L CRES	50
1	FILTER	304L CRES	49
8	WASHER	CRES X	48
12	SCREW	CRES X-20X X	47
1	GUIDE	304 CRES	46
4	INSERT, LOCKING	CRES 4-40	45
4	SCREW, FLAT HEAD	CRES 4-40 X 3/8	44
1	COVER	6061-T6 AL ALLOY	43
12	RIVET	AL ALY	42
1	PLATE, DIAPHRAGM	6061-T6 AL ALLOY	41
1	SUPPORT, DIAPHRAGM	6061-T6 AL ALLOY	40
1	PACKING	VITON	39
1	TUBE	304L CRES	38
1	PACKING	VITON	37
1	PIN, MAIN	440C CRES	36
1	SPRING	302 CRES	35
1	POPPET, MAIN	440C CRES	34
1	SEAT, MAIN	17-4 PH CRES	33
1	SEAT, FLOW LIMITER	17-4 PH CRES	32
1	SPRING	17-7 PH CRES	31
1	PACKING	VITON	30
1	POPPET, FLOW LIMITER	17-4 PH CRES	29
1	COVER, FLOW LIMITER	304 CRES	28

Figure 51. Sectioned Flightweight Regulator Assembly--Side View

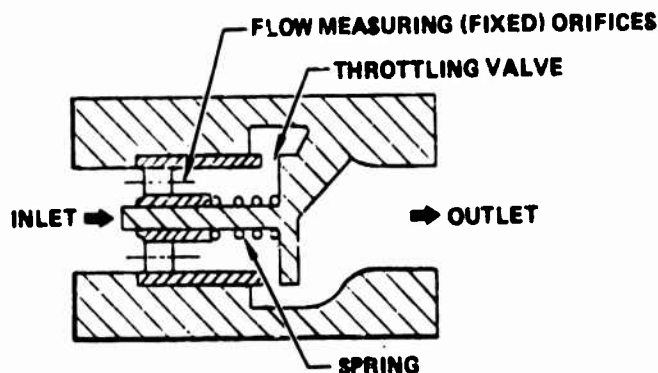


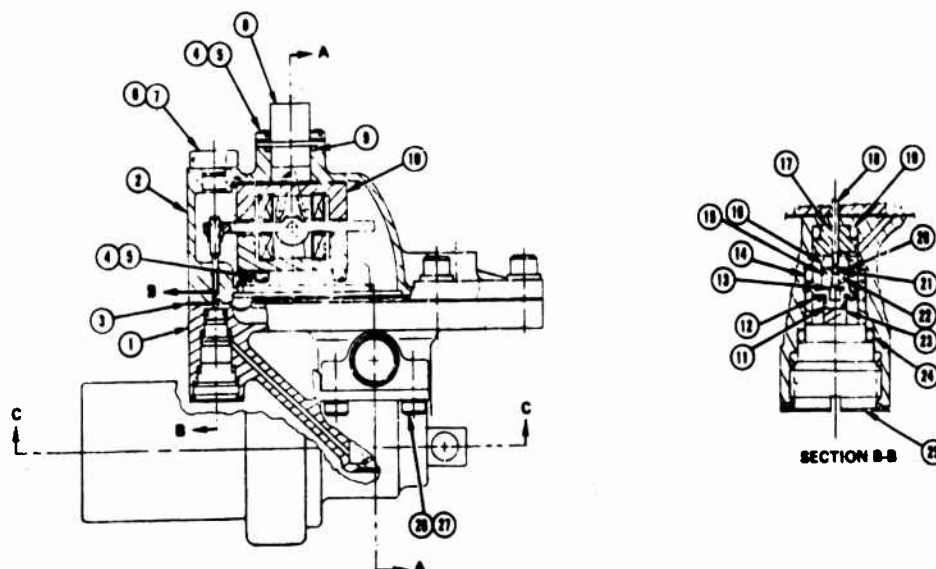
Figure 52. Flow Limiter Schematic

movement. Therefore, the throttling valve remains full open and does not restrict the flow during normal regulator operation. At excessive flowrates, the pressure drop increases and forces the poppet to slide, causing the throttle valve to close and limit the flow. This flow-limiting concept was used in Parker's Apollo Lunar Module (LM) descent engine pressurization subsystem regulator.

It would also be possible to locate the flow limiter at the regulator outlet. This would allow the flow to be limited to a lower level and result in a smaller relief valve; however, the entire regulator, including dome and outlet, then would have to withstand 4000 psia (at 70 F) if the main valve failed open.

The flow limiter design was shown previously in Fig. 51. The poppet and seat are fabricated from 17-4 PH stainless steel. The poppet slides on a center pin guide.

Torquemotor. The torquemotor, which is powered by the output of the electronics package, operates the pilot valve by positioning the valve push rod. Figure 53 shows the Parker design, which is in current production and used on the F-16 and L-1011 aircraft and the Walleye missile. Mass balancing to meet operational shock and vibration requirements is the only modification



QTY	PART NO.	NOMENCLATURE	MATERIAL	ITEM NO.
4		WASHER	CRES NO. 10	27
4		SCREW	CRES 10-32 X 1/2	26
1		PLUG	304L CRES	25
1		PACKING	VITON	24
1		RETAINER	302 CRES	23
1		GUIDE, PIN	303 CRES	22
1		BALL	TUNGSTEN CARBIDE (1 MM)	21
1		SEAT	NYLON	20
1		PACKING	VITON	19
1		ROD	302 CRES	18
1		GUIDE, ROD	304L CRES	17
1		ANVIL	304L CRES	16
1		SPRING	302 CRES	15
1		PACKING	VITON	14
1		PIN	302 CRES	13
1	M810625-4031	SNAP RING	CRES	12
1		SPRING	302 CRES	11
1		TORQUEMOTOR ASSEMBLY	4750 STEEL ALNICO V MAGNET MAGNET WIRE, AL ALLOY POT COMP	10
1		PACKING	VITON	9
1		CONNECTOR	CRES, GLASS INSERT	8
1	AN814-2J	PLUG	CRES	7
1		PACKING	VITON	6
8		SCREW	CRES 4-40 X 3/8	5
8		WASHER	CRES NO. 4	4
1		DIAPHRAGM	FAIRPRENE-VITON/DACRON	3
1		COVER	A356-T61 AL ALLOY CAST	2
1		BODY	CRES	1

Figure 53. Sectioned Flightweight Regulator Assembly--End View

required. The armature and C-cores are fabricated from annealed 4750 steel, and the permanent magnets are Alnico V. The coils are each wound with 800 turns of 36 HML wire to a resistance of 80 ohms on anodized aluminum bobbins. The current required as a function of regulator inlet pressure for maximum and zero propellant flowrates is presented in Fig.54.

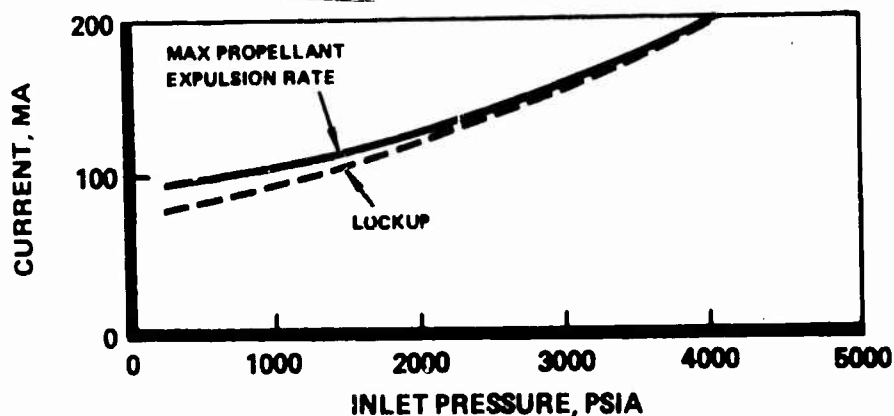


Figure 54 Torquemotor Current

Pilot Valve. The pilot valve is normally closed and requires a displacement of the push pin by the torquemotor to lift the spring-loaded ball off the seat. High-pressure pressurant gas then flows from the inlet of the main valve, through the pilot valve, to the regulator dome as shown in Fig. 55. The dome volume was minimized to achieve the equivalent of a high dynamic spring rate. A small fixed orifice provides for a constant bleed flow from the dome to the main valve outlet, which is at a lower pressure. During lockup, the pilot valve closes and the dome reference pressure drops to the regulator outlet pressure.

Figure 53 shows the pilot valve design, which is unchanged from that utilized in Parker's Viking helium regulator. The seating surface is a thin nylon film hot formed on 304L stainless steel. A 1-mm tungsten carbide ball is used for the poppet. Leakage on the Viking regulator was less than 10^{-5} SCCS helium. The ball is held in place with a pin fabricated from 302 stainless steel. The spring preload on the pin is adjusted with stainless-steel shims. The pin assembly used to lift the ball off the seat is

fabricated from 302 stainless steel and slides in a 304L stainless-steel guide. All other parts except the seals and thin backup rings are fabricated from stainless steel.

Main Valve. The main valve is normally closed and requires a displacement of the diaphragm and push pin to lift the spring-loaded poppet off the seat. Pressurant then flows through the main valve to the PSA's as shown in Fig. 55. Because the main valve is normally closed there is no slam-start requirement imposed on the design.

The diaphragm, shown in Fig. 51, is made from du Pont Fairprene and is clamped between the stainless-steel main body and the A356-T61 aluminum cover, which are serrated. The diaphragm cover plates are fabricated from 6061-T6 aluminum. The lower plate pushes against a 302 stainless-steel spring to contact the 440C stainless-steel push pin with flow deflector, which fits in the 440C steel poppet that is preloaded with a 302 steel spring. The seat is fabricated from 17-4 PH stainless steel; both it and the poppet are flat-lapped. This design is a duplication of Parker's LM helium regulator.

Relief Valve. Figure 56 shows the relief valve, a poppet-type valve, actuated by a spring-loaded diaphragm. When the regulator outlet pressure, acting on the diaphragm, overcomes the preloaded force of the coil spring, the diaphragm lifts the poppet off the seat and vents the pressurant flow.

When the valve is closed, the poppet is mechanically separated from the diaphragm support. Instead, it is held in position by the fluid pressure force and a small spring. The main spring and diaphragm rest on their own positive stop. This approach ensures ample poppet seating forces for low leakage, but limits the seating force to a value that will preclude damage.

The relief valve design, shown in Fig. 57, duplicates Parker's Space Shuttle RCS/OMS helium relief valve. The diaphragm is multi-ply Teflon that has been proven to withstand high pressure differentials while maintaining the

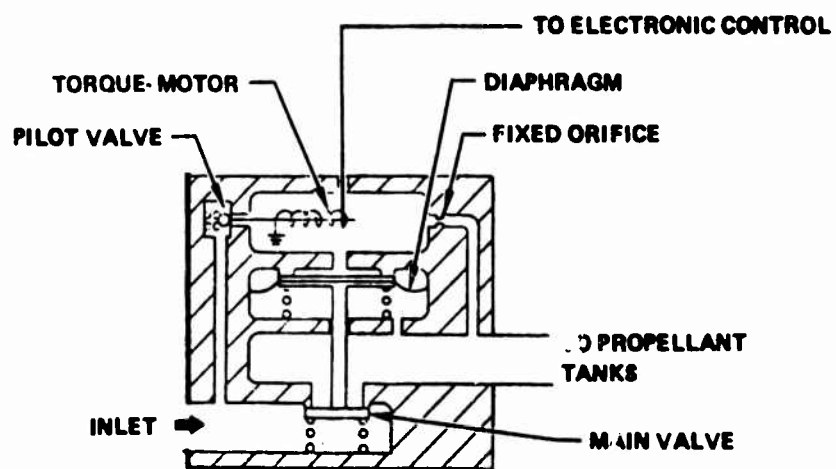


Figure 55. Pressure Regulator Schematic

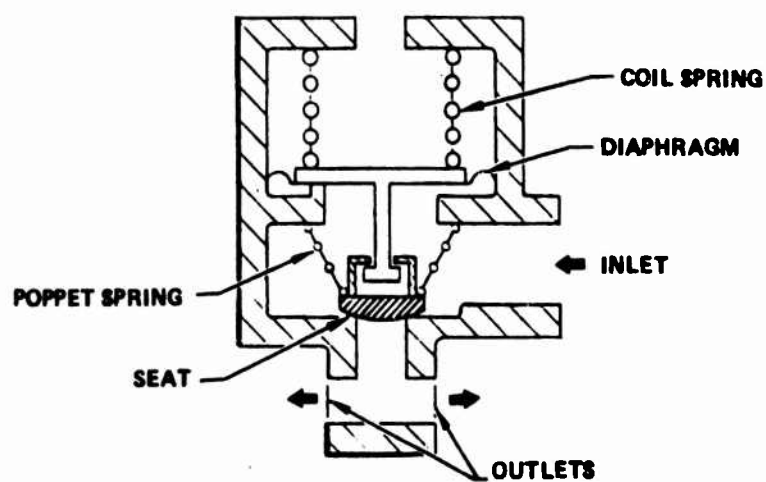
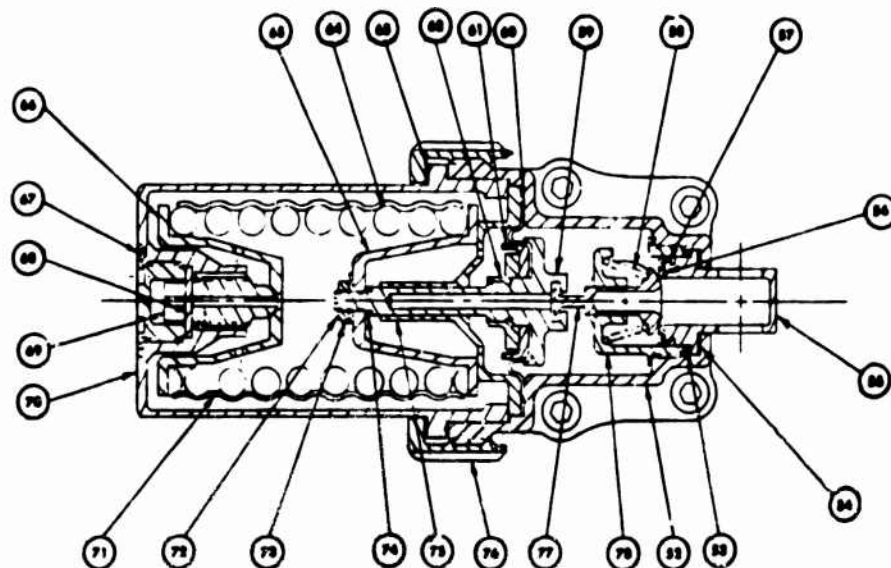


Figure 56. Relief Valve Schematic



QTY	NOMENCLATURE	MATERIAL	ITEM NO.
1	GUIDE, POPPET	17-4 PH CRSS	76
1	POPPET	17-4 PH CRSS	77
1	NUT, COVER	2024-T3 AL ALY	78
1	GUIDE, DIAPHRAGM	17-4 PH CRSS	78
1	ARM	302 CRSS	74
1	WASHER, TAB LOCK	304 CRSS	78
1	NUT, SPINDLE	302 CRSS	78
1	DAMPENER, SPRING	RTV 661U	71
1	HOUSING	6061-T6 AL ALLOY	78
1	SCREW, ADJUST	302 CRSS	80
1	PIN, ADJUSTING LOCK	302 CRSS	80
1	PLUG, LOCK	302 CRSS	87
1	SEAT, SPRING, UPPER	AAY-4830 AL BRONZE	86
1	SEAT, SPRING, LOWER	6061-T6 AL ALY	86
1	SPRING, PRESSURE RELEASE	17-7 PH CRSS	84
1	WASHER, THRUST	302 CRSS	83
1	NUT	304L CRSS	82
1	PISTON	2024-T3 AL ALY	81
1	DIAPHRAGM	FEPS00L FILM TEFLON ARMALON 27-001, T83 WOVEN TEFLON	80
1	SUPPORT, DIAPHRAGM	17-4 PH CRSS	88
1	SPRING, POPPET	17-7 PH CRSS	88
1	RETAINER, SEAT	302 CRSS	87
1	SEAT	FEF 100 TEFLON	86
1	BODY, SEAT	304 CRSS	86
1	WASHER	304 CRSS	84
1	GASKET	TFE TEFLON	83
1	BODY, RELIEF VALVE	ASB-701 AL ALLOY CAST	82

Figure 57. Sectioned Relief Valve

required flexibility. The diaphragm support, poppet, and poppet guide are fabricated from 17-4 PH stainless steel. The FEP 100 Teflon seat is held mechanically with a 302 stainless-steel retainer.

Pressure Transducer. A Kulite miniature solid-state pressure transducer, model HKMS-28-375-250A, is used to sense the delivered MMH pressure. The transducer utilizes a 17-4 PH stainless-steel diaphragm and an integrated sensing unit consisting of a silicon wafer on which a four-element Wheatstone bridge has been diffusion bonded for good stability during long-term storage. Miniaturization yields a marked increase in the natural frequency of the transducer, making it better suited for a shock and vibration environments. The transducer is constructed using electron beam welding and has been used in at least five aerospace applications including Viking. The transducer is integrally packaged with the electronics package as shown in Fig. 58.

The expected accuracy of the transducer is summarized in Table 16. The maximum predicted rms error is ± 1.9 psi and would occur at 40 and 100 F. Transducers normally have both zero shift and scale errors. In the subject application, however, only the accurate measurement of small pressures changes from the 300-psia setting is of interest. Therefore, the transducer bridge is balanced for zero output at the desired setting and scale errors have no effect on the transducer's accuracy. For the same reason, variations in the supply voltage do not cause errors.

Effects due to vibration are negligible. The maximum 15-g axial acceleration causes an error of less than 0.02 psi. Vibration causes a high-frequency variation in the output, but this averages out to zero because the circuits are linear. For 8.8 g rms vibration, the amplitude would be equivalent to less than 0.01 psi.

As shown in Table 16, the error is dominated by the effect caused by the temperature range. This is to be expected with the selected transducer

QTY	NOMENCLATURE	MATERIAL	ITEM NO.
AR	ETCHANT		111
AR	SILICONE INSULATION		110
AR	WIRE, SAFETY	CRES 0.032 DIA	109
AR	TUBING	MIL-I-22179C	108
AR	CATALYST		107
AR	PRIMER		106
AR	POTTING		105
AR	WIRE, STD. 24 AWG	MIL-W-18878D4	104
AR	SOLDER	QQ-S-571D	103
AR	CONFORMAL COAT		102
AR	SEALANT	MIL-S-22973 GRADE AV	101
AR	HEAT SINK COMP		100
4	SPACER, FIBRE	0.250 OD X 0.14 ID X 0.887 LG	99
4	SLEEVE		98
2	WASHER, FLAT	NYLON NO. 8	97
1	TRANSISTOR		96
1	INSULATOR		95
2	SPACER, HEX	TMD 6-32 THRU X 0.80 LG	94
1	LUG TERMINAL	22 AWG WIRE, NO 8 LUG	93
2	NUT HEX	CRES NO. 6-32	92
2	SCREW, PAN HEAD	NYLON 6-32 X 3/8 LG	91
5	SCREW, DR. FIL. HEAD	CRES. 6-32 X 1/16 LG	90
4	WASHER, FLAT	CRES. NO. 6	89
2	WASHER, LOCK	CRES. SPLIT NO. 6	88
2	WASHER, FLAT LT	CRES. NO. 8	87
1	CONNECTOR, RECEPTACLE		86
1	WIRE LIST		85
REF	SCHEMATIC		84
DOC			
RES			
DOC			
1	PLATE, IDENTIFICATION		83
1	ENCLOSURE		82
1	TRANSDUCER, PRESSURE		81
1	ASSEMBLY, P.W.B		80
1	ASSEMBLY, BASE		79

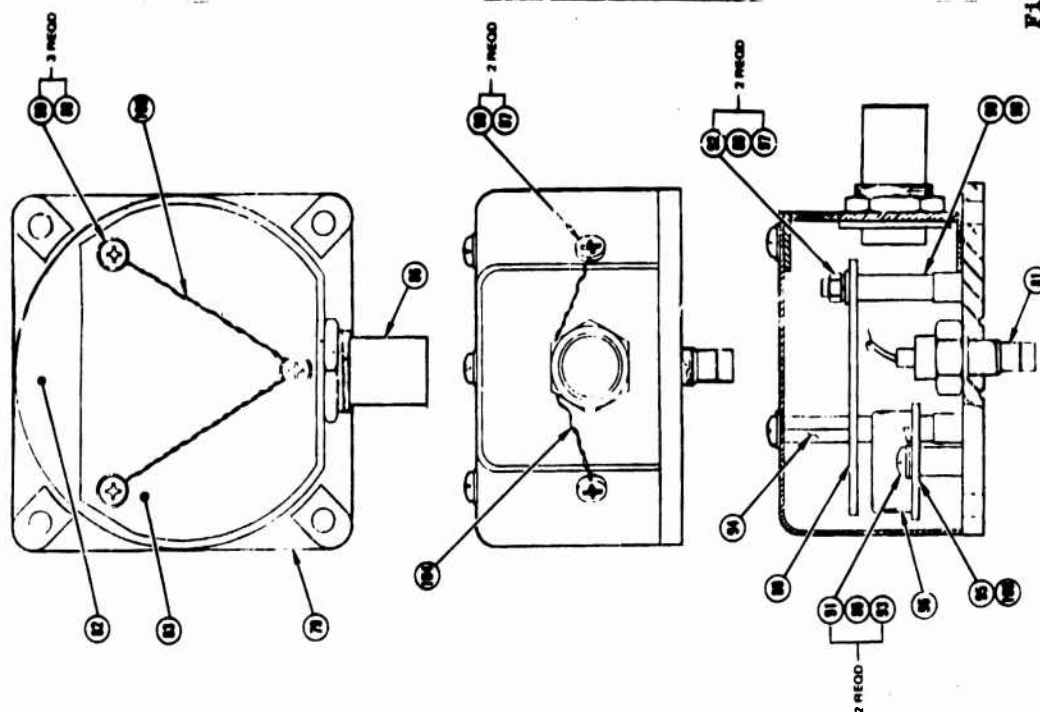


Figure 58. Sectioned Flightweight Controller Assembly

TABLE 16. PRESSURE TRANSDUCER ACCURACY

Characteristic	Kulite Specification	Error, psi
Supply Voltage Sensitivity	Cancelled Out	0
Nonlinearity	Does Not Apply	0
Repeatability	$\pm 0.25\%$ FS	± 0.375
Thermal Error: Zero	$\pm 1\%$ FS/100 F	± 1.80
Thermal Error: Scale	Does Not Apply	0
Resolution	Infinite	0
Acceleration Sensitivity	0.0003% FS/g	Negligible
Control Circuit Drift	$\pm 0.1\%$	± 0.30
Overall Accuracy (rms)		± 1.9

because it uses a piezoresistive strain gage (also referred to as semiconductor strain gage). It is also harder to temperature-compensate than a metal-foil strain gage. A metal-foil type, however, has a smaller output voltage and tends to yield a large drift in the operational amplifier that converts the error signal to the control signal. If problems are encountered in meeting the tolerance on delivered propellant pressure over the 40 to 100 F temperature range, the error tradeoff between the two types of strain gages will be investigated.

Electronics. When 24- to 30-volt dc electrical power is supplied to the electronics, all of the circuitry becomes energized from the output of the 15-volt dc voltage regulator. The reference voltage generator produces a linear ramp corresponding to a 0- to 300-psia command over a 10-second period. The command then saturates at 300 psia. As a result, the pressurant isolation and PSA pressurant inlet valves must be opened when the circuitry is energized or before. Otherwise, an increasingly larger error would exist when the valves are opened.

An error signal is generated by comparing the reference and pressure transducer signals as shown in Fig. 59. The error signal is amplified and then transmitted to the proportional and lead-lag compensation networks. The lead-lag compensation network consists of an amplifier with the maximum required gain and a variable attenuator to vary the gain as a function of the torque-motor current. The gain schedule is shown in Fig. 60.

The attenuator is controlled by the pulse-width-modulated output of a summing amplifier that compares the torque-motor signal to a reference triangular wave generator. The nominal pulse rate is several thousand per second. With a torque-motor current of less than 80 ma, the summing amplifier output is maximum, i.e., there is no attenuation because the triangular pulses are unmodified. Above 80 ma, the sides of the triangular pulses are clipped, resulting in a constant low voltage between pulses. The time duration of the low voltage increases linearly up to a torque-motor current of 180 ma, which causes the effective output of the summing amplifier to be attenuated.

Operation of the proportional compensation maximum gain amplifier and variable attenuator are similar to the integral compensation network, although the gains are different. The signals from the two compensation networks are summed and input to a power amplifier, which drives the torque-motor.

All of the electronic components will be mounted on a single printed circuit board and enclosed in a metallic container as shown in Fig. 58. Parker's analysis and design efforts were conducted without nuclear survivability design criteria. Instead, their designs were reviewed by Physics International (a ROCKOR Subsidiary) and Autonetics Division (Rockwell International), and modifications were recommended.

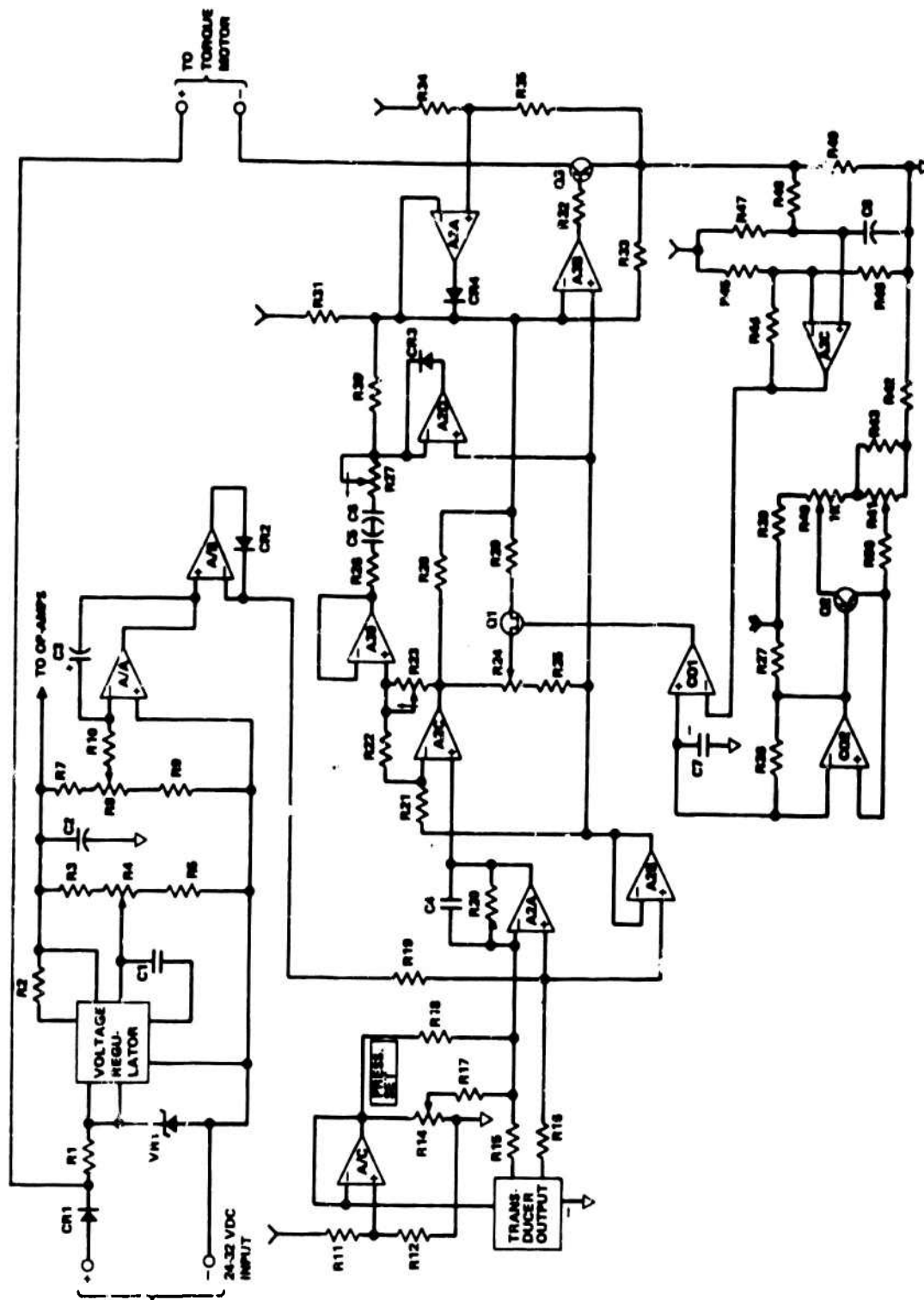


Figure 59. Flightweight Electronics Schematic

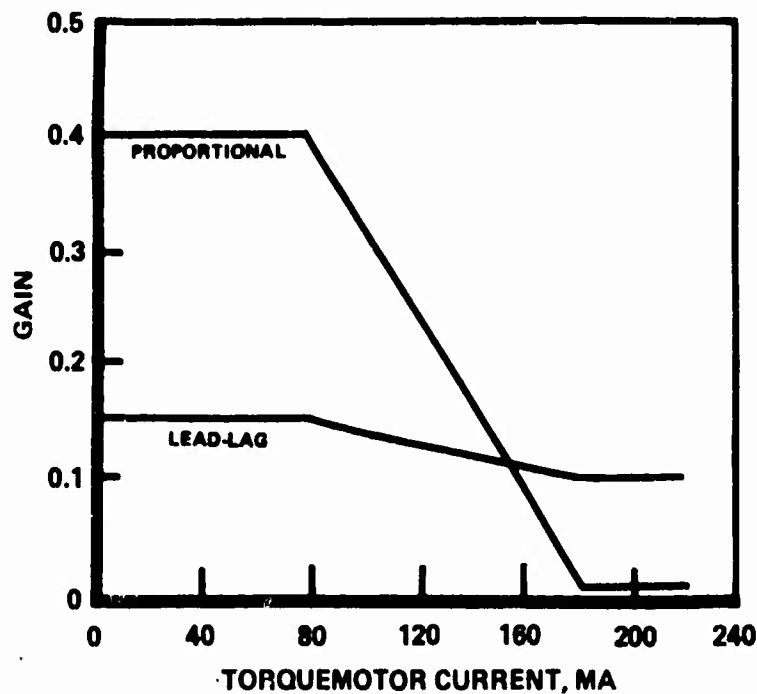


Figure 60. Gain Schedule

Catalytic Reactor

Tridyne is supplied at a regulated pressure to the catalytic reactor where the oxygen and hydrogen are reacted to convert the cold Tridyne to a heated mixture of helium and water vapor. The catalyst bed size, static stress, and thermal analyses and reactor design are presented in the following sections.

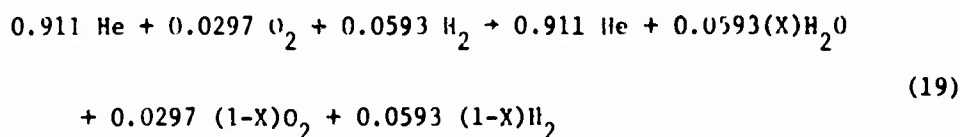
Catalyst Bed Size. Calculation of the catalyst volume was based on an empirical relationship derived from testing of a 2.0-in.³ bed with Tridyne containing nitrogen (instead of helium) during a previous contract. The catalyst volume of 2.49 in.³ was calculated from Eq. 18.

$$V = \frac{\dot{Q}}{Kp} (1 + \epsilon) \left[\ln \left(\frac{1}{1-X} \right) \right] - \epsilon X \quad (18)$$

where

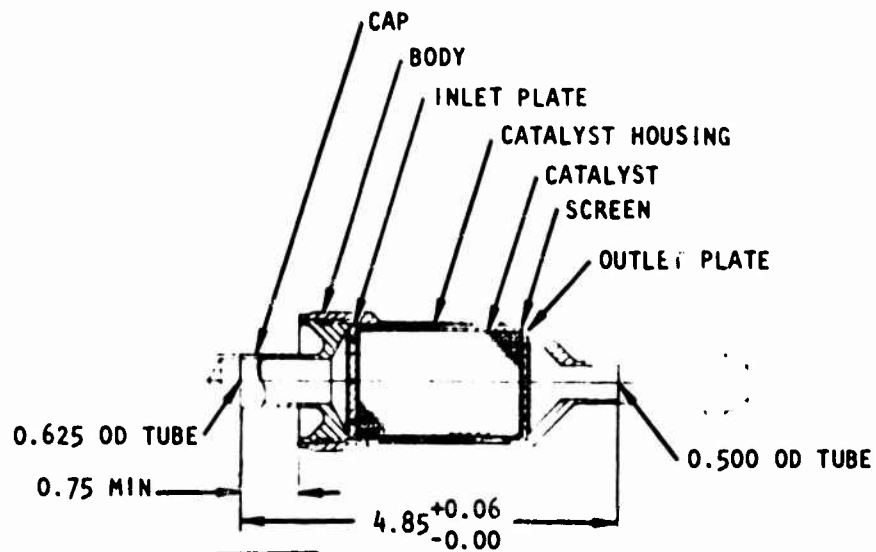
- V = volume, in.³
- \dot{m} = mass flowrate, lb/sec
- ρ = inlet gas density, lb/ft³
- K = empirical reaction coefficient (0.133)
- X = fractional completion of reaction
- ϵ = fractional decrease in moles during reaction

The reaction is shown in Eq. 19.



The parameter ϵ is equal to $0.0297 X$ for this reaction. A value of 0.995 was selected for the fractional completion of reaction to intentionally yield a relatively large catalyst bed. In addition, a mass flowrate of 0.035 lb/sec was used, which is approximately 25% higher than the flow required during propellant expulsions. The catalyst bed diameter was selected to be 1.25 inches, the same as the reactor tested in a previous nitrogen-Tridyne program.

Reactor Design. The reactor design is presented in Fig. 61. Except for the catalyst and wire screens, the complete assembly is made from 321 stainless steel. The catalyst, designated DEOXO MFSA by Engelhard Industries, consists of platinum-group metals on the surface of 0.0625-inch-diameter aluminum oxide spheres contained in a cylindrical housing with drilled end plates. The 302 stainless steel, 26 mesh, 0.015-inch-diameter wire screens prevent the catalyst spheres from obstructing the 17 0.032-inch-diameter injection orifices in the inlet plate and from migrating through the 52 0.125-inch-diameter holes in the outlet plate. The injection orifices are used to distribute the Tridyne flow and prevent channeling within the catalyst. The area of the exit plate holes is 5.3 times the area of the exit tube.



Dimensions in inches

PART NO.	MATERIAL	SIZE	SPECIFICATION
016	321 CRSS BAR	1.438 DIA X 0.28	QQ-S-763 CL321 COND A
013	CRSS WIRE CLOTH	26 BZEM 6.815 WIRE TWILLED	
008	321 CRSS TUBE	1.438 OD X 0.068 WT	MIL-T-8808 COMP 321 TYPE II
087	321 CRSS BAR	1.438 DIA X 0.18	QQ-S-763 CL321 COND A
006	321 CRSS BAR	1.88 DIA X 2.00	QQ-S-763 CL321 COND A
003	321 CRSS BAR	1.88 DIA X 8.00	QQ-S-763 CL321 COND A

Figure 61. Flightweight Catalytic Reactor

The catalyst assembly is positioned in the main body to form a double-walled reactor. This design feature minimizes conduction heat losses and provides for a fast thermal response time, both of which are important goals in maximizing pressurization subsystem performance, especially for the long, pulsed MDC 11.

The inlet cap and the main body are threaded to ensure a tight fit of the internal catalyst assembly. The reactor is sealed with a burn-down weld. The inlet tube is fabricated with a closed end, and the outlet tube is threaded to permit proof pressure and leak testing. Tube ends are subsequently removed prior to installation in the pressurization subsystem.

Static Stress Analysis. A static stress analysis was conducted at twelve locations using maximum operating pressures and temperatures. The lowest safety factors occur near the mid-point of the thin wall section of the main body. These safety factors are approximately 1.8 on yield and 5.2 on ultimate.

Thermal Analysis. A thermal analysis of the reactor was performed to predict its transient response time, maximum operating temperatures, material thermal gradients, and heat soakback to the electronically controlled regulator. For this analysis, the maximum gas outlet temperature of 1061 F (storage at 100 F) was used. This temperature allows for a 10-degree drop in the gas temperature as it flows to the PSA's in insulated lines.

Rocketdyne's Differential Equation Analyzer Program (DEAP) was utilized with the nodal model shown in Fig. 62. Forced convection was assumed to be the primary heat transfer mode from the gas to the catalyst and hardware. A standard Dittus-Boelter type of equation was used to determine the convective film coefficient. Heat loss caused by conduction and radiation from the noninsulated outer surface was taken into account. An emittance of 0.5 was used as being typical for a machined steel surface.

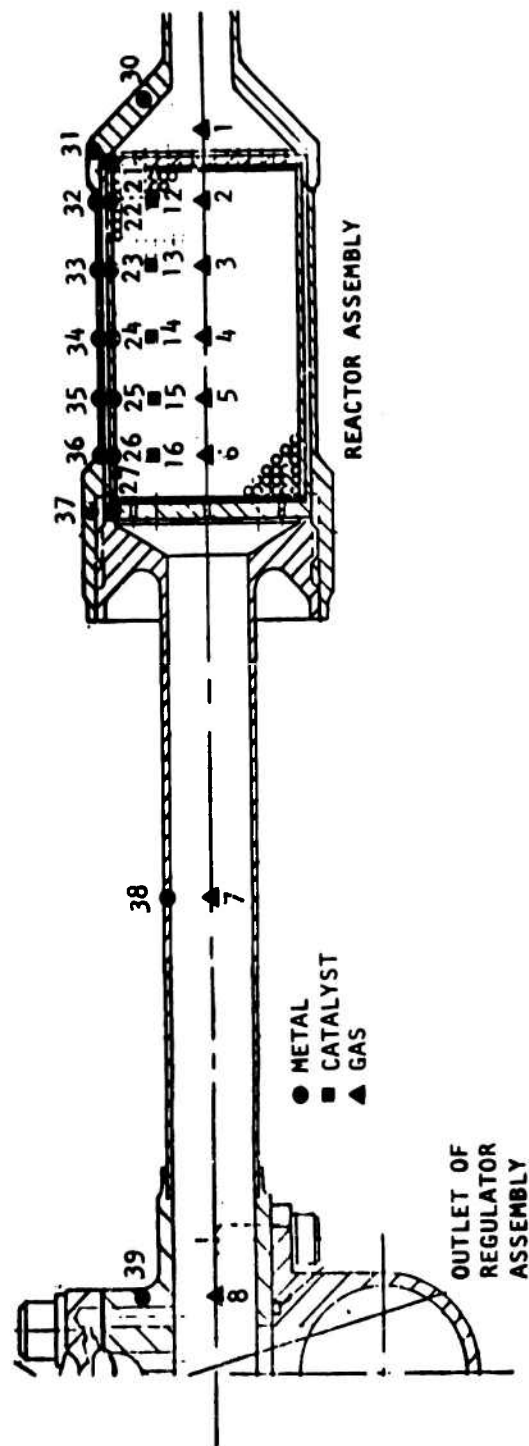


Figure 62. Reactor Nodal Model

The reaction temperature profile of the gas was determined by using the terms of Eq. 18 and parametrically varying the fractional completion of reaction, which implies a temperature, and calculating the corresponding volumes. As a result, the axial locations of the respective temperatures were determined for a fixed diameter, assuming no heat loss. The results are presented in Fig. 63.

Simulation of the initial pressurization with the DEAP nodal model is presented in Fig. 64. The reactor gas outlet temperature reaches 90% of the reaction temperature in less than 2 seconds. This rapid response is partially the result of the double-wall design, which minimizes losses from the main body. The effectiveness of the design is demonstrated by comparing the temperatures of the catalyst housing and the main body.

The results of simulating MDC I are presented in Fig. 65. The 10-second initial pressurization was followed by a 128-second coast and the 122.5-second expulsion. A second coast then was simulated to determine if the regulator would overheat. This sequence represents a worse case from a thermal soakback standpoint than the pulsed MDC II. As shown, the regulator assembly outlet remains cold during the long coast. Even the line between the reactor and the regulator reaches only 150 F.

The reactor outer body temperature peaks at approximately 870 F. Although the effect of radiation heat loss on reactor performance is not appreciable, it may be advisable to insulate the reactor to protect adjacent components from thermal radiation. A 0.125-inch-thick layer of insulation such as Johns-Manville MIN-K would be adequate.

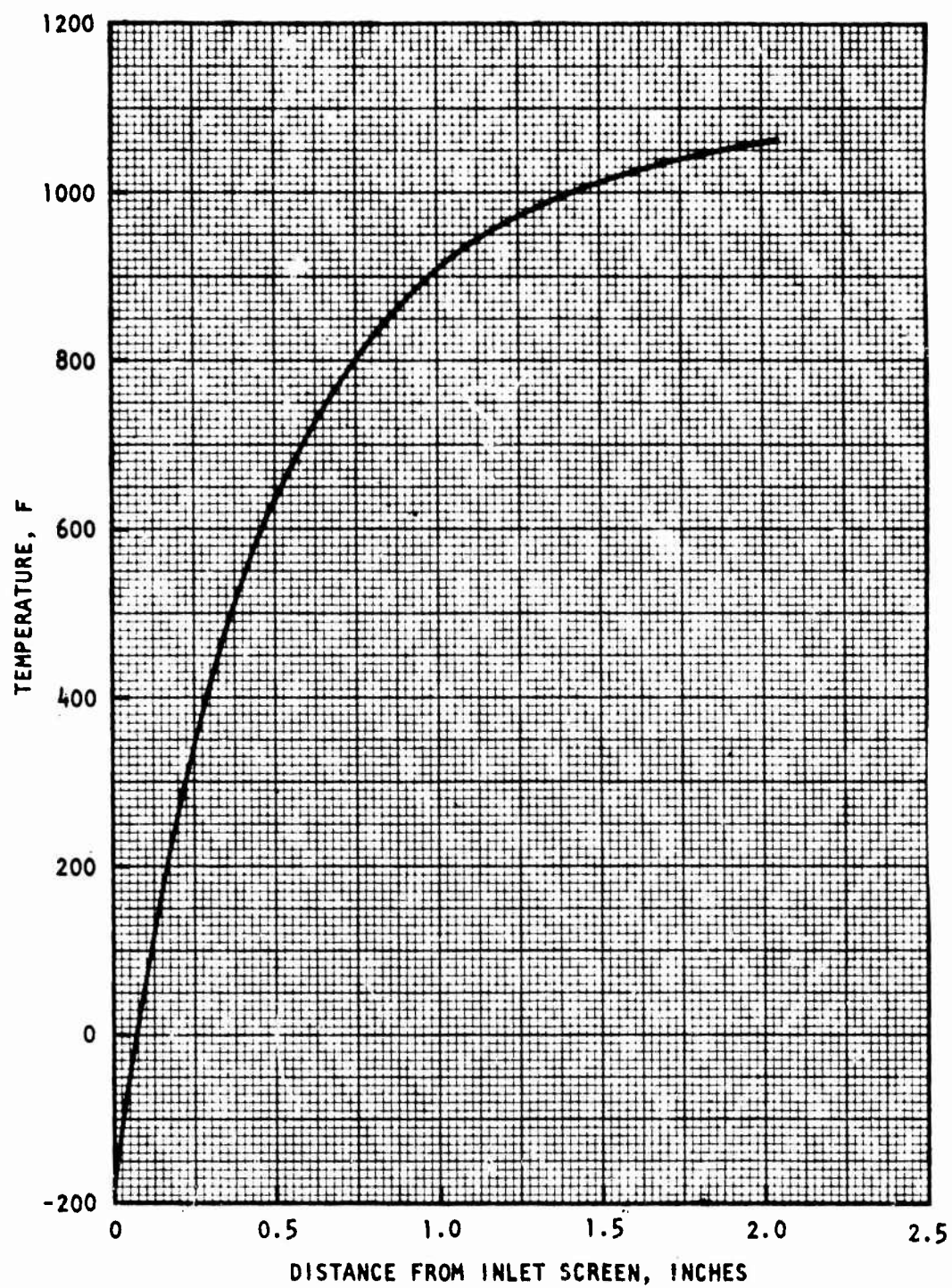


Figure 63. Catalyst Bed Temperature Profile

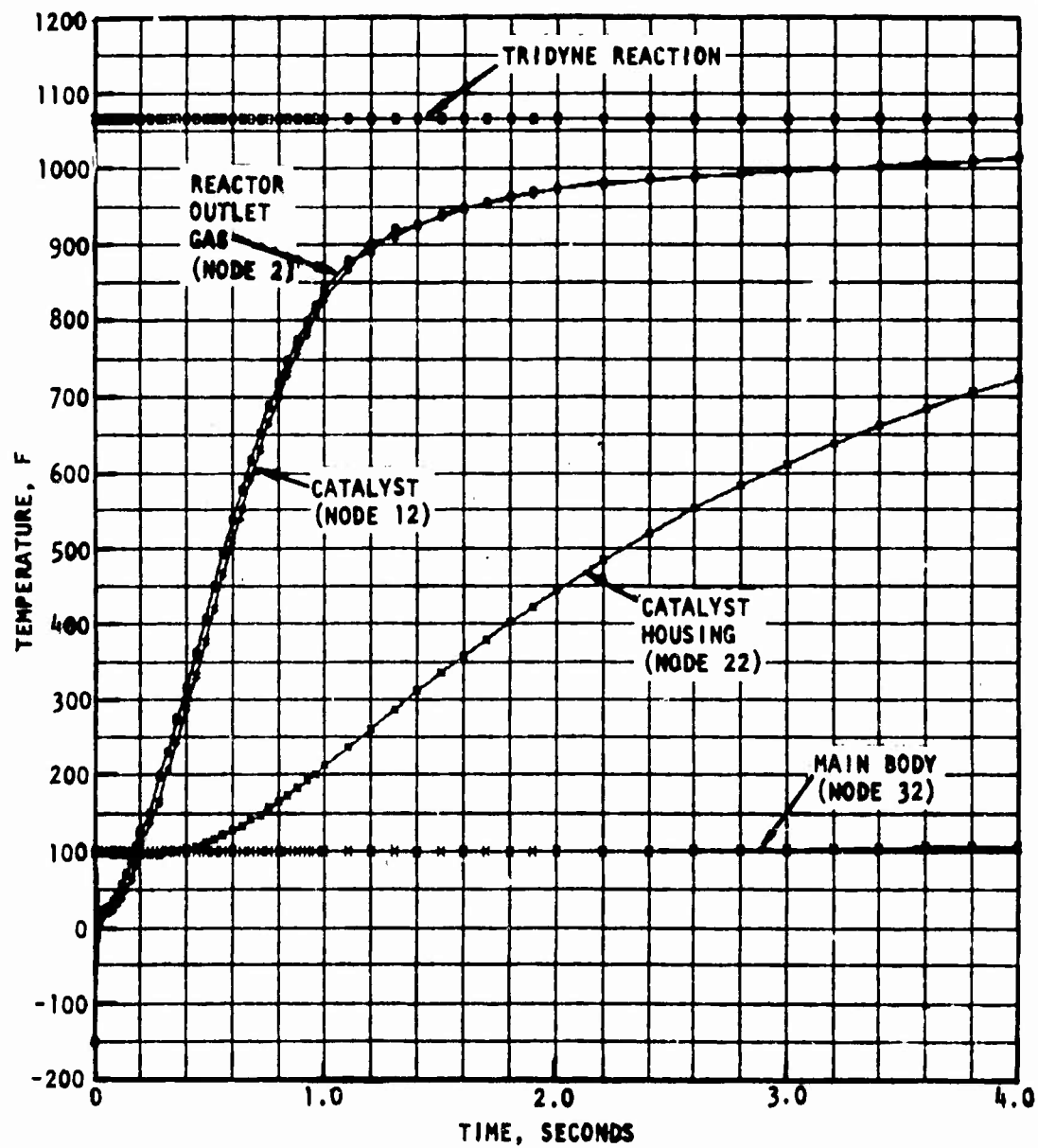


Figure 64. Reactor Temperature Transients During Initial Pressurization

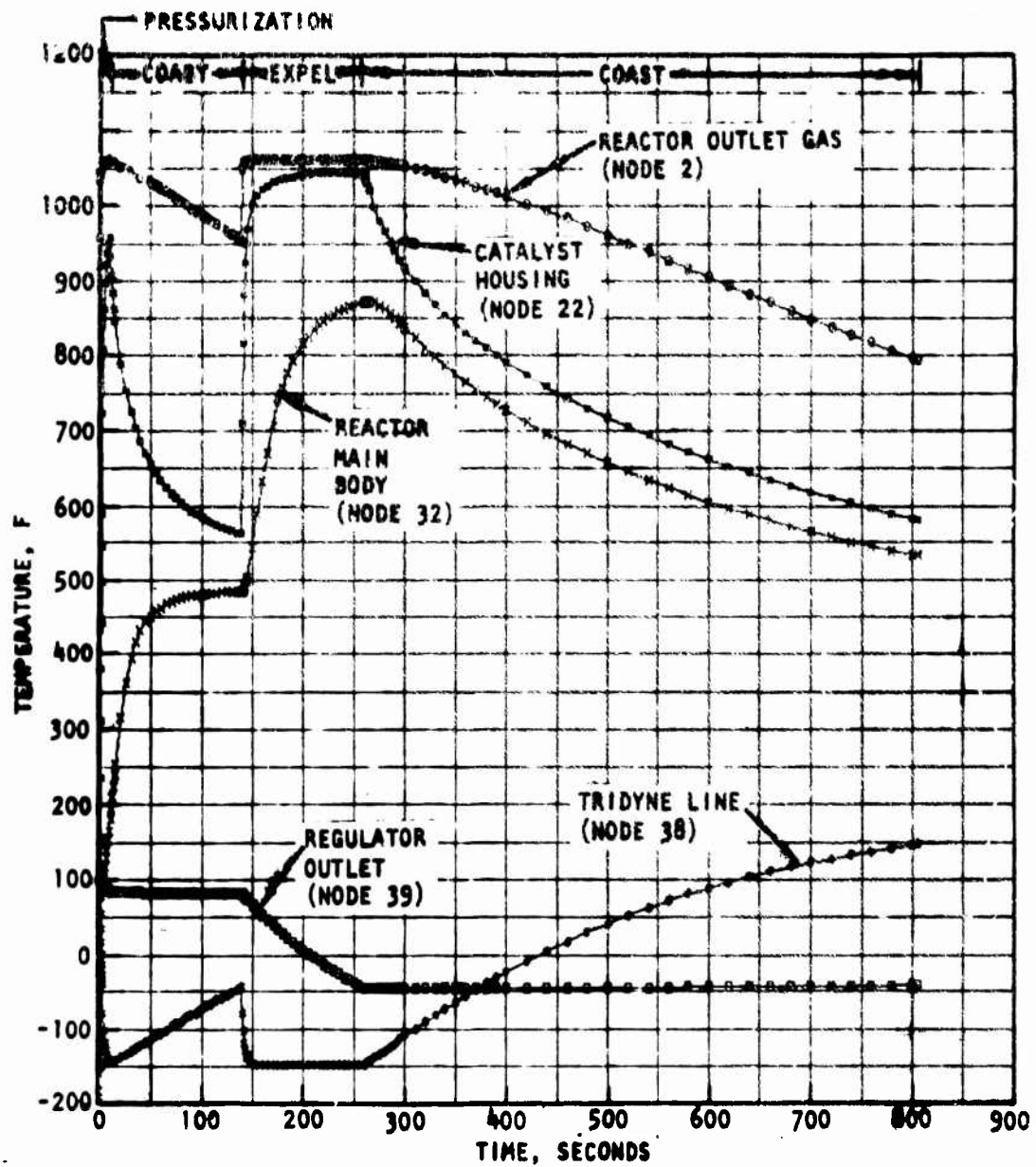


Figure 65. Reactor Temperature Transients During MDC I

PROTOTYPE PRESSURIZATION SUBSYSTEM

The prototype pressurization subsystem differs from the flightweight design in two respects. First, facility components will be used instead of flightweight hardware for the pressurant tank fill and drain valve, the tank leak detector, the pressurant isolation valve, and the regulator assembly filter, flow limiter, and relief valve. In addition, design modifications were made to the pressurant tank, the electronically controlled regulator and the catalytic reactor for reasons discussed in the following sections.

Pressurant Storage Tank

Brunswick is currently fabricating composite-wrapped spherical tanks for the Space Shuttle Orbiter being developed by Space Division, Rockwell International. These RCS helium tanks have a minimum volume of 3008 in.³ at one atmosphere after proof sizing. This size is approximately 5% larger than required for the flightweight design. Because of availability, one of these tanks has been acquired for use during the program.

The Brunswick Shuttle tank (Fig. 66) has maximum operating, proof, and burst pressures of 4000, 5270, and 6000 psig, respectively. The liner is titanium 6Al-4V with a 1.5-inch-diameter, threaded outlet port. The liner is filament wrapped with Kevlar 49, which is impregnated with epoxy resin. The weight is 25.7 pounds and the outer diameter is 18.7 inches. Space Division's specification number is MC282-0082 and their part control number is MC282-0082-0032.

Electronically Controlled Regulator

The prototype electronically controlled regulator design duplicates the flightweight design in those areas required to demonstrate its functional adequacy. Not included in the prototype regulator assembly are the integrally packaged inlet filter and flow limiter and the outlet relief valve. In addition, the torque motor will be used "as is" from current production

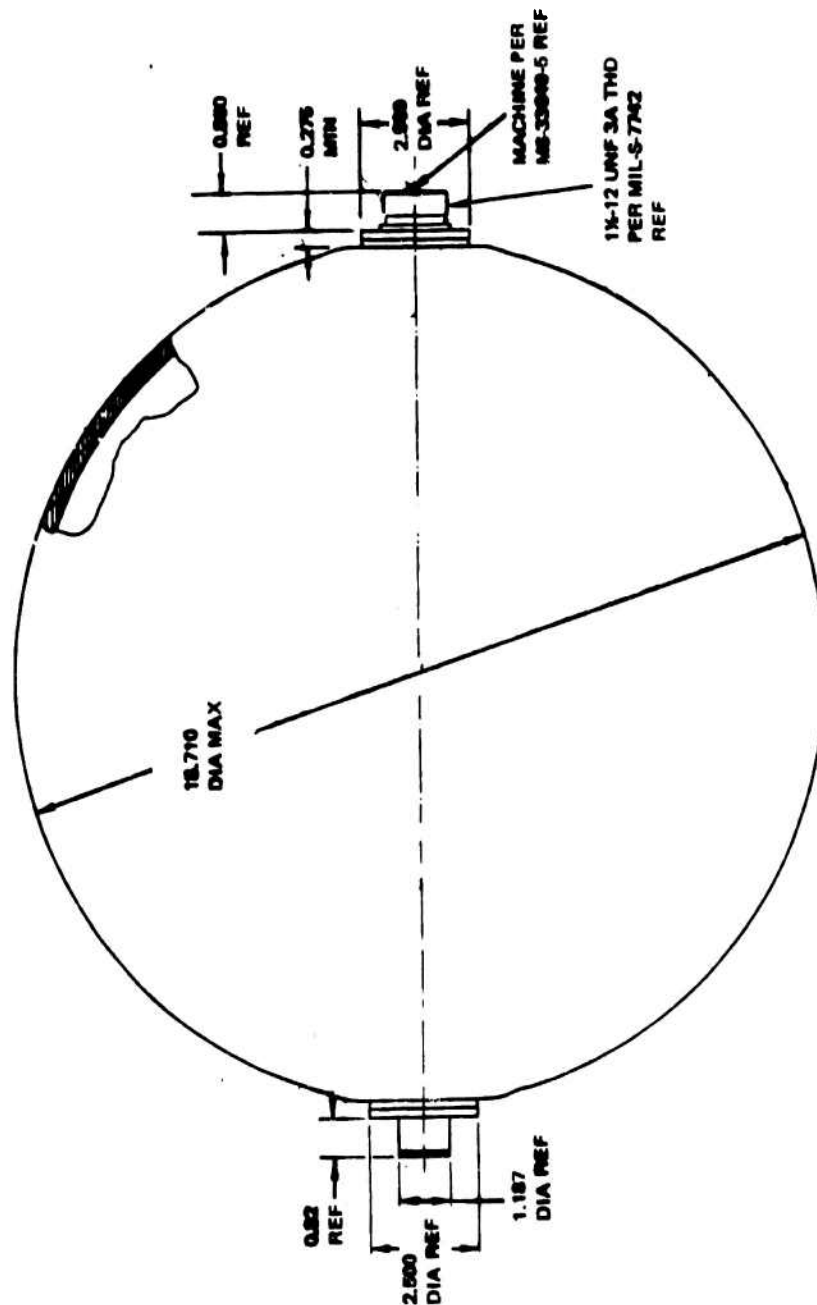


Figure 66. Prototype Pressurant Tank

without mass balancing. The main body will be heavyweight and machined from 6061-T6 aluminum bar stock with threaded stainless-steel inlet and outlet fittings rather than a lightweight stainless-steel body with welded tube stubs. The cover also will be heavyweight machined 6061-T6 rather than a lightweight A356-T6 aluminum casting.

Exterior and sectioned drawings of the prototype regulator assembly are shown in Fig. 67 and 68, respectively. The lightweight poppet, seat, and diaphragm materials are utilized and all-stainless-steel construction of other pilot valve and main valve parts is maintained.

Variations from the lightweight controller assembly include provisions for varying the gain schedules. Also, the electronics will be breadboarded in a less compact housing. Figures 69 and 70 show the electronics to be utilized during regulator component testing by Parker.

Catalytic Reactor

The prototype and lightweight catalytic reactor designs are very similar in the areas important to demonstrating performance during development testing. Because six catalysts beds will be tested, modifications to the main body are required, as shown in Fig. 71, to permit interchangeability. These modifications are restricted primarily to the relatively cool inlet end, however, to ensure similar thermal characteristics.

Because the largest catalyst bed diameter is the same as the lightweight design, the reactor main body diameters are the same. The outlet converging section and tube dimensions also are identical to the lightweight design; however, a threaded outlet fitting is used instead of a tube stub. Construction of the three 1.25-inch-diameter catalyst beds, including the inlet and outlet plates, is identical to the lightweight design, except one is shorter and one is longer. The three 1.00-inch-diameter beds will have a larger annular gap between the bed housing and main body.

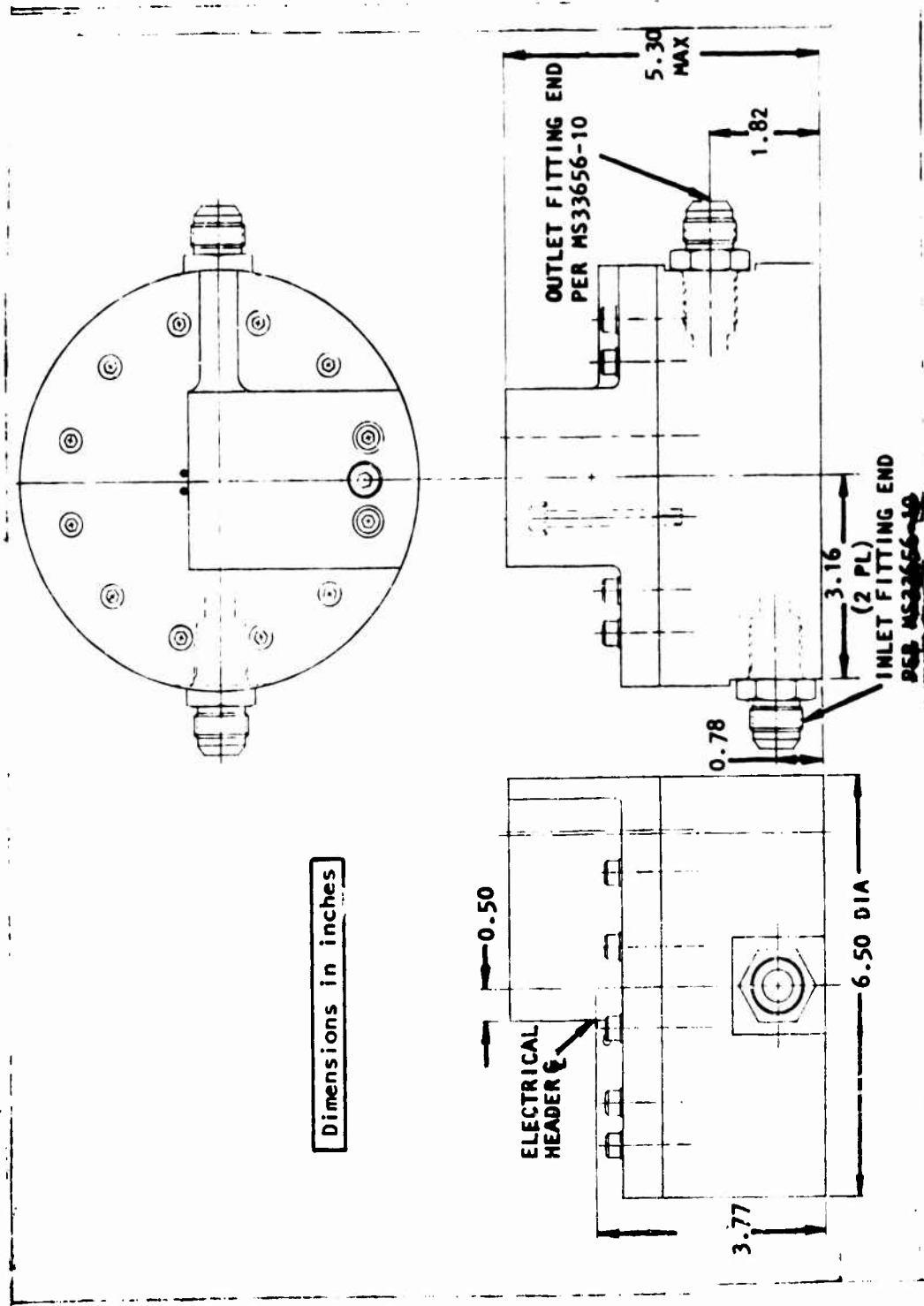


Figure 67. Prototype Regulator Assembly

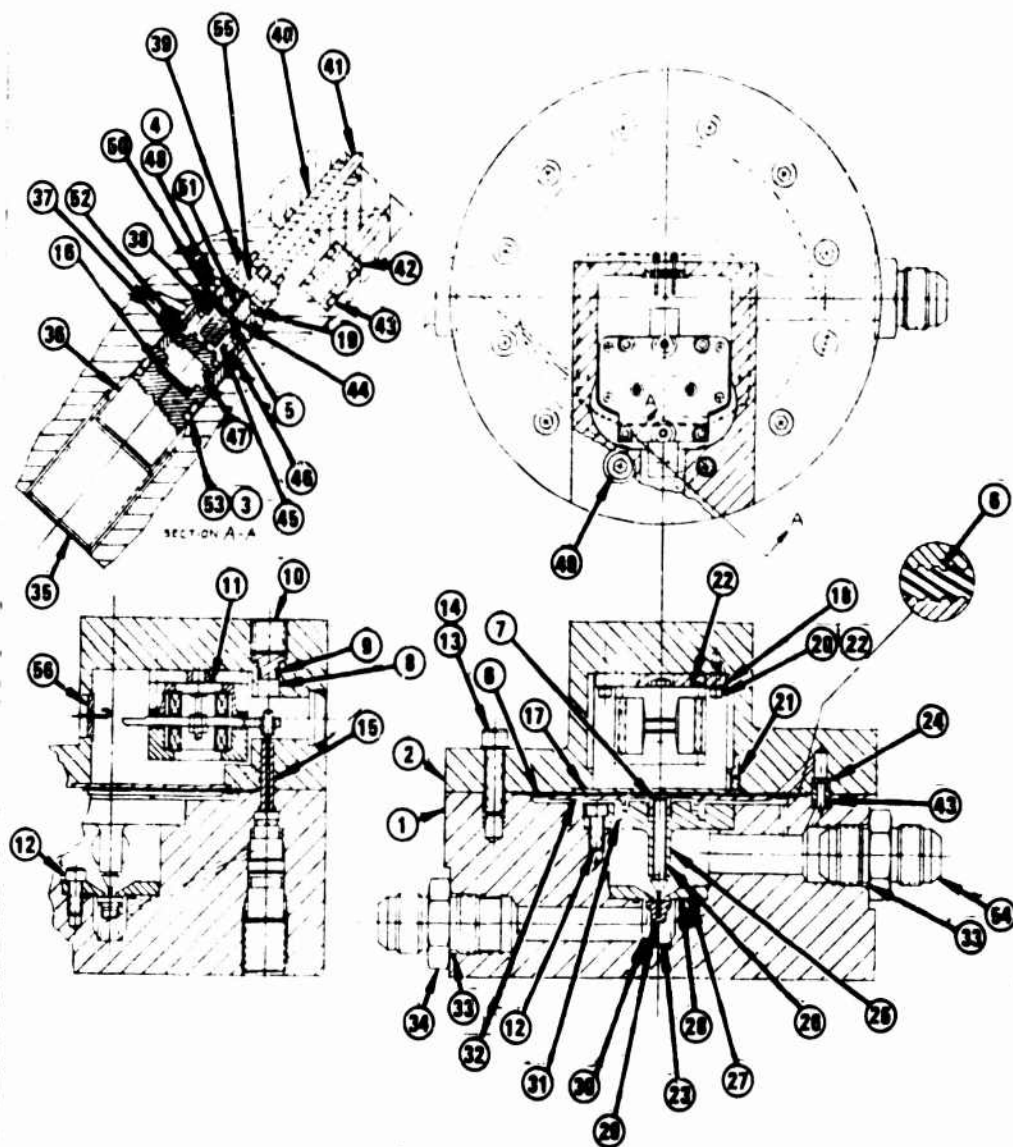


Figure 68. Sectioned Prototype Regulator Assembly

QTY	PART NO.	NOMENCLATURE	MATERIAL	ITEM NO
1	N230048-2A-MP80	ELECT HEADER		88
1	5778184-101	PIN, SPACER	17-4 PH CRES	86
1	AN815-10J	FITTING	CRES	84
1	MS28774-013	BACKUP RING	TETRAFLUOROETHYLENE	83
1	5778186-101	SPRING, BIAS	17.7 PH CRES	82
1	5778186-101	PIN, ANVIL	17-4 PH CRES	81
1	5778184-101	PIN, BALL	17-4 PH CRES	80
2	NAS1352C4H36	SCREW	CRES 1/4-20 X 2-1/4	79
1	MS28774-012	BACKUP RING	TETRAFLUOROETHYLENE	78
1	5778182-101	SPRING, PILOT	17.7 PH CRES	47
1	5778181-101	BODY, PILOT	304 CRES	46
1	5778180-101	SPRING, RETAINER	17.7 PH CRES	45
1	5778179-101	SEAT, PILOT	NYLON 8	44
4	PARKER # 2-007	PACKING	BUTYL	43
1	5778178-101	TUBE, TRANSFER	304 CRES	42
1	5778177-101	PUSH ROD, PILOT	17-4 PH CRES	41
1	5778176-101	TUBE, PILOT	304 CRES	40
1	5778175-101	SPACER, PILOT	304 CRES	38
1	5778174-101	GUIDE, PILOT	303 CRES	38
1	5778172-101	SPACER, SPRING	304 CRES	27
1	5778172-101	RETAINER, SPRING	304 CRES	36
1	STOCK NO 3275	SCREW, SET	CRES 5/8-18 X 3/4	36
1	20011-10-17W	FILTER	10000 300 SERIES CRES TRI-DOT ELECTRON INO	34
2	PARKER # 2-910	PACKING	BUTYL -10 PORT	33
1	5778171-101	PLATE, LWR, DIAPH	8081-T8 AL ALY	32
1	5778170-101	SPRING, DIAPH	302 CRES SPG TEMP	21
1	5778169-101	SPRING, POPPET	302 CRES SPG TEMP	30
1	5778168-101	POPPET, MAIN	440C CRES RC37-82	28
1	PARKER # 2-018	PACKING	BUTYL	27
1	5778167-101	SEAT, MAIN	17-4 PH CRES H800	26
1	5778166-101	PIN, MAIN	440C CRES RC 80 MIN	25
1	5778165-101	GUIDE, MAIN	17-4 PH CRES H800	24
1	5778164-101	ORIFICE	304 CRES	23
AR	5778165-AR	SHIM, SPG MAIN	CRES 204	22
8	NAS620C04	WASHER	CRES NO 4	21
4	MS24893 C3	SCREW, EL HD	CRES 4-40 X 5/16	20
4	NAS1252C04H8	SCREW	CRES 4-40 X 2/8	19
1	5778182-101	ANVIL	304L CRES 8HN 180 MIN	18
1	5778181-101	PLATE, ADAPTER	8081-T8 AL ALY	17
1	5778157-101	PLATE, COVER	8081-T8 AL ALY	16
A/P	5778180-AR	SHIM, PILOT	304 CRES	15
2	PARKER # 2-009	PACKING	BUTYL	14
10	NAS1352C4H18	SCREW	CRES 1/4-20 X 1	13
12	NAS620C4	WASHER	CRES 1/4	12
7	NAS1351C3H6	SCREW	CRES 10-32 X 1/2	11
1	2782004-101	TORQUE MOTOR ASSY	4750 STL, ALNICO V MAGNET MAGNET WIRE, AL ALY, POT COMP	10
1	AN565AC820H6	SCREW, SET	CRES 1/2-20 X 1/2	8
1	PARKER # 2-008	PACKING	BUTYL	8
1	5778159-101	PLUG, ADJUSTING	304 CRES	7
AR	5778163-AR	SHIM, MAIN VALVE PIN	304 CRES	6
1	5778158-101	DIAPHRAGM	CHLOROPHYORIN ON DACRON	5
1	5723183-1	BALL	TUNGSTEN CARBIDE IMM	4
1	PARKER # 2-012	PACKING	BUTYL	2
1	PARKER # 2-012	PACKING	BUTYL	2
1	5778157-101	COVER ASSY	8081-T8 AL ALY	1
1	5778156-101	BODY	8081-T8 AL ALY	1

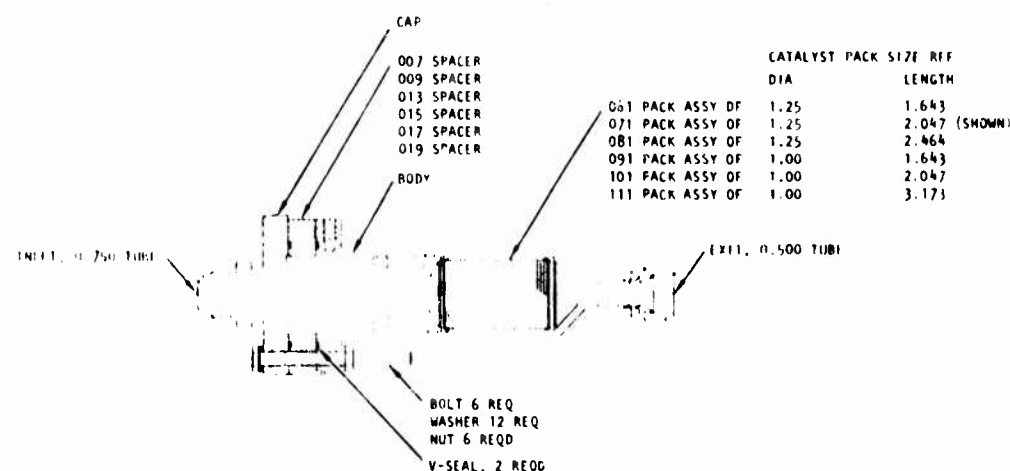
Figure 68. (Concluded)



Figure 69. Variable Gain Controls



Figure 70. Electronic Components



PART NO.	SIZE	MATERIAL	SPECIFICATION
000	MAKE FROM -033 OR -036		
057	1.25 X 1.25	INCONEL 000 SCREEN 40 MESH 0.010 WIRE	
056	1.50 X 1.50	INCONEL 000 SCREEN 40 MESH 0.010 WIRE	
053	MAKE FROM NAS1004 -36A BOLT		
049	1.25 X 1.25	INCONEL 000 SCREEN 40 MESH 0.010 WIRE	
047	1.50 X 1.50	INCONEL 000 SCREEN 40 MESH 0.010 WIRE	
045	0.047 X 3.38 X 3.25	304L CRSS SHEET	QQ-S-785 CL304L COND A
043	0.047 X 3.38 X 2.13		
039	0.047 X 3.38 X 1.70		
037	0.047 X 4.13 X 2.53		
036	0.047 X 4.13 X 2.13		
033	0.047 X 4.13 X 1.70	304L CRSS SHEET	QQ-S-785 CL304L COND A
029	1.25 X 0.19	304L CRSS BAR	QQ-S-785 CL304L COND A
027	1.25 X 0.25		
026	1.50 X 0.18		
023	1.50 X 0.25		
019	3.00 X 1.75		
017	3.00 X 0.75		
015	3.00 X 0.25		
013	3.00 X 1.08		
009	3.00 X 0.75		
007	3.00 X 0.25		
006	3.00 X 5.00		
003	3.00 X 7.50	304L CRSS BAR	QQ-S-783 CL304L COND A

Figure 71. Prototype Catalytic Reactor

The inlet end is substantially different from the flightweight design. The inlet cap, which holds the catalyst bed in place, slides within the main body to accommodate the different bed lengths. It has a 0.75-inch-diameter threaded inlet port instead of a 0.625-inch-diameter tube stub. The inlet cap is secured to the main body with six bolts, and six spacers are required for the different beds. Sealing is accomplished with two metal V-seals. Nonmetallic seals will be used during short-duration tests (with inert gas purging after cutoff), when heat soakback will be minimal. The flange at the inlet end of the main body has two threaded holes for mounting the reactor. Because of availability, the prototype reactor was made from 304L instead of 321 instead of 321 Cres and the screens from 40 mesh 0.010 Inconel 600 wire instead of 26 mesh 0.015 Cres wire.

FLIGHTWEIGHT FEED SYSTEM

Additional supporting studies were conducted for the flightweight feed system. These analyses included performance, stage installation layouts, mass properties (weight and center of gravity), unit production costs, system safety and reliability, and nuclear hardness and survivability. Feed system design characteristics are summarized in Table 17.

Performance

Two types of performance analyses were performed for the propellant feed system. The first involved determination of the pressurant flowrate requirements during various propellant expulsions with transient heat transfer. The second was a prediction of the transient errors in delivered propellant pressure.

Pressurant Flowrate. Since modeling of the pressurant flowrate thermodynamics is relatively straightforward, the equations were included in the complex heat transfer model of the PSA described in the flightweight PSA section. Quasi-steady fluid flow relationships were assumed, i.e., pressure oscillations were precluded by setting the pressurant flowrate equal to that required to maintain the required pressure schedule in the tank during the expulsion duty cycle. This pressure schedule is a function of diaphragm pressure differential, which varies with percent diaphragm reversal.

TABLE 17. FEED SYSTEM DESIGN CHARACTERISTICS

Propellant Pressure Performance, psia	300 \pm 2.55
Maximum Pressurant Flowrate, lb/sec	
Initial Pressurization	0.046
MDC I	0.028
MDC II	0.027
Weight, pounds	
Loaded Feed System (two PSA's, pressurization subsystem, propellants, Tridyne)	1594
N ₂ O ₄ (loaded)	900
MMH (loaded)	554
Feed System at End of Mission	187
Feed System Hardware Plus Tridyne	140
Feed System Hardware	134
PSA Hardware (two, including mounting rings)	98
Pressurization Subsystem (including Tridyne, excluding mounting plate and fasteners)	41
Unit Production Cost, 1977 dollars	
Feed System	47,800
Two PSA's	31,200
Pressurization Subsystem	16,600
Reliability	0.9963

During the 10-second initial pressurization, the flowrate decreases from 0.046 to 0.028 lb/sec. This range is the highest imposed on the pressurization subsystem. During the long MDC I expulsion at 275 in.³/sec, the pressurant flowrate starts at 0.020 lb/sec, increases to 0.028, and then decreases slightly to 0.027. For conversion to volumetric flowrates, 0.01 lb/sec of pressurant equals 184 in.³/sec at 307 psia and 1025 F.

MDC II starts off with a 275-in.³/sec expulsion, which requires a flowrate of 0.020 lb/sec. During the intermediate pulses, the maximum expulsion rate

is 205 in.³/sec, which reduces the pressurant flowrate to a range from 0.015 to 0.019 lb/sec as the expulsion cycle progresses. At the end of the cycle, the expulsion rate oscillates between 205 and 255 in.³/sec, requiring a maximum of 0.022 lb/sec of pressurant. The low expulsion rates, simulating attitude control engine burns, require less than 0.001 lb/sec pressurant gas.

Propellant Pressure. A previously developed dynamic performance model was utilized to simulate feed system operating conditions and determine resultant transient pressure errors. The mathematical model contains descriptions of the flow processes and operational characteristics of the regulator's mechanical and electronic components. Not included were the errors associated with the transducer, which are additive.

Development of the model, conducted prior to this program, evolved in three steps. First, a computer program was written to determine the steady-state flow and force balances. The one-dimensional isentropic compressible flow equation was used to relate pressures, temperatures, areas, and flows through the main and pilot valves, and orifices. The main valve force balance includes pressure forces on the poppet and diaphragm, the spring force and friction. Pilot valve force balance includes the aerodynamic force on the ball, spring forces, and the torquemotor force, which is a function of current. Simultaneous solutions of these equations were used to iterate design parameters (dimensions, spring rates, and torquemotor rating). After selecting optimum values, the main valve stroke requirement was calculated as a function of inlet pressure, regulated pressure, and flowrate. The torquemotor current also was determined from these equations.

The governing equations for the various components were then represented by their appropriate transfer functions and a block diagram was constructed. Since the valve inertia and outlet line acoustical characteristics are associated with very high frequencies (beyond the bandpass of the electronic controller), these phenomena were not included in the diagram. By reducing the various inner feedback loops, an overall transfer function was obtained (Fig. 72).

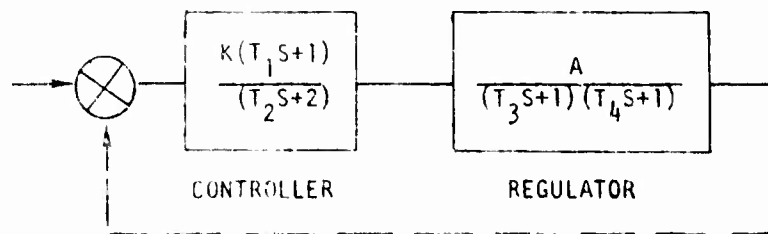


Figure 72. Reduced Block Diagram

Parameters K , T_1 and T_2 are related to controller gains and time constants, and A , T_3 , and T_4 are related to physical properties of the regulator components.

The stability margin of the regulator was evaluated by constructing Bode charts for both open-loop and closed-loop responses with selected controller gains. The open-loop analysis, with a proportional gain of 0.001 and an integral gain of 0.03, indicated a phase margin of 40 degrees and a corresponding damping ratio of 0.35. Closed-loop analysis showed a cutoff frequency of 119 Hz. Because this frequency is relatively low, high-frequency effects such as line dynamics and their interaction with the regulator performance should be adequately damped.

Except for minor changes, design of the flightweight regulator was accomplished prior to this program. The adequacy of the design with respect to meeting updated requirements was verified, but this did not necessitate repeating the steady-state design iterations or the linear frequency response analysis.

Having determined preliminary values for the time constant and gains with the linear frequency response analysis, a dynamic performance model was constructed. In addition to the steady-state relationships already mentioned, the electronic controller was modeled with the following equation,

$$\frac{dI}{dt} = K_p \frac{dE}{dt} + K_I E - \frac{I}{T_c} \quad (20)$$

where

- I = torquemotor current
- E = error in regulated pressure
- K_p = equivalent proportional gain
- K_I = equivalent integral gain
- T_c = time constant
- t = time
- d = differential operator

$$I = \int \frac{dI}{dt} dt \quad (21)$$

The change in pressure of the pressurized volume was calculated with the following equation

$$\frac{dP}{dt} = \frac{\gamma}{V} \left(RT \frac{dW}{dt} - P \frac{dV}{dt} \right) \quad (22)$$

where

- P = pressure
- V = volume
- R = gas constant
- T = temperature
- W = mass
- γ = specific heat ratio
- t = time
- d = differential operator

$$P = \int \frac{dP}{dt} dt \quad (23)$$

Because the heat transfer process between the pressurant gas and PSA hardware is relatively slow compared to the pressurization subsystem response, the bulk gas temperature was programmed as a function of time for each duty cycle, based on the PSA thermal transient model results. The effect of the transient

diaphragm pressure drop on pressurant pressure also was programmed as a function of time.

Simulations of the initial pressurization sequence and MDC's I and II were repeated during the program with the dynamic performance model. Table 18 shows the initial pressurant tank pressure and initial pressurized volume for the five cases that were run. Three separate sequences were investigated for MDC II (at the beginning, middle, and end) to determine the effect of simultaneously decreasing the regulator inlet pressure and increasing the downstream pressurized volume. It was during this analysis that the controller gain schedule was synthesized.

TABLE 18. INITIAL CONDITIONS FOR FEED SYSTEM
DYNAMIC PERFORMANCE PREDICTIONS

Duty Cycle	Initial Regulator Inlet Pressure, psia	Initial Pressurized Volume, ft ³
Initial Pressurization	4000	0.75
MDC I	3960	0.75
MDC II		
Sequence 1	3960	0.75
Sequence 2	2000	10.5
Sequence 3	450	19.0

Figure 73 shows the regulator response to be very stable during initial pressurization. The overshoot in propellant pressure at the end of pressurization was 0.25 psi (0.08%), as determined from digital data printouts. The decay in regulator inlet pressure is also shown.

BEST AVAILABLE COPY

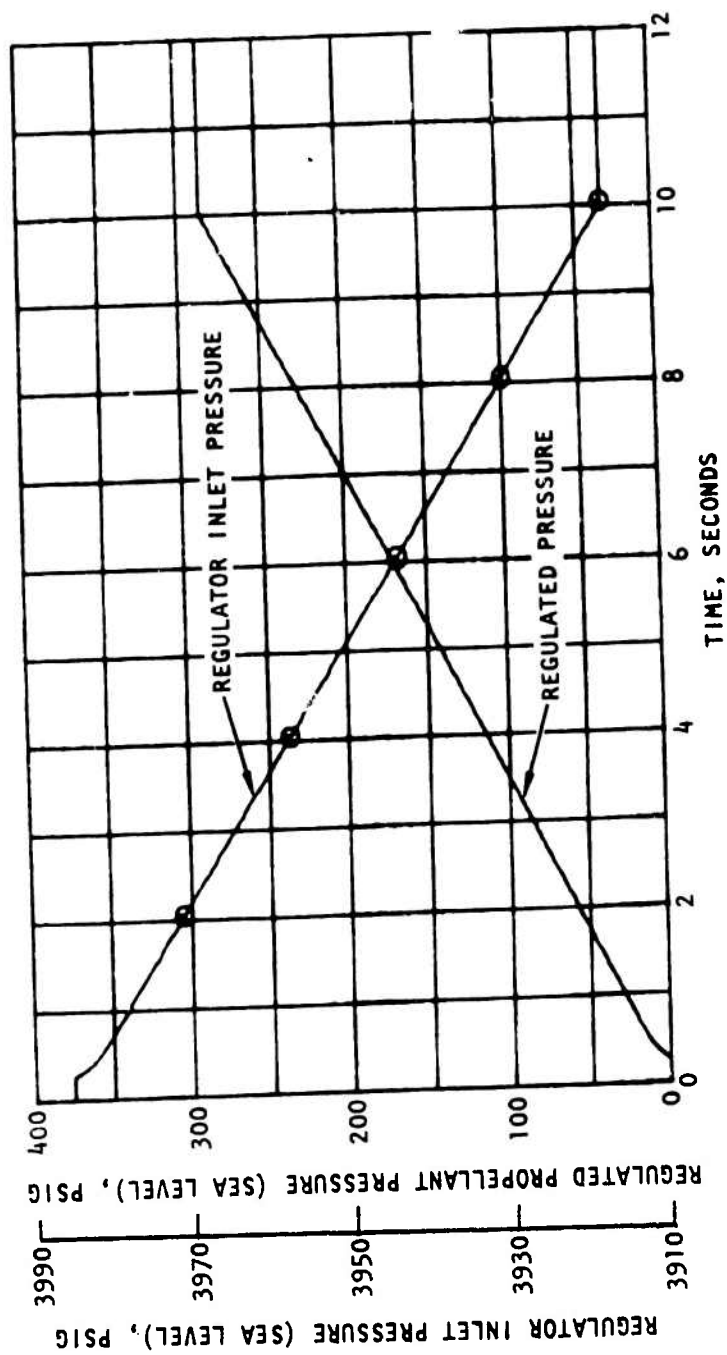


Figure 73. Regulator Dynamic Performance for Initial Pressurization

The maximum error for MDC I occurred at the start of expulsion (at 275 in.³/sec), as shown in Fig. 74 . The magnitude of the small oscillation in propellant pressure was 0.65 psi (0.22%). The increasing pressurized volume and decaying regulator inlet pressure are also shown.

Because MDC II starts with this same (maximum) propellant demand, it has the same initial error in delivered pressure. However, the magnitude of the error is smaller for the lower flowrates. The transient data (expulsion flowrate, regulator inlet pressure, and delivered propellant pressure) for the start of MDC II are presented in Fig. 75 .

During subsequent selected MDC II pulses, the maximum errors were ± 0.29 and ± 0.21 psi (± 0.10 and $\pm 0.07\%$), respectively. These two cases had lower regulator inlet pressures, larger pressurized volumes, and lower expulsion rates. The results are presented in Fig. 76 and 77.

The regulator dynamic errors are summarized in Table 19. Data are also presented for the additive regulator and transducer errors as a function of duty cycle. Transducer errors are for the 40 to 100 F operating range. The maximum error in delivered pressure is ± 2.55 psi (0.85%).

Stage Installation Layout

A typical installation for the flightweight propellant feed system in an advanced post-boost vehicle was presented in Fig. 7 and 8. The AGE locations are in accord with Ref. 5, but the IFSS and MGS drawer locations correspond with an earlier version (3 Dec. 1976).

The PSA's are located on opposite sides of the axial engine and expel inwardly. Each PSA is attached to the stage structure by six pin-connected struts. The pressurization subsystem is mounted under the IFSS drawer.

Ref. 5: Specification No. S-M-X-41016, Prime Item Development Specification For MX Stage IV, Headquarters, Space and Missile Systems Organization, Air Force Systems Command, 8 September 1977, Confidential.

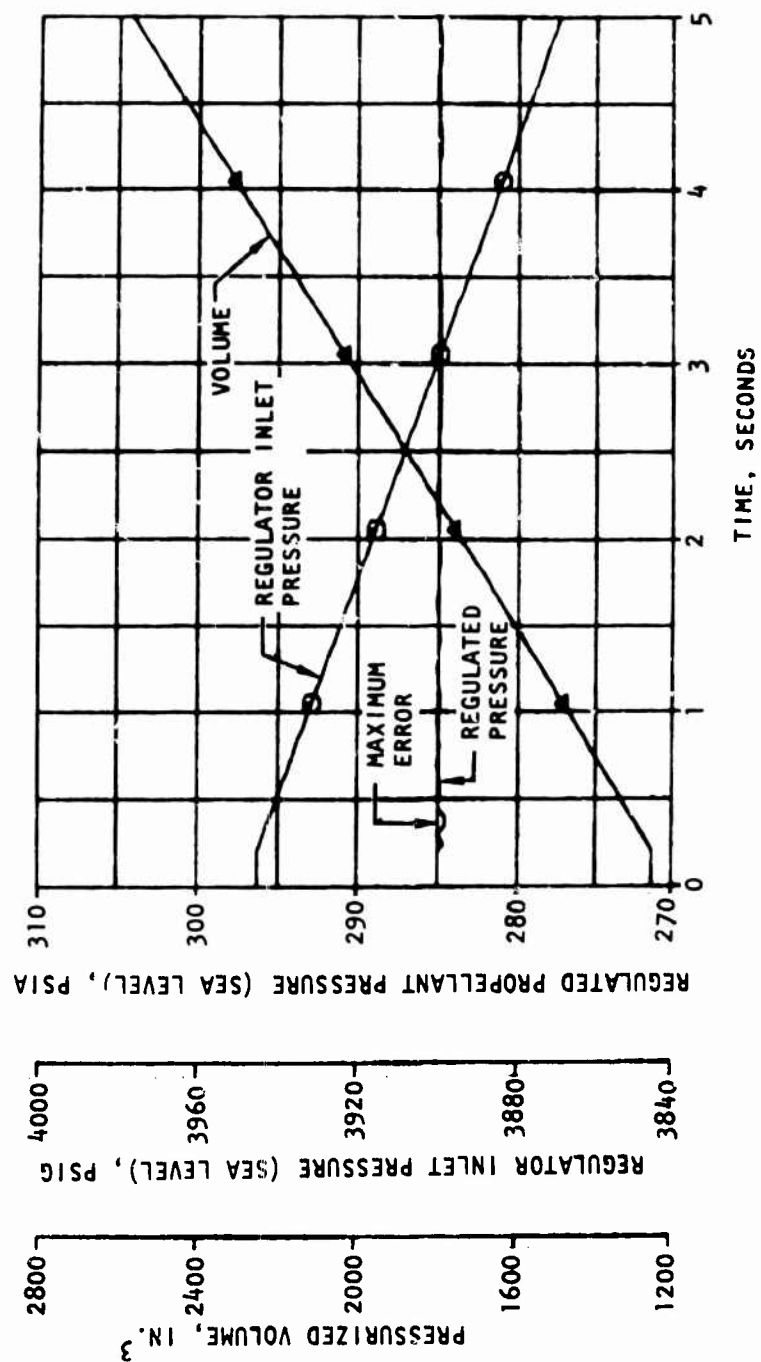


Figure 74. Regulator Dynamic Performance for Start of MDC I

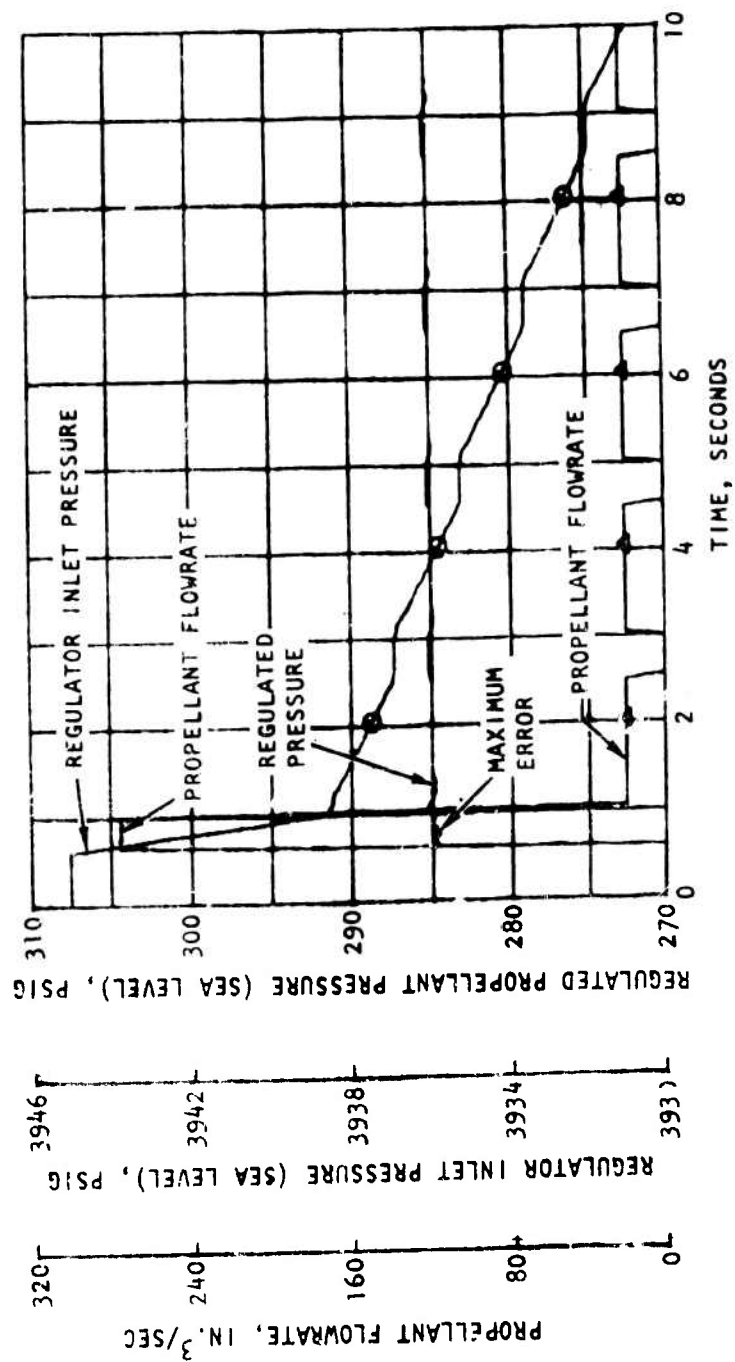


Figure 75. Regulator Dynamic Performance for Start of MDC II

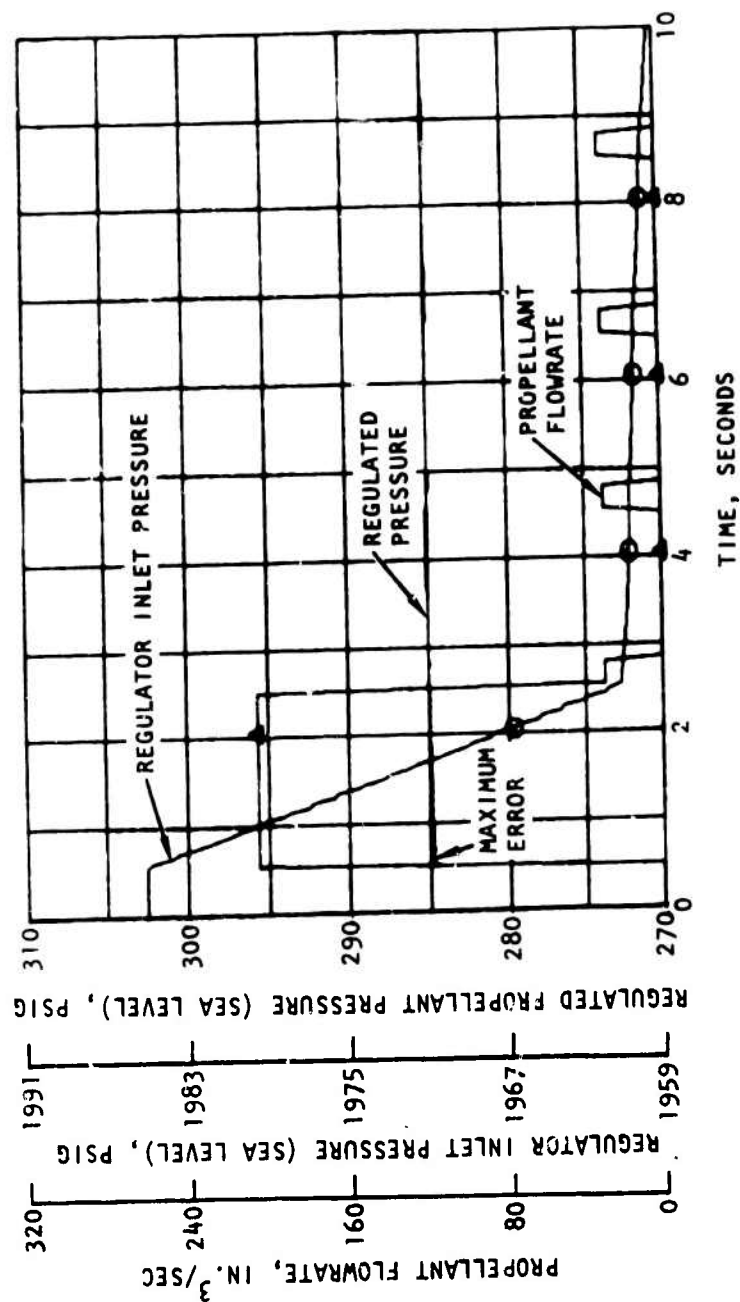


Figure 76. Regulator Dynamic Performance for Middle of MDC II

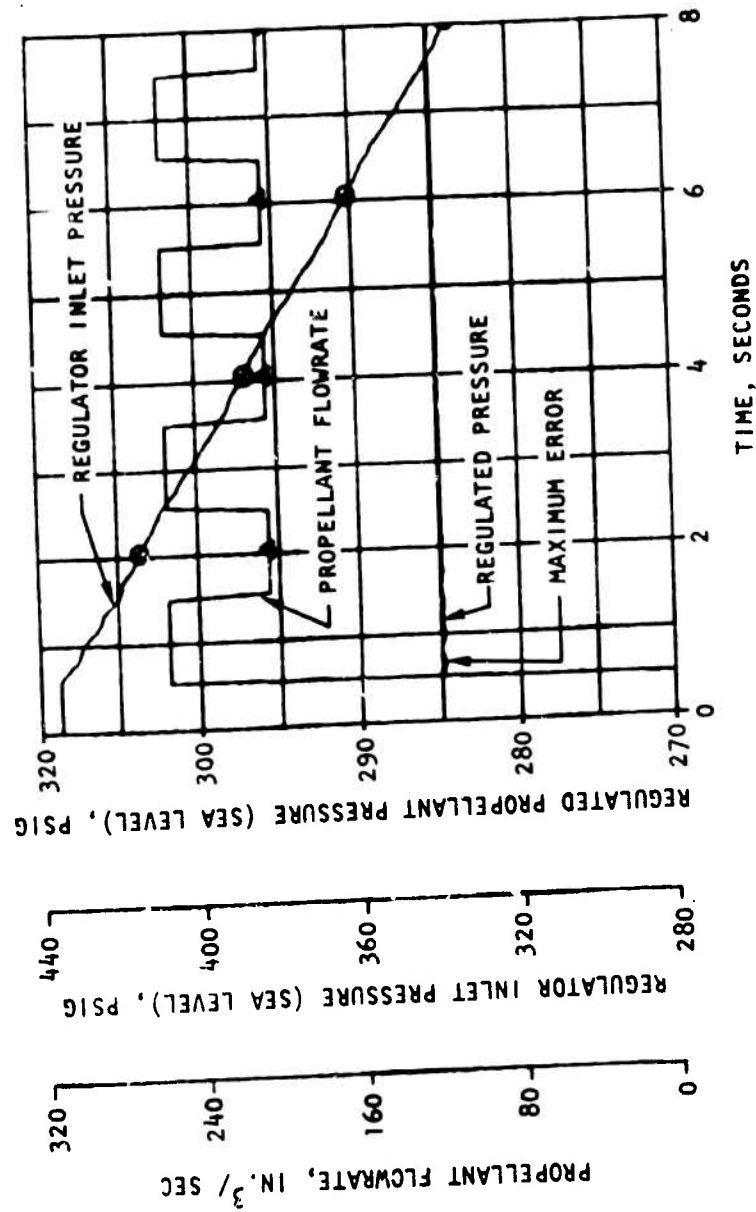


Figure 77. Regulator Dynamic Performance for End of MDC II

TABLE 19. FEED SYSTEM DYNAMIC ERROR SUMMARY

Source	Error, psi(%)
Transducer	± 1.90 (± 0.63)
Initial Pressurization	
Regulator	+0.25 (+0.08)
Regulator plus Transducer	+2.15 (+0.72)
MDC I and Start of MDC II	
Regulator	± 0.65 (± 0.22)
Regulator plus Transducer	± 2.55 (± 0.85)
Middle of MDC II	
Regulator	± 0.29 (± 0.10)
Regulator plus Transducer	± 2.19 (± 0.73)
End of MDC II	
Regulator	± 0.21 (± 0.07)
Regulator plus Transducer	± 2.11 (± 0.70)

Mass Properties

The weight breakdown for the flightweight propellant feed system is presented in Table 20. Each PSA weighs 59.2 pounds while the pressurization subsystem weighs 41.4 pounds. The PSA's are designed to deliver 1400 pounds of propellants to the engines and have an assumed expulsion efficiency of 98.1%. The feed system weight of 189 pounds, which includes the Tridyne and residual propellants, represents a 27 to 35% reduction from earlier feed system technology programs.

To make center of gravity (CG) calculations, it was necessary to assume a displacement of each PSA envelope from the stage centerline. A distance of 12.3 inches was assumed, which leaves 1.3 inches on the outboard side for a 92.2-inch-diameter stage. Each PSA was centered in its respective envelope.

TABLE 20. FEED SYSTEM WEIGHTS
(POUNDS)

Oxidizer PSA (59.24)	
Liner, Diaphragm, Valves, Leak Detector	34.48
Mounting Ring	12.19
Helical Composite Wrap	10.86
Circular Composite Wrap	1.71
Fuel PSA (59.24)	59.24
Pressurization Subsystem (41.42)	
Storage Tank	26.40
Tridyne	5.12
Leak Detector	0.44
Fill Valve	0.30
Isolation Valve	1.95
Regulator Assembly	4.25
Electronics/Pressure Transducer Assembly	0.60
Catalytic Reactor	0.77
Lines	<u>1.59</u>
Total Feed System Hardware (including Tridyne)	159.9
N ₂ O ₄ (loaded)	889.3
MMH (loaded)	<u>547.3</u>
Total Feed System (loaded)	1596.5

The results of these calculations are presented in Table 21 and Fig. 78. The feed system CG shifts 2.0 inches aft (+X) because of the increasing influence of the pressurization subsystem weight as the propellants are expelled. The feed system CG also shifts 5.1 inches toward the stage centerline in the radial Z direction and 5.3 inches away from the stage centerline in the radial Y direction. The CG shift of the PSA's is primarily toward the centerline in the Z direction (5.1 inches) with no movement in the Y direction and only 0.1 inch aft in the X direction.

Unit Production Costs

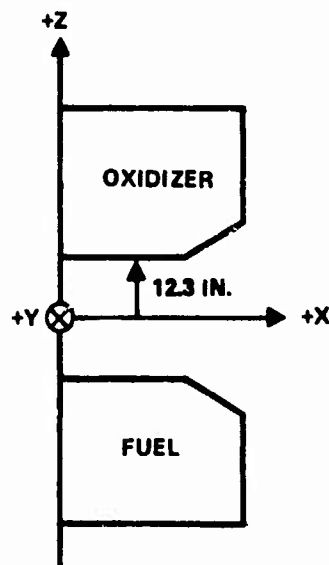
Feed system unit production costs were estimated on the basis of 400 systems at a production rate of 10 per month, using inputs from the Engineering, Manufacturing, Purchasing and Pricing departments. Initially, assessments were made to determine where each component fabrication process would be conducted, i.e., in-house or by a vendor. Vendors were requested to submit cost estimates for purchased fabrication processes and components. The list of vendors contacted to update the information received during preparation of the proposal included Aircraft Hydro-Forming (PSA diaphragms and liners), Brunswick (PSA composite wrap and pressurant tank), Pyronetics (valves), Jewett (PSA leak detector), Parker-Hannifin (regulator), Gulton (pressurant leak detector), and Engelhard (catalyst).

In-house fabrication included the PSA polar boss, inlet diffuser plate, outlet collector plate, mounting ring, fittings, and assembly. Also included were the pressurization subsystem reactor, lines, fittings, mounting hardware, and assembly. Detailed manufacturing planning documents for all parts were used to subdivide the in-house fabrication by department and operation from the time a number was applied to the raw material until the finished part was inspected. An example, for the PSA leak detector boss, is shown in Fig. 79. These documents were used to estimate both setup and run times.

The unit production costs, exclusive of fee, are presented in Table 22. A breakdown showing Rocketdyne labor and purchased material/labor for the PSA's,

TABLE 21. FEED SYSTEM CENTER OF GRAVITY*

	X Axis		Y Axis		Z Axis	
	Initial	Final	Initial	Final	Initial	Final
PSA's	20.7	20.6	0	0	6.4	1.3
Pressurization Subsystem	32.3	32.4	30.9	30.6	0.1	0.1
Feed System	21.0	23.0	0.8	6.1	6.2	1.1
*All centers of gravity in inches						



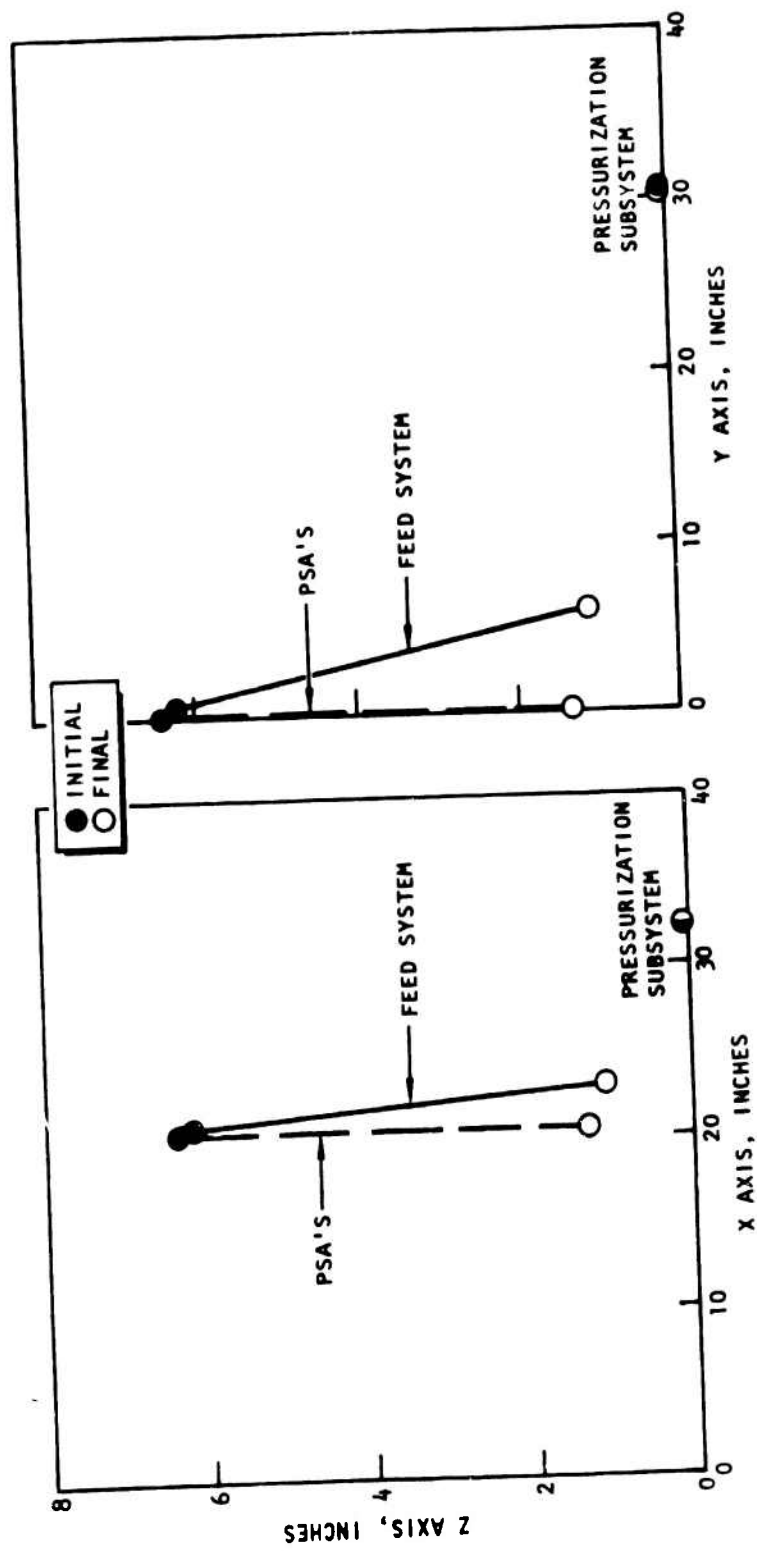


Figure 78. Feed System Center of Gravity

JUPITER		NO. NO.	CO.	NEW	OPC	CHG	DATE PRG	ORDER NO.	DWG SET	INITIAL STG	FINAL STG						
<div style="text-align: right;">23</div>																	
MANUFACTURING ORDER																	
QTY	PLAN	PAGE	OF	REMARKS													
PART NO.	AN 77 206 24																
PART NAME	BOSS LEAK																
	11 LOCATOR																
PLANNED BY	NEW 11																
REVISED																	
UNIT NO. PART NO.				REVISED				DATE									
AN 77 206 24				11X													
THIS COPY USED ON				THIS PART SET ON													
<div style="display: flex; justify-content: space-between;"> <div> LAST WEEK INSP. CYS <input type="checkbox"/> WIP-UP <input type="checkbox"/> NO. SHG <input type="checkbox"/> SHG LTR <input type="checkbox"/> NO. S.S. <input type="checkbox"/> S.S. NO. </div> <div>DATE</div> </div>																	
LINE	UNIT QTY	DEPT	1	2	DATE	WEEK / LTR	OPERATION	MATERIAL	DATE	INSP	TEST / CAT NO.	DATE	SET UP	SPEED	FEED	WTC	COOL T
1							1" DIA X 1 3/4	5086 AL BAR					(4.25)	(0.70)			
2							5086 AL BAR										
3							5086 AL BAR										
4							5086 AL BAR										
5							5086 AL BAR										
6							5086 AL BAR										
7							5086 AL BAR										
8							5086 AL BAR										
9							5086 AL BAR										
10							5086 AL BAR										
11	5086						5086 AL BAR										
12							5086 AL BAR										
13							5086 AL BAR										
14							5086 AL BAR										
15							5086 AL BAR										
16							5086 AL BAR										
17	5086						5086 AL BAR										
18							5086 AL BAR										
19							5086 AL BAR										
20							5086 AL BAR										
21							5086 AL BAR										
22							5086 AL BAR										
23							5086 AL BAR										
24							5086 AL BAR										
25							5086 AL BAR										
26							5086 AL BAR										
27							5086 AL BAR										
28							5086 AL BAR										
29							5086 AL BAR										
30	5086						5086 AL BAR										
31							5086 AL BAR										
32							5086 AL BAR										
33							5086 AL BAR										
34							5086 AL BAR										
35							5086 AL BAR										
36							5086 AL BAR										
37							5086 AL BAR										
38							5086 AL BAR										
39							5086 AL BAR										
40							5086 AL BAR										
41							5086 AL BAR										
42							5086 AL BAR										
43							5086 AL BAR										
44							5086 AL BAR										
45							5086 AL BAR										
46							5086 AL BAR										
47							5086 AL BAR										
48							5086 AL BAR										
49							5086 AL BAR										
50							5086 AL BAR										
51							5086 AL BAR										
52							5086 AL BAR										
53							5086 AL BAR										
54							5086 AL BAR										
55							5086 AL BAR										
56							5086 AL BAR										
57							5086 AL BAR										
58							5086 AL BAR										
59							5086 AL BAR										
60							5086 AL BAR										
61							5086 AL BAR										
62							5086 AL BAR										
63							5086 AL BAR										
64							5086 AL BAR										
65							5086 AL BAR										
66							5086 AL BAR										
67							5086 AL BAR										
68							5086 AL BAR										
69							5086 AL BAR										
70							5086 AL BAR										
71							5086 AL BAR										
72							5086 AL BAR										
73							5086 AL BAR										
74							5086 AL BAR										
75							5086 AL BAR										
76							5086 AL BAR										
77							5086 AL BAR										
78							5086 AL BAR										
79							5086 AL BAR										
80							5086 AL BAR										
81							5086 AL BAR										
82							5086 AL BAR										
83							5086 AL BAR										
84							5086 AL BAR										
85							5086 AL BAR										
86							5086 AL BAR										
87							5086 AL BAR										
88							5086 AL BAR										
89							5086 AL BAR										
90							5086 AL BAR										
91							5086 AL BAR										
92							5086 AL BAR										
93							5086 AL BAR										
94							5086 AL BAR										
95							5086 AL BAR										
96							5086 AL BAR										
97							5086 AL BAR										
98							5086 AL BAR										
99							5086 AL BAR										
100							5086 AL BAR										

Figure 79. Sample Manufacturing Planning Sheet

TABLE 22. UNIT PRODUCTION COST

Purchased Material/ Labor	Propellant Storage Assemblies (2)	Pressurization Subsystem	Feed System
	Composite Wrap	Tank	\$ 5,276
	Tank Labor	Regulator	4,431
	Tank Material	Pressure Switch	1,563
	Pressurant Inlet Valve	Isolation Valve	423
	Propellant Outlet Valve	Other Materials	303
	Fill/Drain Valve	Fill/Drain Valve	98
	Leak Detector	Catalyst	22
	Vacuum Service Valve		
	Subtotal	Subtotal	\$12,116
	Tooling		
	Subtotal		\$23,587
Rocketdyne Labor	Fabrication and Support Tooling	Fabrication and Support Assembly	2,711
Total			1,808
	Subtotal	Subtotal	4,519
			\$24,200
			\$47,787

pressurization subsystem, and feed system is provided. Only in-house tooling is identified; vendor tooling was prorated and included in the cost of purchased components and processes.

The costing methodology for in-house fabrication was based on the following ground rules.

1. All costs were based on fabrication performed at October 1977 rates.
2. The selection of special tooling was based on producing 400 systems at 10 per month in an economical manner.
3. The costs reflect the average of the first 200 systems.
4. Five parts were produced per each operation setup.
5. A 10% upward adjustment was made to setup and run hours to account for the fact that estimates were based on preliminary design drawings.
6. A 22% "realization" factor was added to the "shop standard" hours shown on the manufacturing planning sheets, which are the minimum achievable.
7. A parts mortality rate of 7% was applied to labor and material, based on previous experience.
8. An additional 35.2% of the fabrication hours was included for manufacturing services and expediting.
9. A material adjustment of 3.25% was added for use of in-house material such as tubing.
10. A material procurement expense of 7.16% was added.
11. Quality control and quality assurance were estimated to be an additional 25 and 10% respectively, of the labor hours.
12. Average rates for each department were used.
13. Overhead and G&A (general and administrative) were included.

Hazards Analysis

A preliminary system safety analysis was performed with the primary objective being to minimize or eliminate potential hazards that could cause physical harm to personnel or damage to or failure of hardware. Safety hazards inherent in the propulsion feed system were identified and design criteria and operational constraints were reviewed to ensure that the hazards were reduced to a reasonable level. The analysis covered the loading, handling, storage, checkout, shipment, and flight phases of the hardware life.

The procedure followed in conducting the analysis was to (1) define the extreme conditions for each life cycle environmental requirement, (2) identify the applicable operating phase, (3) list the possible failure modes, (4) classify the severity of each assumed failure, and (5) identify the design and procedural controls to prevent, detect, and react to impending hazards. Definitions of the hazard classifications are provided in Table 23. The hazard control entries in Table 24 are the most important information in

TABLE 23. HAZARD CLASSIFICATION

Classification	Description
IV	<u>Catastrophic</u> . Will cause death or severe injury to personnel, or loss of system. Leakage of propellant in the immediate vicinity of personnel (handling operations) is classified as catastrophic.
III	<u>Critical</u> . Will cause personnel injury or major system damage, or will require immediate corrective action for personnel or system survival. Leakage of propellant during storage without presence of personnel is classified as critical.
II	<u>Marginal</u> . Can be encountered or controlled without injury to personnel or major system damage. This category includes an indication of loss of tank integrity by the leak detector.

TABLE 24. PRELIMINARY HAZARD ANALYSIS

Hazard Source	Operational Phase	Hazard	Hazard Classification	Hazard Control
High Temperature 170 F maximum	Mobile Deployment, transportation, storage, handling, and flight (100 F)	1. Rupture of diaphragm due to: a. Increased propellant vapor pressure b. Decreased tensile strength of diaphragm material with increased temperature	1. II Marginal Loss of diaphragm integrity and well redundancy; leak detector indicator (except flight)	1. a. Pressure increase is negligible compared to operating pressure. Diaphragm fully supported by outer tank wall. b. No significant change in 1100-0 diaphragm material strength at 120 F
		2. Local leakage of diaphragm or diaphragm/liner weld caused by accelerated chemical reaction combined with local reactive impurities	2. II Marginal Loss of well redundancy; leak detector indicator (except flight)	2. Minimum 0.03-inch aluminum thickness. EB weld used, which does not introduce weld rod impurities; thus material homogeneity is maintained
		3. Rupture of pressurant storage storage vessel due to increased pressure from: a. Thermal expansion of the pressurant b. Thermally initiated chemical reaction	3. IV Catastrophic Probable extensive damage of other hardware in vicinity as well as destruction of the storage vessel	3. a. Safety factor is applied to worstcase condition. b. Tridyne is inert at the specified storage temperature
Low Temperature -40 F minimum	Mobile deployment, transportation, storage, handling, and flight (40 F)	1. Leakage of diaphragm due to local cracks, fracture, or other integrity failure due to: a. Reduced propellant vapor pressure b. Loss of ductility at low temperature. Could be aggravated by mechanical stresses (handling and transportation loads)	1. II Marginal Loss of diaphragm integrity and well redundancy; leak detector indicator (except flight)	1. a. Evacuated pressurant volume provides a positive outward pressure on the diaphragm at all times. b. Diaphragm ductility will not decrease significantly at low temperature.
		2. Fracture of outer tank wall due to differential expansion at welds; brittleness.	2. II Marginal Loss of outer wall integrity; leak detector indicator (except flight)	2. Outer wall strength does not decrease at low temperature. All structural welds are EB welds, thus preserving material homogeneity
		3. External leak in propellant or pressurant tank due to differential expansion or brittleness of metal or filament wrap	3. III Critical Leaks in pressurant side of propellant tank will be detected. Leaking Tridyne is neither toxic nor flammable.	3. Engineering analyses of aluminum and filament wrap thermal characteristics considered in design.
Thermal Cycling 170 to -20 F	Mobile deployment, transportation, storage, and handling	1. fatigue cracking and leakage of diaphragm due to pressure and mechanical stress cycling	1. II Marginal Loss of inner wall integrity and redundancy; leak detector indicator	1. The 1100-0 aluminum diaphragm is not susceptible to fatigue or work hardening under the low-level thermal and mechanical stresses applied by thermal cycling. The diaphragm will remain pressed against the tank wall at any temperature in the specified range.
		2. External tank leakage; fracture of wall	2. III Critical Leaks in pressurant side of propellant tank will be detected.	2. Engineering analyses of aluminum and filament-wrap thermal characteristics are considered in design.
Storage Duration Up to 15 years under specified environmental conditions	Mobile deployment or storage	1. Leakage of diaphragm due to: a. Chemical attack and decomposition of diaphragm by propellant	1. II Marginal Propellant leakage will cause loss of well redundancy; leak detector indicator.	1. a. 5-year storage data show no significant chemical attack on aluminum by MMH or N ₂ O ₄ . b. Propellant purity and loading controls must ensure that moisture is not introduced into the N ₂ O ₄ tank.
		2. Leakage of fluid from pressurant tank due to chemical attack by active constituents of Tridyne	2. II Marginal Loss of pressure is detectable. Leaking Tridyne is not toxic or flammable.	2. Tridyne contains a low proportion of combustible gases and is an inert fluid under storage conditions.

TABLE 24. (CONTINUED)

Hazard Source	Operational Phase	Hazard	Hazard Classification	Hazard Control
External Pressure 1.5×10^{-12} to 15 D axle	Transportation and Handling	1. Collapse of outer propellant tank wall due to high external pressure	1. III Critical Diaphragm will buckle, tank rupture would cause toxic fumes, fire hazard, Corrosive liquid release (H_2O_2)	1. Engineering analysis and considered buckling in design
		2. Rupture of outer propellant tank wall due to low external pressure	2. III Critical Would cause toxic fumes, fire hazard, Corrosive liquid release (H_2O_2)	2. Increase of stress on tank due to decreased ambient pressure is negligible
		3. Rupture of pressurant tank	3. IV Catastrophic	3. Increased pressure differential at its negligible
	Flight	1. Rupture of outer propellant wall due to combined increase of internal pressure and decreased external pressure	1. III Critical Would cause toxic fumes, fire hazard, Corrosive liquid release (H_2O_2)	1. Increase of stress on tank wall due to combined pressure effects is within tank design criteria
		2. Rupture of pressurant tank	2. IV Catastrophic	2. Increased pressure differential due to external pressure is negligible, but considered in design
Humidity 0 to 100% including condensation	Mobile deployment, transportation, storage, and handling	1. Corrosion at weld or other outer tank wall discontinuity, propagating through outer wall	1. III Critical Loss of outer wall integrity, leaks in pressurant side of propellant tank will be detected.	1. Aluminum is resistant to corrosion from atmospheric conditions due to natural, thin protective oxide coating. 5086 aluminum is not susceptible to stress corrosion. Filament winding is coated with moisture barrier.
Shock	Mobile deployment, transportation and handling	1. Rupture of diaphragm due to a. Liquid peak lined pressure/ fluid inertia b. Mechanical stress generated by acceleration forces	1. II Marginal Loss of diaphragm integrity and wall redundancy; leak detector indication	1. Peak pressures and mechanical stresses have been considered in design. Diaphragm conforms to the shape of the tank inner wall, minimizing differential motion between diaphragm and tank.
		2. Crack of outer propellant tank due to mechanical stresses	2. III Critical Loss of outer wall integrity. Leaks in pressurant side of propellant tank will be detected.	2. Peak mechanical stresses have been considered in design.
		3. Rupture of both diaphragm and outer tank wall due to mechanical stresses	3. IV Catastrophic Release of toxic fumes; fire hazard. Release of corrosive liquid (H_2O_2)	3. Peak pressures and mechanical stresses have been considered in design. Diaphragm conforms to the shape of the tank inner wall, minimizing differential motion between diaphragm and tank.
		4. Mechanical stress on pressurant tank filament wrap causes relaxation, resulting in rupture or leakage.	4. IV Catastrophic Rupture of Tank II Marginal Leakage	4. Mechanical properties of the filament wrap under shock were considered in design.
	Flight	1. Rupture of diaphragm	1. III Critical Loss of inner wall integrity	1. Tank designed for operational stresses combined with shock/ acceleration loads.
		2. Leakage or rupture of pressurant tank	2. IV Catastrophic Rupture of Tank II Marginal Leakage	2. Mechanical properties of filament wrap under shock were considered in design.
Vibration	Mobile deployment, transportation, and handling	1. Diaphragm leak or rupture due to: a. Mechanical stress, cyclic fatigue b. Fatigue from propellant sloshing c. Diaphragm/tank shell rubbing and wear d. Resonant vibration at propellant vapor ullage	1. II Marginal Loss of inner wall integrity and redundancy; leak detector indication	1. a. Stresses will not be transmitted to diaphragm but will be borne by tank. Levels negligible compared to strength. b. 1100-D material not susceptible to fatigue. c. Diaphragm held firmly against wall by propellant. d. Analyzed and considered in design.

TABLE 24. (CONCLUDED)

Hazard Source	Operational Phase	Hazard	Hazard Classification	Hazard Control
	Flight	<p>2. Crack in tank parent material or weld due to resonant vibration failure</p> <p>3. Mechanical stress on pressurant tank filament wrap causes relaxation, resulting in rupture or leakage.</p>	<p>2. II Marginal Loss of outer wall integrity. Leaks in pressurant side of propellant tank will be detected</p> <p>3. IV Catastrophic Rupture of tank II Marginal Leakage</p>	<p>Applied stresses are low compared to strengths. Propellant provides vibration damping.</p> <p>3. Mechanical properties were considered in design. Filament winding acts as a vibration damper and keeps a compressive static load on the tank under all specified conditions.</p>
	Flight	<p>1. II Marginal Loss of inner wall integrity and redundancy; leak detector indication</p> <p>2. Crack in tank parent material or weld due to resonant vibration failure</p> <p>3. Mechanical stress on pressurant tank filament wrap causes relaxation, resulting in rupture or leakage</p>		<p>1. a. Stresses will not be transmitted to diaphragm but will be borne by tank. Levels negligible compared to strength. b. 1100-B material not susceptible to fatigue. c. Diaphragm held firmly against wall by propellant. d. Analyzed and considered in design.</p> <p>2. Applied stresses are low compared to strengths. Propellant provides vibration damping</p> <p>3. Mechanical properties were considered in design. Filament winding acts as a vibration damper and keeps a compressive static load on the tank under all specified conditions.</p>
Nuclear Radiation	Storage, flight	1. Deterioration in mechanical or chemical properties	1. II Marginal	1. Anticipated levels analyzed and considered in design.

the analysis. They consist of brief descriptions of the design techniques implemented or design margins provided. These features provide evidence of the safe nature of the flightweight design.

In addition to the single-point hazards mentioned, multiple failures may combine to result in hazardous situation. The fault logic diagrams presented in Fig. 80 and 81 show the areas of greatest concern.

Failure Modes And Effects Analysis

A failure modes and effects analysis (FMEA) was conducted for the flightweight feed system. Results of the FMEA (Table 25) describe discrete component failure modes and their effects on subsystem operations during flight and mission completion. Design features or criteria for controlling each failure mode are listed.

Reliability

Failure rate data for the flightweight feed system are presented in Table 26. The rates shown are based on Rome Air Development Command RADC-TR-75-22 and related data, modified by engineering judgment for design complexity and technology status. The analysis considered all components whose failure modes could result in partial or complete loss of mission while the system is in the flight operating mode. It does not include ground failure modes that would not affect mission reliability, such as functional failure of leak detectors. The reliability corresponding to the system failure rate of 11,061 failures per million hours is 0.9963.

Nuclear Hardness And Survivability Analysis

The environment produced by nuclear explosions will be a threat to the post-boost vehicle from storage to re-entry vehicle deployment. A nuclear explosion releases large quantities of energy directly in the form of X-rays, neutrons, and gamma rays, and indirectly in the form of electromagnetic pulse

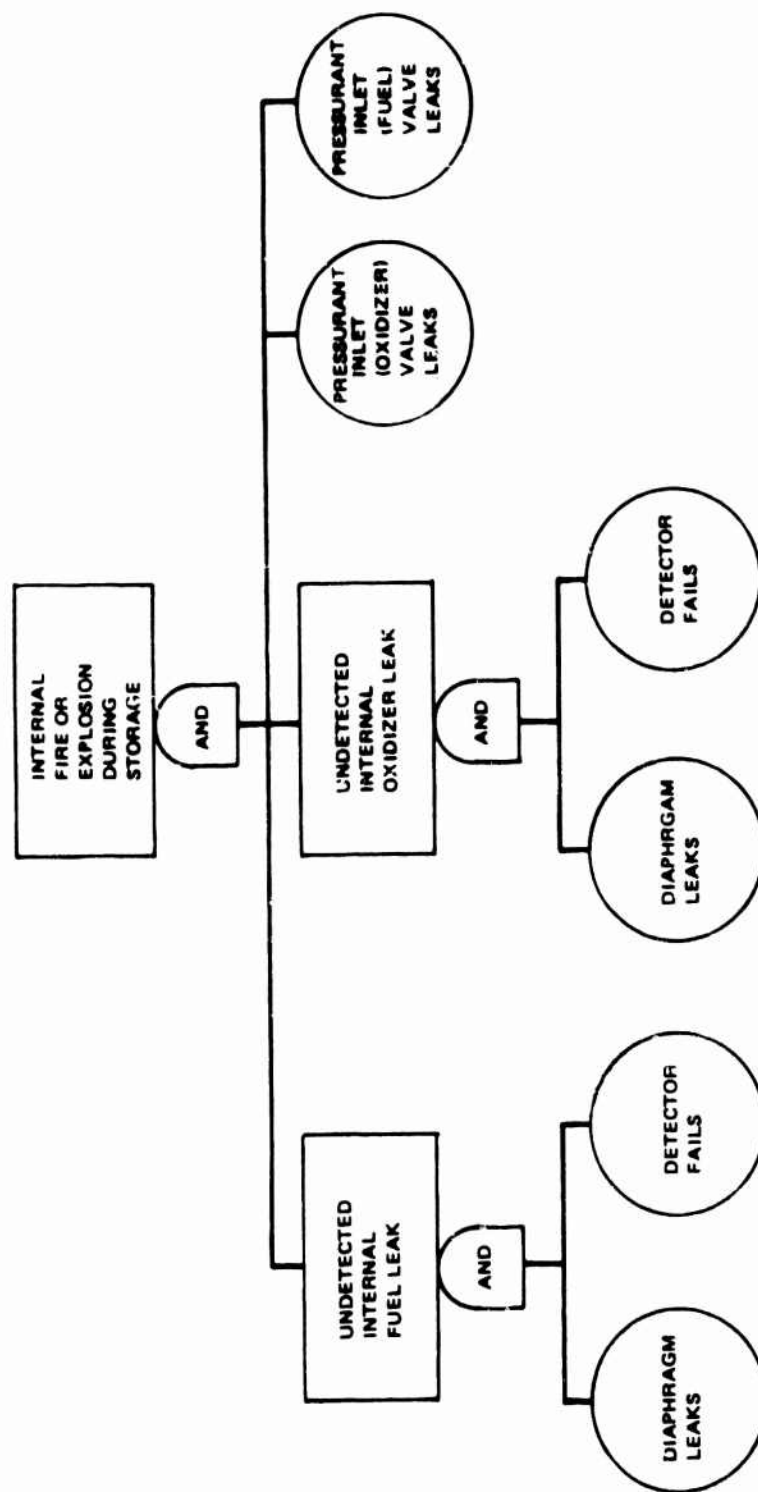


Figure 80. Fault Logic Diagram for Fire or Explosion Internal to Feed System During Storage

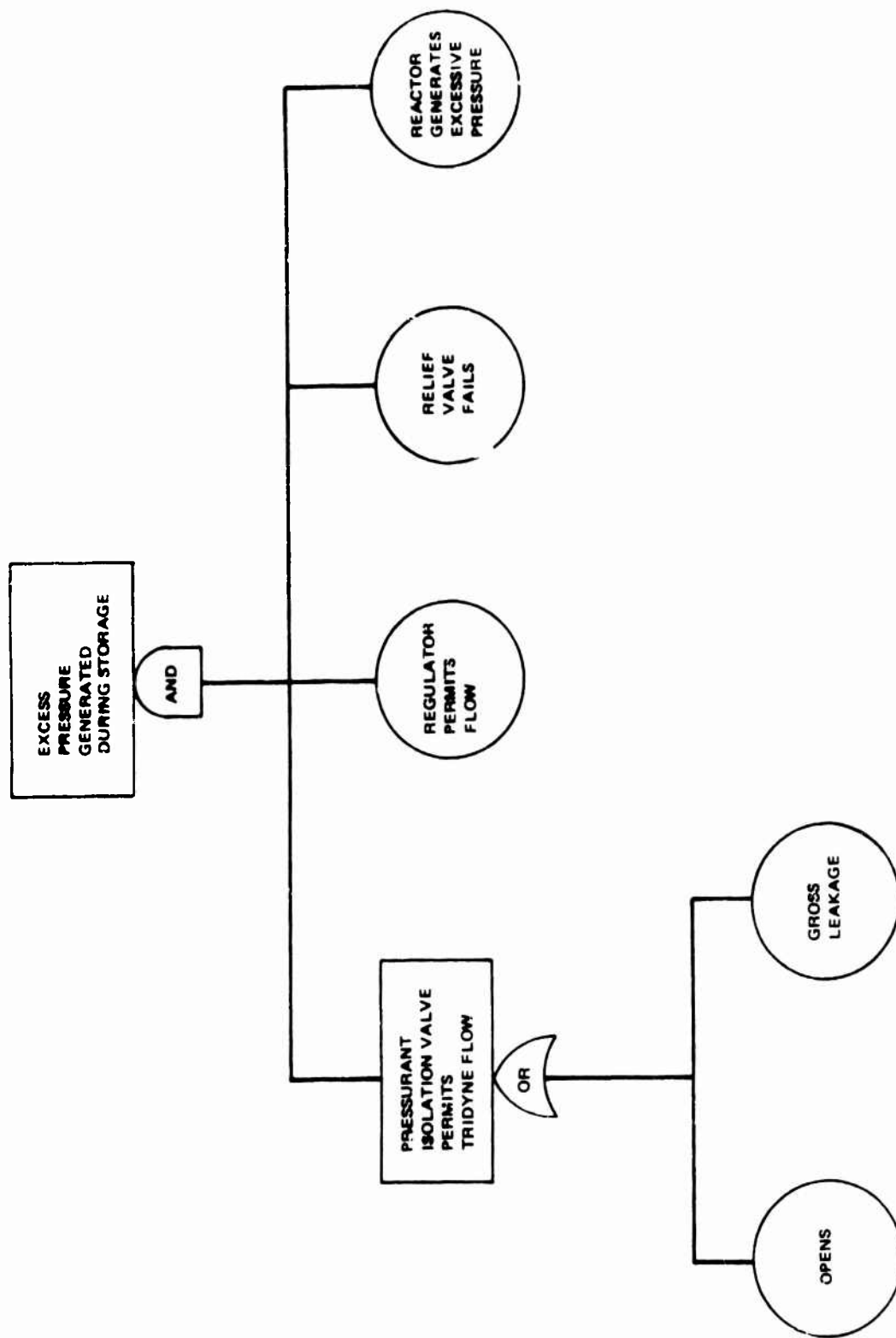


Figure 81. Fault Logic Diagram for Excess Pressure Buildup in Feed System During Storage

TABLE 25. FAILURE MODES/EFFECTS ANALYSIS

PNE Item	Nomenclature	Function	Failure Mode/Mechanism	Failure Effect on Subsystem	Failure Effects on Mission	OPERATING MODE FLIGHT	
						Controls in Effect to Eliminate or Reduce Failure Mode Occurrence - Effects	Critical Yes No
1	Pressurant Tank and Associated Elements (Fill Valve), Pressure Switch, Isolation Valve, Lines	Store high-pressure gas (Trigyne) to expel propellant	1. External leakage 2. Structural failure	1. Negligible: Accumulation of inert, noncorrosive gas in compartment 2. Complete loss of pressurant	Partial loss of mission	All-welded construction Leak detection provided in strategic alert	X
2	Pressurant Isolation Valve	Normally closed squib valve is opened to initiate pressurization of system	1. Internal leakage or premature opening 2. Fails to open when charge fired	None Backed up by normally closed regulator No pressurization	Complete loss of mission	Safety factors of 2:1 plus use of inert pressurant and filament wrap will ensure structural integrity	X
3	Catalyst Reactor and Associated Pressurant Lines	Reacts pressurant to increase its temperature and expel propellant	1. Outlet temperature low due to contamination of catalyst 2. External leakage	Regulator will attempt to compensate for decrease of reaction efficiency by increasing flowrate of pressurant and thus resulting in its probable early depletion Negligible: Accumulation of inert, noncorrosive gas in compartment	Partial loss of mission	Extensive testing will confirm valve opening	X
4	Internal Filter	Located at inlet to regulator to prevent debris or contamination from damaging downstream components	1. Blockage of filter 2. Filter shreds	Complete loss of pressurant Reduced pressurant flowrate resulting in engine degradation Possible damage to downstream components leading to performance degradation	Complete loss of mission	Controls on fabrication and processing of catalyst, reactor, and pressurant, plus internal filters, will preclude contamination	X
5	Electronic Regulator/Relief Valve/Pressurizer/Transducer/Electronics	Provide regulated pressure to expel propellant gases	1. Outlet pressure high (full open) - Transducer low - Electronics fail open/short - Control circuit fails open/short - Internal regulator fails open 2. Outlet pressure low (full closed) - Vehicle power lost (interface mode) - Transducer fails high - Electronics fail open/short - Control circuit fails open/short - Internal regulator fails closed	Pressurant delivered at higher than normal. Relief valve open to prevent excessive pressure Pressurant delivered at lower than normal. Relief valve open to prevent excessive pressure No pressurization or lockup of pressure if already pressurized	Higher than normal flow through regulator sized to maintain capacity of relief valve on outlet side, precludes overpressurization of regulator and downstream components Complete or partial loss of mission	All-welded construction Safety factors 2:1 will ensure structural integrity Filter sized with adequate margin to ensure required minimum pressurant flowrate Verification/acceptance tests will ensure structural integrity of filter Use of flow limiter on inlet side of regulator sized to maintain capacity of relief valve on outlet side, precludes overpressurization of regulator and downstream components Use of proven, high-reliability components in regulator control circuitry with conservative testing will minimize probability of failure occurrence	X R X R X

TABLE 25. (CONCLUDED)

PNEA Item	Item Nomenclature	Function	Failure Mode/Mechanism	Failure Effect on Subsystem	Failure Effects on Mission	OPERATING MODE FLIGHT		Critical
						Controls in Effect to Eliminate or Reduce Failure Mode Occurrence or Effects	Yes	No
6	Propellant Tank Isolation Valves (four required)	Normally closed squib valves retain and provide dual isolation of fuel and oxidizer. Valves are opened to permit pressurization and expulsion of propellants to engines.	3. Outlet pressure out of tolerance - Transducer/electronic components drift - Regulator mechanism binding due to contaminants or damage	Slight performance degradation	Possible partial loss of mission	Environmental tests will verify necessary performance of components. Pressurant purity and servicing controls, plus internal filters, will preclude hazardous contaminants.	X	
			4. Flow limiter/regulator/relief valve leaks externally	Negligible: Accumulation of inert, noncorrosive gas in compartment	Partial loss of mission	Verification/acceptance tests will ensure integrity for leakage during ground handling, storage, and flight.		X
			5. Relief valve fails to reseal (requires prior regulator failure)	Probable early depletion of pressurant	Partial loss of mission	Secondary failure mode	X	
			1. Internal leakage or premature opening	None: Tank diaphragms and engine valves prevent fuel/oxidizer mix.	None			X
			2. Fails to open when charge fired	Precludes delivery of either fuel or oxidizer to engines. Overpressurization of either propellant tank is prevented by relief valve in regulator.	Complete loss of mission	Extensive testing will confirm valve opening.	X	
7	Propellant Leak Detectors (two required)	Detect internal leakage of either propellant during prelaunch modes	1. Functional	Not applicable	None	Detector function is only critical to monitor status of system integrity prior to launch		X
8	Positive Propellant Expulsion Diaphragms (two required)	Expel undiluted propellants as pressurant is introduced into tanks	1. Rupture or tear 2. Internal leakage	Performance degradation: Mixing of pressurant with either fuel or oxidizer will reduce thrust Negligible: Leak detectors will ensure no leakage prior to launch and subsequent short-term leakage will have minimal effect on engine performance	Partial loss of mission	Extensive testing for all loads/environments will minimize probability of failure	X	
9	Propellant Tanks and Associated Components (Fill valves, vacuum service valves, lines; two each required)	Contain propellants and pressurant gas used to expel propellants to engines	1. External leakage 2. Structural failure	Negligible: Accumulation of corrosive propellant component if propellants are noncorrosive and inert Complete loss of either propellant (possible fire hazard) or inert pressurant	Partial loss of mission Complete loss of mission	Redundant welds or dual-wall containment are used. Leak detectors are used. Strategic alert for leaks on pressurant side. Safety factors of 1.25 will ensure structural integrity.	X	

TABLE 26. FAILURE RATES

Assembly or Component	Failure Rate
<u>Pressurization</u>	
Tridyne Tank and Associated Pressurization Components	58.9
Isolation Valve	90.0
Filter	20.0
Pressure Transducer and Electronics	2,201.0
Pressure Regulator and Flow Limiter Assembly	3,340.8
Relief Valve	501.3
Catalytic Reactor and Associated Pressurant Lines	758.2
Electrical Harness and Connectors	<u>10.0</u>
Subtotal	6,980.3
<u>Propellant Storage</u>	
Squib Isolation Valves	4 x 90
Propellant Tank and Associated Components	2 x 1,860.3
Subtotal	<u>4,080.6</u>
Total System Failure per Million Hours	11,060.9

(EMP) radiation, blast, thermal radiation, dust, and debris. A limited nuclear hardness and survivability (NH&S) analysis was performed by Physics International, a subsidiary of Rockcor, using the MX threat environment (Ref. 6). The critical components were analyzed to provide (1) maximum front face temperatures, (2) melt depth, (3) average temperature rise, (4) maximum dose, and (5) X-ray stresses. The study is summarized in subsequent sections.

Principal computations performed were energy deposition, thermal diffusion, and transient stresses. These calculations determine the heat loads and sub-microsecond stress waves imposed by nuclear environments and are additive to propulsion system thermal and stress computations. The computerized models utilized have been verified by laboratory and underground test correlations. Energy depositions were computed by the KNISH code, based on axisymmetric

Ref. 6: Specification No. S-M-X-41016, Prime Item Development Specification For MX Stage IV, Appendix I, Headquarters, Space and Missile Systems Organization, Air Force Systems Command, 22 June 1977.

photoelectric/compton single scattering. Submicrosecond stresses were computed with the PISCES one-dimensional program, which is a PUFF-type, finite-difference shock wave and material response code.

Three separate configurations were considered: (1) unshielded exposure of components, (2) shielded by a structure of 0.138-inch nitrile EPM and 0.143-inch magnesium-2% thorium, and (3) shielded by an aft thermal blanket of 0.25 lb/ft² of Astroquartz and 0.066 lb/ft² stainless steel. The X-ray radiation environment is of greatest concern. Unshielded exposure of the components is clearly unacceptable; however, adequate protection for most of the components can be provided, after staging, by the structure, intervening components, and an aft thermal blanket. The most susceptible component is the electronically controlled regulator. If the forward payload does not protect the feed system components after the shroud has been jettisoned, additional local shielding or a forward bulkhead could be required.

Propellant Tanks. Critical view paths were selected at the points of (1) minimum composite thickness, (2) minimum propellant shielding, (3) diaphragm weld attachment, and (4) mount ring attachment. The failure modes of concern were excessive temperature excursions of materials and propellants, stress wave damage (spall), and debonding of the liner prior to pressurization. Unshielded exposure resulted in critical debonding of the liner (if unpressurized) and composite temperatures exceeding the cure temperature. Noncritical effects included a small loss in composite thickness, negligible liner surface spall, and small temperature increases in the diaphragm and propellants. Protection provided by the thermal blanket reduced response levels to acceptable levels, and shielding by the structure was considerably greater.

Catalytic Reactor. An unshielded exposure would possibly cause some internal spall of the housing, but would not degrade the catalyst. Adequate shielding would be provided by an aft thermal blanket.

Relief Valve. Unshielded exposure might produce internal spall of the housing; however, no performance degradation would be expected. Depending on its orientation, the vent poppet could be directly exposed through the vent ports. Local shielding may be required to prevent surface etching/spall of the seat surface.

Lines. Unshielded exposure probably would cause both external and internal spall of the tubing and weld joints. Shielding with the aft thermal blanket would be sufficient.

Electronically Controlled Regulator. Unshielded exposure of the regulator assembly would result in possible spall of the cast housing, which could cause fragments to reach the main and pilot valve poppets and seats. Aft thermal blanket shielding would be sufficient to prevent damage.

Unshielded exposure of the torquemotor housing would probably cause damage to the copper windings and solder joints. Some local shielding in addition to that afforded by the aft thermal blanket may be required to protect the solder.

Energy deposition in the gold material contained in the electronic components was critically high with only the thin aluminum housing. Local shielding would be required to reduce the dose to a safe level. Shielding also would reduce the peak dose in copper, solder, and silicon materials.

Because the electronically controlled regulator is the most susceptible component, an additional NH&S study was conducted by Autonetics Division, Rockwell International. The MX nuclear environment specified in Ref. 7 was utilized. Analyses were conducted to determine the effects of EMP, system-generated EMP (SGEMP), X-ray, neutron fluence, total ionizing dose, and ionization dose rate.

Ref. 7: Specification No. S-M-X-41017, Prime Item Development Specification For MX Guidance and Control System, Appendix IV, Headquarters, Space and Missile Systems Organization Air Force Systems Command.

Electromagnetic Pulse And SGEMP. Shielding of the cable between the d-c power source and the electronics and between the electronics and the regulator assembly are required. Additionally, filtering of the electronics assembly d-c power input and signal output is needed to protect against burnout of the interface circuits. Parker's electronics piece part and sub-assembly packaging will minimize the effects on internal circuits, but a hardened housing would be beneficial. The adequacy of the housing to protect against EMP/SGEMP burnout was not evaluated because a hardened design already was required by other environments. The regulator assembly is not expected to respond to EMP/SGEMP transients from a single event.

X-ray. Shielding of the cables is required to protect against X-ray effects. The electronics housing requires a layer of high molecular weight material to reduce the ionization dose deposited by a criteria-level X-ray environment. This will prevent damage caused by thermomechanical and conductivity modulation effects. A hardened housing also may be required to prevent damaging thermomechanical stresses in the pressure transducer Wheatstone bridge element mounting structure. Additional analysis is required to verify that regulator assembly parts surrounding the tungsten carbide ball in the pilot valve will adequately attenuate the X-ray environment to avoid thermomechanical effects.

Neutron Fluence. Key parameters of the power amplifier, operational amplifiers, bipolar transistors, and integrated circuits (IC's) within the electronics package would be severely degraded with only an aluminum housing. Changes in resistivity of the diffused resistors in the pressure transducer were insignificant for dopant levels $>5 \times 10^{14}$ carriers/cm³.

Total Ionizing Dose And Dose Rate. The mosfet and bipolar transistors, diodes, and IC's would be degraded significantly by the total ionizing dose. Parker's design does contain adequate current limiting in piece part circuits to guard against burnout due to ionization dose rates, with the exception of the IC's, where inadequate test data exist for analysis. Transient ionization effects would momentarily saturate the output transistor and

increase the power amplifier output current. Whether hardening would be required depends on the response time of the regulator assembly and the recovery time of the electronics.

Recommendations. Cables that interface with the electronics and regulator assemblies should have a minimum length and be shielded. Electromagnetic (EM) shields must provide on the order of 100 db attenuation for burnout protection against conducted EMP transients. Crimped or welded connectors are required to protect against X-ray thermomechanical effects and twist-on signal return pairs are necessary to guard against SGEMP effects.

The electronics assembly requires EM shielding of the housing to the same level as the cable design. A high molecular weight material X-ray shielding is also required on the inside of the housing. Filtering of the d-c power input and electronics output will be required as a minimum. The need for filtering the transducer input must be evaluated further. Proposed MX program electronics piece parts should be utilized, especially in place of the power amplifier, mosfet transistors, and IC's. Semiconductors should not contain high molecular weight materials in metallization, bonds, or packaging.

FEED SYSTEM PARAMETRICS

Parametric analyses were conducted to evaluate the effect of a wide range of design variables on the propellant feed system weight, envelope and unit production cost. Each of the feed system design requirements used in establishing the flightweight feed system design were taken into account, except when they were independent variables. Design layouts were drawn for the flightweight design concept with delivered propellant loads of 900, 1400, and 1800 pounds, and three a/b ratios each. Layout drawings also were prepared for alternate tank materials of titanium and all-aluminum. These designs served as the basis for generating parametric data over a range of delivered propellant loads between 800 and 2400 pounds.

The data presented in this section is internally consistent, but the absolute values may not agree with information found elsewhere in this report because of subsequent design changes. This does not, however, affect the validity of the trends.

COMPOSITE-WRAPPED ALUMINUM PSA DESIGN LAYOUTS

The baseline flightweight PSA was designed to deliver 1400 pounds of propellants and has a volume of 18,413 in.³. Parametric design layouts were made for different propellant loads and tank volumes. Figure 82 illustrates the design configurations for delivered propellant loads of 900, 1400, and 1800 pounds with a contour a/b ratio of approximately 1.4. Parameters held constant included the 10.0-inch-diameter polar boss opening, the 6.00-inch-diameter polar wrap opening, the 0.030-inch minimum liner thickness and the diaphragm wall thickness profile. The baseline design concepts of the valves, leak detector, mounting ring, and pressurant inlet and propellant outlet assemblies did not require any changes. Material processing and weld joining for all components also did not require any changes from the baseline PSA design. No significant variations are anticipated in the diaphragm reversal mode.

To maintain an optimum liner contour for the different volumes, i.e., minimum stress, a variation in the conical length near the equator was required. The effect of this variation on the stability of the diaphragm reversal was evaluated and the results indicated that adequate margin exists between the buckling and rolling differential pressures.

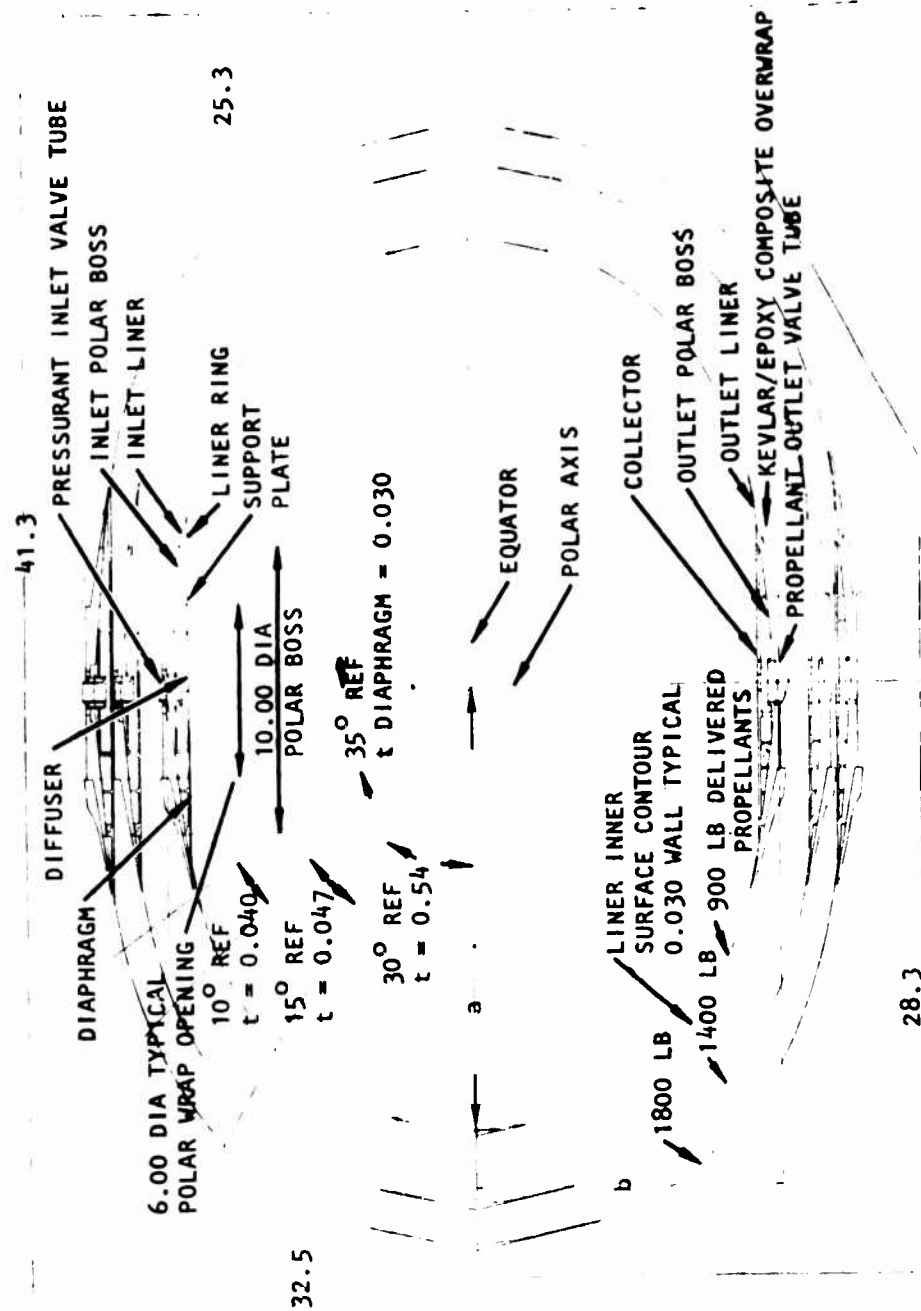


Figure 82. Parametric Propellant Tank Layouts for $a/b = 1.4$

Parametric design layouts also were made for PSA delivered propellant loads of 900, 1400, and 1800 pounds with a/b ratios of approximately 1.2 and 1.9. These design layouts are presented in Fig. 83 .

The lower a/b limit was based on maintaining a sufficient diaphragm reversal stability to preclude buckling. The upper end of the a/b range was limited by the large deflections near the poles under pressure and inward buckling of the tank under vacuum propellant storage conditions. The upper limit of 1.9 also was considered the practical limit for the composite-wrap stress patterns. In addition it should be noted that deflections at the equator under proof and operating pressures must be controlled by the mounting ring and the circular wrap as the a/b ratio deviates from the baseline design (1.42), which has negligible movement. Deflection control, required to maintain integrity of the diaphragm girth weld, can be maintained by the mounting ring design and composite wrap for a/b ratios between 1.2 and 1.9.

ALL-ALUMINUM AND TITANIUM PSA DESIGN LAYOUTS

The design of an all-aluminum tank to support the calculation of parametric data is presented on the left side of Fig. 84 . A true elliptical contour rather than the shape of the baseline composite-wrapped tank was used. This shape is optimal for metal tanks to minimize deflections and stresses. Because of the isotropic nature of metal, the allowable stresses are substantially the same in all directions, as opposed to the wrapped tank where the allowable stress is a maximum in the direction of the fiber. The tank is sized to deliver 1400 pounds of propellants and has an a/b ratio of 1.40. This a/b ratio results in a negligible change in the girth diameter under pressurized conditions.

Minimum allowable yield and ultimate strengths of 2219T6 aluminum are 36 and 54 ksi, respectively. Considering the proof and burst safety factors of 1.1 and 1.25, respectively, a maximum tank wall thickness of 0.140 inch was determined. Except for the deviation in tank contour, the design concept for

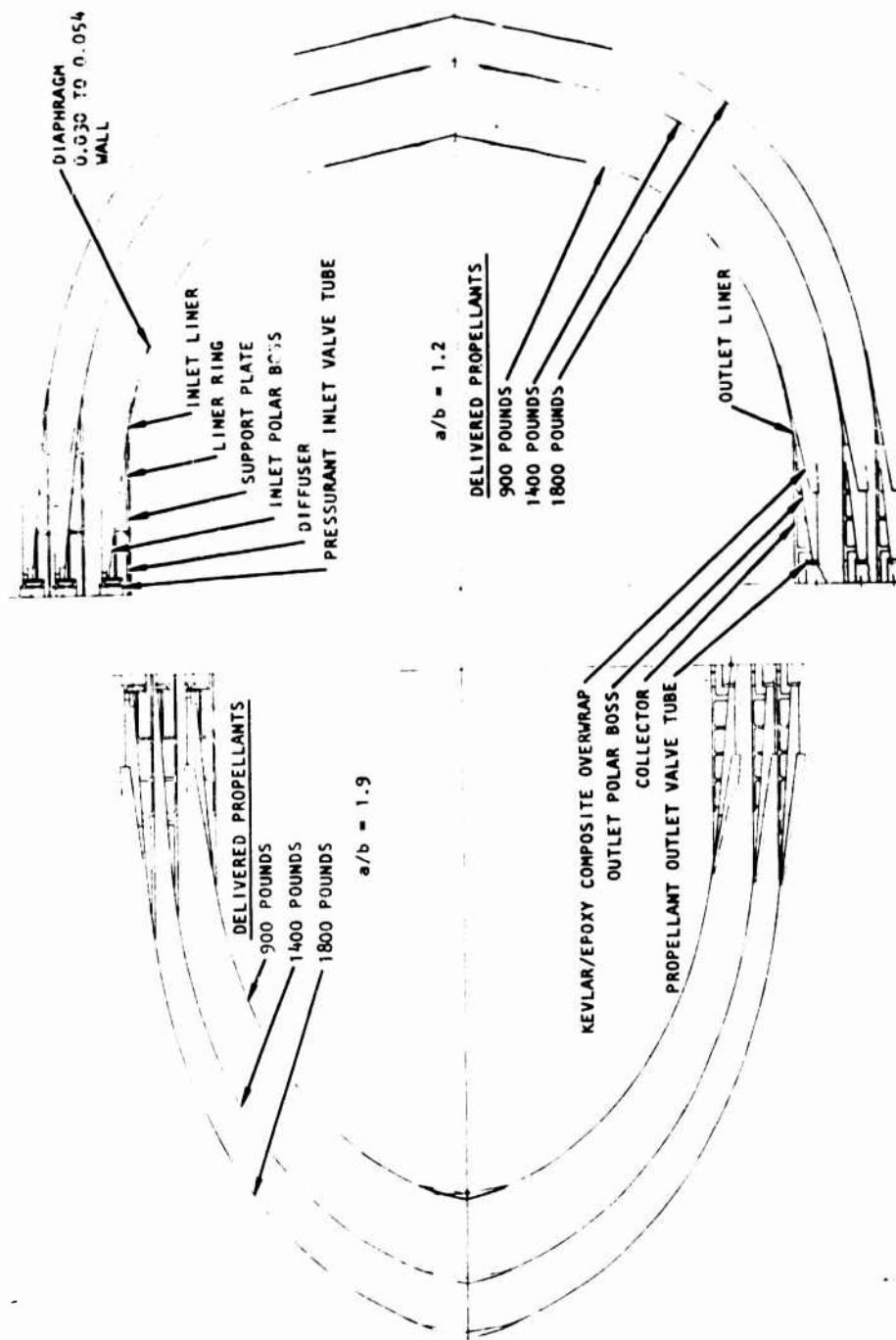


Figure 83. Parametric Propellant Tank Layouts for $a/b = 1.2, 1.9$

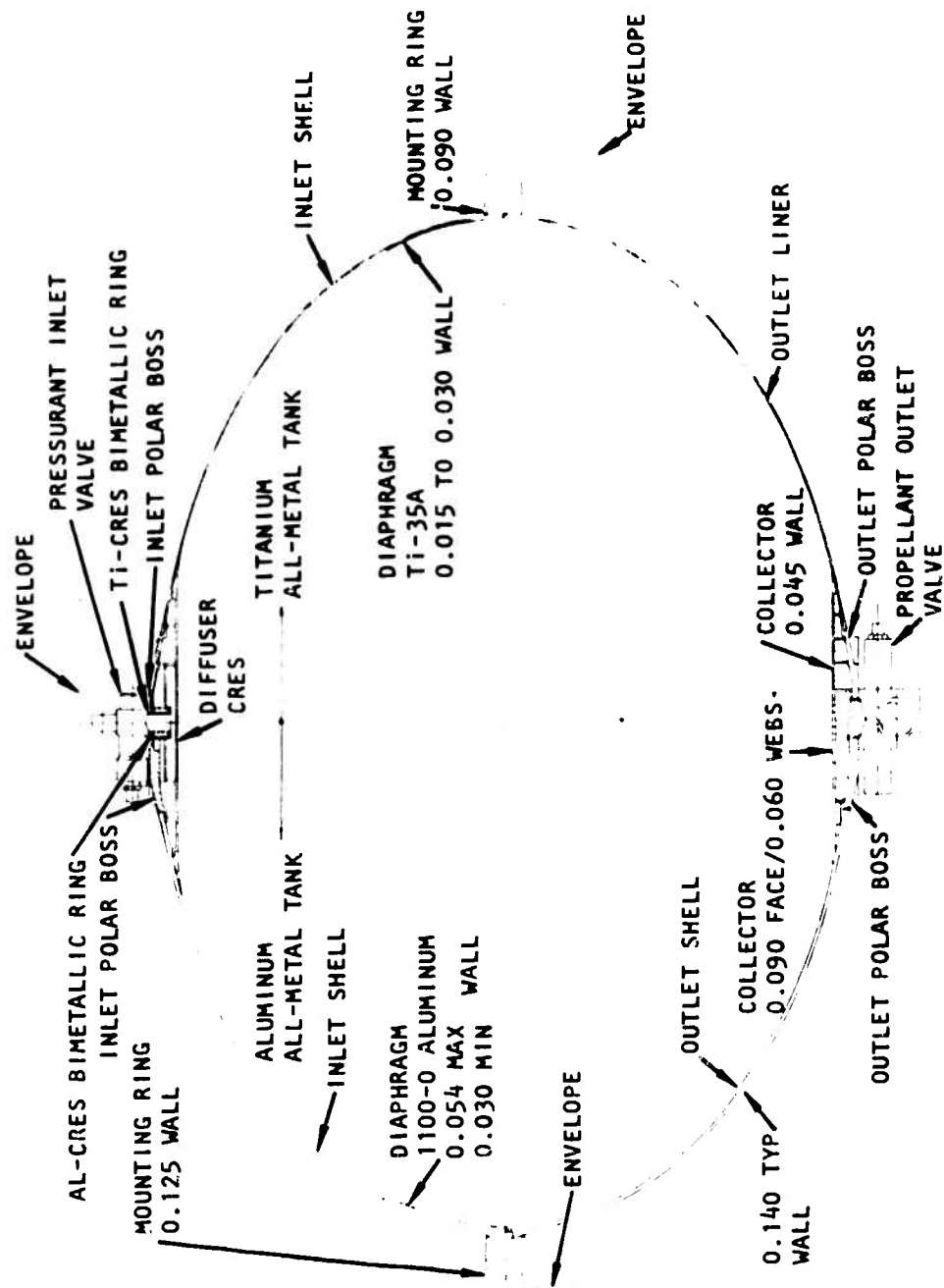


Figure 84. All-Aluminum and Titanium Flightweight Tank Layouts

the all-aluminum PSA is essentially the same as the tank liner assembly of the baseline wrapped PSA.

Figure 84 also presents the design of an all-titanium tank using 6Al-4V for the structure and Ti-35A for the diaphragm. Again, the design concept is like that of the baseline PSA liner assembly, as are the joining concepts. The structural shell surface is elliptical and of the same geometry as the all-aluminum tank. The titanium tank wall thickness, sized on burst pressure conditions, can be as low as 0.040 inch. However, to maintain inward buckling stability under vacuum storage conditions, a minimum constant thickness of 0.061 inch was required.

PARAMETRIC DATA

Parametric data were generated to determine the effect of a wide range of design variables on component and feed system weights, envelopes, and unit production costs. Each of the feed system design requirements used in establishing the flightweight feed system design were taken into account, except when they were independent variables. The following three sections present the analytical results for the PSA's, pressurization subsystem and propellant feed system.

Propellant Storage Assembly

The range of parameters considered for the PSA calculations are presented in Table 27. PSA weight data are presented in Fig. 35 to 88 as a function of delivered propellant weight and pressure, a/b , material, and pressurant inlet temperature. Figure 85 shows individual PSA weights as a function of delivered propellant weight and pressure for aluminum, titanium, and composite-wrapped aluminum at an a/b of 1.4. Composite-wrapped tanks do not have a large advantage at the lower pressures, especially when compared to titanium, because they are over-designed. This is caused by the lower limit on the wind density (filaments/inch) with a single-layer wrap. Figures 86 and 87 show the additional effect of a/b variations (1.2, 1.4, and 1.9) for

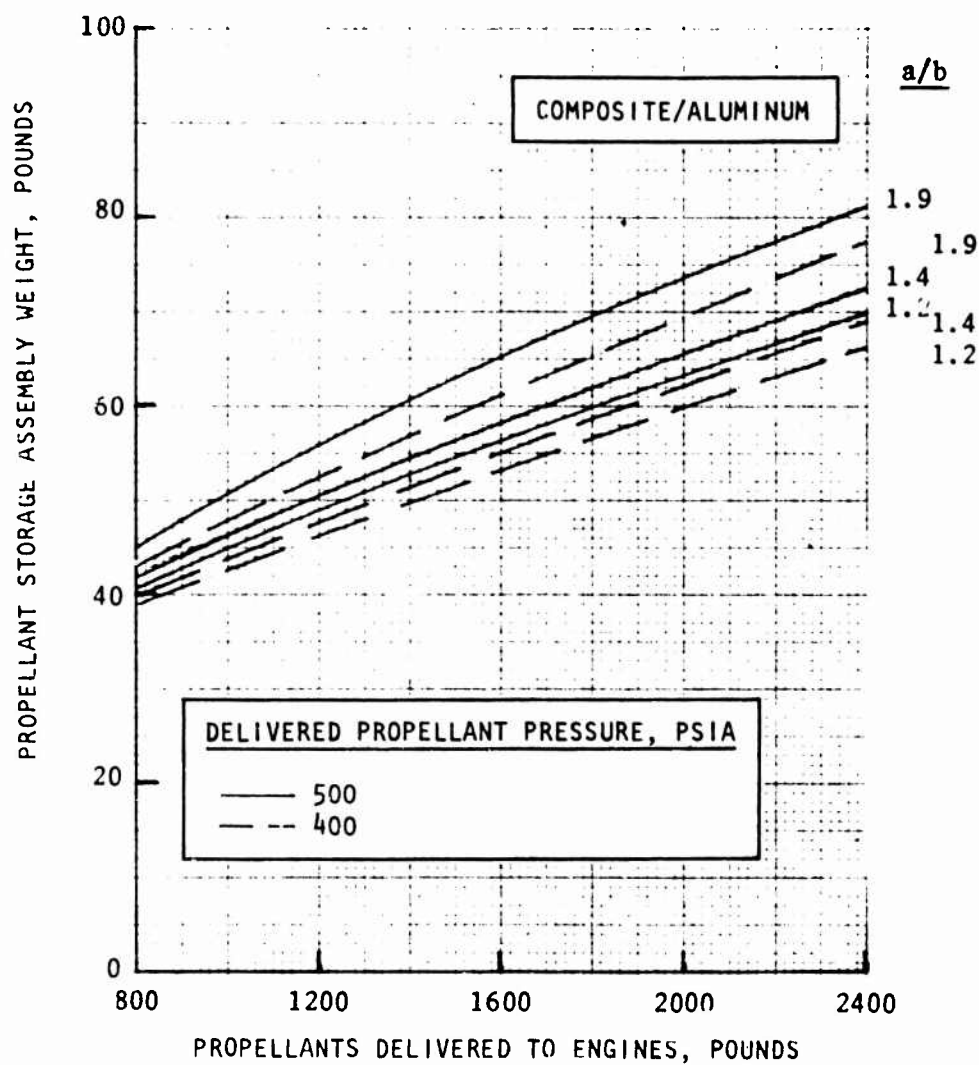


Figure 86. Parametric PSA Weights as a Function of a/b and Propellant Weight at Pressures of 400 and 500 psia

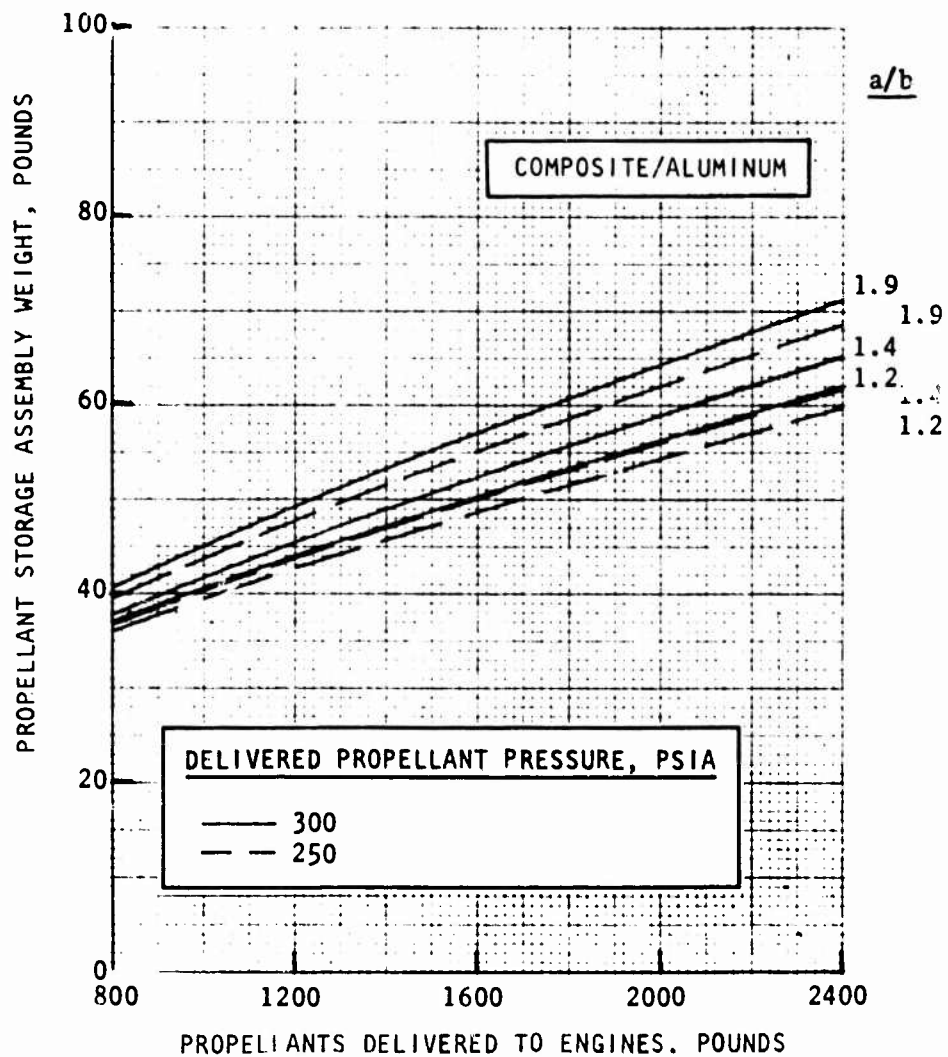


Figure 87. Parametric PSA Weights as a Function of a/b and Propellant Weight at Pressures of 250 and 300 psia

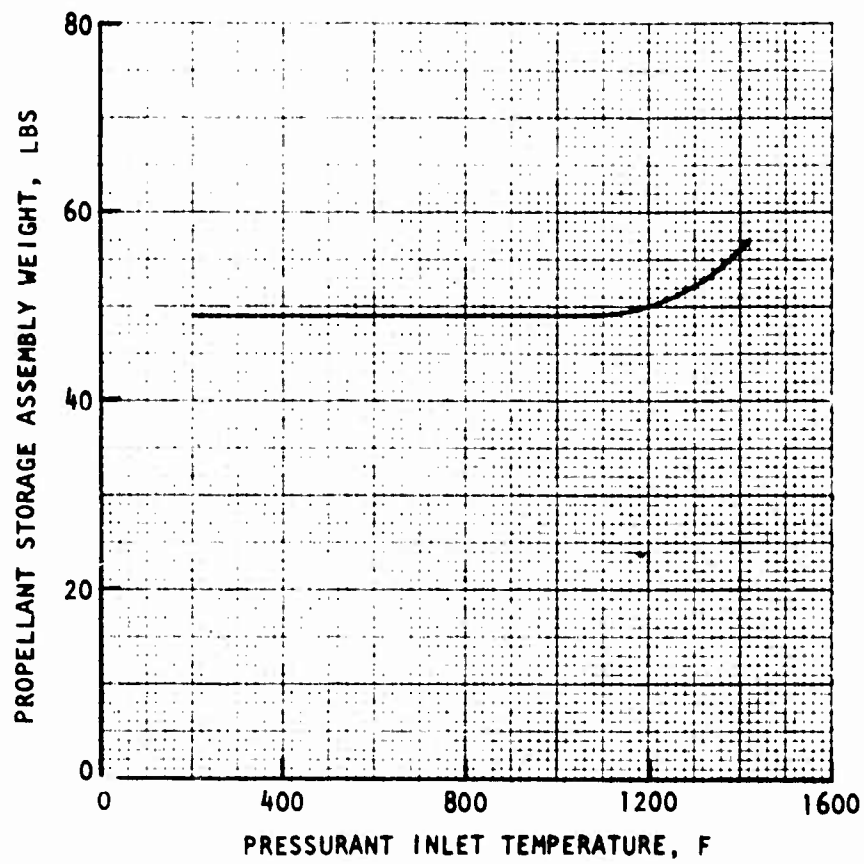


Figure 88. Parametric PSA Weights as a Function of Pressurant Temperature

TABLE 27. PSA RANGE OF PARAMETERS

	Nominal	Minimum	Maximum
Delivered Propellants, pound	1400	800	2400
Delivered Pressure, psia	300	250	500
a/b	1.4	1.2	1.9
Pressurant Inlet Temperature, F	1025	225	1425
Number of Systems	400	200	400
Production Rate, Systems/Month	10	3	10
Expulsion Efficiency, %	97	90	99
Maximum Aluminum Diaphragm Thickness, inch	0.054	0.030	0.060
Maximum Titanium Diaphragm Thickness, inch	-	0.015	0.040
Material	Composite/ Aluminum	Aluminum, Titanium	
Metal Parts Fabrication	Draw/ Machine	Spin/Machine	

the composite-wrapped aluminum tanks. As expected, the weight decreases with a/b as the shape approaches a sphere. The effect of pressurant inlet temperature on PSA weight is minimal (Fig. 88). As the temperature is increased above the baseline value of 1025 F, it becomes necessary to increase the thickness of the aluminum liner to act as a heat sink and prevent overheating of the epoxy resin. At very low temperatures it would be possible to use an all-aluminum inlet diffuser plate, but the weight savings would be minimal.

Figure 89 presents PSA envelope data, i.e., the length (stage axial direction) and height (stage radial direction) dimensions, as a function of delivered propellant weight and liner a/b. The plotted dimensions include the mounting ring, valves, and displacements due to pressurization. The lightweight concept is capable of delivering approximately 1580 pounds to the engines without violating the envelope requirement.

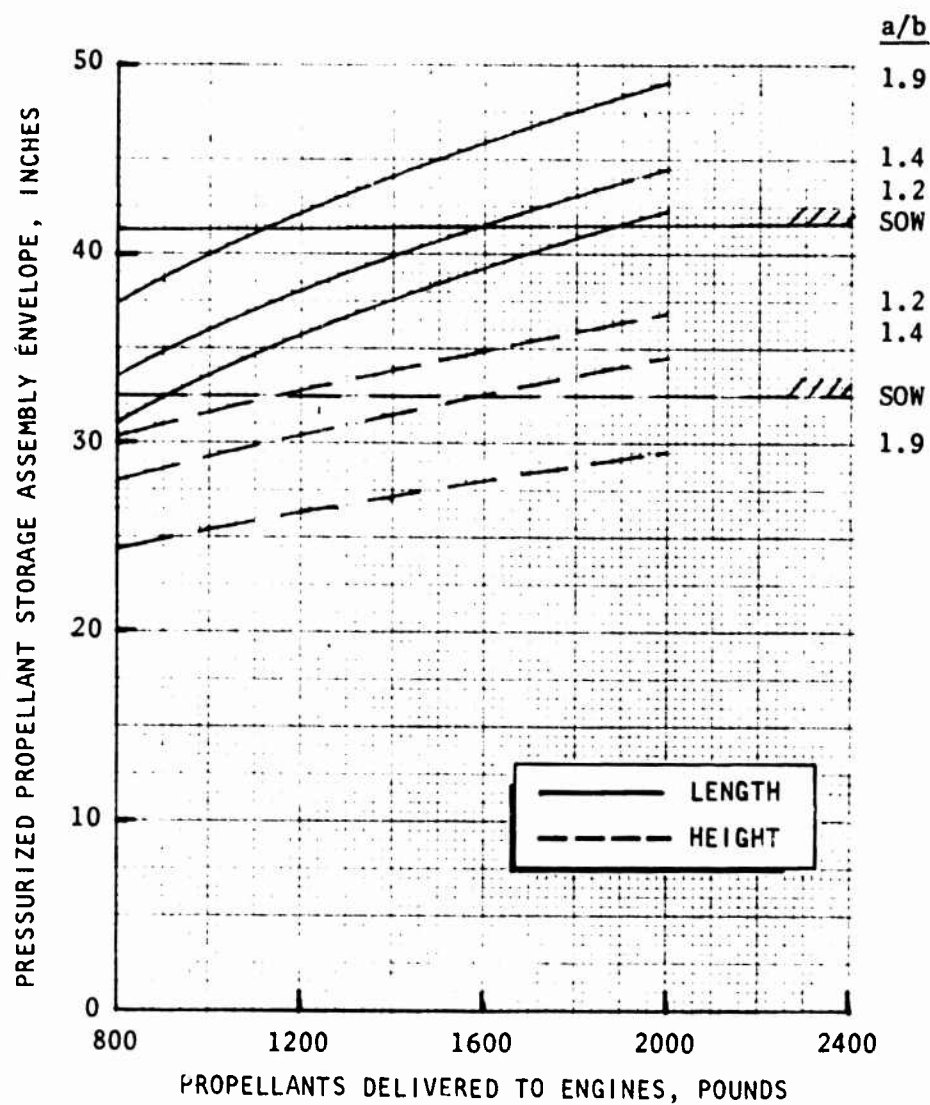


Figure 89. Parametric PSA Envelopes as a Function of Propellant Weight and a/b

Because of the shape of the tank, which results in a volumetric efficiency exceeding 99%, little benefit is to be gained in terms of envelope dimensions by placing the valves inside the tank. The polar axis dimension could be minimized, however, by placing the valves on the PSA mounting ring and routing lines to the polar bosses.

The unit production cost of two PSA's is shown in Fig. 90 and 91. Figure 90 shows cost as a function of delivered propellant weight and pressure, and a/b for composite-wrapped tanks with aluminum parts that are initially draw-formed, then machined (liners) or chemically etched (diaphragms). The variation in cost of fabricating the metal parts is relatively small for the small range in the tank size required. Further, the cost is virtually unaffected by a/b and the design pressure (only a small portion of the metal parts is load-carrying). Also, the cost of wrapping is only slightly sensitive to these parameters. Approximately half of the designs represented have only a single layer and the cost of a second layer is minimal. The cost of an alternative metal fabricating process, spinning, is also presented. Figure 91 shows the effect of varying the production rate and total number of systems.

The envelopes of PSA valves and the leak detector are presented in Table 28. These dimensions are not a function of any of the parameters considered.

TABLE 28. VALVES AND LEAK DETECTOR ENVELOPES

Component	Dimensions, inches
Vacuum Service Valve	0.86 X 0.86 X 1.17
Fill/Drain Valve	1.09 X 1.09 X 1.73
Pressurant Inlet Valve	1.00 X 2.00 X 3.88
Propellant Outlet Valve	2.00 X 2.30 X 6.25
Leak Detector	1.12 X 1.12 X 1.70

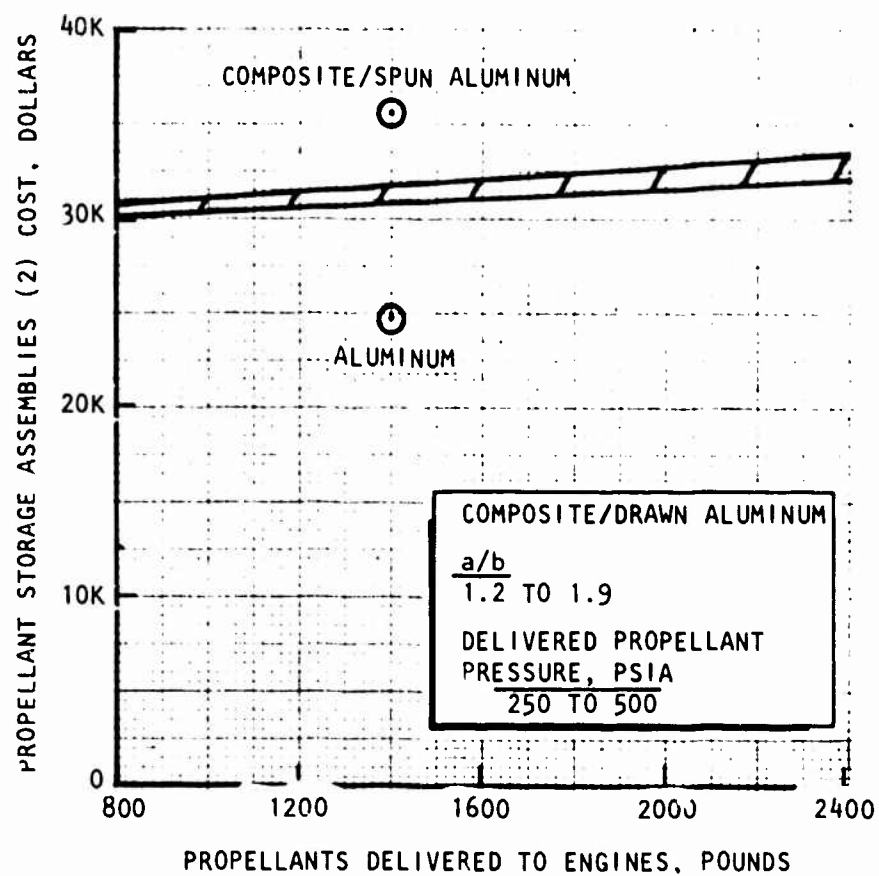


Figure 90. Parametric PSA Costs as a Function of a/b, Metal Fabrication Process, and Propellant Weight and Pressure

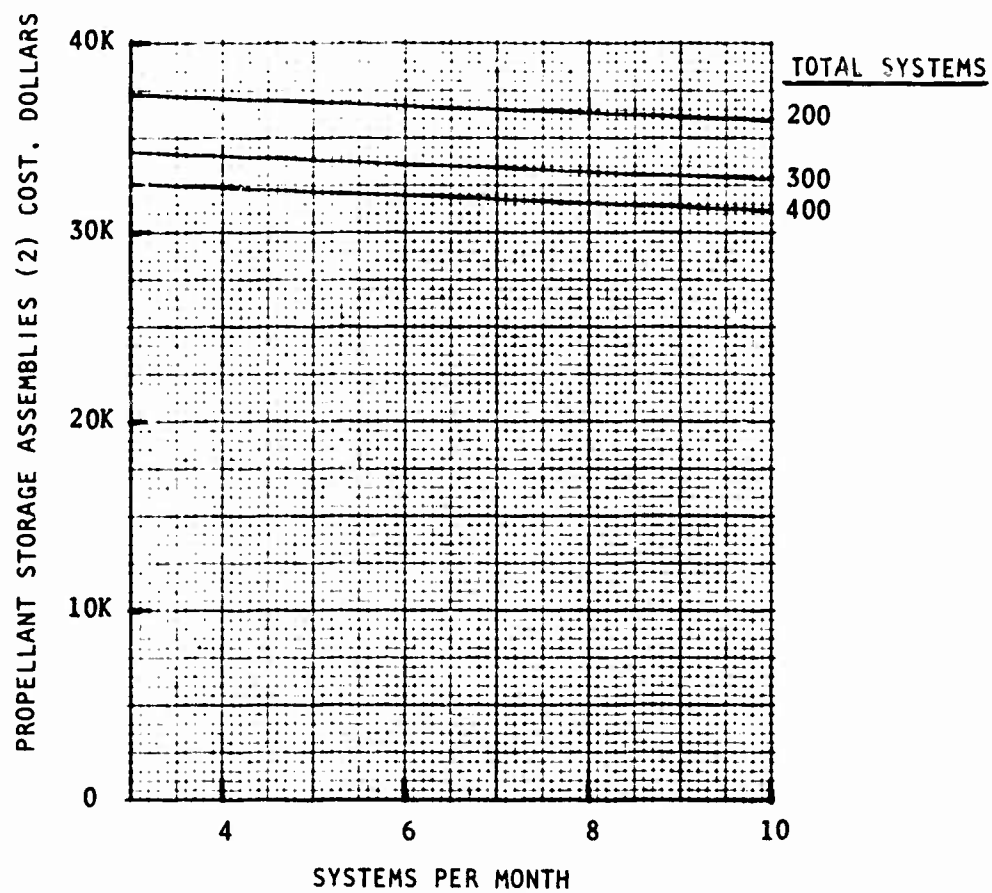


Figure 91. Parametric PSA Costs as a Function of Rate and Quantity

Figures 92 to 96 present a series of curves characterizing the diaphragm. Figure 92 shows the pressure drop required to achieve a given expulsion efficiency for thicknesses between 0.030 and 0.060 inch for 1100-0 aluminum, and 0.015 and 0.040 inch for Ti-35A titanium. When considering multiple-thickness diaphragms, the thickest dimension is applicable. A 0.030-inch-thick aluminum diaphragm is near the minimum because of pitting during storage. Titanium thicknesses below 0.015 inch would be possible because it is more compatible with the propellants; however, fabricability may be a problem. The propellant weight penalty associated with a given expulsion efficiency is shown in Fig. 93. Additionally, there is a small increase in hardware weight to store the extra propellant, which can be determined from previous figures. Approximately 7 pounds are required to prime the propellant lines. The parametric diaphragm weights as a function of delivered propellant weight, thickness and a/b for aluminum and titanium are presented in Fig. 94 to 96 for a/b's of 1.2, 1.4, and 1.9, respectively. These weights are for constant thicknesses, but a representative variable thickness (0.030/0.040/0.047/0.054 inch) diaphragm is shown in Fig. 95. Its effective thickness is approximately 0.046 inch.

Pressurization Subsystem

The range of parameters considered for the pressurization subsystem calculations are presented in Table 29. Tridyne weight data are presented in Fig. 97 to 99 as a function of delivered propellant weight and pressure, duty cycle, and pressurant inlet temperature. Figure 97 shows that pulsed MDC II requires additional pressurant because the longer mission allows more heat transfer from the fluid to the PSA hardware. Figures 98 and 99 show the effects of delivered propellant pressure and pressurant inlet temperature for MDC II. The Tridyne weight required as a function of temperature initially decreased, reached a minimum, and then increased as the PSA inlet temperature was reduced from 1425 F. As expected, the end-of-mission gas temperature decreased continuously, tending to increase the weight required; but the percentage of relatively heavy oxygen/hydrogen mix decreased, having the opposite effect.

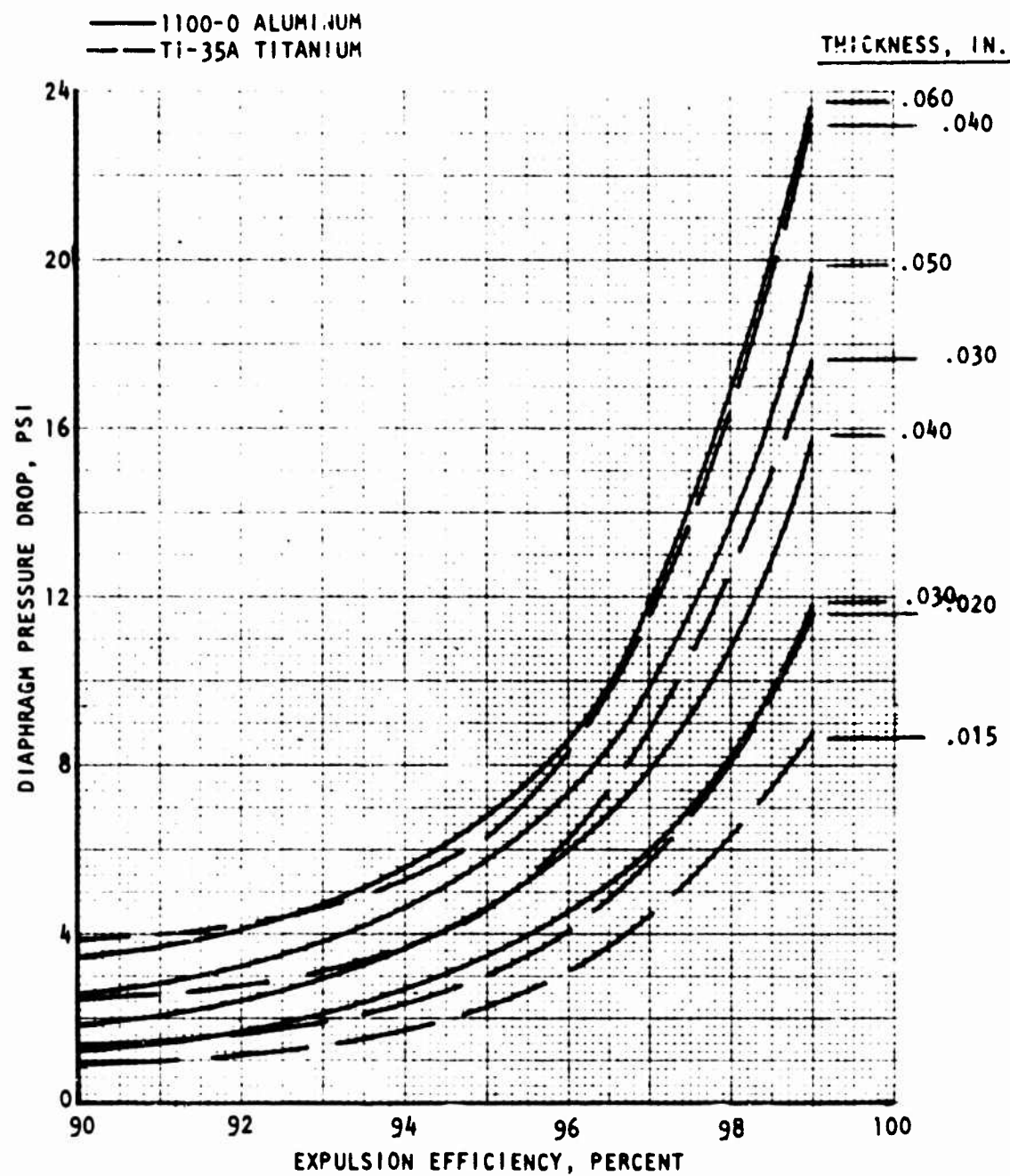


Figure 92. Parametric Diaphragm Pressure Differential as a Function of Expulsion Efficiency, Thickness and Material

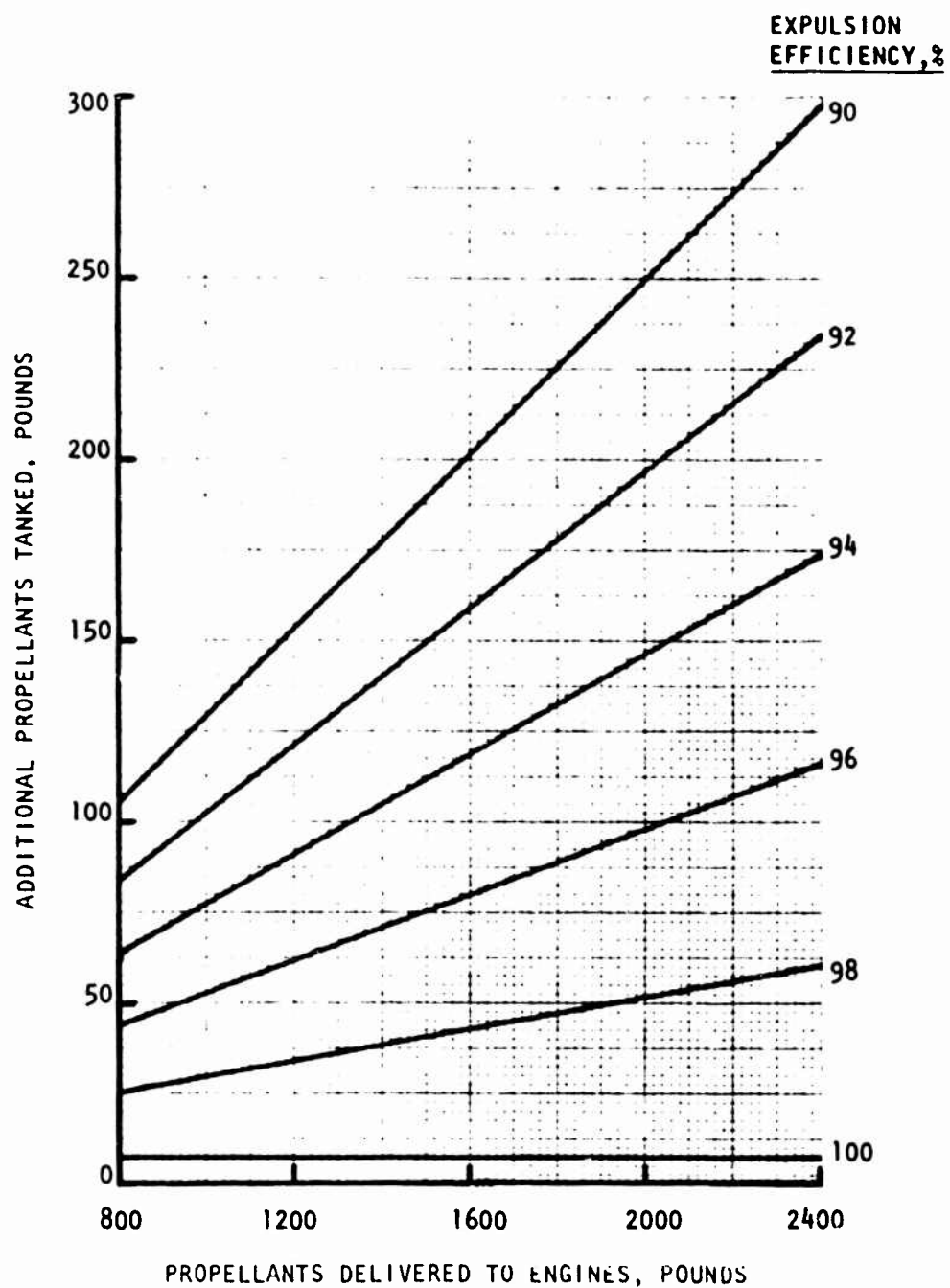


Figure 93. Parametric Additional Propellant Requirements as a Function of Delivered Propellant Weight and Expulsion Efficiency

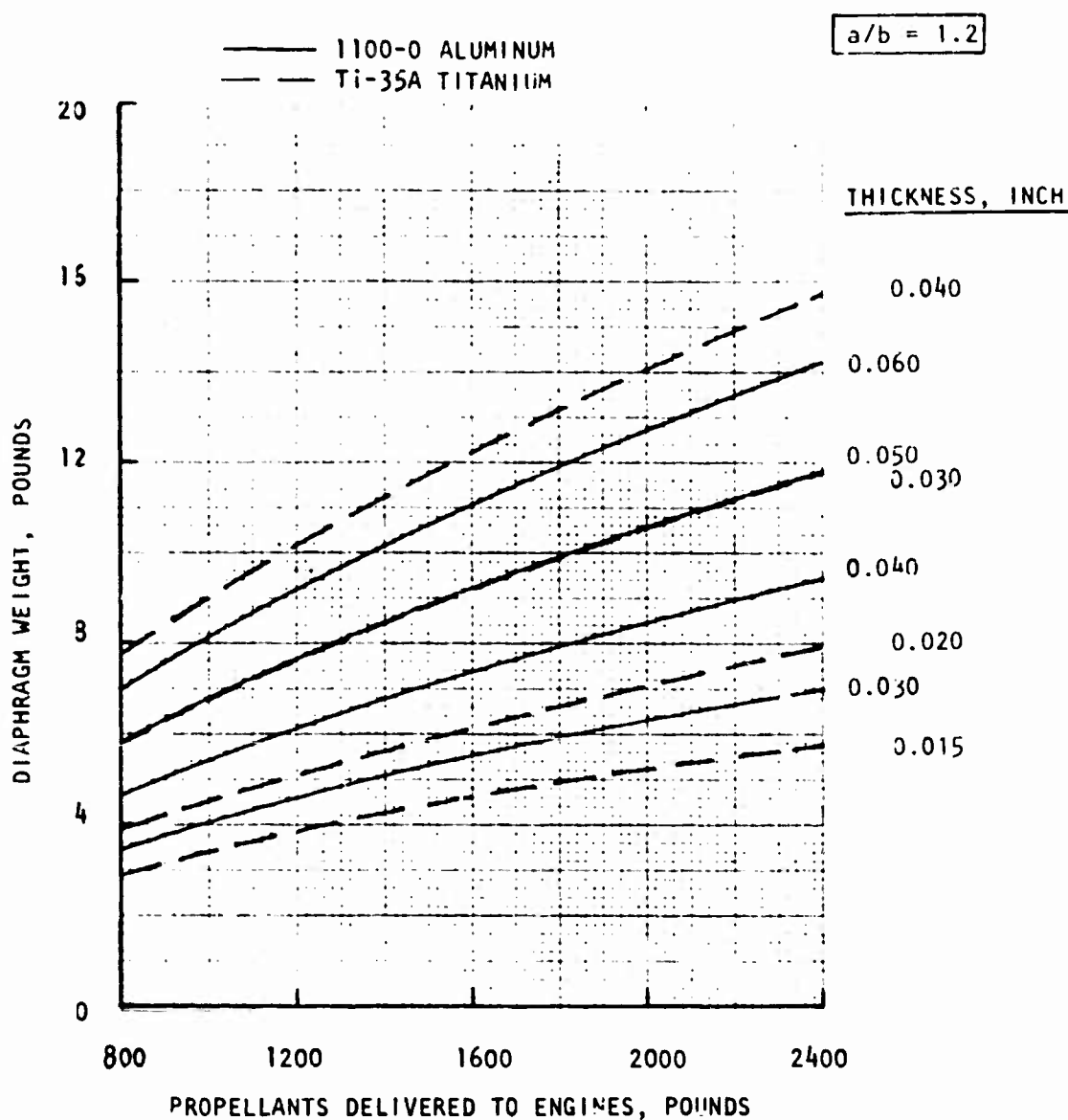


Figure 94 Parametric Diaphragm Weights as a Function of Propellant Weight, Thickness, and Material for $a/b = 1.2$

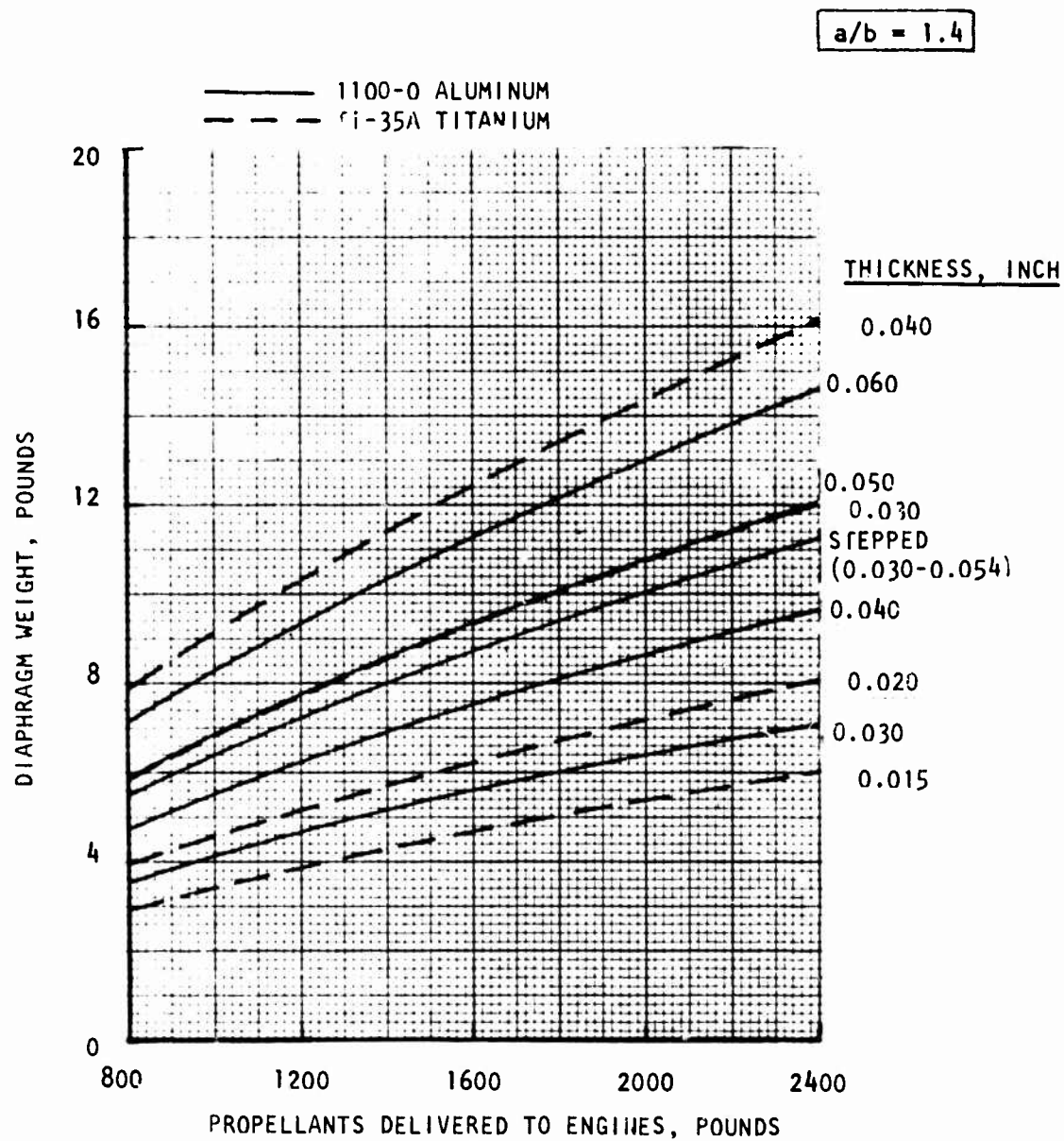


Figure 95. Parametric Diaphragm Weights as a Function of Propellant Weight, Thickness, and Material for $a/b = 1.4$

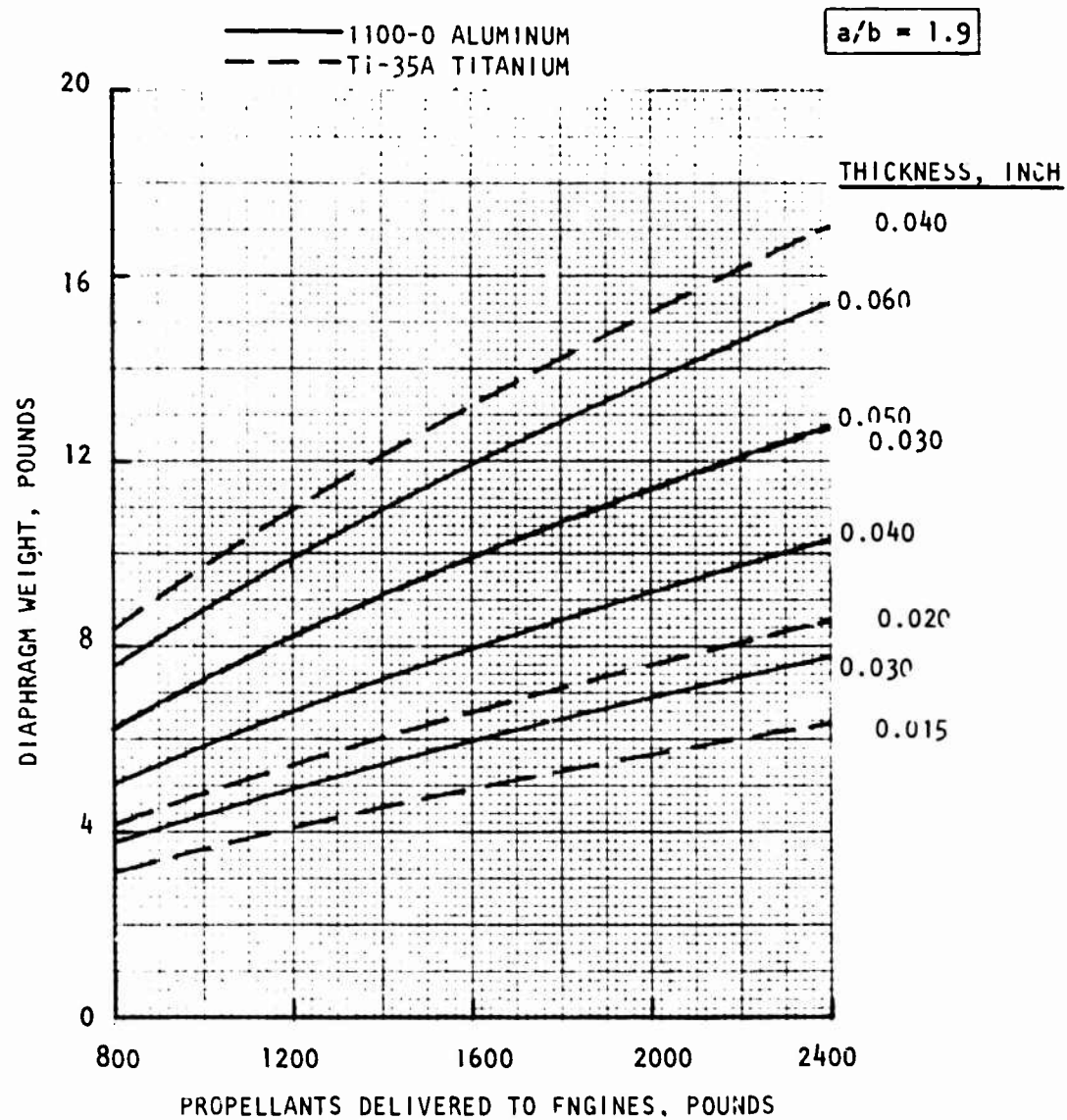


Figure 16. Parametric Diaphragm Weights as a Function of Propellant Weight, Thickness, and Material for $a/b = 1.9$

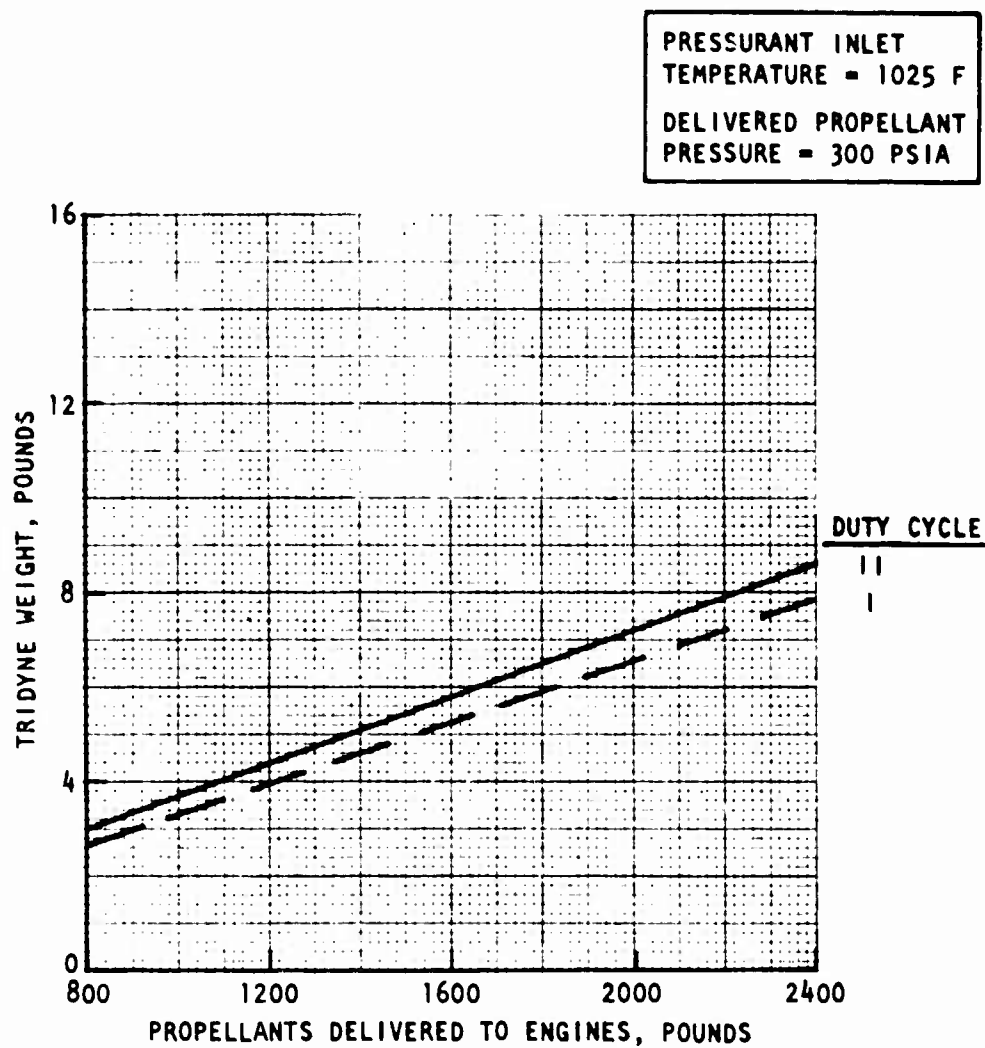


Figure 97. Parametric Pressurant Weight as a Function of Propellant Weight and Mission Duty Cycle

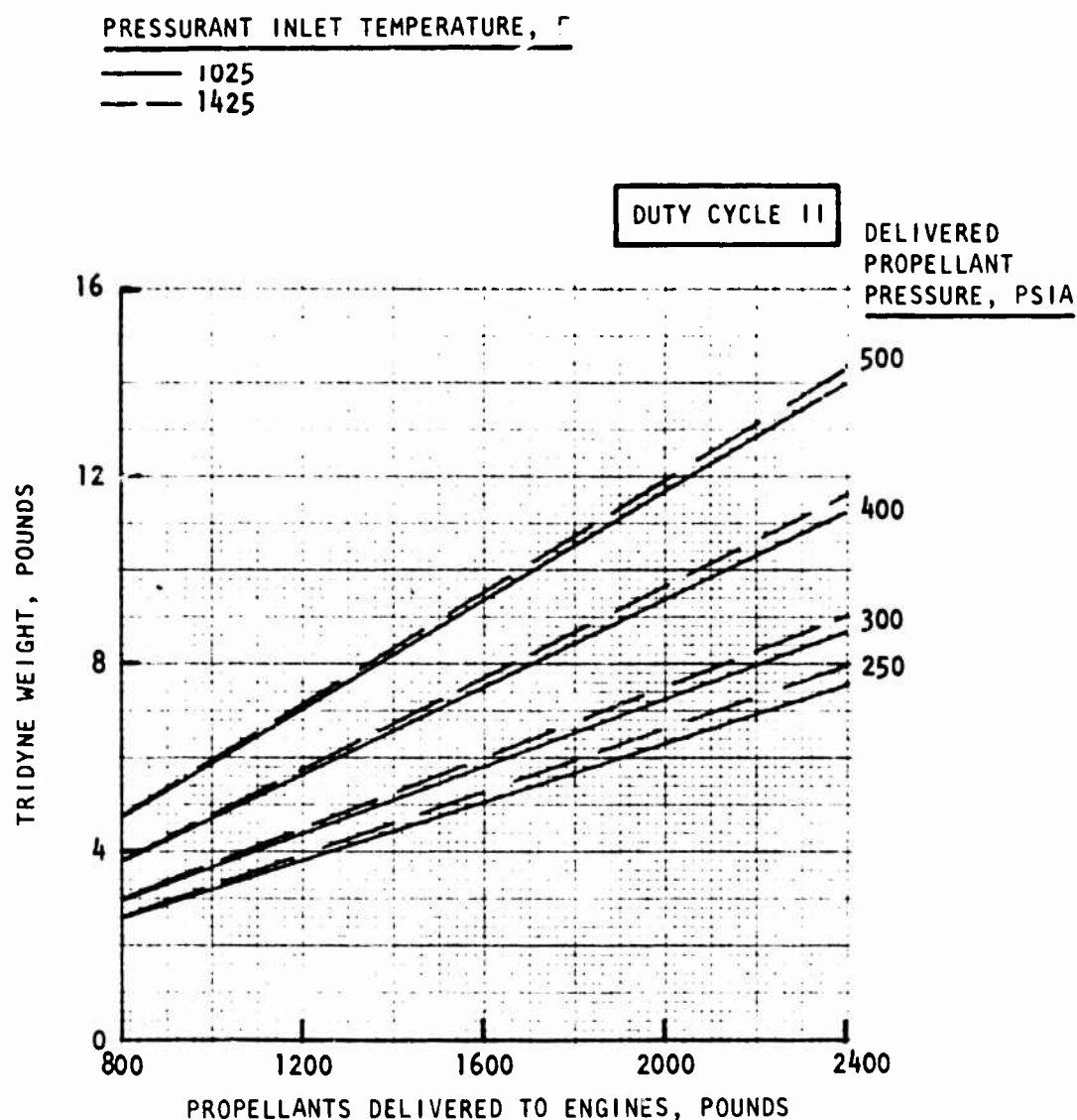


Figure 98. Parametric Pressurant Weight as a Function of Propellant Weight and Pressure for PSA Inlet Temperature = 1425 and 1025 F

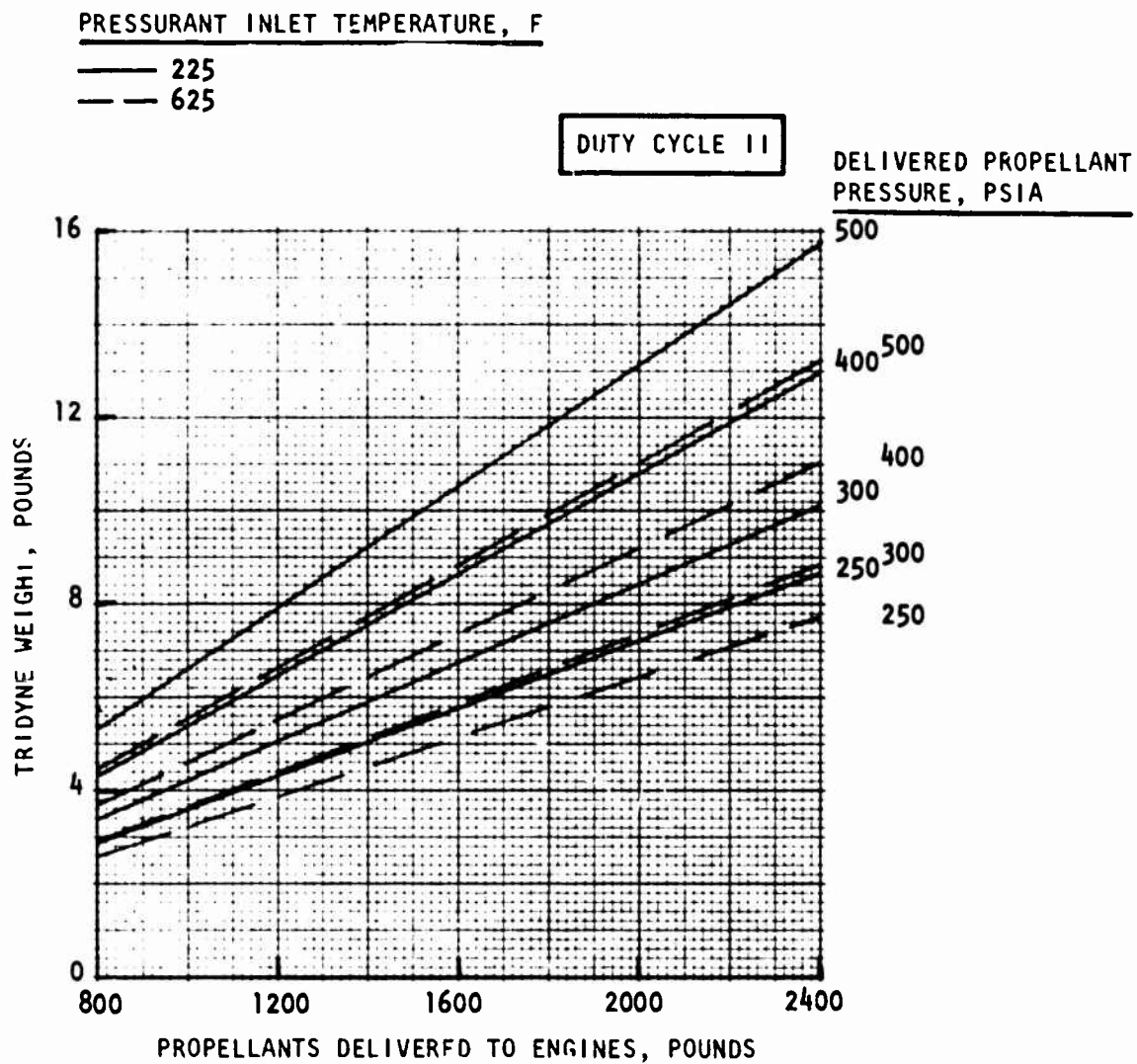


Figure 99. Parametric Pressurant Weight as a Function of Propellant Weight and Pressure for PSA Inlet Temperature = 625 and 225 F

TABLE 29. PRESSURIZATION SUBSYSTEM RANGE OF PARAMETERS

	Nominal	Low	High
Delivered Propellants, pounds	1400	800	2400
Delivered Propellant Pressure, psia	300	250	500
Propellant Flowrate, in. ³ /sec	275	150	500
Pressurant Inlet Temperature, F	1025	225	1425
Pressurant Storage Pressure, psia	4000	3000	5000
Pressurant Tank Material	Composite/ Aluminum	Titanium	

The corresponding Tridyne volume requirements are presented in Fig. 100 to 102, respectively. Unlike the weight, volume continuously increases with decreasing temperature.

Pressurant tank weight data are presented in Fig. 103 and 104 as a function of delivered propellant weight, pressurant inlet temperature, and pressurant storage pressure for MDC II using titanium and composite-wrapped 5086-0 aluminum. The weight advantage of the composite-wrapped tanks is substantial at these elevated pressures.

The corresponding composite-wrapped pressurant tank outer diameters are presented in Fig. 105 and 106. These diameters do not include polar boss fittings.

Pressurant tank cost data are presented in Fig. 107. The entire range of data for wrapped tanks falls within the band shown. As with PSA's, the cost is fairly insensitive to the ranges of size and pressure considered. In addition to being lighter, composite-wrapped aluminum tanks also are significantly lower in cost.

The remaining pressurization subsystem component weights are presented in Fig. 108 as a function of the delivered propellant flowrate, which directly

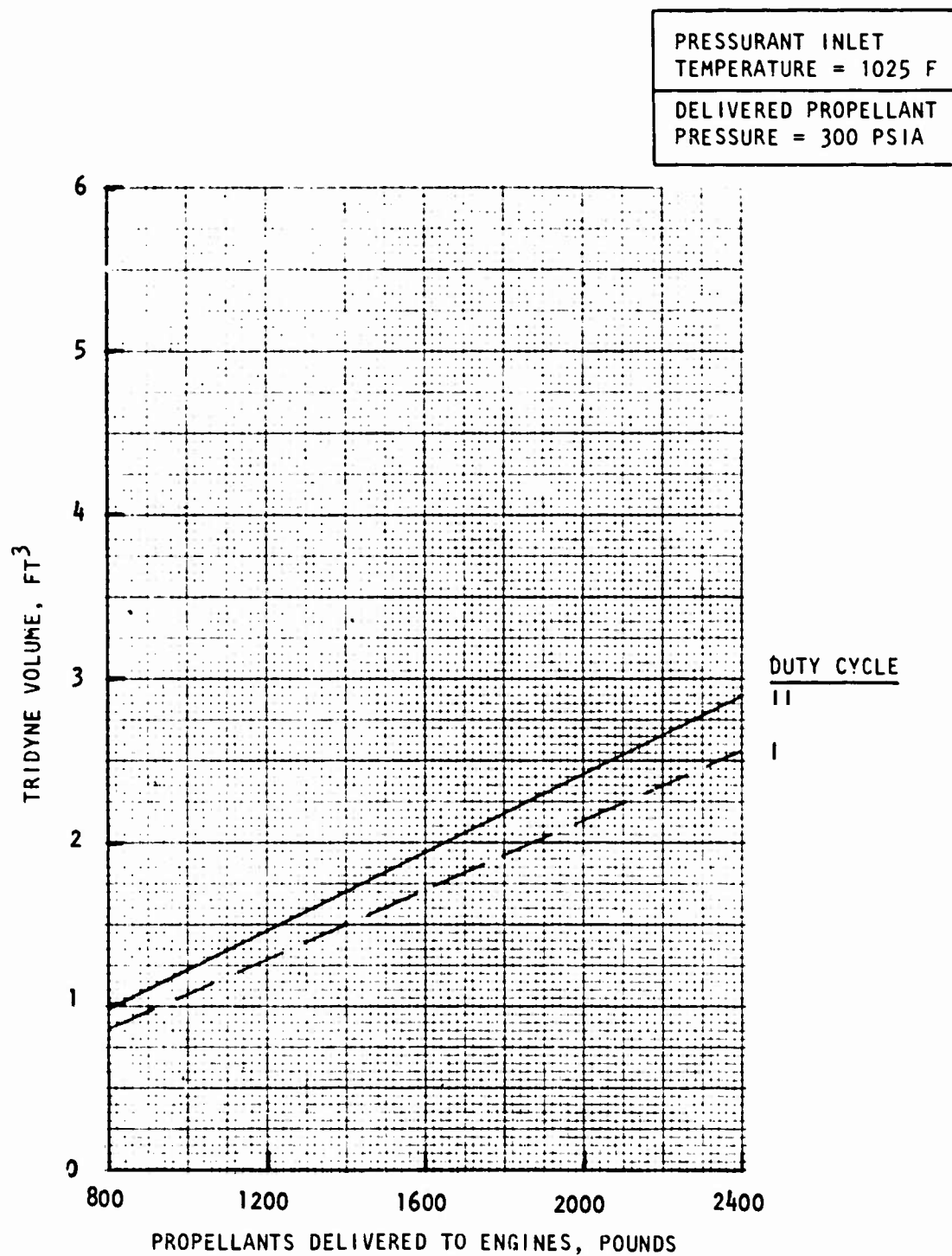


Figure 100. Parametric Pressurant Volume as a Function of Propellant Weight and Mission Duty Cycle

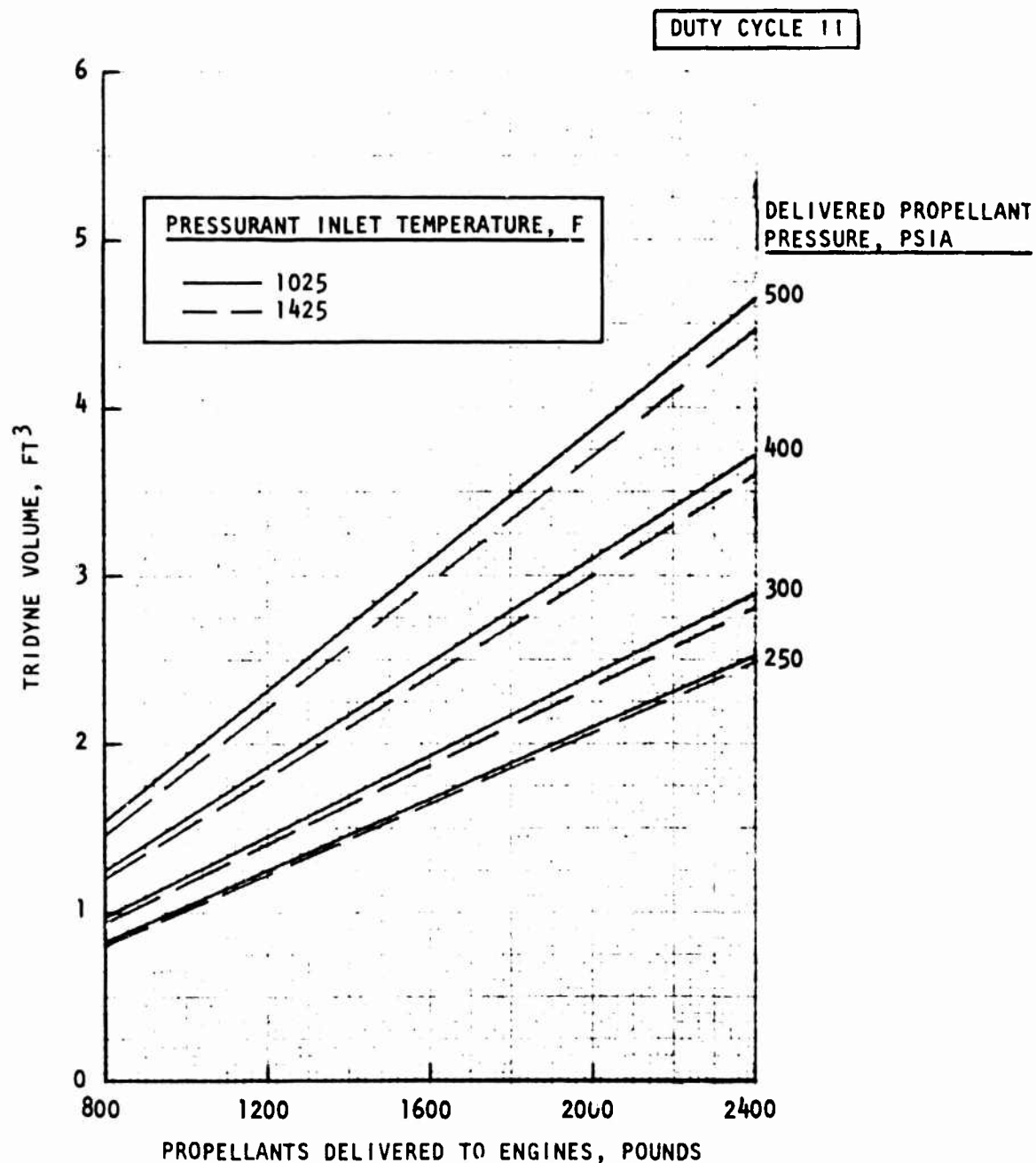


Figure 101. Parametric Pressurant Volume as a Function of Propellant Weight and Pressure for PSA Inlet Temperature = 1425 and 1025 F

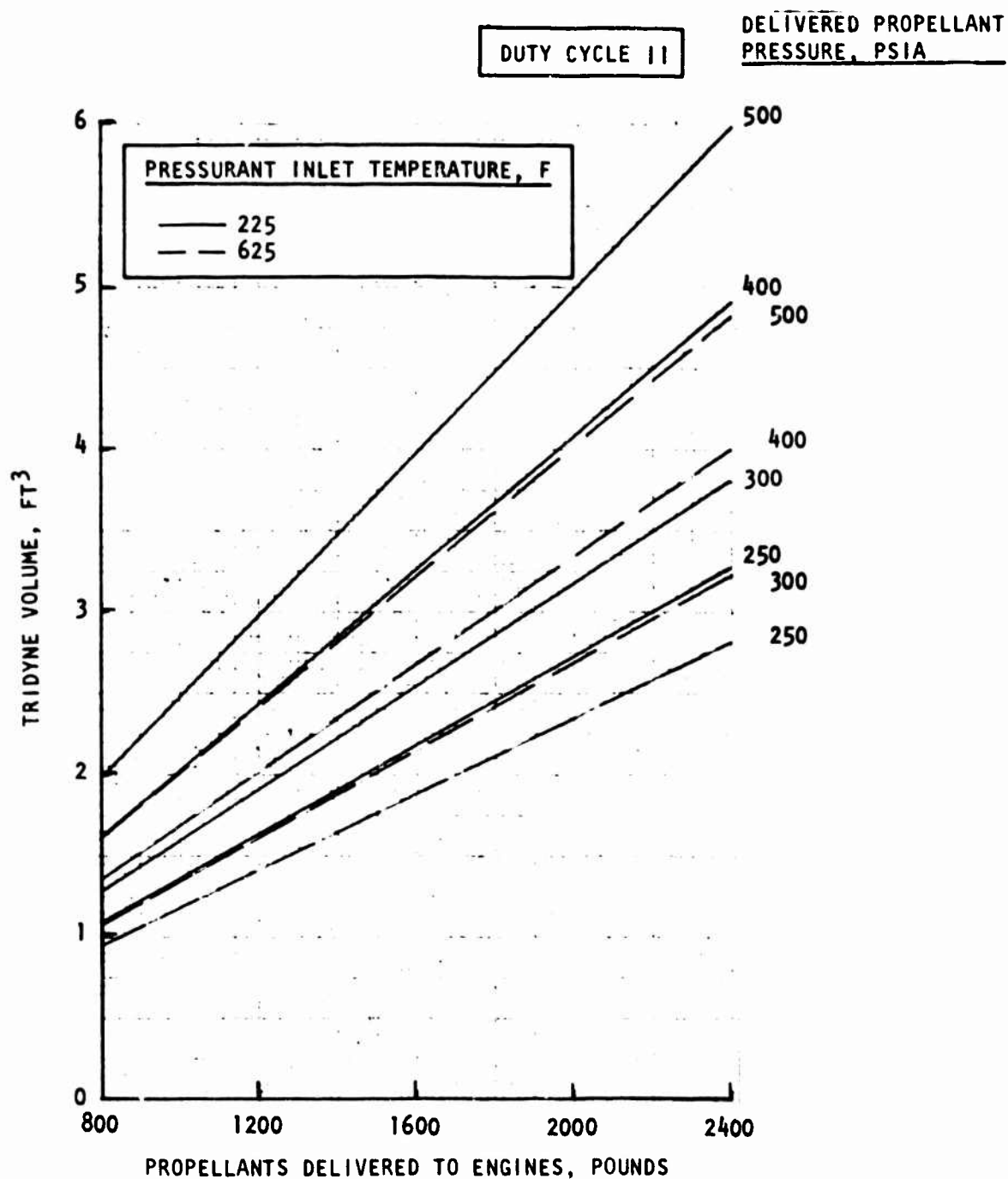


Figure 102. Parametric Pressurant Volume as a Function of Propellant Weight and Pressure for PSA Inlet Temperatures = 625 and 225 F

MATERIAL, PRESSURANT INLET TEMPERATURE, F

— TITANIUM, 1025
— COMPOSITE, 1025

DUTY CYCLE II

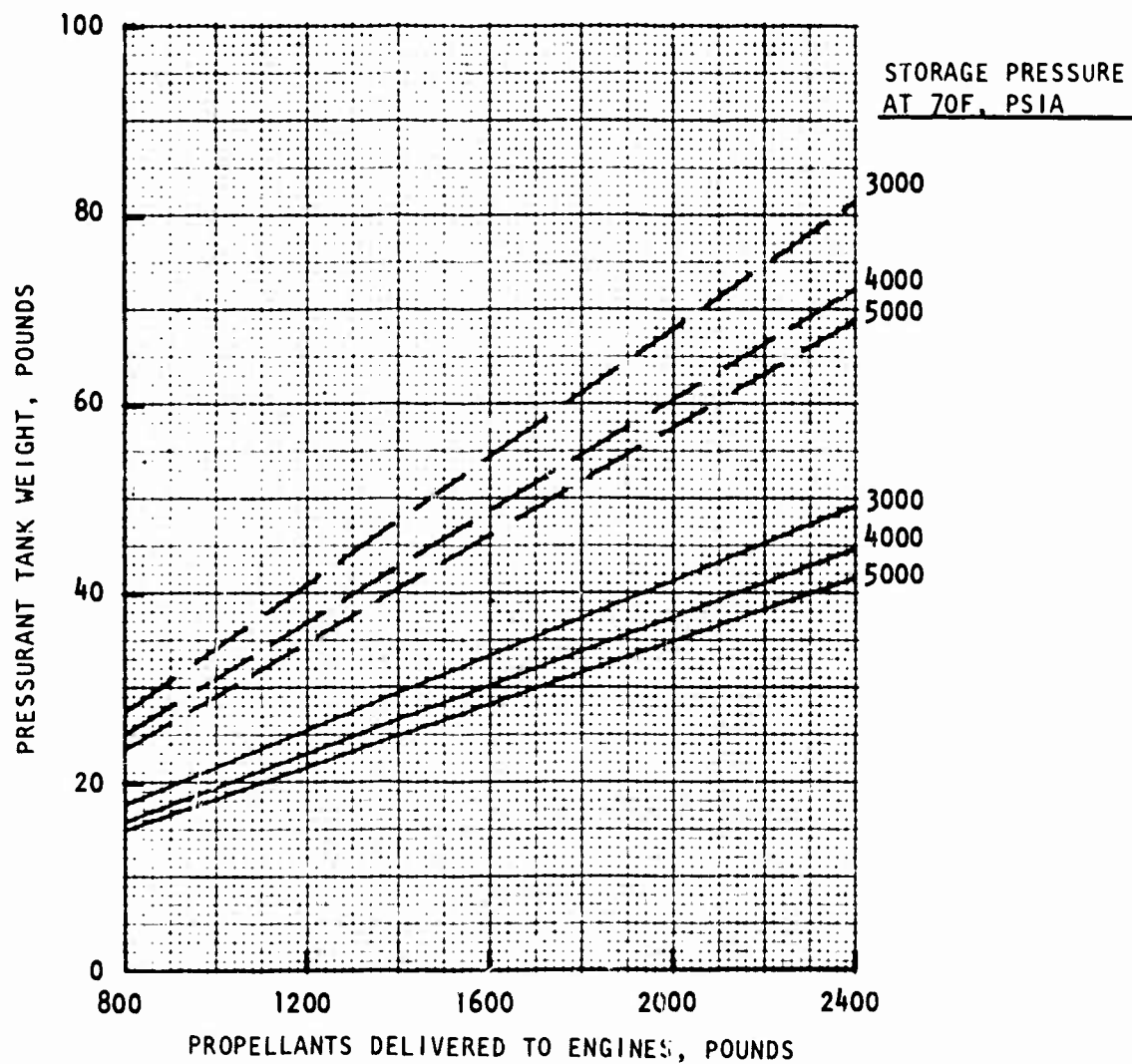


Figure 103. Parametric Pressurant Tank Weight as a Function of Storage Pressure, Material, and Propellant Weight for PSA Inlet Temperature = 1025 F

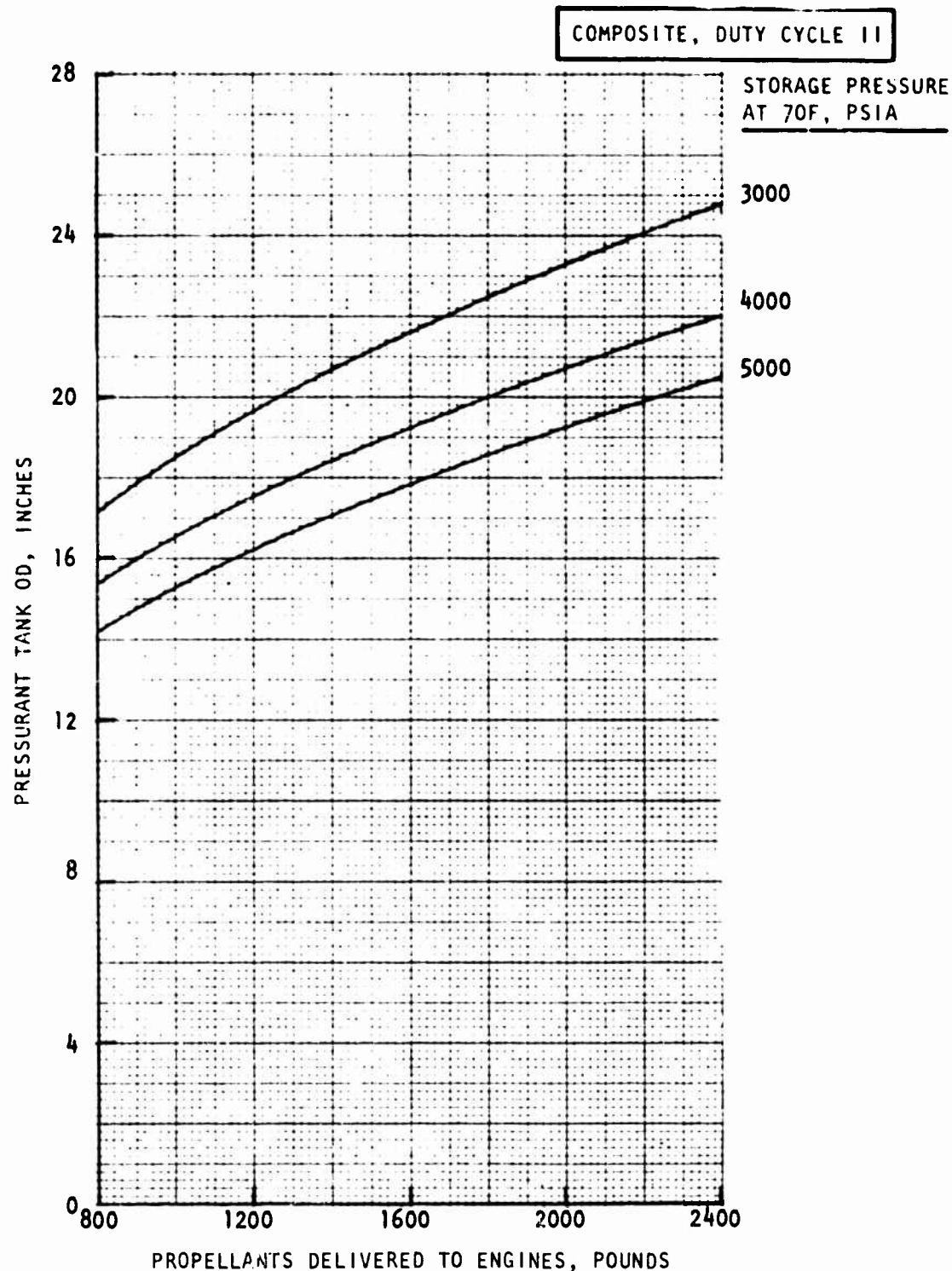


Figure 105. Parametric Pressurant Tank Diameter as a Function of Storage Pressure and Propellant Weight for PSA Inlet Temperature = 1025 F

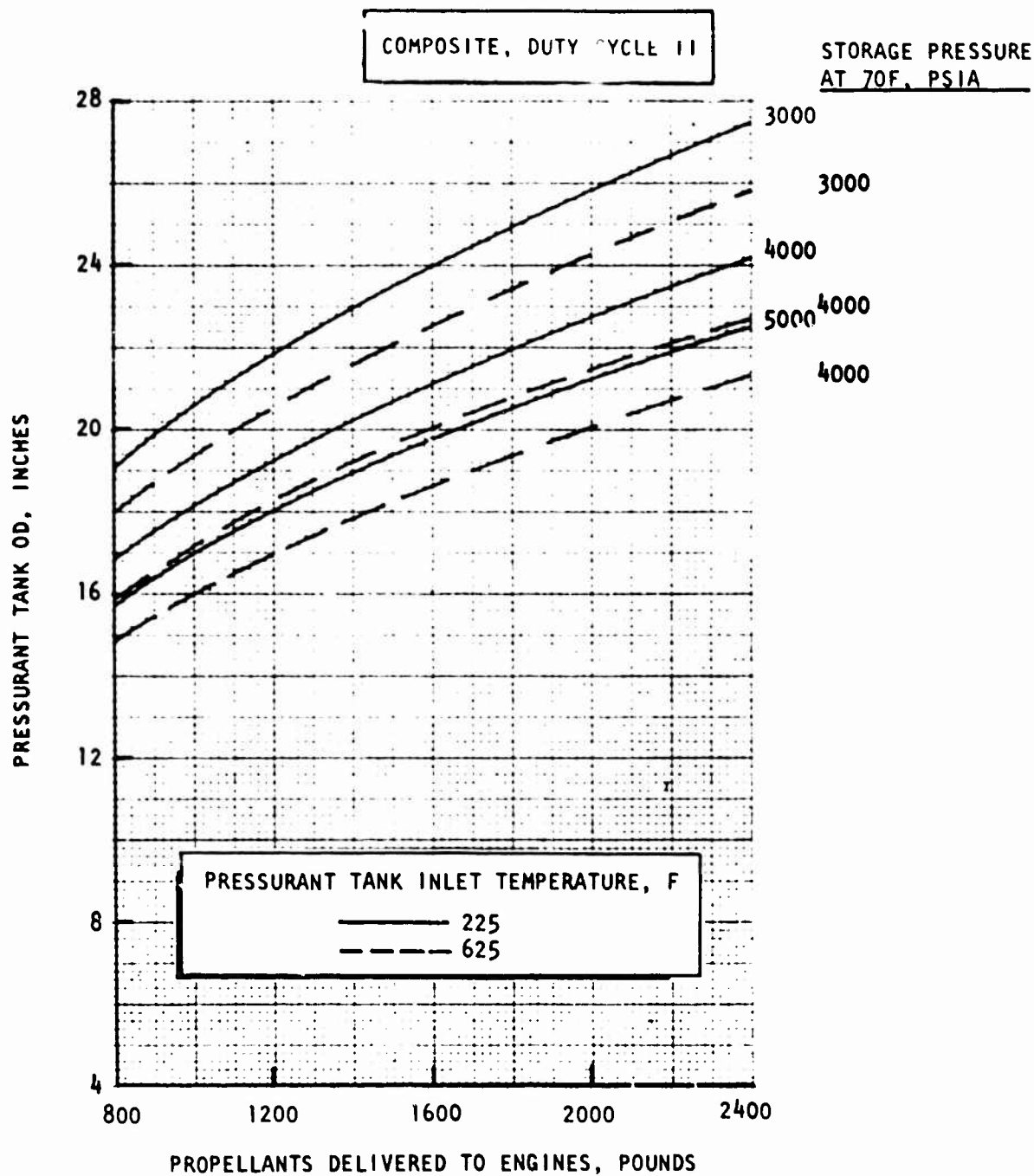


Figure 106. Parametric Pressurant Tank Diameter as a Function of Storage Pressure and Propellant Weight for PSA Inlet Temperatures = 625 and 225 F

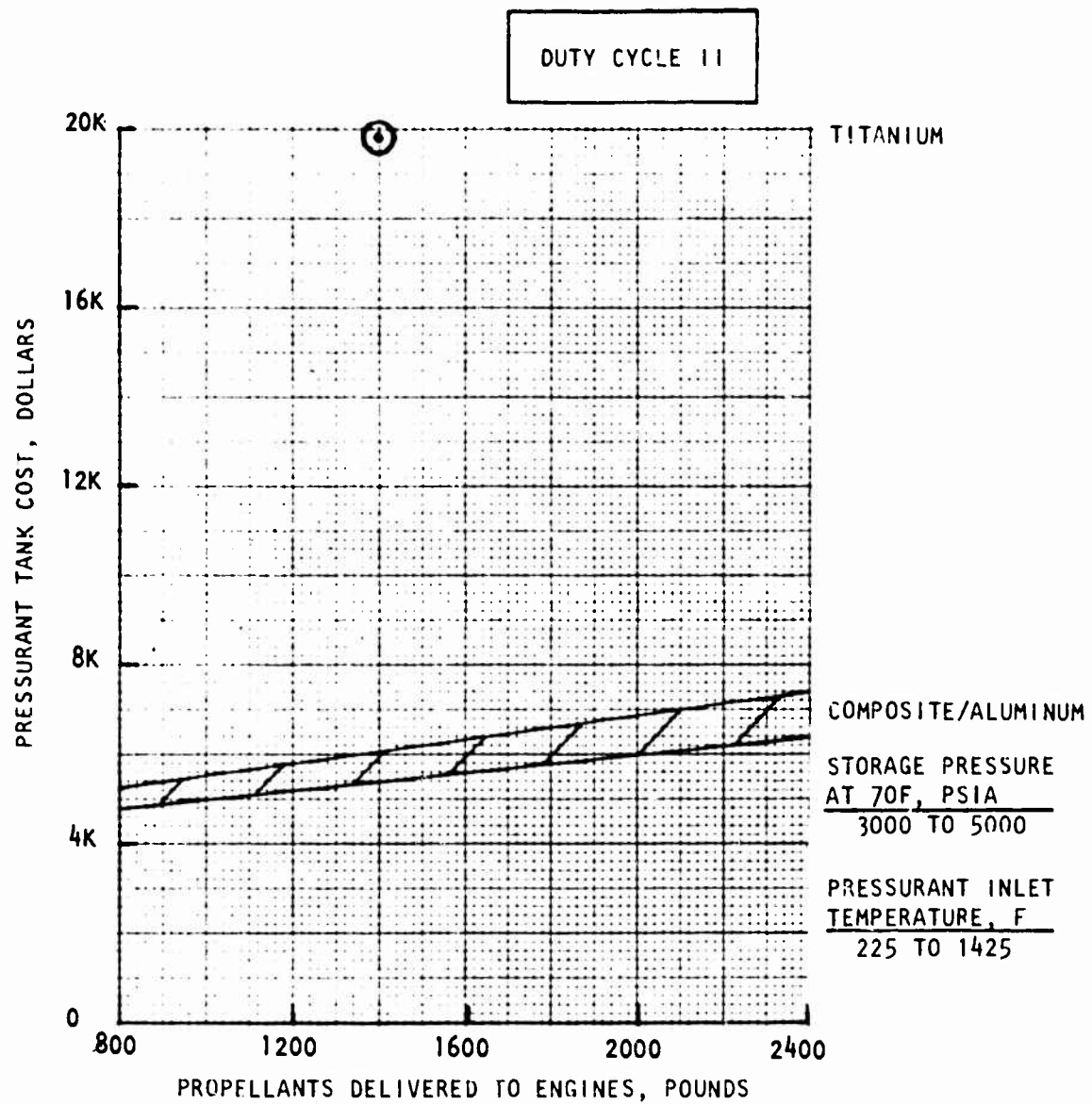


Figure 107. Parametric Pressurant Tank Costs

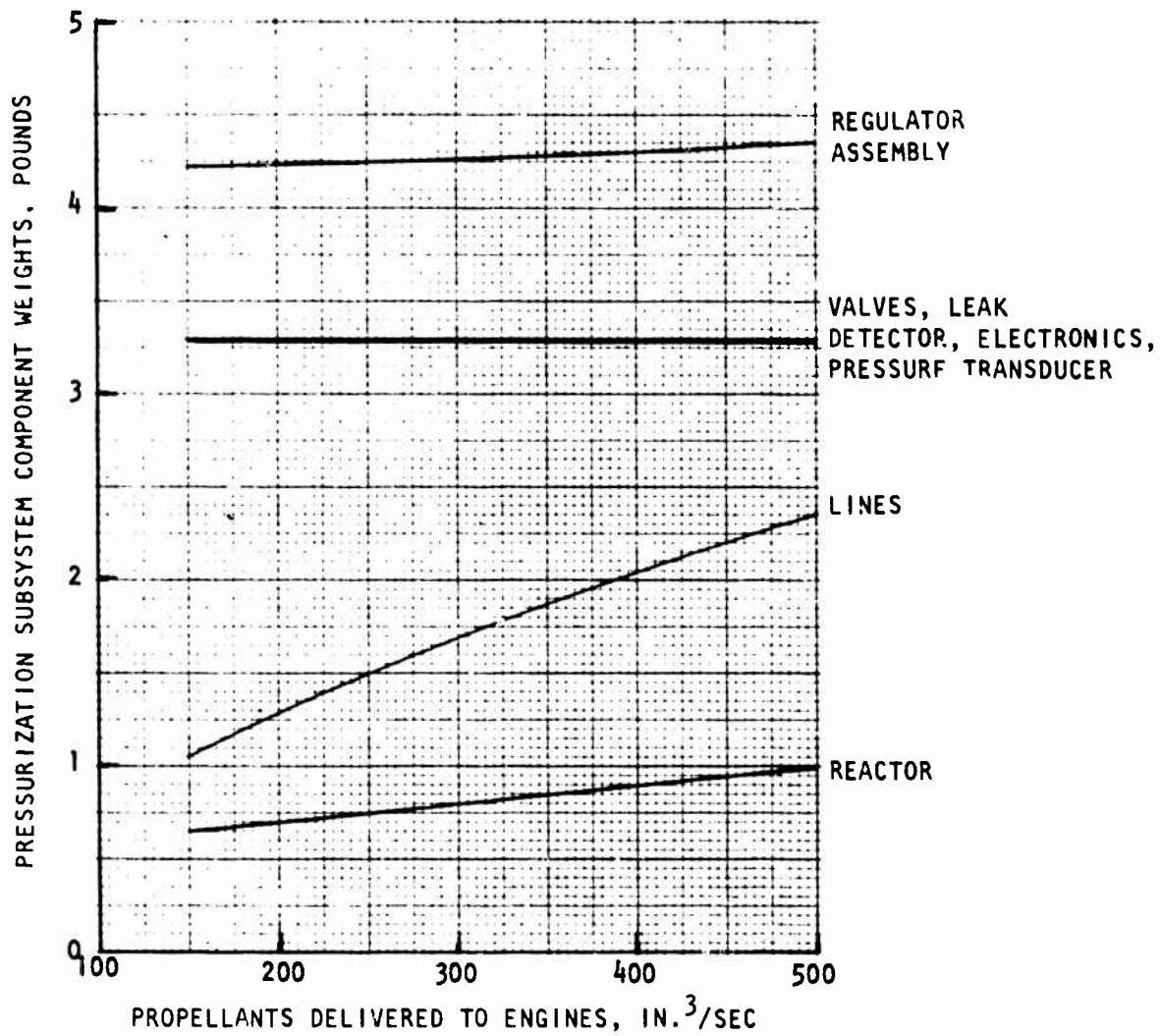


Figure 108. Parametric Pressurization Subsystem Weights

affects the pressurant flowrate. The small regulator assembly variation is due to the relief valve. Line sizes were varied to minimize the pressure drops, which affect the regulator performance when the flowrate demand changes. The reactor volume and weight vary with flowrate to achieve 1035 F outlet gas.

The envelopes of these pressurization subsystem components are presented in Table 30. The values shown are fairly independent of the ranges of parameters considered, except for the reactor. Its diameter would vary approximately ± 0.5 inch.

Pressurization subsystem envelope data are presented in Table 31. Comparisons for the three pressurant fluids are shown. Hydrazine is the most compact, followed by Tridyne.

TABLE 30. PRESSURIZATION SUBSYSTEM COMPONENT ENVELOPES

Component	Dimensions, inches
Regulator Assembly	5.62 X 5.96 X 6.50
Pressure Switch Leak Detector	1.73 X 1.73 X 4.80
Fill Valve	0.75 X 0.75 X 1.18
Isolation Valve	1.00 X 1.12 X 3.88
Electronics/Pressure Transducer Assembly	3.00 X 3.00 X 2.45
Reactor	1.51 X 1.51 X 3.56

TABLE 31. PRESSURIZATION SUBSYSTEM ENVELOPES

Pressurant Fluid	Dimensions, inches		
	Width	Height	Length
Hydrazine	9.9	13.7	27.8
Tridyne	18.9	18.7	26.5
Helium	23.1	23.1	26.8

The effect on the pressurization subsystem of varying the time allowed to pressurize the PSA's from 10 to 40 seconds was considered and found to be insignificant. The flightweight system design was based on a 10-second pressurization. The resultant maximum pressurant flowrate requirement was 0.046 lb/sec compared to 0.028 lb/sec during MDC 1 expulsion. Some allowance was made for this fact by designing the reactor for a flowrate of 0.035 lb/sec. The reactor flowrate exceeds this value for only 6 seconds during initial pressurization, and a flowrate of 0.046 lb/sec has negligible effect on the reactor gas temperature rise (<50 F) and overall performance.

If the pressurization time were increased from the design value of 10 seconds, it would reduce the maximum flowrate and permit a slightly smaller reactor; however, the current design weighs only 0.8 pound. The detrimental effect of increasing the pressurizing time is that it requires larger capacitors in the regulator electronics assembly, which have to be hardened for nuclear survivability.

Feed System

Feed system weight data are presented in Fig. 109 as a function of delivered propellant weight and propellant tank material. A comparison between pressurant fluids (helium, hydrazine, and Tridyne) also is shown for composite-wrapped propellant tanks. The low weight of the hydrazine pressurized system is due to its small pressurant (hydrazine) tank, which is pressurized by a small helium tank. The small size is because of the performance advantage associated with warm-gas pressurization and storage of the hydrazine as a high-density liquid. Tridyne maintains the warm-gas performance advantage over helium, but is stored as a low-density gas.

Table 32 presents feed system cost data as a comparison between propellant tank material (composite/aluminum, aluminum, and titanium) and pressurant. The higher cost of the hydrazine pressurized system is caused by the need for two pressurization subsystem tanks, one of which has positive expulsion, and a

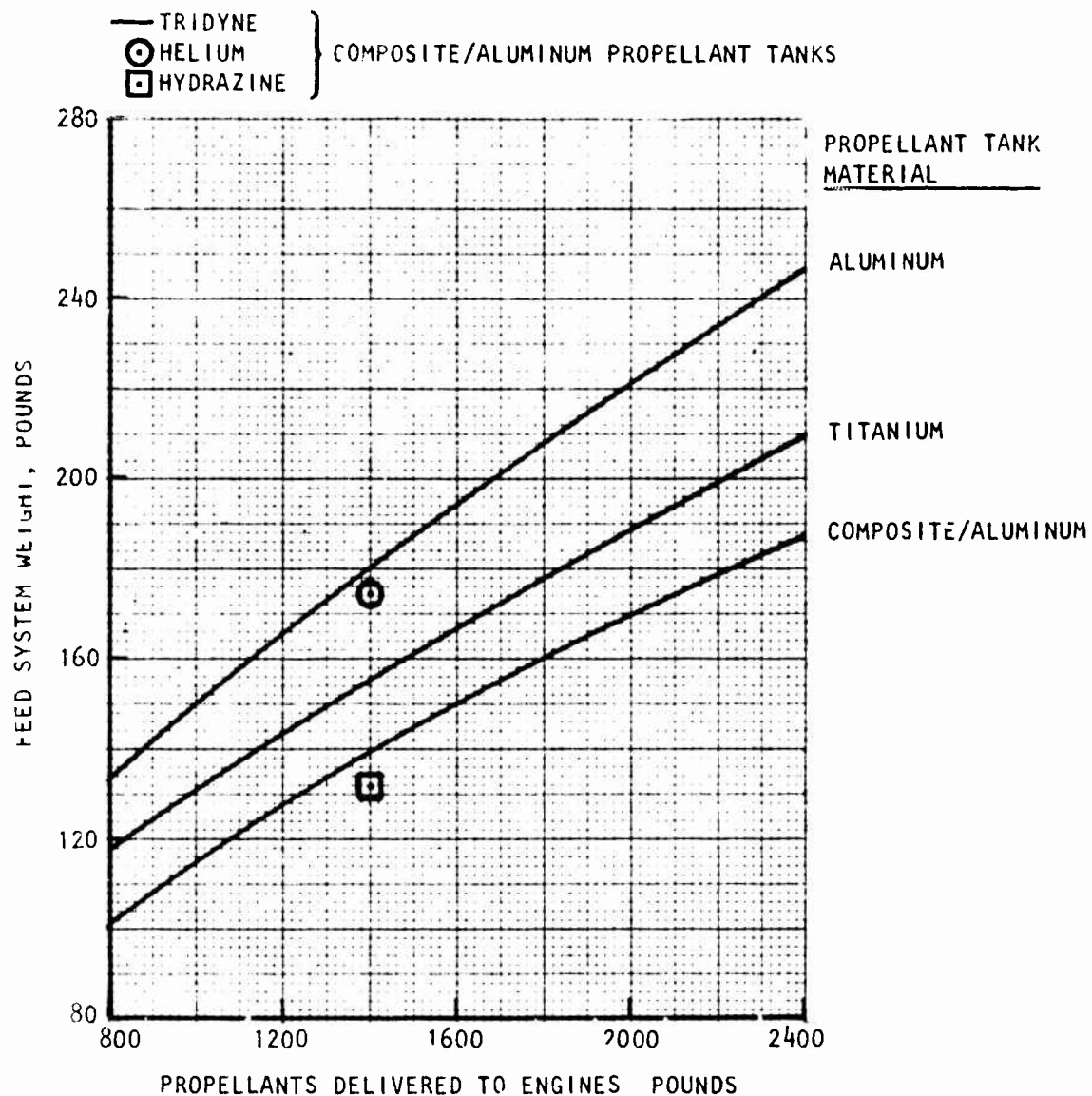


Figure 109. Parametric Feed System Weights

TABLE 32. FEED SYSTEM UNIT PRODUCTION COSTS

Propellant Tank Material	Pressurant Fluid		
	Tridyne	Helium	Hydrazine
Composite/Aluminum	\$47.8K	47.8K	62.3K
Aluminum	41.4K	--	--
Titanium	≥100.0K	--	--

relatively expensive gas generator. Because of difficulty in obtaining vendor quotes for fabricating titanium PSA parts, there was considerable uncertainty in the calculated costs for this alternative material. It is fairly certain, however, that the feed system would cost in excess of \$100K.

PROPELLANT STORAGE ASSEMBLY FABRICATION AND TEST

Fabrication and testing of the propellant storage assembly was subdivided into three parts:

1. Plastic Workhorse Tank
2. Aluminum Workhorse Tank
3. Flightweight Tank

These activities are reported herein under these three headings.

PLASTIC WORKHORSE TANK

A reliable positive-expulsion diaphragm was developed that resulted in repeatable expulsion performance and met program objectives. Design requirements were defined, manufacturing processes were developed, and expulsion performance was verified experimentally. Tests were designed to demonstrate successful operation of the selected diaphragm design. The goals were repeatable expulsion efficiency, center-of-gravity control, and mechanical integrity.

Tank Fabrication

A sketch of the plastic tank was shown in Fig. 109. It consisted of two flanged plastic half-shells and a replaceable expulsion diaphragm. A large and small port were in each half-shell at the polar axis for pressurization, expulsion, propellant filling, and instrumentation. The tank weighed approximately 450 pounds.

The two plastic tank half shells were fabricated by All Plastic Fabricators (APF, Duarte, CA). After forming and partially machining the half shells, it was discovered that the flange was not thick enough to permit additional machining to achieve the correct polar axis dimension. The problems associated with forming and machining the plastic half shells were resolved and

corrective actions were made. APF layered thermal-setting acrylic to the half shells to build up the inside surface in the region near the flange radius. This was required for remachining of this surface by APFs vendor.

Washer-shaped pieces of acrylic were machined and bonded to the outer surface of the flanges with thermal setting acrylic to increase the thickness to the design dimension (1 inch). Washer-shaped pieces were also required at the poles because of excessive thinning during forming. The 1.5 inch stock thinned to 1.1 inches, compared to a required thickness of 1.4 inches to match the aluminum parts.

Additional stress analyses were conducted for the polar region because of concerns related to the plastic-to-plastic bond. Based on these analyses, a decision was made to modify the aluminum casing plugs to relieve the stress concentrations at their outer diameters. Modifications included tapering the plug and welding on an extension to make it flexible. The modified and original designs were compared in Fig. 110.

Diaphragm Forming

The diaphragms were draw formed in an HPM 3200-ton vertical hydraulic press by Aircraft Hydro-Forming (Gardena, CA). The 0.090 inch thick 1100-0 aluminum was held between two draw rings and pulled down over a stationary male die (punch). The aluminum feeds inward between the rings in a controlled manner to preclude tearing or wrinkling. Control was accomplished with a "draw bead" consisting of a rounded groove machined in the surface of one ring, and a matching protrusion from the surface of the other.

The initial forming resulted in a diaphragm flange radius of approximately 3/8 inches. This large radius (on the upper draw ring) was required to allow the 1100-0 aluminum to feed between the ring and the male die during the draw process. This draw ring was then replaced with a "coining" ring for the next step. The coining operation resulted in a 1/8 inch radius.

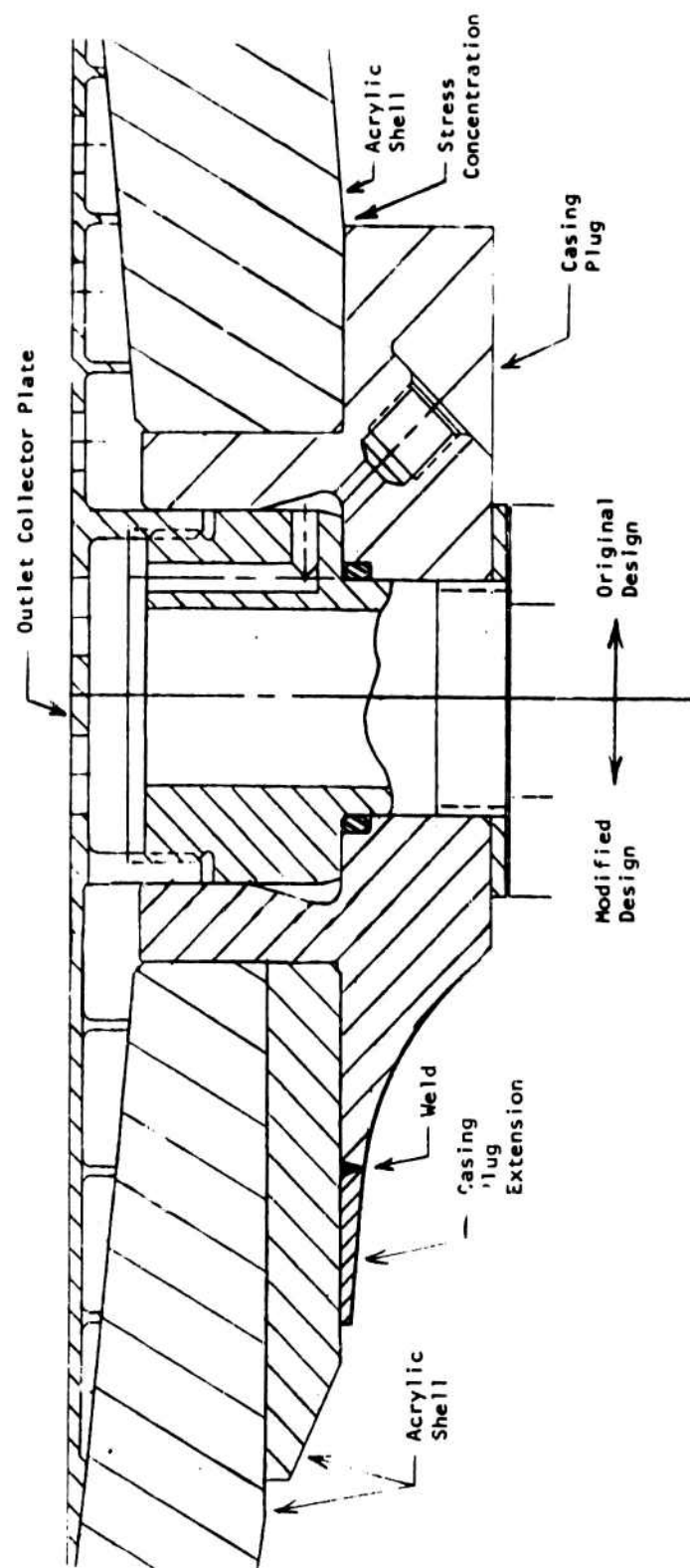


Figure 110. Plastic Tank Design Modification

Initially, a second coining operation was used to achieve the final flange radius. The other side of the coining ring, which had a 0.020 inch radius was utilized. Excessive dimensional variations and material thinning led to stress relieving and "rolling" the radius in a lathe after the first coining operation. During rolling of the first diaphragm, the small radius was reduced from a range of 0.051-0.096 to 0.046-0.048 inches. The large radius was reduced from 0.160-0.200 to 0.064-0.070. The diaphragms were then annealed.

The variations in thickness of four diaphragms after draw-forming are presented in Table 33. The diaphragms were formed from nominal 0.090 inch sheets. Diaphragm No. 1 shown in Table 33 had variations along meridians and lines parallel to the equator as presented in Tables 34 and 35, respectively. It can be seen that the largest amount of thinning occurred midway between the pole and equator. Also, the variation between concentric circles is greater than between meridians. The distribution of measured thicknesses is presented in Fig. 111.

Diaphragm Chem-Milling

Three different diaphragm chem-mill thickness profiles, with material removed from the outer surface, were fabricated and tested to determine their effect on expulsion efficiency and center-of-gravity (CG) control. The thickness profiles in inches, are presented in Table 36. The chem-milling was done by Aerochem (Orange, CA) and Chemical Energy of California (San Diego).

Configuration No. 3 was selected and the chem-mill tolerances shown in Table 37 were established. An additional restriction was specified requiring the three steps nearest the polar axis to be at least 0.003 inches, based on the mean thickness for each region. These tolerances resulted in negligible variations in diaphragm pressure drops (ΔP s) and are not difficult to achieve.

TABLE 33. DIAPHRAGM-TO-DIAPHRAGM THICKNESS VARIATIONS

DIAPHRAGM NO.	MAXIMUM THICKNESS, INCH	MEAN THICKNESS, INCH	MINIMUM THICKNESS, INCH
1	0.083	0.077	0.072
2	0.086	0.080	0.072
3	0.086	0.080	0.072
4	0.087	0.080	0.074

TABLE 34. DIAPHRAGM MERIDIONAL THICKNESS VARIATIONS

MERIDIONAL LINE NO.	MAXIMUM THICKNESS, INCH	MEAN THICKNESS, INCH	MINIMUM THICKNESS, INCH
1	0.082	0.076	0.072
2	0.082	0.077	0.072
3	0.082	0.076	0.072
4	0.082	0.078	0.074
5	0.083	0.078	0.074
6	0.081	0.078	0.075
7	0.083	0.077	0.073
8	0.080	0.077	0.074
9	0.082	0.077	0.073
10	0.082	0.076	0.072

TABLE 35. DIAPHRAGM THICKNESS VARIATIONS

LINE NO.	MAXIMUM THICKNESS, INCH	MEAN THICKNESS, INCH	MINIMUM THICKNESS, INCH
1 (NEAR POLE)	0.080	0.080	0.079
2	0.083	0.078	0.076
3	0.080	0.078	0.077
4	0.079	0.076	0.075
5	0.079	0.076	0.072
6	0.077	0.074	0.072
7	0.075	0.073	0.072
8	0.077	0.074	0.072
9	0.079	0.077	0.074
10	0.083	0.082	0.079
11 (NEAR EQUATOR)	0.082	0.078	0.076
12	0.079	0.077	0.076

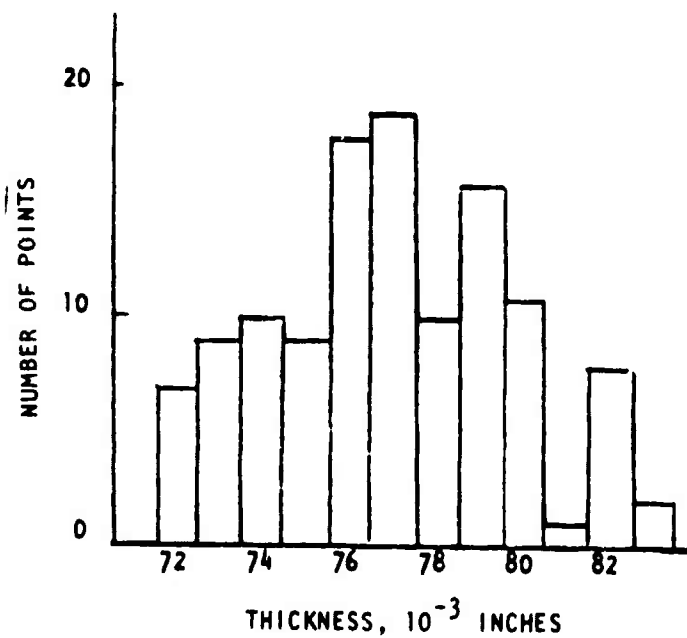


Figure 111. Thickness Distribution

TABLE 36. DIAPHRAGM NOMINAL THICKNESSES

ANGLE FROM POLAR AXIS, DEGREES	CONFIGURATION NUMBER		
	1	2	3
0 - 35	0.030	0.030	0.026
35 - 45	0.047	0.040	0.034
45 - 50	0.054	0.047	0.034
50 - 60	↓	0.047	0.039
60 - 70		0.054	0.039
70 - FLANGE RADIUS		0.054	0.044
FLANGE RADIUS		0.073	0.061

TABLE 37. CHEM-MILL TOLERANCES

NOMINAL, INCH	(+) TOLERANCE, INCH	(-) TOLERANCE, INCH
0.026	0.002	0.001
0.034	0.003	0.002
0.039	0.003	0.002
0.044	0.003	0.002
0.061	0.003	0.002

A comparison of thicknesses from diaphragm-to-diaphragm is presented in Table 38 for units chem-milled by Aerochem and used in tests 3, 4, and 5. The values shown are averages for each step based on vidi-gage measurements to the nearest thousandth of an inch. The maximum variation in means is 1.2 thousandths or 3.6 percent.

Thickness measurements of diaphragm No. 5 indicated the chem-milled steps were within tolerances. Only 1 measurement out of 140 was out-of-spec. Table 39 summarizes the results (measurements are in thousandths of an inch).

TABLE 38. CHEM-MILL VARIATIONS

NOMINAL	DIAPHRAGM		
	NO. 3	NO. 4	NO. 5
0.026	27.0	26.9	26.9
0.034	34.1	32.9	33.8
0.039	38.2	38.5	37.4
0.044	43.7	43.0	42.7
0.061	63.2	62.0	62.1

TABLE 39. DIAPHRAGM NO. 5 THICKNESS

NOMINAL	NUMBER OF MEASUREMENTS	MINIMUM	MEAN	MAXIMUM
0.026	30	26.0	26.9	28.0
0.034	20	32.0	33.8	37.0
0.039	30	36.0	37.4	39.0
0.044	30	42.0	42.7	45.0
0.061	30	60.0	62.1	64.0

Diaphragm Tests

Eight diaphragms were tested in the plastic tank. The first six were expelled at Rocketdyne's Engineering Development Lab (Canoga Park, CA) between August and December, 1978. The last two were subjected to an acceleration environment and expelled at AETL (Fullerton, CA) during May, 1979. Table 40 summarizes the parameters used and the results.

Diaphragm Integrity. There were no tight folds or tears in any of the diaphragms tested resulting from nominal operation. The radius of curvature at the rolling plane decreased during the expulsion cycle from approximately 1 to 1/4 inch.

TABLE 40. PLASTIC TANK TESTS

DIAPHRAGM	CONFIGURATION/ THICKNESS PROFILE, INCH	WIRE RIBS	SPACER THICKNESS, INCHES	ACCELERATION	EXPULSION DIRECTION	EXPULSION EFFICIENCY AT 25 PSIG (>97% REQUIRED)	MAXIMUM CG DISPLACEMENT (1.3 INCHES REQUIRED)
1	2	NO	0.00	NO	VERTICAL	93.3	1.4
	0.032 - 0.072		1.00			NO DATA	
2	1	NO	0.75	NO	VERTICAL	96.6	2.3
	0.031 - 0.072						
3	3	NO	0.00	NO	VERTICAL	94.2	1.0
	0.027 - 0.063		0.50			97.1	
4	3	8 SHORT	0.00	NO	VERTICAL	98.2	1.0
	0.027 - 0.062						
5	3	36 LONG	0.00	NO	HORIZONTAL	98.1	1.9
	0.026 - 0.064						
6	3	36 LONG	0.00	NO	HORIZONTAL	98.2	1.9
	0.026 - 0.064						
7	3	36 LONG	0.00	YES	HORIZONTAL	-	-
8	3	36 LONG	0.00	YES	HORIZONTAL	98.2	-

The only unexpected occurrence was the formation of several buckles oriented along meridians around the circumference. There were generally nine of these of similar size and fairly equally spaced. Referenced to the final chem-mill profile, they started in the 0.039 inch region and grew as the expulsion cycle progressed until they were approximately 8 inches long and within 1 to 2 inches of the equator. After the diaphragm rolled through at the equator, the buckles straightened out as the surface was pressed against the tank wall.

These buckles are inherent to the diaphragm's shape and the thicknesses tested. The physical explanation for their formation is that as the diaphragm rolls inward, the distance from the polar axis to a point on the surface decreases, creating an excess surface area. This excess area is accommodated by the formation of buckles with large radii of curvature.

Expulsion Efficiency. Eight diaphragms were tested using gaseous nitrogen at 25 psig as the pressurant. Tests 3 through 8 had identical diaphragms (the selected configuration) and tests 5 through 8 had identical outlet rib designs. Test No. 4 had only 8 short ribs instead of 36 long ones. While the difference in rib configuration had no effect on expulsion efficiency, the additional ribs were required to preclude high flow ΔP s in the tank near the end of the expulsion cycle. The expulsion efficiency with the major axis horizontal and the outlet flow vertically upward (test No. 4) was 98.2 percent at a diaphragm ΔP of 25 psi, compared to a required minimum of 97 percent. Turning the tank 90 degrees to expel the flow horizontally did not have any effect on expulsion performance as evidenced by efficiencies of 98.1 and 98.2 percent at 25 psi during tests 5 and 6.

The diaphragms used in tests 5 and 6 demonstrated that the quality of chem-milling also had little effect on expulsion performance. Test No. 5 used the fifth diaphragm supplied by Aerochem, which was the best one tested with respect to thickness variations, surface finish and roughness (dents).

Test No. 6 used the first diaphragm supplied by Chemical Energy, which was the worst with respect to thickness variations and surface finish. Approximately 15 percent of the surface exceeded allowable thickness tolerances. This diaphragm was relatively free of dents, which had been shown to have no effect on expulsion performance by comparing the results of diaphragms supplied by Aerochem. These dents were smoothed out by pressurizing the diaphragm with gaseous nitrogen prior to testing, a process that apparently resulted in negligible work hardening.

Tests 4 through 6 each consisted of 12 or 13 pulses at flowrates up to $116 \text{ in}^3/\text{sec}$, which is 85 percent of the maximum required rate. This is the highest flowrate obtainable with 25 psig pressurant. Testing did not reveal any effects on diaphragm rolling due to the flowrate.

Diaphragm ΔP , as a function of percent reversal, is shown in Fig. 112 to be very repeatable. Inlet and outlet pressure measurements were made at the polar axis during all tests. As a result, the amount of hydrostatic pressure at the outlet is higher during tests 5 and 6 because of the tank orientation and accounts for the higher ΔP .

Center-of-Gravity. Three load cells were utilized to measure shifts in CG during the first 4 tests, with the major axis horizontal. Since the test set-up did not include provisions for continuously balancing the load cell output signals, readings were available only between flow pulses. Dimensional of the location of the rolling radius were made after each flow pulse during the last 2 tests and the CG profiles were calculated from estimates of their diaphragm shapes.

CG displacements from the polar axis are shown in Fig. 113. Although test No. 3 did not have ribs along the outlet half shell, the diaphragm was identical to those in tests 4, 5 and 6 and CG data comparisons are therefore valid. The data shown reflect a substitution of the heavier of the two propellants (NTO) for the water and factoring in the stationary weight of the flightweight tank. The allowable $3-\sigma$ variation is 3 inches.

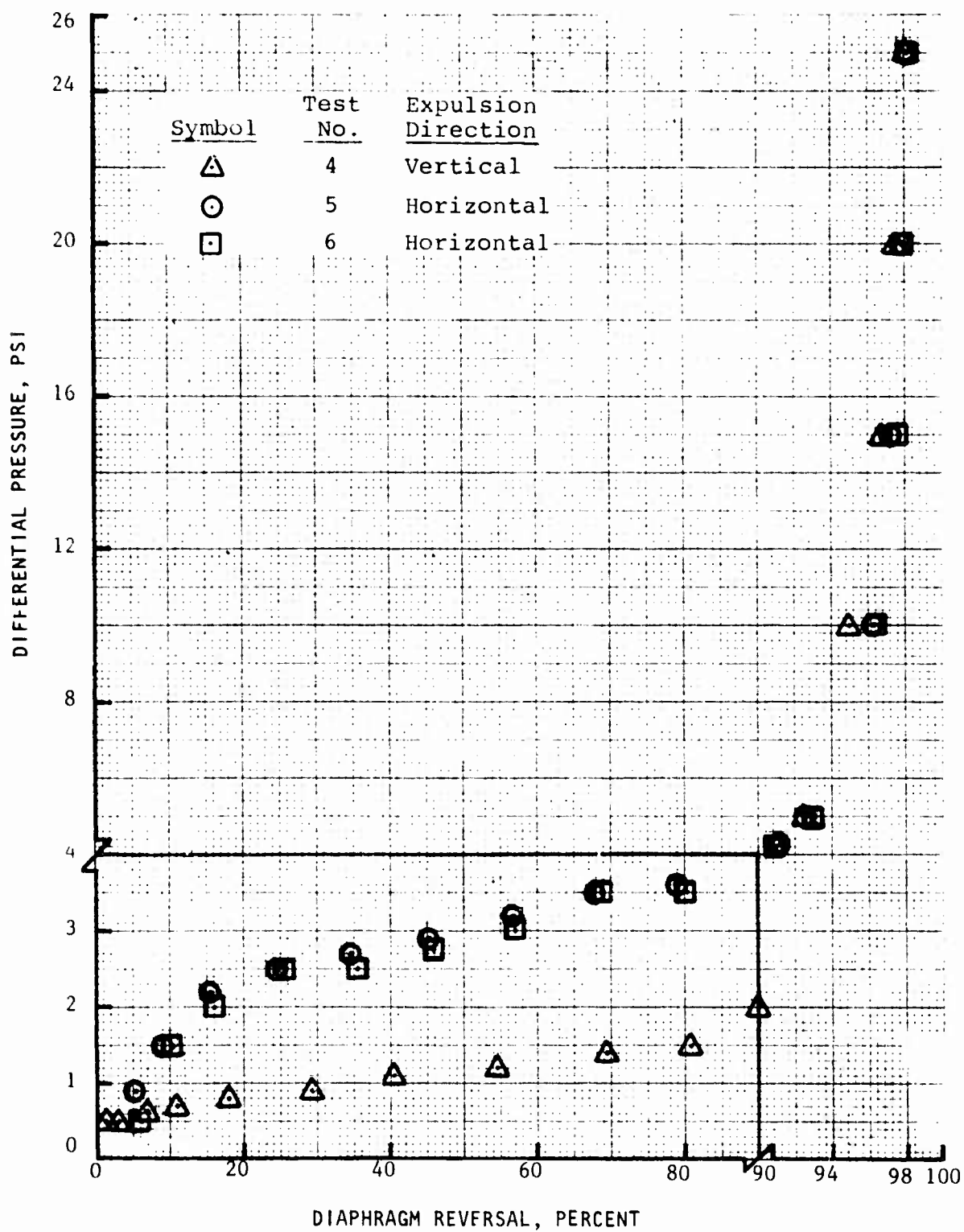


Figure 112. Pressure Differential at Tank Centerline

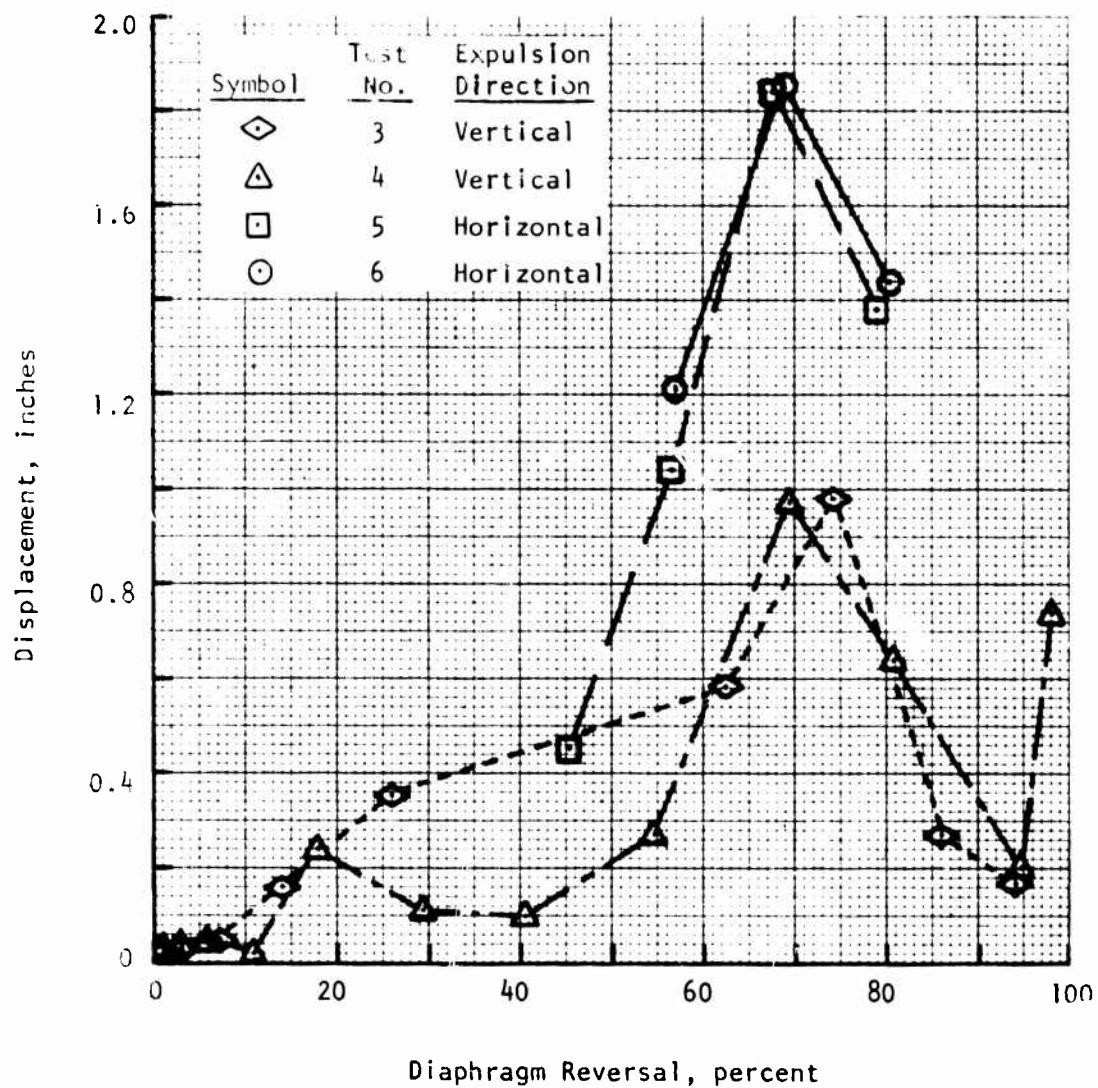


Figure 113. Flight NTO Tank CG Displacement From Polar Axis

Variations in CG profiles along the polar (expulsion) axis were always less than 0.2 inches, as expected. Since the locus of points rolling away from the tank wall defined a relatively flat plane, the effect of one side of the diaphragm being reversed more than the nominal amount was balanced by the other side being displaced a correspondingly smaller amount (for a given percent diaphragm reversal).

The increased CG displacement observed in the two tests with the major axis vertical is due to the effect of the asymmetric hydrostatic pressure gradient about the polar (expulsion) axis. This gradient was 1.3 psi at the equator compared to a range from approximately 0.6 to 2.5 psi in the NTO tank and 0.4 to 1.5 psi in the MMH tank during a typical fourth stage duty cycle.

The CG displacement from the polar axis reached a maximum at approximately 70 percent expelled. This is due to the fact that the bulk of the residual propellant occupies an annulus at a large distance from the polar axis and is therefore sensitive to even small amounts of asymmetry. Later in the expulsion cycle, the propellant weight is overshadowed by the fixed weight of the tank, whose CG is located on the polar axis. Since the maximum CG displacement occurs late in the duty cycle, it is important that diaphragm thickness steps be located near the equator to provide corrections even though they are not required to provide a stability margin between buckling and the rolling reversal mode. As the angular location of the last step, measured from the polar axis, was increased from 45 to 60 to 70 degrees (tests 2, 1 and 3, respectively), the maximum CG displacement decreased from 2.3 to 1.4 to 1.0 inches.

Test 1. A total of 674 pounds of water was loaded in the tank. Assuming the water to be at 68 F, the plastic tank and diaphragm were oversized by 2.4 percent. The oversizing was primarily due to a change in the shell and diaphragm contour near the equator, from conical to spherical during the design phase of the program without resizing. The water was expelled on 9 August 1978 in eight pulses at flowrates between 97 and 108 in³/sec, compared to a maximum required rate of 137.5. The lower test flowrate,

which should not influence reversal of the diaphragm, is a result of limiting pressure in the plastic tank to 30 psig. Testing was conducted with the system shown in Fig. 114 and 115.

Initial reversal of the diaphragm occurred at a ΔP of 0.8 psi. Reversal progressed in a very uniform manner with large rolling radii. No tight folds were experienced during the test. As shown in Fig. 116, nine chords developed around the rolling circumference in the middle of the 0.049 inch thick section. Locations of step thickness changes are marked with solid lines. These chords were uniformly spaced and therefore had little effect on the CG as the test progressed. Since the rolling circumference was not a circle, the excess surface area formed "buckled" regions, which can be seen in Fig. 116 by observing the waviness of the lines on the diaphragm.

The diaphragm stopped rolling before it flipped through at the equator, resulting in an expulsion efficiency of only 93.3 percent, compared to a predicted minimum of 97 percent. The diaphragm ΔP at the end of the test was 25 psi. The diaphragm ΔP during the test is shown in Fig. 117 along with the thickness profile. The ΔP was less than 3 psi until 90 percent reversal, at which time the ΔP increased rapidly.

The shift in CG of the water and diaphragm is shown in Fig. 118. Load cells were located under the bolt flange at 0, 120 and 240 degrees. The data points shown correspond to the conditions existing at the end of each of the 8 pulses. The test setup did not include provisions for continuously balancing the load cell output signals. The corresponding percent reversals for these 8 data points are the 7 points shown in Fig. 117 between 8 and 79 percent, inclusive, and the final point (93.3 percent).

The measured loads were corrected by substituting the heavier of the two propellants (NTO) for the water and including the stationary weight of the flightweight tank. The resulting maximum shift in CG from the polar axis was 1.36 inches, compared to the three σ allowable of 3 inches. The CG was contained within a 50 degree sector.

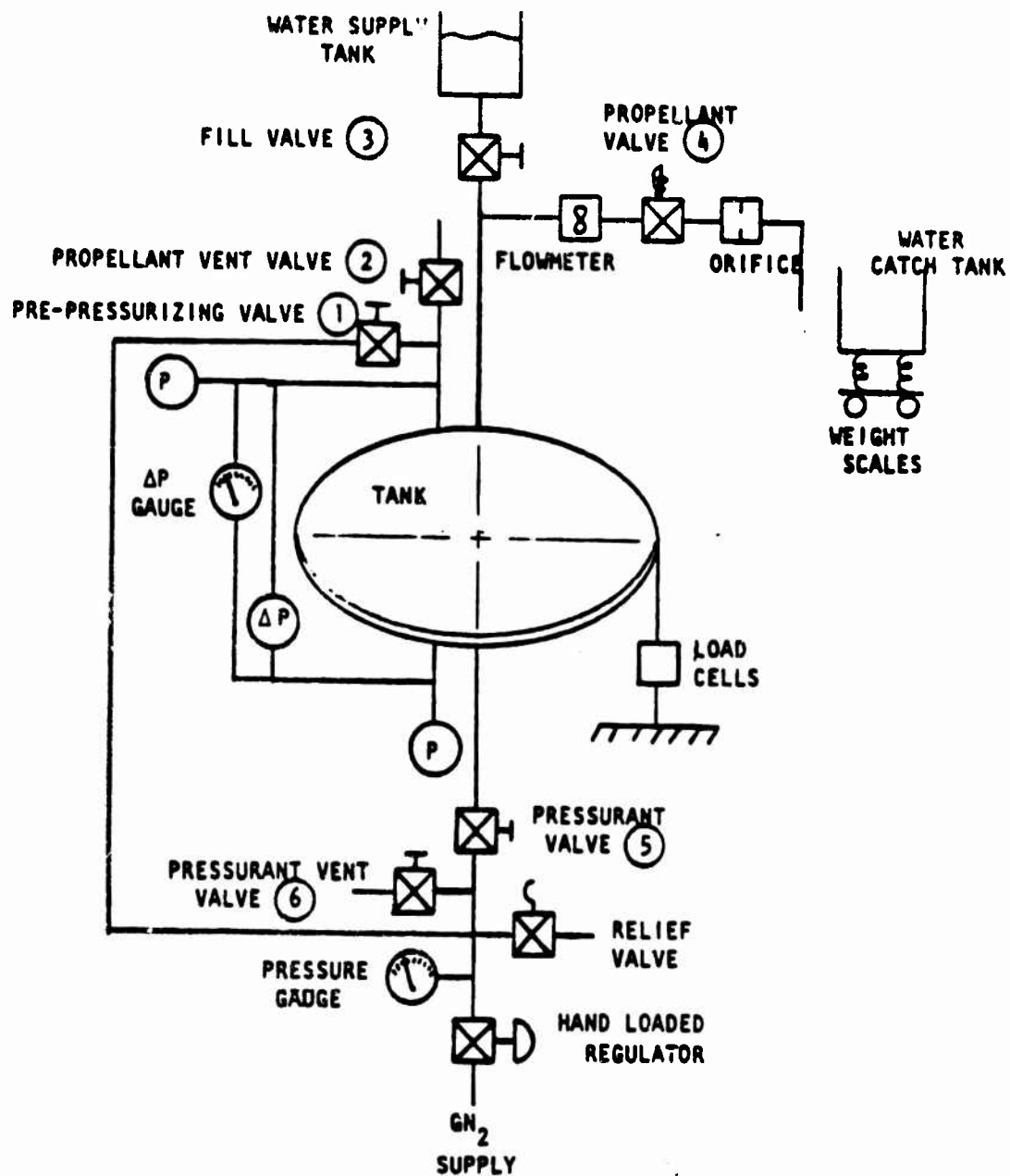
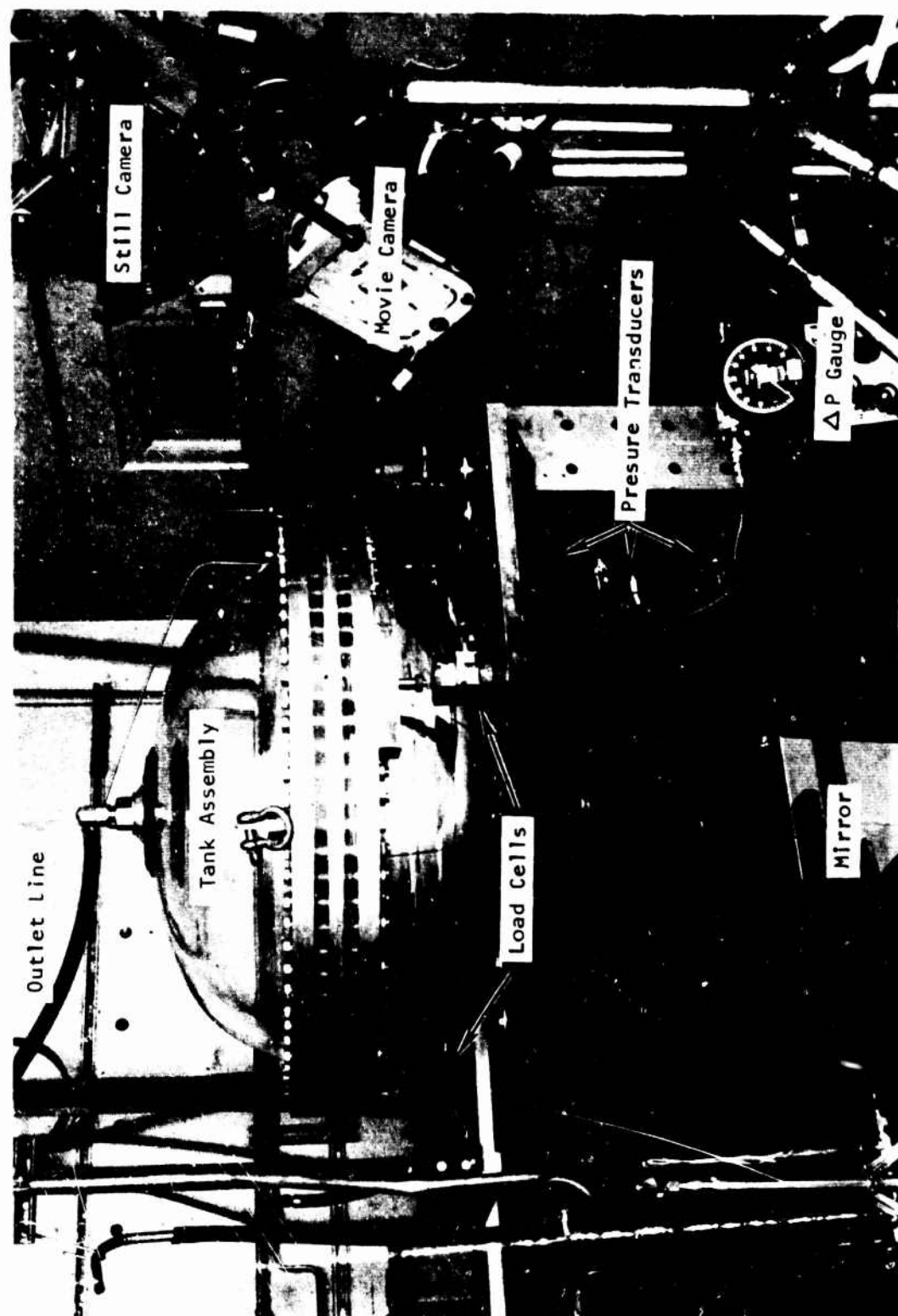


Figure 114. Test Schematic



1XZ65-8/10/78-C1J

Figure 115. Plastic Tank Test Setup



1XZ65-8/10/78-C1C

Figure 116. Development of Buckles

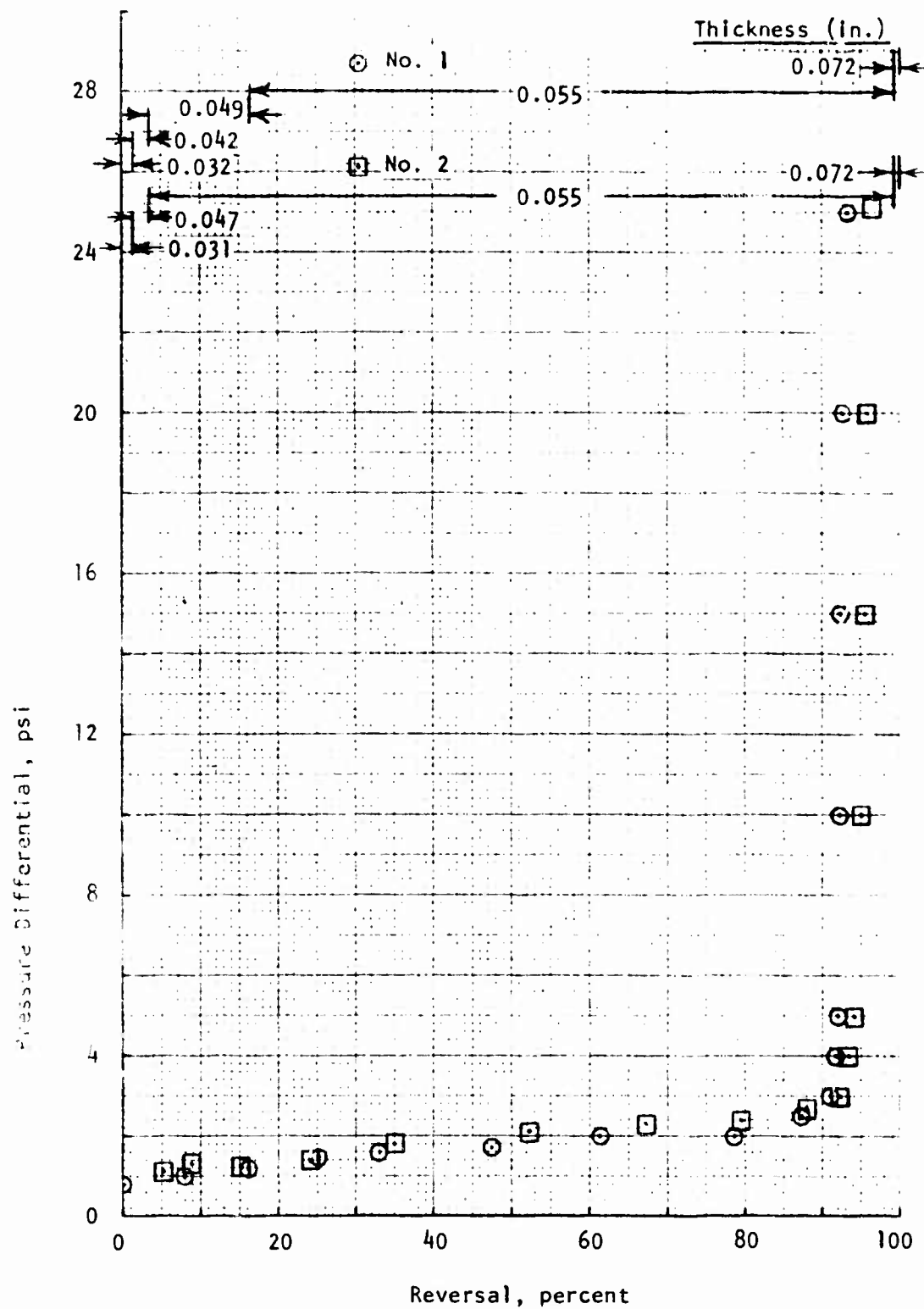


Figure 117. Diaphragm ΔP for Plastic Tank Tests 1 and 2

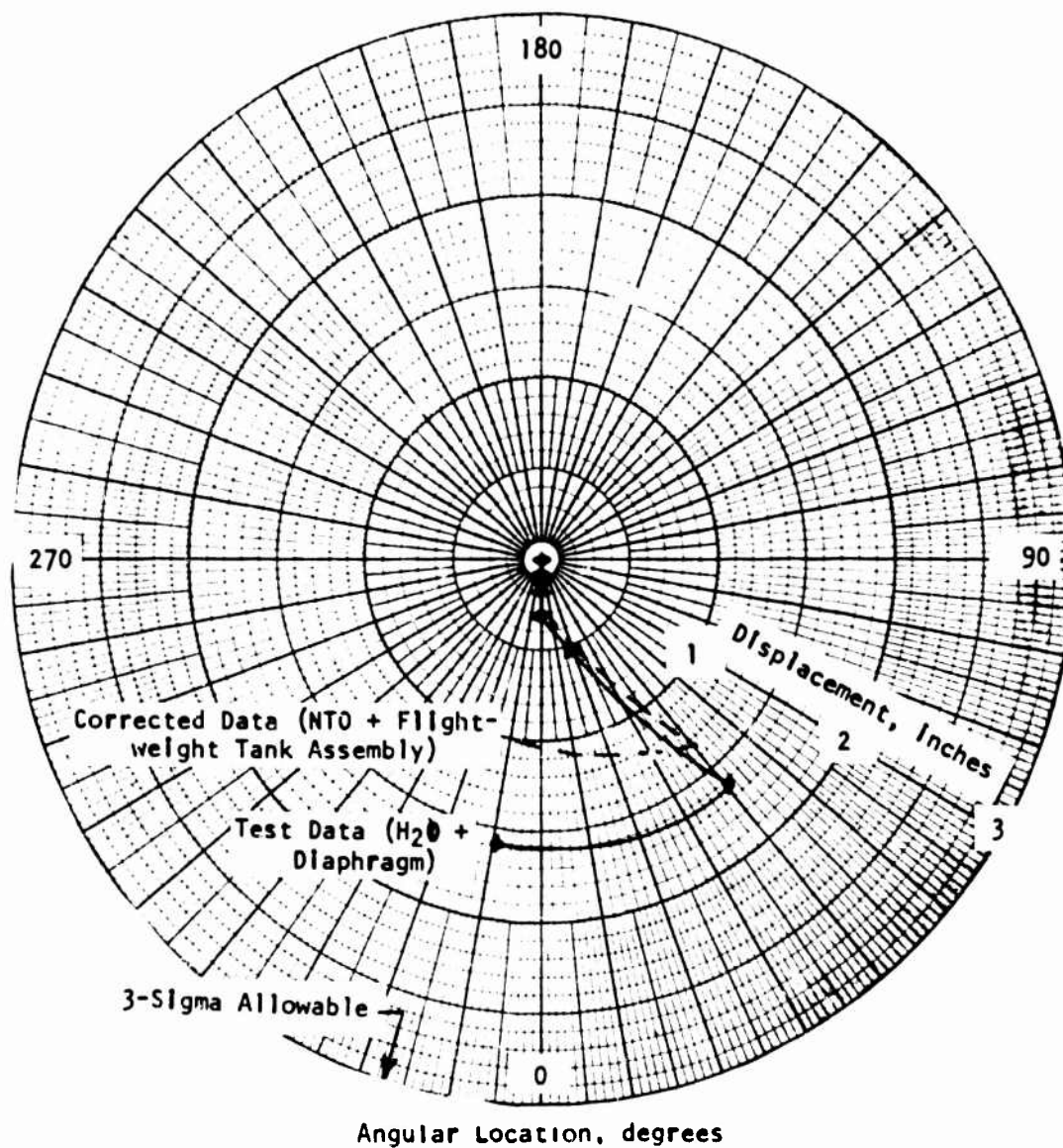


Figure 118. CG Shift for Plastic Tank Test 1

Although the diaphragm bottomed out in the region near the polar axis, there was no indication that the holes in the outlet plate were sealed. The flow meter was still spinning at the end of the test and there were no circular marks on the diaphragm to indicate it was being extruded through the holes. Measurements showed the outlet plate was 0.15 inches farther from the equator than the inlet plate so there was sufficient volume in the outlet half shell for complete reversal of the diaphragm. In addition, there was no material thinning as determined by comparing vidi-gage measurements before and after the test at 14 locations in the 0.032 inch section and 5 in the 0.042 inch section.

A sketch of the diaphragm shape after completion of the test is shown in Fig. 119 and a photograph is presented in Fig. 120.

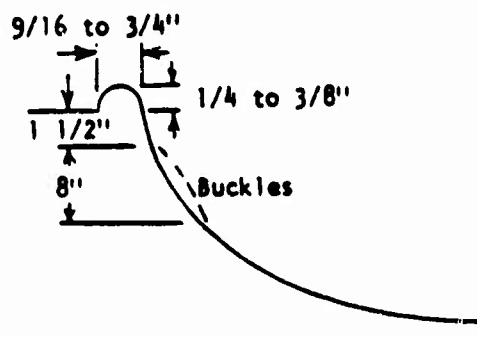


Figure 119. Sketch of Diaphragm Number 1 After First Part of Expulsion

It appeared that as the diaphragm rolled inward, the radial distance from the polar axis of a point on the surface decreased, creating an "excess" surface area. This excess area was accommodated by the formation of buckles, which, together with the fact that the diaphragm bottomed out against the outlet plate, stiffened the diaphragm and prevented it from being pressed outward against the wall. This problem was compounded by the fact that any increase in pressure to force the diaphragm against the wall also reduced the rolling radius at the equator, which increased the pressure required for rolling.



1XZ65-8/16/78-C1

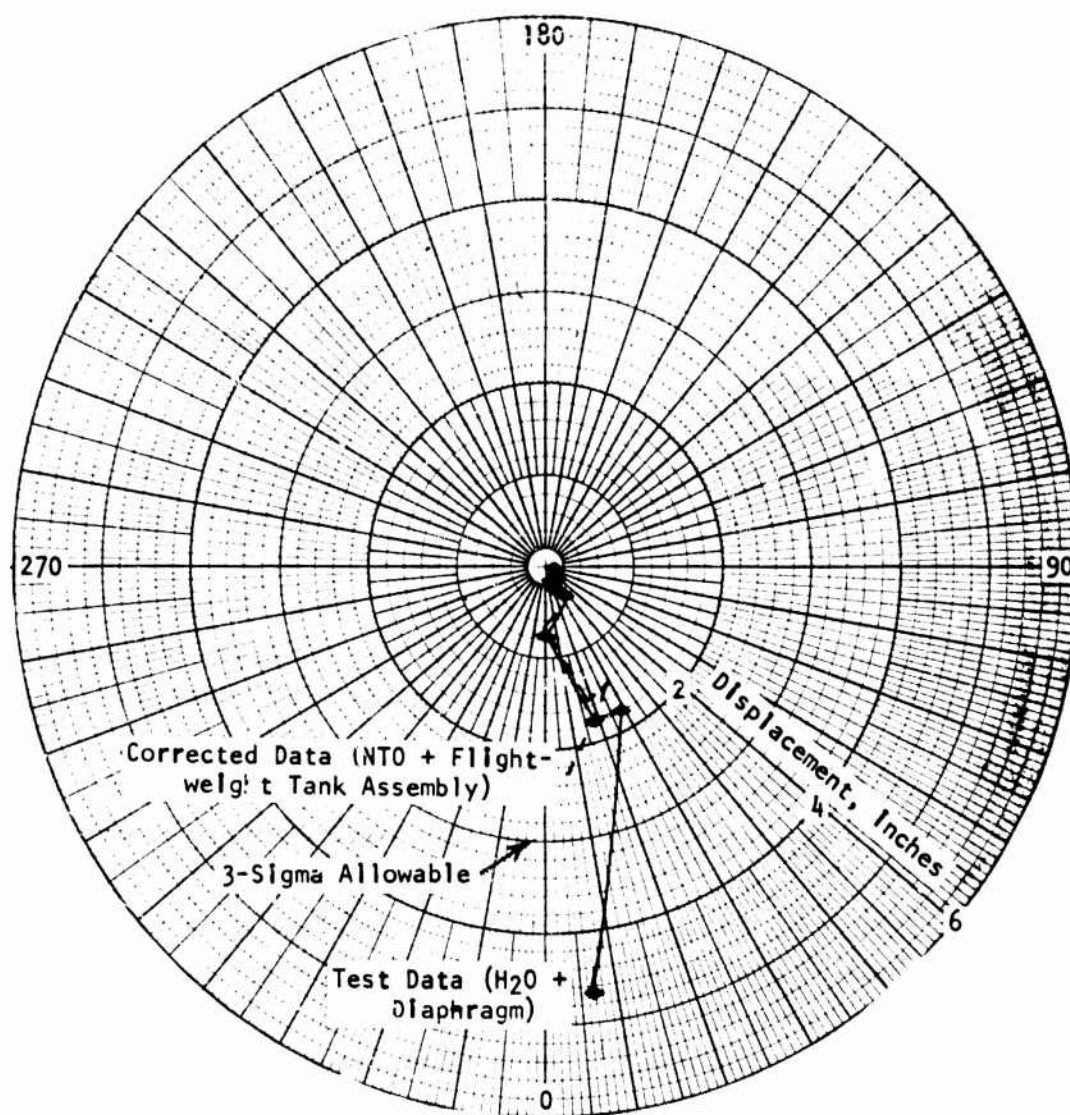
Figure 120. Diaphragm Number 1 After First Part of Test

In order to gain further insight into the problem, a 1 inch thick spacer was inserted at the equator on the outlet side of the tank. This increased the surface area by 114 in^2 and the volume by 1030 in^3 (5.5 percent). The tank was assembled with the previously used diaphragm, filled with water and slowly pressurized on 18 August 1978. The increased size of the tank permitted the diaphragm to roll through at the equator (4 to 5 psi) and the major portion of the buckles were straightened out (12 psi). The diaphragm again bottomed out against the outlet plate. No CG or expulsion efficiency measurements were made.

Test 2. At this point it appeared that the primary objective would be to reduce the thickness of the diaphragm to reduce its stiffness and permit it to roll through at the equator with the minimum sized spacer. Rather than wait for another diaphragm to be chem-milled, the second diaphragm was installed in the tank. This diaphragm had one less step, but the thickness in the region of the equator (0.055 inches) was the same. This diaphragm was tested in order to start minimizing the spacer width.

The spacer was reduced to 0.75 inches for this test, which was conducted 25 August 1978. The spacer increased the surface area by 85 in^2 and the volume by 772 in^3 (4.1 percent). The water was expelled in nine pulses at flowrates between 73 and $105 \text{ in}^3/\text{sec}$. As expected, the diaphragm reversal was very similar to the first one tested with respect to ΔP , the large rolling radii and the development of nine chords around the circumference. The diaphragm rolled through at the equator and the expulsion efficiency was 96.6 percent at a ΔP of 25.1 psi. The diaphragm ΔP s during the expulsion cycle were included in Fig. 117. As shown, they were nearly identical to those experienced during the first test.

The shift in CG of the water and diaphragm is shown in Fig. 120. The nine points correspond to the eight data points in Fig. 117 between 5 and 80 percent reversal, inclusive, and the final point (96.6 percent). The corrected CG data shows a maximum variation from the polar axis of 2.26 inches.



Angular Location, degrees

Figure 121. CG Shift for Plastic Tank Test 2

Test 3. The third diaphragm was tested in the plastic workhorse tank on 3 October 1978. The objectives of this test were to minimize the width of the spacer in the outlet half of the tank as a means of increasing the expulsion efficiency above the 96.6 percent achieved during the second test and to determine the effect of a thinner diaphragm. Because of the possibility that this thinner diaphragm might roll through at the equator without a spacer, it was initially tested without a spacer.

Expulsion consisted of twelve pulses at flowrates up to $109 \text{ in}^3/\text{sec}$, which is 79 percent of the maximum requirement. The flowrate is limited by the necessity of keeping the pressurant pressure below 30 psig in the plastic tank. This does not compromise the test results, however, since there has not been any visual evidence of diaphragm reversal characteristics being dependent on flowrate. The expulsion efficiency achieved at 26.4 psid was only 94.2 percent because the diaphragm did not roll through at the equator. The effect of reducing the diaphragm thickness was to increase the expulsion efficiency by 0.9 percent, as shown in Table 40 by comparing diaphragms 1 and 3.

A 0.5 inch spacer was then installed in the tank and the expulsion cycle was completed with the same diaphragm after re-filling the tank with water. The spacer increased the tank volume by 515 in^3 (2.75 percent). Because of the additional space in the outlet half of the tank, the diaphragm rolled through at the equator and the expulsion efficiency was 97.1 percent at 25.0 psid. The diaphragm pressure differential is shown as a function of percent expulsion in Fig. 122. As with the first two tests, several equally-spaced buckles oriented along meridional lines developed in the region near the equator. There were no tight folds associated with the buckles, however, and the minimum diaphragm rolling radius was approximately $3/4$ inch.

The maximum displacement of the CG of the water and diaphragm from the polar axis during the test was 1.18 inches. Converting the water weight to NTO and adding the weight of the flightweight tank reduces the CG displacement to 1.01 inches. This is an approximate maximum in that the load cells are

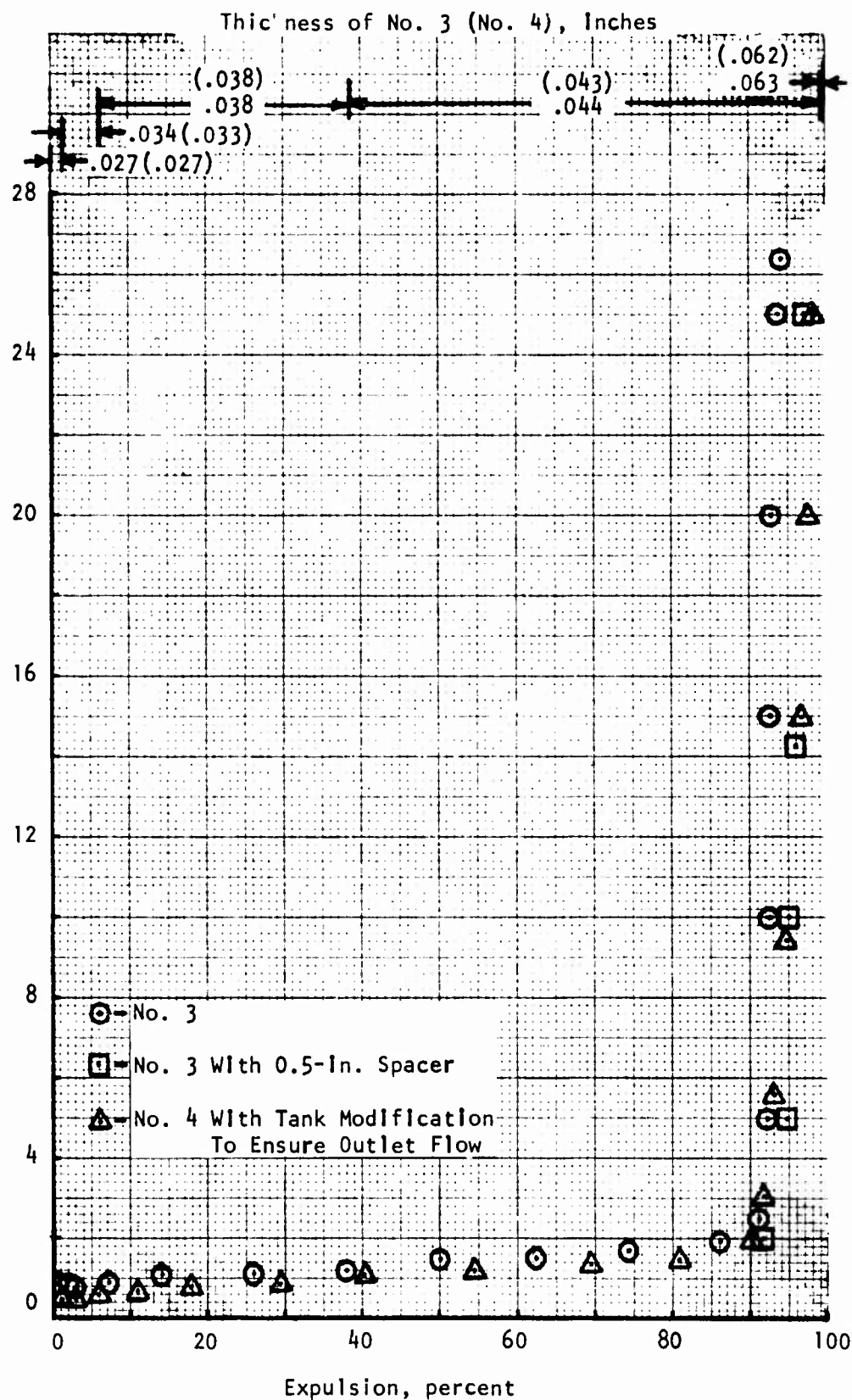


Figure 122. Diaphragm Differential Pressure as a Function of Percent Expulsion

balanced only between expulsion pulses, rather than continuously. The 1.01 inch displacement occurred at 74.4 percent expelled. The displacement was 0.59 inches at 62.6 percent and 0.28 inches at 86.1 percent. The CG movement is plotted in Fig. 123.

Test 4. In order to determine if the flow between the diaphragm and tank wall was being restricted enough to prevent the diaphragm from rolling through at the equator, the tank was modified to ensure there would be an outlet flow path near the end of the expulsion cycle. This was accomplished by spacing eight small-diameter (0.026 inches) wires along meridional lines near the outlet. One end of each wire was placed between the collector plate and tank wall.

The fourth diaphragm was tested without a spacer on 6 October 1978, and resulted in an expulsion efficiency of 98.2 percent at 25.0 psid. A total of 12 pulses were run with flowrates up to $116 \text{ in}^3/\text{sec}$, which is 85 percent of the maximum requirement. The diaphragm ΔP s during the expulsion cycle are presented in Fig. 122. This test provided evidence that the previous low expulsion efficiencies were due to flow restrictions near the end of the expulsion cycle.

The maximum water/diaphragm CG displacement was 2.03 inches and occurred at the end of the cycle as shown in Fig. 124. After correcting the data to NTO and adding the flight tank weight, the maximum CG displacement was calculated to be 0.99 inches at 69.6 percent expelled. The CG displacement was 0.27 inches at 54.7 percent and 0.66 inches at 80.9 percent.

The relatively small CG displacements with the third and fourth diaphragms is a result of the last step thickness change, neglecting the one at the equator, being closer to the equator than with diaphragms 1 and 2. The second diaphragm's last step was the furthest away and had the largest CG displacement, 2.3 inches.

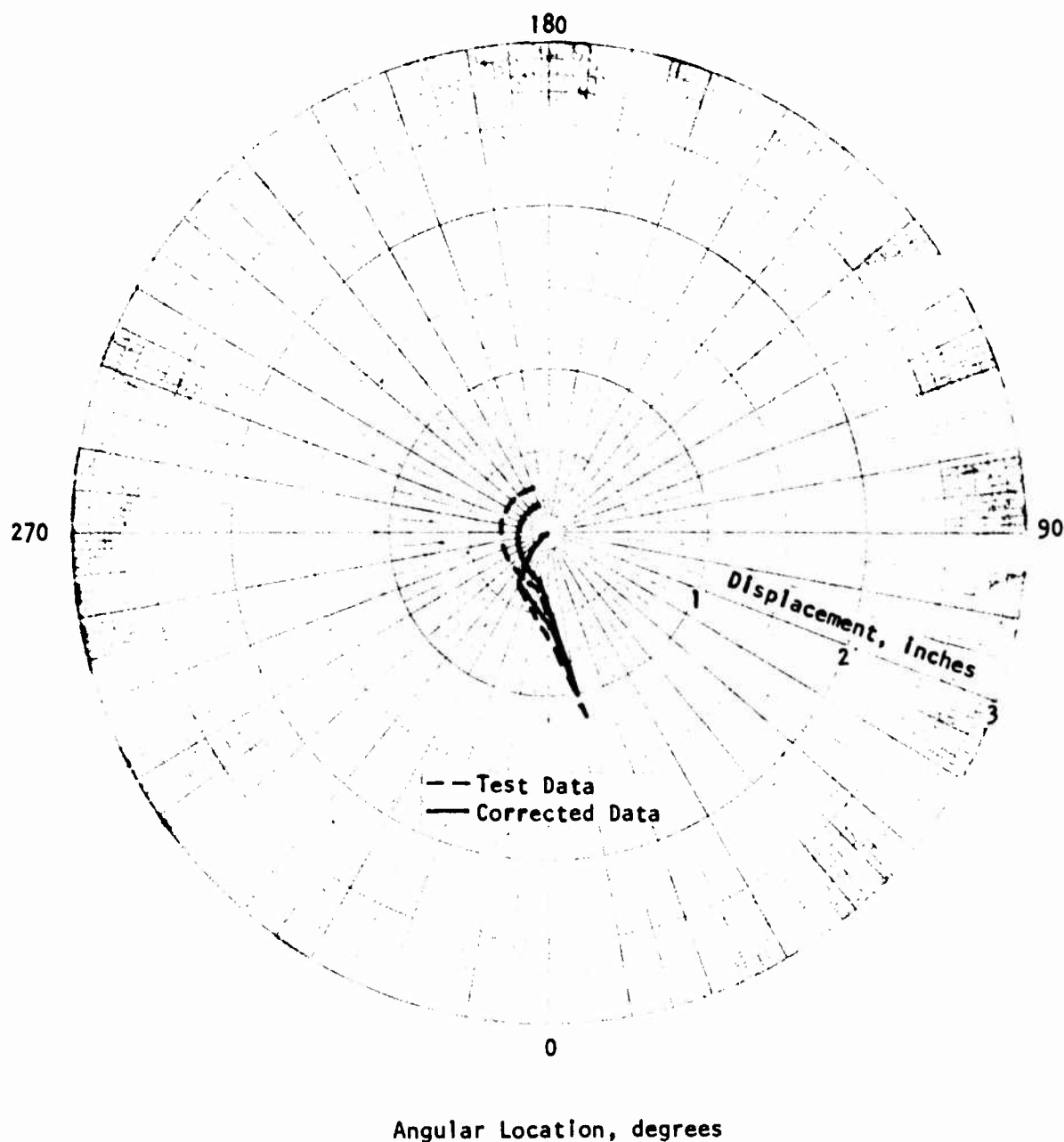


Figure 123. Center-of-Gravity Movement During Third Test

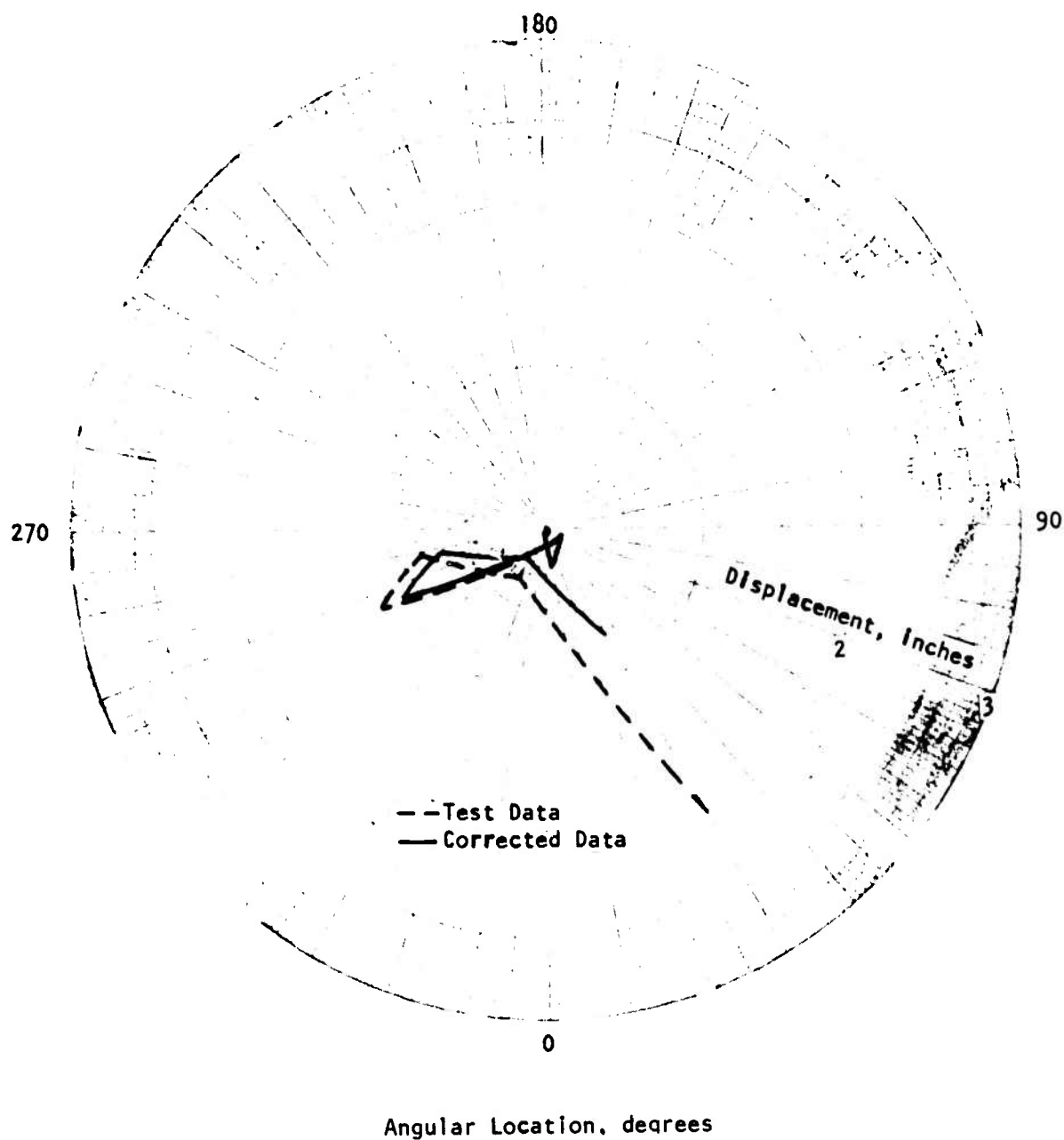


Figure 124. Center-of-Gravity Movement During Fourth Test

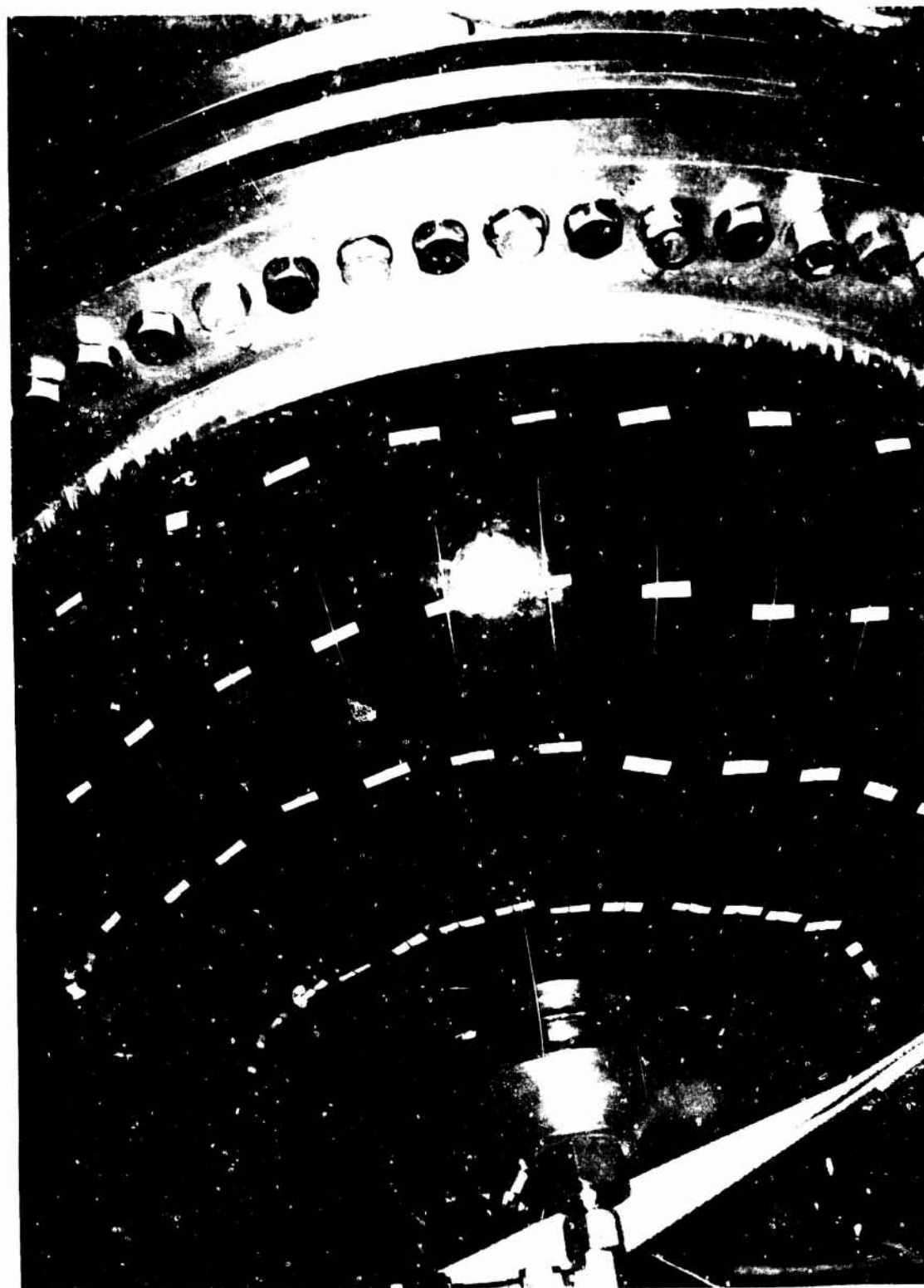
This data provides evidence of the effectiveness of the stepped thickness profile controlling non-symmetrical rolling. Since the maximum CG displacement occurs at 70 to 75 percent expelled, when the residual propellant occupies an annulus with the bulk of the weight located at a large distance from the polar axis, it is important that thickness steps be located near the equator even though they are not required to provide stability margin between the buckling and rolling modes.

Test 5. The fifth diaphragm was tested in the plastic tank on 16 November 1978. This was the first diaphragm with the flange radius formed by a one-step "coining" in the hydraulic press, followed by "rolling" in a lathe.

As a result of the success of the No. 4 unit with the wires to provide a flow path near the end of expulsion, the internal surface of the flight tank outlet liner was redesigned to include chem-milled ribs to provide flow channels along meridional lines. These ribs were simulated in the plastic tank by attaching 0.032 inch diameter wires to the wall as shown in Fig. 125. Ribs would not be required with an all aluminum tank because the fluid outlet port would be relocated near the equator where it would not get covered by the diaphragm.

Expulsion with the fifth diaphragm consisted of 13 pulses at flowrates up to $104 \text{ in}^3/\text{sec}$, which is 76 percent of the maximum requirement. Since the tank was oriented with the minor (expulsion) axis horizontal, there was a hydrostatic pressure gradient of approximately 1.3 psi at the equator. The actual gradient during a typical fourth stage duty cycle will range from approximately 0.6 to 2.5 psi in the NTO tank and 0.4 to 1.5 psi in the MMH tank.

The expulsion efficiency at a diaphragm differential pressure of 25 psi was 98.1 percent, compared to 98.2 percent in the previous test, which utilized 8 short wires to ensure outlet flow. The increased number and length of wires were of benefit, however, in that the observed expulsion efficiency was achieved without the diaphragm completely straightening out at the equator.



10769-11/16/78-C1H

Figure 125. Wires Attached to Plastic Tank

It did not straighten out because the diaphragm was formed slightly too deep. Evidence of this was noticed during assembly when the diaphragm buckled in the flat region near the polar axis when the flange bolts were tightened.

The pressure across the diaphragm as a function of percent fluid expelled is presented in Fig. 112. Due to a small zero shift of unknown quantity, the pressures shown are slightly high.

The relatively high pressure required to achieve a high expulsion efficiency is the result of the thickness of the diaphragm near the equator (0.043 inches). Expelling additional fluid requires sizing of this region against the tank wall, which requires a higher pressure than during the rolling mode. The thickness cannot be reduced without reducing the size or number of steps, or reducing the minimum thickness (at the polar axis). None of these alternatives are recommended, however.

No CG measurements were made because the tank design is not readily adaptable to the installation of load cells when oriented to expel horizontally. However, measurements of the location of the rolling radius were made at the top and bottom of the tank after each flow pulse and the CG profile was calculated from estimates of the diaphragm's shape. The locations of the rolling radius at the end of several pulses are shown in Fig. 126. The figure shows that diaphragm rolling slowed up at both the top and bottom of the tank whenever a step was traversed.

The maximum CG displacement of the water from the polar axis was calculated to be 2.1 inches after expelling 67.8 percent. After converting the water weight to NTO and factoring in a flight tank, the maximum CG shift from the polar axis was calculated to be 1.9 inches. A comparison of the CG profiles for vertical and horizontal expulsions is presented in Fig. 113. As expected, the CG shifted farther from the polar axis during the horizontal expulsion test because of the asymmetric hydrostatic pressure gradient.

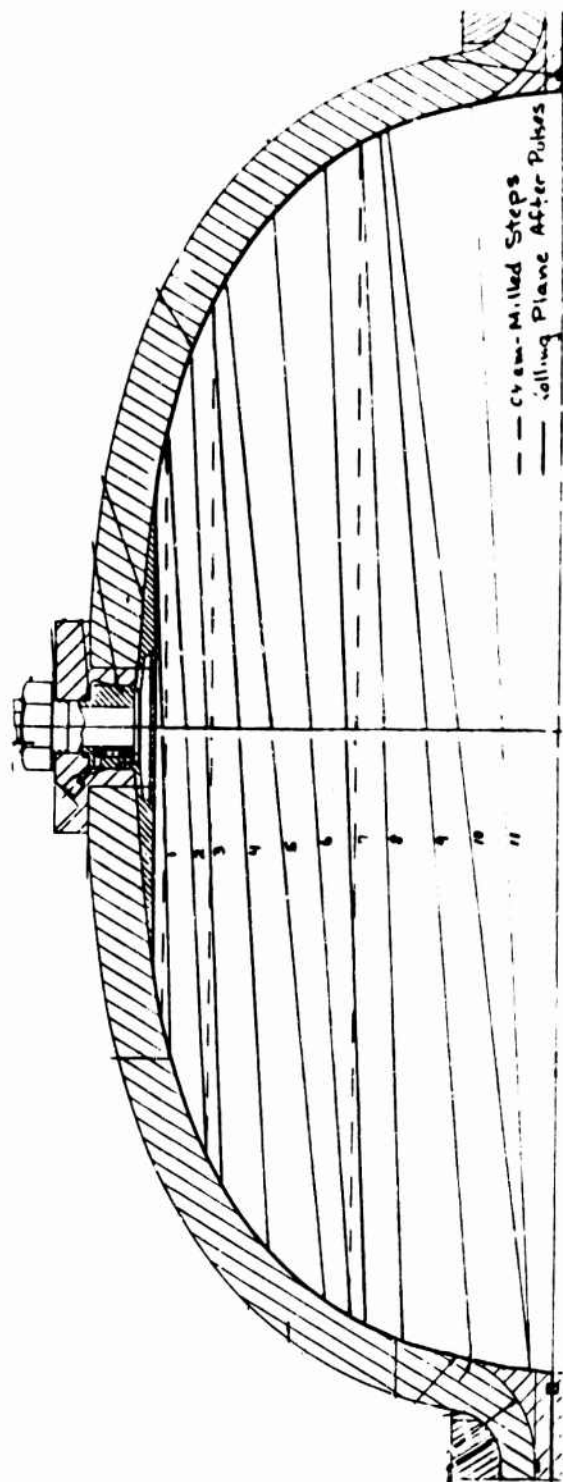


Figure 126. Orientation of Diaphragm Rolling Radius After Pulses

Test 6. The sixth diaphragm was tested in the plastic tank on 20 December 1978. This diaphragm, the first chem-milled by Chemical Energy, had a rough surface finish characterized by small platelets, giving the surface a large-grained appearance.

Fifteen percent (18 out of 121 measurements) of the surface area exceeded allowable thickness tolerances by a maximum of 0.002 inches, even after local chem-milling following the initial inspection. Except for the flange, this was the thickest diaphragm tested with the final nominal profile.

This diaphragm was tested with the major axis vertical and served as a check on repeatability of the previous test. It also demonstrated the effect of diaphragm thickness variations and surface condition on performance since the fifth and sixth diaphragms were the best and worst tested.

Pre-test sizing of the diaphragm to the tank shell at 25 psig resulted in a tight fold in the region near the polar axis. The relative excess diaphragm surface area was due to local buckling of the flat region during handling at Chem-Energy and the tank shell not being a true contour.

The expulsion duty cycle consisted of 13 pulses at flowrates up to $102 \text{ in}^3/\text{sec}$, which is 74 percent of the maximum requirement. The expulsion efficiency at 25 psid was 98.2 percent, compared to 98.1 in the previous test, and 98.2 with the major axis horizontal. A comparison of diaphragm ΔP s for tests 5 and 6 is presented in Fig. 112.

For the first time during any tests, two small ($1/2'' \times 1-1/2''$, $1'' \times 3''$), adjacent buckles occurred slightly ahead of the rolling radius. Pre-test inspection measurements were not made within the boundaries of the buckles and adjacent measurements did not indicate any thinning. However, there are hand-working marks on the diaphragm that are the same shape as the two buckles. This area is clearly visible in photographs taken during the test. It is probable that the area in question is thin, regardless of adjacent inspection measurements.

Test 7. Test 7 with the plastic workhorse tank was run on the centrifuge shown in Fig. 127 at AETL (Fullerton, CA) on 3 and 4 May 1979. During this

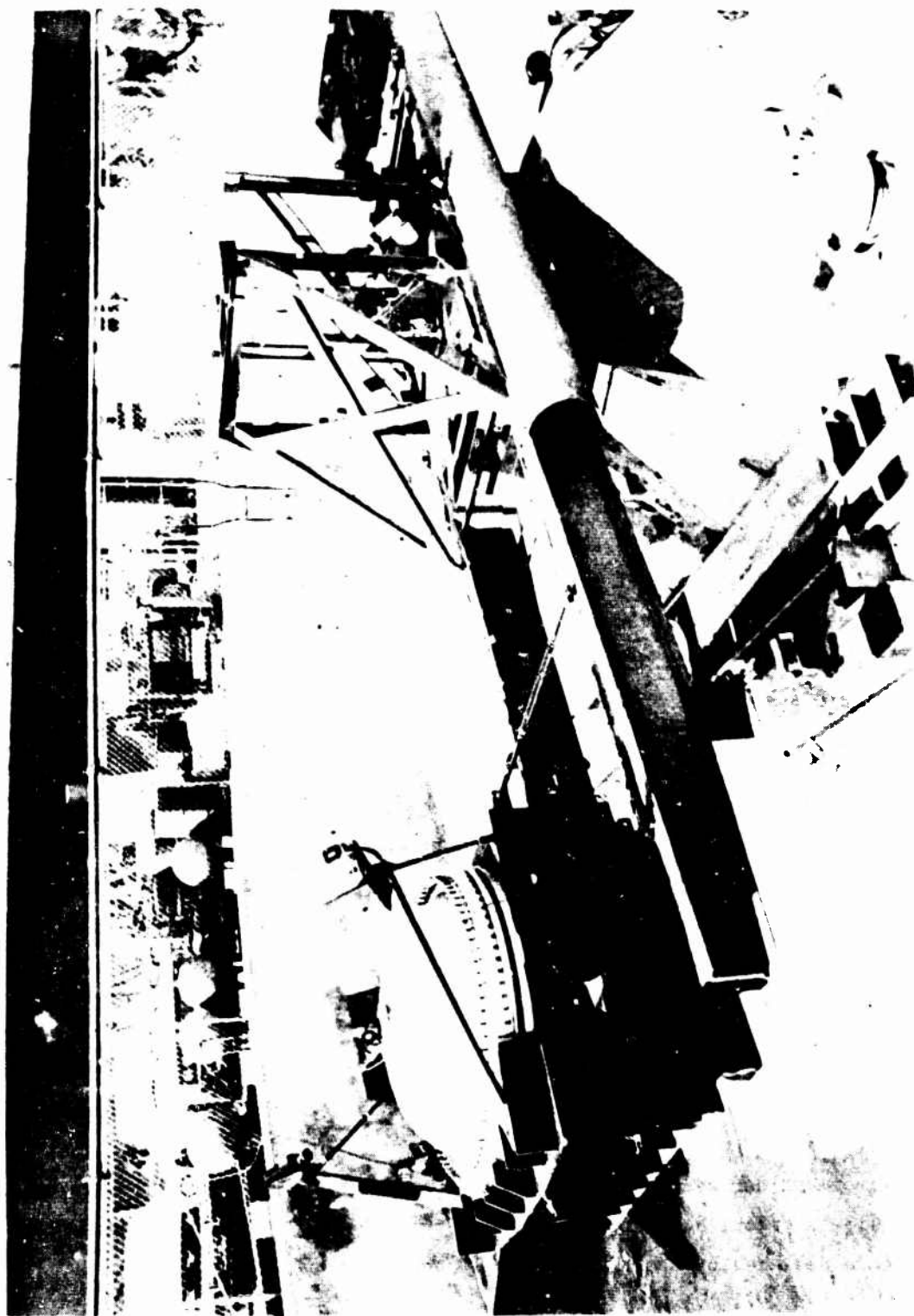


Figure 127. Centrifuge Test Setup

test, the tank was pressurized at 5.1 g, subjected to 15.4 g and subsequently expelled a 1 g. These accelerations were nominal to the polar (expulsion) axis.

The purpose of this test was to provide experimental data relative to the geometric distortion of the expulsion diaphragm due to a typical flight environment and determine the effect of this distortion on expulsion performance.

Initial vacuum leak checks were unsuccessful, which required disassembly of the tank to inspect the o'rings. A 1-in. section of one o'ring was out of its groove, causing the leak. Upon reassembling the tank, the diaphragm buckled in a continuous ring all the way around the circumference a couple inches above the flange. This was caused by the diaphragm being slightly too large as a result of pressure sizing which occurred during vacuum leak checking. Overgrowth of the diaphragm occurred because the pressurant inlet half shell was displaced slightly by the misplaced o'ring mentioned above, and possibly because of stress relieving when the tank shell was removed during disassembly. There was no indication the buckle had any effect on the test results.

The pressure sizing during leak checking also caused a four-legged wrinkle extending across the flat section of the diaphragm near the polar axis. This was caused by the plastic tank not being a true contour and occurred on some of the other plastic tank tests. As a result of this wrinkle, no further pressure sizing was done so as not to reduce the wrinkle's radius of curvature.

The tank was vacuum loaded to 90.1 percent of capacity with Freon-11. During loading, the adhesive tape used to attach the wire ribs to the propellant outlet half liner came loose. This tape, used primarily in an acidic environment during metallic plating processes, had been successfully tested in liquid Freon, but the bond between the adhesive and the tape material became weakened by the Freon vapor as the tank was filled.

The tank was pressurized to 22 psig to collapse the liquid-side vapor ullage when the centrifuge rotation reached a speed corresponding to 5.1g at the tank's polar axis. The corresponding acceleration levels along the major

axis ranged from 4.6 to 5.6g from inboard to outboard. The centrifuge speed was increased to a maximum tank polar axis acceleration of 15.4g. The corresponding acceleration levels along the tank's major axis were 13.9 to 16.9g. These calculated accelerations, based on accelerometer measurements, are lower than the values calculated based on a visual display of the centrifuge's rotational speed, by at least 0.6g. This discrepancy was not resolved.

Acceleration and pressure histories during the test are presented in Fig. 128. Based on accelerometer measurements, the tank's polar axis exceeded 14.5g for 30 seconds. This is lower than the 30 second 15g requirement because the digital display of the centrifuge's rotational speed was used by the operator to control the test.

As the acceleration level was increased to 15.4g after pressurization, the plane defining the locus of points on the diaphragm where it was rolling away from the tank wall moved around toward the equator as shown in Fig. 129. After bringing the tank to rest, the diaphragm was seen to be relatively free of wrinkles.

Time did not permit expulsion of the Freon immediately following the acceleration test. Although it was recognized that the Freon would cool overnight, thereby causing a small amount of diaphragm reversal, it was decided the test results would not be compromised since the reversal would be no different than the first expulsion pulse. The tank was not rotated 90 degrees, however, which caused the diaphragm movement to be symmetrical about the polar axis. This in turn created a "ledge" at the intersection of the two planes of reversal as shown in Fig. 130 (after the tank was rotated 90 degrees to achieve 1g along the tank's major axis).

When the first flow pulse was initiated, both deflected regions continued to reverse, causing severe wrinkling along the ledge. As the expulsion continued, the ledge gradually disappeared. There were no cracks or tears in the diaphragm during the test and the wrinkles had no apparent effect on

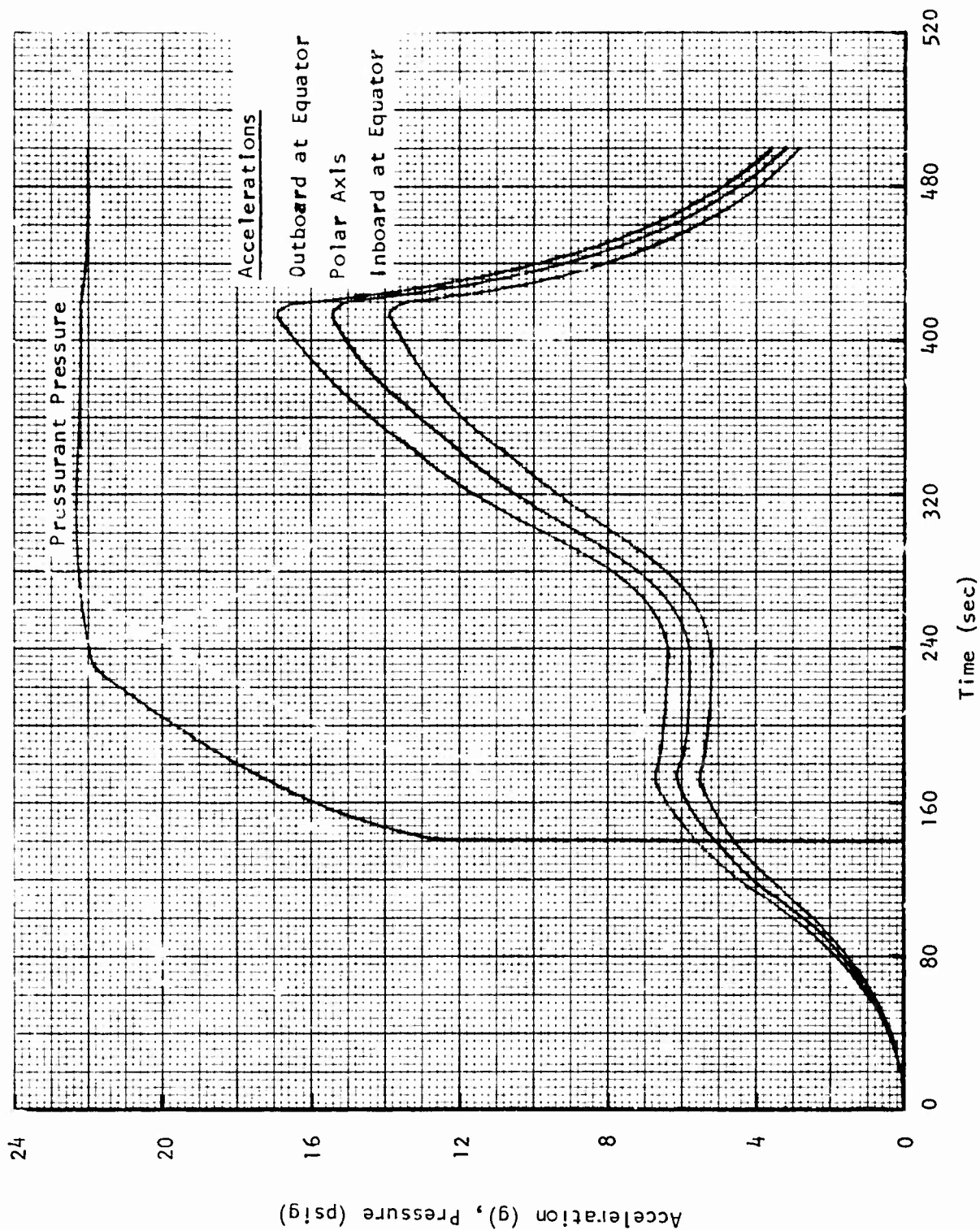


Figure 128. Tank Pressure and Accelerations During Test 7

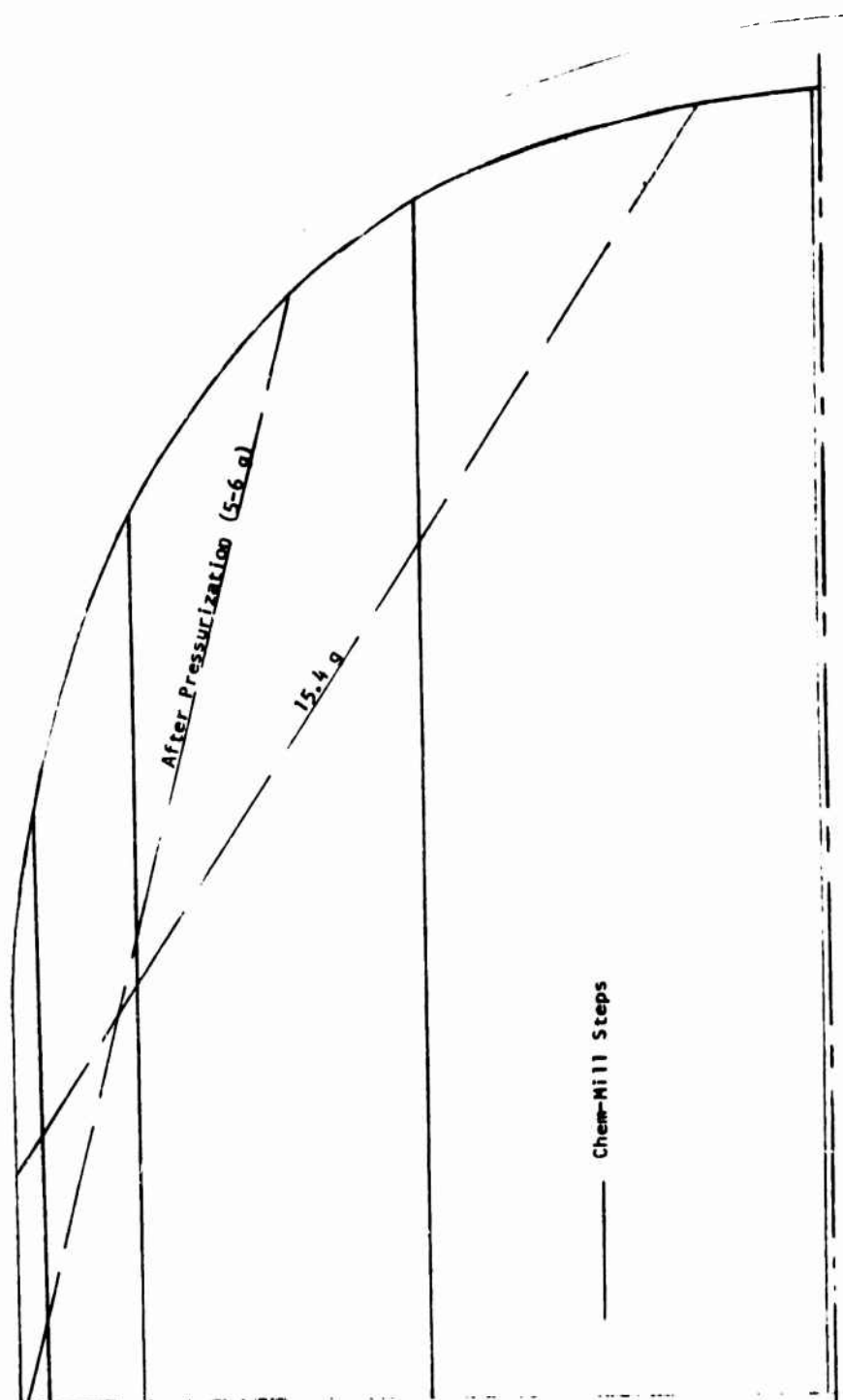


Figure 129. Movement of Deflected Section of Diaphragm During Test 7



Figure 130. Diaphragm Shape Prior to Expulsion During Test 7

expulsion efficiency. After the test was completed, the pressurant was inadvertently vented first, causing the diaphragm to reverse halfway back toward the inlet. This did not cause any cracks or tears, however.

The Freon was expelled in 12 pulses at pressures up to 28 psig and flowrates between 21 and 75 in³/sec. This was the highest flowrate that could be attained due to plastic tank pressure limitations established after the Freon caused stress relieving and crazing of the outlet half-shell. The expulsion cycle was terminated at 94 percent to preclude tearing the diaphragm with the ends of the loose wire ribs.

Because of the hardware/test anomalies and the severe wrinkling, another test was run. Precluding these conditions from occurring during the second test produced remarkably different results.

Test 8. Prior to running the second centrifuge test, the wire ribs were epoxied to the plastic tank. No problems were experienced with the ribs coming loose during the test.

After filling the tank to 90.1 percent of capacity with Freon-11, it was accelerated to 5.2g at the polar axis (4.6 to 5.7g along the major axis). The tank was then pressurized to 20 psig and the centrifuge speed was increased to a maximum tank polar axis acceleration of 14.6g (13.2 to 16.1g along the major axis). The display of the centrifuge rotation speed indicated an acceleration of at least 15.2g at the polar axis.

Acceleration and pressure histories during the test are presented in Fig. 131. Based on accelerometer measurements, the tank's polar axis exceeded 14.2g for 30 seconds. As the acceleration level was increased to 14.6g, the plane defining the locus of points on the diaphragm where it was rolling away from the tank wall moved around toward the equator as shown in Fig. 132. This movement was significantly less than the first test because of the lower maximum acceleration level.

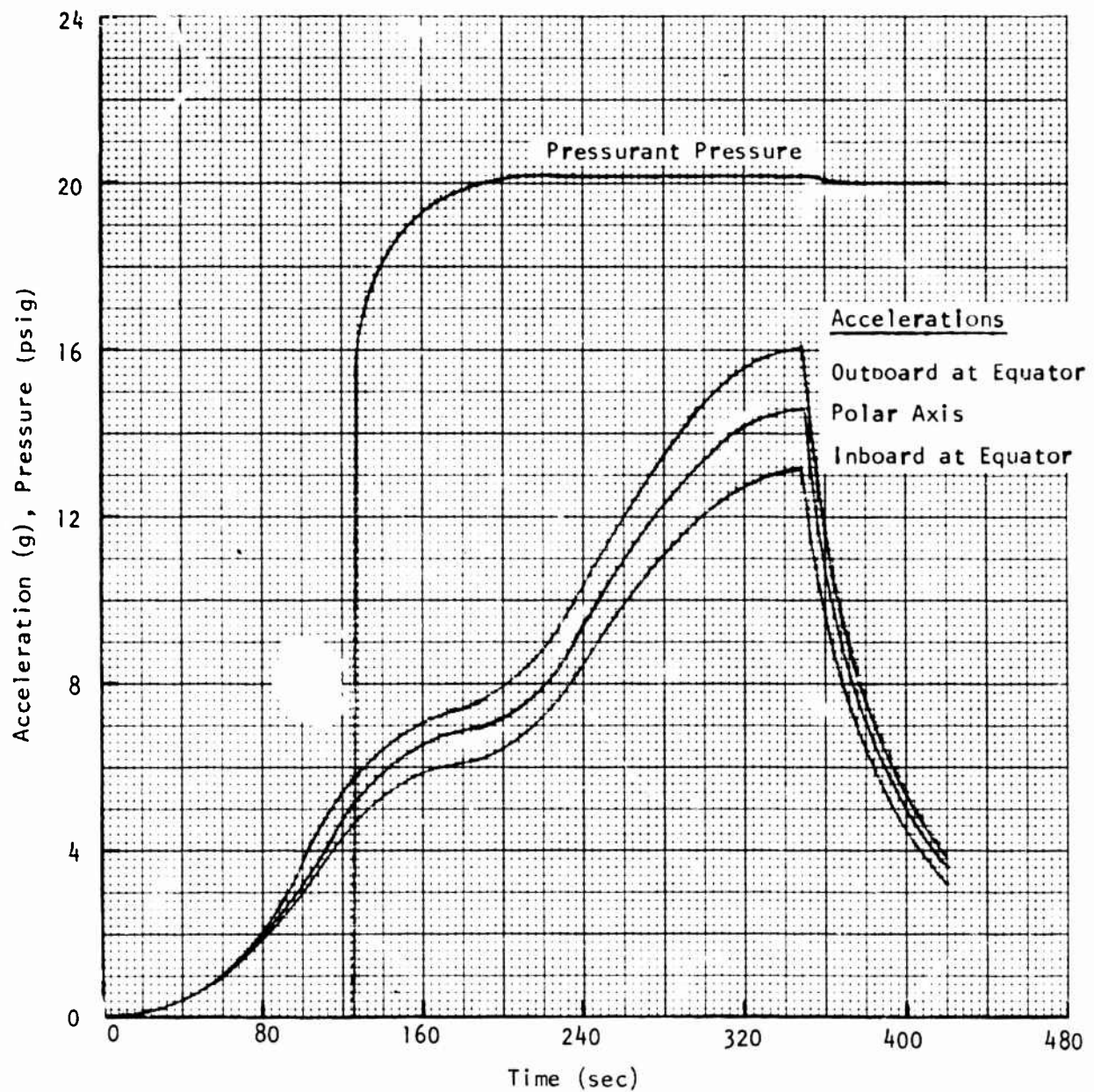


Figure 131. Tank Pressure and Accelerations During Test 8

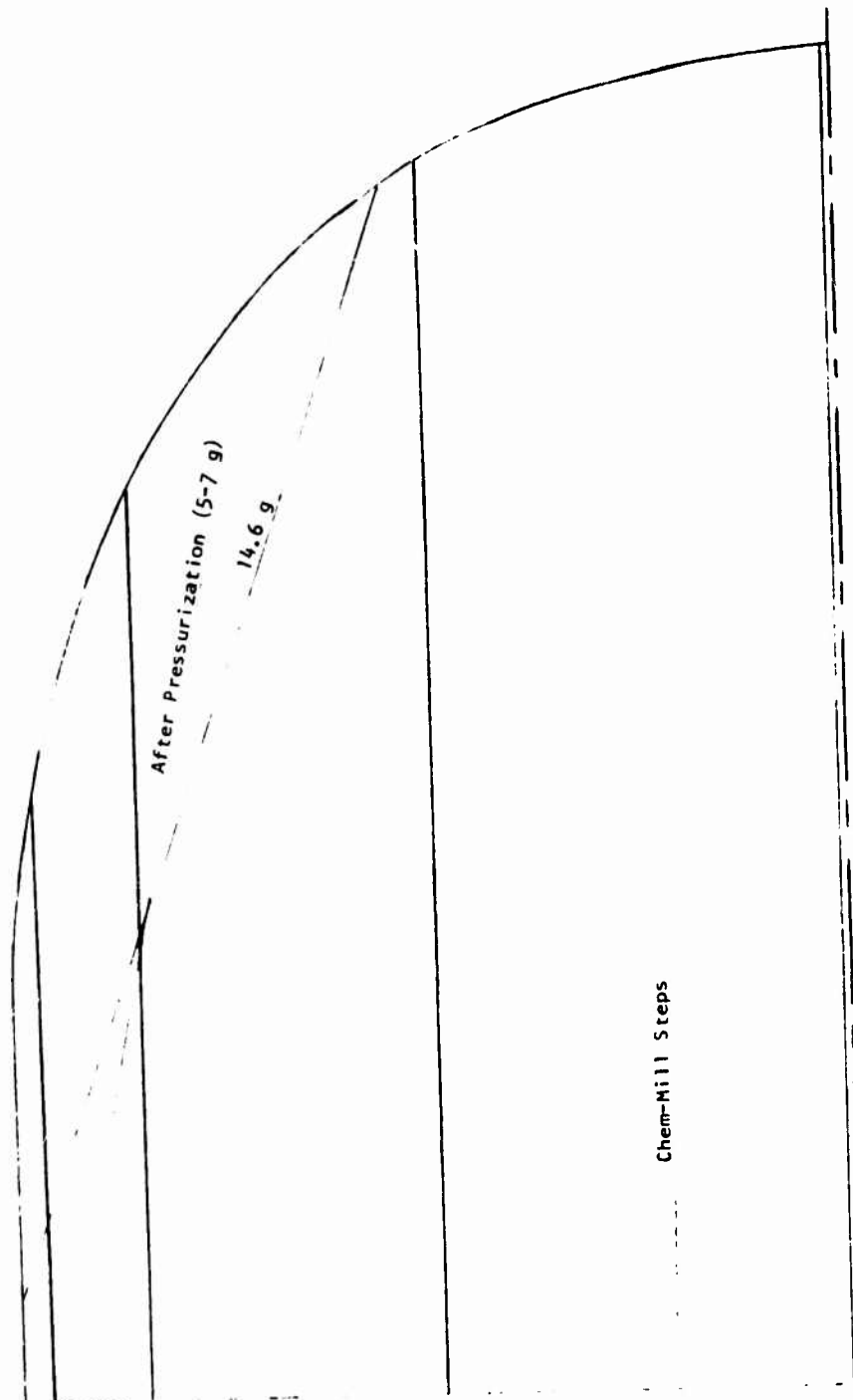


Figure 132. Movement of Deflected Section of Diaphragm During Test 8

Since the deflected region did not roll around toward the equator as far as the previous test and the tank did not sit in a horizontal position overnight, initiation of the expulsion cycle did not create a ledge at the intersection of the two planes of reversal because of the larger angle created. Figure 133 shows the diaphragm after the first pulse. The different results from these two tests illustrate the importance of the difference in acceleration levels normal to the polar axis experienced during launch and post-boost operation after pressurization with a large initial ullage volume.

The region of the diaphragm near the top of the tank was relatively free of any of the nine bulges which typically formed during the expulsion cycle. This is believed to be the result of the initial reversal being shifted around toward the equator during the acceleration portion of the test.

The Freon was expelled in 14 pulses at pressures up to 30 psig and flowrates between 22 and 62 in³/sec. The expulsion efficiency was 98.2 percent.



Figure 133. Diaphragm Shape During Expulsion Portion of Test 8

ALUMINUM WORKHORSE TANK

An aluminum workhorse tank with replaceable expulsion diaphragms was fabricated and tested. Three of the tests were conducted to demonstrate expulsion performance and mechanical integrity of the diaphragm selected during the plastic workhorse tank tests. These tests utilized the Tridyne pressurization subsystem to evaluate its performance.

A fourth diaphragm was subjected to vibration and shock environments to demonstrate the diaphragm's mechanical integrity and establish its fundamental response characteristics. The workhorse tank was used because it permitted accessibility for inspection, redesign, and additional testing of the diaphragm without using the relatively expensive flightweight tanks.

Tank Fabrication

A sketch of the aluminum tank is presented in Fig. 134. It consists of two flanged half-shells and a replaceable expulsion diaphragm. A large and small port are located in each polar boss for instrumentation, propellant filling, pressurization, and expulsion.

The 2219 aluminum half-shells were draw-formed by Aircraft Hydro-Forming (Gardena, California) in two steps with an intermediate annealing step. It was necessary to restrain the shells during the final heat treatment to preclude distortion. Machining and welding were done by Rocketdyne. After machining to compensate for shrinkage near the polar bosses and tilting of the flanges during welding, it was necessary to machine flange spacers to increase the polar axis dimensions of the shells.

Strips of aluminum were spot-welded to the outlet half shell to simulate the chem-milled ribs in the flight tank. This design modification was accomplished in this manner because the tank was fabricated prior to establishing the requirement for the ribs.

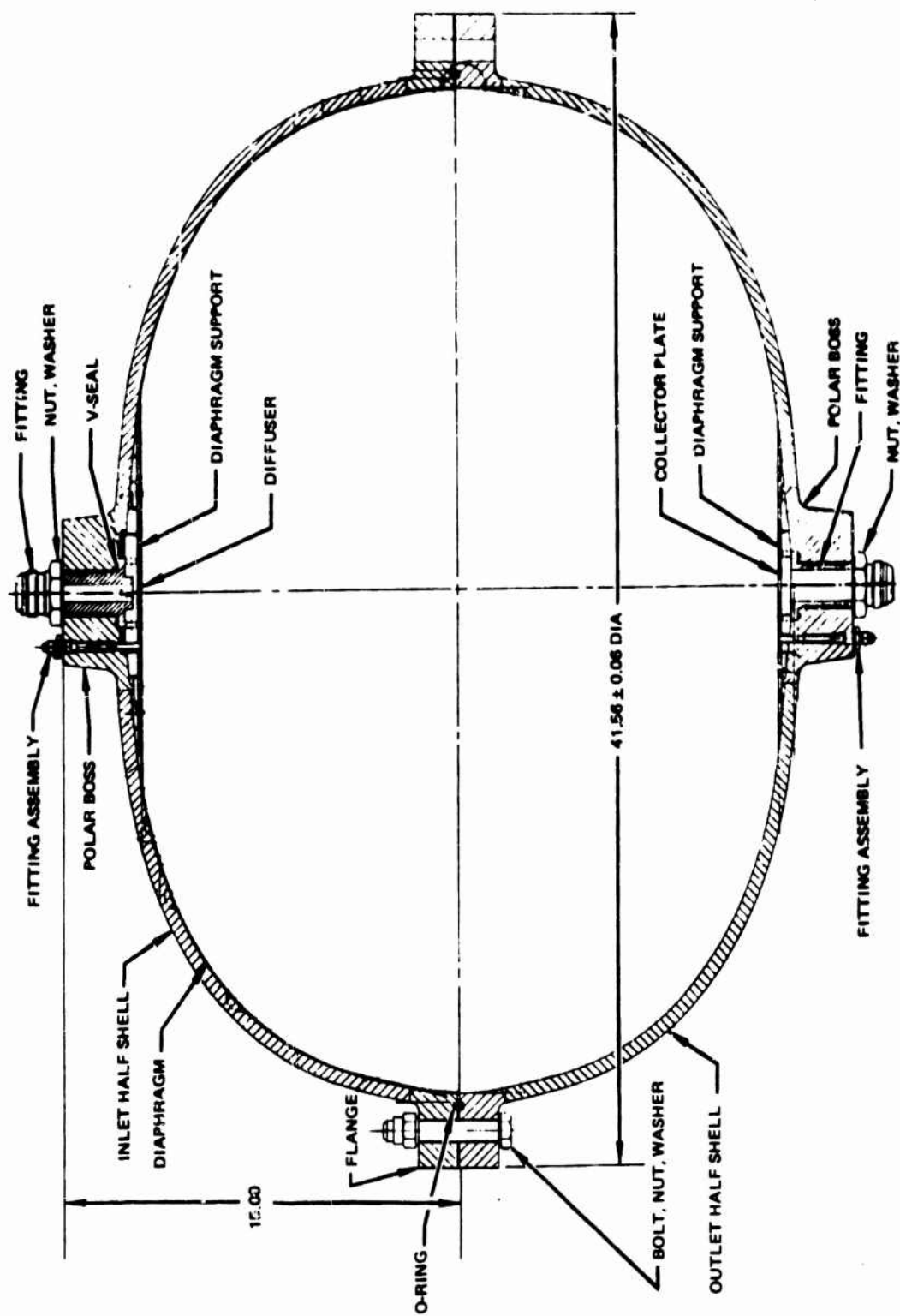


Figure 134. aluminum Workhorse PSA

Diaphragm Expulsion Tests

Three diaphragms were tested in the metal workhorse tank at Rocketdyne's Santa Susana Field Lab (Santa Susana, California) between February and April 1979. A propellant simulant (water) was expelled from the tank with the Tridyne pressurization subsystem.

Expulsion efficiency data was obtained from two of the tests that confirmed the plastic tank test data and demonstrated that expulsion at design pressure (300 psi) with warm gas (up to 1192 F at the tank interface) has no measurable effect on diaphragm ΔP . The efficiency for both tests was 99.3 percent at 50 to 54 psi differential.

There was no posttest evidence that the warm gas affected the aluminum diaphragm as a result of impingement. The mechanical integrity of the diaphragm flange radius during expulsion was demonstrated by the fact that a ΔP of 162 psi was insufficient to cause any cracks, even with a 0.015 inch chem-mill undercut.

Thermal data were obtained that showed the effectiveness of the tank design near the gas inlet in minimizing heat transfer from the pressurant to the outer shell and propellant. The maximum increase in bulk propellant (water) temperature was 8 to 11 degrees (F), depending on the duty cycle, and it occurred at the end of the expulsion.

Test 1-A. The first test using the metal workhorse tank was conducted 15 February 1979. Because of problems created by a very fast response facility valve and subsequent damage to the regulator's remote sensing pressure transducer, the test was run in three segments. The first segment (Test 1-A) of the pulsed duty cycle was controlled by a magnetic tape and consisted of initial pressurization, a hold period and one high-flow pulse, which generated a pressure redline cutoff.

The aluminum workhorse tank was vacuum loaded with water to 97.5 percent of capacity and the Tridyne tank was filled to a pressure of 2216 psia. At the start of the test, the Tridyne isolation valve was opened and the regulator assembly was energized to pressurize the propellant tank. These components are shown schematically in Fig. 135 and photographically in Fig. 136. During pressurization, gas flowed only to the propellant tank, i.e., no gas was dumped through the orifices used to simulate the second tank. The propellant tank inlet and outlet pressures are shown in Fig. 137.

When the flow demand control valves were opened after a 142 second hold period, the tank outlet line pressure dropped below the redline value, which was established to preclude a very high differential pressure across the diaphragm at the end of the expulsion cycle. When the high-flow valve, a high pressure Annin, was automatically closed due to the redline after 0.2 seconds of flow, a severe pressure oscillation resulted as shown in Fig. 138. A check of the valve with micro-switches indicated an effective travel time of approximately 5 to 10 msec, much faster than the axial engine valve specification. Since the valve could not be modified without venting the propellant and pressurant tanks, it was decided to continue testing by disarming the pressure redline until the final duty cycle pulse. Table 41 shows the sequence of test events.

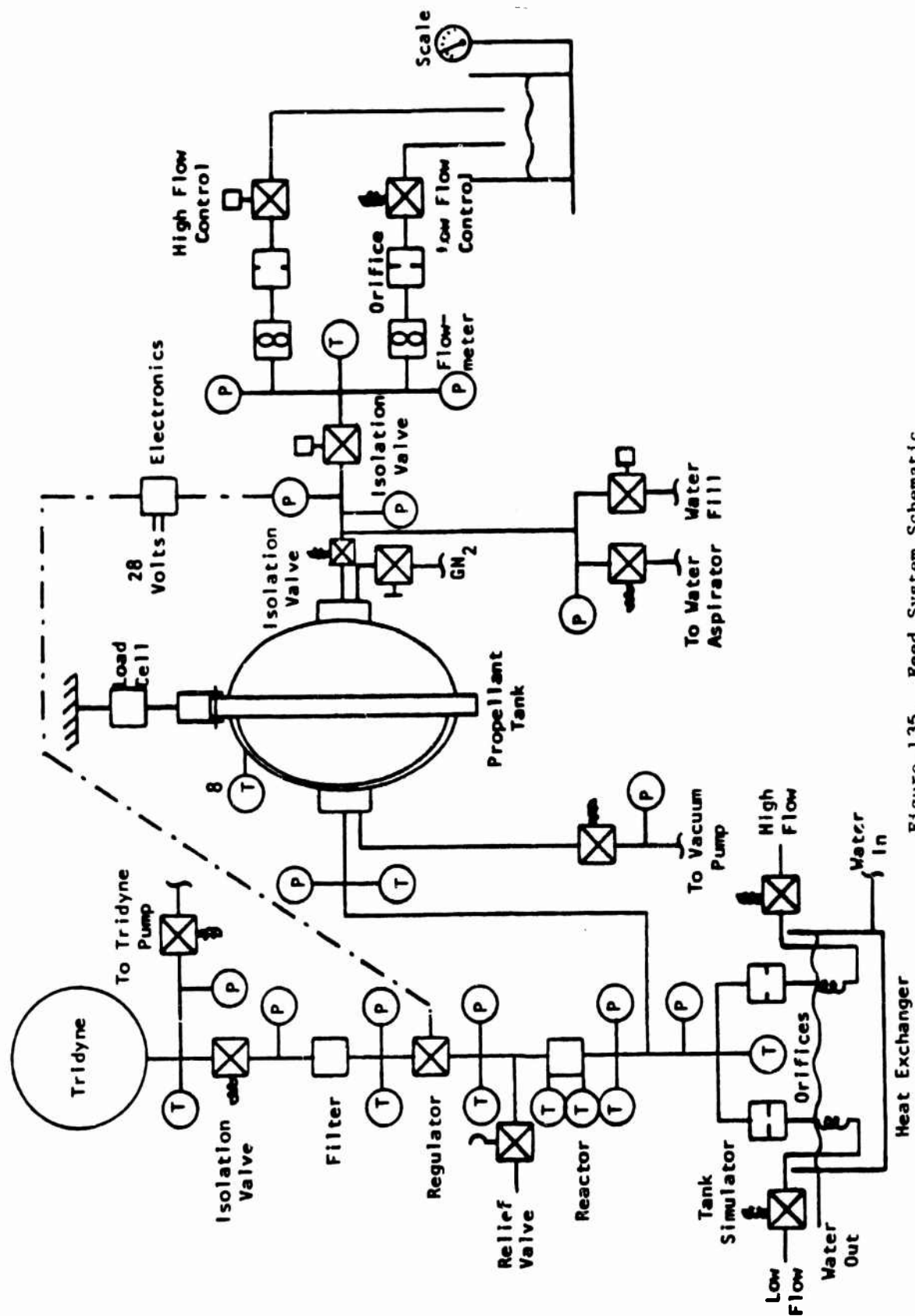
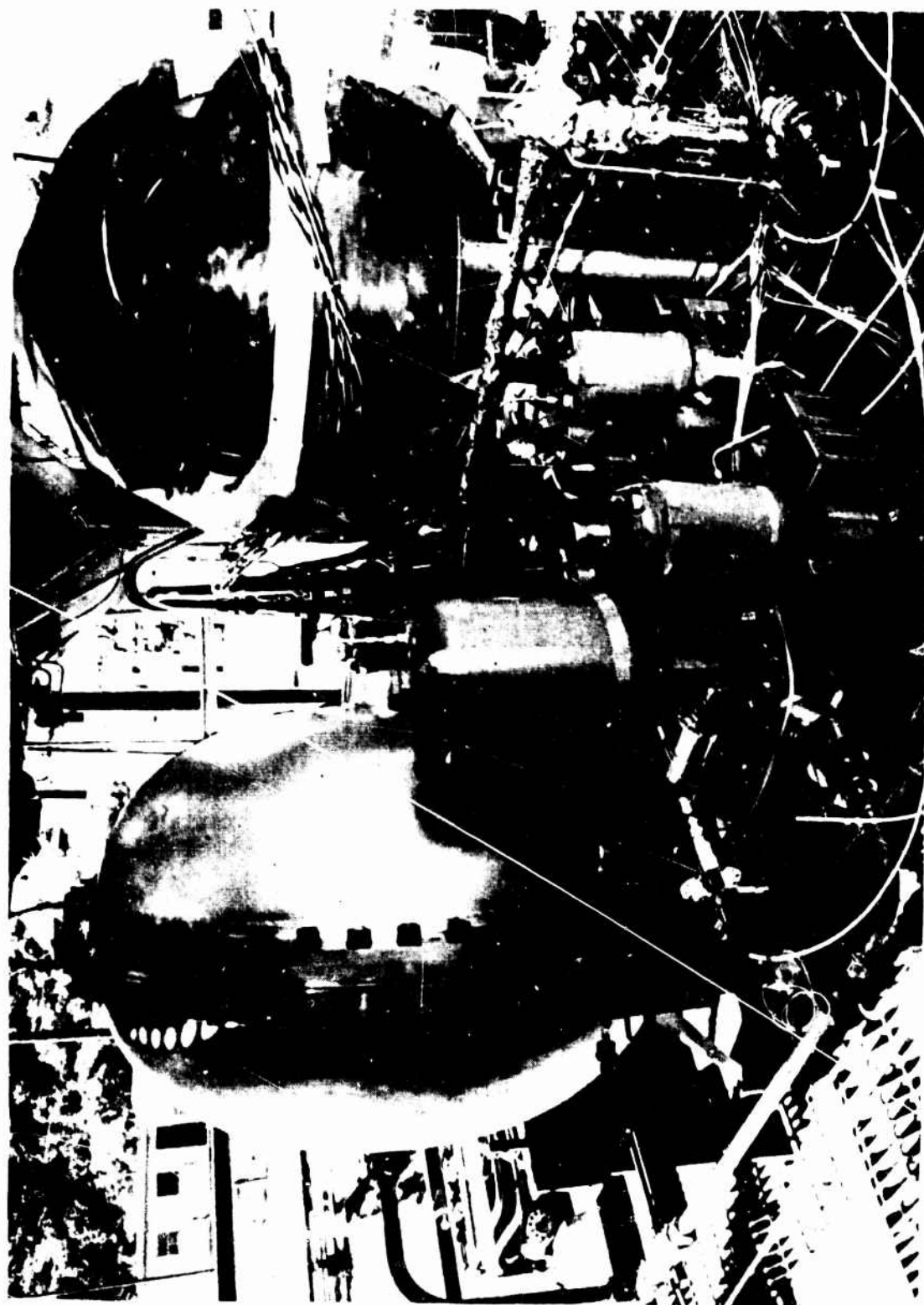


Figure 135. Feed System Schematic



LX263-2/9/79-S1A

Figure 136. Feed System Test Setup

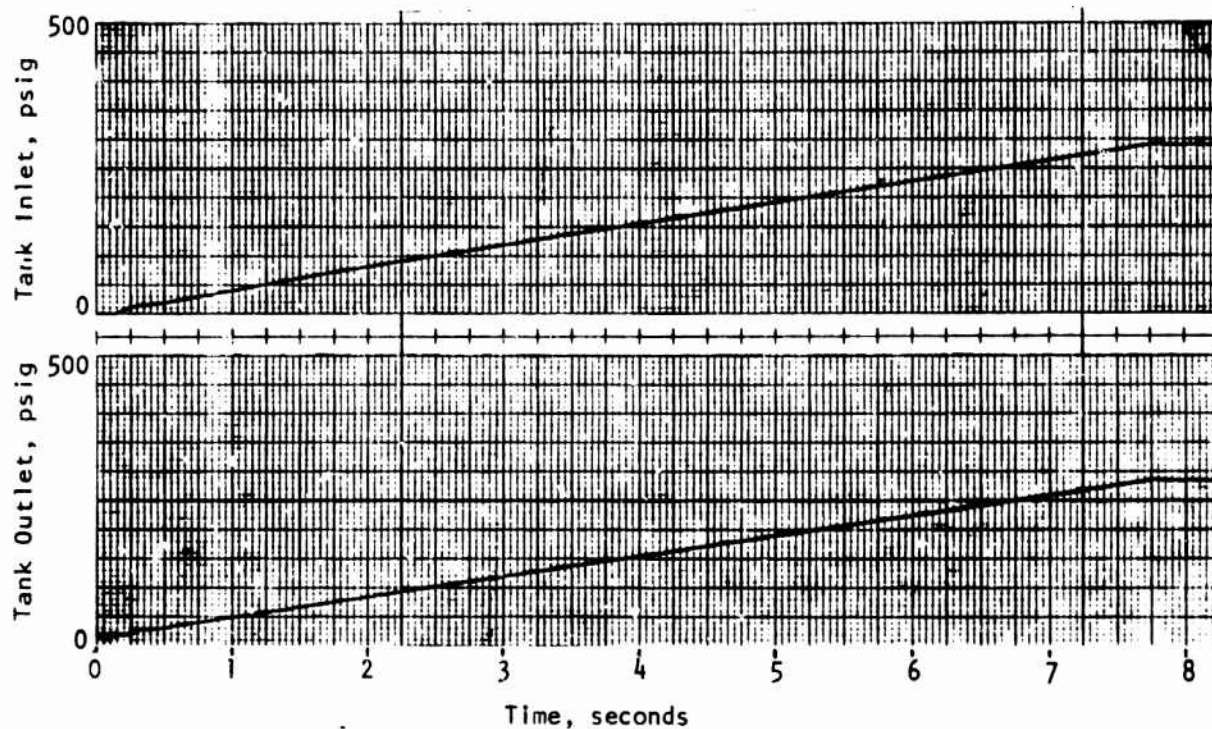


Figure 137. Pressure Transients During Initial Pressurization

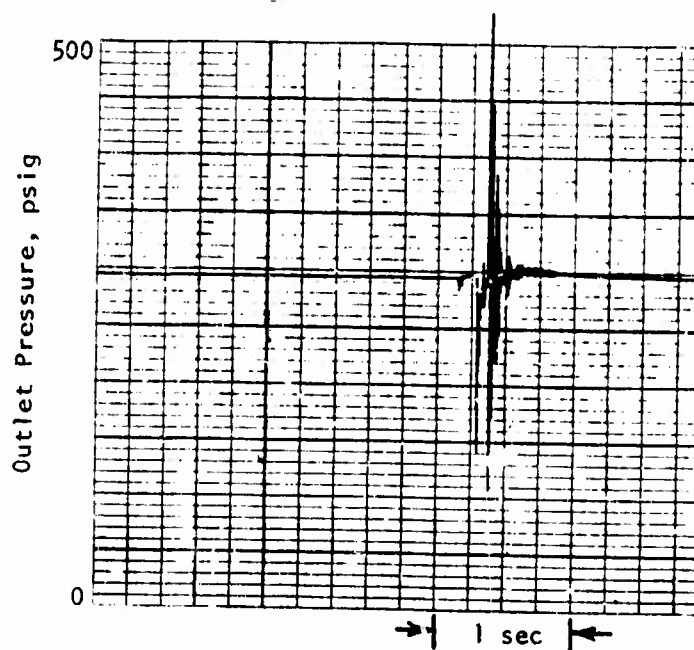


Figure 138. Tank Outlet Pressure During First Pulse

TABLE 41. TEST EVENT DURATIONS

TEST NO.	1-A		1-B		1-C	
	7.5 SEC 142.		6.5 SEC -		18.0 SEC 36.3	
	HIGH FLOW	LOW FLOW	HIGH FLOW	LOW FLOW	HIGH FLOW	HOLD
INITIAL PRESSURIZATION HOLD	0.2 (CUT)		-	15.9	9.0	50.1
1ST CYCLE			3.0	10.0	10.1	49.6
2ND CYCLE			0.4	15.0	10.8	48.8
3RD CYCLE			2.0	6.0	11.0	49.4
4TH CYCLE			8.0	15.0	10.3	49.8
5TH CYCLE			3.0	3.6(CUT)	10.3	49.7
6TH CYCLE					10.3	49.9
7TH CYCLE					15.0	44.9
8TH CYCLE					10.2	?
9TH CYCLE					21.6	
10TH CYCLE						

Test 1-B. Because the pressurant cooled off and a small amount leaked through a line fitting, it was necessary to repressurize the tank from 70 psia. The drop in pressure caused the diaphragm to reverse direction as the small amount of air on the liquid side expanded, but there was no evidence of damage during posttest inspection.

Since the flow-demand control valves were positioned by a magnetic tape which was not reset after Test 1-A, the low flow valves were open during pressurization and for 15.9 seconds afterwards, until the high-flow pulse was initiated. After the fourth high-flow pulse in this test, the regulator failed and remained closed. After the fifth high-flow pulse, it was noticed that the propellant tank was operating in a blowdown mode and the test was manually terminated.

Posttest examination by Parker-Hannifin revealed the propellant pressure control transducer failed in a manner that resulted in a high output voltage, which signaled the mechanical regulator to close after the fourth pulse. Also, the regulator had been forced to flow an abnormally high amount of Tridyne because of slow thermal transients in the simulated tank subsystem. Because there was no warm gas flow in these lines during initial pressurization and the lines are relatively long, the gas temperature at the orifices was colder than the value used in their sizing calculations.

A few superficial checks were made on the regulator assembly while it was still on the test stand, but they did not reveal the mode of failure. It was therefore decided to replace it with a facility regulator and continue the expulsion cycle.

Test 1-C. The pressurant gas was vented to atmospheric pressure to replace the regulator, once again causing the diaphragm to partially reverse itself as the air on the liquid side expanded. The feed system was then pressurized for the third time and water was expelled by manually pulsing the high-flow demand valve nine times. Each cycle was approximately 60 seconds long and all but one included a 10 second flow pulse. The exception had a 15 second

pulse. Finally, the valve was opened (tenth pulse) with the pressure redline set at a value to terminate the test when the diaphragm pressure differential (ΔP) reached 50 psi. The flowrate range was 129 to 135 in³/sec during the pulses, except at the end of the last one when flow dropped to 116 in³/sec as the diaphragm ΔP increased.

The thermal efficiency of the catalytic reactor was only 70 percent during the test, compared to 93 percent during component testing a year earlier. The low outlet temperature was observed during Test 1-B, but it was assumed to be the result of the abnormally high gas flowrate mentioned previously. Component testing during March 1979 indicated the problem was associated with a bad Tridyne gas mix, rather than catalyst degradation or contamination. Because of the discontinuous nature of this first test and the low gas temperature, the data were not used to calculate PS performance.

The initial workhorse PSA wall temperatures along the meridian running through top-dead-center were 70 F at the three thermocouples closest to the polar boss (as a result of heating from Test 1-B) and 52 F at the three nearest the flange (due to the influence of the remaining water, which was also 52 F).

The tank inlet-gas temperature was approximately 880 F and resulted in the tank wall temperature profile shown in Fig. 139, after the ninth pulse. These were the maximum temperatures because of the relatively long hold period before the tenth pulse, during which the pressure redline was rearmcd. The lower temperatures at the side and bottom of the tank were due to the cooler gas migrating to the bottom of the tank and also cooling by the cold water propellant, which is asymmetric about the polar axis due to the hydrostatic pressure gradient.

The water outlet temperature was 54 F at the end of the ninth pulse and 60 F when the test was terminated. The increase in water temperature was therefore eight degrees during the duty cycle expulsion.

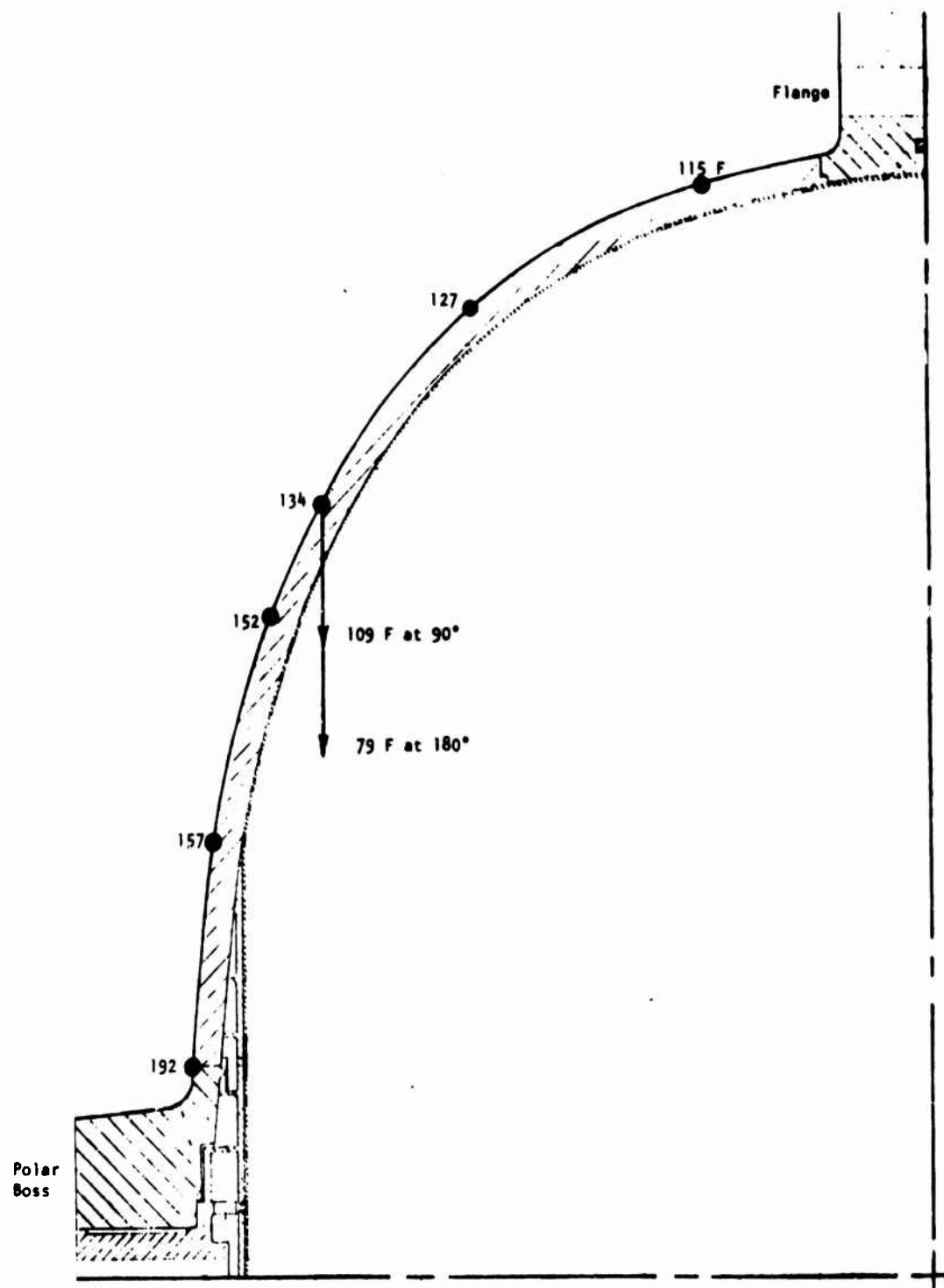


Figure 139. Maximum Tank Outer Wall Temperatures

The expulsion efficiency was 99.3 percent with a final diaphragm ΔP of 54 psi. This high efficiency shows agreement with the 98.1 to 98.2 percent achieved with the plastic tank at 25 psi. The ΔP as a function of percent diaphragm reversal during the final pulse is shown in Fig. 140. Because a ΔP transducer capable of withstanding all of the pretest and test pressure environments was not available, diaphragm ΔP s were calculated from two separate pressure transducers. The errors associated with these transducers and the recording devices resulted in invalid data at low ΔP s, i.e., at expulsion percentages up to approximately 70 to 80 percent.

The diaphragm ΔP was maintained after the test was completed, indicating the absence of any tears. Also, posttest inspection did not reveal any indication of effects due to the warm gas pressurant. The propellant side of the diaphragm is shown in Fig. 141.

There was one wrinkle in the diaphragm, in the thinnest section, that did not straighten out at the end of the test as shown in Fig. 142. This wrinkle was probably created during pretest sizing of the diaphragm to the inlet half shell or during venting and repressurization.

The diaphragm tested was chem-milled by Chemical Energy in San Diego and had a chem-milled undercut at the flange radius of approximately 0.015 inch. This undercut extended from between meridians numbered 1 and 2 to between numbers 6 and 7. There are a total of 12 equally spaced numbered meridians. Posttest inspection indicated the diaphragm rolled down to the flange radius and then yielded from meridian No. 1 to between No.'s 6 and 7, where the undercut was located, but the diaphragm did not leak.

Test 2. Since the electronically controlled regulator had not been repaired, test 2 was run with a facility regulator. The continuous-expulsion duty cycle was utilized. The diaphragm tested was chem-milled by Chemical Energy. Thickness measurements indicated 109 out of 121 locations were within specifications. The maximum variation from the tolerance band was 0.002 inches.

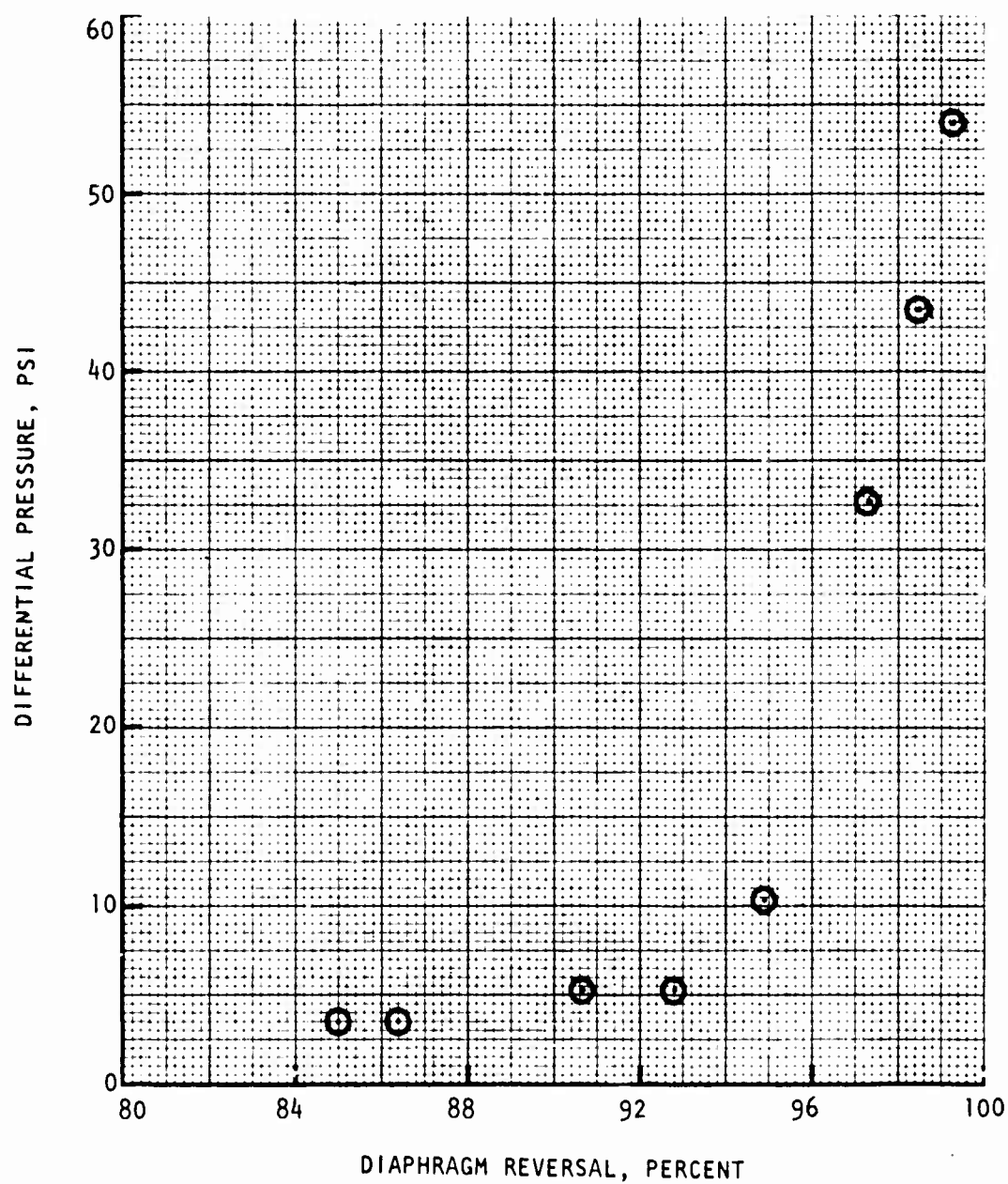
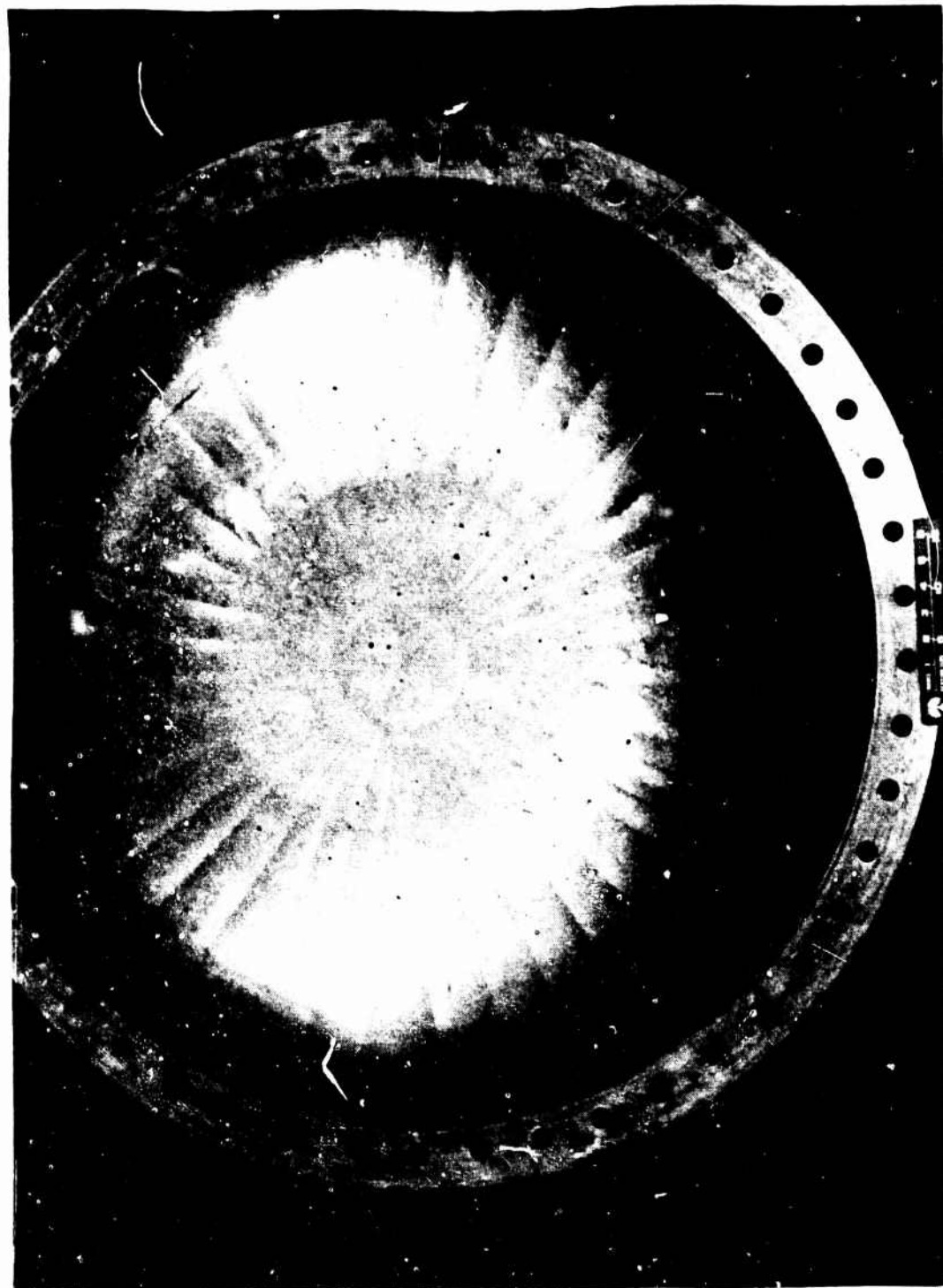


Figure 140. Diaphragm Differential Pressure at Tank Polar Axis



1XZ65-2/16/79-S1A

Figure 141. Propellant Side of Diaphragm 1



1XZ65-3/5/79-C1A

Figure 142. Wrinkle in Diaphragm 1

There were chem-milled undercuts approximately 0.015 inches deep at the flange radius between meridians numbered 1 and 2, 4 and 6, 7 and 9. There were a total of 10 equally spaced, numbered meridians.

The tank was vacuum loaded with water to 90.3 percent of capacity to yield the largest required liquid-side ullage volume and result in the maximum amount of heat transfer from the warm gas to the diaphragm during pressurization. The oversized Tridyne tank was filled to yield a pressure of 983 psia.

At the start of the test on 5 April 1979, the Tridyne isolation valve was opened and the tank was pressurized to 333 psia in 11 seconds. During the pressurization and subsequent expulsions, gas flowed only to the propellant tank, i.e., no gas was dumped through the orifices used to simulate the second tank. This had the effect of increasing the reactor thermal response time and changing the steady state gas temperature by minor amounts.

Following pressurization and a hold period, a 4.5 second, $8 \text{ in}^3/\text{sec}$ pulse was initiated at 86 seconds into the test. The purpose of this pulse was to provide data to assist in the calculation of diaphragm pressure differentials. At 98 seconds into the test, the high-flow valve was opened. This valve remained open until a downstream propellant pressure redline terminated the test. This redline precludes the diaphragm ΔP from exceeding a preset value. Temperature transients were monitored for 225 seconds after termination of flow.

A flowrate of $133 \text{ in}^3/\text{sec}$ was maintained for 128 seconds except for the last couple seconds of the test when the flowrate dropped to $118 \text{ in}^3/\text{sec}$ as the diaphragm ΔP increased. Except at the end of the test, the delivered propellant pressure was 300 psia.

The tank wall temperature transients are presented in Fig. 143 for the thermocouple (T/C) locations numbered 1 to 6 in Fig. 144. The temperatures ranged from 148 to 188 F at the end of the expulsion with the warmest region being at the polar boss. These wall temperature transients reflect the influence of several heat transfer phenomenon including:

1. Different initial temperatures influenced by sunlight, ambient air, water and thermal isolation from the water as a result of the mechanical design.
2. A varying inlet gas temperature
3. Thermal isolation from the warm gas as a result of the mechanical design
4. Conduction along the wall
5. Natural convection
6. Forced convection
7. A bulk gas temperature gradient due to gravity
8. Condensation of the water vapor in the pressurant

The effectiveness of the mechanical design in thermally isolating the tank wall near the warm gas inlet is evidenced by the transients during and immediately after pressurization. In spite of T/C No. 6 being closest to the gas inlet line, T/C's numbered 5, 4 and 3 registered higher temperatures. This cannot be completely explained by the relatively large mass of the inlet boss because T/C No. 4 registered a higher temperature than T/C No. 5, and both are located along the constant thickness wall. The explanation for this observance is that the wall on one side of T/C No. 5 is isolated from the warm gas by the flat-plate extension of the diffuser. T/C's numbered 1 and 2 remained relatively cold during pressurization because this region of the wall does not get exposed to the warm gas.

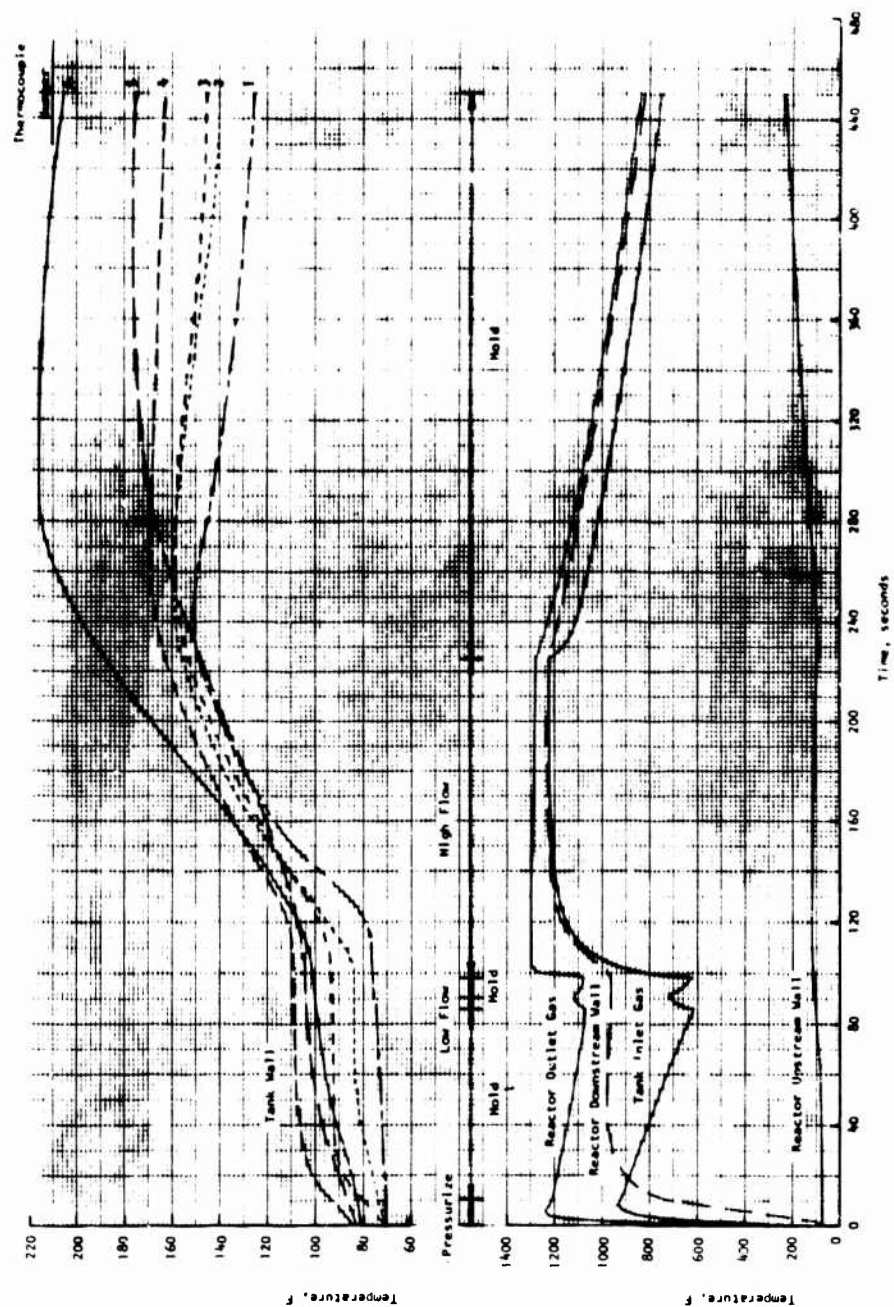


Figure 143. Test Temperature Transients

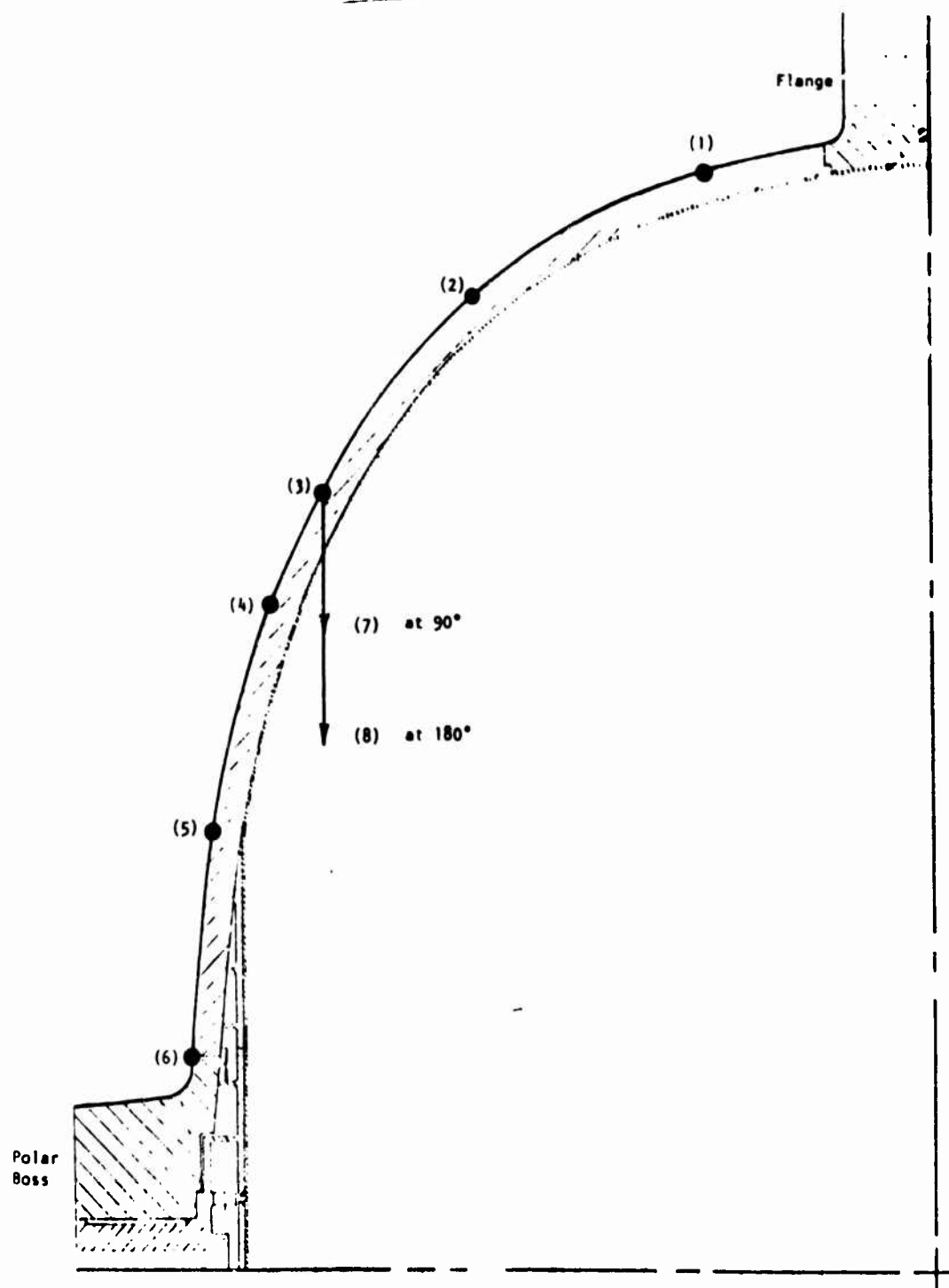


Figure 144. Tank Wall Thermocouple Locations

Further evidence of the effectiveness of the thermal isolation design can be observed during the high-flow expulsion. It took 22 seconds after initiation of the flow for T/C No. 6 to exceed T/C No. 5 and 58 seconds for T/C No. 6 to exceed T/C No. 4. T/C No. 5 did not exceed T/C No. 4 until 60 seconds after the propellant was expelled.

The wall temperatures discussed above were the result of the gas inlet temperature profile shown in Fig. 143. This measurement was made 30.5 inches downstream of the catalytic reactor and 14 inches upstream of the tank in an insulated line. The gas temperature varied between 1220 and 1225 F during the last 55 seconds of the expulsion. The initial water temperature in the tank was 69 F.

Because the warm gas flows to the highest point in the tank that has been exposed as the diaphragm reverses, and the water cools the bottom of the tank longer than the top due to the diaphragm being slightly skewed as a result of the hydrostatic pressure gradient, there is a large wall temperature gradient from the top to the bottom. The magnitude of the gradient is shown in Fig. 145 for T/C's numbered 3, 7 and 8, which were located at the top, side and bottom, respectively.

The water outlet temperature, measured 8 to 9 feet downstream of the tank, was 69.5 F at the start of the test and 69.8 with 60 percent expelled. The temperatures at 80 and 90 percent, and at the end of the expulsion cycle were 70.9, 74.6 and 79.5 F, respectively.

The expulsion efficiency was 99.3 percent, the same as the first test with the aluminum workhorse tank, at 50.2 psi. The diaphragm ΔP as a function of percent reversal is shown in Fig. 146.

The diaphragm ΔP was maintained after the test was completed, indicating the absence of any tears. Also, a visual posttest inspection did not reveal any effects due to the warm-gas pressure.

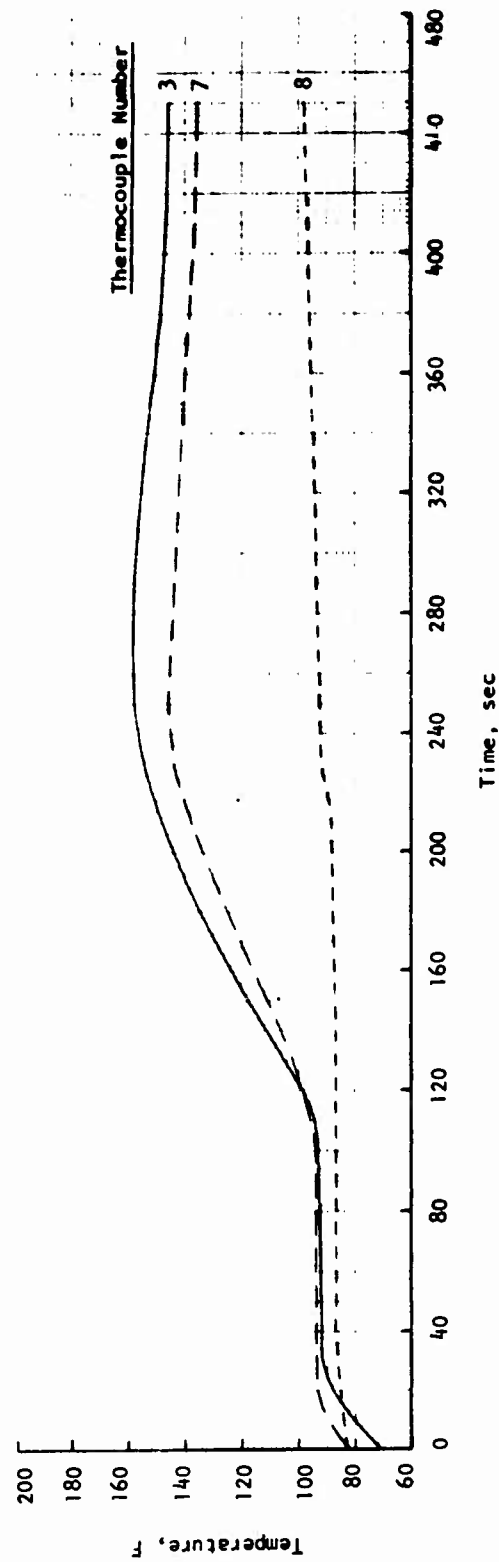


Figure 145. Tank Wall Temperature Transients for Test 2

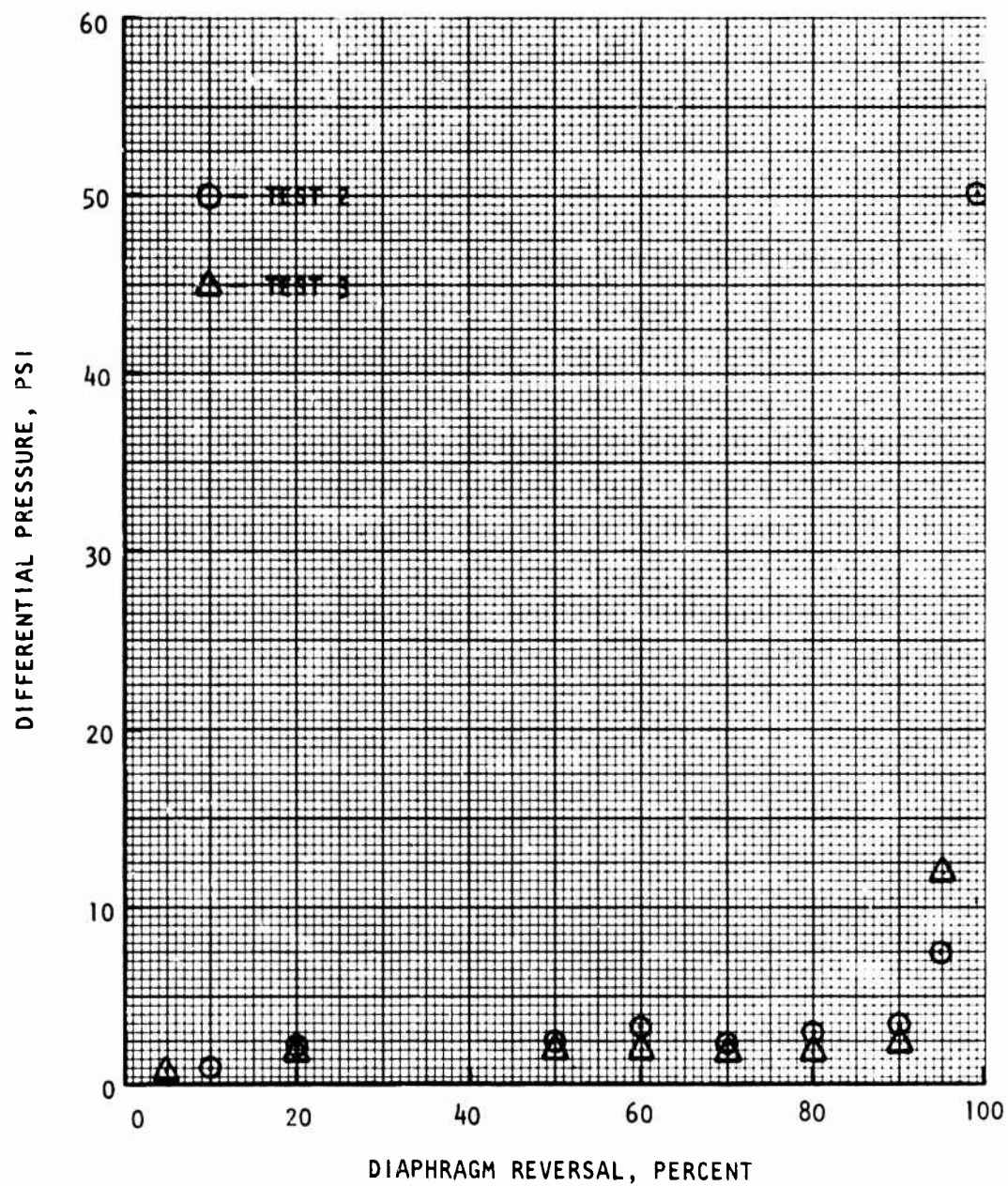


Figure 146. Diaphragm Differential Pressure

Venting of the propellant simulant and pressurant gas after the test resulted in a maximum diaphragm ΔP of 162 psi without tearing, in spite of the chem-mill undercuts. There were 4 circular marks on the liquid side of the diaphragm corresponding to the 4 center holes in the outlet collector plate, but the ΔP was insufficient to cause any dents.

Test 3. The third diaphragm tested in the aluminum workhorse tank was chem-milled by Chemical Energy. Thickness measurements at all 121 locations were within tolerances. There were chem-mill undercuts of approximately 0.015 inches depth, however, at the flange radius between meridians numbered 2 and 6, and 9 and 10. These undercuts were marked prior to assembling the tank. There were a total of 10 equally spaced, numbered meridians.

The tank was vacuum loaded with water to 95.0 percent of capacity. The oversized Tridyne tank was filled to yield a pressure of 1174 psig.

At the start of the test on 10 April 1979, the Tridyne isolation valve was opened, but the facility regulator reference pressure had not been set. This caused the regulator to remain closed. The isolation valve was then closed and the line vented through the regulator, reactor and gas orifice simulating the second propellant tank. This caused the reactor to be at slightly elevated temperatures at the start of the actual test.

The propellant tank was pressurized to 333 psia in 9 seconds. During pressurization and subsequent expulsions, gas flowed only to the propellant tank, i.e., no gas was dumped through the orifices used to simulate the second tank. Cutting the Tridyne flow in half increased the reactor thermal response time and changed the steady state gas temperature by minor amounts.

Following pressurization and a hold period, the pulsed duty cycle was initiated at 95.5 seconds into the test with a low-flow pulse of 7 in³/sec for 60.5 seconds. Starting with closure of the low-flow valve at the end of the 60.5 second pulse, the 59.4 second valve sequence shown in Fig. 147 was repeated six times.

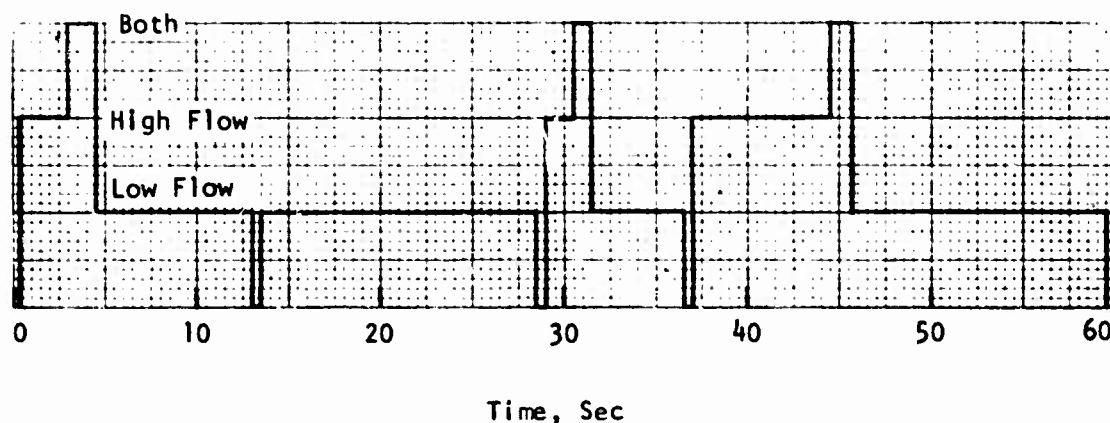
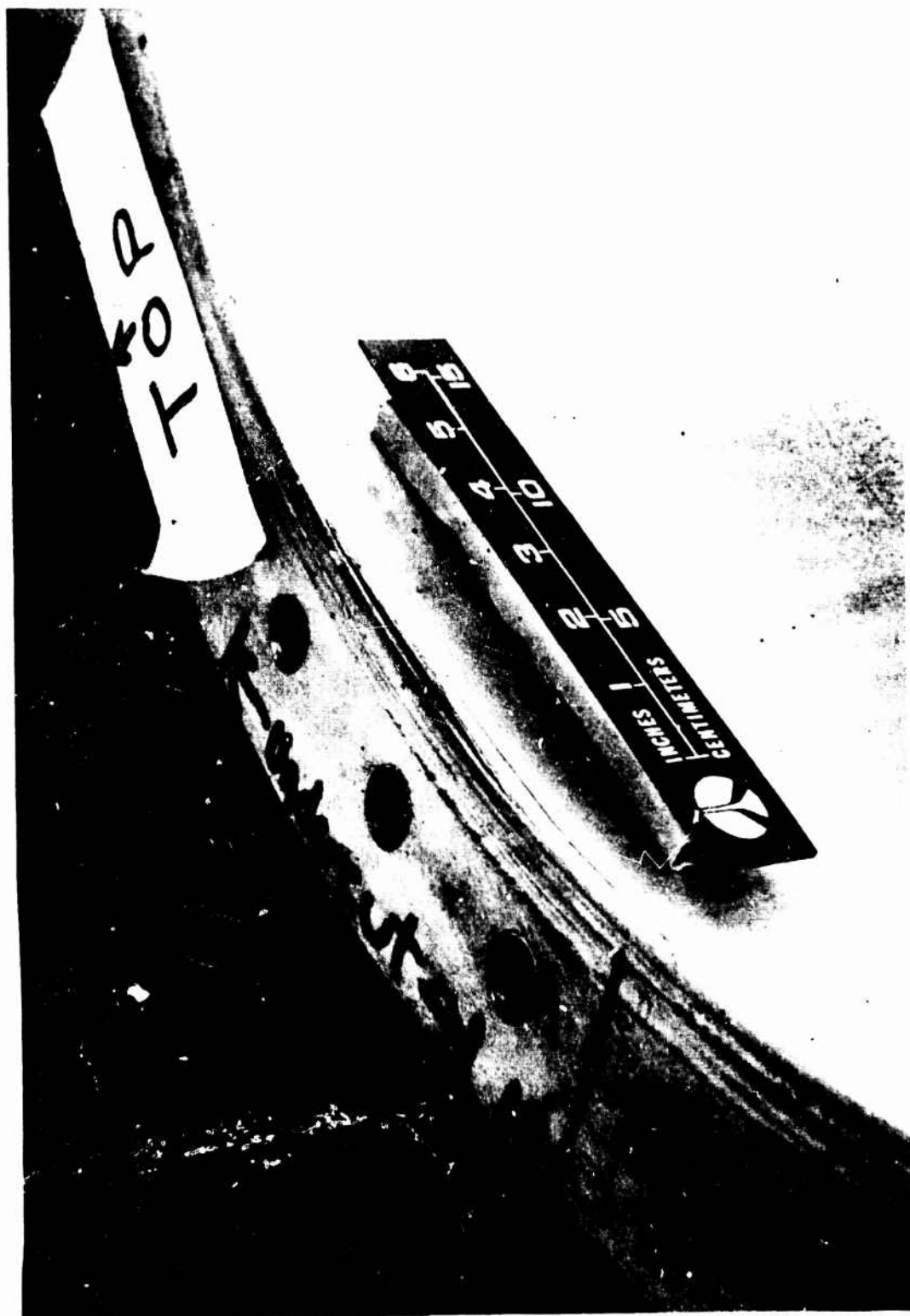


Figure 147. Pulse Series

During the third high-flow pulse of the seventh series, the valve control mode was transferred from magnetic tape to manual, the liquid outlet pressure redline was energized and a redline cut of the test was immediately encountered. The test engineer mistakenly thought the redline was caused by energizing the redline too soon after transferring to the manual control mode and he quickly reset the control console and opened the high-flow valve. The redline cut was actually a normal end-of-test cut caused by the outlet liquid pressure dropping below the preset value. When the high-flow valve was opened, the diaphragm ΔP reached an exceedingly high value before the redline once again caused the valve to close.

Data analysis indicated diaphragm ΔP s as shown in Fig. 146 and 63 psi at the end of the test, i.e., at the first redline cut. When the valve was reopened, a crack in the diaphragm developed at one of the previously mentioned chem-mill undercuts as shown in Fig. 148. The undercut region, marked prior to the test, is also shown. It was not possible to determine the diaphragm ΔP at the time the crack developed; however, there were four distinct dimples in the diaphragm corresponding to the four holes in the center of the outlet collector plate. Based on a visual comparison with the previously tested diaphragm, it would appear the ΔP exceeded 162 psi since the previous diaphragm was not dimpled at that value.



IX265-4/12/79-S1A

Figure 148. Diaphragm Crack

The flowrate through the small valve ranged between 7.0 and 7.7 in³/sec during the test and the large valve flowed 131 to 135 in³/sec except for the last couple seconds when it dropped to 105 in³/sec as the diaphragm ΔP increased. Except at the end of the test, the delivered propellant pressure was approximately 308 psia.

The tank wall temperature transients are presented in Fig. 149 for the T/C locations numbered 1 to 6 in Fig. 144. The primary difference between these profiles and the ones from the previous test is the final temperatures. They ranged from 159 to 240 F from near the equator to the polar boss for the pulsed duty cycle compared to 148 to 188 F at the end of the continuous expulsion. The higher temperatures are a result of the longer time available for heat transfer from the pressurant gas to the tank wall.

The gas inlet temperature profile for this test was also presented in Fig. 149. The gas temperature was fairly steady after the first series of pulses and remained within the band shown. The maximum peak-to-peak variation after the first series of pulses was 68 F. The average temperature during the last few series of pulses was 1106 F compared to 1222 F during the continuous expulsion. The initial water temperature was 59 F, 10 degrees cooler than the continuous-expulsion test.

The variation in tank wall temperatures from top to bottom are presented in Fig. 150. The temperature profile is more uniform than the continuous-expulsion test, as expected, because of the longer time during which thermal conduction occurred along the wall.

The water outlet temperature increased from 58.8 to 70.0 F during the test. This increase, 11.2 degrees, was slightly larger than the 10.0 degrees during the continuous-expulsion test. Again, this is due to the longer duty cycle.

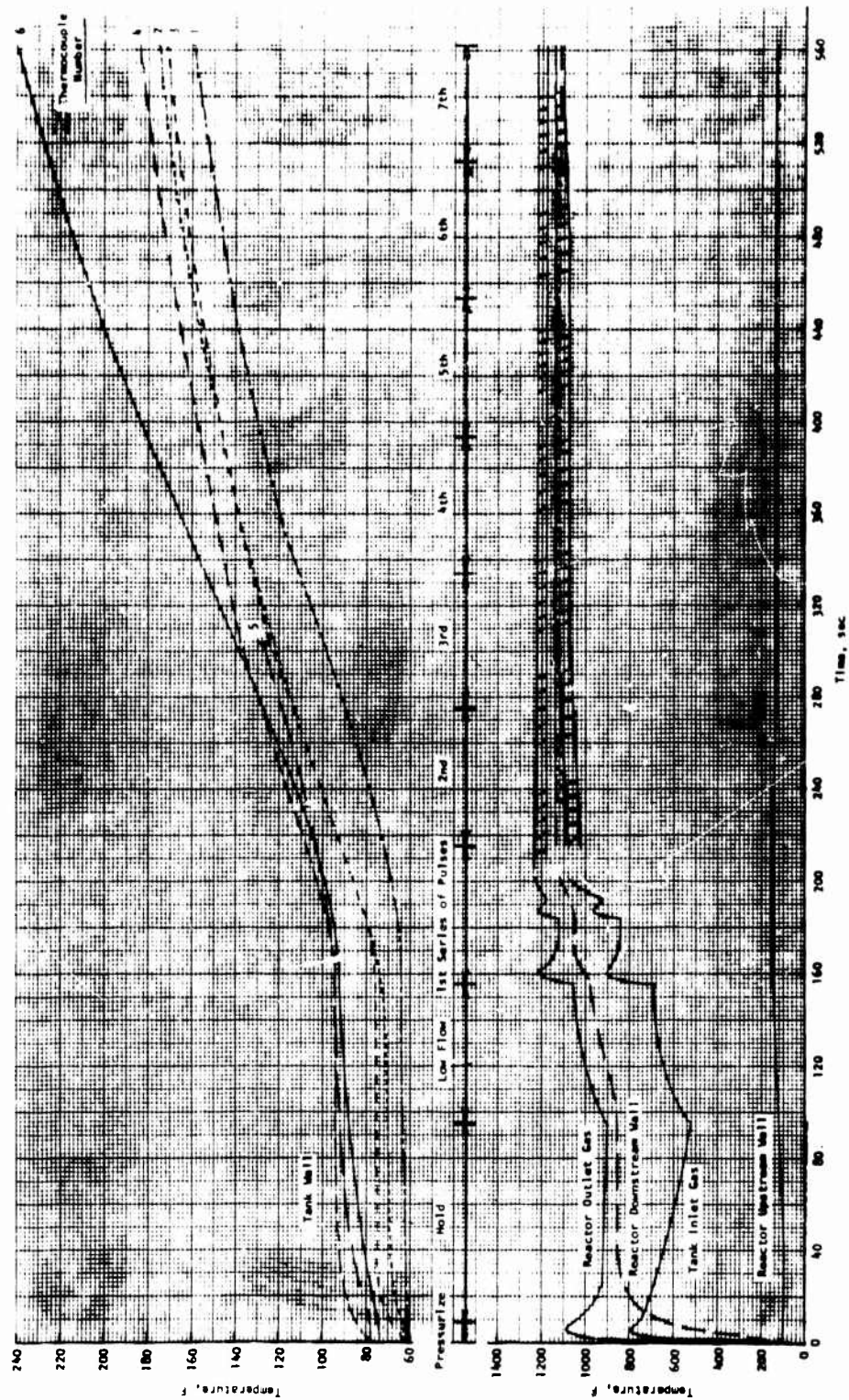


Figure 149. Test Temperature Transients

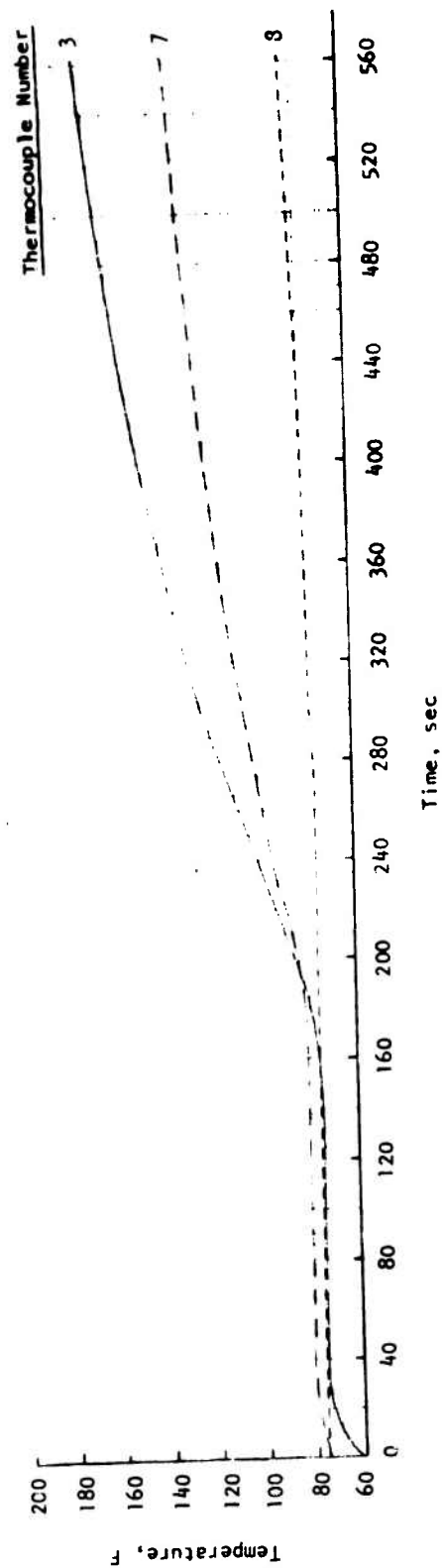


Figure 150. Tank Wall Temperature Transients for Test 3

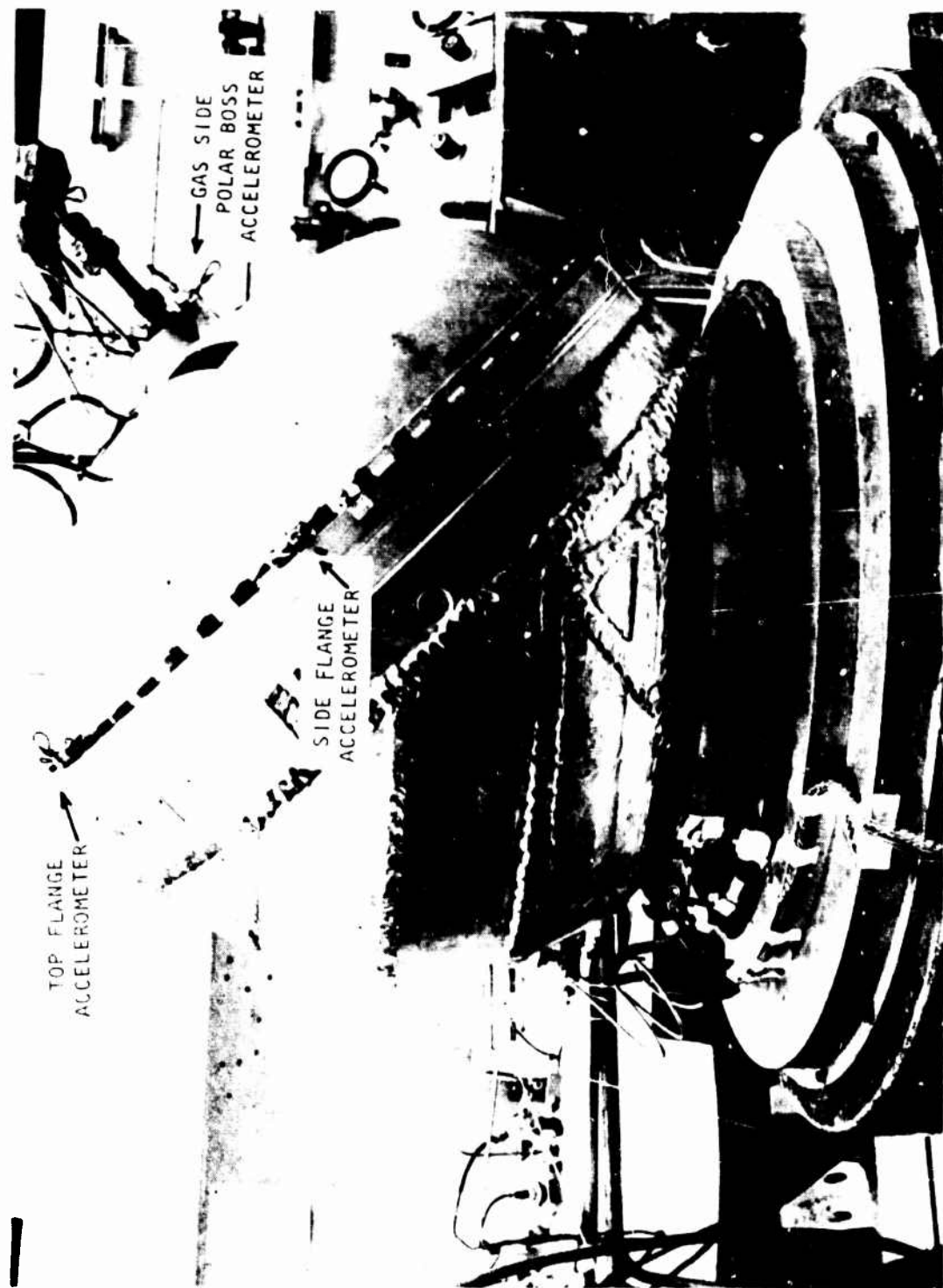
Diaphragm Structural Dynamic Test

A diaphragm was installed in the metal workhorse tank and subjected to vibration and shock environments at Rocketdyne's Engineering Development Lab during June 1979. The environments included ground random vibration with the tank unpressurized, and stage separation shock and Stage II/III flight random vibration with the tank pressurized.

Diaphragm structural dynamic response modes were determined and diaphragm strains resulting from the workhorse tank structural response were measured. Three cracks in the diaphragm, including one through-crack that permitted Freon leakage during Stage II/III vibration, developed as a result of fatigue. Since additional diaphragm vibration tests were deleted, the effects of using the workhorse instead of the flightweight tank were not determined. Also, although the dynamic environments were derived from MX requirements, they were applied as inputs rather than response environments, which increased the test levels. Finally, the unintentional presence of a non-condensable gas on the liquid-side of the diaphragm may have contributed to the failure.

Test Fixture. The one-piece welded test fixture was designed and fabricated from magnesium plate and bar stock by Kimball Industries (Monrovia, California). A photograph of the fixture is presented in Fig. 151. The tank is shown mounted in the fixture with the polar axis at 45 degrees to the shaker. With the tank oriented in this manner, two axes were tested simultaneously. Since the tank and diaphragm are symmetrical about the polar axis, it was not considered necessary to test in the third axis.

Single-axis input tests are more conventional, but the selected test method minimizes costs associated with fixture fabrication, test setup, and test time. In addition to cost benefits, two-axes tests more closely simulate flight conditions since all axes are excited simultaneously.



1XZ69-b/25/79-C1B

Figure 151. Shock/Vibration Test Setup

The disadvantage is that confidence has been developed in multiple single-axis testing because, historically, hardware that survived these types of tests has performed satisfactorily in flight.

Control Method. Initially, the tests were to use response limiting rather than controlling the input to the tank at the fixture. Response limiting implies adjusting the input such that the envelope of response peaks of accelerometers on the tank matches the required environment. This is the control method used on the MX program. Because of cost reasons and to be consistent with the control methods used on the other AFRPL feed system technology programs, it was decided to control to an accelerometer on the fixture. It should be noted that controlling the input resulted in higher tank responses than response-limiting control.

Test Results. The diaphragm was sized to the tank shell with gas at 53 psig. The pressurant and propellant sides of the tank were then evacuated. After bleeding Freon (3.5 lb) into the lines and tank, the tank was evacuated again. This procedure was used as a means of ensuring that virtually all the noncondensable gas was removed.

The tank was loaded to 90.7 percent of capacity with Freon-113. The resulting pressure was 7.5 psig, indicating the presence of non-condensable gas. This was unexpected because extreme care was taken to seal the fittings. Subsequent calculations indicated that sufficient gas could have been in solution in the Freon to cause the observed pressure. This gas would come out of solution when the Freon was pumped into the evacuated tank. Prior to conducting the ground random vibration test, the pressure slowly decayed to 7.2 psig, possibly indicating that some gas was going back into solution.

Five-step computer controlled equalization to full level ground random vibration was then initiated. A minor problem was encountered prior to reaching full level and the test was terminated. Although the test lasted for only a couple of minutes at very low levels, the liquid-side pressure decayed from 7.2 to 5.4 psig.

Full level was achieved on the second attempt after approximately 11 minutes of automated equalization. Approximately seven minutes at full level were required to bring the control accelerometer within the specified tolerance band (+3 db, -1.5 db). While plotting power spectral densities (PSDs) at full level, it was noticed that the input appeared to be too high, in spite of the analyzer indicating that conditions were within tolerance. The test was therefore terminated after 26 minutes and 31 seconds at full level. The problem was associated with patch-board wiring and no over-testing actually occurred.

The pressure dropped from 5.4 to -0.1 psig during this portion of the test. Since the gas bubble would have been at the top of the tank, away from all fittings, and leakage through the tank o-rings is extremely unlikely, a substantial amount of gas apparently went into solution. The only other explanation for this drop in pressure would be a large leakage of Freon and no leakage was observed.

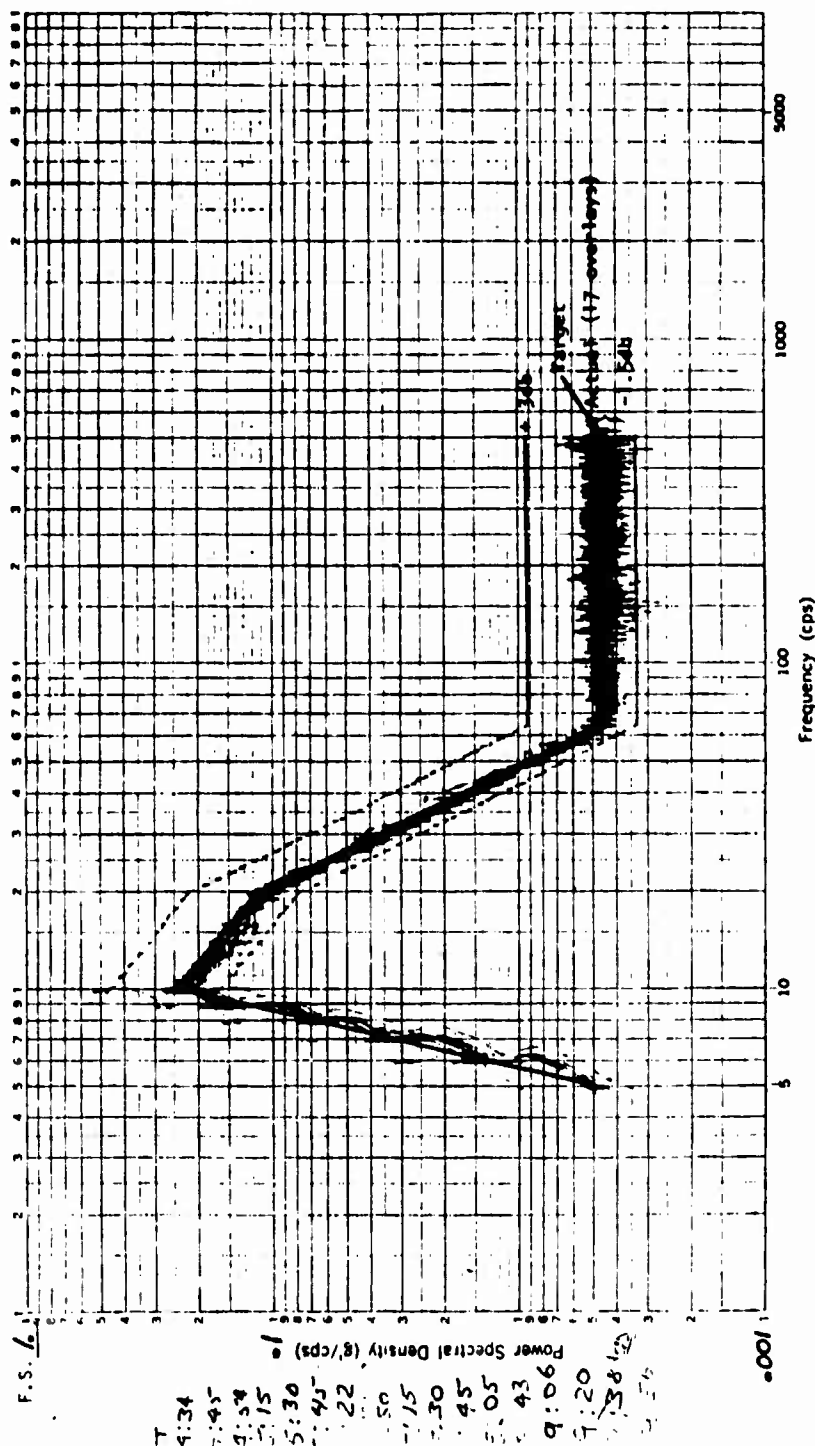
The automated equalization sequence was repeated and the test was continued until 3 hours was accumulated at full level. The test was then continued the next day.

On the second day of testing, the equalization sequence was repeated twice, once at the start and again 2 hours of testing. The test was interrupted after 2 hours to conduct a routine fitting inspection. There were no diaphragm leaks at the conclusion of 10 hours of accumulated full level ground random vibration. The PSDs plotted during the test are shown in Fig. 152 through 160 for the tank accelerometers. The locations and directions of accelerometers are noted in Table 42, along with acceleration meter readings (g rms). This tank data is presented as a reference to indicate the input to the diaphragm, whose response is the real objective of this test.

Three 45 degree strain gage rosettes were attached to the propellant-side of the diaphragm along the meridian containing the highest point above the shaker. One was at the polar axis and the other two at the two chem-mill steps closest to the polar axis. The gages were oriented to measure strain along the meridian and normal to it. The maximum strain during ground random vibration was 22 μ -in./in. peak, which is equivalent to 216 psi peak stress. This level is too low to cause any damage, even for 10 hours duration.

Prior to running the stage separation shock test, the automated equalization sequence was verified for both launch and post-boost propulsion system (PBPS) random vibration. Full level launch vibration was achieved in 2 minutes and run for several seconds. It also took 2 minutes to reach full level PBPS vibration, which was run for 42 seconds.

Run = 3 ^{Time} LWFS-04
 Axis V Accel Loc. C4V Axis V
 Date 6/24/9 Grms 2.24



Frequency Bandwidth 15 Hz. No. Averages 64

Figure 152. Control Accelerometer Response (Fixture Base, V)

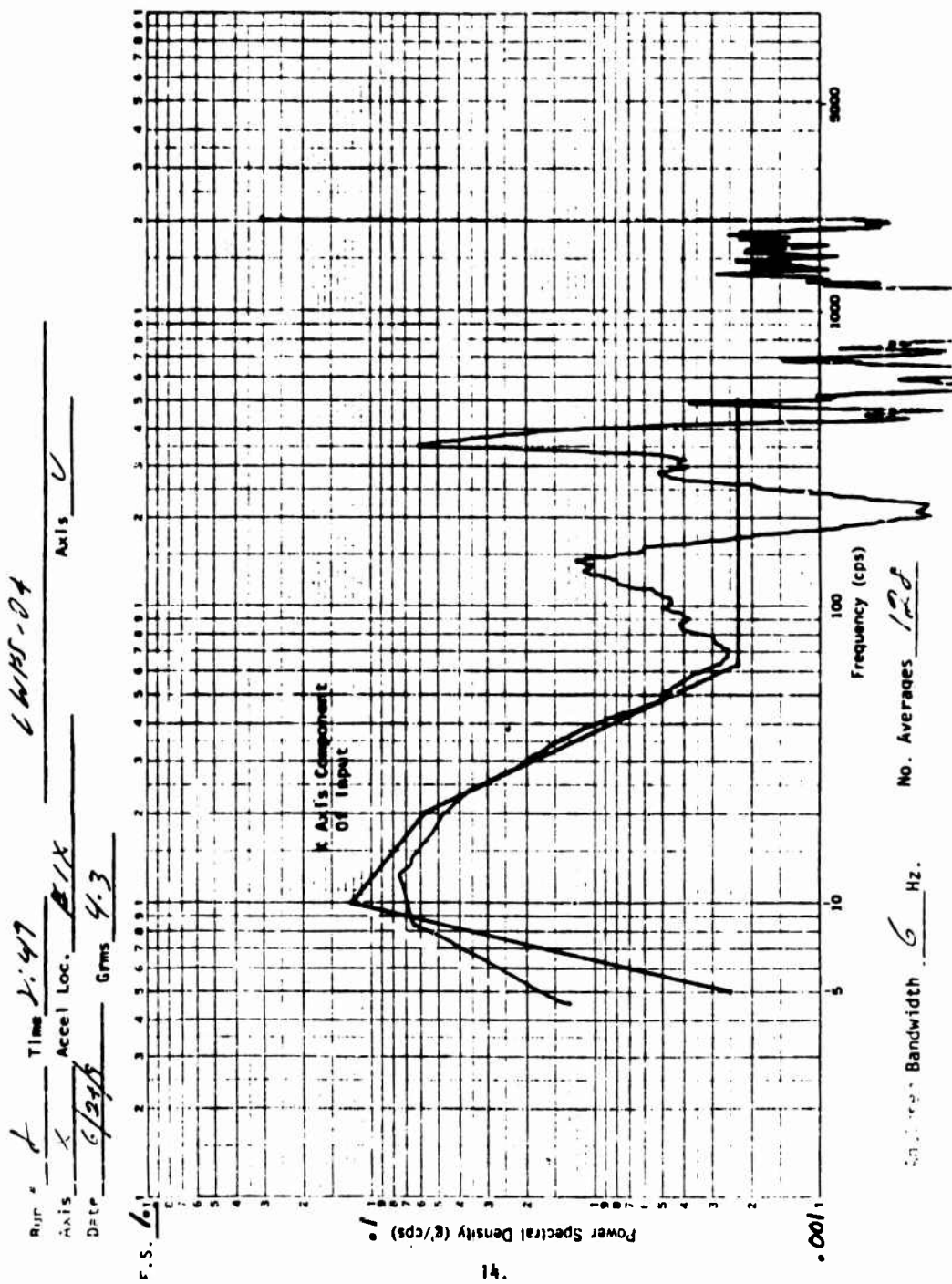


Figure 153. Response of Flange at Top (X axis)

Run # 8 Time 2:50 CWIS-04
 Axis Y Accel Loc. 124 Axis ✓
 Date 6/24/68 Grms 8

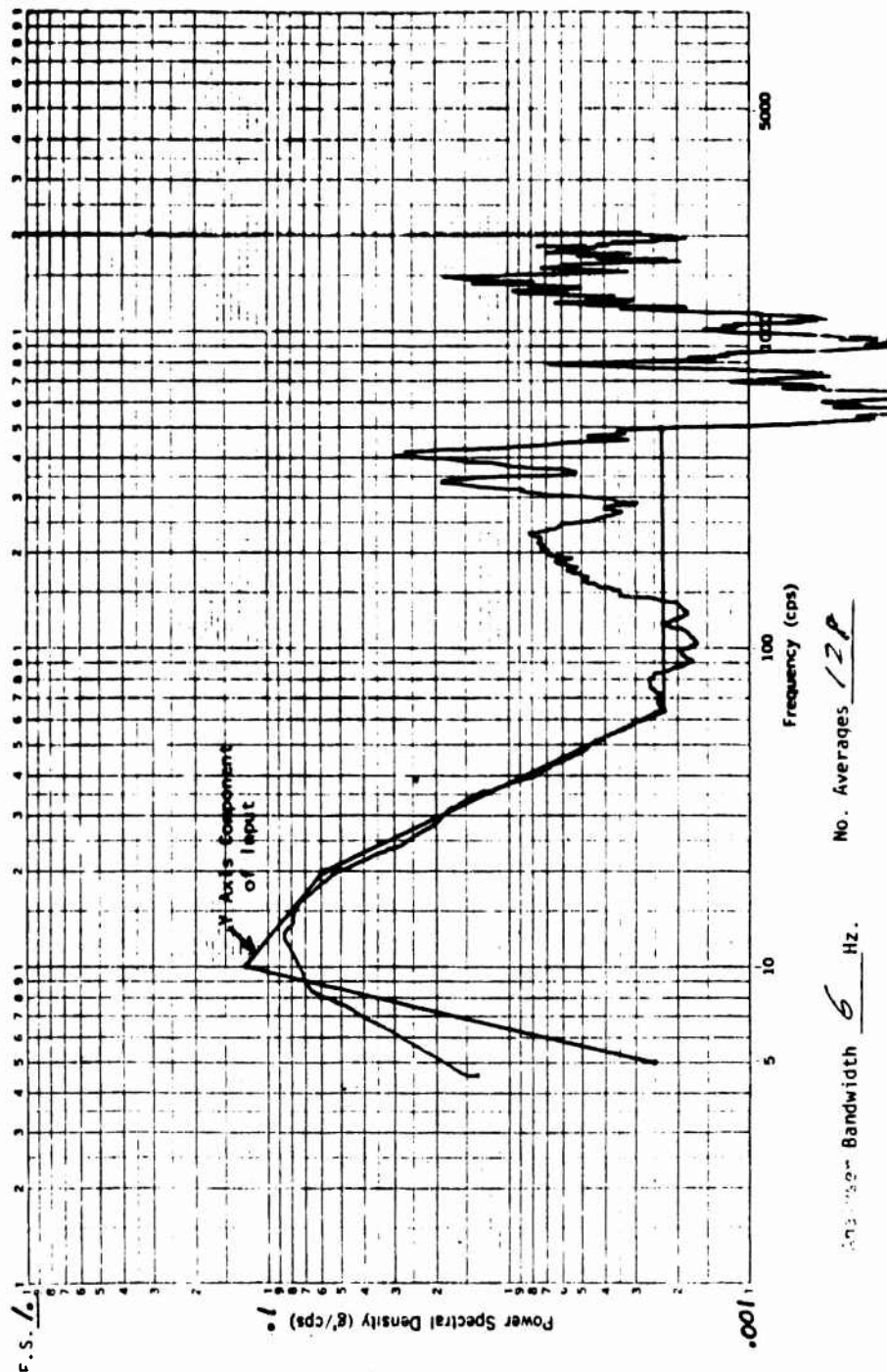


Figure 154. Response of Flange at Top (Y axis)

Pur # 8 Time 9:02 LT. JTF-04
 Axis X Accel Loc. F13X Axis ✓
 Date 5/24 Grms 4.2

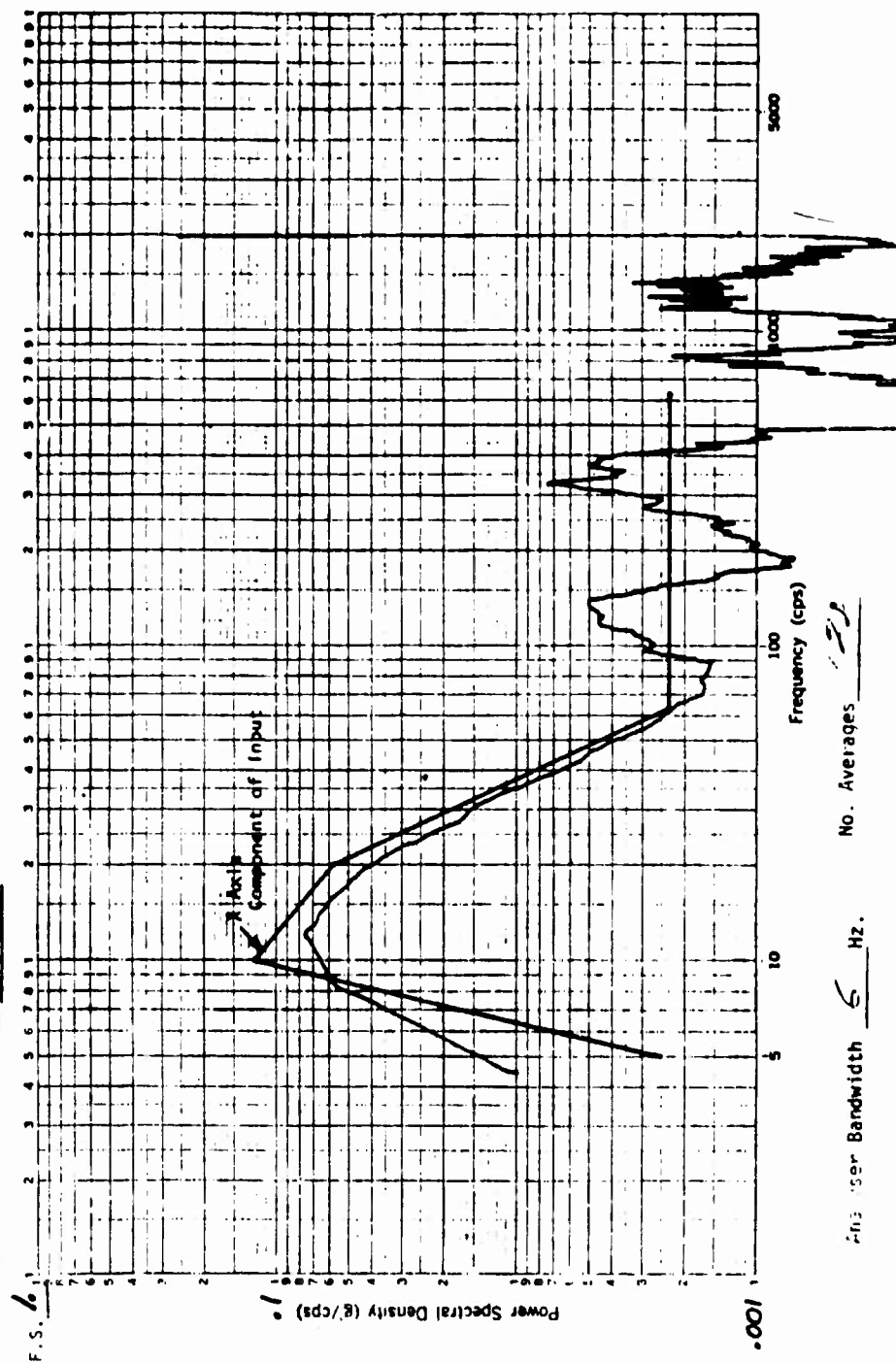


Figure 155. Response of Flange at Side (X axis)

Run # 5 Time of Day LTF5-04
 Axis Y Accel Lvl: F14Y Axis V
 Date 6/20/5 Grms 4

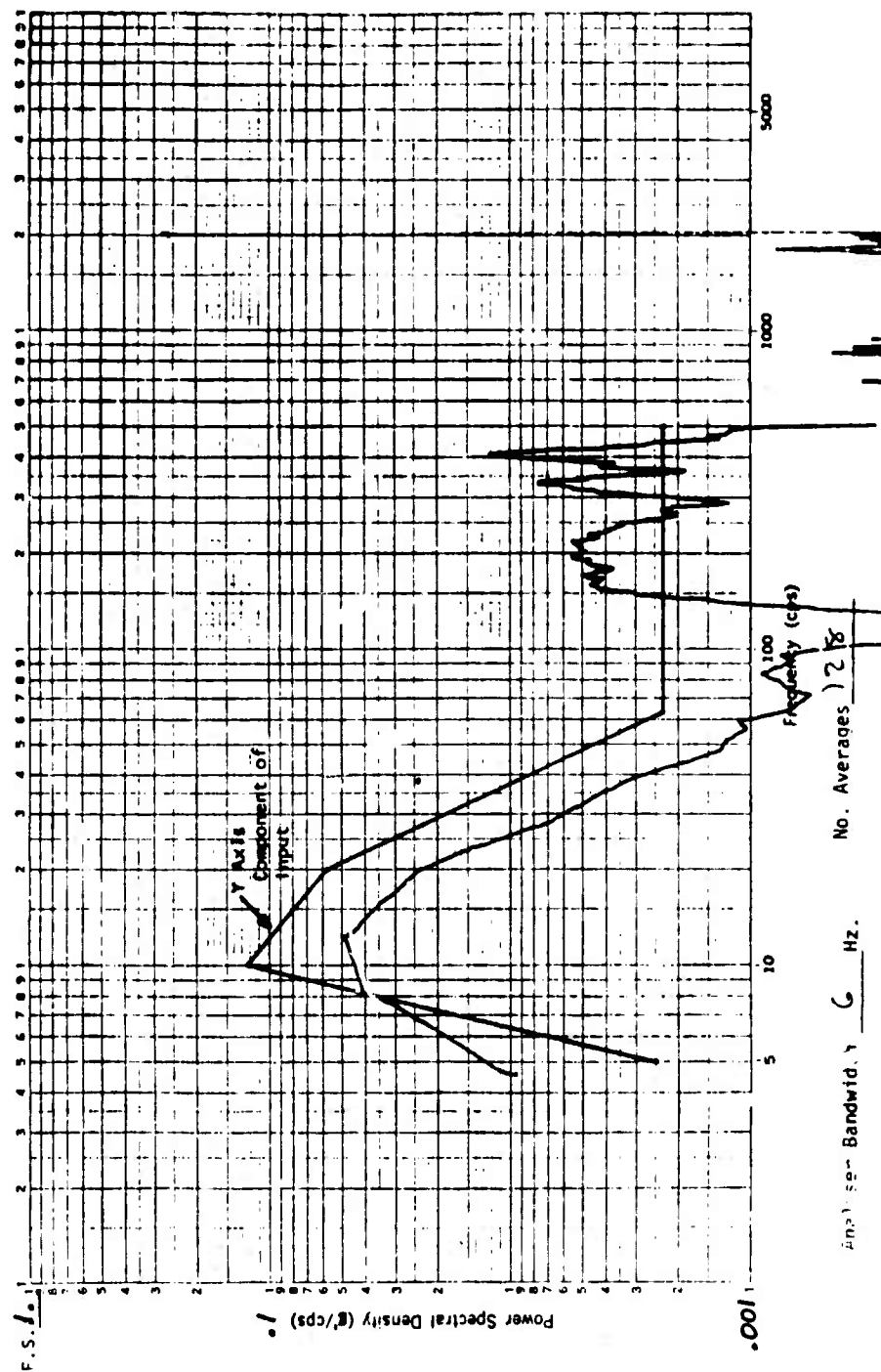


Figure 156. Response of Flange at Side (Y axis)

Cur. # 8 Time 8:31 LWFS-09
 Axis Y Accel Loc. RTX Axis ✓
 Date 11-24-59 Grms 17

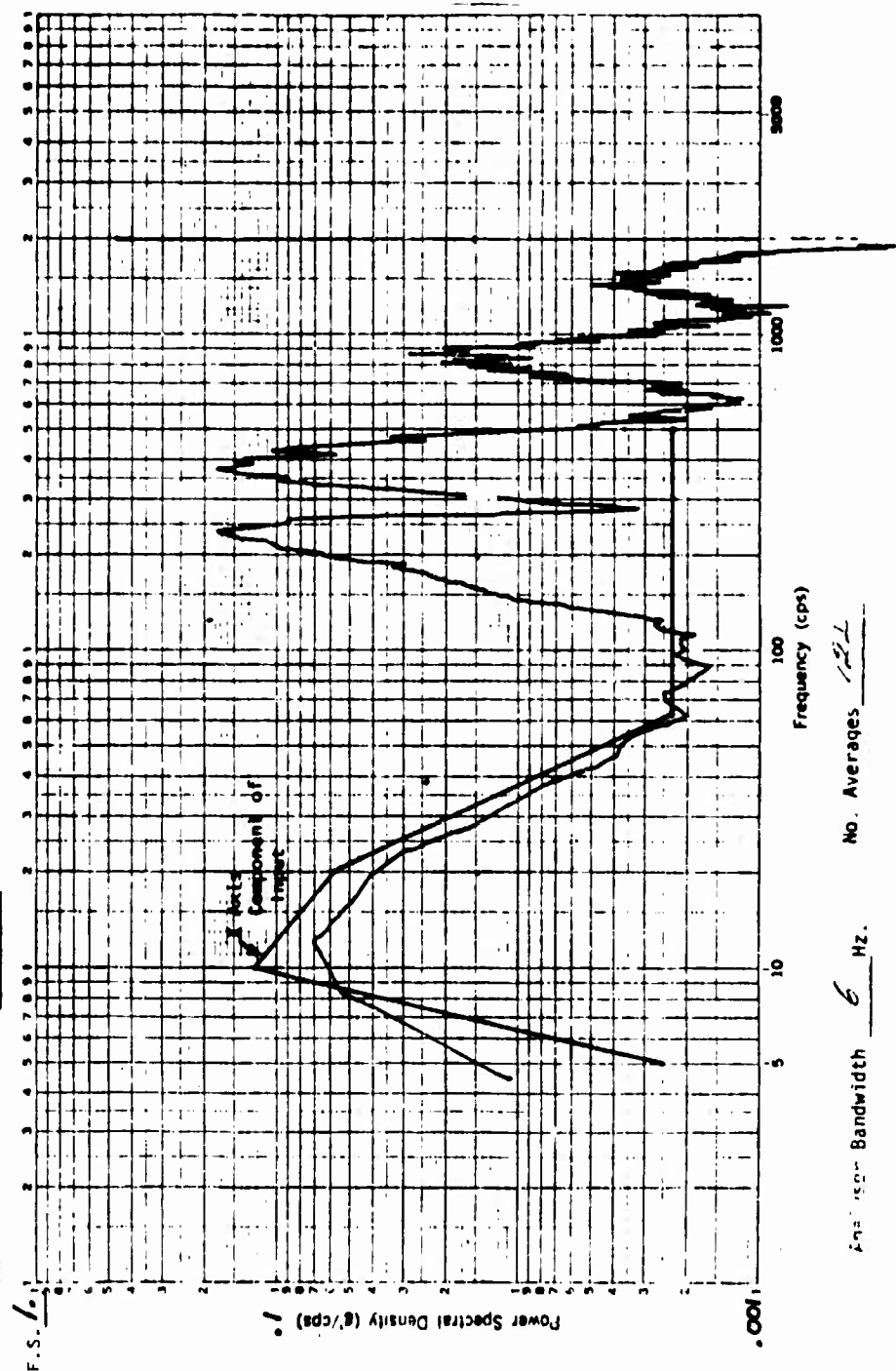


Figure 157. Response of Gas Side Polar Boss (X axis)

Run: 8 Time 0:39 0205.04
 Axis Y Accel Loc. 104 Axis U
 Date 6/24/69 Gms 17

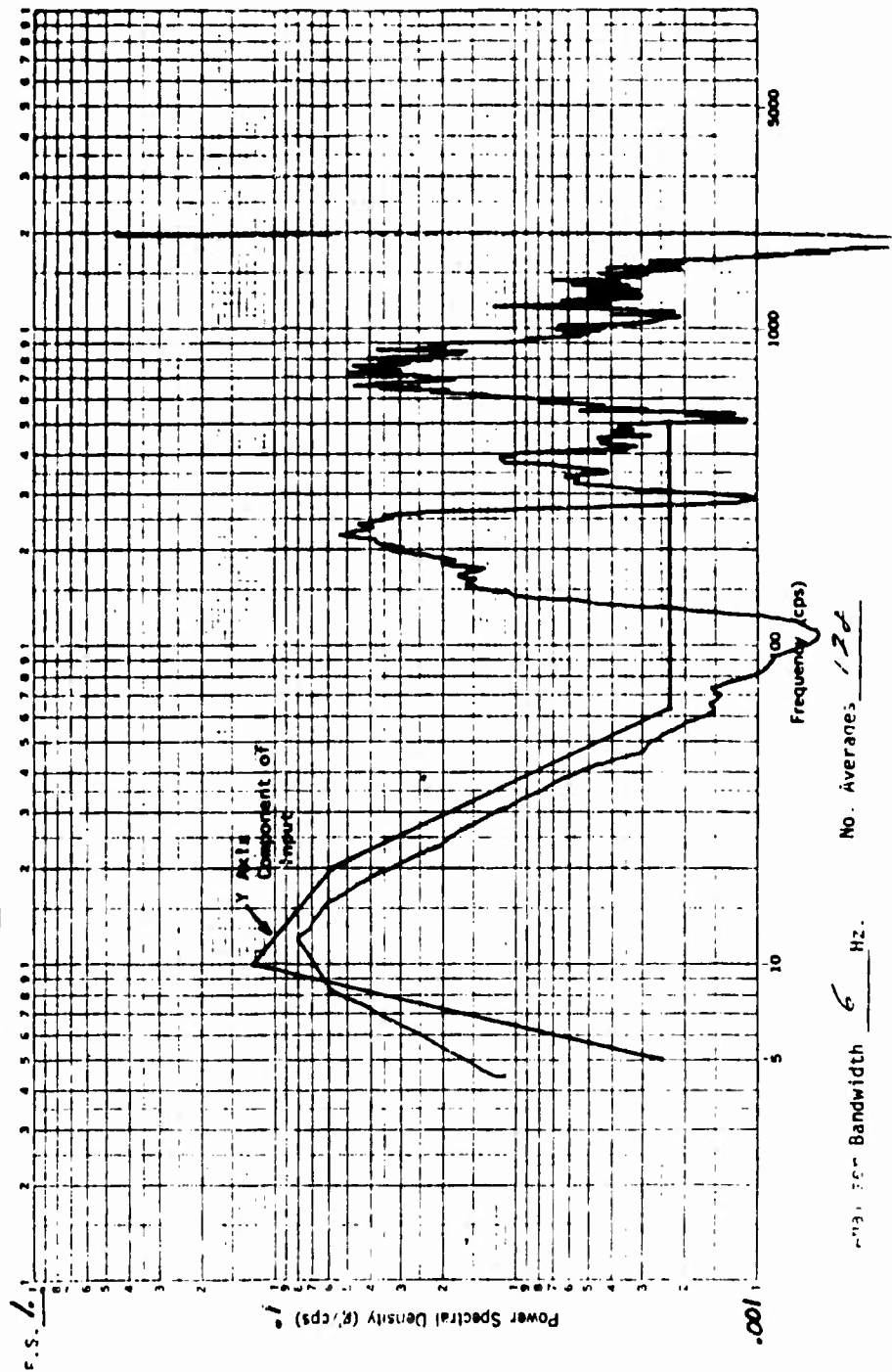
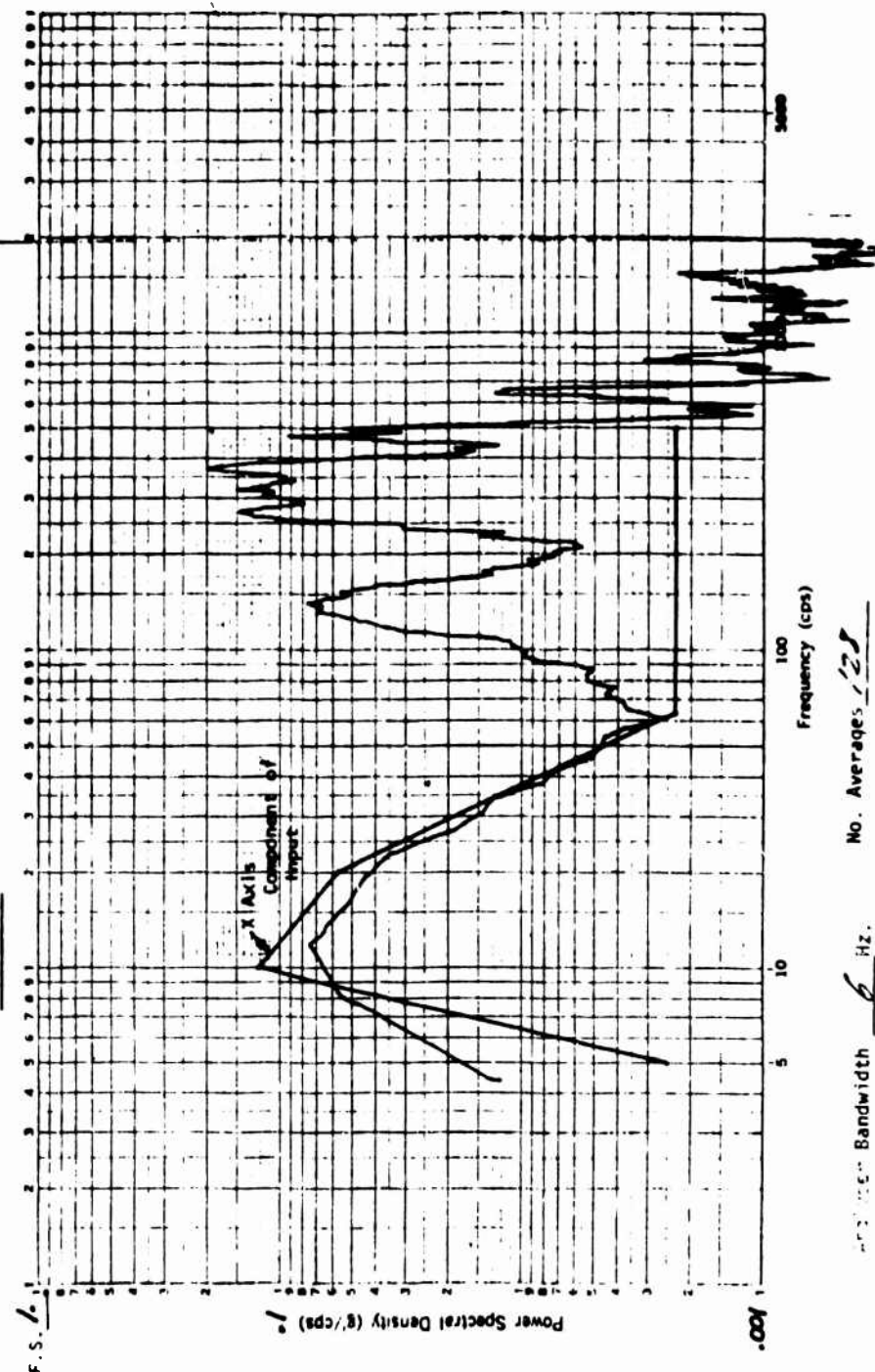


Figure 158. Response of Gas Side Polar Boss (Y axis)

Run - 1 Time 8:54 LINKS-09
 Axis 1 Accel Loc. R10X Axis U
 Date 6, 24/6 Grms 15



No. Averages 128

Bandwidth 6 Hz.

Figure 159. Response of Liquid Side Polar Boss (X axis)

Run # 2 Time 8:38 1265-04
 Axis Y Accel Loc. F11Y Axis V
 Date 6/24/9 Grms 7

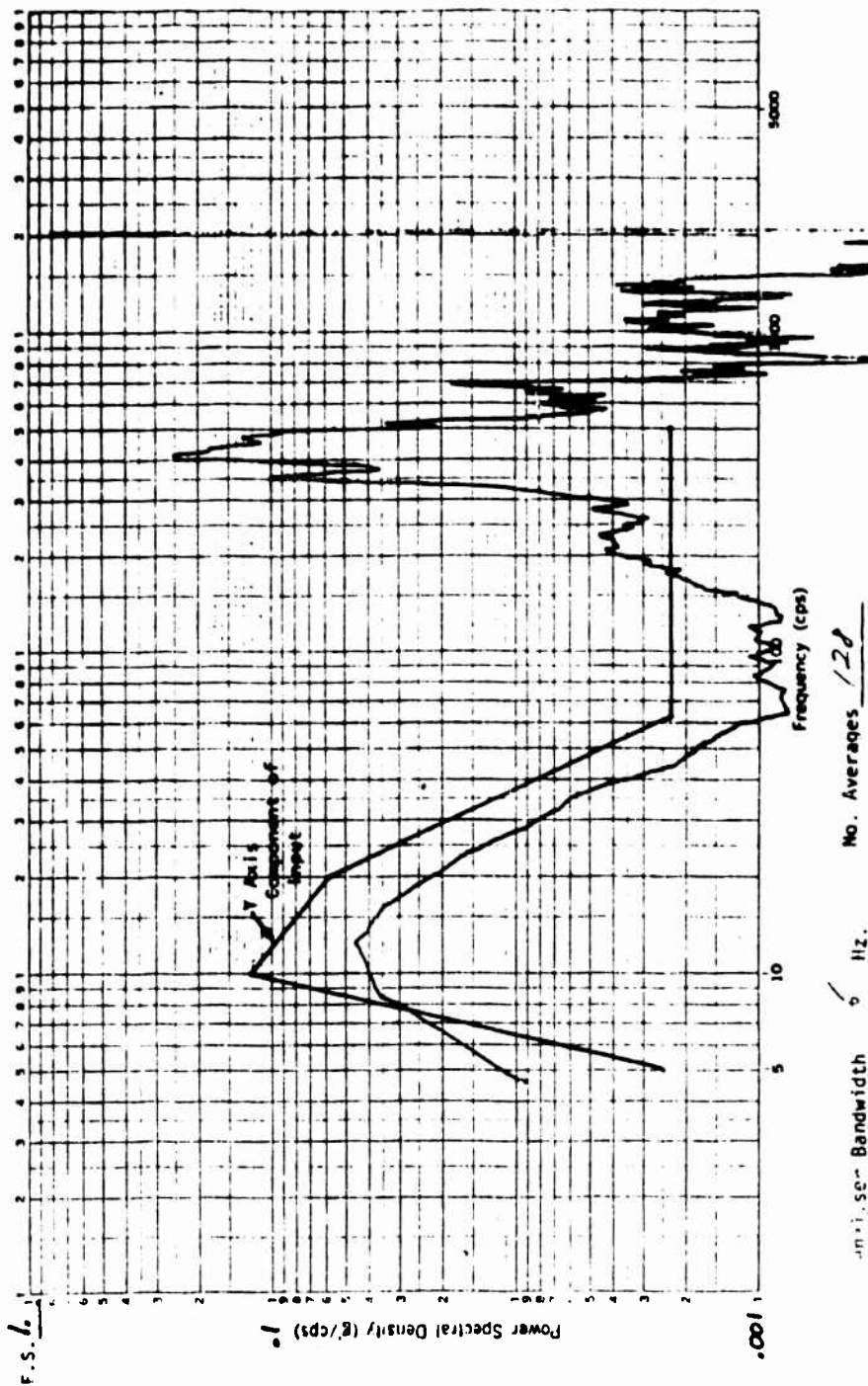


Figure 160. Response of Liquid Side Polar Boss (Y axis)

TABLE 42. GROUND RANDOM VIBRATION ACCELERATION LEVELS

LOCATION	AXIS	ACCELERATION (grms)	
		AT 1 HOUR	AT 9 HOUR
FIXTURE BASE	V* (SHAKER VERTICAL)	2.2**	2.2**
	W	4.	-
	Z (SAME AS TANK OFF AXIS)	3.5	-
FLANGE AT TOP	X (TANK POLAR)	4.5	4.3
	Y	8.5	8.
	Z (TANK OFF-AXIS)	4.5	-
FLANGE AT SIDE	X	4.5	4.2
	Y	4.2	4.
	Z	6.	-
GAS SIDE POLAR BOSS	X	20.	17.
	Y	20.	17.
	Z	18.	-
LIQUID SIDE POLAR BOSS	X	15.	15.
	Y	7.	7.
	Z	6.	-
*THE TANK X AND Y AXES ARE THE COMPONENTS OF THE SHAKER V AXIS **THESE VALUES CORRESPOND TO A SMALL BANDWIDTH, APPROXIMATELY 0-600 Hz. ALL OTHERS CORRESPOND TO A BANDWIDTH EXCEEDING 10 KHz			

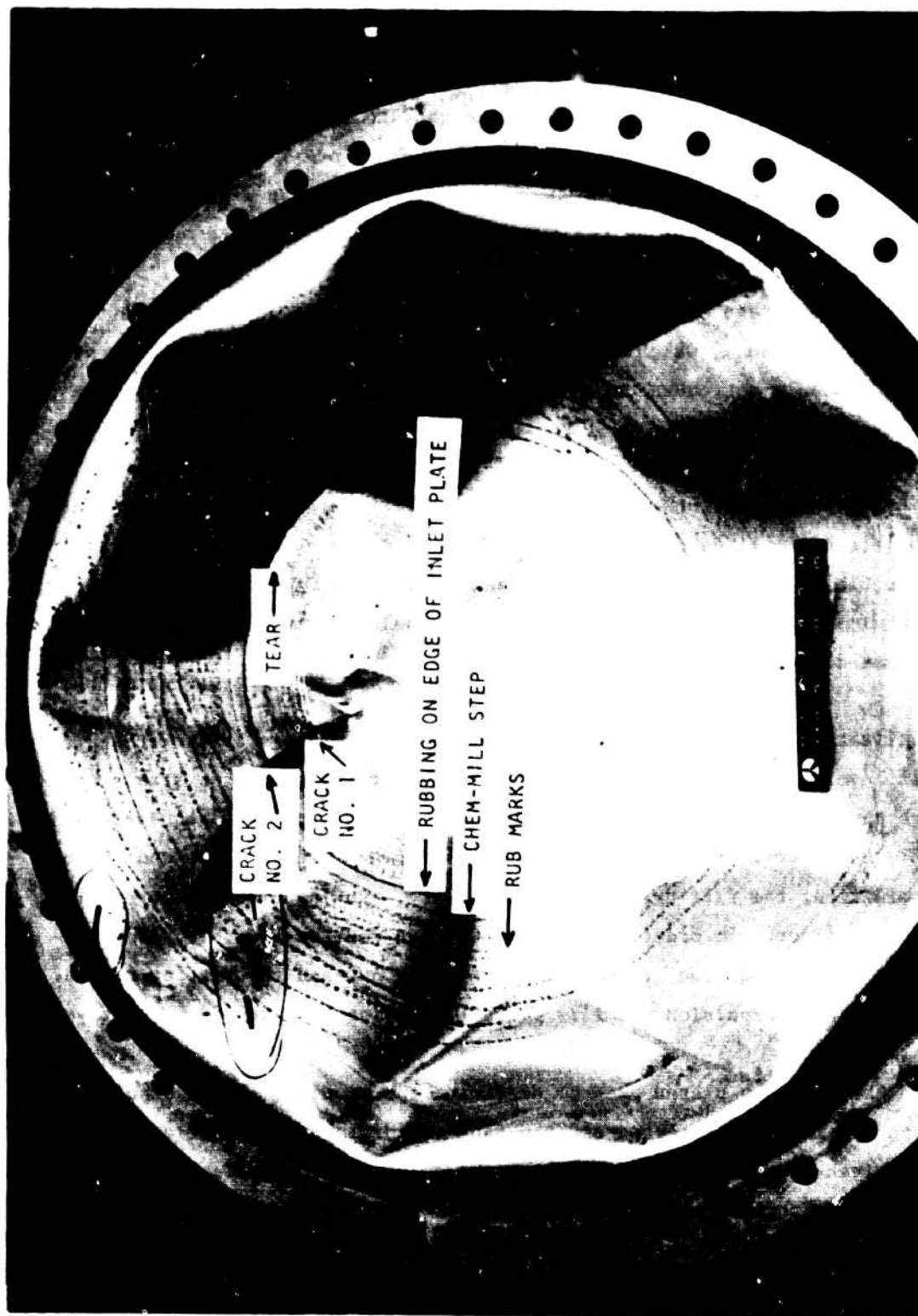
Several "1/10 - level" stage separation shocks were run while adjusting the potentiometer sliders to achieve equalization. Two "1/5 - level" shocks were also run prior to pressurizing the tank to 50 psig. After pressurization, the maximum shock capable with the shaker (overloading the power amplifier) was run. No Freon vapor was detected during a partial venting of the pressurant, indicating the absence of any leaks in the diaphragm.

The highest strain at low frequency during the separation shock was 380 μ -in./in. peak, which corresponds to 3800 psi peak stress. This stress would probably not cause any fatigue damage since only four cycles were observed.

At high frequencies, the highest strain was 180 μ -in./in. peak (1800 psi peak stress). Although this level is not of concern and only occurred for one cycle, the full shock level was not achieved at frequencies above approximately 110 Hz. A full-level shock could potentially cause bladder fatigue damage.

Equalization of launch random vibration took two minutes. After reaching full level, a Freon leak was noticed at the fitting where the strain gage wire pass-through was located. Termination of the test was requested and achieved after 22 seconds at full level. Approximately 0.5 seconds before termination, the fitting came completely off, causing Freon to be expelled onto the floor. In order to stop the flow as fast as possible, the pressurant was vented, the strain gage wires were cut and the fitting capped. The resultant expulsion was 11.7 percent, leaving the tank 79 percent full.

When the tank was pressurized to determine the amount of Freon expelled, a diaphragm leak was detected and the tank was drained. Inspection revealed a 1/4 inch through-crack (tear) near the point where the diaphragm rubbed against the edge of the inlet diffuser plate. This through-crack also had a short crack normal to it. There were also two sets of intersecting cracks in another area near the tear. These cracks and the through-crack are shown in Fig. 161 to 164. The dark concentric rings on the diaphragm shown in Fig. 161 and 165 indicate where it was rubbing against the tank.



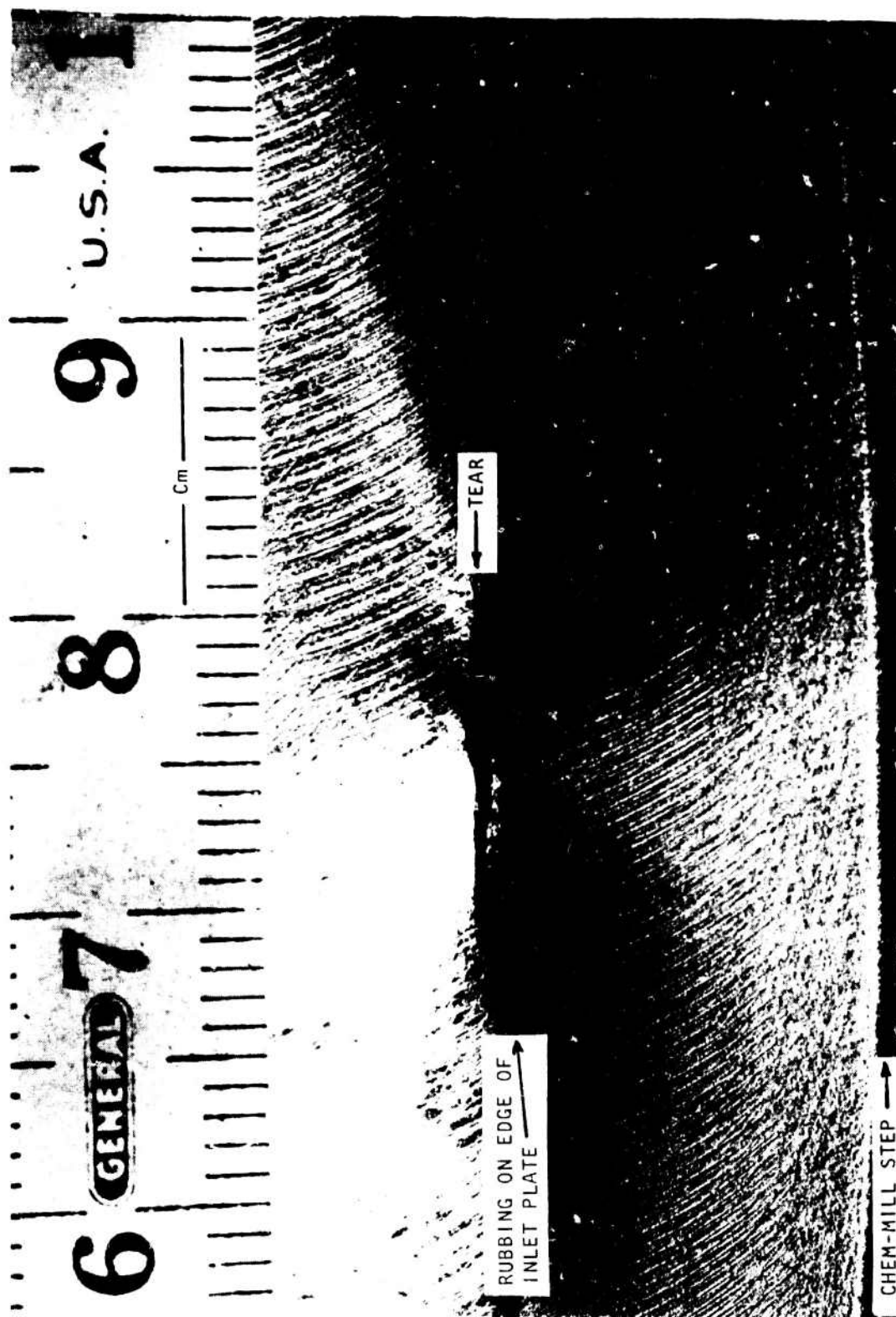
1XZ65-6/27/79-C1A

Figure 161. Post-Test View of Diaphragm



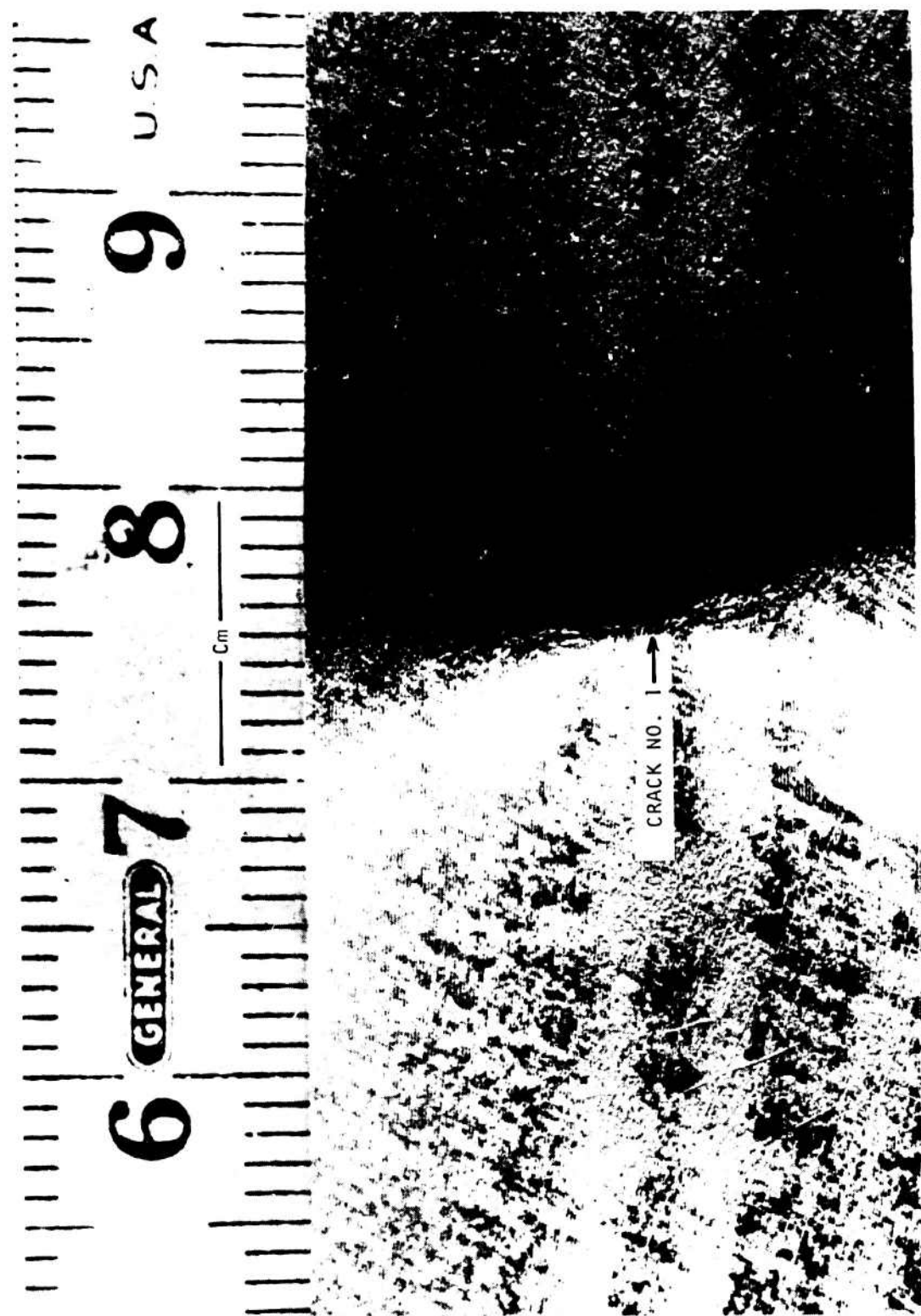
1XZ65-6/27/79-C1E

Figure 162. Post-Test View of Tear and Cracks



1X265-6/27/79-CID

Figure 163. Post-Test View of Tear



1XZ65-6/27/79-CLC

Figure 164. Post-Test View of Crack No. 1



1XZ65-6/27/79-C1B

Figure 165. Post-Test View of Rub Marks

The control accelerometer response is presented in Fig. 166. The composite level was 15.1 g rms, the maximum capability of the shaker. This corresponds to 10.7 g rms in each of the two tank axes. As during the ground random vibration test, the highest tank responses were measured on the liquid side polar boss. The X and Y axes responses were 45.1 and 56.9 g rms, respectively.

The highest strain gage readings were 144, 133, 120 and 104 μ -in./in. rms for the gages whose power spectral densities are presented in Fig. 167 through 170. As shown, the bladder response rolled off beyond 225 Hz. The maximum peak strain was 650 μ -in./in., which corresponds to 6500 psi peak stress. This level, when coupled with factors associated with folds in the aluminum, is sufficient to cause fatigue cracks for the subject test durations.

Metalurgical Evaluation. Crack initiation and propagation was confirmed to be due to fatigue, however the fold lines undoubtedly accelerated the failures by creating stress concentrations. The primary and cross crack patterns were oriented along compound folds that were formed like saddles. The three failure points were located along two meridionally oriented folds located in the middle of two of the "lobes" that typically form during diaphragm reversal (Fig. 161).

In order to determine if folds could cause cracks without being exposed to vibration, a diaphragm that had been expelled in the plastic tank and accidentally partially reversed again at AETL, was examined. Although numerous severe folds of several shapes were created, as shown in Fig. 171, no cracks were found. It was therefore concluded that the severity of the folds was insufficient to cause the cracks.

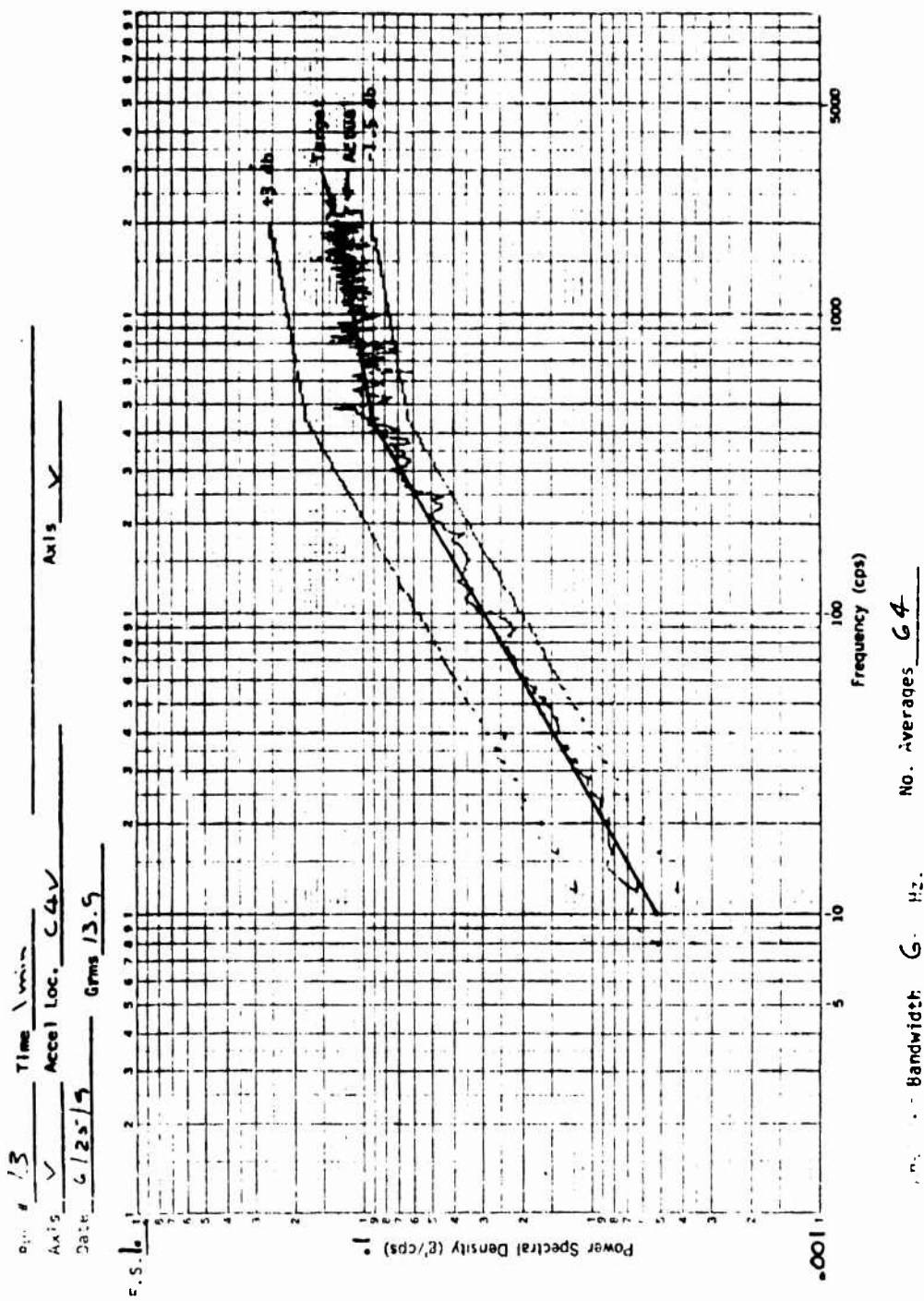


Figure 166. Control Accelerometer Response (Fixture Base, V)

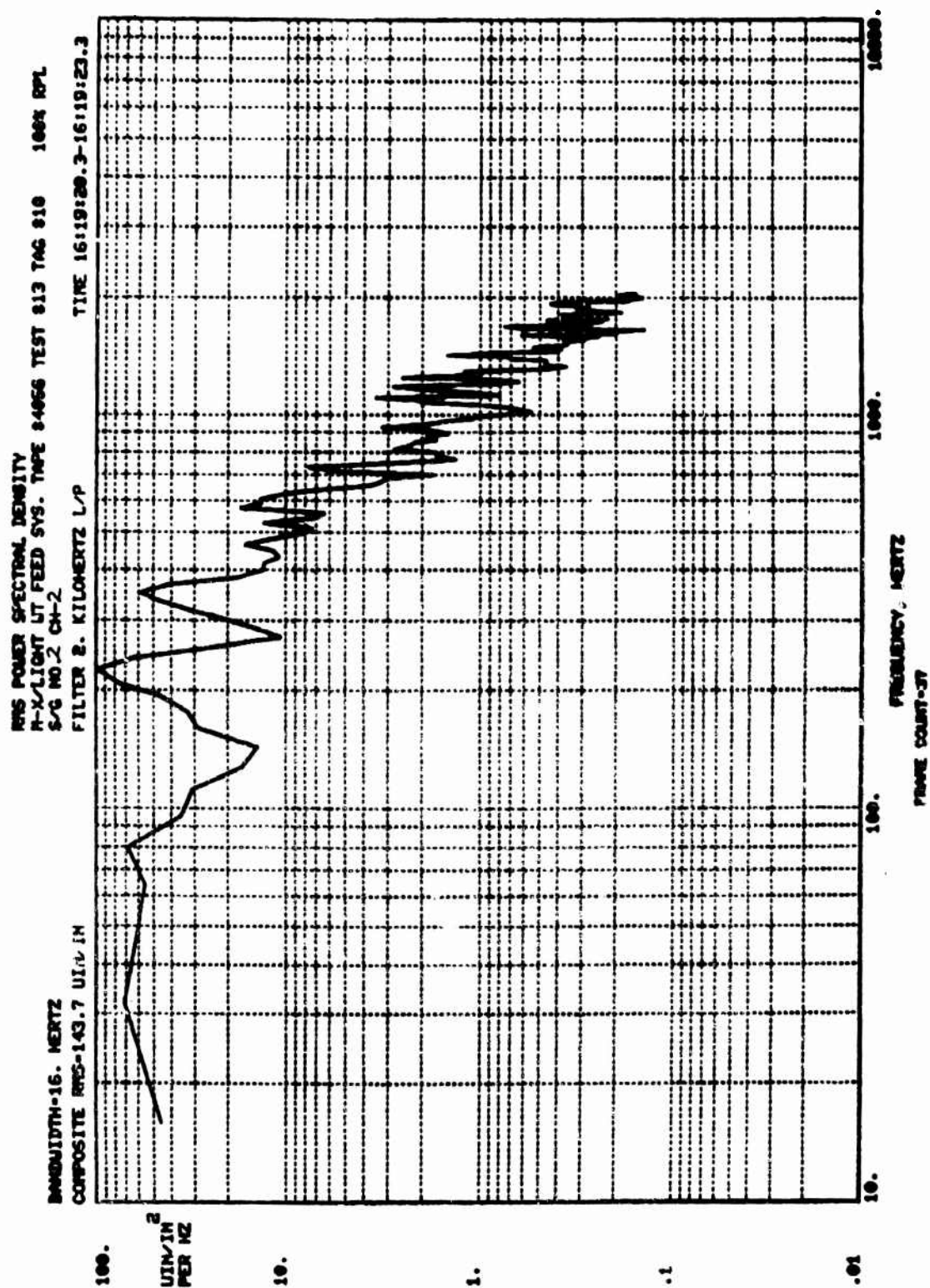


Figure 167. Strain Gage 2 PSD

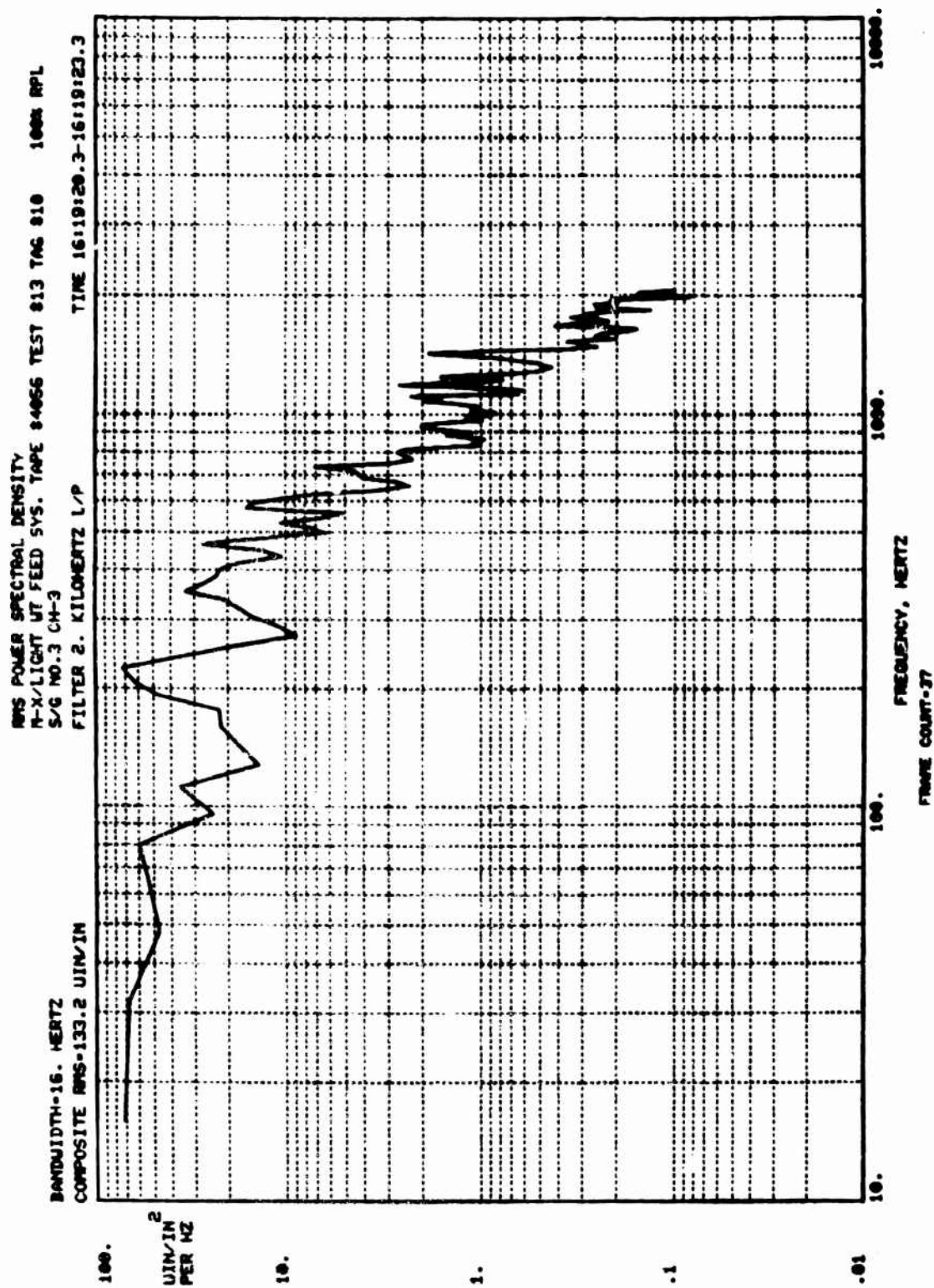


Figure 168. Strain Gage 3 PSD

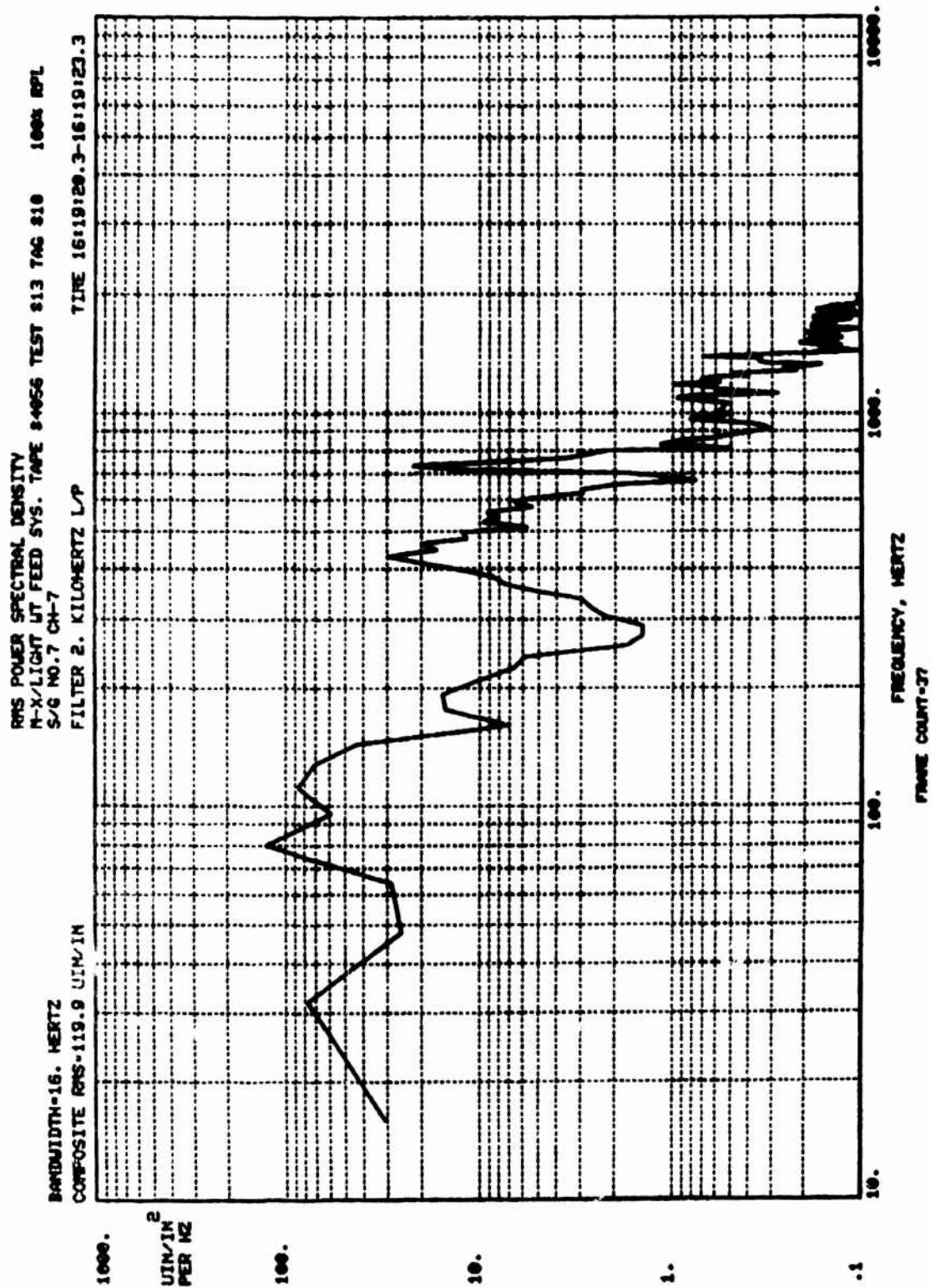


Figure 169. Strain Gage 7 PSD

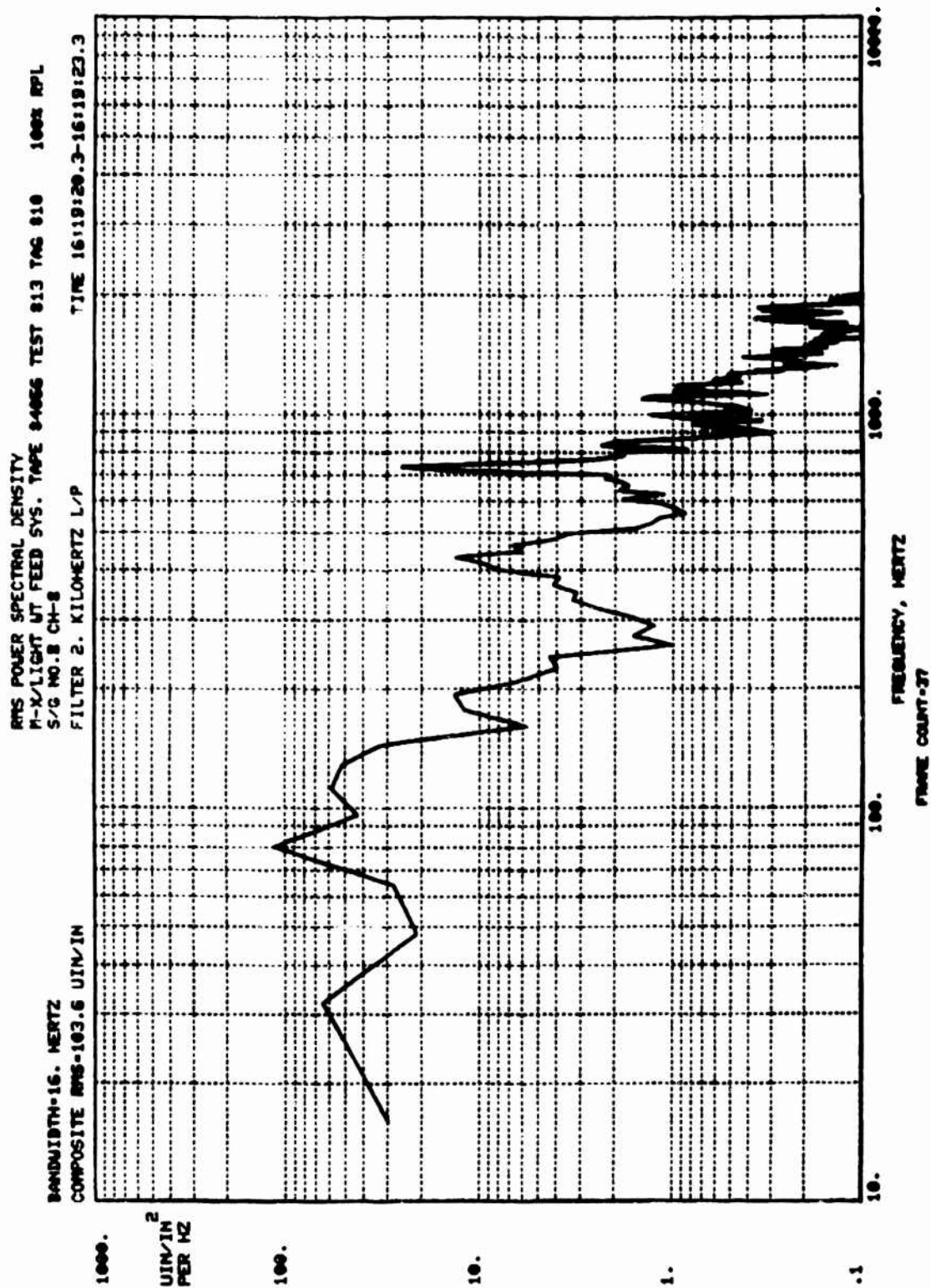


Figure 170. Strain Gage 8 PSD



18Z65-7/9/79-C1D

Figure 171. Compas 2 Diaphragm

Further metalurgical evaluations failed to provide any evidence of abnormal material properties that would have an appreciable effect on fatigue life. The hardness close to the cracks was the same as that in an area of the bladder that had not been deformed (R = 56 vs 58), although hardness is admittedly difficult to measure on thin, annealed 1100 aluminum. Also, there was no evidence of thinning. The aluminum exhibited a normal structure and conformed to MIL-A-250/1 composition except the copper content was less than 0.05 to 0.20. The yield and ultimate strengths were 7.2 and 9.9 ksi, respectively, for 0.25 inch wide specimens. This ultimate strength is lower than MIL-A-250/1 (11 to 15.5 ksi), but the values are not directly comparable because the standard is based on 0.5 inch specimens. If not attributable to specimen size, the low ultimate strength might be due to the low copper content. The elongation was 22.3 percent in one inch, compared to 25 percent in two inches per MIL-A-250/1.

Since potential diaphragm fatigue-life problems related to vibration of 1100-0 aluminum had been identified during the metal workhorse tank vibration test and other AFRPL feed system technology contracts, it was decided to resolve the problem by changing the scope of one of the other contracts, and additional diaphragm structural dynamic tests were deleted from this contract.

FLIGHTWEIGHT TANK

One flightweight tank was fabricated, proof and leak tested, expelled using the Tridyne pressurization subsystem, subjected to structural dynamic tests, and burst tested. Fabrication processes developed for Kevlar wrapping of the liner assembly in a heated environment are documented in the Materials Processing Development Section of this report. Experiments were conducted that demonstrated that laser holography is an extremely useful technique for locating unbonded regions between the tank liner and the composite wrap.

Since determination of the thermal characteristics of the flightweight propellant tank was of higher priority than the structural dynamic response of the composite-wrapped shell, the expulsion test with warm-gas pressurization was run first. Additional objectives of this test were: demonstration of the mechanical integrity of the diaphragm-to-liner EB weld, evaluation of the performance of the electronically controlled regulator, and confirmation of the expulsion efficiency data accumulated in the workhorse tank tests.

The structural dynamic tests were run to determine the response characteristics and demonstrate the mechanical integrity of the tank shell and mounting ring. A subsequent shell-burst test was run to determine the posttest design margin.

Tank Fabrication

The flightweight tank design and fabrication sequence were described in the Engineering Analysis and Design section of this report. Additional information related to the liner assembly, bi-metal joints, composite wrapping, and PSA weight are discussed in this section.

Liner Assembly. The two 5086 aluminum liners were draw formed by Aircraft Hydro-Forming (Gardena, CA) in the same manner as the metal workhorse half-shells. After rough machining at Rocketdyne, they were chem-milled, including the flow ribs in the outlet liner, by Aerochem (Orange, CA).

Final machining was then completed at Rocketdyne to prepare the inlet liner, shown in Fig. 172, for weld assembly of the components shown in Fig. 173. Figure 173 includes the leak detector, the vacuum service valve, and the threaded port substituted for the isolation valve.

After final machining of the polar boss region of the outlet liner, weld assembly was completed as presented in Fig. 174 and 175. Figure 175 shows the propellant fill valve and cap, and the threaded port substituted for the isolation valve.

After EB welding the diaphragm to the outlet liner (Electron Beam Welding, Los Angeles, CA), the weld was helium leak tested at 0.25 psig and a small hole was EB-weld repaired. The weld passed a subsequent leak check and dye-penetrant inspection. The outlet and inlet liners were then match-machined, EB welded (Fig. 176), helium leak checked, X-rayed and shipped to Defense Division of Brunswick Corp. (Lincoln, Neb) with the girth mounting bracket assembly shown in Fig. 177 for composite wrapping. Nine small flat spots on the liner surface, resulting from handling at Rocketdyne and/or Electron Beam Welding were documented. Although not visually detectable, they were located by rubbing. They did not have a detrimental effect on the wrap process or tank performance.

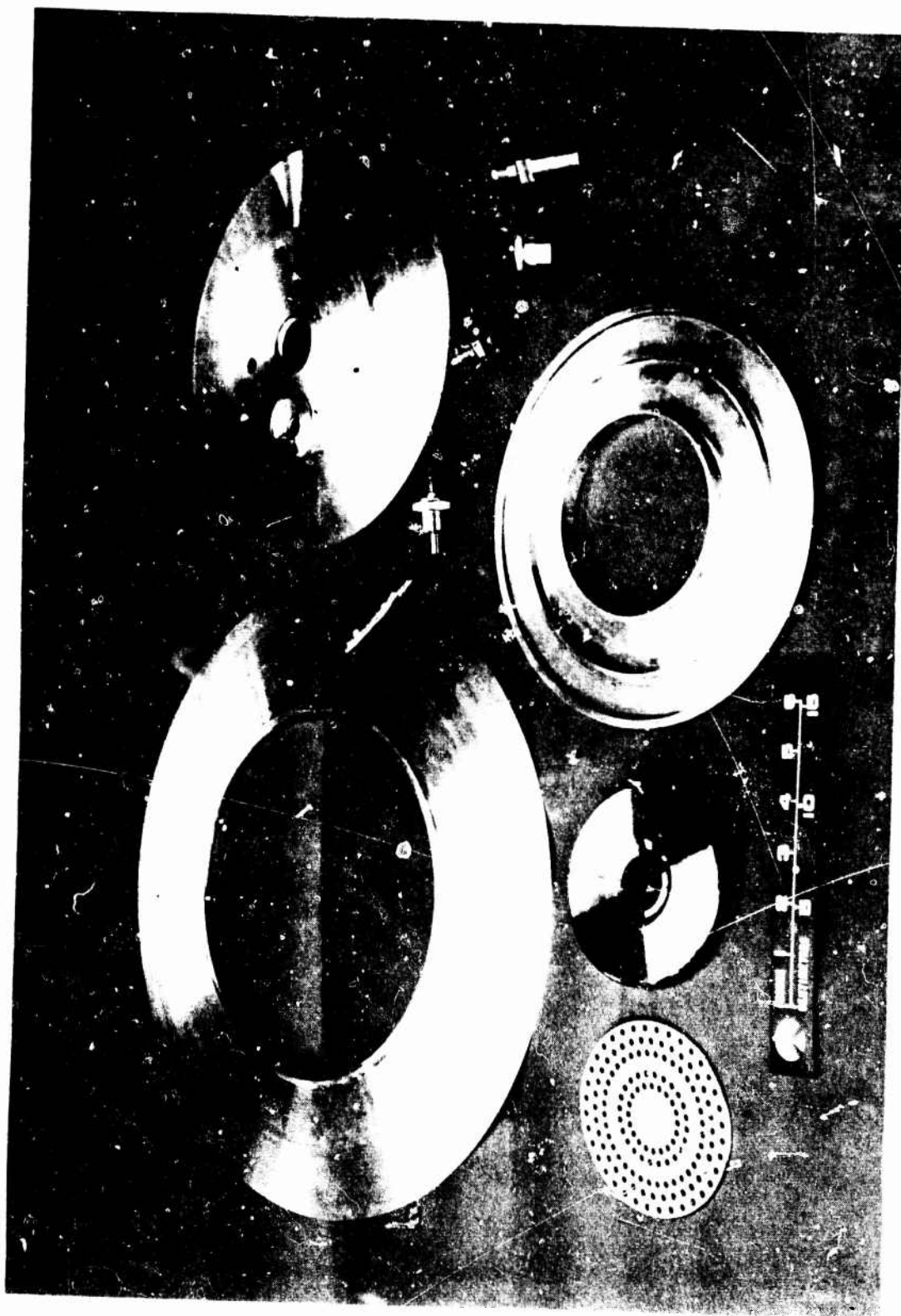
Bi-metal Joints. Bi-metal joints are required for mounting the steel vacuum gage tube leak detector and pressurant isolation valve to the aluminum liner assembly. Based on an evaluation of inertia welded, explosively bonded (Northwest Industries, Port Angeles, Wash.), extruded (Nuclear Metals, Concord, Mass.) and salt bath brazed (Bi-Braze, Glen Head, N.Y.) joints, inertia welding was selected because of the minimum development required for the desired alloys and cost (\$75 to \$125 each, unmachined).

An off-the-shelf 6061-T6 aluminum/304 stainless steel inertia welded joint suitable for the leak detector was purchased from Interface Welding (Carson, CA). A tube was machined from the first part, including grinding of the final outer surface to preclude gouging at the bi-metal interface.



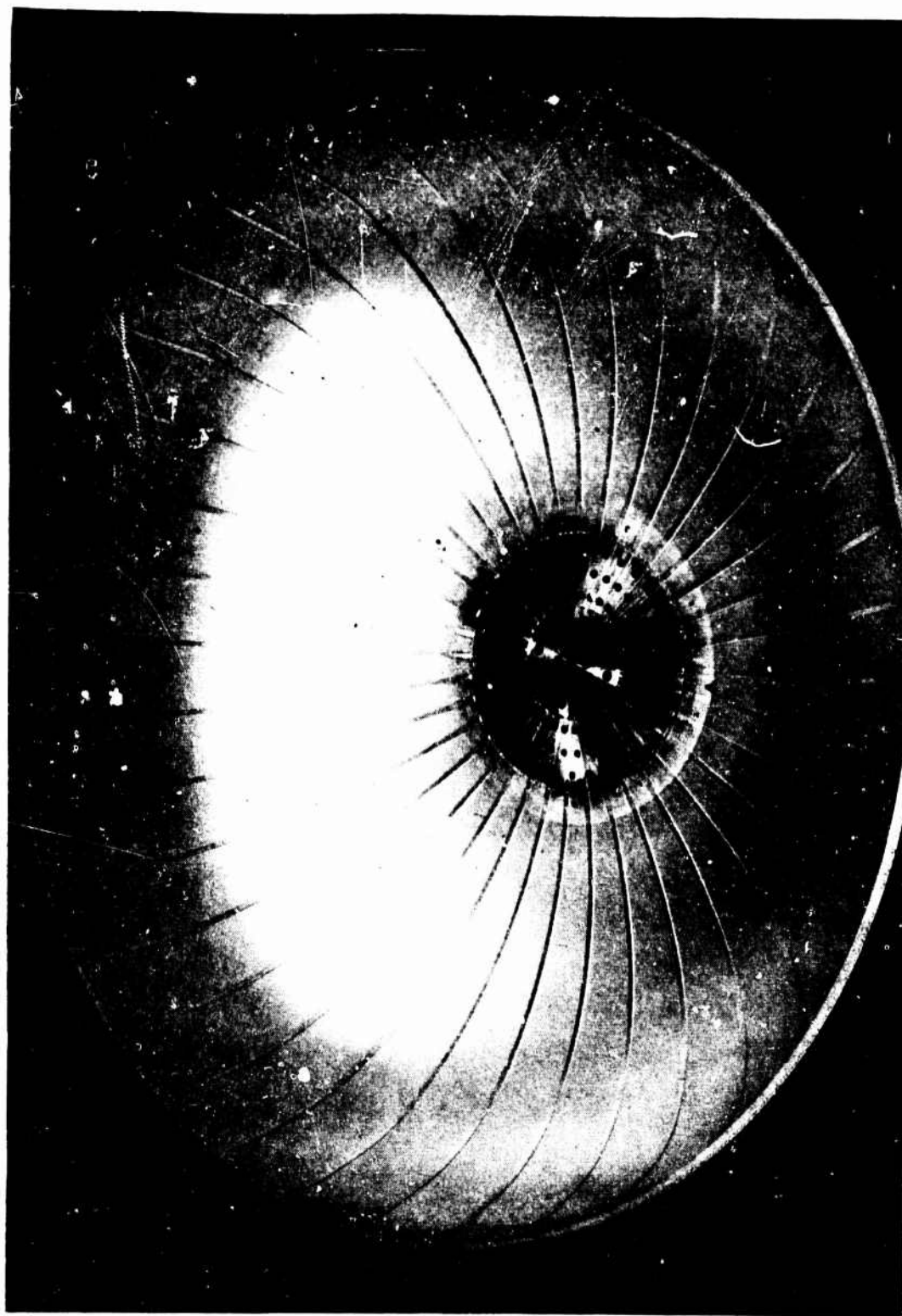
1X762-5/25/79-C1C

Figure 172. Inlet Liner



IX262-5/25/79-CIA

Figure 173. Inlet Polar Boss and Diffuser Plate Parts



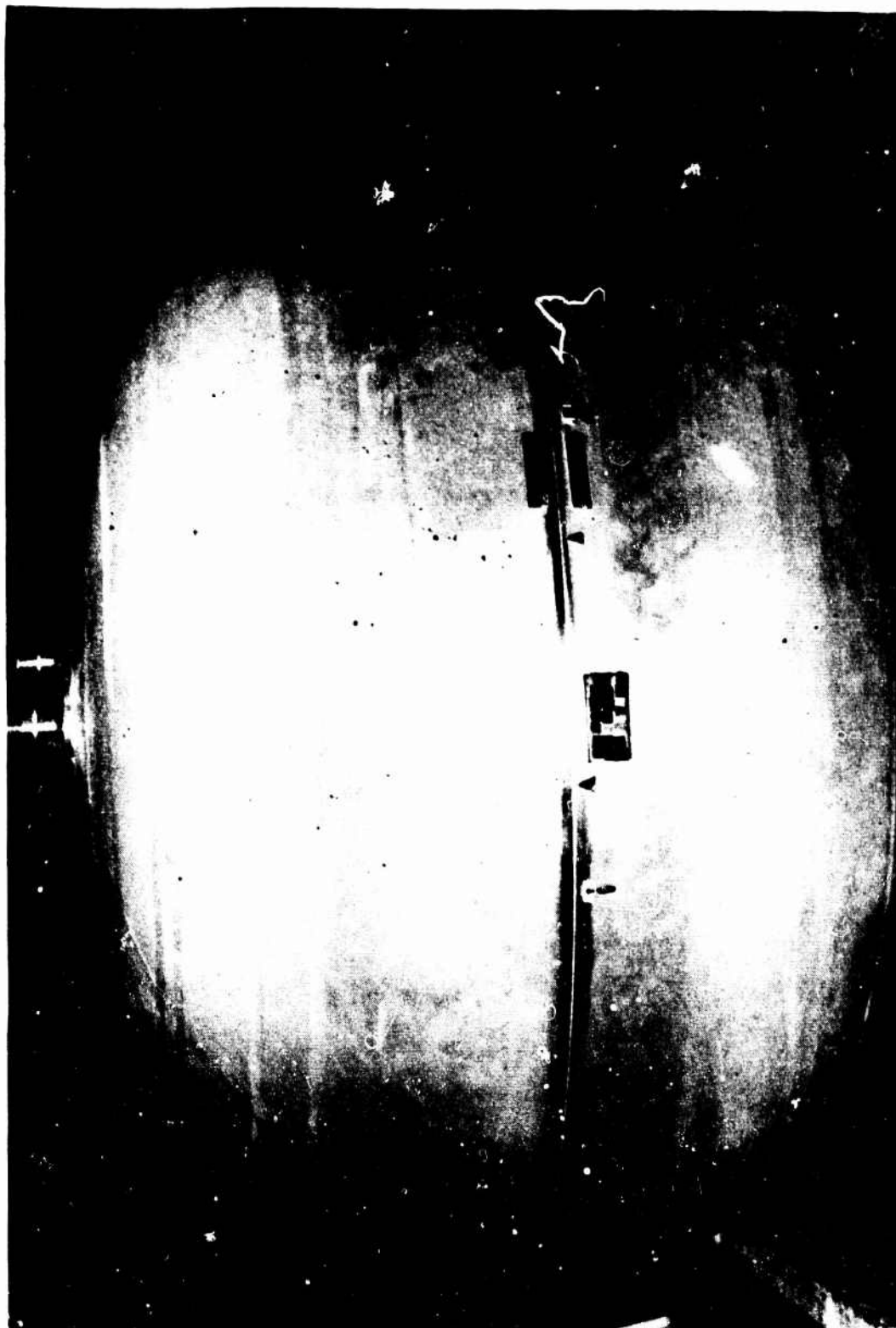
IXZ62-6/13/79-C1B

Figure 174. Outlet Liner Assembly



1X262-6/13/79-CLA

Figure 175. Outlet Liner Assembly



1X262-7/24/79-C1

Figure 176. Tank Liner Assembly



IXZ62-3/25/79-C1B

Figure 177. Girth Ring Assembly

The machined tube was proof tested at 450 psig for five minutes and bubble leak tested at 350 psig.

Development of the larger diameter joint, used with the isolation valve, consumed only eight sets of material. Two of the production parts were tensile tested at elevated temperatures. Since the test apparatus was limited to approximately 10,000 pounds force, the tube walls were machined to half their design thickness.

Both tubes failed in the aluminum adjacent to the joint interface in the weld affected zone in a typical ductile fashion. The ultimate strengths at 250 and 350 F were 39.5 and 37.2 ksi, respectively. These values are approximately 88 and 83 percent, respectively, of the strength of 6061-T6 aluminum at room temperature.

Composite Wrap. Upon receipt of the liner assembly, Brunswick decided it was stiff enough to withstand the filament tension during wrapping without pressurizing (4.5 psig). This decision was based on wrap process development with 490 in.³ spherical liner assemblies.

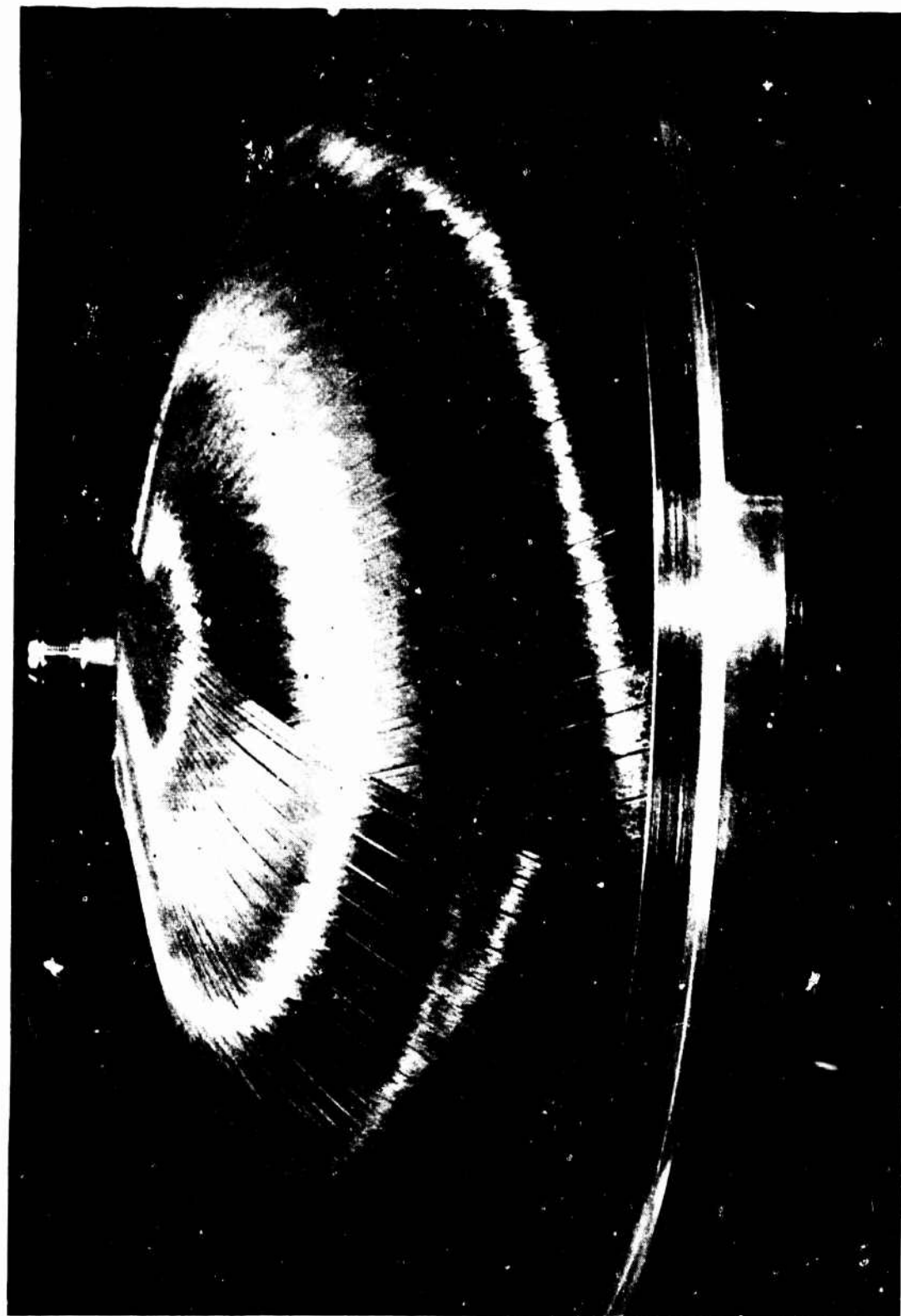
Composite wrapping and acceptance testing of the tank were performed the week of 10 September 1979. After cleaning and acid etching the liner assembly surface, it was preheated and placed in the numerically controlled winder in a heated enclosure. Eight spools of dry Kevlar roving were set up and their tensions adjusted. The flat band roving ran through an epoxy resin bath to a heated eye to the liner assembly. Use of eight spools resulted in a band density near the lower end of the normal range and some gapping between adjacent bands on the liner. This required two layers (four plies) of helical wrapping, which was preferred to one layer from sixteen spools. One layer would have resulted in a density at the high end of the normal range and some overlapping of bands.

After aligning the winding eye relative to the liner assembly, the tank was helically wrapped without any problems. During wrapping, the tank rotated about its polar axis and the eye moved back and forth parallel to the polar axis. There were no restarts requiring any filaments to be stripped off or cut. Bridging of the roving across the liner surface was observed in a region extending approximately three inches from the wrap polar boss opening. Cab-O-Sil filled resin was hand worked into this region during wrapping to fill the void.

During "B-stage" curing in the heated enclosure used for wrapping, excess resin was wiped from the tank. The composite wrap was subsequently cured in an oven. The elastomer band and mount ring were then positioned on the wrapped liner assembly and the ring was circularly wrapped on both sides to hold it in place. A second cure cycle was performed to cure the circular wrap. The completed assembly is shown in Fig. 178.

PSA Weight. The liner assembly weighed 34.5 pounds. This is heavier than necessary as a result of a loose tolerance (+0.010 inches) specified for the minimum liner thickness (0.032) because it was the first unit. The actual thicknesses were 0.037 to 0.042 inches for the inlet and 0.034 to 0.043 inches for the outlet, with averages of 0.039 and 0.038, respectively. The liner was also slightly oversized due to achieving a minimum of 98.1 percent expulsion efficiency during whorhorse tests compared to 97 percent used for design purposes. The baseline weights contained in the Engineering Analyses and Design section were adjusted for liner thickness and volume, and valves were substituted for the threaded ports.

The mounting ring weighed 12.3 pounds. Its weight could be reduced by reducing its size or drilling holes between the mounting points. A "universal" design was selected because the mounting requirements were not specified.



14-361-9/27/79-CLB

Figure 178. Flight Tank

The helical composite wrap weighed 11.1 pounds. This weight could be reduced slightly by increasing the radius of curvature of the liner near the polar axis to prevent bridging of the filaments, which required filler material (Cab-O-Sil and resin). The circular wrap used to hold the mount ring in position weighed 1.71 pounds. As fabricated, the complete PSA weighed 59.6 pounds.

Acceptance Tests. The proof pressure test was conducted by Brunswick. Both sides of the diaphragm were pressurized simultaneously with helium from a common source through identical lines at a very slow rate (3.5 psi/min). The slow rate was required to avoid transient pressure differences that could collapse the diaphragm. Pressurization was controlled with a 10-turn 0.02 inch variable orifice and the diaphragm pressure differential was monitored with a digital voltmeter.

The proof pressure was established at 389 psig. This pressure represents 1.1 times the design pressure of 350, plus one percent margin for test error. The actual proof test pressure exceeded 385 psig for a couple minutes and was maintained at 389 psig for 30 seconds.

As the pressure was vented, a single "pop" was heard; however, no evidence of damage was found. Several sources of this noise are possible including: (1) breaking of the bond between the wrap and liner near the polar wrap opening where the growth due to pressure is greatest, (2) movement of the mounting ring relative to the liner assembly, (3) movement of the inlet diffuser plate (which has equal pressure on both sides) relative to the liner assembly, and (4) breaking one of the internal plate welds. The pressure was vented slowly to 315 psig and held for 30 minutes during the leak test.

Prior to running the proof test, the tank was encased in a polyethylene bag and sealed. A mass spectrometer probe was placed in the bag at the top of the tank. External PSA leakage was measured at less than 10^{-8} sccs helium. The tank was vented at 6.8 psi/min.

The tank was to have been inspected for unbonded regions between the composite wrap and the aluminum liner by Rocketdyne, using holographic interferometry. One of Brunswick's small-scale tanks with intentionally placed imperfections was used to set up the inspection equipment, but the argon ion laser malfunctioned during initial inspection of the flight tank and had to be repaired. When these repairs started to impact the expulsion test schedule, holographic inspection was eliminated.

Non-Destructive Inspection Experiments.

Current state-of-the-art non-destructive inspection (NDI) techniques were compared to select the best method of evaluating the integrity of the bond between the Kevlar/epoxy wrap and the 5086 aluminum liner. In addition to the problems created by the physical properties and geometry of the materials involved, the tank design does not permit access to the interior volume to insert equipment. The study was conducted by Brunswick between March and July 1979 and the following NDI techniques were considered: ultrasonics, dielectric capacitance, infra-red photography, X-ray image enhancement, acoustics, and optical holography.

A sub-scale tank with intentional unbonded regions was used for the experiments. The results using laser holography were extremely successful. The threshold size of detection was approximately 0.25 inches.

Sub-Scale Tank Description. Two sub-scale (10 inch diameter) spherical tanks were fabricated to facilitate an evaluation of the NDI techniques. The materials used for the liner (5086-O aluminum) and composite wrap (Kevlar/epoxy) were the same as the flightweight tank. Also, the thicknesses of the liner (0.030 to 0.050 inches) and composite (0.039 to 0.273 inches) were nearly the same as the flightweight tank. A polar winding pattern was used to approximate the pattern on the flightweight tank.

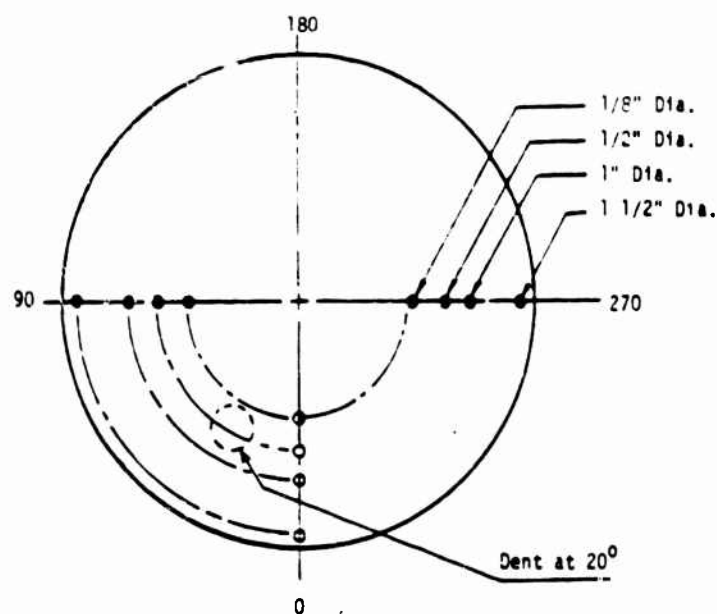
Intentional unbonded regions of known size and location were created on the sub-scale tanks. Four areas were created by each of three materials applied to the liner: adhesive backed Teflon (TFE) tape, thin Teflon (FEP) film, and Parafilm (high temperature paraffin) mold release spray. Both square and circular unbonded regions with basic dimensions of 0.125, 0.5, 1.0 and 1.5 inches were positioned as presented in Fig. 179. Only the second tank had the flat spot shown.

Ultrasonics. The first sub-scale tank was transported to Sonic Industries (Trenton, N.J.) for a demonstration of the capabilities of ultrasonic techniques. Both submerged and transducer couplant techniques were used with continuous frequency ranges from 2.5 to 20 MHz. Experiments were conducted with four different systems using several transducers of various shapes and sizes.

The only combination that produced any positive results was the Mark IV with two 54 degree, focused, 0.25 inch transducers used in the through-transmission reflective mode. Only the 1.5 inch Teflon tape area could be located, and that with questionable repeatability. The poor results were apparently due to distortion of the reflective characteristics of the aluminum liner by the composite's non-uniform surface and structure, and the intimate contact maintained, even in the absence of a bond.

Dielectric Capacitance. Dielectric capacitance experiments were to have been conducted by Brunswick, but were deleted based on literature search findings that indicated a low probability of detecting unbonded areas for materials that are in intimate contact. Contact is ensured by the compressive nature of the composite wrap acting on the liner.

Infra-Red Photography. A literature search revealed test results indicating that unbonded regions of composite wrapped aluminum could be detected for minimum diameters of 2.0 inches and maximum thicknesses of 0.25 inches. A further condition was that the unbonded materials could not be in intimate contact. Experiments with the sub-scale tanks were therefore not conducted.



LEGEND

- - Teflon Square
- ⊙ - FEP Square
- - Parafilm Circle

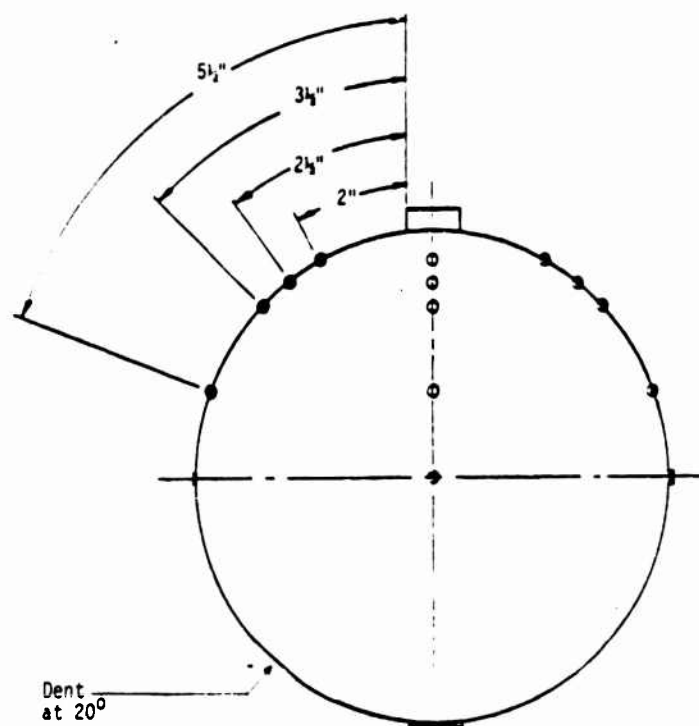


Figure 179. Subscale NDI Tank

X-Ray Image Enhancement. The capabilities of real-time radiography with video image enhancement were demonstrated by Lockheed Research Laboratory (Palo Alto, CA). Lockheed's equipment has sensitivity capabilities to detect defects as small as 0.0005 inches in width with a radiographic density contrast as low as 0.01. The only unbonded area that could be located was the 1.5 inch square Teflon tape. The radiation path was tangent to the defect and indicated the presence of foreign material, not the unbond. As with the other techniques investigated, the absence of any separation between the materials contributed to unsatisfactory results.

Acoustics. Two companies were contacted for demonstrations of acoustical techniques, including holography. Unfortunately, Lockheed's (Palo Alto, CA) equipment was being moved to new facilities and was inoperative. Holosonics was experiencing similar problems as a result of their move from Washington to San Jose, CA. It is generally thought that acoustical techniques would yield at least partial success in detecting unbonded regions, but because of the excellent results using optical holography, acoustic methods were not pursued further.

Optical Holography. The optical holography demonstrations were conducted by Chemical Systems Division (CSD), United Technologies Corporation (UTC), at their Coyote Plant (San Jose, CA). The technique consisted of making a hologram of the illuminated tank in a reference stress condition. The stress is then changed, e.g., by pressurization, and a second hologram is superimposed on the plate. This results in a holographic interferogram with fringes appearing wherever a dimensional change of half the light's wavelength occurs. Irregular displacements, including those caused by unbonded regions, cause fringe patterns that are distinguishable from the generally uniform pattern of the tank. Fringe patterns at unbonded regions occur because of the altered load-sharing relationship between the aluminum liner and composite wrap.

The experimental NDI system was mounted on an air suspension table for isolation and is shown in Fig. 180. A commercial Lexel Model 95, continuous wave, two-watt argon ion laser was used. The actual operating power was 0.7 to 0.8 watts and the laser was water cooled. The wavelength was 5145 Angstroms. The tank was sprayed with dye-penetrant developer to enhance reflectivity.

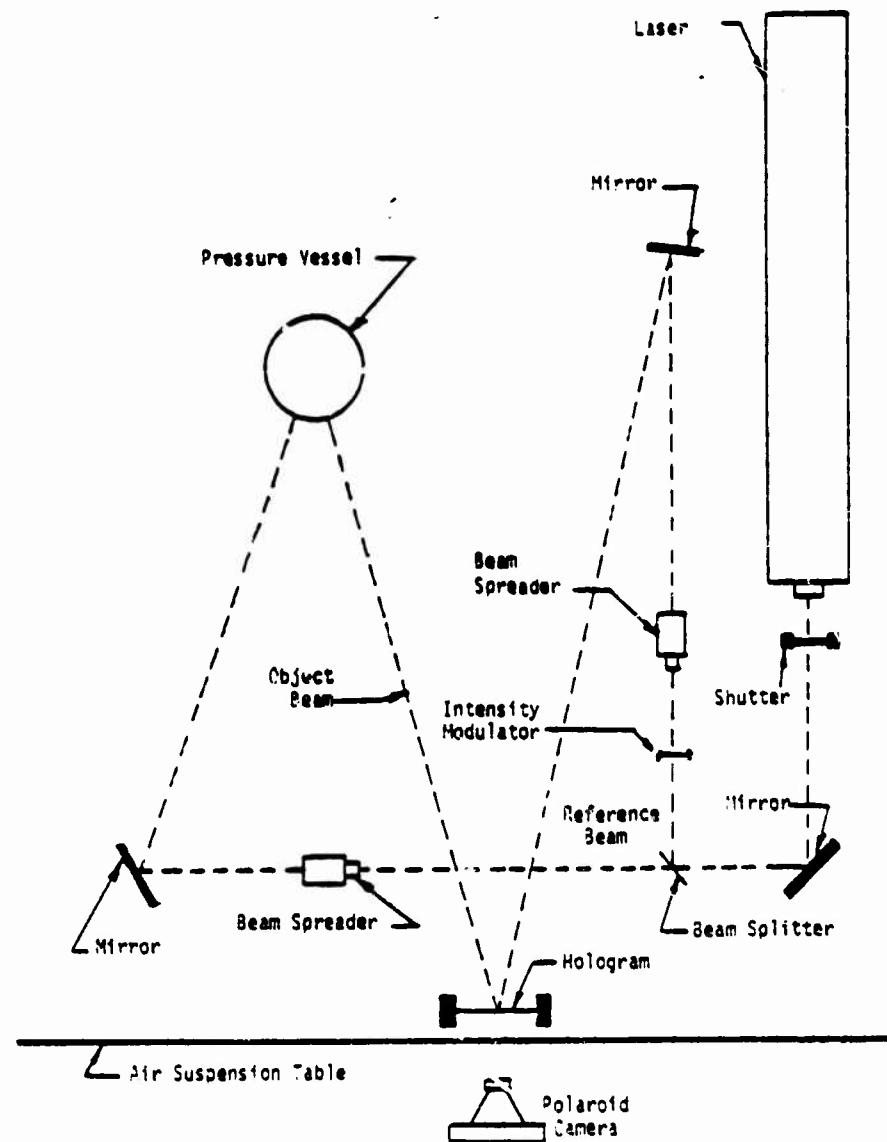


Figure 180. Holographic Setup

The tank was pressurized with water and a change in pressure of 6 psi was found to produce the best fringe spacing to determine the location, size and shape of defects. There was no effect due to the absolute pressure level (up to 50 psig) at which the 6 psi delta was applied. All unbonded regions except the 0.125 inch size were readily identifiable. Figure 181 shows holograms of sides of the tank with and without defects. The photo on the right shows two unbonded regions at the top and a bonded flat spot at the bottom. Because of the similarity in fringe patterns, tangential X-rays would be required to differentiate unbonded regions and flat spots on the liner. The influence of the aluminum liner weld and a circular wrap at the girth (center of photos) on the fringe pattern, is also visible.

Additional experiments were conducted using thermal excitation rather than pressure. The results were unsuccessful, however the tank was only heated by 3 to 5 degrees F and there was no means of maintaining the temperature.

The equipment used in these experiments could be purchased for approximately \$41,000. This includes \$21,000 for the laser and \$12,000 for the table.

Performance Tests.

Performance tests were conducted with the flightweight tank between October 1979 and March 1980. A propellant simulant (water) was expelled from the tank during a pulsed duty cycle with the Tridyne pressurization subsystem. The maximum pressurant temperature at the tank inlet was 1042 F. The thermal characteristics of the tank were obtained and they demonstrated the adequacy of the design in minimizing the heat transferred to the tank shell. There was no evidence of any temperature effects on the composite wrap. The final bulk pressurant gas temperature, which is duty cycle dependent, was 150 F for a 61 F initial temperature.

The expulsion efficiency and pressure drop data were consistent with the data obtained in the workhorse tests. The integrity of the diagram-to-liner weld during expulsion was demonstrated.

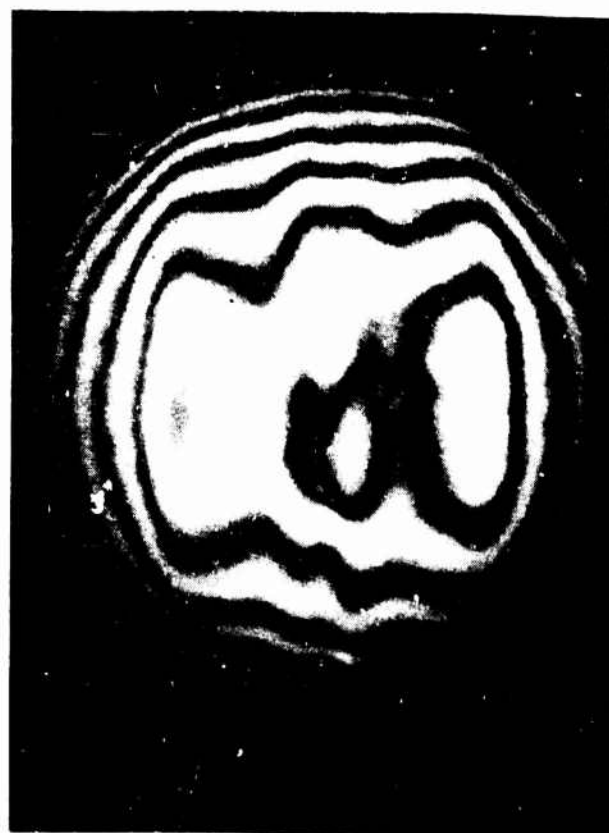


Figure 181. Optical Holograms of Wrapped Tank

The structural dynamic response characteristics of the tank shell and mounting ring were determined. Transfer function analyses indicated there were no significant resonances below 80 Hz. There was no evidence that pressurization to 75 psig had any affect on dynamic response. There was no visible damage due to short duration ground random vibration, nominal duration flight random vibration, or flight shock tests.

A burst pressure test demonstrated the adequacy of the tanks structural design. A weld tensile failure occurred at burst pressure, but a subsequent analysis indicated that it was due to weld porosity and corrosion, which can be precluded.

Expulsion Test. The flight tank was expelled at Rocketdyne's Santa Susana Field Laboratory (Santa Susana, CA) on 16 October 1979. The test setup was basically the same as used with the metal workhorse tank (Fig. 135), with the following exceptions. The pressurant gas thermocouple, 14 inches upstream of the tank inlet, was moved to within a couple inches. The water temperature measurement was made within a few inches of the tank outlet instead of 8 to 9 feet downstream. A total of 12 thermocouples were attached to the tank outer surface. The most significant change was moving the electronic regulator's Kulite pressure transducer from the water flow line to a short dead-ended line connected to the propellant fill valve. This was necessary because the facility pulse-flow control valve could not be slowed down sufficiently to eliminate pressure surges that might damage the Kulite transducer. This resulted in the feed system pressure being controlled inside the tank. Pressurant gas and diaphragm pressure variations were still compensated for, but liquid flow pressure variations were not.

After sizing the diaphragm to the shell at 50 psig with gaseous nitrogen and performing a leak check, the tank was completely filled with water (10.57 ft³). Water was then removed (0.64 ft³) to create a liquid-side ullage (6.1 percent). The Tridyne pressurant storage tank was pressurized to 1217 psig.

The mission duty cycle was initiated by simultaneously opening the Tridyne isolation valve and energizing the electronic regulator. Due to a sequencing problem, the instrumentation recorders were not activated until after the system was pressurized. As a result, no transient pressurization data were recorded. The instrumentation was activated approximately 45 seconds after opening the Tridyne isolation valve. The pulsed expulsion duty cycle included 8 low-flow ($7.5 \text{ in.}^3/\text{sec}$) and 17 high-flow ($130 \text{ in.}^3/\text{sec}$) pulses and is presented in Fig. 182.

The thermocouple installed to measure the gas temperature at the inlet to the propellant tank did not operate properly during the test. Using data from the metal workhorse tank pulsed-flow test, the gas temperature at the tank interface was estimated to be 410 F lower than the reactor outlet temperature at the start of the flow expulsion cycle, and 115 F lower at the end. This results in a maximum tank inlet temperature of 1042 F. The thermocouple on the outer surface of the tank inlet fitting at $1/8$ inch from the polar boss surface measured a peak temperature of 793 F as shown in Fig. 183. This thermocouple is noted as number 8 in Fig. 184. The tank was mounted with thermocouple No. 1 near top-dead-center.

The locations of the 11 thermocouples on the tank shell are presented in Fig. 184. Their temperature transients are shown in Fig. 182 and 185. Number 7 was on the polar boss, $1/8$ inch from the inlet fitting, and number 6 was on the boss, $1/8$ inch from the Kevlar wrap. Their peak temperatures were 359 and 276 F, respectively, and occurred slightly after the last pulse. The maximum temperature measured on the Kevlar overwrap was 202 F. There was no posttest visual or tactile evidence of any temperature effects on the Kevlar. Figure 185, in conjunction with Fig. 182 shows the temperature gradient from the top of the tank to the bottom.

The water outlet temperature was unchanged (61 F) through the first 360 seconds of recorded data. It was 62 F at 420 seconds, 63 F at 480 seconds, 66 F at 550 seconds and 68 F at 7.7 seconds prior to flow termination. The maximum temperature was 75 F at the end of the expulsion cycle, 14 F higher than the initial temperature.

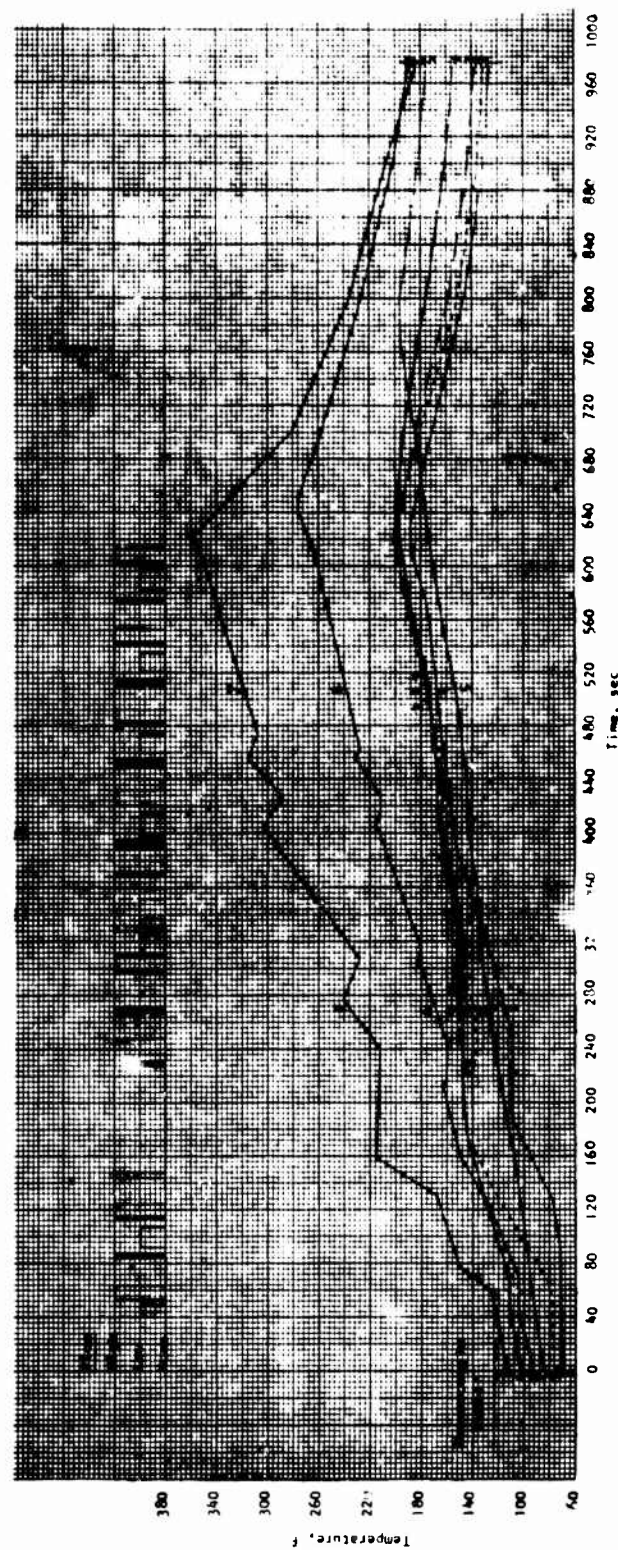


Figure 182. Tank Wall Temperature Transients

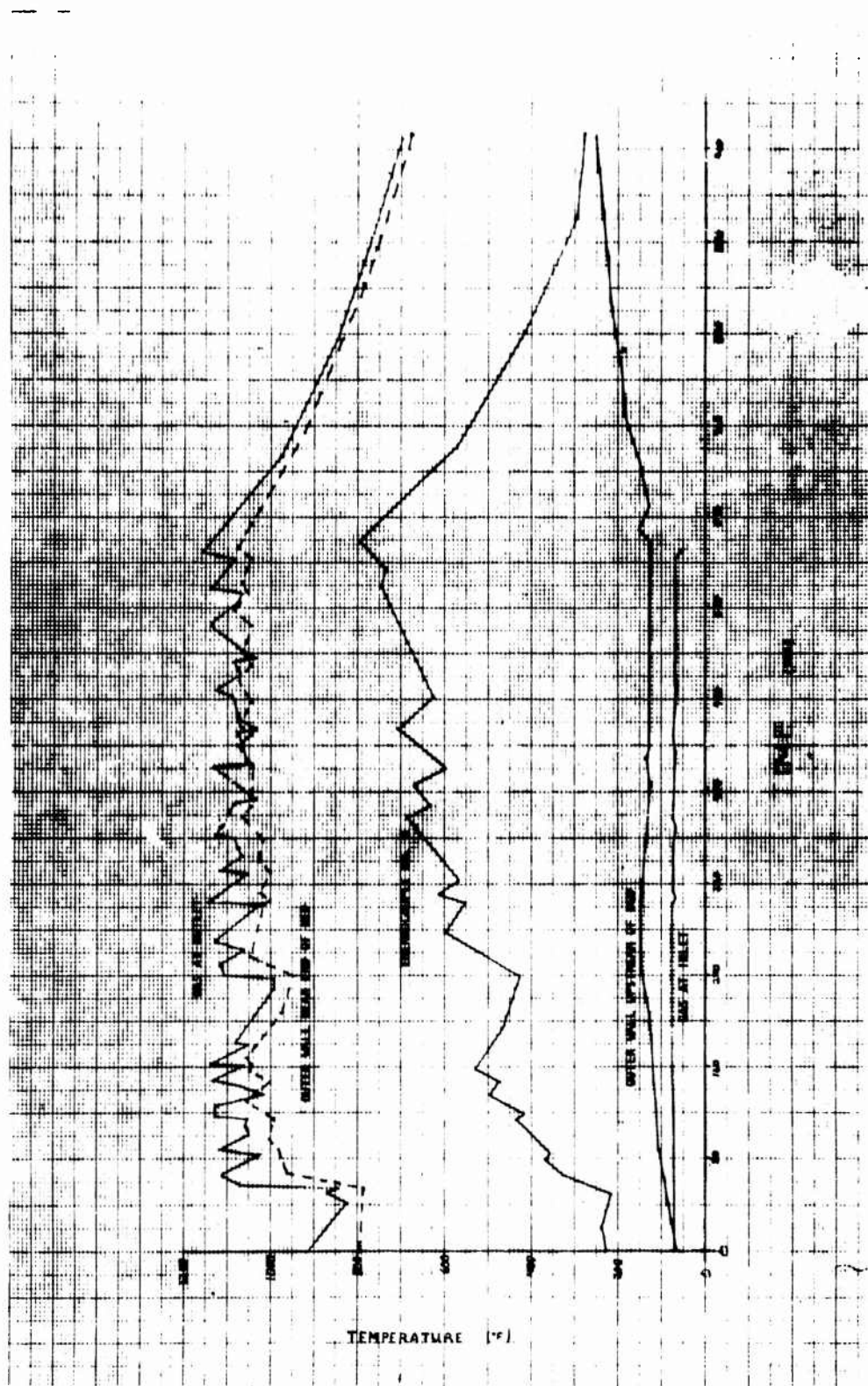


Figure 183. Reactor Temperatures

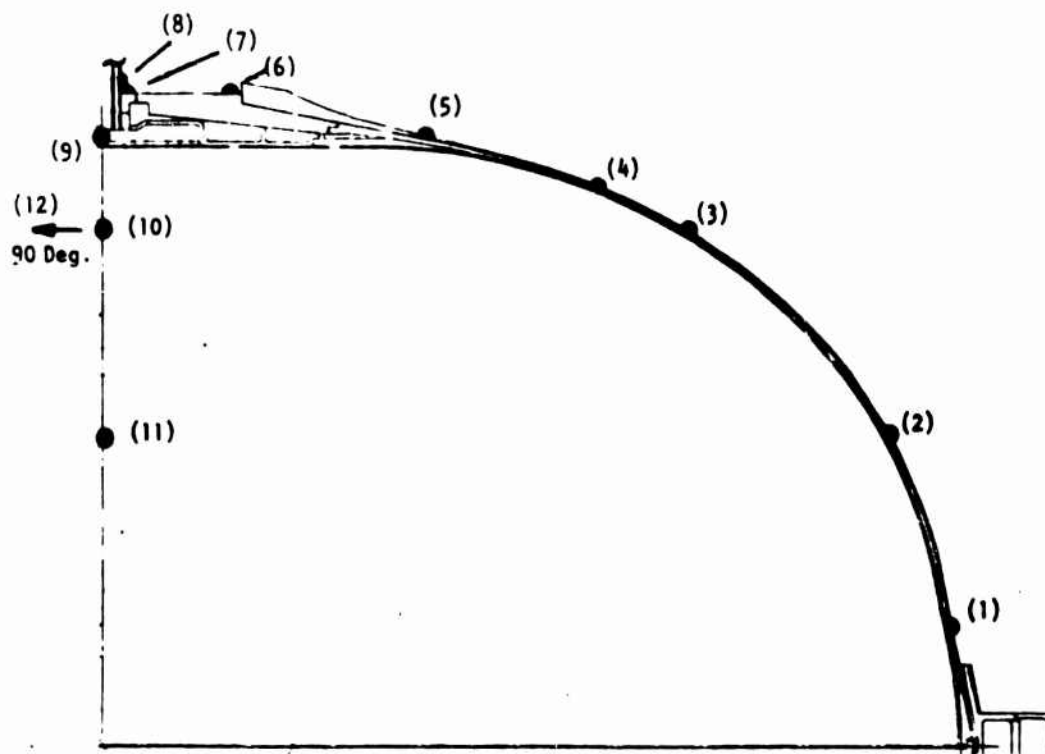


Figure 184. Tank Outer-Wall Thermocouple Locations

The Tridyne tank pressure decreased from 1217 to 673 psig during the test, representing a usage of 3.0 pounds. The amount of water condensation in the propellant tank during expulsion is unknown; however, from thermodynamic calculations, the final bulk gas temperature had to be between 147 and 153 F, and the condensation between 85 and 100 percent, respectively, at the end of the expulsion cycle.

The tank expulsion efficiency could not be calculated because virtually all the water was expelled when a problem with the automatic sequencing caused a diaphragm differential pressure of nearly 300 psi. The diaphragm did not tear or leak, however. The diaphragm ΔP 's at 90 and 95 percent reversal were approximately 3 and 11 psi, respectively, which is consistent with the metal workhorse tank test data. The ΔP data up to this point in the duty cycle appear questionable, primarily because they are small values that are calculated as the difference between two high pressures.

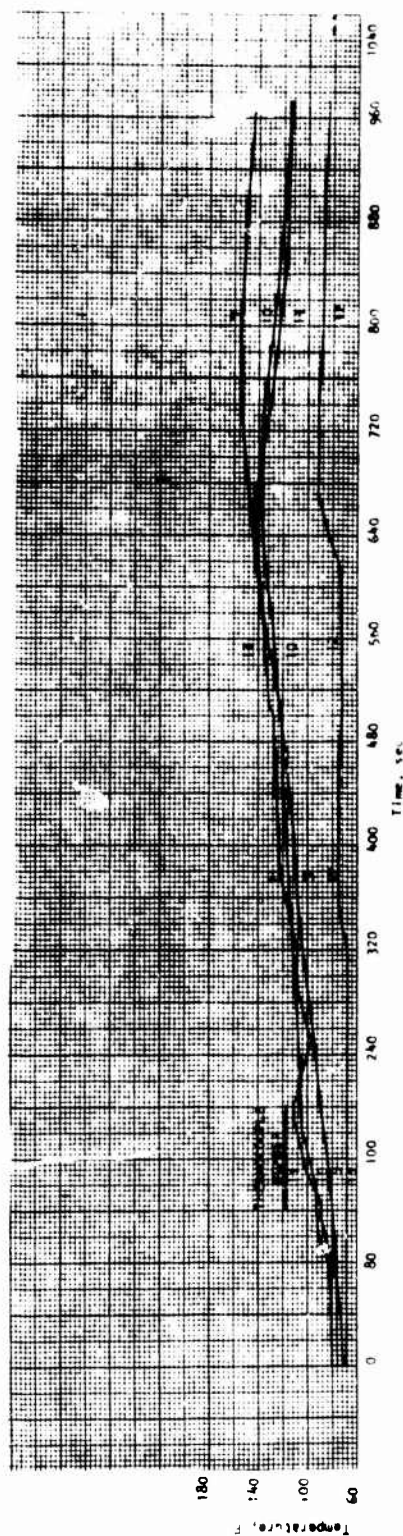


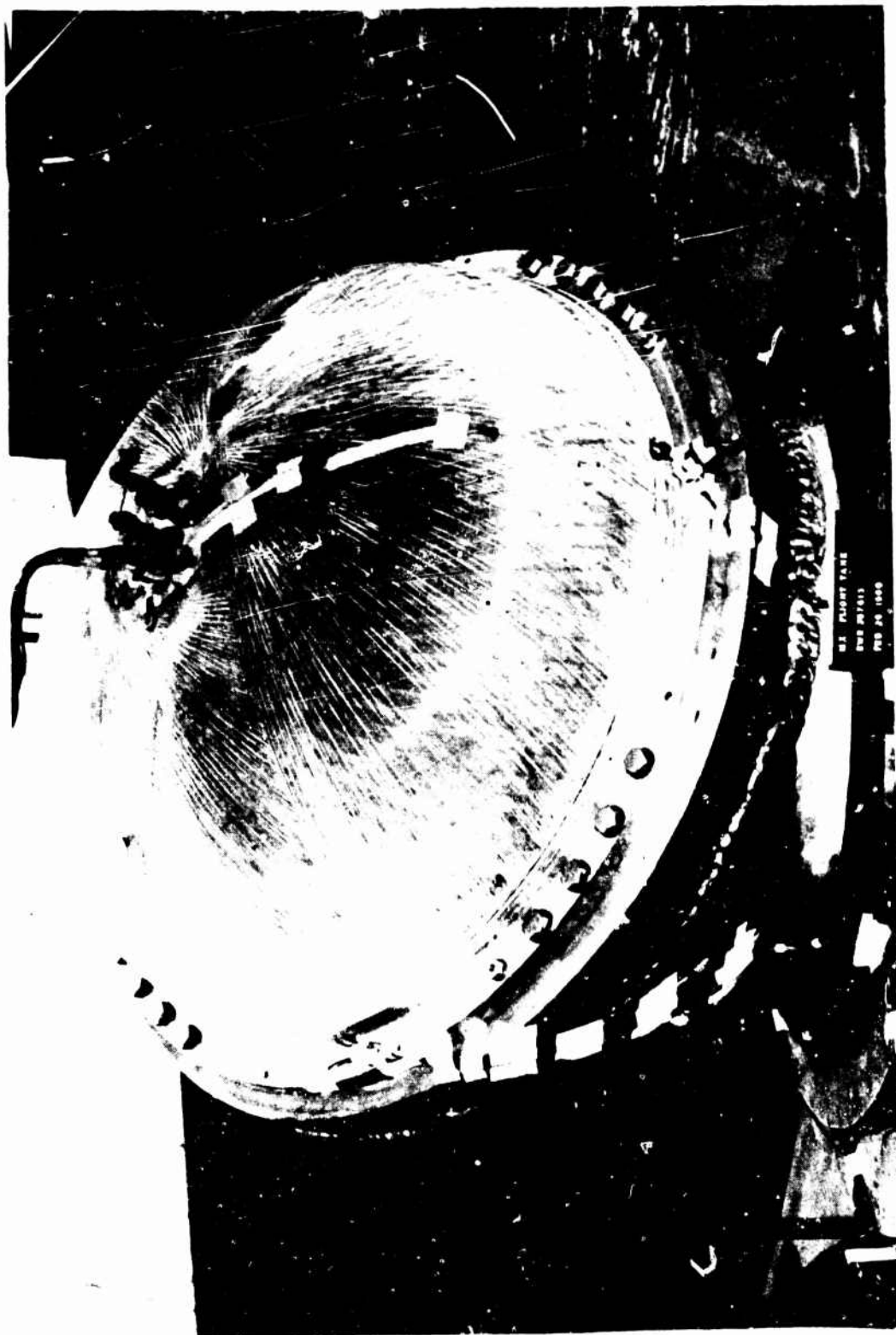
Figure 185. Tank Wall Temperature Transients

Structural Dynamic Tests. Structural dynamic tests were run at Rocketdyne's Engineering Development Laboratory (Canoga Park, CA) from 20 through 28 February 1980. As a result of the diaphragm failure in the workhorse dynamic test program, it was decided to limit the flightweight dynamic testing to determination of the structural dynamic response characteristics of the tank shell and mounting ring during ground and flight random vibration and flight shock. The tank is shown mounted with four sets of four bolts in the 45 degree test fixture in Fig. 186. The rationale for testing two tank axes simultaneously was presented in the workhorse tank structural dynamic test section. Unlike the workhorse tank, the flight tank vibration tests were response limited. Response limiting is also discussed in the workhorse section.

The ground random vibration test was run from the shaker's lower frequency limit, approximately 5 Hz, up to 500 Hz. Rather than run a 10 hour duration test, the objective was limited to characterizing the response of the composite wrapped tank. A tenth-power input test was run for 19 minutes to provide data to adjust the input spectrum to achieve response limited levels. A tenth-power response limited test was then run for 23 minutes. After readjusting the input, a 28 minute half-power test was run. Finally, 41 minutes of testing were conducted at full power.

Nearly all of the test axes (X and Y) control accelerometers (Fig. 187) responded at approximately the same level up to about 20 Hz. Above 20 Hz, the x-axis control accelerometers mounted on the polar bosses measured the highest responses. Their PSDs are presented in Fig. 188 and 189. The composite g's rms were 0.88 and 0.84 on the pressurant and propellant sides, respectively. The two accelerometers mounted on the composite wrap, normal to the surface, measured low values except for the accelerometer nearest the polar boss in the 40 to 80 Hz frequency range. The PSD is shown in Fig. 190.

Transfer function gains are presented in Fig. 191 and 192 for y-axis accelerometers on the mounting flange. The maximum gain was approximately 5.5 at 400 Hz. Two additional modes between 400 and 500 Hz were evident with gains



12869-2/26/80-C1A

Figure 186. Structural Dynamic Test Set-Up

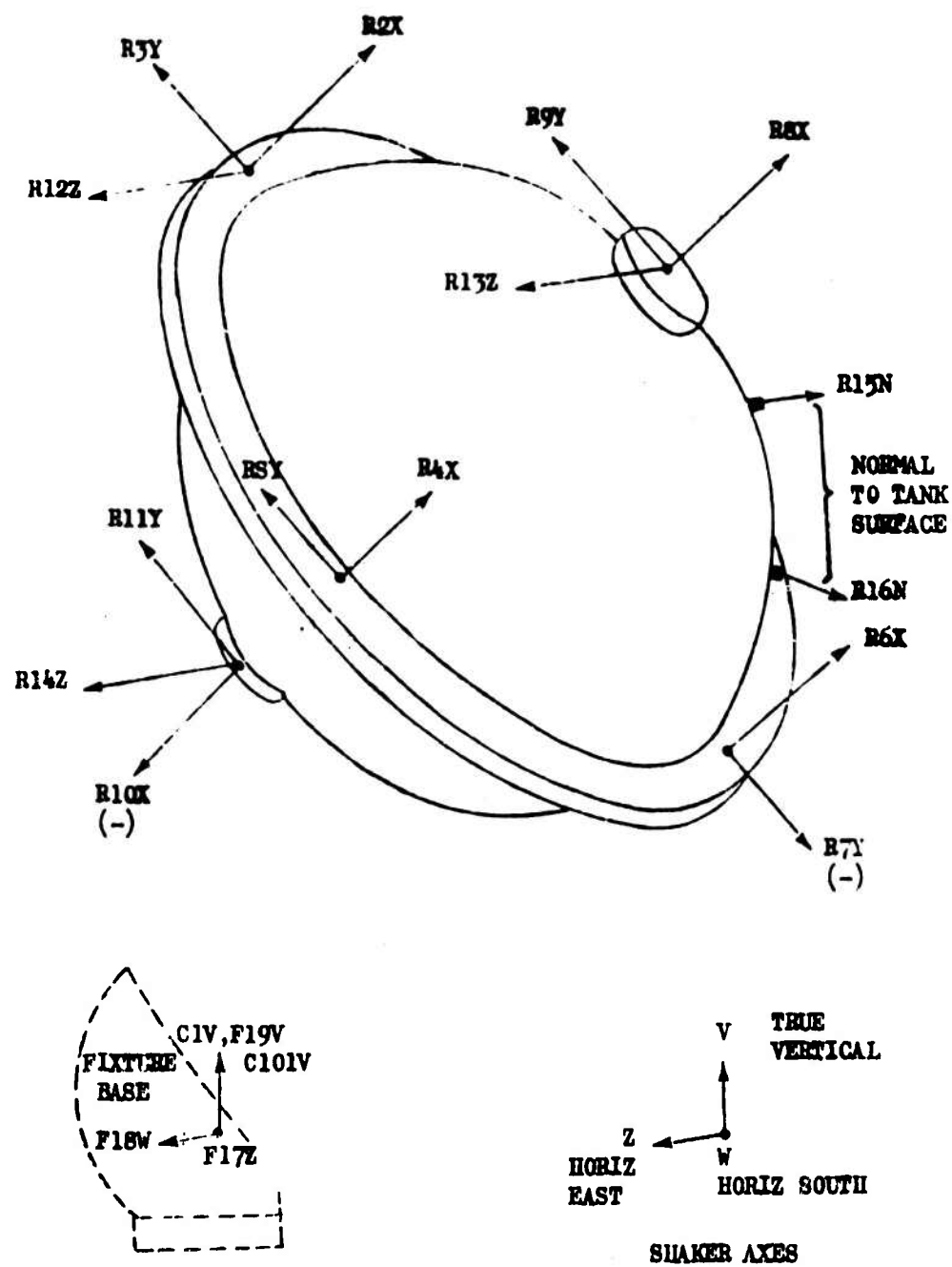


Figure 187. Flight Weight Tank Accelerometer Locations

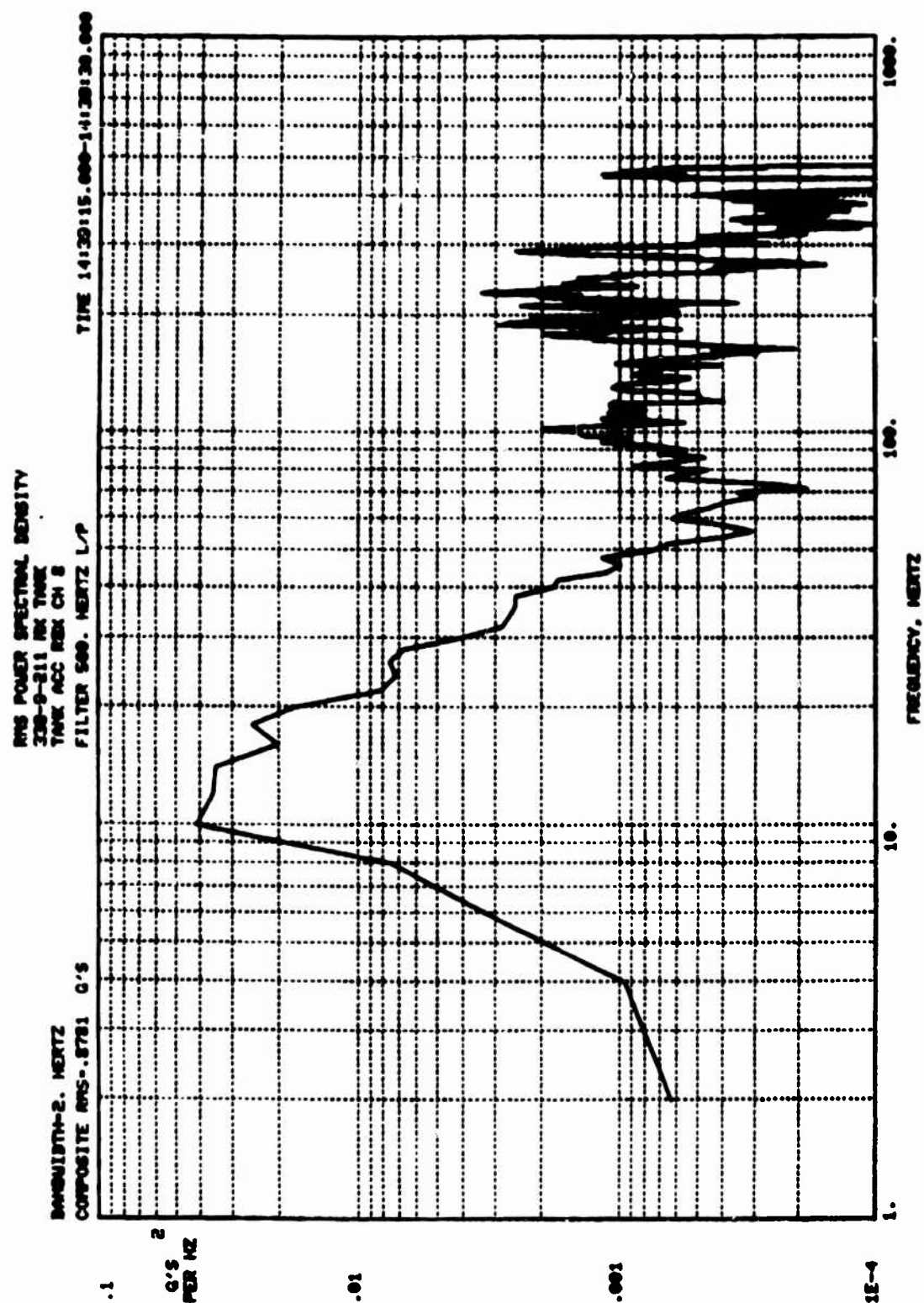


Figure 188. Pressurant Boss X-Axis PSD

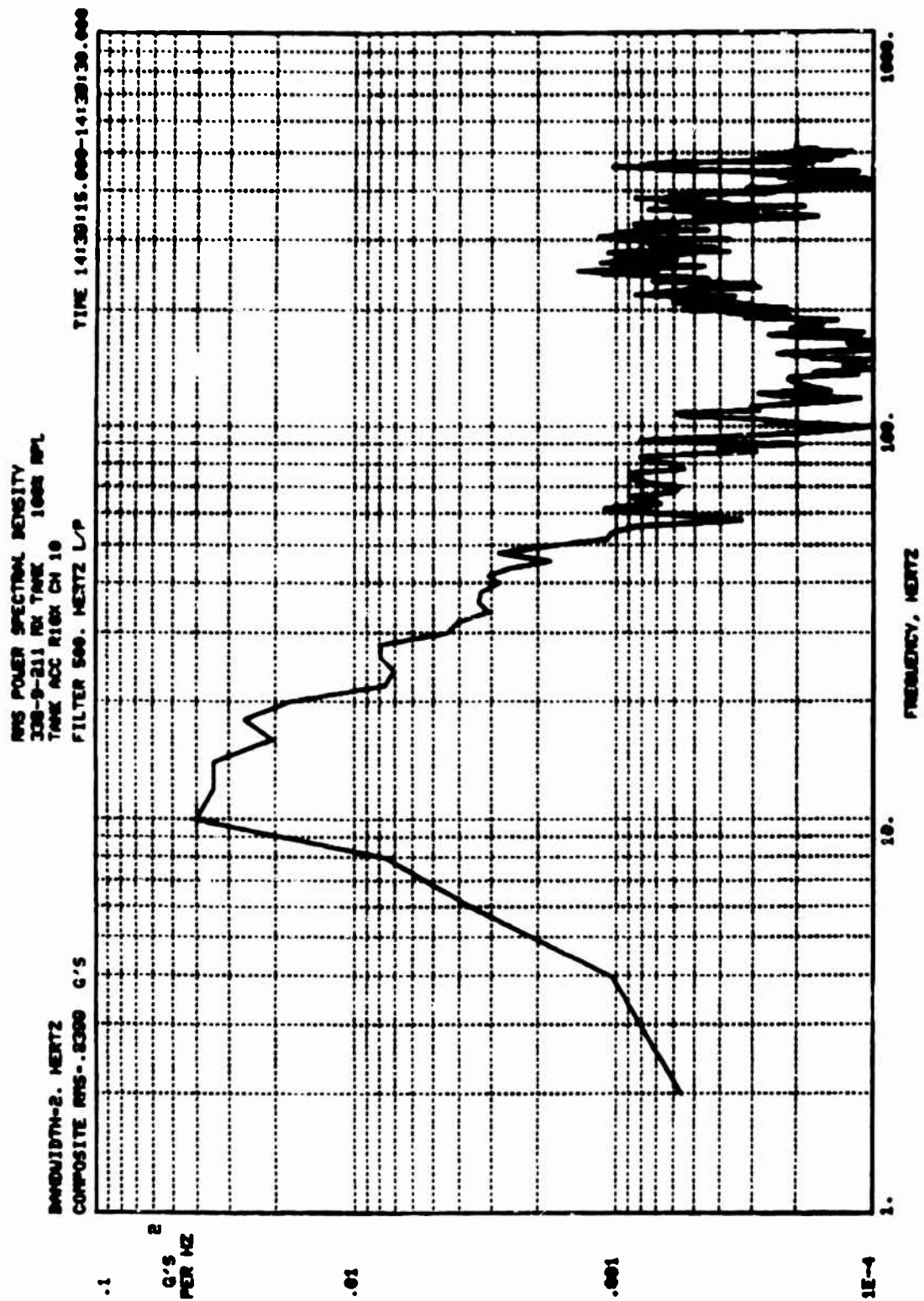


Figure 189. Propellant Boss X-Axis PSD

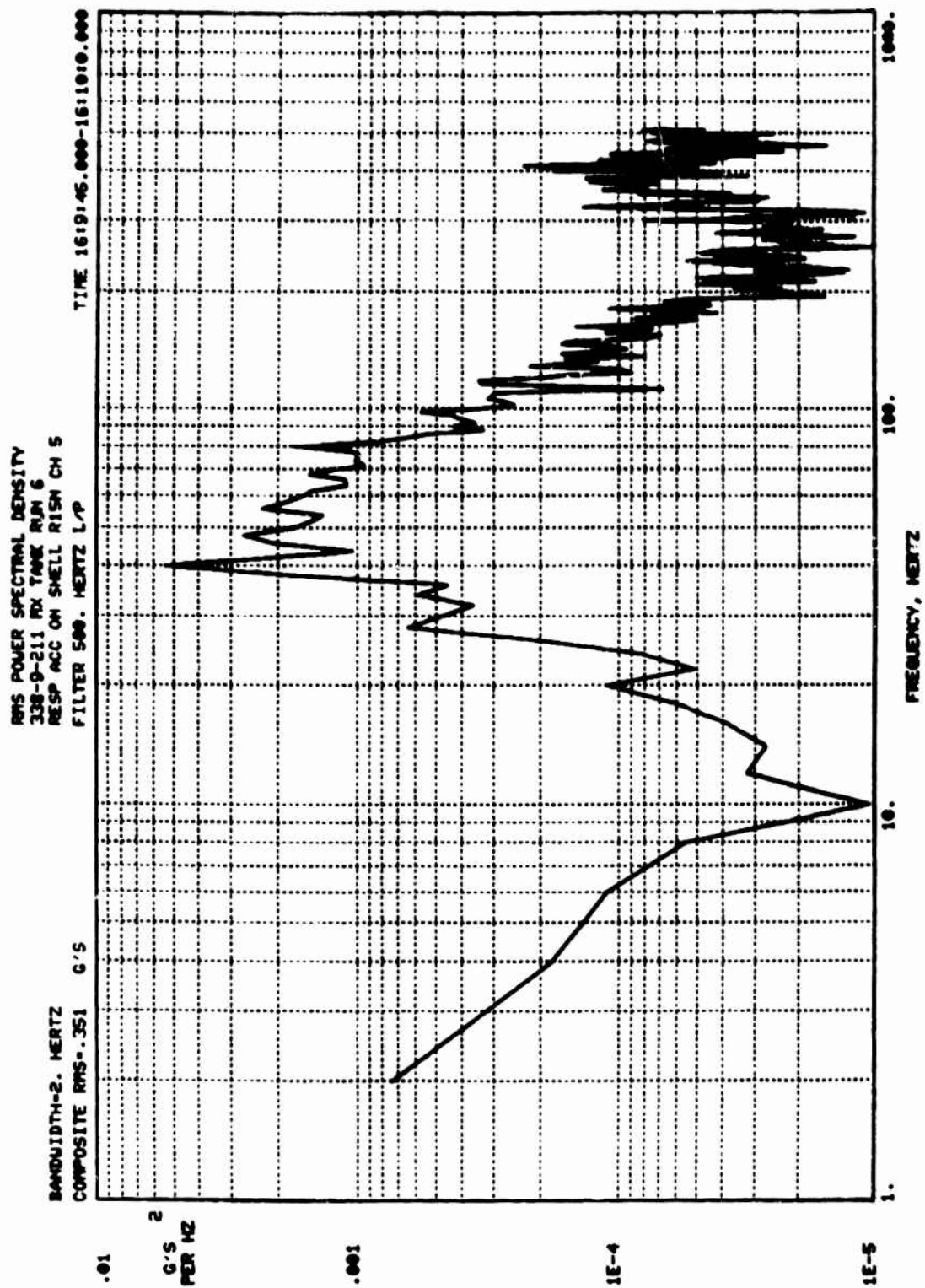


Figure 190. Composite Wrap PSD - Near Pressurant Boss

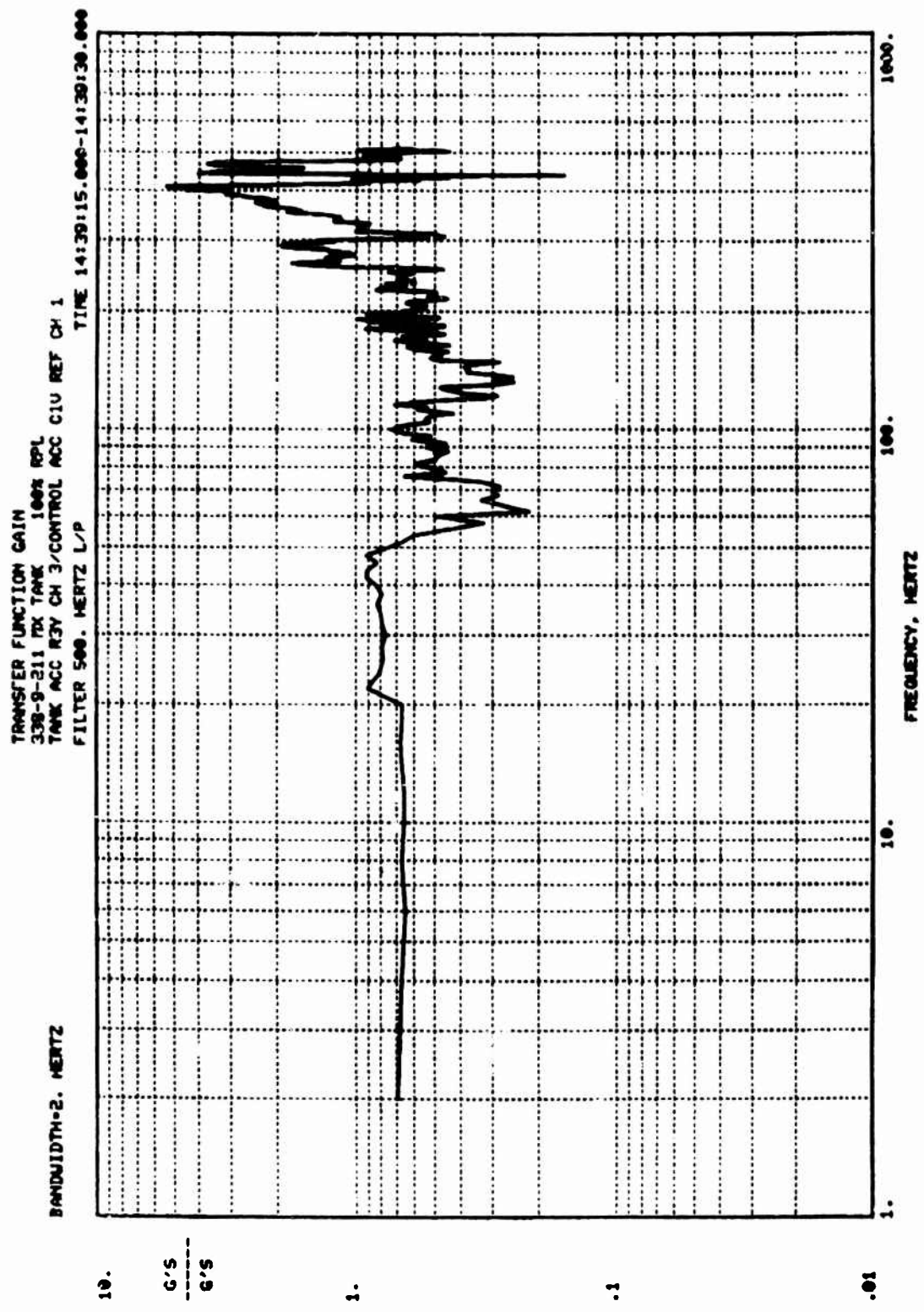


Figure 191. Flange Top Y-Axis Gain

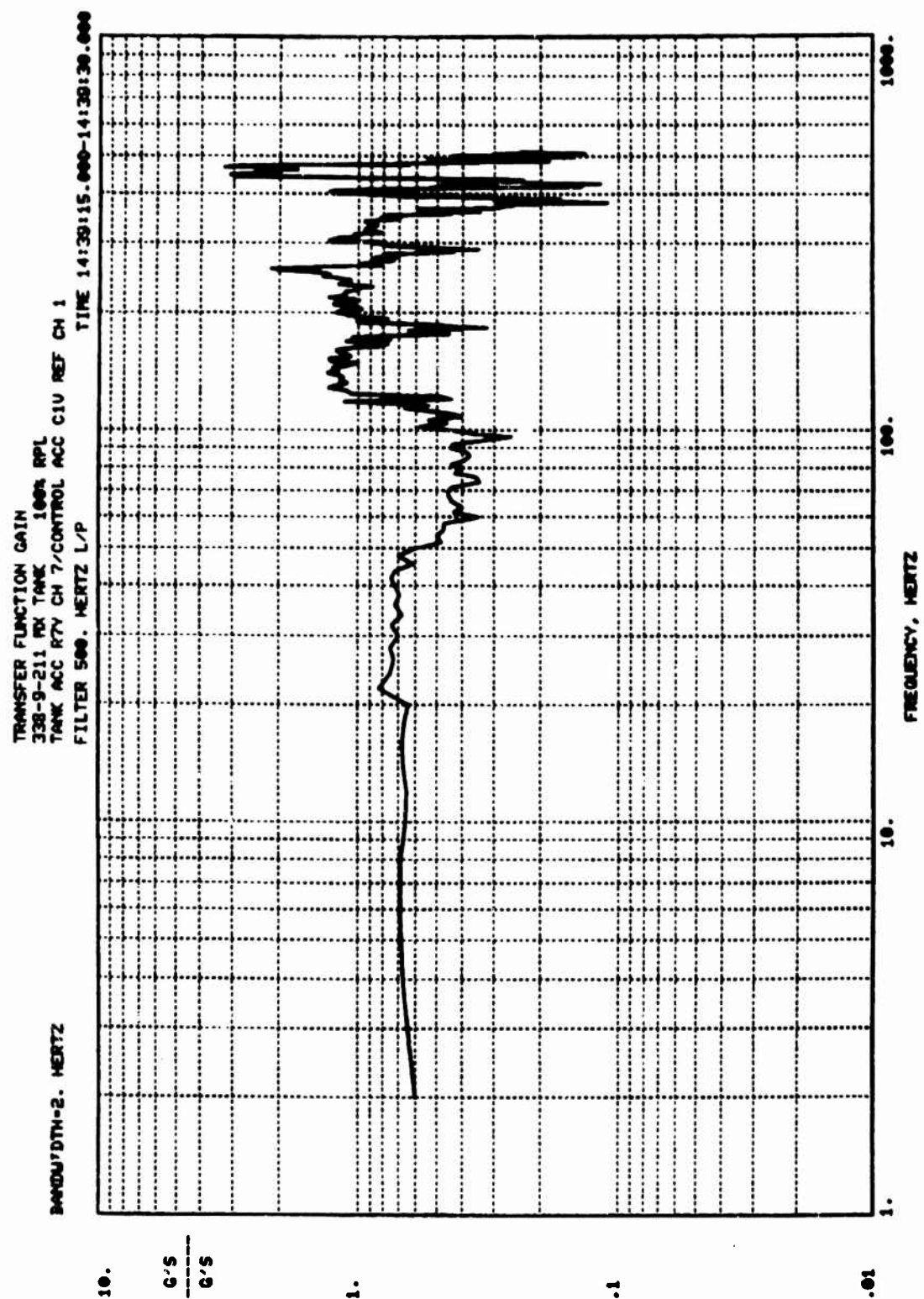


Figure 112. Flange Bottom Y-Axis Gain

of 3 to 4. The y-axis accelerometers on the polar bosses indicated that the highest gains at the bosses (3 to 3.5) were at these same frequencies (Fig. 193 and 194).

In addition to the modes just mentioned, the x-axis accelerometer on the pressurant-side polar boss measured high gains at several frequencies between 100 and 300 Hz, as shown in Fig. 195. The highest (5.5 to 6) were at 190 and 290 Hz. The gains shown in Fig. 196 for the x-axis accelerometer on the liquid-side polar boss indicate maximums of 3 to 4 at approximately 280 and 480 Hz.

The accelerometer mounted on the composite wrap nearest the polar boss measured relatively low gains, with a maximum of nearly 2 at 400 Hz (Fig. 197). The other accelerometer on the composite material measured gains less than 1.

Low-level input (-13 db) and response-limited (tenth-power) unpressurized launch random vibration runs from 10 to 2000 Hz were made to adjust the input level. The durations were 3.4 and 1.6 minutes, respectively. Full-level tests were then run for 1.2 minutes unpressurized, and 1.3 minutes pressurized to 75 psig. This pressure was selected for safety reasons and was limited by the fact that the tank had already been subjected to an expulsion duty cycle and had no previous vibration test history, i.e., was the first unit.

A comparison of data for the two tests indicated there was no significant effect of pressure (75 psig) on the response characteristics (modes and gains) of the tank. The highest gains at the response control points (5 to 10) were at frequencies between 400 and 1500 Hz in the Y direction at two places on the mounting ring, and in the Y direction on the pressurant polar boss as shown in Fig. 198, 199, and 200, respectively. Gains between 10 and 26 at frequencies between 400 and 1000 Hz were measured on the composite wrap as presented in Fig. 201 and 202.

TRANSFER FUNCTION GAIN
 338-9-211 NX TANK RUN #5 TAPE 4219
 TANK RESPONSE ACCEL 89/CONTROL ACCEL C1U
 FILTER 500. HERTZ L/P

TIME 14:39:15.000-14:39:30.000

BANDWIDTH=2. HERTZ

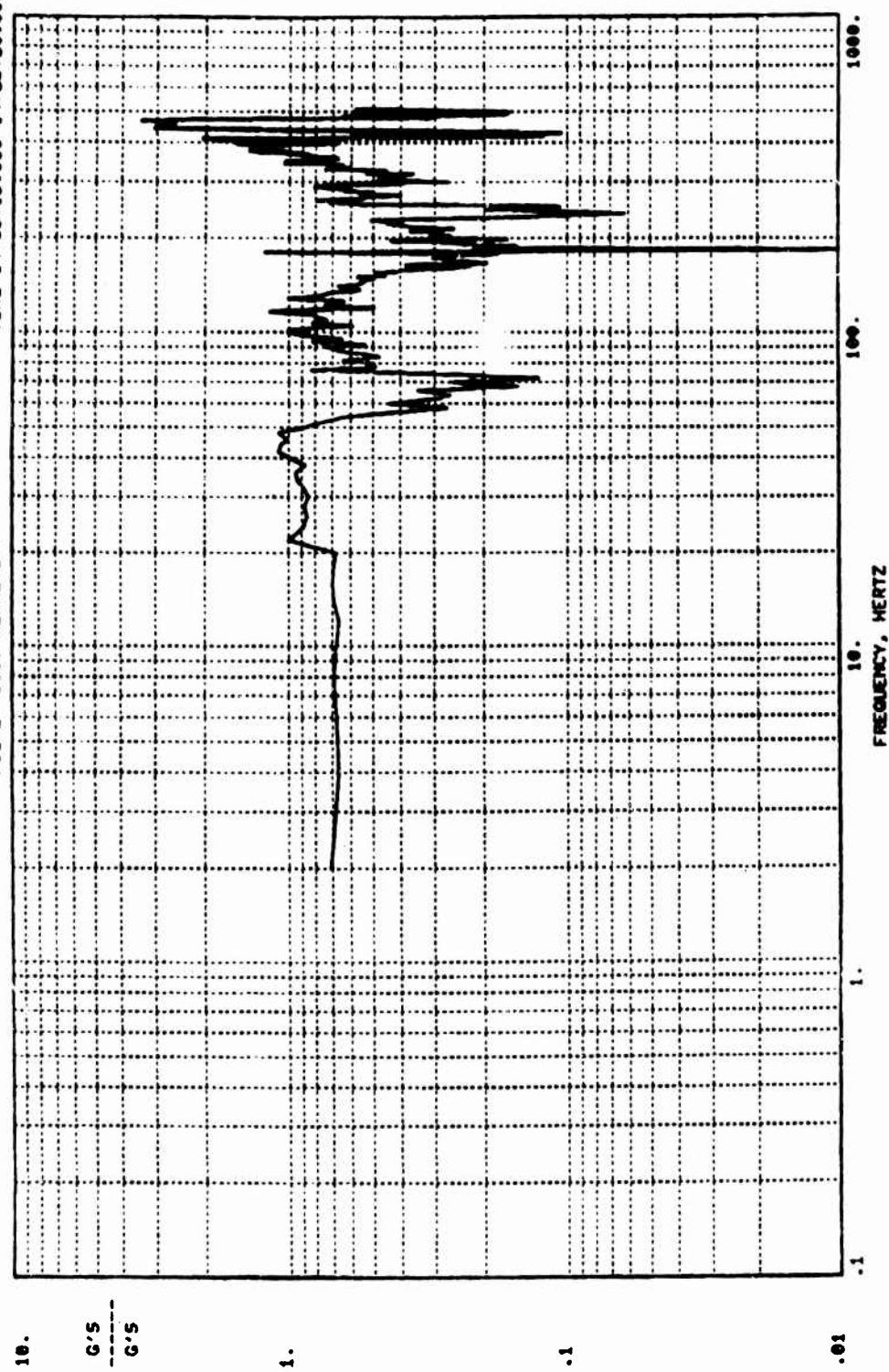


Figure 193. Pressurant Boss Y-Axis Gain

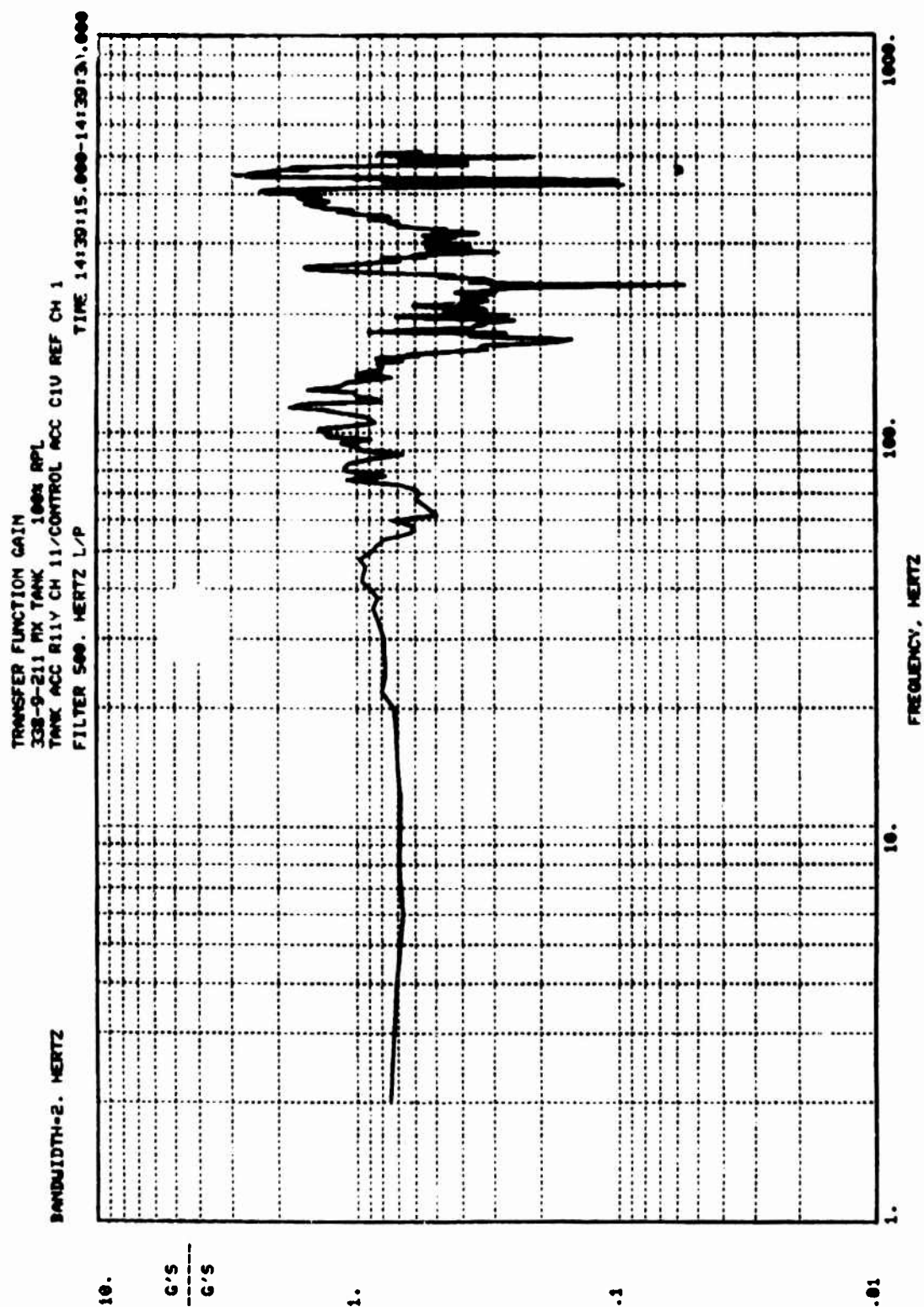


Figure 194. Propellant Tank Y-Axis Gain

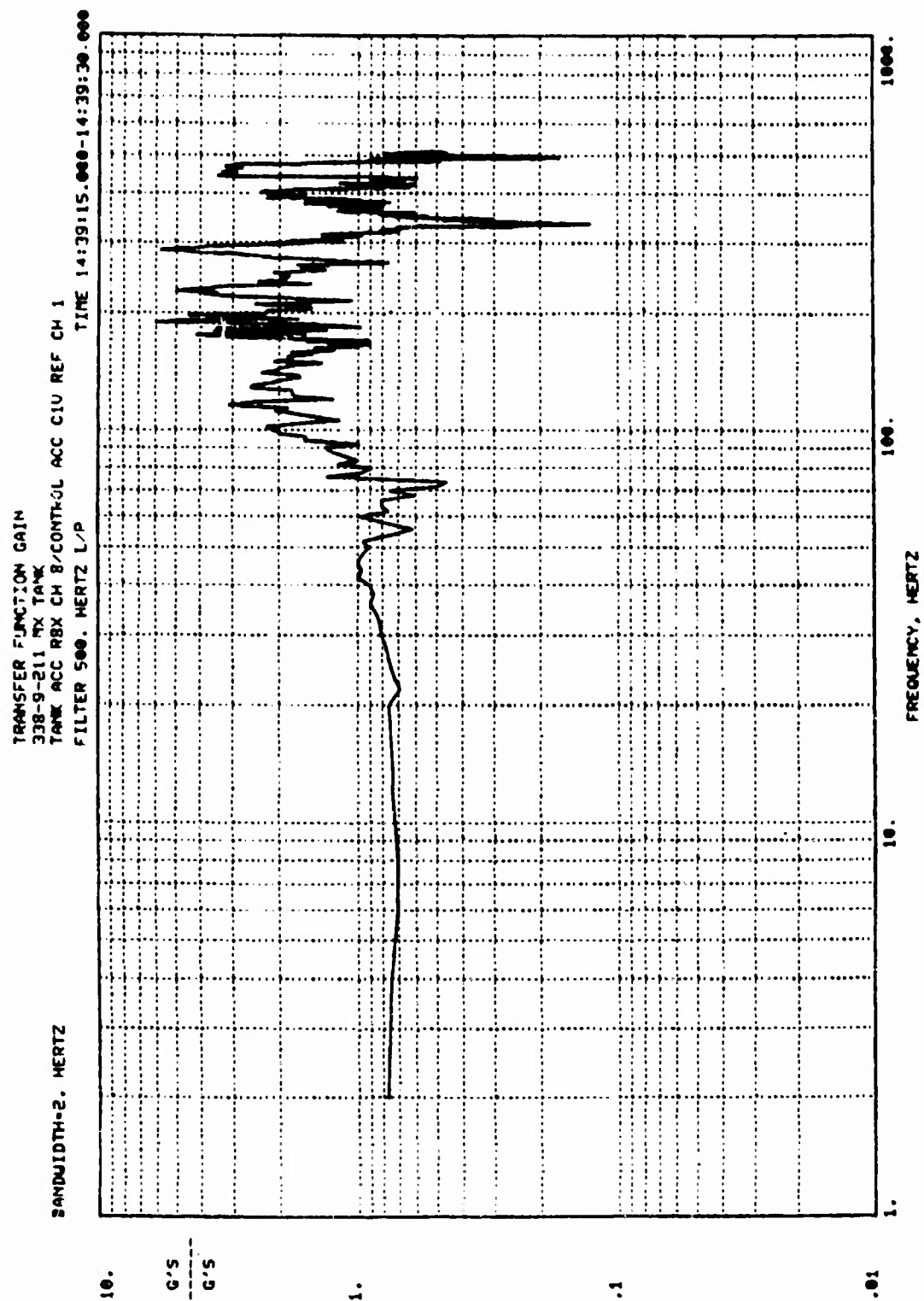


Figure 195. Pressurant Tank X-Axis Gain

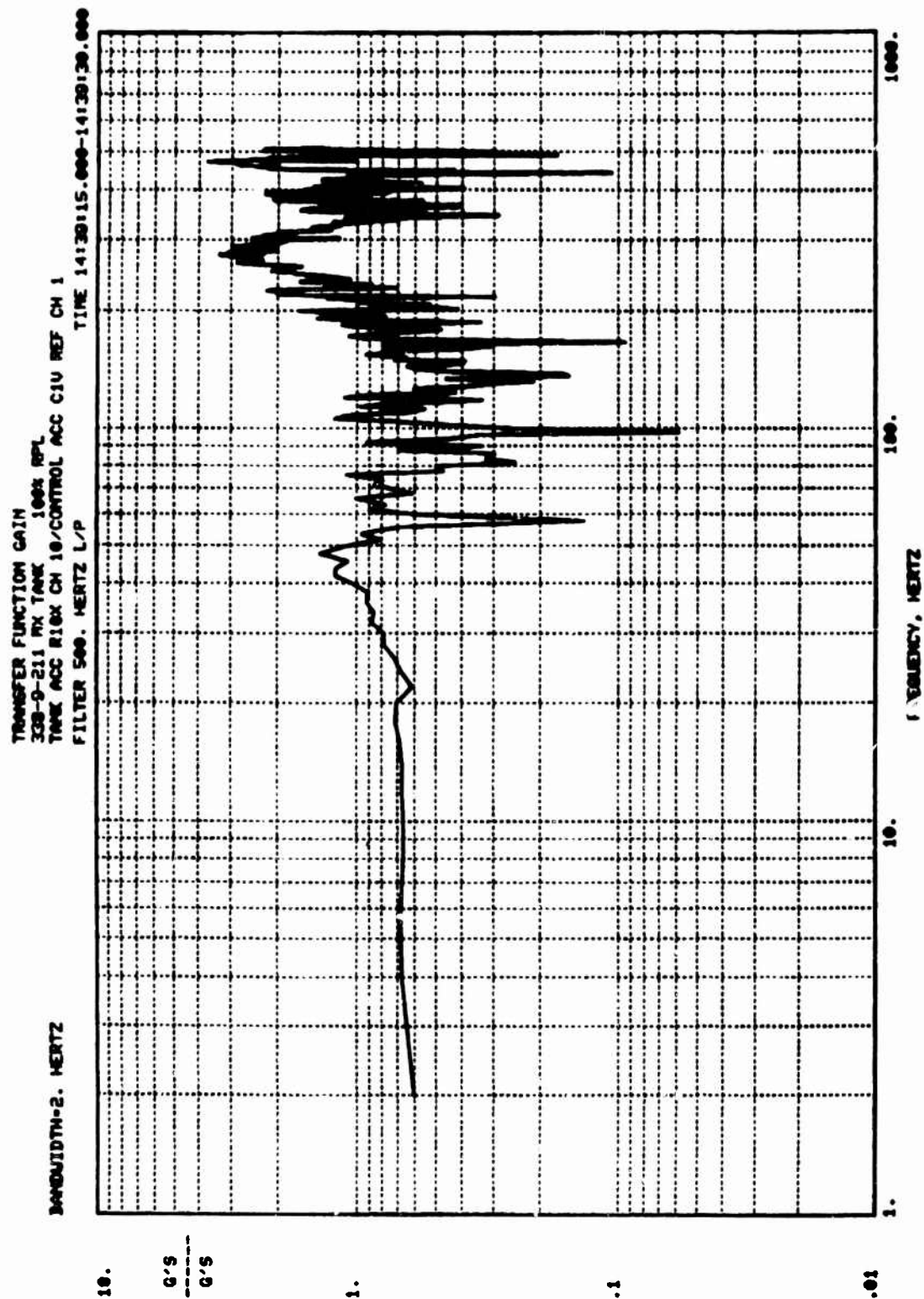


Figure 196. Propellant Boss X-Axis Gain

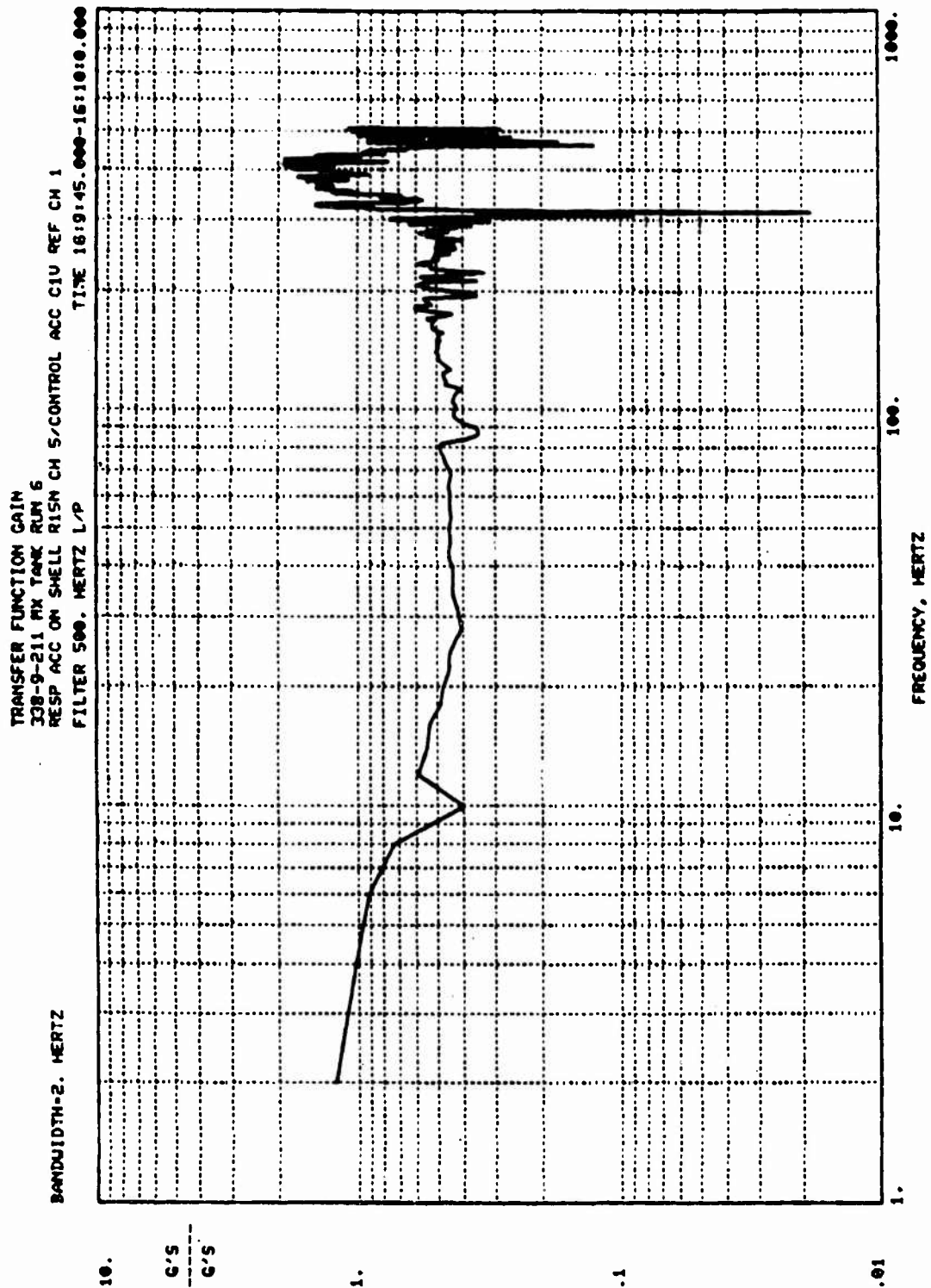


Figure 197. Composite Wrap Gain - Near Pressurant Boss

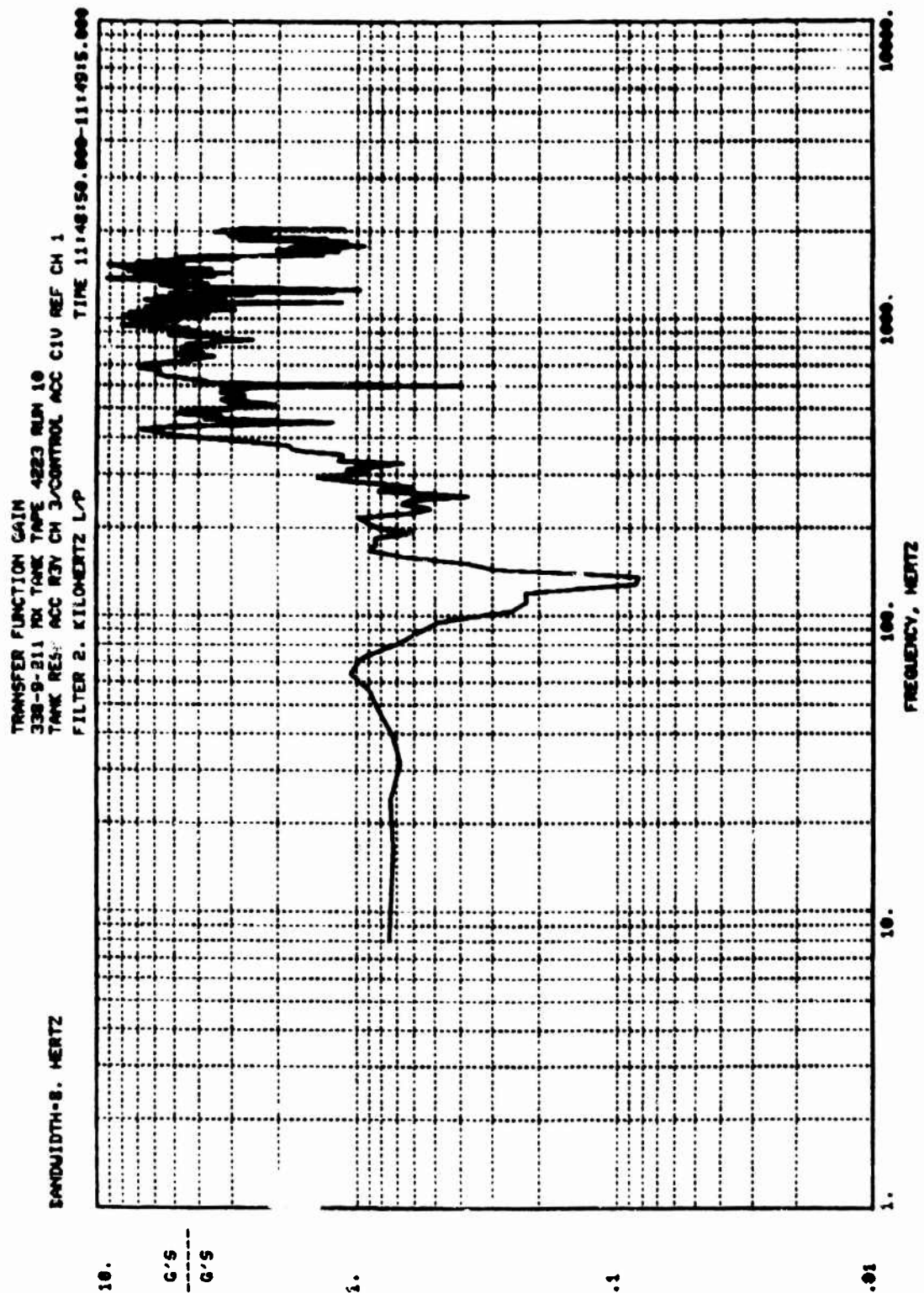


Figure 198. Flange Top Y-Axis Gain

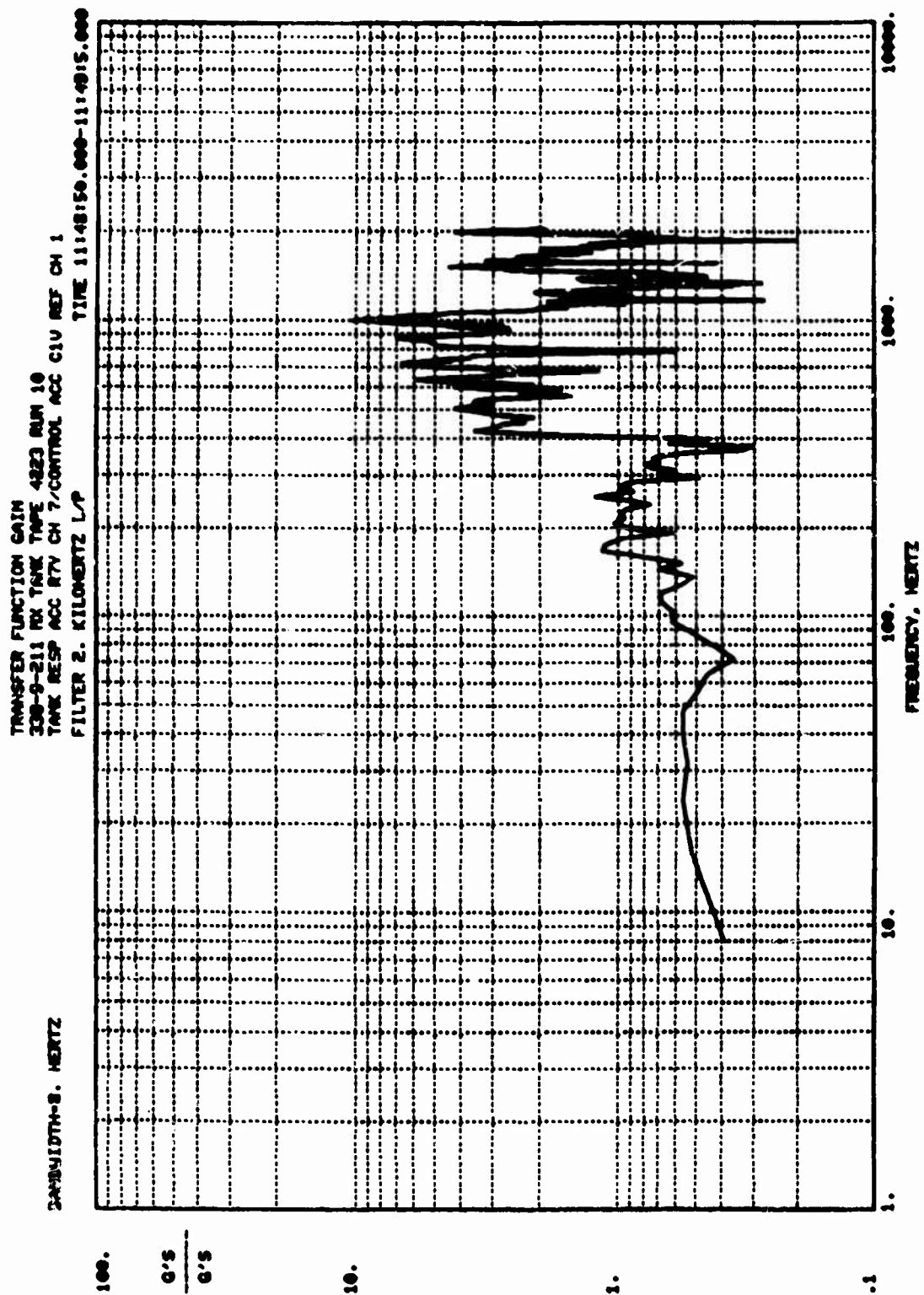


Figure 199. Flange Bottom Y-Axis Gain

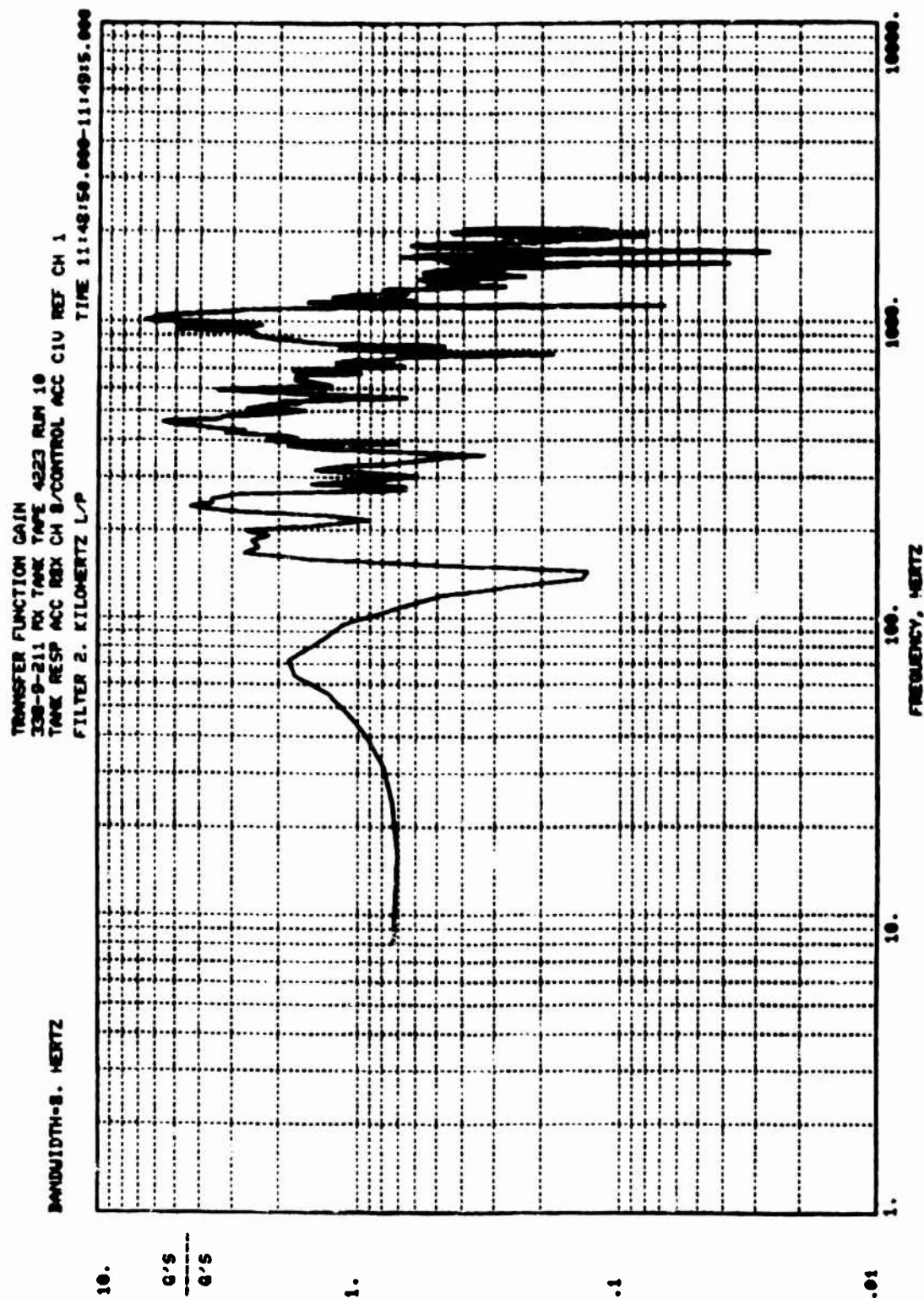


Figure 200. Pressurant Boss X-Axis Gain

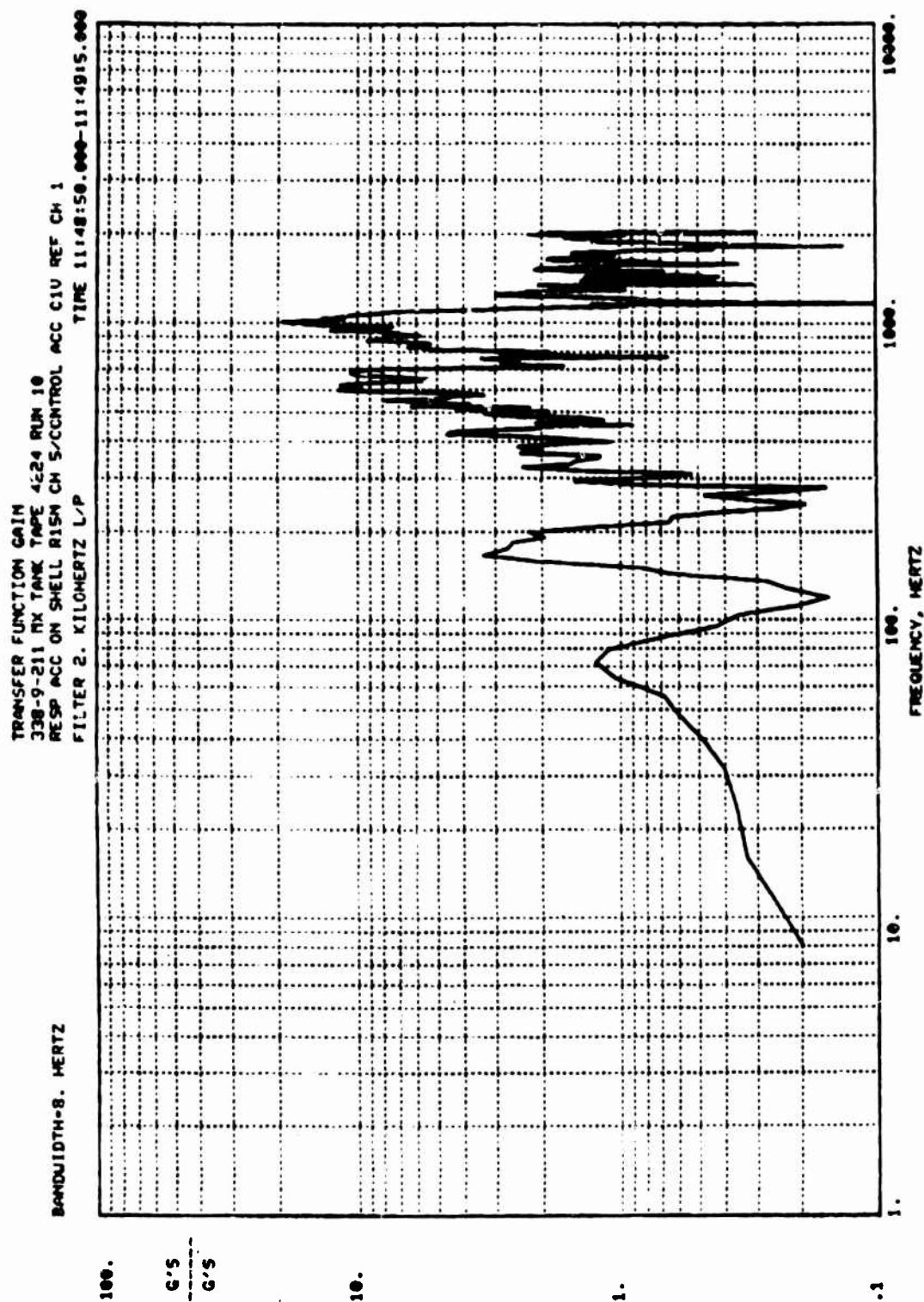


Figure 201. Composite Wrap Gain - Near Pressurant Boss

TRANSFER FUNCTION GAIN
 338-9-211 RX TANK TAPE 4224 RUN 10
 RESP ACC ON SHELL RIGN CH 6/CONTROL ACC C1U REF CH 1
 FILTER 2. KILOWERTZ L/P TIME 11:48:50.000-11:49:15.000

BANDWIDTH-8. HERTZ

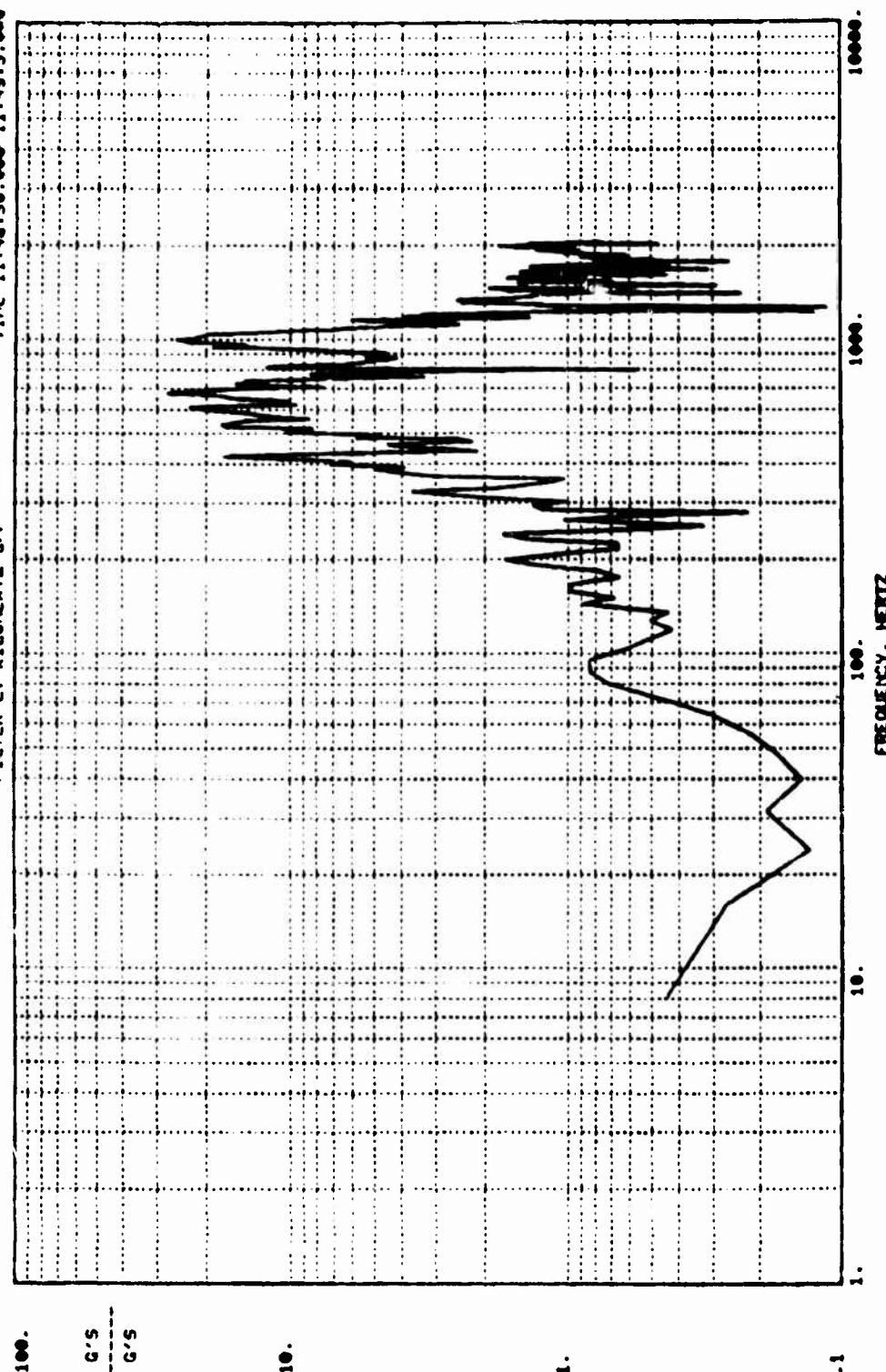


Figure 202. Composite Wrap Gain - Near Flange

Equalization of the pressurized (75 psig) shock spectrum was conducted at one-tenth level from 40 to 160 Hz using a Q of 1.0 and a one-third octave bandwidth. Approximately 100 shocks were required at this level. The required spectrum could not be simulated at higher frequencies because of shaker limitations. One shock was also run at one-fifth and one-half levels to improve the equalization.

The fixture accelerometer data for the full-level shock is presented in Fig. 203. It shows that the test significantly exceeded requirements at low frequencies. The highest level tank responses were measured at the polar bosses and are shown in Fig. 204 through 207. One attempt was made to run a 100-g shock between 100 and 500 Hz, but the results were not significantly different from the 40 to 160 Hz test. There was no visible damage to the tank shell or mounting ring as a result of the vibration or shock tests.

Burst Test. A hydrostatic pressure test was conducted with the flightweight tank at Rocketdyne's Engineering Development Laboratory (Canoga Park, CA) in March 1980. The tank was loaded with water, and pressurized at approximately 8 psi/sec to proof pressure (385 psig) and held for 30 seconds. Pressurization to burst pressure (438 psig) occurred at 4 psi/sec. This pressure was held for 90 seconds. A liner-to-liner weld crack occurred as the burst pressure was attained. There was no evidence of any other damage to the tank, including the composite wrap.

The weld failure was sectioned and analyzed. A continuous line of 0.025 inch porosity was found to extend in both directions from the extremities of the crack. This porosity accentuated crevice-type corrosion at the weld. Corrosion products were visible half-way through the weld. The corrosion resulted from residual water after the expulsion test in October 1979. The tank had been flushed with alcohol, but it was virtually impossible to remove the water trapped near the girth weld between the diaphragm and shell.

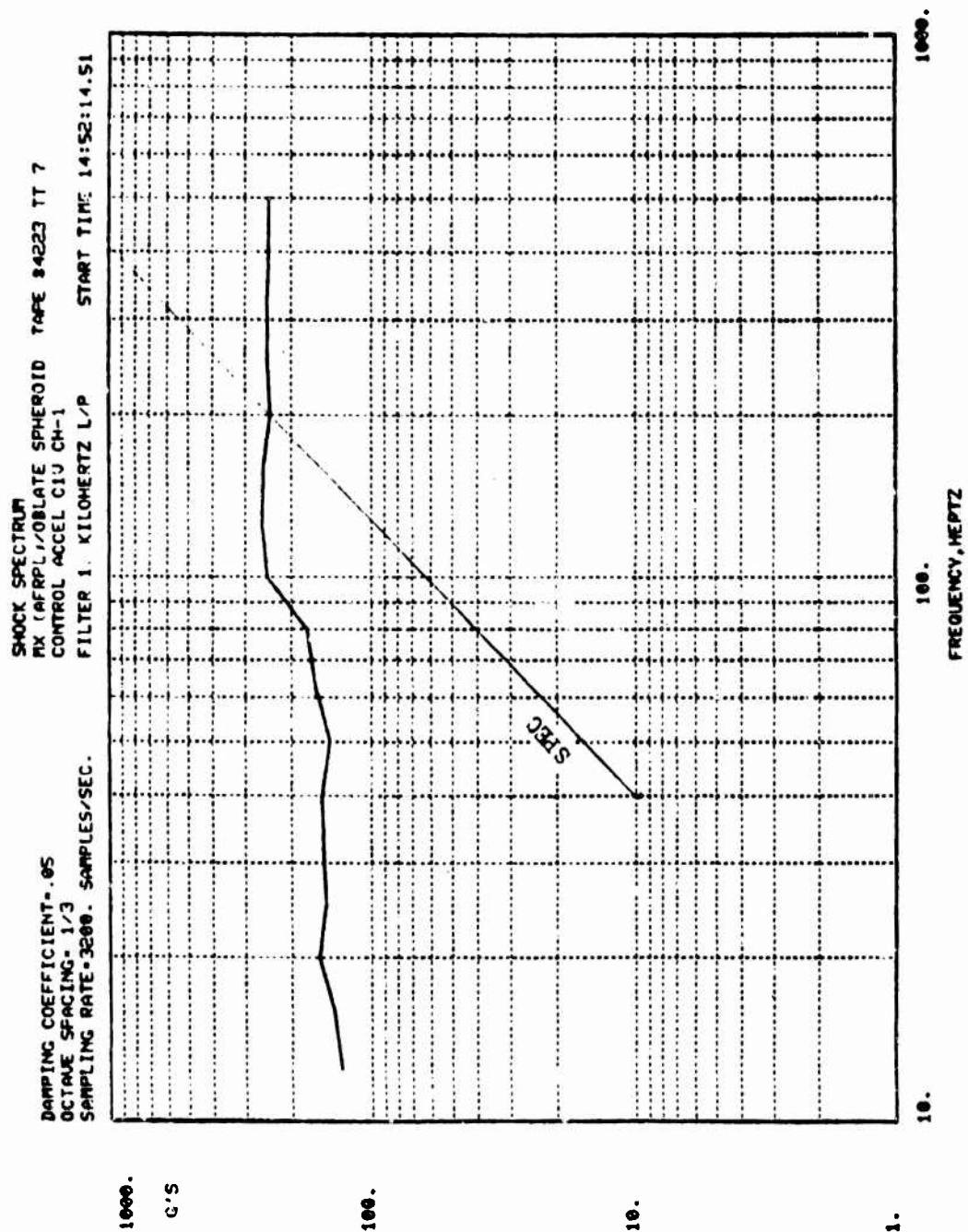


Figure 203. Test Fixture Flight Shock Spectrum

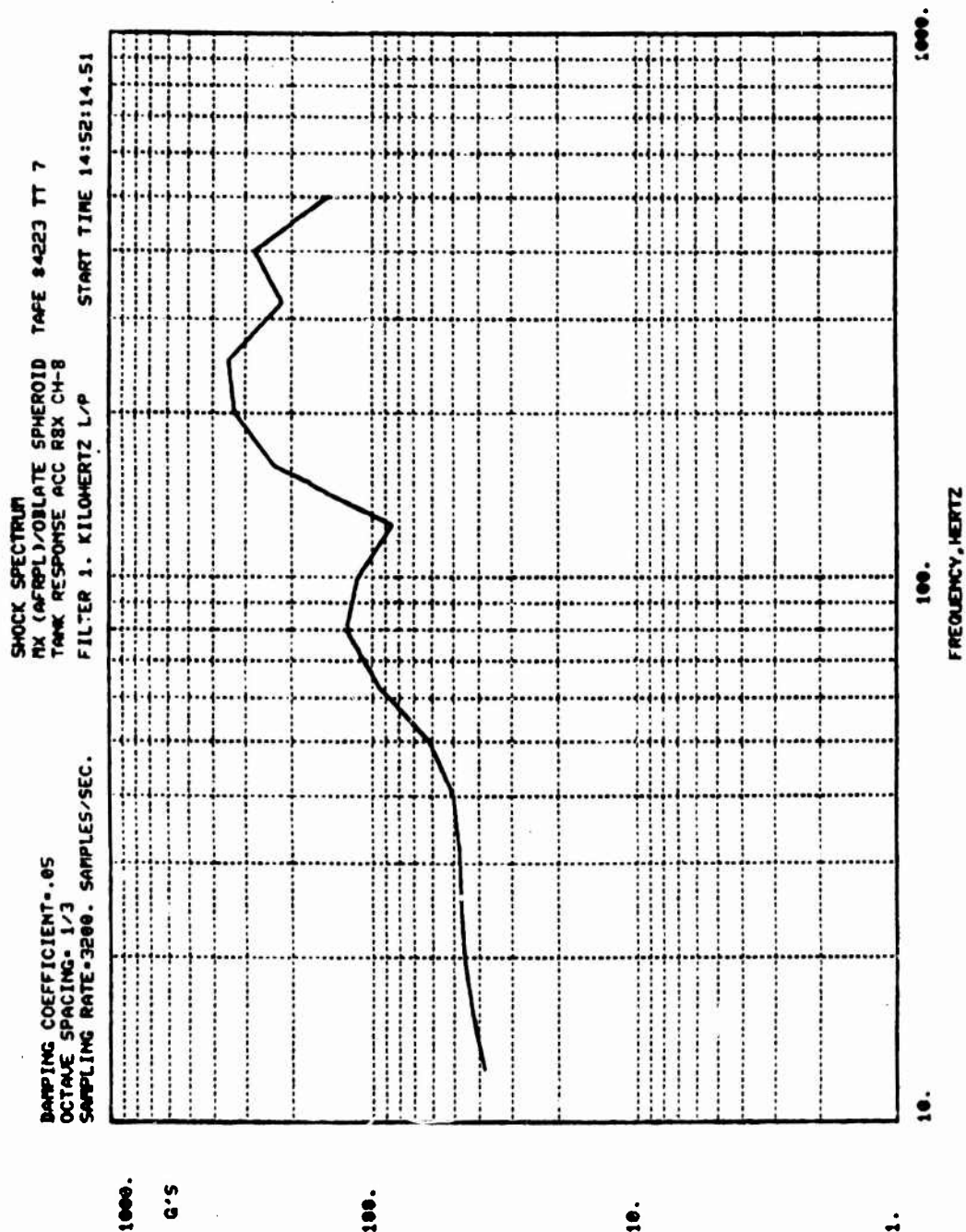


Figure 204. Pressurant Ross X-Axis Shock Spectrum

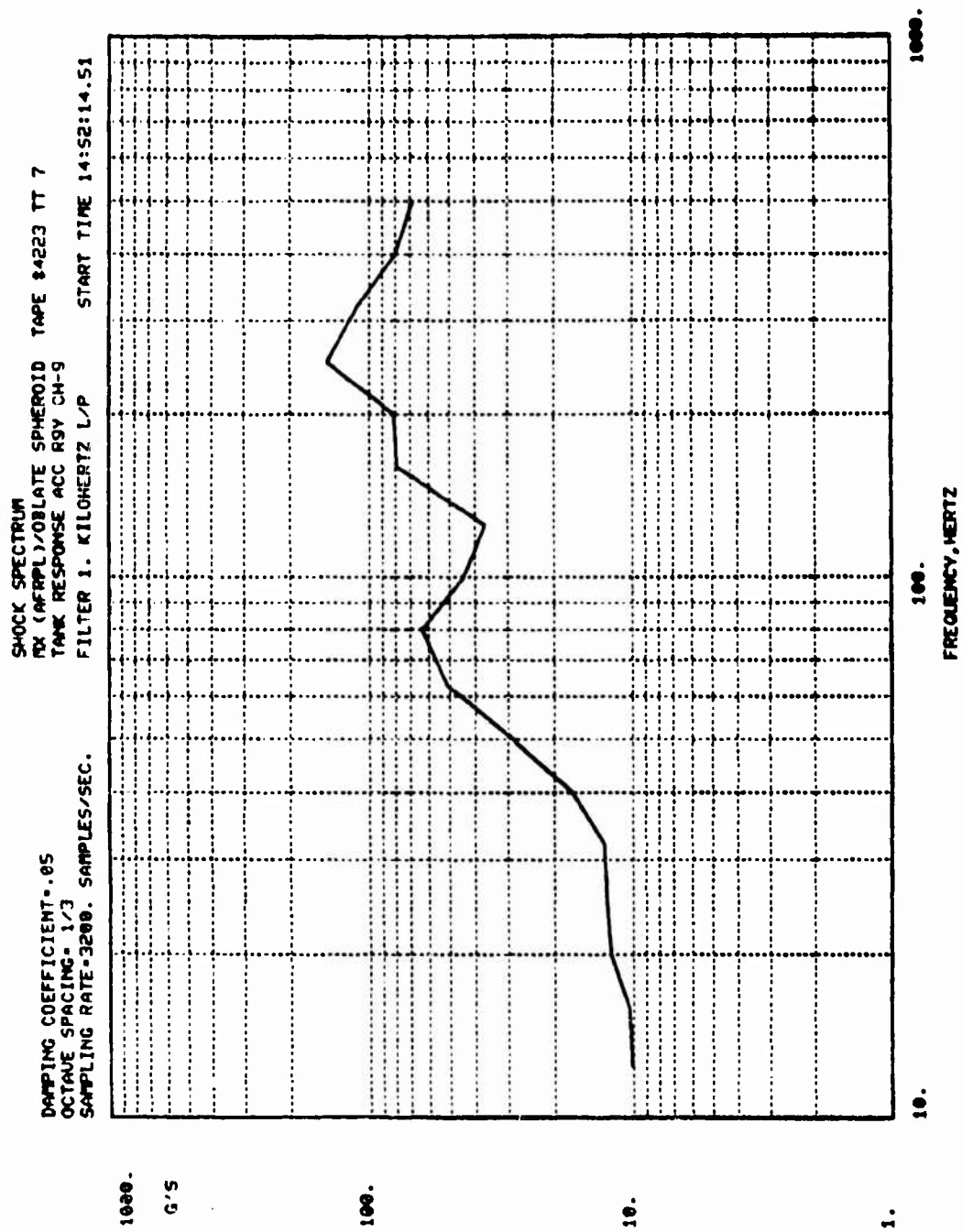


Figure 205. Pressurant Boss Y-Axis Shock Spectrum

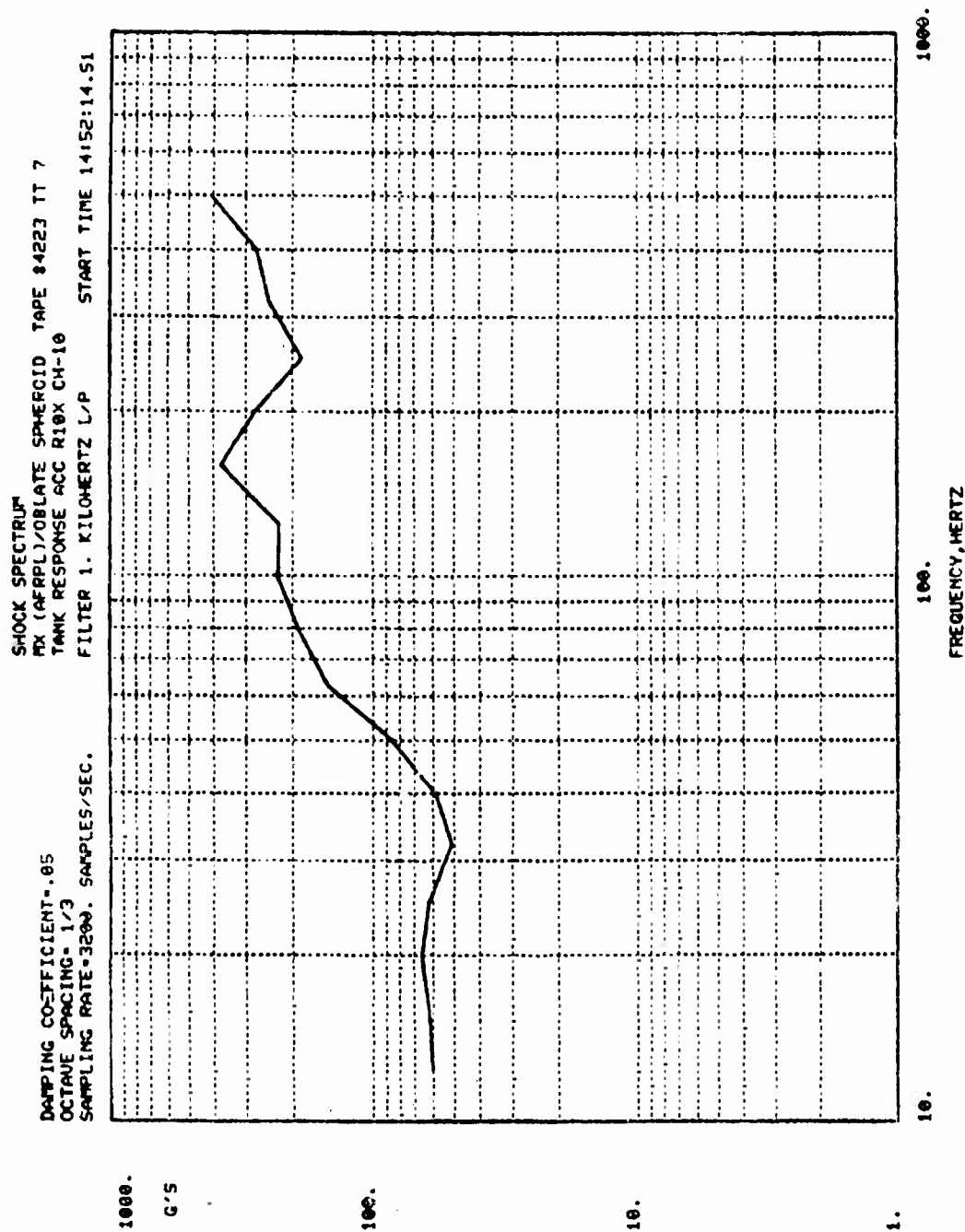


Figure 206. Propellant Boss X-Axis Shock Spectrum

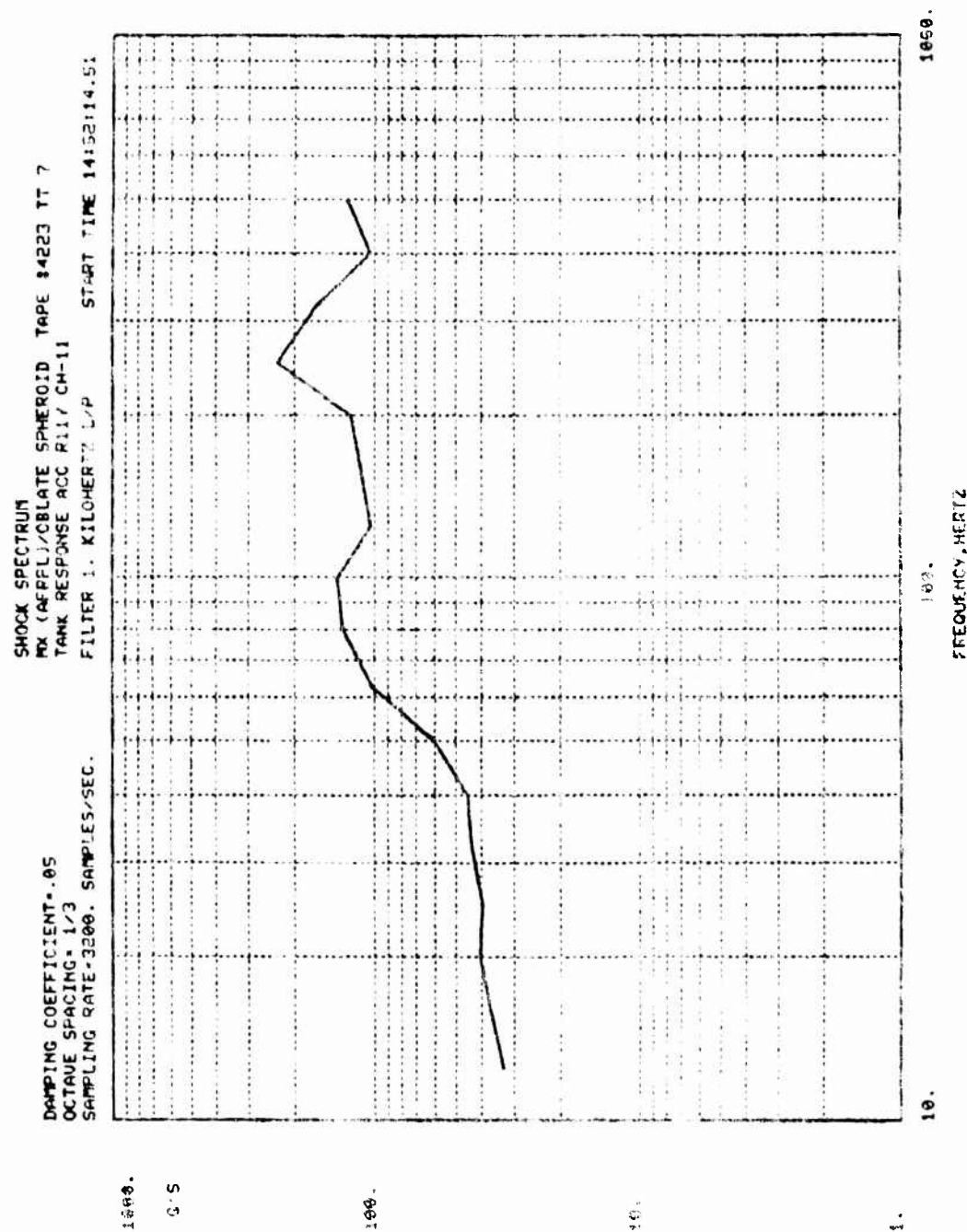


Figure 207. Propellant Boss Y-Axis Shock Spectrum

There was a single-line crack in the weld with only minor branch cracks. Failure was the result of a tensile overload, with no evidence of fatigue, showing that the vibration testing did not contribute to the failure.

PRESSURIZATION SUBSYSTEM FABRICATION AND TEST

A prototype catalytic reactor and two prototype electronically controlled regulators, both described in the Engineering Analyses and Design section, were fabricated and initially tested as components. The reactor and the first of the regulators, along with the prototype pressurant storage tank and facility components were then assembled into a pressurization subsystem and used with Tridyne pressurant during the metal workhorse and lightweight propellant tank expulsion tests.

CATALYTIC REACTOR

A prototype catalytic reactor was fabricated and twelve tests were run at Rocketdyne's Santa Susana Field Lab (Santa Susana, CA) between 22 and 27 March 1978. The test objectives were to select the optimum catalyst bed geometry and determine the effect of flowrate and mission duty cycle on performance. The reactor was subjected to structural dynamic tests with the regulator at Parker Hannifin during June and July 1978 to determine the effect on the catalyst.

Reactor Fabrication

The prototype reactor, which incorporates design features for testing several catalyst bed sizes, is shown in Fig. 208 and 209 with the baseline bed. Additional parts for the other five beds are shown in Fig. 210. The inlet screens were trimmed to fit inside their respective catalyst housings. Without trimming, there would have been a leak path between the inlet plate and the catalyst housing.

Reactor Testing

An acceptable catalyst bed geometry ($D=1.25"$, $L=2.0"$) was established and the effects of flowrate and MDCs I and II were determined. A net reaction temperature rise (uncompensated for heat loss) of 92 to 93 percent of the theoretical maximum was demonstrated.

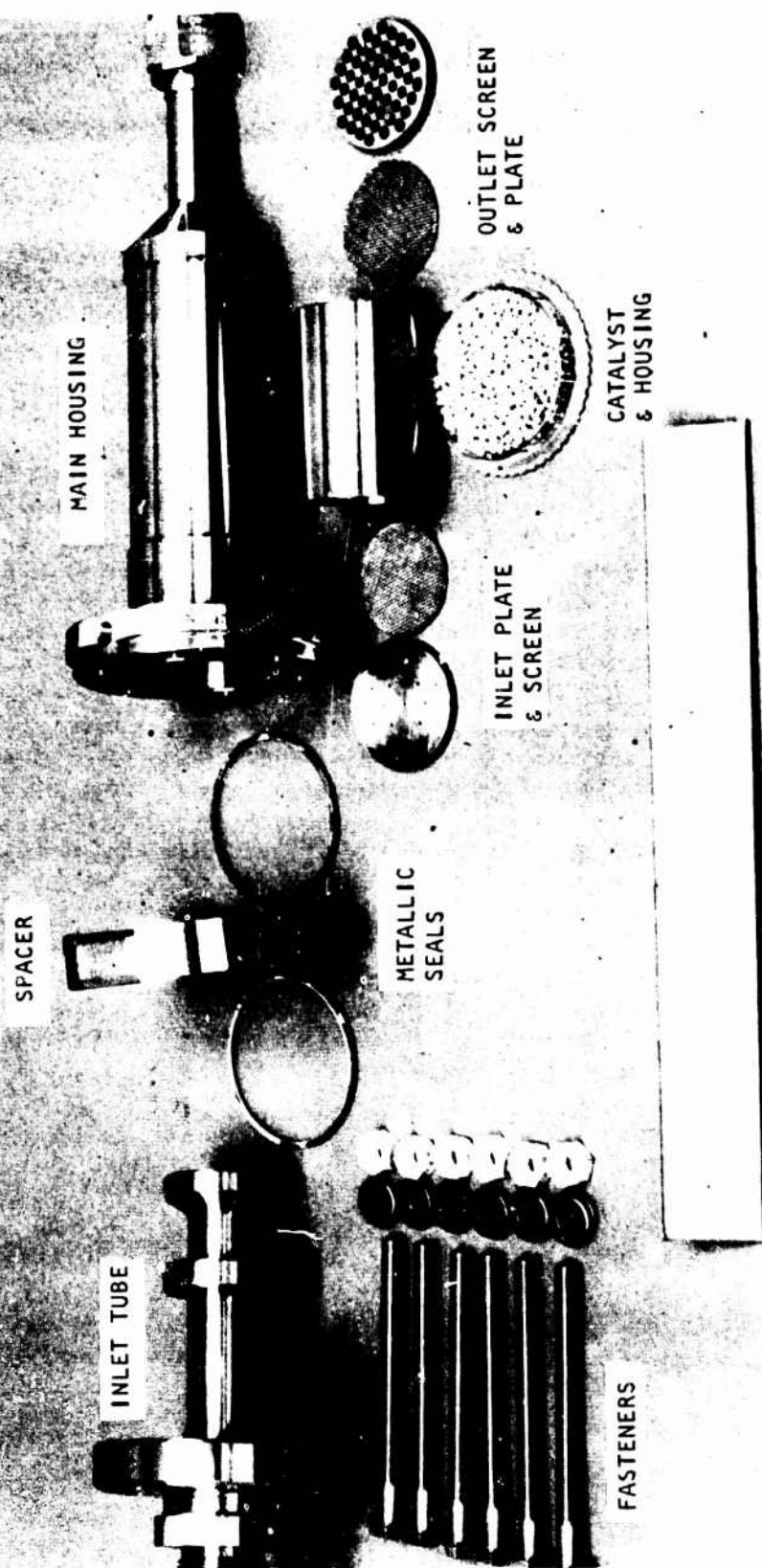
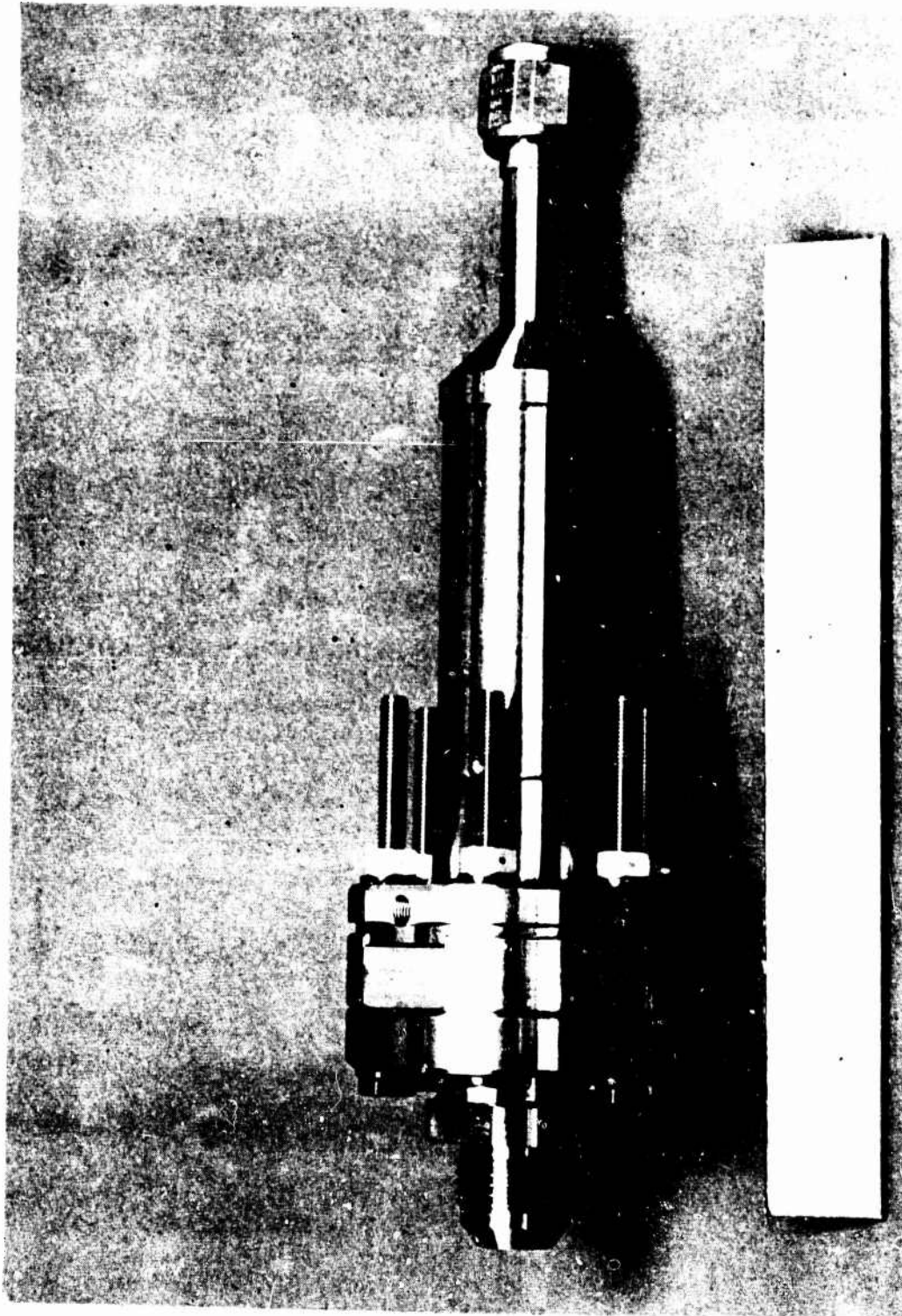


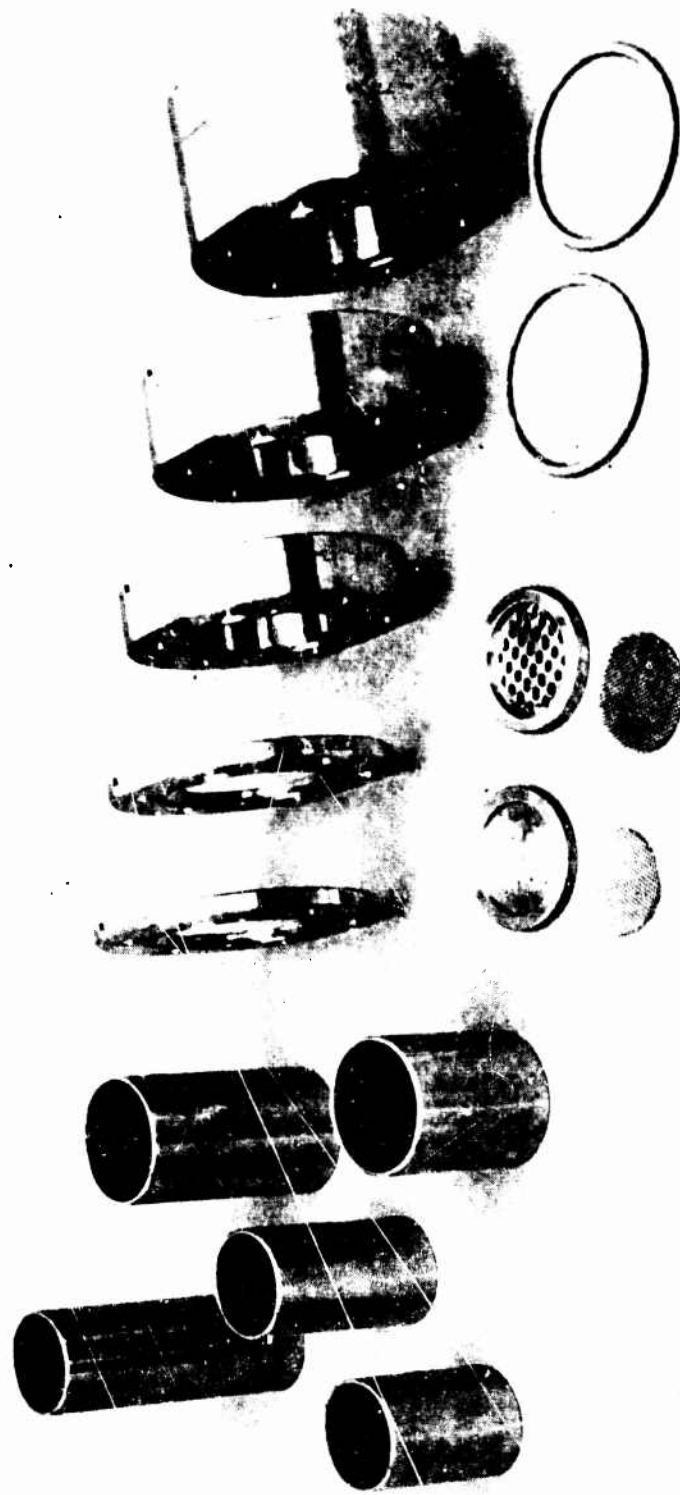
Figure 208. Catalytic Reactor Parts

1X762-3/16/78-C1B



1XZ62-3/16/78-C1C

Figure 209. Assembled Catalytic Reactor



IXZ62-3/16/78-CIA

Figure 210. Interchangeable Reactor Parts

A reactor outlet gas temperature of approximately 1200 F was achieved with the optimum bed, which is 175 F warmer than the propellant tank inlet design temperature. The relatively high outlet temperature is due to the warm reactor inlet gas temperature. The selected Tridyne composition was based on flightweight design analyses assuming a polytropic process exponent of 1.33, which yields colder gas at the reactor inlet than was achieved with the large mass of the facility storage tanks and supply lines.

As a result of performance test observations, it is recommended that the angle of convergence at the outlet of the main housing be made shallower (from 45 to 30 degrees) on the flightweight design. This will permit fuller utilization of the outer portion of the catalyst bed.

A simplified schematic of the performance test facility is presented in Fig. 211. The Tridyne was stored in K-bottles and flowed through two isolation valves to a Fairchild Space Shuttle Orbital Maneuvering System (OMS) series-redundant helium regulator. Only the upstream module was operative and the reference pressure was supplied by a hand-loaded GN_2 facility regulator. After catalytic reaction in the reactor, the gas was split and flowed through parallel high and low flow orifices. In order to preclude use of hot-gas valves, the flow was cooled in a water heat exchanger. The test stand, set up for the initial test, is shown in Fig. 212. The reactor was wrapped with Johns Manville No. 475, 3/16 inch insulation. The parameters that were varied during each test are presented in Table 43.

Structural dynamic testing did not cause any damage to the catalyst. Post-test inspection did not reveal any broken particles or dust.

Tests 1 and 2. The first test was conducted with the large diameter (1.245 inches), short length (1.623) catalyst bed with a nominal regulated pressure of 347 psia for 15 seconds. Flow was initiated by opening the solenoid valve upstream of the regulator with the downstream high-flow solenoid valve open and the low-flow valve closed.

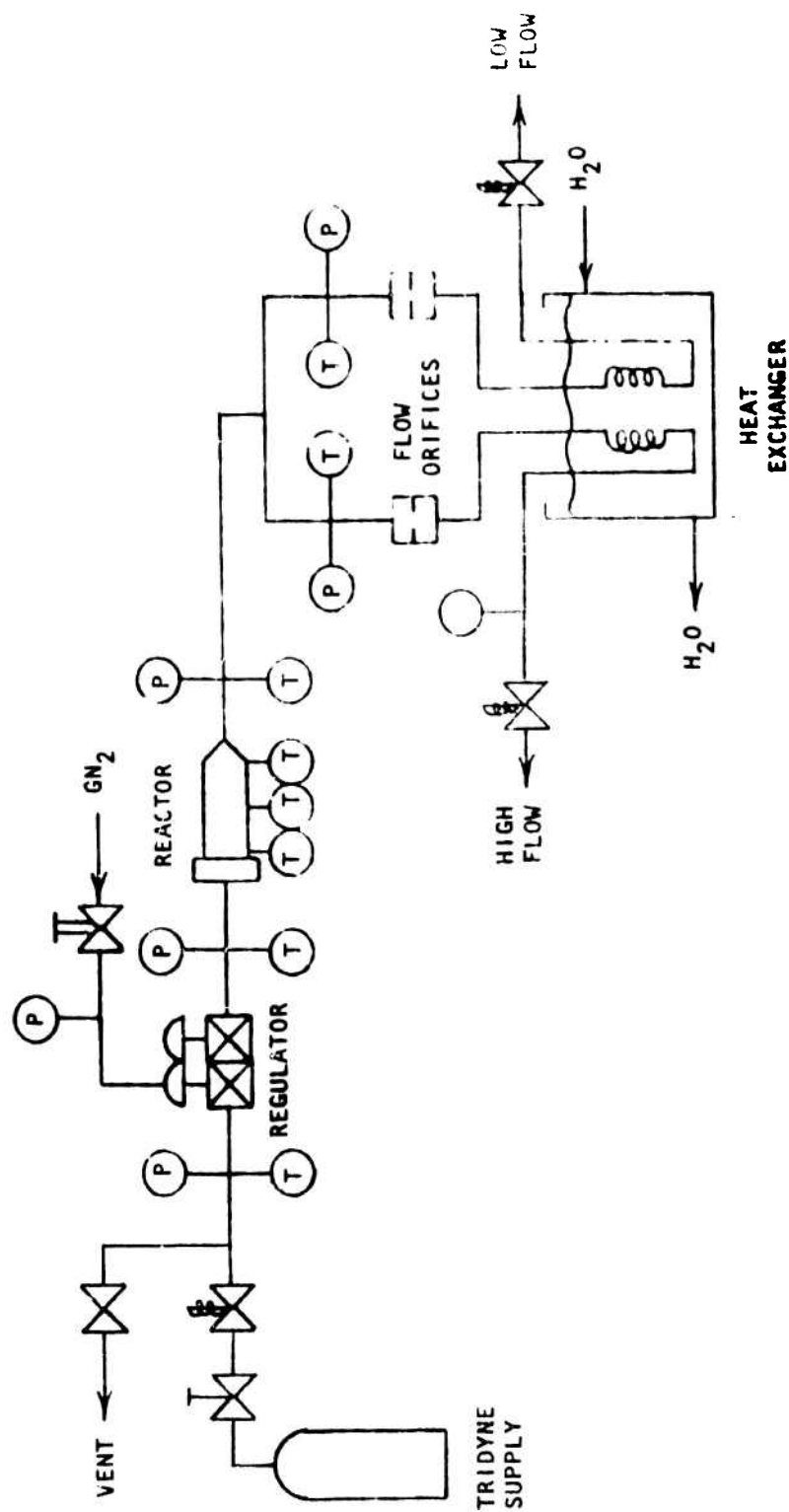
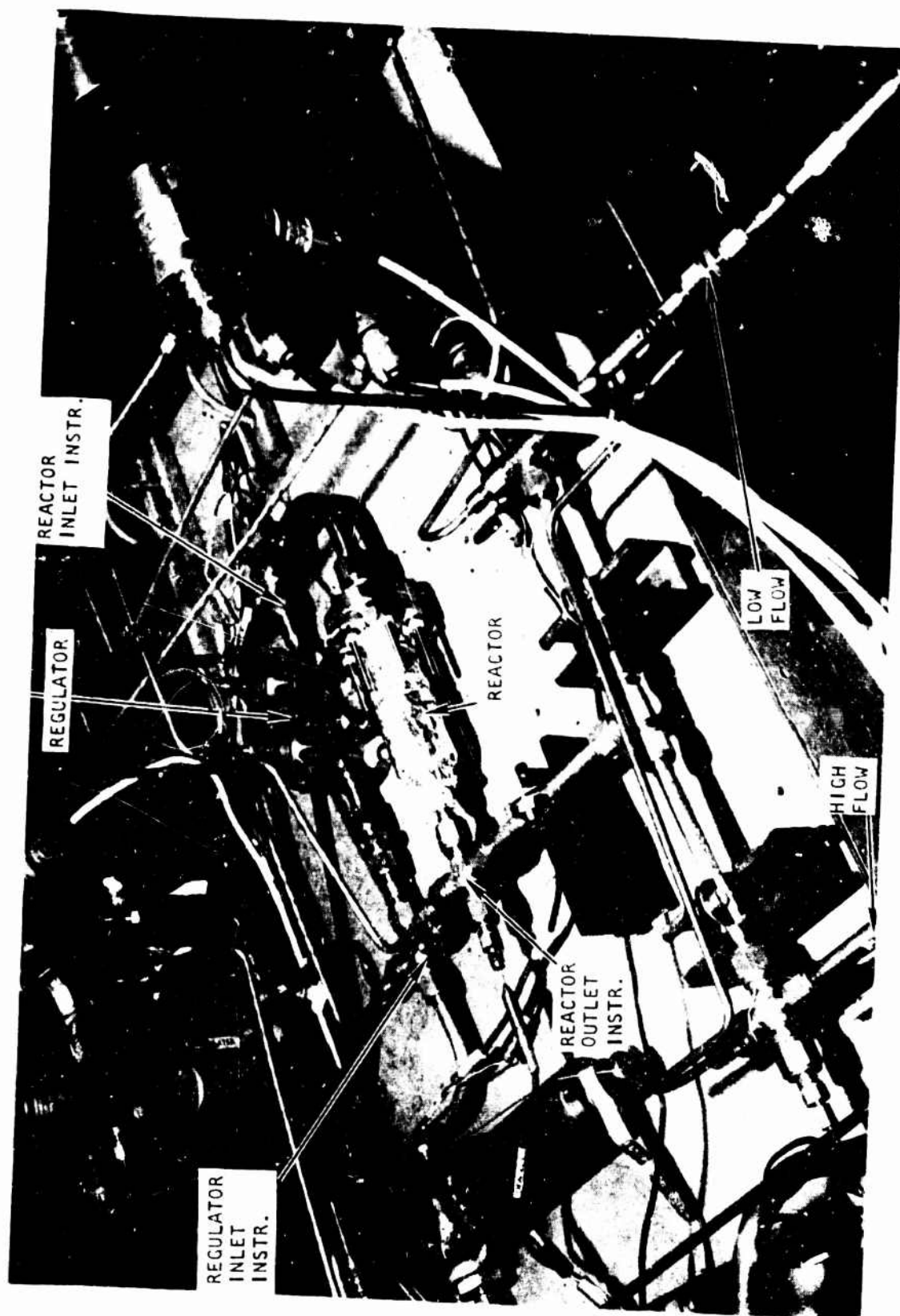


Figure 211. Test Schematic



5DZ34-3/22/78-S1A

Figure 212. Test Stand

TABLE 43. CATALYTIC REACTOR TEST OBJECTIVES

Test No.	Bed Dia. (in.)	Bed L/D	Bed Vol. (in. ³)	Pressure (psia)	Objective (Effect of)
1	1.25	1.3	2.0	350.	Bed Size
2	↓	↓	↓	↓	Repeat No. 1
3	↓	↓	↓	300.	Repeat No. 1
4	1.00	3.2	2.5	↓	Bed L/D
5	1.25	1.6	↓	↓	Bed Length
6	↓	2.0	3.0	↓	Bed Length, Flowrate
7	↓	1.6	2.5	400.	Flowrate
8	↓	↓	↓	300.	MDC 1
9	↓	↓	↓	400.	Repeat No. 7
10	↓	↓	↓	300.	Repeat No. 8
11	↓	↓	↓	400.	Repeat No. 7
12	↓	↓	↓	300.	MDC 11

The nominal regulator inlet pressure decayed from 1380 to 690 psia during the test. The regulated pressure overshoot to 515 psia and oscillated ± 55 psi about the nominal pressure at 17 Hz initially. At the end of the run, the oscillation was ± 48 psi at 11.5 Hz. The oscillation propagated through the reactor to the flow orifice.

The second test was run with both discharge valves initially closed and the system pre-pressured to preclude slam-start conditions. Once again the regulated pressure oscillated (364 ± 80 psia). The nominal regulator inlet pressure decayed from 1965 to 1365 psia during the 10 second test. The frequency of the oscillation decreased from 18 to 17 Hz during the test.

The only explanation that Fairchild had for the instability was the extremely small volume between the regulator and the flow orifice (approximately 10 to 15 cubic inches). A facility regulator was therefore installed for the third test. It was also decided to reduce the nominal reactor inlet pressure to 300 psia to reduce the flowrate, which was higher than desired. The high flowrate was because of significant heat loss from the tubing which increased the gas density.

Test 3. The third test with the large diameter, short length catalyst bed (1.98 cubic inches) was successful. The reactor inlet pressure was 302 psia and the duration was 9.5 seconds. The reactor outlet gas temperature was 1152 F at the end of the run, which corresponds to a temperature rise (ΔT) of 1093 F. This ΔT is 89.4 percent of the theoretical maximum. The flowrate at the end of the run was 0.023 lb/sec. The outerwall temperatures from upstream to downstream were 60, 60 and 96 F, respectively. The first two of these thermocouples were upstream of the inlet plate as shown in Fig. 213. The data at the end of the run is summarized in Table 44.

The reactor gas transient temperature rise, as a percentage of the theoretical maximum, is presented in Fig. 214. This format was chosen for comparative purposes because the inlet temperature varied during the run and also from run to run, as did the Tridyne composition. The irregularity in the curve at the beginning of the test is due to the regulator pressure (and therefore flowrate) transient.

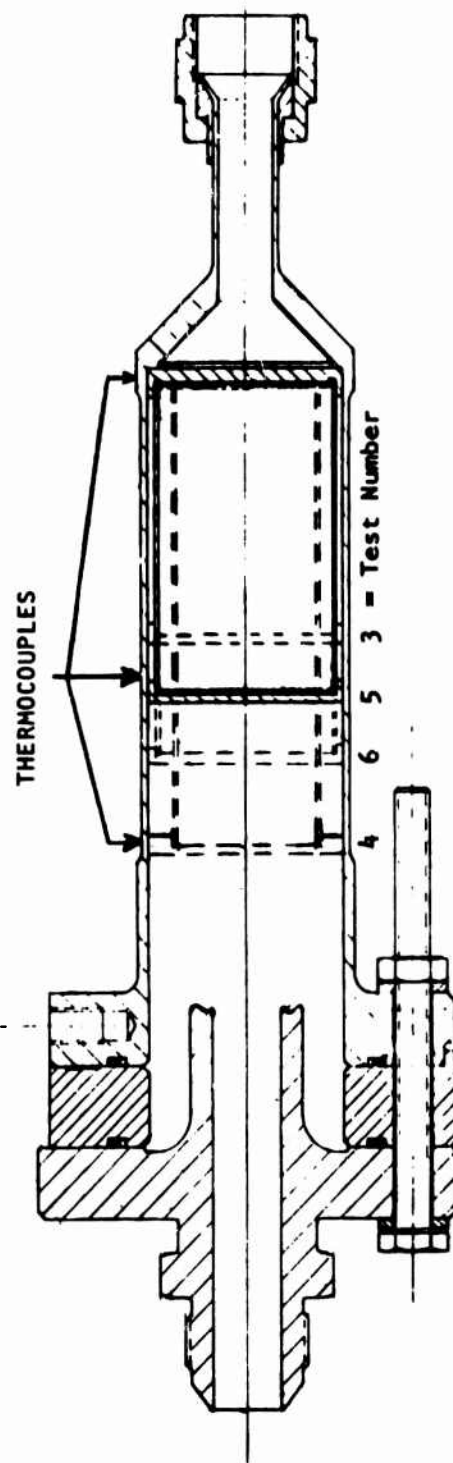


Figure 213. Thermocouple Locations Relative to Catalyst Beds

TABLE 44. TEST DATA SUMMARY

TEST NUMBER	DATE	CATALYST DIA. (IN)	CATALYST LENGTH (IN)	CATALYST VOLUME (IN ³)	REACTOR INLET PRESS. (PSIA)	REACTOR GAS INLET TEMP. (°F)	REACTOR GAS OUTLET TEMP. (°F)	REACTOR GAS TEMP. INCREASE (°F)	REACTOR UPSTREAM WALL TEMP. (°F)	REACTOR MIDSTREAM WALL TEMP. (°F)	REACTOR DOWNSTREAM WALL TEMP. (°F)	REACTOR FLOWRATE (L/P/SEC)	REACTOR GAS TEMP. INCREASE (°F)	COMMENTS
1	22MAR78	1.245	1.523	1.38	347 ± 40	1113	1075		69	68	91	-	-	Regulator oscillated
2	23MAR78	1.245	1.523	1.38	344 ± 40	1091	1039		94	80	118	-	-	Regulator oscillated
3	23MAR78	1.000	3.153	2.48	302	1192	1073		60	60	56	0.023	89.4	Good data
4		1.245	2.827	2.57	304	1120	1045		72	230	175	0.019	87.2	Good data
5		1.245	2.827	2.57	296	1194	1131		72	101	245	0.018	90.5	Good data
6		1.245	2.827	2.57	298	1082	1033		70	93	229	0.008	83.6	Good data
6C		1.245	2.827	2.57	299	1085	946		73	260	267	0.004	77.4	Good data
7	23MAR78	1.245	2.827	2.57	297	1099	1002		79	127	395	0.000	81.9	Internal leak
8		1.245	2.827	2.57	295	1095	896		85	130	167	0.000	69.5	Internal leak
9		1.245	2.827	2.57	295	1095	896		89	145	157	0.001	69.3	Internal leak
10		1.245	2.827	2.57	295	1095	896		122	267	430	0.0	87.6	Internal leak
10A		1.245	2.827	2.57	295	1095	896		79	61	127	0.021	87.3	Internal leak
10B		1.245	2.827	2.57	295	1095	896		92	129	407	-	83.3	Internal leak
10C		1.245	2.827	2.57	295	1095	896		70	94	220	0.19	92.8	Internal leak
11		1.245	2.827	2.57	295	1095	896		121	305	570	0.0	87.6	Internal leak
12	27MAR78	1.245	2.827	2.57	294	1124	1052		104	80	240	0.019	86.3	Internal leak
12A		1.245	2.827	2.57	291	1151	1046		95	75	246	0.005	86.9	Internal leak
12B		1.245	2.827	2.57	290	1151	1046		80	76	237	0.022	77.8	Internal leak
12C		1.245	2.827	2.57	290	1151	1046		122	264	455	0.0	87.6	Internal leak
13		1.245	2.827	2.57	290	1151	1046		85	78	205	0.000	71.1	Internal leak

Test No.	Diameter (in)	L/D	Volume (in ³)
3	1.25	1.3	2.0
4	1.00	3.2	2.5
5	1.25	1.6	2.5
6	1.25	2.0	3.0

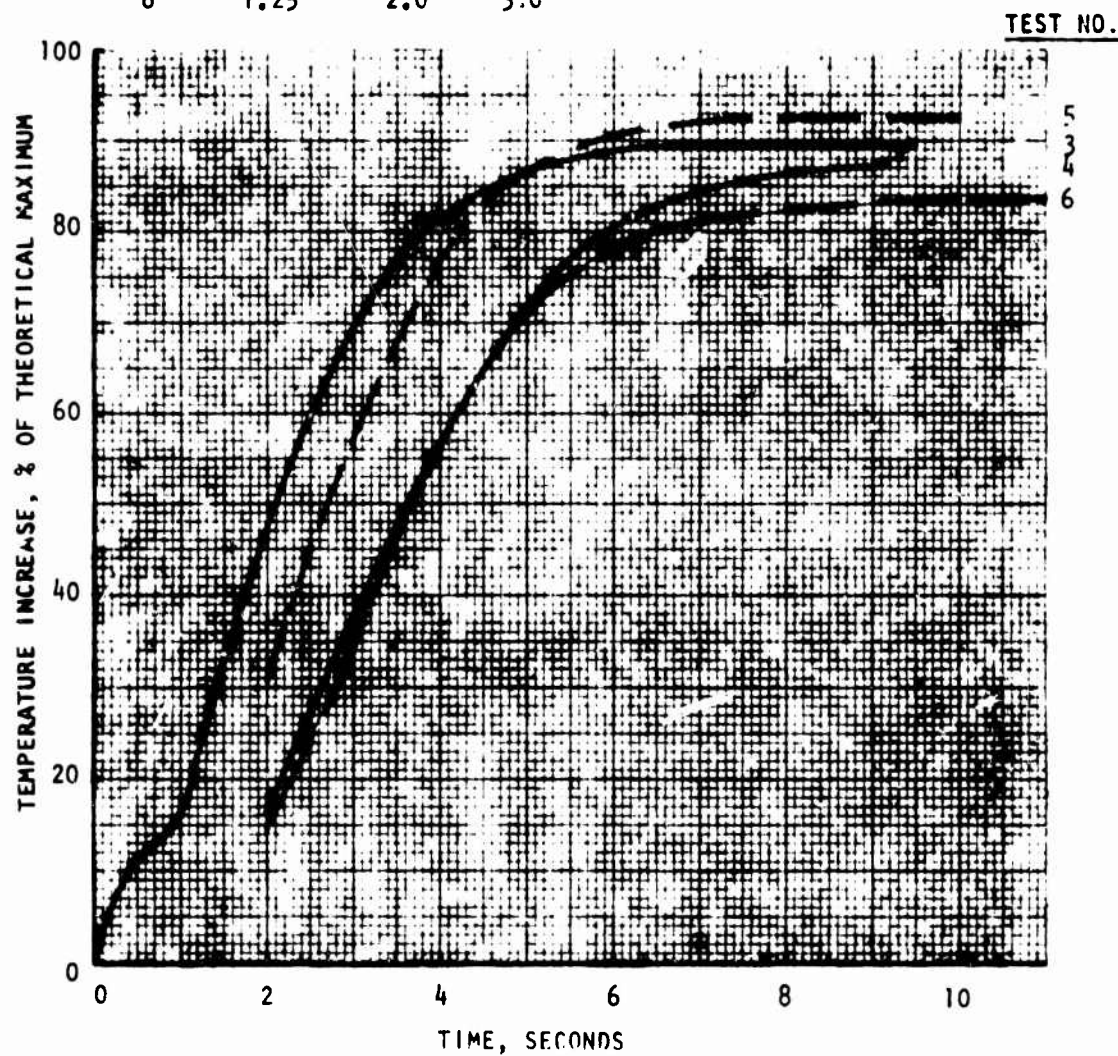


Figure 214. Reactor Temperature Increase Transients

In disassembling the reactor for the next test it was observed that the downstream screen was discolored by the warm gas only at the center. The diameter was approximately the same as the outlet tubing, indicating the angle of contraction of the housing was probably too steep. This flow pattern would have reduced the effectiveness of the catalyst.

Test 4. The fourth test was with the small diameter (1.0 inch), long length (3.153 inches) catalyst bed. The volume (2.48 cubic inches) was approximately 25 percent larger than the previous bed tested. The two shorter lengths were not tested because of the relatively low efficiency (89.4 percent) achieved in test No. 3.

The nominal reactor inlet pressure was 304 psia and the test duration was 9 seconds. The reactor outlet gas temperature was 1120 F at the end of the run, which corresponds to a ΔT of 1065. This is 87.2 percent of the theoretical maximum, slightly lower than the previous test. Because of the larger volume, it also had a slower response. The flowrate at the end of the run was 0.019 lb/sec.

Test 5. The fifth test was conducted with the large diameter (1.245 inches), medium length (2.027 inches) catalyst bed at a nominal reactor inlet pressure of 296 psia for 10 seconds. This bed had the same volume as the previous test. The reactor outlet gas temperature at the end of the run was 1194 F, with a corresponding ΔT of 1131 F. This corresponds to 92.5 percent of the theoretical maximum, the highest efficiency of the three beds tested.

Because of the larger bed volume, its response was slower than with the other large diameter bed (test No. 3). The flowrate at the end of the run was 0.018 lb/sec.

Test 6. The sixth test used the large diameter (1.245 inches), long length (3.153 inches) catalyst bed with a volume of 2.98 cubic inches. Since the trend with the large diameter beds was an increasing gas temperature with increasing bed length, it was assumed this test would result in the highest temperature.

Therefore, the test was set up to determine the effect of flowrate. After 11 seconds of nominal flow, the high flow valve was closed and the low flow valve was opened for 9 seconds. The valve positions were then switched for 2 seconds of nominal flow.

The reactor inlet pressure ranged between 297 and 299 psia during the test. The reactor outlet gas temperature was 1082 F ($\Delta T = 1023$ F) at the end of the first 11 seconds of nominal flow (0.020 lb/sec). The reactor ΔT was only 83.6 percent of the theoretical maximum (the lowest of the four beds tested). Being the largest, this bed also had the slowest response. The test data appeared to show that heat loss from this large catalyst bed more than offset the expected increase in reaction completion.

During the subsequent period of low flow (0.001 lb/sec), the reactor outlet temperature had dropped to 959 F ($\Delta T = 899$ F) at 3 seconds, but slowly increased to 1005 F ($\Delta T = 946$ F) at 9 seconds and was still increasing when the high flow was initiated again. The high flow was for only 2 seconds, but was sufficient to increase the reactor outlet gas temperature to 1059 F ($\Delta T = 1002$ F). Had the test not been terminated, the 1023 F ΔT achieved during the first part of the test would probably have been duplicated.

Test 7. Since the large diameter (1.245 inches), medium length (2.027) catalyst bed had resulted in the largest reaction temperature rise, it was selected for use in all the remaining tests. The seventh test was conducted for 10.5 seconds with a reactor inlet pressure of 396 psia to investigate the effect of flowrate on performance. The outlet gas temperature was 938 F ($\Delta T = 856$ F) at the end of the run. This ΔT is only 69.5 percent of the theoretical maximum. It was thought that the flowrate (0.028 lb/sec) was too high for the bed volume.

Test 8. The eighth test simulated Mission Duty Cycle (MDC) I. After simulating a 13 second initial pressurization and 125 second coast, flow was sustained for 122.5 seconds. During the initial 13 seconds of the test, the reactor inlet pressure was 295 psia and the reactor outlet gas temperature

was 885 F ($\Delta T = 804$ F). This temperature is more than 300 F lower than test number 5 with the same bed. The flowrate at the end of the flow period was 0.021 lb/sec.

It was subsequently discovered that the catalyst bed housing was loose within the main housing. This was caused by thermal growth of the cylindrical section of the catalyst housing, which depressed the downstream screen into the undercut in the outlet plate as intended. However, the screen did not return to its original position when the bed cooled. This would permit leakage of unreacted Tridyne around the inlet plate before passing through the orifices or around the catalyst bed housing after flowing through the orifices.

In retrospect, tests 1, 2 and 3 were conducted without disassembly. Because of the short bed length and therefore small thermal growth, there may have been very little leakage due to a depressed screen during the second and third tests. Also, the reaction temperature was relatively high during the third test. Since only one test was conducted with the small diameter screen, data for test number 4 is also thought to be valid. Tests No. 5 and 6 were each conducted with new screens and since neither involved cool-down periods, their data is also thought to be valid. In view of the problems encountered, however, it must be noted that these beds were not checked for tightness before testing which casts some doubt on the results. Although the reaction temperatures were relatively high, the small differences between bed sizes could have been due to small leakages.

It is likely that the low gas temperature resulting from test No. 7 was due to leakage rather than the high flow. It is certainly the cause for the low temperature in test No. 8.

During the 122.5 second flow period after the 125 second coast (unpressurized, no flow), the ΔT was 831 F after 3 seconds and 829 F at the end of the test. Although the bed was leaking internally, the reaction performance remained constant. At the end of the test the reactor inlet pressure was 300 psia and the flowrate was 0.021 lb/sec.

Test 9. After disassembling the reactor to straighten the screen, test No. 9 was conducted to determine the effect of flowrate on performance. This was necessary because of suspected internal leaks in the seventh test. An external leak in a tube fitting caused irregular pressures and flows and the test was rerun as test No. 11.

Test 10. Once again the reactor was disassembled to straighten the screen. Test No. 10 was then run to simulate MDC I. During the initial 10.5 second flow period, the reactor inlet pressure was 295 psia and the reactor outlet gas temperature was 1211 F ($\Delta T = 1134$ F). This corresponds to 92.8 percent of the theoretical maximum, which duplicates test number 5. The flowrate was 0.019 lb/sec.

During the 126 second coast, the thermocouple measuring the reactor outlet gas dropped from 1211 to 540 F. The upstream, midstream and downstream outer wall temperatures increased from 78 to 121, 94 to 305, and 220 to 570 F, respectively.

Flow was then initiated for 20 seconds rather than the full 122.5 seconds. The reactor inlet pressure was 294 psia and the reactor outlet gas temperature was 1124 F ($\Delta T = 1052$ F). This ΔT was 82 F lower than during the initial 10.5 second flow period, indicating an internal leak due to cooling during the coast period. The flowrate was 0.019 lb/sec. Before the bed had a chance to cool, the pressure was increased to once again attempt to determine the effect of flowrate on performance (test No. 11).

Test 11. The reactor inlet pressure was 393 psia during this 14 second test and the outlet gas temperature was 1151 F ($\Delta T = 1086$ F). This ΔT is 34 F higher than during the last part of test No. 10. This result is reasonable, but is questionable because the relative amounts of leakage are unknown. The flowrate for the test was 0.025 lb/sec.

Test 12. After straightening the screen, a test was run to simulate MDC II. The sequence, controlled by magnetic tape, is shown in Table 45. The reactor inlet pressure varied between 290 and 298 psia during the test. At the end of the initial 10 seconds of flow the reactor outlet gas temperature was 975 F (AT = 900 F). Although there obviously was internal leakage, the test was completed to give an indication of the effect of a pulsed duty cycle on the reactor gas temperature. The gas temperatures and flowrates are summarized in Table 46.

Structural Dynamic Tests. The selected size reactor bed was filled with unused catalyst and the reactor was connected to the regulator for structural dynamic testing. These tests are described in the Regulator Tests section. A sample of the tested catalyst is compared to an unused sample in Fig. 215. No evidence of catalyst breakage was found.

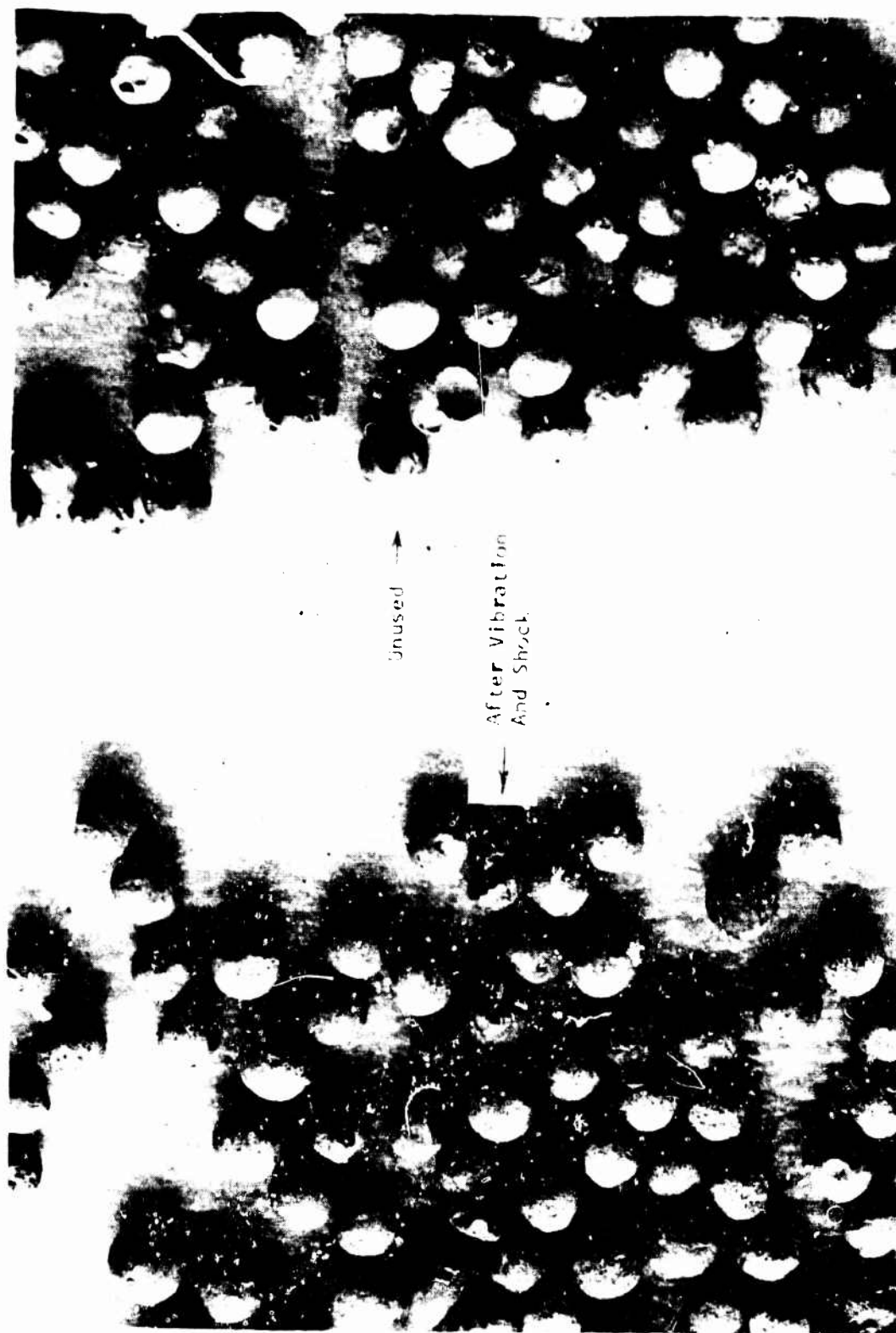
TABLE 45. MDC II SIMULATION

Duration (Sec)	Low Flow Valve	High Flow Valve	Event
10.0	Open	Open	Initial Pressurization
128.0	Closed	Closed	Coast
0.4	O	O	MDC II ↓
60.0	O	C	
3.0	C	O	
10.0	O	C	
0.4	C	O	
15.0	O	C	
2.0	C	O	
6.0	O	C	
8.0	C	O	
15.0	O	C	
13.0	O	C	
1.0	C	C	

Repeated 10 Times

TABLE 46. MDC II DATA SUMMARY

TIME (SEC)		REACTOR ΔT (F)		FLOWRATE (LB/SEC)	
INITIAL	FINAL	INITIAL	FINAL	INITIAL	FINAL
0.0	10.0	0.	900.	0.028	0.022
10.0	138.0	0.	0.	0.	0.
138.0	138.4	368.	452.	0.026	0.025
138.4	198.4	452.	855.	0.001	0.001
FIRST REPEATED CYCLE					
198.4	201.4	855.	946.	0.025	0.020
201.4	211.4	946.	860.	0.001	0.001
211.4	211.8	860.	871.	0.021	0.020
211.8	226.8	871.	830.	0.001	0.001
226.8	228.8	830.	937.	0.022	0.020
228.8	234.8	937.	876.	0.001	0.001
234.8	242.8	876.	898.	0.020	0.020
242.8	257.8	898.	770.	0.001	0.001
TENTH REPEATED CYCLE					
733.0	736.0	760.	890.	0.020	0.020
736.0	746.0	890.	817.	0.001	0.001
746.0	746.4	817.	829.	0.020	0.020
746.4	761.4	829.	787.	0.001	0.001
761.4	763.4	787.	890.	0.020	0.020
763.4	769.4	890.	820.	0.001	0.001
769.4	777.4	820.	872.	0.020	0.019
777.4	792.4	872.	737.	0.001	0.001
792.4	805.4	737.	897.	0.021	0.020
805.4	806.4	0.	0.	0.	0.



5AG43-7/26/79-C1

Figure 215. Catalyst Comparison

ELECTRONICALLY CONTROLLED REGULATOR

Two prototype electronically controlled regulators were fabricated by Air and Fuel Division, Parker Hannifin (Irvine, CA). The first unit was subjected to structural dynamic, development/performance, and acceptance tests at Parker. It was subsequently used during the first metal workhorse and flightweight propellant tank tests at Rocketdyne. Completion of fabrication of the second unit was intentionally delayed to incorporate design changes, which were not required. With deletion of the third phase of this contract, the second unit was not used in feed system tests.

Regulator Fabrication

Both regulators were fabricated as described in the Engineering Analyses and Design section. All machined parts were fabricated by a vendor for Parker. The torquemotors were acquired from Parker's F-16 production line and Parker assembled the regulator and electronics package.

During fabrication Parker evaluated adhesives for bonding the electrical header to the cover. For the first two tests, 3M Scotch-Weld structural adhesive 2214 regular was used. The surface film applied to the aluminum parts to prevent oxidation was not removed from the first sample. The adhesive was cured for 40 minutes at 250 F and left in the oven overnight with the oven off. The second sample had the film removed with a procedure which included deburring with a tool, sanding, and cleaning. The adhesive was cured at 250 F for 2-1/2 hours. Both samples were leak tested at 1500 psig and found to be leak free with a helium "sniffer." A force was then applied to the external surface of the header so that the shoulder would not carry any load. The bond broke at 1275 pounds for the sample without surface preparation and at 1500 pounds for the one with prepared surfaces. This latter force corresponds to a uniformly applied pressure of over 5000 psi. The third sample utilized Armstrong A-12T epoxy adhesive, mixed 1:1, applied to prepared surfaces. Curing was at 200 F, 0.9 psia for 2 hours. This sample

was leak free at 1500 psig, but the bond broke with an applied force of 335 pounds. As a result of these tests, the 3M Scotch-Weld adhesive was selected and the surfaces were prepared.

Regulator Tests

Tests with the first regulator were conducted during June and July 1978. After leak and proof tests, development tests were conducted with the bread-board electronics package to select the optimum control system. Structural dynamic tests with the regulator (exclusive of the electronics and pressure transducer) and catalytic reactor, and performance tests with the complete prototype regulator assembly were then performed.

The first unit (as-fabricated) met all design requirements, except for having a slightly low flow capacity. Operational performance after exposure to the structural dynamic tests was excellent. Initial pressurization in 9 seconds resulted in a 0.5 psi overshoot. The maximum error in regulated pressure was ± 0.75 psi and occurred during pulsing with a high regulator inlet pressure and a small downstream ullage.

The second regulator assembly was tested in December 1979. The performance test results were essentially the same as they were with the first unit. Structural dynamic tests were not conducted.

Dielectric Test. Prior to assembly, the two torque motor coils in each regulator were subjected to a 1000 volt rms, 60 Hz potential for 1 minute. No short circuits were found.

Internal Leakage. After assembly, the first regulator had a small internal leak, which required disassembly and relapping of the main valve sealing surfaces. This was the only time the regulator was taken apart during component testing. No adjustments were made to any springs or orifices, and no seats were machined or replaced.

After pressurizing the regulator inlet to 4000 psig for 5 minutes with helium, leakage through the normally closed pilot and main valves was measured at 0.01 scim. This corresponds to 1.3×10^{-9} lb/sec of Tridyne, which is approximately 5 orders of magnitude less than the flow required to maintain the propellant tank pressure during zero expulsion as the warm pressurant gas cools off. Leakage of the second unit was 0.37 scim at 4000 psig. Although substantially greater than the first regulator, the leakage is still fairly low.

External Leakage. For the external leakage test, the inlet and outlet of the first regulator were pressurized with helium to 4000 and 350 psig, respectively. The second regulator was pressurized to 3000 and 300 psig with nitrogen. There were no observable bubble formations at any joints.

Proof Pressure. The outlet of the first regulator was pressurized to 1275 psig and the inlet to 6000 psig for 5 minutes. There was no observable exterior damage.

Flow Capacity. The flow capacity of the first regulator was measured at the lowest inlet pressure, 400 psig. The helium flowrate was 0.0182 lb/sec, which corresponds to 0.0235 lb/sec Tridyne. This value is lower than predicted. Based on feed system design analyses, this flow is inadequate at the very end of the single burn, maximum expulsion rate MDC 1 for storage temperatures of less than 66 F. Since no two-tank feed system expulsion tests were conducted, it was not determined if the regulator flow capacity was too low and no adjustments were made to the regulator. The flow can be increased by reducing the size of the bleed orifice between the dome and outlet.

The flow capacity of the second unit exceeded 0.02 lb/sec helium with an inlet pressure of 500 psig. The regulated pressure was 281 psig.

Development Performance. The first complete regulator assembly, including the pressure transducer and breadboard variable-gain electronics package, was installed in the flow bench. During a five day period that was interrupted by a facility compressor failure, the flow bench was checked out and the regulator was fine-tuned. All mission flowrate, pressure, and propellant tank ullage conditions were simulated and the maximum regulated propellant pressure error was approximately one psi peak-to-peak. This does not include transducer errors associated with temperature variations, however. The nominal pressure was 297 psi. No attempt was made to correct this value to 300 psi, since the acceptance flow tests were to follow the vibration/shock tests.

Random Vibration. The catalytic reactor and first regulator, exclusive of the pressure transducer and electronics, were subjected to 30 hours (10 hours/axis) of ground random vibration at test (ultimate) levels from 4 to 75 Hz. Parker's electrodynamic shaker (Ling model L-300) was not capable of operating below 4 Hz or matching test requirements between 4 and 20 Hz. Figure 216 shows a trace of the control accelerometer mounted on the regulator. The required test levels are superimposed for comparison. This deviation is of little or no significance since the natural frequencies associated with the spring loaded pilot and main valves, and the diaphragm exceed 100 Hz. The only other movable part, the torque motor armature, is very stiff and not subject to flexure.

The reactor and regulator were also subjected to 30 minutes (10 minutes/axis) of Stage II/III flight random vibration at test levels from 8 to 2000 Hz. Figure 217 shows the control accelerometer output and the test requirement. There were no plans to conduct Stage IV separation shock and random vibration tests because they would have required the regulator to be pressurized to simulate flight conditions.

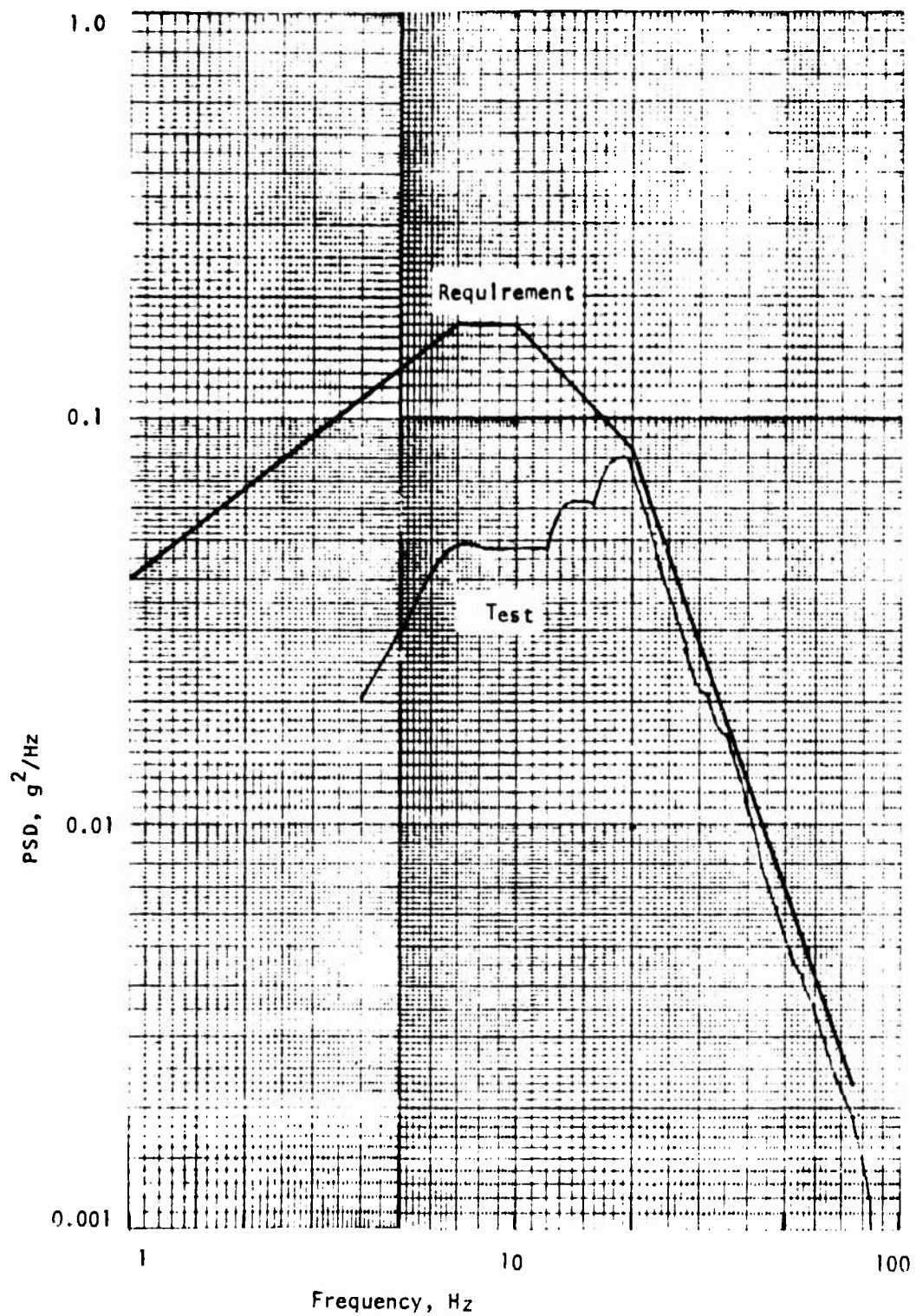


Figure 216. Ground Random Vibration

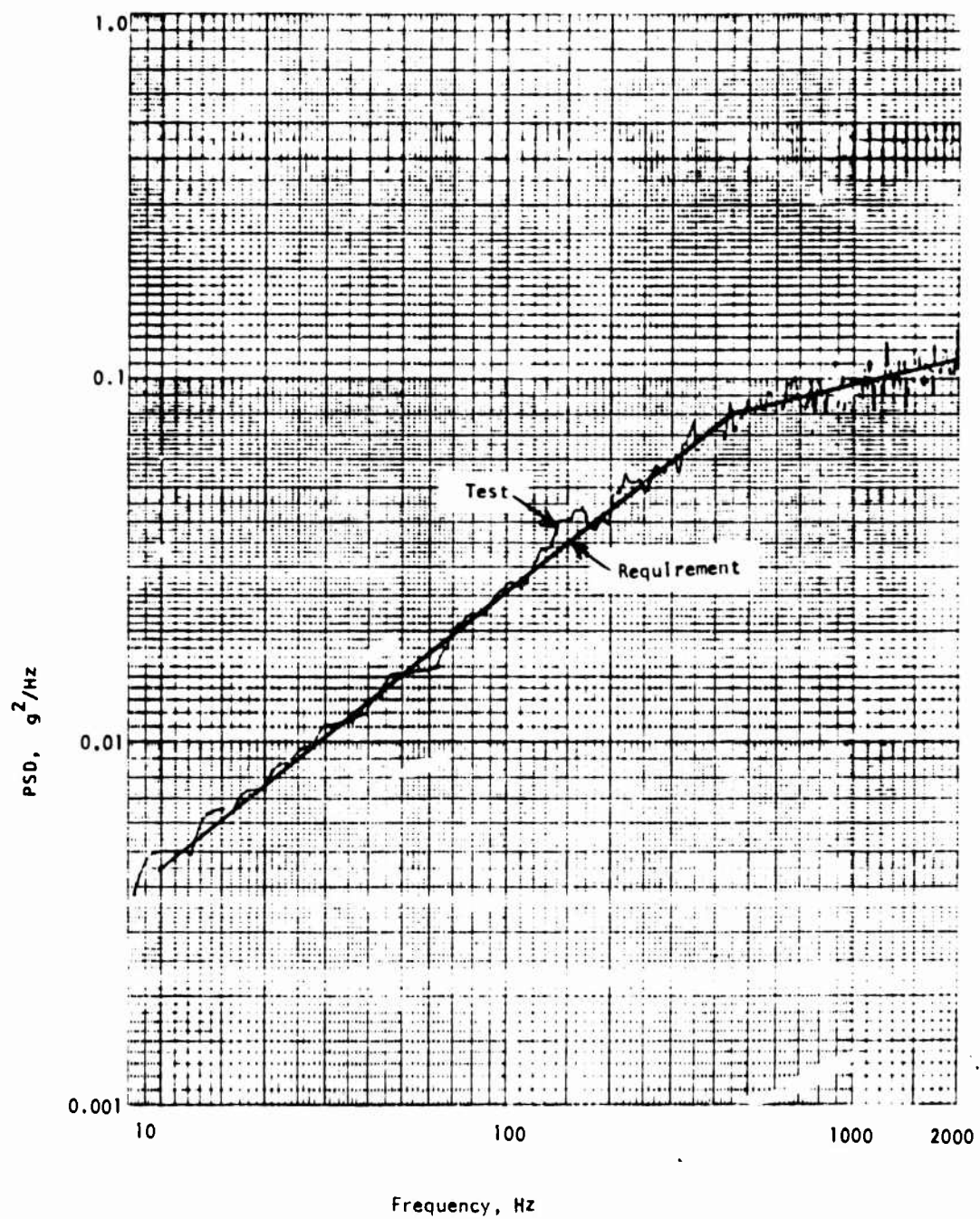


Figure 217. Stage II/III Random Vibration

Three internal leakage tests were performed during the ground and Stage II/III random vibration tests. After the Z-axis tests (perpendicular to main valve motion and the inlet tube flow direction), the leakage was 0 scim at 4000 psig. This is lower than the original leakage rate noted previously (0.01 scim), and is thought to be the result of cycling the valve several times during development performance tests. Leakage after the Y-axis tests (in line with inlet tube flow) was 0.016 scim. After the X-axis tests (in line with main valve motion), the leakage was 0.020 scim. There was no visible external damage to the regulator resulting from the vibration tests.

Ground Shock. A total of 15,000 shock tests (5000/axis) were conducted with the reactor and first regulator. The number of shocks for each amplitude and axis direction are presented in Table 47. A half-sine wave rather than a terminal-peak sawtooth and a 0.025 second pulse width rather than 0.250 second were used because of shaker limitations. Internal leakage after the X-axis tests was 0.015 scim. Leakage was measured at 0.030 scim after the Y-axis and Z-axis tests. This is equivalent to 4.0×10^{-9} lb/sec Tridyne. There was no visible external damage as a result of these tests and mechanical operation was not affected.

TABLE 47. GROUND SHOCKS

<u>No. Shocks</u>	<u>Y/Z - Axis</u>	<u>X - Axis</u>
4400	1.50	0.750
520	2.25	1.125
50	3.00	1.500
25	3.75	1.875
5	4.50	2.250

Slam Start. The regulator pilot and main valves are normally closed and the upstream isolation valve is opened before power is supplied to the regulator electronics. As a result of these initial conditions for the subject application, the regulator is not required to control the propellant pressure under slam-start conditions. However, since a slam start is required in many applications, a test was run with the first regulator. Subjecting the closed main and pilot valves to 4000 psig by opening the isolation valve did not cause any damage.

Initial Pressurization. A schematic of the setup used in the flow tests is shown in Fig. 218. It differs from the one used during development performance tests (prior to the vibration tests) in that the Kulite transducer (P5) was placed at the top of the tank to control the pressurant pressure rather than the water pressure. There were two reasons for this change. First, solenoid valve S2 was producing excessive noise, which resulted in high frequency oscillations.

The second and most important reason for moving the transducer was to solve a problem caused by replacing the original water tank with a larger one (15 ft³). The larger tank was required to more closely approximate the maximum ullage volume (20 ft³). When it was observed that the magnitude of liquid oscillations at the tank outlet were larger than those in the ullage volume, pressure transducers P3 and P4 were switched to see if they were functioning properly. This test confirmed that they were.

A calculation of the first-mode natural frequency of the tank shell indicated it was very close to the frequency of the oscillator (800 Hz) used in the electronics package to provide gain scheduling. It was therefore assumed that the tank shell was vibrating and causing the large liquid pressure oscillations.

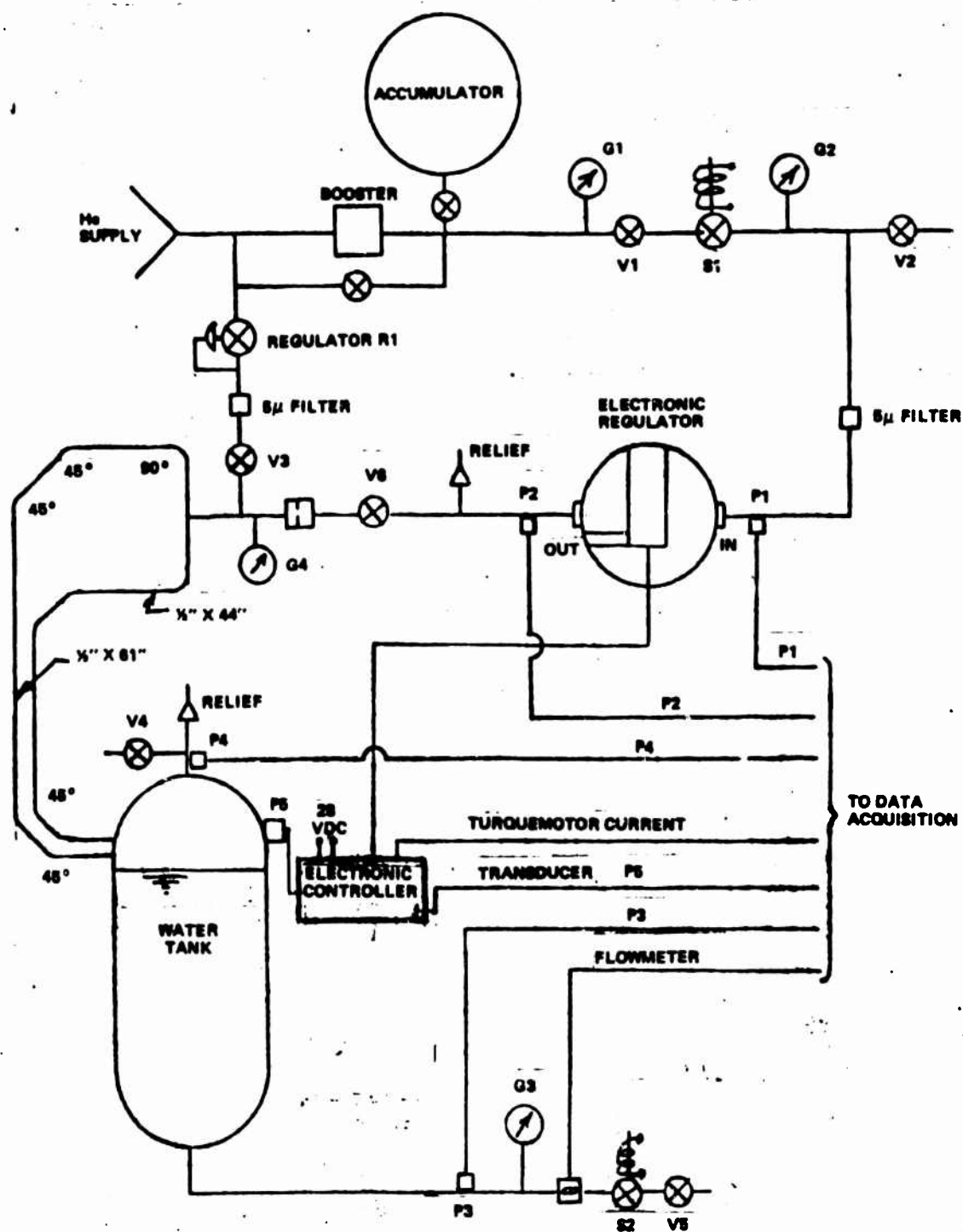


Figure 218. Regulator Test Schematic

Placing the Kulite transducer at the top of the tank to control the ullage pressure did not compromise the results of these component tests. System pressure accuracy was demonstrated at a later date with the aluminum workhorse and flightweight tanks using the Tridyne reactor rather than with a tank having a free liquid surface using cold helium pressurization.

Simulation of initial pressurization (0-300 psig) in approximately 9 seconds with the first regulator is presented in Fig. 219. Two traces of regulated pressure are provided, one for absolute readings and one for errors. The overshoot was approximately 0.5 psi (0.2 percent), but dissipated quickly. When combined with the transducer errors associated with repeatability, temperature extremes and circuit drift, the maximum predicted overshoot would be 2.4 psi (0.8 percent).

The pressurization ramp (0-281 psig) for the second unit was set at 9.5 seconds. No overshoot was observed during testing.

Flow Tests. The initial conditions for the flow tests performed with the first regulator are shown below.

TEST NO.	REGULATOR INLET PRESSURE, PSIG	ULLAGE VOLUME, FT ³	SIMULATED FLOWRATE, ENGINES
1	4000	0.7	ACS
2	3900	1.2	ACS & AXIAL
3	2600	8.2	ACS
4	2500	8.7	AXIAL
5	600 → 400	15.0	AXIAL

The results for test No. 1 are shown in Fig. 220. The variation in pressure for the two low-flow pulses is less than ± 0.5 psi (± 0.17 percent). A maximum-flow pulse with approximately the same initial conditions (test No. 2) resulted in larger errors (± 0.75 psi, ± 0.25 percent). As predicted, this was the largest error during testing (Fig. 221). When combined with transducer errors, the total is ± 2.65 psi (0.88 percent).

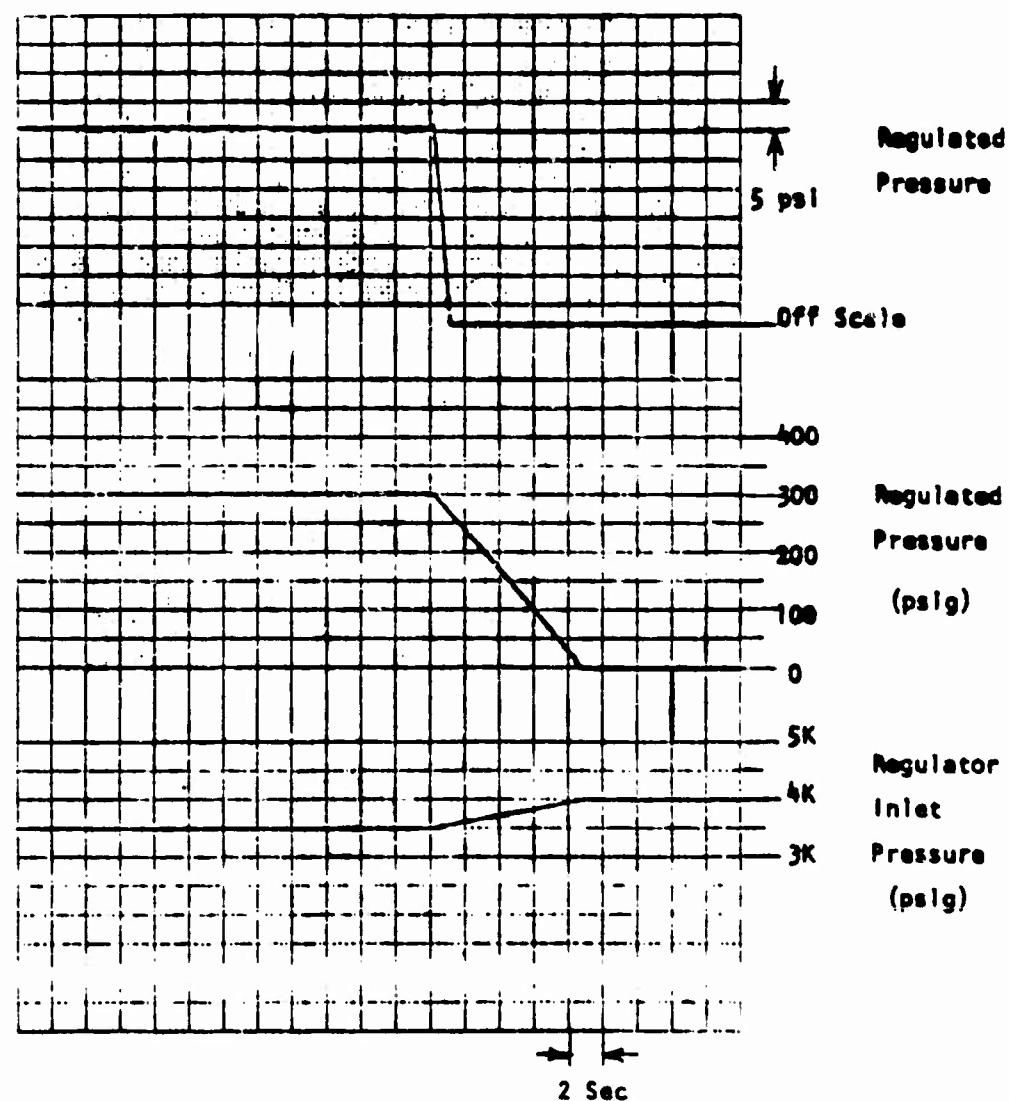


Figure 219. Initial Pressurization

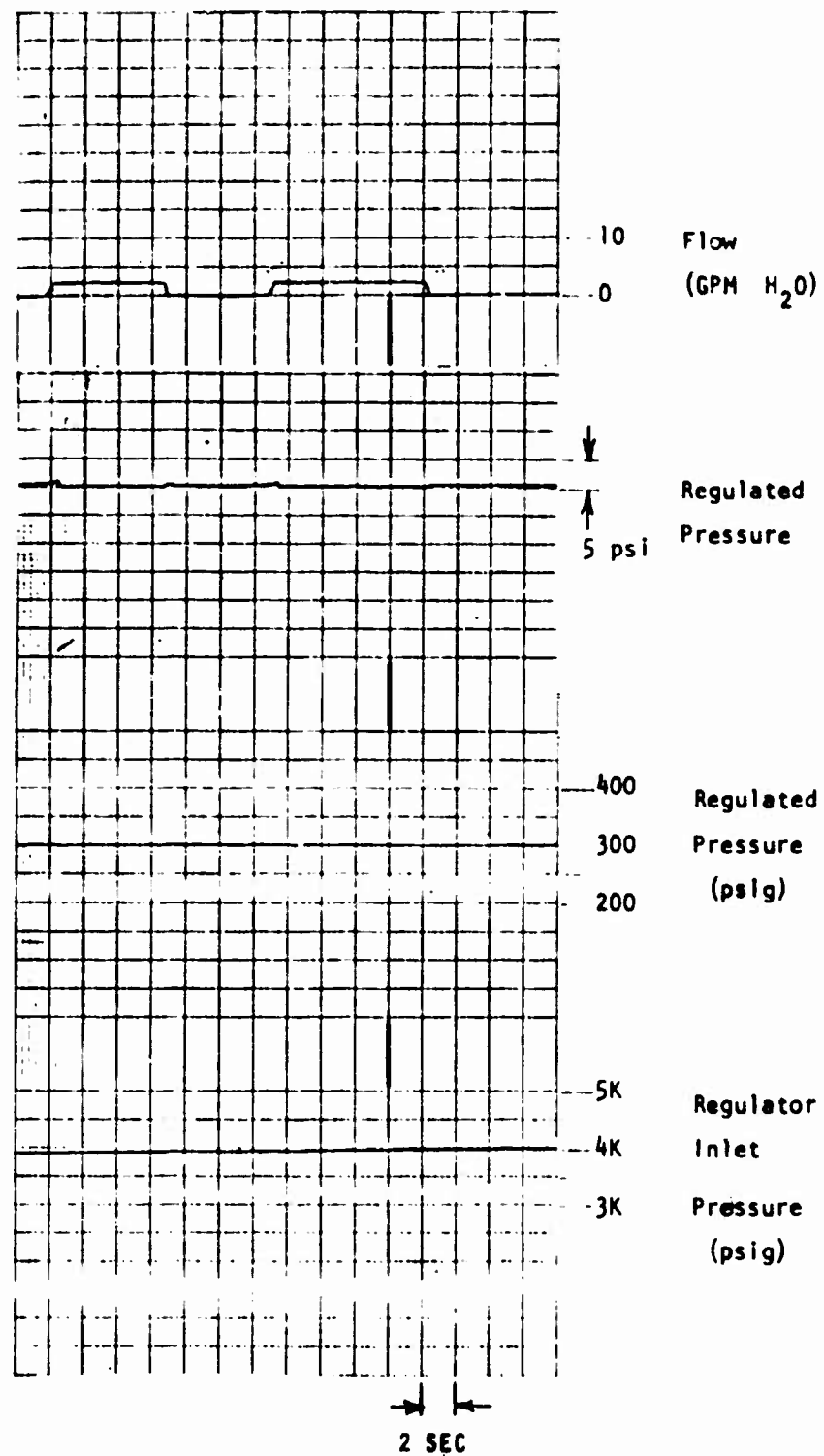


Figure 220. Flow Test No. 1

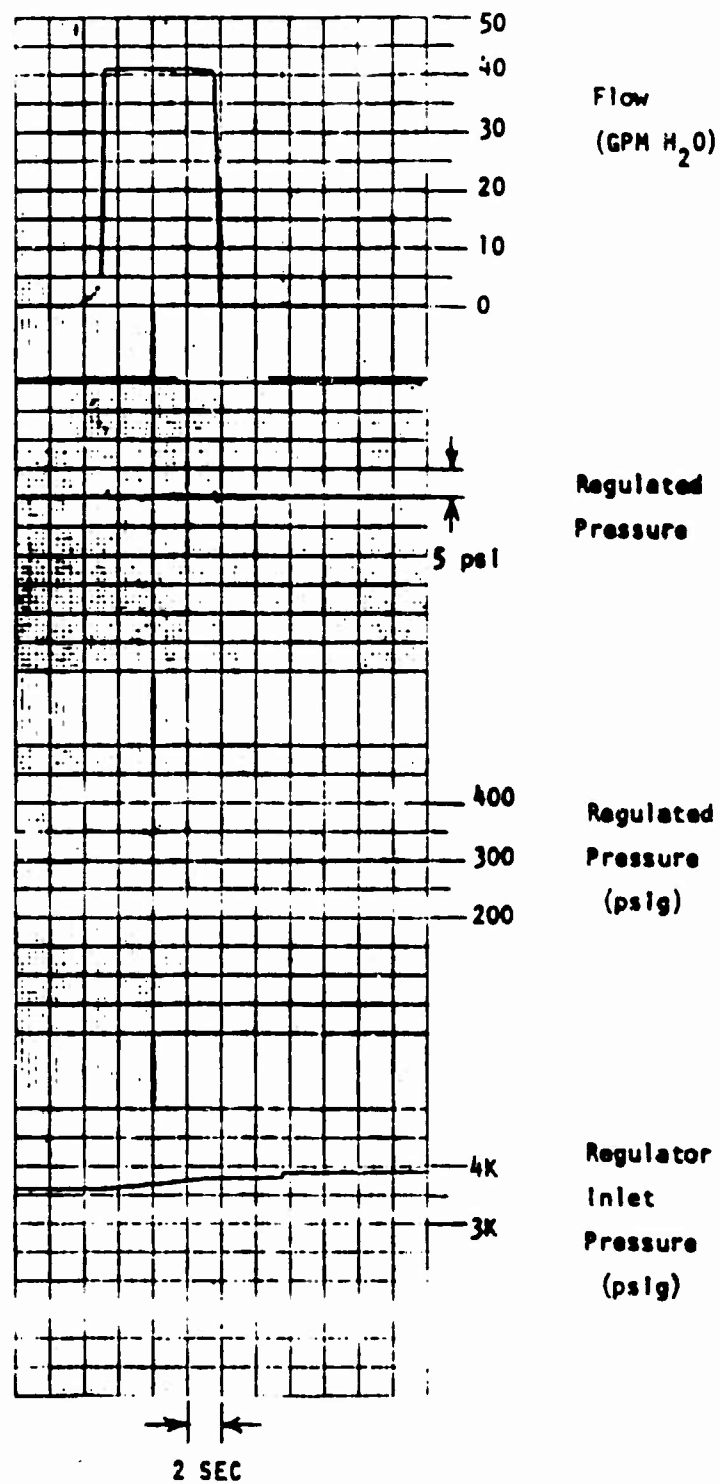


Figure 221. Flow Test No. 2

As the inlet pressure was reduced and the ullage volume increased for tests 3, 4, and 5, the regulator error decreased. The data for test 5 is presented in Fig. 222. During test No. 5, the regulated pressure was inadvertently set below 300 psig. A photograph of the first delivered regulator assembly is shown in Fig. 223.

Flow testing of the second regulator assembly was very limited. With an inlet pressure of 2000 psig and a downstream volume of 1.5 ft^3 , the maximum error during pulsed flow was $\pm 0.25 \text{ psi}$. At an inlet pressure of 500 psig with the same pressurized volume, the maximum error was $\pm 0.38 \text{ psi}$. This trend is opposite that of the first regulator's performance and is undoubtedly due to the fact that the volume was not increased to simulate the propellant tanks as the regulator inlet pressure was reduced.

Another phenomenon attributable to the same cause was the oscillation observed in the regulated pressure with a 500 psig source pressure. The amplitude was $\pm 0.2 \text{ psi}$ and the frequency was 6 Hz. This was the only time that oscillations were observed during component testing of the two regulators.

PRESSURIZATION SUBSYSTEM

Upon completion of the prototype catalytic reactor component tests, the reactor was modified to improve its performance. It was subsequently loaded with the catalyst used during the shock and vibration tests and assembled with the first prototype electronically controlled regulator, the prototype pressurant storage tank, and facility components for use with Tridyne pressurant gas during the first metal workhorse propellant tank expulsion test. The PSA expulsion tests were described in the Aluminum Workhorse Tank and Flightweight Tank sections.

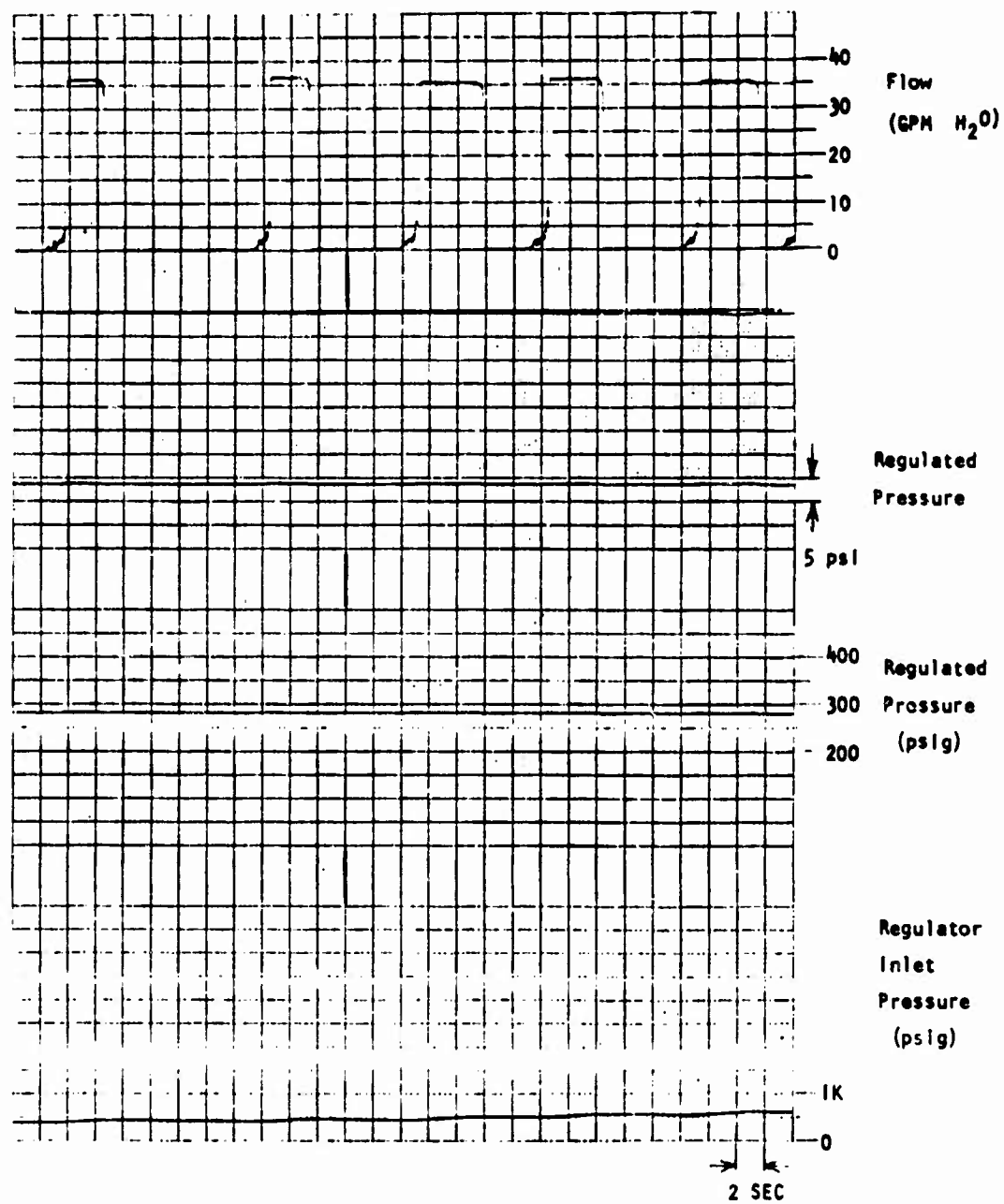
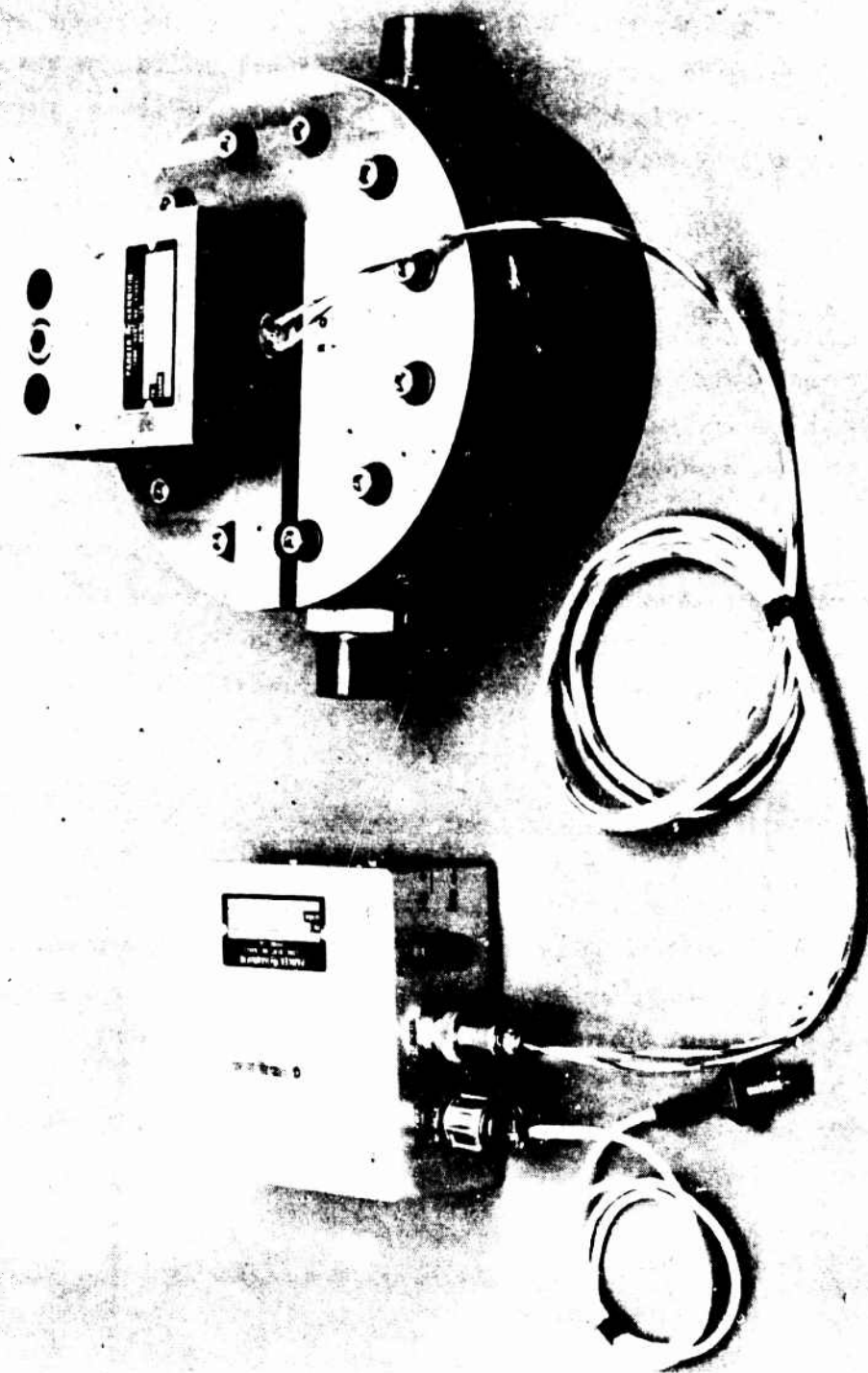


Figure 222. Flow Test No. 5



1AX61-1/24/78-C1

Figure 223 Electronically Controlled Regulator

Due to a malfunction of the regulator's remote sensing pressure transducer, the electronic regulator was replaced with a facility regulator during the first test. The facility regulator was also used for the second and third tests. Replacement of the pressure transducer and checkout of the electronic regulator were accomplished in time to use them during the flight-weight propellant tank expulsion test.

Catalytic Reactor Modifications

The prototype catalytic reactor was modified by trimming the outlet screen to fit inside the catalyst housing and permit the housing to slip into the groove in the outlet plate. The original design utilized the screen as a spring to accommodate thermal expansion of the housing, but the screen did not return to its original position when it cooled down and leakage of unreacted Tridyne occurred. The main housing, catalyst housing, and outlet plate were then EB welded together so that all Tridyne had to flow through the catalyst bed. A wave-spring washer was installed between the inlet tube and inlet plate to provide for thermal expansion of the catalyst bed assembly.

Electronically Controlled Regulator Repairs

The electronically controlled regulator failed closed after five high-flow pulses during metal workhorse tank tests 1-A and 1-B. Posttest analyses indicated that the Kulite transducer used as the remote sensing device was exposed to pressure spikes exceeding 500 psig when the liquid-flow control valve was closed. The actual value of the spikes is not known because the recorder was scaled to only 500 psig. The transducer has a "rated" pressure of 250 psig and a "maximum" pressure of 500 psig.

The transducer resistances were measured and found to be higher than normal. The voltage at zero pressure was 1.7 volts, compared to the original calibration value of 3.9 millivolts, indicating the transducer was inoperative. This output signal is sufficient to cause the regulator to remain in a locked-up (closed) condition. The circuitry in the electronics package was checked and found to be undamaged.

An excessive internal regulator leakage of approximately 30 scim helium was measured at 1000 psig. The primary source of leakage was the pilot valve, which was found to have contamination at the seat. The main valve poppet and seat had fretting marks, but there was no other damage to the regulator. While the regulator was disassembled, the main valve poppet and seat were lapped and nonmetallic parts, including the pilot valve seat, were replaced. The pilot poppet preload (0.55 pound) and torquemotor/pilot push rod clearance were adjusted, the regulator was assembled, and the Kulite transducer was replaced for regulator assembly functional tests.

Proof pressure, internal and external leakage, flow capacity, ramp time, set pressure, and response performance tests were run. Internal leakage was 1.0 scim helium at 1000 psig. The flow capacity exceeded 0.02 lb/sec with an inlet pressure of 500 psig. Other aspects of the tests were also normal. The regulator assembly was subsequently used during the flight-weight tank expulsion test.

Performance Tests

The objectives of these tests were to determine the performance of the modified catalytic reactor, the accuracy of the electronically controlled regulator and the performance of the pressurization subsystem.

Test 1-A With Workhorse PSA. The regulator's facility filter inlet, the regulator outlet, and the catalytic reactor outlet pressures during pressurization are presented in Fig. 224. As shown the regulator pressure oscillations were damped by the reactor. The regulator performance, as

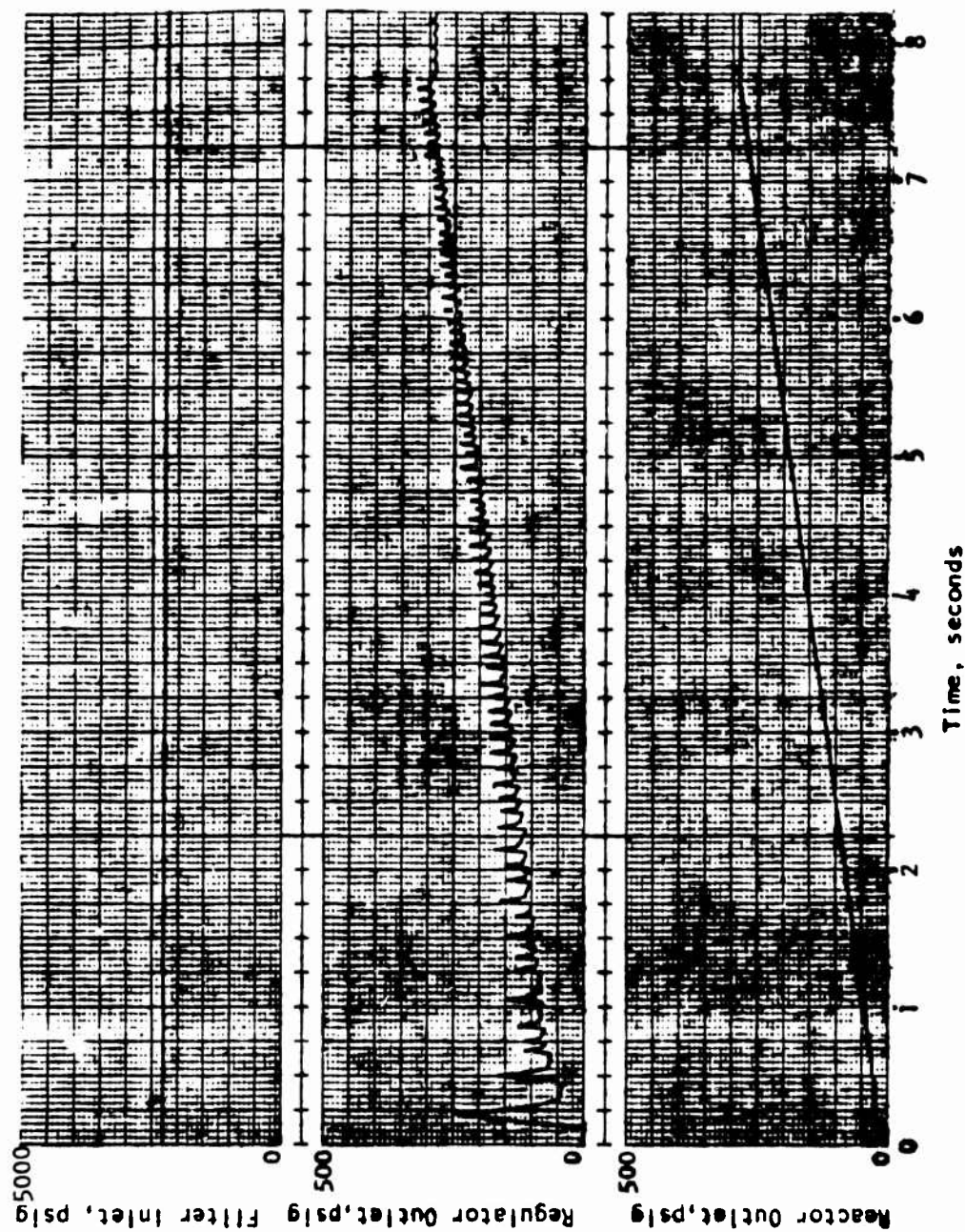


Figure 224. Pressure Transients During Initial Pressurization

measured by the controlled propellant pressure, is indicated in Fig. 225 and 226. The initial overshoot (Fig. 225) was 2.1 psi (0.7 percent), but it dissipated in 0.1 second as the pressurant gas cooled. The pressure then oscillated with a peak-to-peak variation of 1.0 psi during the initial portion of the 142 second hold period. Except for the effect of not having the nominal initial regulator inlet pressure, this variation is the largest anticipated since the ullage volume for this test was approximately equal to the minimum volume that would be experienced with two tanks. At the end of the hold period, just prior to the high-flow pulse, the variation was not measurable (Fig. 226).

Test 2 With Workhorse PSA. The Tridyne mixture used in test 2 was 91.04 He/3.00 O₂/5.96 H₂ (molar percent). The theoretical temperature rise (ΔT) for this mix is 1228 F. During the major portion of the single-pulse expulsion, the reactor gas ΔT was 98.9 to 99.3 percent of this value. The one percent loss was due to both incomplete reaction and heat loss.

The reactor outlet gas temperature transient was presented in Fig. 143. This temperature ranged between 1274 and 1297 F during the continuous expulsion with the variation primarily due to the reactor inlet temperature transient. The response was extremely fast, due to the double-wall design, compared to the "tank inlet" temperature transient, which reflects the time required to heat the heavy-wall tubing.

The reactor downstream outer wall T/C data was also shown in Fig. 143 for the location shown in Fig. 227. Being very close to the end of the catalyst bed and the conduction path between the inner and outer walls, this T/C recorded very high temperatures. The upstream wall T/C remained very cool, however, as shown in Fig. 143.

The amount of Tridyne used was calculated from densities in the gas storage tank to be 2.45 pounds. Calculations of the final gas temperature in the propellant tank, based on gas mixing relationships, resulted in a conclusion that between 65 and 100 percent of the water condensed. The corresponding range in temperatures of the pressurant in the propellant tank is 185 to 201 F.

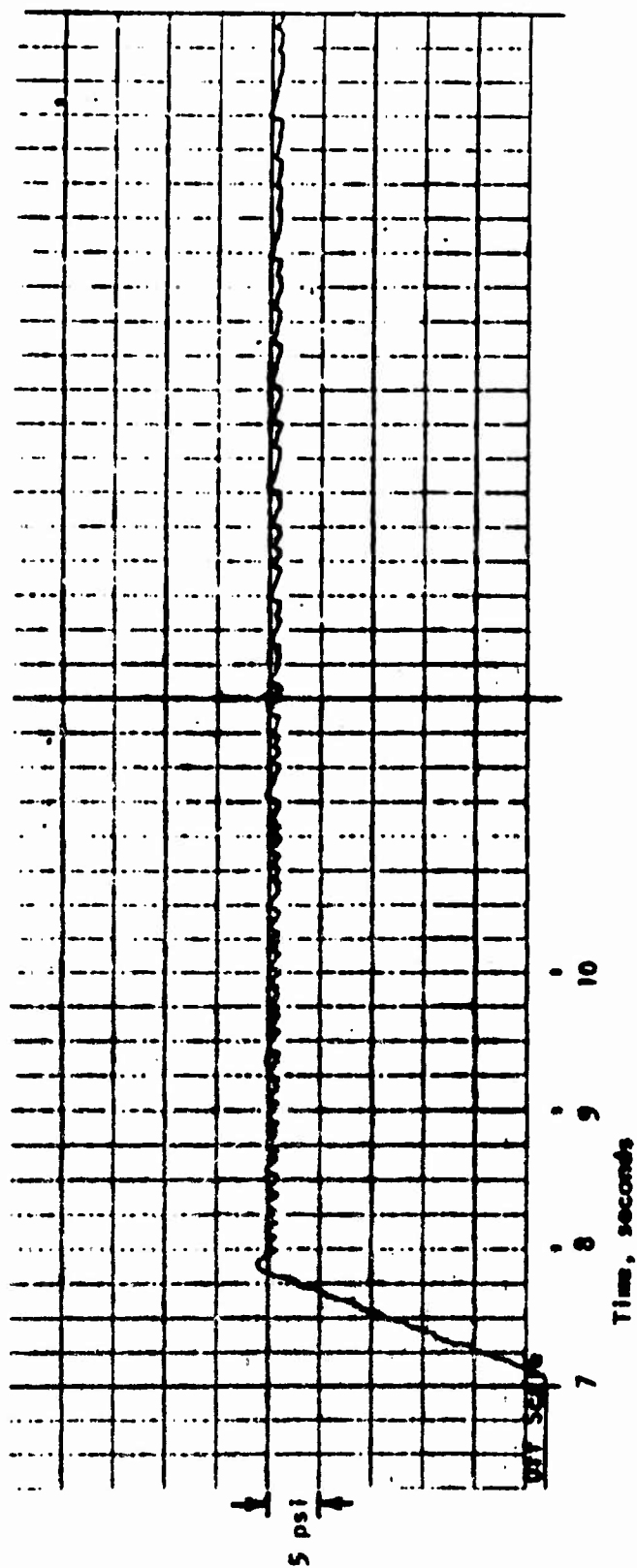


Figure 225. Tank Outlet Pressure Transient During Initial Pressurization

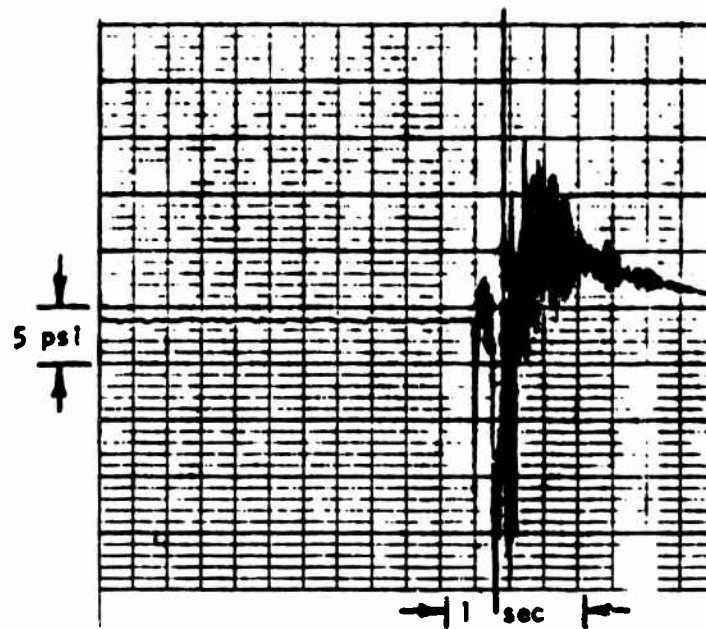


Figure 226. Tank Outlet Pressure Prior to First Pulse

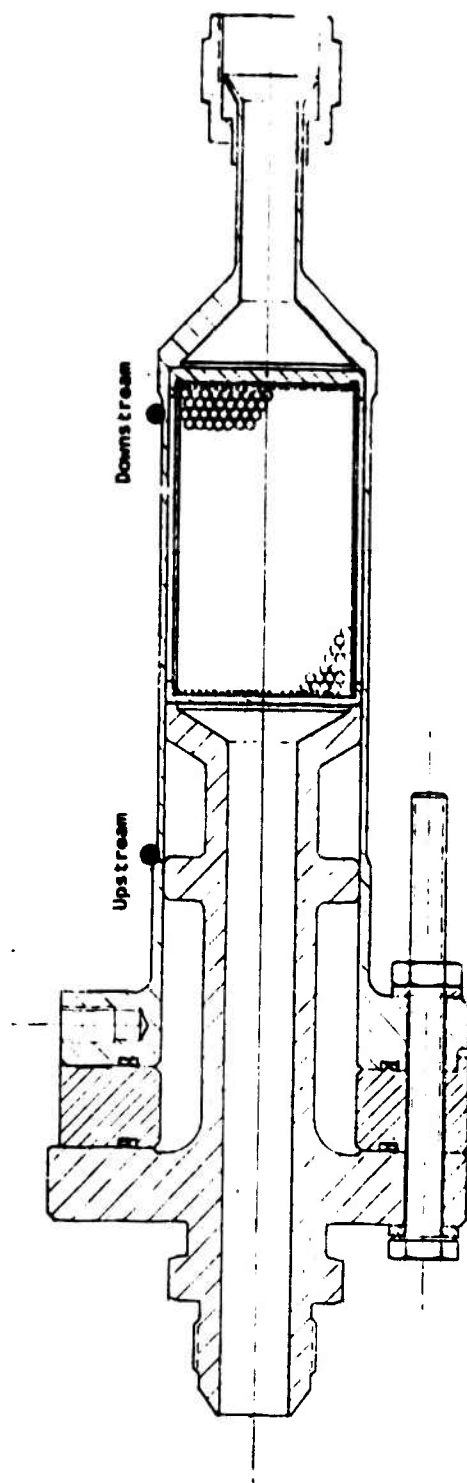


Figure 227. Catalytic Reactor Thermocouples

Test 3 With Workhorse PSA. The Tridyne mixture used in test 3 was 91.03 He/3.00 O₂/5.97 H₂ (molar percent). The corresponding theoretical ΔT is 1229 F, one degree higher than test 2. The analyses supplied with the 49 bottles of Tridyne purchased indicated variations in molar percentages of ± 0.8 H₂, ± 1.2 O₂ and ± 0.1 He. The corresponding maximum variation in reaction temperature is ± 10 F.

Because of the pulsed nature of the expulsion cycle, the reactor ΔT did not reach steady-state conditions. Throughout most of the expulsion cycle, including periods of low flow, the reactor ΔT was 90.8 to 95.3 percent of theoretical. The 5 to 9 percent loss was due to both incomplete reaction and heat loss.

The reactor outlet gas temperature transient was presented in Fig. 149. During the major portion of the expulsion cycle, the outlet gas ranged between 1178 and 1233 F. The reactor wall temperature transients were also presented in Fig. 149 and followed the same trends as test 2.

The amount of Tridyne used was calculated to be 3.06 pound. The pressurant gas temperature in the propellant tank at the end of the expulsion cycle was calculated to be 89 to 90 F for 98 to 100 percent of the water condensed.

Test With Flightweight PSA. The Tridyne molar-percent mixture used was 91.01 helium, 5.98 hydrogen and 3.01 oxygen. The respective mass percentages are 77.08, 2.55 and 20.37. The corresponding theoretical reaction temperature rise is 1230 F. During the pressurization and expulsion cycle, the Tridyne tank outlet gas temperature decreased from 64 to 16 F. The minimum temperature at the inlet to the regulator was 44 F.

The catalytic reactor inlet and outlet gas temperature transients are presented in Fig. 183. Beginning with the peak temperature resulting from the first high-flow pulse, the reactor outlet gas temperature was 1075 plus or minus 83 F. The minimum temperature was after the long pause early in the

expulsion cycle and the maximum was at the end of the cycle. The thermal efficiency of the reactor was 75 to 90 percent. The inefficiency was due to heating the hardware, incomplete reaction and heat loss.

The reactor downstream outer surface temperature was within approximately 100 F of the outlet gas temperature, as shown in Fig. 183, with a maximum of 1083 F. The upstream surface temperature was less than 150 F during the expulsion cycle.

The Tridyne tank pressure decreased from 1217 to 673 psig during the test, representing a usage of 3.0 pound. The amount of water condensation in the propellant tank during expulsion is unknown, however, from thermodynamic calculations, the final bulk gas temperature had to be between 147 and 153 F, and the condensation between 85 and 100 percent, respectively, at the end of the expulsion cycle.

The current from the regulator's electronics package to the torquemotor was monitored to characterize the functioning of the regulator assembly. The wave-form of the current during the first low and high-flow pulse is shown in Fig. 228. During the high-flow pulse, the current established a very distinguishable oscillatory pattern at approximately 2.9 Hz. The regulator's mechanical response to this current, in the form of outlet pressure is also shown in Fig. 228. The pressure oscillation is damped as the Tridyne flows through the catalytic reactor (Fig. 228).

As the mission duty cycle progressed, the regulator current and outlet pressure oscillations increased in magnitude and decreased in frequency. By the end of the third high-flow pulse, the frequency was 2.0 Hz (Fig. 228). During the next-to-last high-flow pulse, the regulator outlet pressure oscillation frequency was 1.0 Hz (Fig. 229). Pressure oscillations were measurable in the tank inlet line, but not at the regulator's remote sensing transducer at the tank outlet.

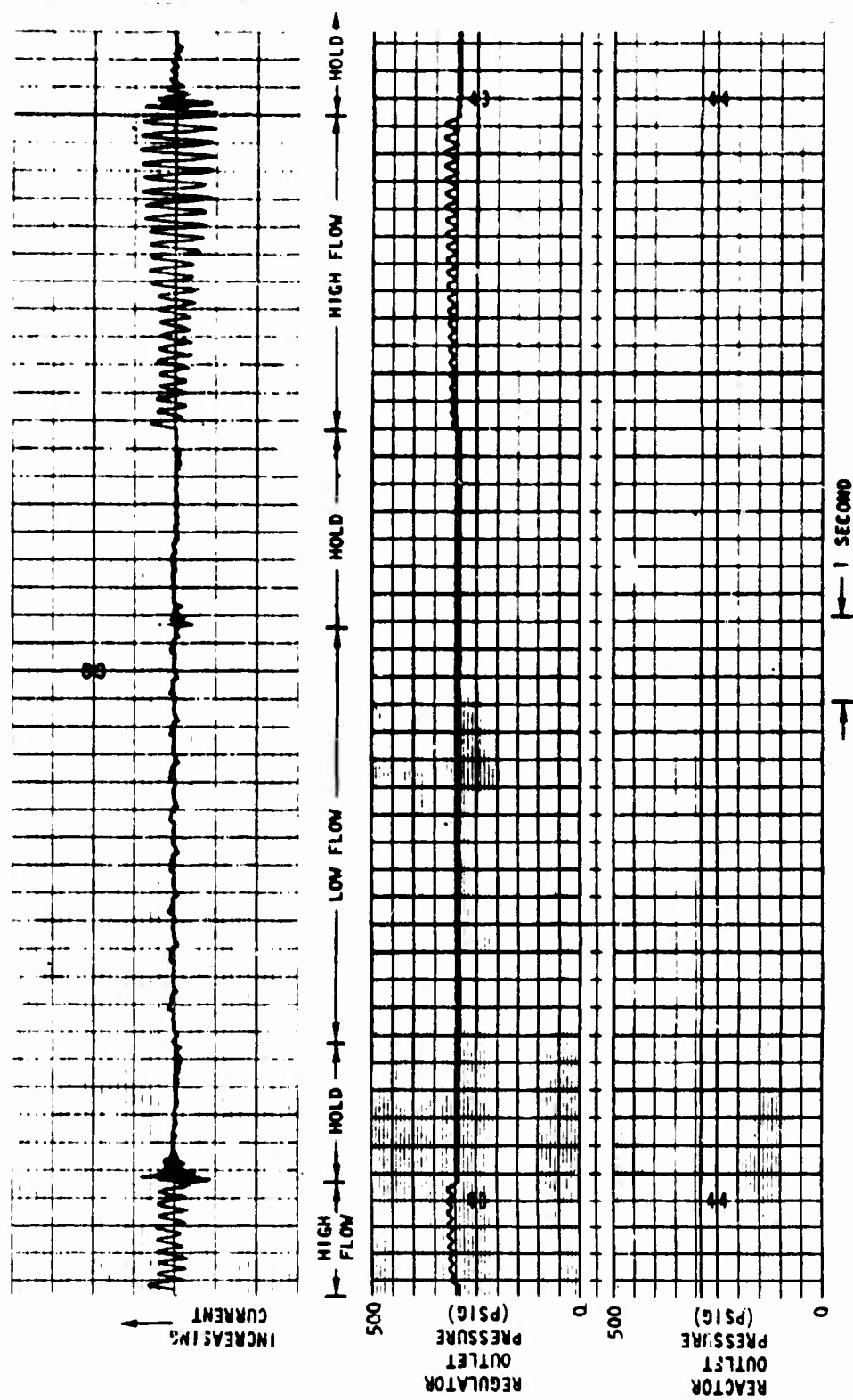


Figure 228. Regulator Transients From Second Through Third High-Flow Pulse

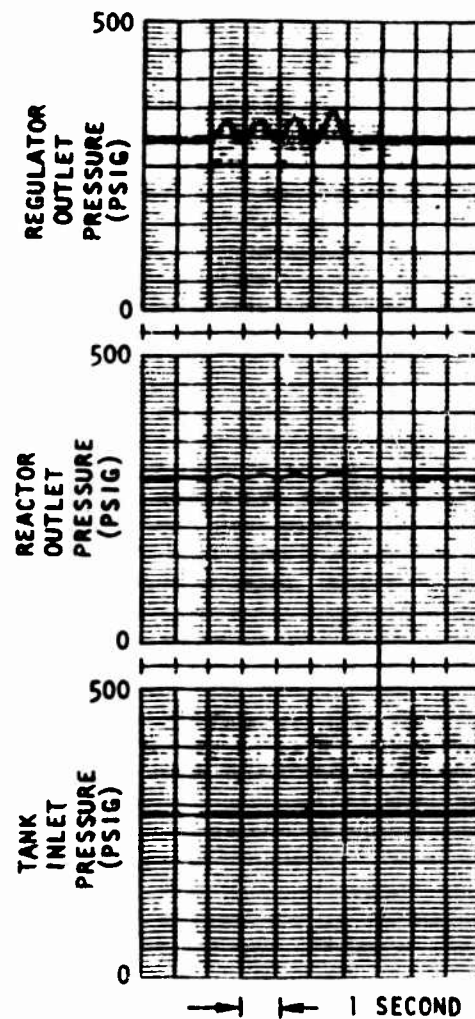


Figure 229. Pressure Transients During Next-to-Last High-Flow Pulse

During the last high-flow pulse, pressure oscillations of ± 1.4 psi were measured by the remote sensing transducer. This is the largest error detected except during the last 0.5 seconds. As the water was depleted during this time period, the pressure decreased gradually by 6.6 psi and then dropped to atmospheric pressure. Up to the last pulse, the pressure at the outlet of the tank was constant within ± 0.4 psi.

DESIGN UPDATE AND NEW TECHNOLOGY

Only two design changes were identified but not incorporated in the prototype hardware that was fabricated. The propellant tank aluminum liner radius of curvature near the polar bosses needs to be decreased to prevent bridging of the Kevlar roving during wrapping. The second design change involves reducing the angle of convergence of the catalytic reactor downstream of the catalyst bed from 45 to 30 degrees to permit fuller utilization of the cylindrical bed shape.

Another potential design modification, not actually defined, is associated with the diaphragm fatigue life during pressurized vibration. The magnitude of this problem is dependent on the structural response of the propellant tank shell and the vibration environment. Solutions will probably require changing the diaphragm alloy or layering non-metallic materials on the diaphragm's outer surface. Further development effort would be required, but the necessary technology is available.

MATERIALS PROCESSING DEVELOPMENT

Two material processes are documented in the following subsections. The first involved draw-forming of sheet aluminum in a hydraulic press. The dramatic effect of incorporating a draw bead in the draw rings is described. Repeatable control of the sheet stock feed rate between the draw rings was achieved by this modification to the tooling.

The second process involved Kevlar/epoxy wrapping of an aluminum tank liner at an elevated temperature (130 to 140 F). Heated wrapping permitted a thinner (lighter) liner and was successfully attempted for the first time by Defense Div, Brunswick Corp.

DIAPHRAGM FORMING

The aluminum expulsion diaphragm was draw-formed by Aircraft Hydro-Forming (AHF) in Gardena, CA. Forming was initially attempted with tooling that did not include a feature (draw bead) normally used by AHF to form sheet stock because of constraints imposed by a subcontractor. Only limited, nonrepeatable success was attained. When the constraints were removed, AHF modified the draw rings to incorporate a draw bead, with remarkably successful results. This information is included in this report to document the dramatic effect of the draw head in providing repeatable control of the sheet stock feed rate between the draw rings.

Diaphragm Description

The diaphragm, a half-shell with a small flange, is made from 1100-0 aluminum. The shape of the inner surface is oblate, i.e., a contour-of-revolution about the minor axis, with a 12.4-inch-diameter flat area at the pole. A section plane containing the minor (polar) axis yields a nearly elliptical contour, except the flat area. Compared to an ellipse, the actual shape bulges outward midway between the pole and equator.

The inside diameter of the diaphragm at the equator is 36.2 inches and the outside diameter of the flange is 36.5 inches. The diaphragm is 12 inches high. Minimizing the thickness of the liner at the equator, where the diaphragm is attached, required a small diaphragm flange radius. A 0.020-inch radius was desired, but a radius of only 0.056 to 0.068 inches was consistently achieved while maintaining the diaphragm thickness.

Draw Forming Problems

Draw forming of the diaphragms was accomplished with an HPM 3200-ton vertical hydraulic press. Lubricated, flat sheet stock, 0.090 inches thick by 60 inches in diameter, was held between two draw rings and pulled down over a stationary male die to achieve the surface contour. The original draw ring design included a "draw bead" to control the inward feed rate of the sheet stock between the rings. This feature was eliminated, however, because of objections to the residual joggle in the flange surface expressed by the subcontractor that was to spin the flange radius.

A total of fourteen pieces of material were formed during tooling tryout. The objective was to determine the proper combination of lubricant and "cushion" pressure between the draw rings to control the sheet stock feed rate. A summary of the variations in processing is presented in Table 48. The first three were formed in one step and the cushion pressure was increased from 50 to 750 psi. The higher pressures restricted the feed rate and resulted in less wrinkling of the contour near the equator. These wrinkles were oriented along meridians.

The fourth and fifth parts were each formed in two steps with pressures between 1200 and 2000 psi. Both fractured near the equator, indicating insufficient material feed, which stretched the material. The sixth part was formed in one step at 1700 psi and had only one 4 by 14 inch area that was wrinkled. The seventh part, completely free of wrinkles, was drawn at 1700 psi to within three inches of the equator and completed at a pressure of

TABLE 40. SUMMARY OF DIAPHRAGM FORMING PROBLEMS

DIAPHRAGM NO.	CUSHION PRESSURE (psi)			RESULTS
	FIRST STEP	SECOND	THIRD	
1	50	--	--	EXTREME WRINKLING
2	250	--	--	LARGE AMOUNT OF WRINKLING
3	750	--	--	MODERATE AMOUNT OF WRINKLING
4	1200	2000	--	FRACTURED
5	1800	2000	--	FRACTURED
6	1700	--	--	WRINKLED AREA LIMITED TO 4" X 14"
7	1700	2000	--	GOOD PART
8	1700	2000	--	WRINKLED ON ONE SIDE
9	1700	2000	--	2 SMALL WRINKLES
10	1700	2000	--	WRINKLED
11*	2200	--	--	WRINKLED
12	1700	--	--	FRACTURED
13	1500	1700	2000	GOOD PART
14	2000	--	--	FRACTURED

*PETROLEUM-BASE LUBRICANT

2000 psi. It was assumed that the forming parameters were close to optimum and forming was stopped to measure the diaphragm.

The eighth, ninth and tenth parts were subsequently formed, but only one came close to demonstrating repeatability. The primary problem appeared to be associated with drawing at a high cushion pressure, which caused deterioration of the nonpetroleum-base lubricant at random locations. This conclusion was reached after observing areas covered with a wax-like substance on the formed parts. A petroleum-base lubricant was used with the eleventh part at a pressure of 2200 psi. Even at this high pressure, there was extreme wrinkling.

Three more attempts were made with the original lubricant. The twelfth diaphragm cracked after drawing only three-fourths of the way down at 1700 psi. This was the same pressure that resulted in varying amounts of wrinkling on other diaphragms. The thirteenth diaphragm was drawn in three steps at 1500, 1700 and 2000 psi and resulted in a good part. The last diaphragm was drawn at 2000 psi all the way and cracked.

Independent of these draw-forming problems, a decision was made to coin the flange radius rather than spin it. Thus, the objectives to the indentation created by a draw bead were no longer applicable and the tooling was modified.

Draw Ring Modifications

A groove was machined in the surface of the lower draw ring and a 1-inch diameter rod, formed into a torus, was placed in the groove. Approximately half of the torus extended above the surface of the draw ring. The diameter at the centerline of this draw bead was 38.5 inches compared to a male die maximum diameter of approximately 36.2 inches. A corresponding groove, 0.63 inches deep, was also machined in the upper draw ring.

As a result of these modifications, inward movement of the sheet aluminum during forming was controlled as it deformed and passed between the bead and

groove rather than by contact with the flat surfaces of the draw rings. Control of the sheet aluminum was accomplished with cushion pressure of 500 psi, which eliminated problems associated with deterioration of the lubricant. One-step draw-forming with the modified tooling netted 22 good diaphragms on the first day.

Selected Processing Steps

The diaphragms were draw-formed from flat sheets 1100-0 aluminum (QQ-A-250/1), 0.090 inches thick by 60 inches diameter. The sheets were lubricated with a drawing compound and formed at a rate of 20 in./min with a cushion pressure of 500 psi. This forming resulted in a flange radius of approximately 3/8 inches. The upper draw ring was then replaced with a coining ring and the flange radius was coined in the press to yield a 1/8-inch radius.

The flange was trimmed to 46 inches in diameter and the diaphragm was alkaline cleaned and stress relieved (Rockwell International Specification RAO 111-010). The flange radius was then reduced to 0.060 inches during a two-step procedure using a lathe and rolling tool with an intermediate alkaline cleaning and stress relieving. Finally, the diaphragm was alkaline cleaned and annealed (RAO 111-010) prior to chem-milling the thickness profile.

COMPOSITE WRAPPING

The propellant tank aluminum liner was wrapped with a Kevlar/epoxy material system by Defense Div., Brunswick Corp. (Lincoln, Neb.). Although Brunswick had wrapped several thousand pressure vessels of various shapes and sizes for a wide range of applications, the requirements imposed by the subject tank were unique enough to require the development of a new process. This process involved wrapping the tank at an elevated temperature - 130 to 140 F.

Wrapping the tank in a heated environment was considered necessary to avoid buckling the aluminum liner during the temperature cycles required for

curing. By wrapping the tank at a temperature close to the cure temperature, compressive loads on the liner due to the larger thermal expansion of the aluminum were minimized and increasing the liner thickness was precluded.

The procedures described in the following subsections were defined by practicing with a small (0.3 ft^3) spherical tank. The full-size tank was successfully wrapped without any significant problems requiring the procedures to be modified.

Tank Description

The propellant tank consists of a composite wrapped 5086-0 aluminum liner assembly with a wrapped aluminum mounting ring installed around the equator. The shape of the liner assembly outer surface is oblate, i.e., a contour-of-revolution about the minor axis. A section plane containing the minor (polar) axis yields a nearly elliptical liner contour. Compared to an ellipse, the actual shape bulges outward midway between the pole and the equator. This contour is based on an analysis that relates the meridional and tangential (hoop) curvatures and the local filament wind angle so that the resultant stress is directed parallel to the fiber.

The volume contained by the liner assembly is 10.66 ft^3 . The outer dimensions of the liner are 36.7 by 36.7 by 26.2 inches. The diameter of the wrap opening at the poles is 6.0 inches.

Helical Wrapping Procedures

The procedures followed in applying the helical wrap to the aluminum liner assembly are discussed in the following subsections. Preparation of the liner, the materials used, setup of the winder in a heated enclosure and winding parameters are addressed.

Tank Preparation. Tank preparation for helical winding consisted of degreasing, etching and preheating. The aluminum liner was degreased using trichloroethane (per Brunswick document BMS 13215) and etched with a sulfuric acid paste (LRF-037) containing sodium dichromate and Cab-O-Sil, to obtain a water-break-free surface. The tank was preheated to 150 F in an oven prior to installing it in the winder.

Material and Equipment Descriptions. The tank was installed in a window (MAW-III) that was located in a temporary enclosure made from wood and mylar. Heat lamps were positioned to maintain the temperature of the tank. The tensions of eight spools of four-end aerospace grade Kevlar (BMS 10195) were adjusted to yield a total tension of 13 pounds. The band of roving was adjusted to a width of 0.982 ± 0.030 inches and routed through a bath of resin (LRF 215) and a heated eye. The winder was programmed for numerical control of the helical winding pattern.

Helical Wrap Parameters. The tank was maintained between 130 and 140 F during winding as measured by an optical pyrometer every 10 minutes. Two layers of 115 circuits each plus one extra circuit were continuously wound to permit positioning of the cut end where it would be covered by the mounting ring. A mixture of resin and Cab-O-Sil was hand worked into the voids created when the roving bridged the regions extending 3 inches from the polar wrap openings.

Curing Procedures. After helical winding of the liner assembly, the tank was cured at elevated temperatures in two steps. The tank was then subjected to a second cure cycle after the aluminum mounting ring was installed and circular wrapped.

Preliminary Cure Procedures. The initial cure was conducted in the wind enclosure for 7 hours with the tank surface maintained between 118 and 125 F. Excess resin was wiped from the tank as required. The tank was then transferred to a heated oven when the surface became tack-free.

Final Cure Procedures. The final cure consisted of placing the tank in a preheated oven at 148 to 150 F for 6 hours. The temperature was then reduced to 100 F over a period of 1.6 hours and the tank was removed for installation of the mounting ring.

After the mounting ring was installed around the tank's equator, it was circular wrapped at ambient temperature to hold it in position. The complete tank assembly was then subjected to a second cure cycle.

PROPELLANT STORAGE ASSEMBLY

Fabrication of the 13 diaphragms tested in the plastic and metal workhorse, and flightweight propellant tanks demonstrated that they can be formed with a minimal scrap rate using standard draw-forming and sheet metal rolling techniques and tooling. Envelope dimensions are important to control since oversizing results in local surface wrinkles after the diaphragm and tank are assembled and the diaphragm is pressure sized. While these wrinkles do not affect expulsion performance, they will have a critical impact on fatigue life during pressurized vibration. A chem-mil thickness tolerance band of 0.005 inches can be consistently achieved and was demonstrated to have no measurable effect on expulsion performance.

The material properties associated with the diaphragm alloy, 1100-0 aluminum, will tolerate even severe folds without cracking during expulsion if they are not exposed to a vibration environment. This was demonstrated after a plastic tank expulsion test when the diaphragm was partially re-reversed. The diaphragm has significant design margin at the equator near the liner attachment point as evidenced by its rolling through 180 degrees without cracking. Even with 0.015-inch chem-mil undercuts in the flange radius, a ΔP of 162 psi did not cause failure.

Based on the limited amount of structural dynamic testing, the limiting design feature of the PSA is the fatigue life of the 1100-0 aluminum diaphragm. The critical environment is after pressurization when the diaphragm is partially reversed and therefore has folds and is not totally supported by the tank shell. Four factors prevented a definitive determination of whether the diaphragm is capable of meeting the specified vibration and shock requirements: testing was conducted in a thick-wall workhorse tank, the environments were applied as inputs instead of tank responses, the propellant simulant contained a noncondensable gas, and limited shaker capabilities prevented reaching required pressurized shock levels at high frequencies. The diaphragm tested in the workhorse tank failed during pressurized flight random vibration after unpressurized ground random and pressurized flight shock. Material evaluations confirmed the three cracks were due to fatigue. No abnormal material properties or defects were found.

The selected diaphragm chem-mill thickness profile and tank outlet liner rib configuration resulted in repeatably uniform and reliable expulsion performance. Four plastic workhorse tank tests yielded expulsion efficiencies of 98.1 to 98.2 percent at a diaphragm ΔP of 25 psi. The efficiency of two metal workhorse tank tests was 99.3 percent at 50 to 54 psi. The maximum CG displacement from the expulsion axis occurred between 67 and 75 percent reversal and was measured at 1.0 inches for two vertical expulsion plastic tank tests and calculated at 1.9 inches for two horizontal expulsion tests. Although it is not required to preclude diaphragm buckling, placement of a chem-milled step near the equator is beneficial to controlling CG. Propellant flow pulses, the rate of flow, the pressure level and warm gas pressurant did not have any effect on the diaphragm reversal mode.

Fabrication of the composite wrapped flightweight tank was relatively free of problems and demonstrated that a lightweight propellant tank shell meeting the subject design requirements is producible. Kevlar/epoxy wrapping of an aluminum liner assembly in a heated enclosure was accomplished and the process can be utilized for thin liners without the risk of buckling due to thermal expansion, when the composite is cured. Laser

holography was shown to be an extremely useful technique in locating unbonded regions as small as 0.25 inches between the composite and the tank liner.

An expulsion test of the flightweight tank was warm gas pressurant up to 1042 F resulted in a maximum composite outer surface temperature of 202 F and demonstrated thermal compatibility. The expulsion efficiency was consistent with the workhorse tank data. Characterization of the structural dynamic response and a burst pressure test provided additional confirmation of the adequacy of the tank shell in meeting design requirements.

PRESSURIZATION SUBSYSTEM

A very accurate electronically controlled regulator was fabricated. Stable operation was achieved through variable-gain scheduling using an electronic compensation circuit that permitted the mechanical regulator to be less precise. Development of a conventional mechanical regulator normally requires extensive development to achieve stable, accurate performance over a wide range of operating conditions. The electronically controlled regulator also allows the pressure to be controlled at a remote location, i.e., the delivered propellant pressure, while regulating the pressure flow.

Accurate propellant pressure regulation was accomplished as evidenced by overshoot during initial pressurization of the PSA of 2.1 psi, which dissipated in 0.1 seconds. This was followed by a maximum peak-to-peak variation of 1.0 psi, which dissipated during the early portion of the 142-second hold period. During pulsed propellant expulsion, the error was ± 0.4 psi, except during the last pulse when it increased to ± 1.4 psi.

A very compact catalyst bed (2.5 in.³) was fabricated capable of reacting Tridyne to yield a steady-state temperature rise in excess of 1200 F at a thermal efficiency greater than 99 percent. This efficiency is uncorrected for heat loss. The pressurant gas bulk temperature in the flightweight propellant tank (150 F) was 89 F higher than initial conditions at the end of the pulsed duty cycle. An even higher temperature would be achieved for a continuous expulsion.

Higher metal workhorse tank wall temperatures occurred during the pulsed MDC than the continuous expulsion duty cycle, in spite of a lower inlet gas temperature, because of the longer time for heat transfer from the pressurant gas. The MDC has very little effect on the increase in propellant temperature. The maximum increase was 14 F. A large tank wall temperature gradient existed about the polar (expulsion) axis because of the tank's orientation. This was caused by the skewed position of the diaphragm and propellant, which was at low temperature, and the gravity effect on the pressurant density, which is a function of temperature.

CONCLUSIONS

A lightweight composite-wrapped propellant tank is both producible and capable of meeting the design requirements. The PSA met all expulsion performance objectives and compatibility with warm-gas pressurant was demonstrated. The only significant potential problem identified was the fatigue life of the diaphragm expulsion device during pressurized vibration.

The advantages associated with the electronically controlled pressure regulator concept, an integration of electronic control circuitry with a conventional mechanical regulator, were demonstrated. Very accurate stable operation was achieved with the first unit after only a week of development testing without modifying the mechanical regulator. Also, a highly efficient compact catalytic reactor to generate warm-gas pressurant from a mixture of helium, oxygen and hydrogen was tested. These components were assembled into a pressurization subsystem and the performance advantages of warm-gas pressurant were demonstrated while expelling the propellant tank.

RECOMMENDATIONS

The following recommendations are made with respect to fabrication precautions, design modifications, vibration test methods, additional diaphragm vibration development tests, and Kevlar/epoxy storage tests. Inspection of the expulsion diaphragm dimensions during fabrication are critical in order to prevent folds from developing after the diaphragm is installed in the propellant tank, when it is pressure sized. Diaphragm handling fixtures are also necessary during manufacturing processing to preclude denting and buckling of the surface. Buckling of the flat section of the diaphragm can result in folds as discussed above.

The number of chem-milled steps in the diaphragm thickness profile is dependent on the contour and size of the tank and CG requirements. Under certain conditions they could probably be eliminated without affecting expulsion performance. The diaphragm ΔP could be lessened by reducing the thickness near the equator. For the subject design, this would require elimination of at least one chem-mill step or reducing the thickness of all regions. The protruding ribs in the outlet line could be eliminated for an all-metal tank by moving the outlet fitting toward the equator.

Heavy workhorse tanks should not be used to demonstrate the adequacy of positive expulsion devices during vibration and shock environments because their structural response characteristics are different from lightweight tanks and this affects the expulsion device. Workhorse tanks should only be used to compare different design configurations. Also, propellant simulant used during structural dynamic tests should be processed as required to match the noncondensable gas content since this parameter can have a significant influence on response characteristics.

Additional diaphragm vibration and shock tests are required for the subject application to determine compatibility with the requirements. The fatigue limits of 1100-0 and other aluminum alloys need to be determined for specific contours, i.e., radius of curvature and fold pattern. Nonmetallic backings may also be required for damping and propellant containment insurance.

A more uniform propellant tank temperature profile resulting from warm-gas pressurization would be beneficial to pressurization efficiency. Improvement could be achieved by nonuniform injection into the propellant tank cavity.

Placement of the remote sensing pressure transducer used in the electronically controlled regulator assembly is dependent on the magnitude of propellant line pressure surges. Pressure oscillations must be avoided by judicious placement of the transducer or use of damping devices.

The final recommendation is that long-term storage tests be conducted for Kevlar/epoxy composite wrapped storage vessels. The degrading effect on material properties should be determined.

APPENDIX A

TECHNICAL REQUIREMENTS

The program requirements include delivery of 1400 pounds of N_2O_4 and MMH at a mixture ratio of 1.623, which corresponds to equal volumetric flowrates at 120 F. Figure A-1 presents the envelope constraints. A further stipulation is that the tank centerlines be coplanar with the stage longitudinal axis.

Storage life is a minimum of 15 years with a temperature range of 20 to 120 F and a relative humidity range of 0 to 100%, including condensation at the 88 F dew point. The external pressure varies between 15 psia on the ground to 3.5×10^{-12} psia during flight.

Table A-1 presents the limit nonoperating shock environment.

TABLE A-1. NON-OPERATING SHOCK

Number of Shocks	Amplitude, g	
	Y/Z-Axes	X-Axis
4400	1.0	0.50
520	1.5	0.75
50	2.0	1.0
25	2.5	1.25
5	3.0	1.50

Each of these terminal peak sawtooth shape pulses have a duration of 0.25 second. The stage separation shock spectra with the system activated but not operating is shown in Fig. A-2. The ground random vibration power spectral density (PSD) for 3000 hours duration at 1.3 g RMS is presented in Fig. A-3. Stage II/III and Stage IV flight vibration PSD's are shown in Fig. A-4. Since the feed system is activated during Stage II flight, these PSD's apply to the operating condition. The nonoperating acoustic environment is presented in Fig. A-5.

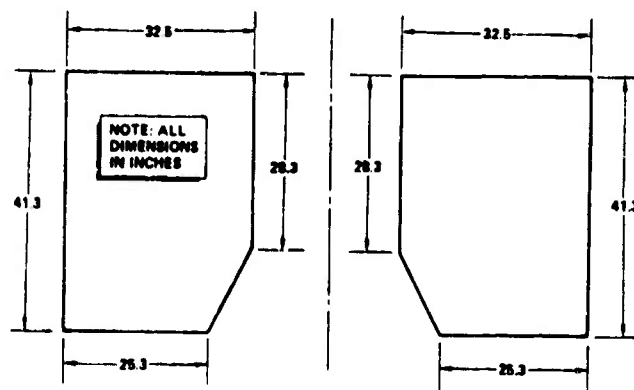


Figure A-1. Feed System Envelope

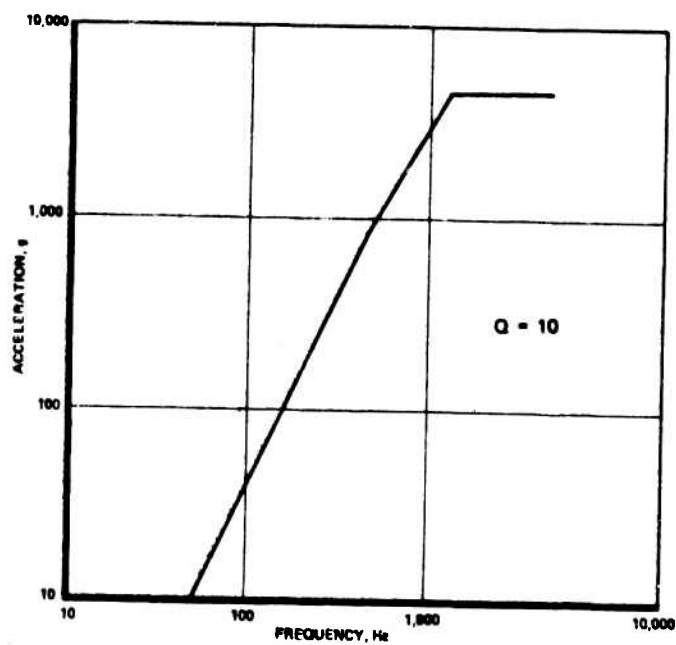


Figure A-2. Separation Shock Spectra

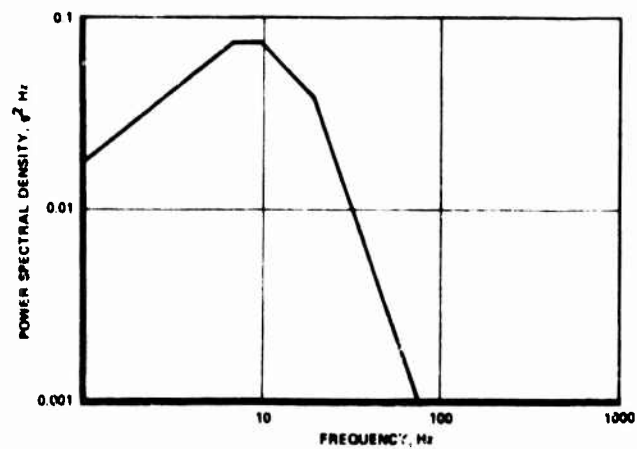


Figure A-3. Ground Random Vibration

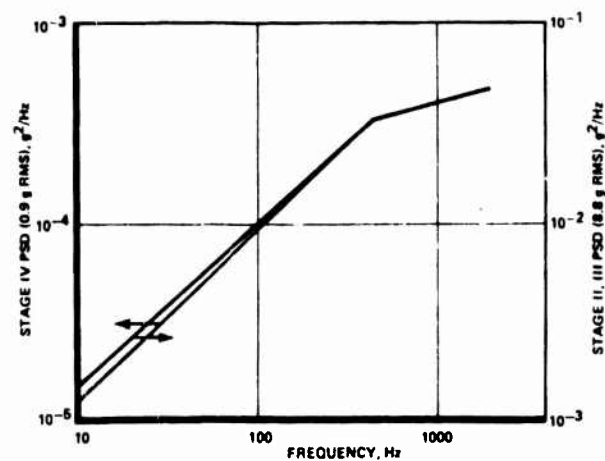


Figure A-4. Flight Random Vibration

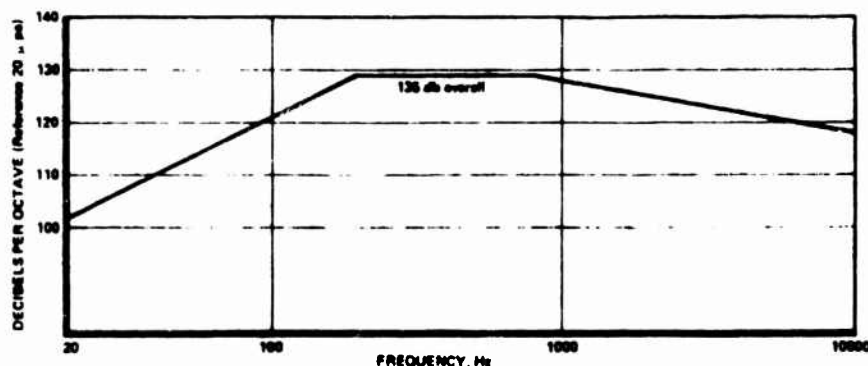


Figure A-5. Acoustic Requirements

A shock and vibration intensification factor of 1.5 is applied to the limit levels presented in Table A-1 and Fig. A-2 to arrive at test (ultimate) levels. This arbitrary factor accounts for the limited sample size, hardware tolerances, environmental tolerances, and uncertainties. For random vibration (Fig. A-3 and A-4), the factor is 2.25 applied to the PSD values. A +4 db per octave factor is applied over the entire spectrum in Fig. A-5. The maximum axial acceleration is 15 g axial. The feed system is subjected to a classified nuclear environment.

The feed system operating temperature range is 40 to 100 F and the two propellant demand duty cycles are presented in Table A-2. The maximum volumetric flowrate is 275 in.³/sec. The allowable delivered propellant pressure is 300 to 400 psi \pm 1%. The propellant storage assemblies must be designed for a pressurant inlet temperature of at least 1025 F. The initial pressurization sequence may take from 10 to 40 seconds.

The minimum proof pressure safety factor is 1.1 applied to the maximum operating pressure at 100 F. The corresponding minimum burst safety factor is 1.25. Finally, the 3 σ standard deviation of the center of gravity from the nominal profile shall not exceed 3 inches during expulsion.

TABLE A-2. PROPELLANT DEMAND DUTY CYCLES

<u>DUTY CYCLE I</u>					
<u>Axial Engine</u>			<u>Attitude Control Engine</u>		
On Time, seconds	Off Time, seconds	Demand, In. ³ /sec	On Time, seconds	Off Time, seconds	Demand, In. ³ /sec
122.5	0	205	122.5	0	70
<u>DUTY CYCLE II</u>					
0.4	—	205	0.4	—	70
—	60	0	1.5	0.5	20 (1)
<u>Run The Following 10 Times</u>					
3.0	—	205	0	3.0	0
	10.0	0	0.3	1.7	30 (2)
0.4	—	205	0	0.4	0
—	15.0	0	0.3	1.7	30 (2)
2.0	—	205	0	2.0	0
—	6.0	0	0.3	1.7	30 (2)
8.0	—	205	0	8.0	0
—	15	0	0.3	1.7	30 (2)
<u>Run The Following Once</u>					
13.0	—	205	1.0	1.0	50 (3)
—	1.0	0			
<u>Note</u>	<u>Average Demand</u>				
(1)	15.0				
(2)	4.5				
(3)	25.0				

GLOSSARY OF TERMS AND ABBREVIATIONS

a	Propellant tank liner inside surface major axis
ACE	Attitude control engine
ACS	Attitude control system
AETL	Approved Engineering Test Labs
AFRPL	Air Force Rocket Propulsion Laboratory
AHF	Aircraft Hydro-Forming
APF	All-Plastic Fabricators
b	Propellant tank liner inside surface minor axis
CG	Center of gravity
cps	Cycles per second
D	Diameter
DEAP	Differential Equation Analyzer Program
EB	Electron beam
EM	Electromagnetic
EMP	Electromagnetic pulse
EPM	External protection material
Exp	Expulsion
FEP	Fluorinated ethylene propylene
GN ₂	Gaseous nitrogen
Hz	Hertz
IC	Integrated circuit
IFSS	Instrumentation and flight safety system
L	Length
L/D	Length-to-diameter ratio
LM	Lunar Module
MDC	Mission duty cycle
MGS	Missile guidance set
MMH	Monomethyl hydrazine
MX	Missile X
NDI	Non-destructive inspection
NH&S	Nuclear hardness and survivability
NTO	Nitrogen tetroxide

OMS	Orbital maneuvering system
P	Pressure
PBPS	Post-boost propulsion system
PSA	Propellant storage assembly
PSD	Power spectral density
PSRE	Propulsion system rocket engine
Q	Quality factor, related to structural damping
RCS	Reaction control system
rms	Root mean square
sccs	Standard cubic centimeters per second
scim	Standard cubic inches per minute
SGEMP	System generated electromagnetic pulse
SOW	Statement of Work
T	Temperature
TAP	Thermal Analyzer Program
T/C	Thermocouple
TIG	Tungsten inert gas
Tridyne	Gaseous mixture of helium, oxygen, and hydrogen
Δ	Difference
η	Efficiency